THERMO-ELECTRICAL AND MECHANICAL STUDIES ON POLYMER – ORGANICALLY MODIFIED MONTMORILLONITE COMPOSITES

By

NORHANA ABDUL HALIM

Physics Department
Faculty of Science, University Malaya

A Thesis Submitted
In Fulfillment Of The Requirements For
The Degree Of Doctor Philosophy

FACULTY OF SCIENCE
UNIVERSITY OF MALAYA
KUALA LUMPUR
2010

Acknowledgment

بسم الله الرحمن الرحيم

In the Name of Allah, the Beneficent, the Merciful

All Thanks are due only to **Almighty Allah,** the most gracious merciful. Who is giving me this opportunity, the strengths, the patience and enabled me to complete this thesis after all the difficulties and challenges. My special praise is to the **Holy Prophet Muhammad** (Peace Be upon Him) who is forever a torch of guidance and knowledge to humanity.

The research work presented in this thesis has been done under the supervision of Assoc. Prof. Dr. Abu Bakar Ahmad and Assoc. Prof. Dr. Zainol Abidin Ibrahim. I owe my sincere gratitude to them for giving me a chance to do this research at Physics Department, University of Malaya. It has been excellent opportunity for me and I have experienced much. Their guidance and supports enabled me to complete this thesis. All through the years that finally resulted in the publication of the present study, I have received abundant help from many parties and persons. I would like to express my appreciation first of all to the Ministry of Science, Technology and Innovation, Malaysia for having provided me with the National Science Fellowship to attend Advanced Masters Program, and subsequently with a PhD grant to explore the field of advanced material science. I also wish to thank Dr. Abu Amu and the staffs at Rubber Research Institute of Malaysia, RRIM for kindly providing me the materials as well as valuable information about Malaysian natural rubbers.

Special thank to the Faculty of Science - University Malaya, its leadership and the staff for providing me with an academic base, which has enabled me to take up this study. I am particularly grateful to Professor Gan Seng Neon from Chemistry Department, Professor Yeap Ea Beng (Geology Department) and Professor Wan Haliza Abdul Majid (Physics Department) for their worthy contribution. I am also indebted to our former technician at the Material Laboratory, Mr. Yusof Zaki for his great assistance in this research work.

All through the hurdles, I've been blessed with such wonderful people as Hidayanti Hamdan and Mohd Imran Zulkifli who taught me the true meaning of a friendship. Special thanks, tributes and appreciations to them and all professional, colleague, friends, family and those their names do not appear here who have contributed much to the successful completion of this study. May Allah bless and grant them all with His Mercy, Peace and Goodness.

I am truly grateful to my dearest parents Haji Abdul Halim and Hajjah Hamisah for their everlasting inspiration and giving me all the opportunities in the world to explore my potentials and pursue my dreams. I owe my deepest gratitude to my beloved husband Hanafi and my dearest children Hanis and Harith, for their infinite patience and understanding on the importance of this work. Their sincere flow of love has accompanied me all the way in my long struggle and has pulled me through many hurdles. Hence, this thesis is dedicated to them.

UNIVERSITY OF MALAYA

ORIGINAL LITERARY WORK DECLARATION

Name of Candidate : **Norhana binti Abdul Halim**

I.C/ No : **740117-11-5252**

Matric No : **SHAQ01300**

Name of Degree : **Doctor of Philosophy**

Title of Thesis : **Thermo-Electrical and Mechanical Studies on Polymer – Organically Modified Montmorillonite Composites**

Field of Study : **Advanced Materials**

I do solemnly and sincerely declare that:

1) I am the sole author/writer of this Work;
2) This Work is original;
3) Any use of any work in which copyright exists was done by way of fair dealing and for permitted purposes and any excerpt or extract from, or reference to or reproduction of
4) any copyright work has been disclosed expressly and sufficiently and the title of the
5) Work and its authorship have been acknowledged in this Work;
6) I do not have any actual knowledge nor do I ought reasonably to know that the making of this work constitutes an infringement of any copyright work;
7) I hereby assign all and every rights in the copyright to this Work to the University of
8) Malaya ("UM"), who henceforth shall be owner of the copyright in this Work and that any reproduction or use in any form or by any means whatsoever is prohibited without the written consent of UM having been first had and obtained;
9) I am fully aware that if in the course of making this Work I have infringed any copyright whether intentionally or otherwise, I may be subject to legal action or any other action as may be determined by UM.

Candidate's Signature — Date: 12/05/10

Subscribed and solemnly declared before,

Witness's Signature — Date: 12/05/10

Profesor
Jabatan Fizik, Fakulti Sains
UNIVERSITI MALAYA

Name: PROF. DR. ZAINOL ABIDIN IBRAHIM
Designation: LECTURER

Abstract

The field of polymer-nanoclay composite has attracted a lot of attention in materials studies due to the dramatic improvement on polymers characteristics. For example mechanical and thermal properties, chemical resistance as well as the reduced gas permeability. However, structural changes and the mechanisms that may contribute to these improvements are not fully understood. In this work, the study on polymer nanoclay composite concentrates on the effects of *OMON* inclusion within different polymer matrix systems. The matrixes are a series of natural rubbers (Standard Malaysia Rubber – Latex grade (*SMRL*); Deproteinized Natural Rubber (*DPNR*) and Epoxidized Natural Rubber (*ENR-50*)), plasticized Polyvinyl chloride (*pPVC*) and Polyethylene (*PE*). *OMON* is a renewed Montmorillonite (*Mon*) clay mineral, where chemical modifications carried out had changed the organophobic property of this mineral into organophylic. XRD analyses demonstrate the intercalation of polymeric chains, showing the increase in *OMON* basal spacing d_{001} from 1.840 nm to 3.864 nm. From the FTIR spectra of *polymer-OMON* composites, matrix-*OMON* silicates interaction is shown with the appearance of (*Si-O-R*) band and the changes in *SiH* (ν*SiH* and *∂SiH*) vibrations.

Investigation on the improved *matrix-OMON* interactions within *polymer-OMON* composites concentrates on their thermo-electrical and mechanical responses. TSC measurement is chosen to carry out the thermo-electrical studies, which involves instrumentation of TSC system. The high sensitivity of TSC technique is capable to detect various dipoles and space charges relaxations, as shown with the emergence of β, α and ρ peaks. Observations and analyses on α and ρ *OMON* peaks reveal the effects of matrix-alkyl and matrix-silicate interactions on methylene groups (CH_2) and alkyl chains $(CH_2)_n$ within *OMON* gallery in the composites. Decomposition on TSC peaks confirm the involvement of various distributed relaxation processes. It also reveals the existence of molecular-ion deep traps with high activation energy *E* (> 4eV). Analyses on pre-exponential factor τ_n from *N-fitting* method distinguish a range of dipole relaxations. It gives characteristic relaxation time τ_n that suggest the occurances of dipole (10^{-10} s to 10^{-13} s), dipole-segmental (10^{-14} s to 10^{-17} s) and segmental (10^{-18} s to 10^{-28} s) relaxation modes. Several τ_n (10^{+1} s to 10^{-4} s) from experimental TSC peaks also confirm the cooperative relaxation around the glass transition temperature T_g.

Analyses and observations on some basic mechanical properties generated from tensile test demonstrate structural effects on the entire composite system. Various matrix-alkyl chains and matrix-silicate interactions induce interfacial adhesion, interparticle bridging flocculated and stacking layer structure, which influence the elasticity modulus Young *Y*, Tensile strength σ_{max} and Maximum elongation ε_{max}. Polar matrix-silicate interactions within *CENR-50* (30%) composite had improved the interfacial adhesion, which contributed to the significant increase in modulus *Y* (15420 %) compares to that of pristine *ENR-50*. Similarly, *CpPVC* (30%) that is a *pPVC* composite with the improved *OMON* stacked structure (*N* ~21 layers) also demonstrates the increased modulus *Y* (2323 %). Polymers intercalation into *OMON* gallery can promote certain chemical reactions, which affect the inner structure of a composite. For example, chains crosslinking within *OMON* gallery that creates the interparticle bridging flocculated structure also promotes more slippage on the matrix chain during stress loading. As a result, it improves the Maximum elongation ε_{max} with the increase of *OMON* content as shown by the *CSMRL* (30%) (ε_{max} ~70 %) and *CDPNR* (30%) (ε_{max} ~125 %) composites.

Abstrak

Bidang komposit polimer-nanoclay menarik banyak perhatian dalam pengkajian bahan disebabkan oleh peningkatan mendadak ke atas ciri-ciri polimer. Sebagai contoh, sifat-sifat mekanikal dan terma, kerintangan kepada bahan kimia dan juga pengurangan ketelusan gas. Walaubagaimana pun perubahan-perubahan struktur dan mekanisma yang mungkin menyumbang kepada peningkatan tersebut belum dapat difahami sepenuhnya. Dalam projek ini, kajian ke atas komposit polimer ditumpukan kepada kesan penambahan *OMON* keatas pelbagai sistem matriks polimer. Bahan matriks tersebut terdiri daripada satu siri getah asli (Getah Malaysia Standard – gred Lateks (*SMRL*); Getah Asli Nyahprotein (*DPNR*) dan Getah Asli Terepoksida (*ENR-50*)), Polivinil klorida terplastik (*pPVC*) dan Polietilena (*PE*). *OMON* adalah mineral lempung (clay) Montmorillonite (*Mon*) yang diperharui, dimana ubahsuai kimia yang dijalankan telah mengubah sifat organofobik mineral ini kepada organofilik. Analisa keputusan XRD menunjukkan penyisipan rantai polimer dengan peningkatan ruang basal d_{001} *OMON* daripada 1.840 nm kepada 3.864 nm. Dari spektra FTIR bagi komposit-komposit *polimer-OMON*, interaksi matrik-silikat *OMON* ditunjukkan dengan kemunculan jalur penyerapan (*Si-O-R*) dan perubahan keatas jalur-jalur bagi *SiH* (ν*SiH and ∂SiH*).

Kajian peningkatan interaksi *matrik-OMON* dalam komposit-komposit *polimer-OMON* ditumpukan kepada tindakbalas termo-elektrikal dan mekanikal komposit tersebut. Kaedah Pengukuran TSC telah dipilih untuk kajian termo-elektrikal yang melibatkan instrumentasi sebuah sistem TSC. Kaedah TSC yang sensitif ini mampu untuk mengesan pelbagai santaian dwikutub dan cas ruang seperti yang ditunjukkan dengan kemunculan puncak-puncak β, α dan ρ. Pemerhatian dan analisa ke atas puncak-puncak α dan ρ *OMON* menunjukkan kesan-kesan interaksi matrik-alkil dan matrik-silikat ke atas kumpulan methilena (CH_2) dan rantai-rantai alkil $(CH_2)_n$ di dalam ruang galeri *OMON* bagi komposit-komposit tersebut. Kaedah Pemisahan (decomposition) ke atas puncak-puncak TSC membuktikan penglibatan pelbagai proses santaian. Ia juga menunjukkan kehadiran "molecular-ion deep trap" yang bertenaga pengaktifan *E* yang tinggi (> 4eV). Analisa ke atas faktor pre-exponential τ_n dari kaedah *N-fitting* membezakan pelbagai santaian dwikutub. Ia memberikan masa santaian ciri τ_n yang mencadangkan kewujudan mod-mod santaian dwikutub (10^{-10} s ke 10^{-13} s), dwikutub-segmental (10^{-14} s ke 10^{-17} s) dan segmental (10^{-18} s ke

10^{-28} s). Beberapa τ_n (10^{+1} s ke 10^{-4} s) untuk puncak-puncak eksperimen TSC juga mengesahkan santaian kooperatif yang berlaku sekitar suhu peralihan kekacaan, T_g.

Pemerhatian dan analisa ke atas beberapa sifat mekanikal asas yang diperolehi dari ujian tensil menunjukkan kesan-kesan struktur ke atas sistem komposit secara menyeluruh. Pelbagai interaksi rantai-rantai matrik-alkil dan interaksi matrik-silikat merangsang pembentukan perlekatan antaramuka, struktur-struktur "interparticle bridging flocculated" dan "stacking layer" yang mempengaruhi modulus elastik Young *Y*, Tegasan maksima σ_{max} dan Regangan maksima ε_{max}. Interaksi matrik berpolar dalam komposit *CENR-50* (30%) umpamanya, telah berjaya memperbaiki perlekatan antaramuka tersebut dan menyumbang kepada peningkatan mendadak ke atas modulus *Y* berbanding dalam kes *ENR50* tulen. Begitu juga dalam kes *CpPVC* (30%) iaitu komposit *pPVC* yang mempunyai *OMON* dengan penambahan lapisan dalam struktur berlapisnya (*N* ~21 lapis), juga telah menunjukkan peningkatan dalam modulus *Y* (2323 %). Penyisipan polimer ke dalam galeri *OMON* boleh menggalakkan tindakbalas kimia tertentu yang mempengaruhi struktur dalaman sesuatu komposit. Sebagai contoh, sambung-silang rantai dalam galeri *OMON* yang mewujudkan struktur "interparticle bridging flocculated" juga menggalakkan lebih gelongsoran rantai polimer ketika dikenakan tegasan. Hasilnya, ia meningkatkan Regangan maksima ε_{max} pada komposit dengan penambahan kandungan *OMON* seperti yang ditunjukkan oleh komposit-komposit *CSMRL* (30%) (ε_{max} ~70 %) dan *CDPNR* (30%)(ε_{max} ~125 %).

List of Content Page

Appendices

List of Tables

List of Figures

Chapter 1

Introduction

Chapter 1: INTRODUCTION

1.1 Background

Composite by definition is a multicomponent material comprises of several different phase domains, where at least one of the phase domains is a continuous phase [1.1] for example polymers. Polymer composites typically have been made of synthetics or natural organic fillers in order to improve the polymer properties, or else simply to reduce production cost. Among the frequently used conventional fillers are in the form of fiber (e.g. glass fiber), particulate particle (e.g. carbon black) and flake particle (e.g. mica) [1.2, 1.3 and 1.4]. The presence of these filler within conventional composites however creates disadvantages to the resulting materials, for instance the increase in weight, opacity and brittleness. Polymer nanocomposites on the other hand are a new class of composites with particle dispersion in nanometer range [1.5, 1.6, 1.7 and 1.8]. These composites offer extraordinary large contact area for matrix-filler interactions, which may give better polymer properties and also broaden their utilities in many applications.

The field of polymer nanocomposite attracts a large number of research groups to explore the potential offered by this polymer matrix composite in many areas. It is well established that dramatic improvements in physical properties can be achieved by adding just a small fraction of clay minerals into a polymer matrix. Such as tensile strength σ_{max}, elasticity modulus *Y*, heat distortion temperature (HDT) and gas permeability resistance [1.9, 1.10, 1.11, 1.12 and 1.13]. Martinez-Gomez and his group [1.9] have shown that the elasticity modulus *Y* of neat poly(triethylnene glycol p, p'-bibenzoat) PBET can be increased up to 200 % with modified clay addition. In fact, thermal properties and solvent resistance of polymers can also be improved as revealed by Lin and co-authors [1.11] in their studies on composite poly(amide-imide) with organoclay. On the other hand, studies by Adame and Beall [1.12] on organically modified clay composites with poly(amide) demonstrated the

decrease in gas permeability. The effect that is caused by structural modifications however benefits the field of air-insulated packaging, especially for food and medical supplies.

1.2 Research Objective

Despite all the improvements and recent progresses of polymer nanocomposites, many fundamental questions have not been answered. For example, the mechanisms which make the changes in polymer crystalline structure which are induced by clay affected the overall composite properties; the right organoclay chemistry to reach certain degree of polymer matrix-filler reaction or modification for a given polymer-clay system and also the role of processing parameters in influencing nanocomposite properties [1.14]. Further studies that address on such issues have stimulated many researchers to diversify their research area. In fact, these issues create momentum for this present work on polymer nanocomposites.

The primary objective in this work is to characterize *polymer-OMON* composites thermo-electrically and mechanically. Preliminary works involved the chemical modifications on Montmorillonite (*Mon*) property from organophobic into organophylic. This renewed clay mineral is recognized as organically modified *Mon*, which is abbreviated as *OMON*. The fabrications of *polymer-OMON* composites in this work utilized series of natural rubbers: Standard Malaysia Rubber – Latex grade (*SMRL*), Deproteinized Natural Rubber (*DPNR*) and Epoxidized Natural Rubber (*ENR-50*). It also involved plasticized Polyvinyl Chloride (*pPVC*) and Polyethylene (*PE*) polymers. Thermo-electrical and mechanical studies on the polymers composites with *OMON* and *Mon* clay minerals were carried out by means of TSC measurement and tensile test, respectively.

1.2.1 Thermo-electrical Study – TSC Measurement

Thermally Stimulated Current (TSC) is a thermal analysis technique that is used to resolve molecular ability in dielectric materials. The basic principle behind TSC technique is that

electrical field F_p can induce charges carrier mobility in non-conductive materials, such as dipoles, ions and space charges. This principle is used by applying a DC electrical field F_p to shift the potential of charge carrier to a higher energy state. These excited charge carrier inside electrets are then frozen in the polarize state by reducing its temperature *T*, while maintaining the applied field. This electrical field is removed at low temperature, T_o where the carrier mobility is minimal. Reheating the electret will induce depolarization processes, where sufficient thermal energy supply promote the motions of polarized charge carriers [1.15, 1.16 and 1.17]. These relaxation processes finally can be detected on the current trends of image charges with the rise in temperature *T*. Analyses on the current (*I*) versus temperature (*T*) plot from the TSC measurement reveal a lot of information regarding the relaxation behaviors of a material. For example, activation energy *E* and characteristic relaxation time, which is also known as pre-exponential, factor τ_o.

1.2.2 Mechanical Study – Tensile Test

Tensile test that is also known as tension test is one of the fundamental technique, which is commonly used in mechanical study. This test measures the elongations of tested specimen due to the applied external forces [1.18 and 1.19]. Therefore, it is a destructive test in the sense that tested specimen is finally broken or fractured into pieces. From the applied load against extension data, a stress-strain diagram can be plotted for tensile test. Analyses on this stress-strain diagram reveal many mechanical properties that describe the mechanical responses in a material. Such as elasticity modulus *Y*, tensile strength σ_{max} and maximum elongation ε_{max}. From the stress-strain diagram, the energy density *U* can also be estimated that describes the toughness of a material.

It is well established that the high sensitivity of the TSC technique make it a powerful tool for dielectric spectroscopy [1.20, 1.21 and 1.22]. This technique has an advantage to detect

various types of relaxations caused by of structural effects even at molecular level. For that reason, TSC technique is useful to study the effect caused by structural modification on *OMON* internal structures. Mechanical response is closely related to the inner structure of materials. It means that any changes to such structure can alter their mechanical behaviors. Investigation on basic mechanical properties from tensile test can highlight the effects due to matrix-*OMON* interaction on the whole system of *polymer-OMON* composites.

1.3 Nature of Polymers and Montmorillonite (*Mon*)

In order to identify the changes in mechanical behavior and to appreciate the improvement in composite properties, it is a necessary to priory understand the basic nature of polymers matrix. Similarly, the knowledge about *Mon* is very important before any modification can be performed on this material. The nature of *Mon* and *OMON* clay must be well recognized even though they may take just a small fraction in composite composition. This would help to understand their influence on matrix-filler interactions in composite.

1.3.1 Polymers

Polymer in general is a long chain molecule that is composed of repeating structural units, which is typically connected by covalent chemical bonds. Polymeric materials are found in nature such as cellulous, protein and isoprene polymer. Synthetic polymers on the other hand are made of monomers obtained mainly from petrochemical and alternative resources such as coal, sugar, wood, alcohol and furfural [1.23].

1.3.1.1 Polymer Classification

The large number of natural and synthetic polymers can be divided into two major groups. The polymers are either thermoplastic or thermoset polymer which depend on their thermal processing behaviors [1.23, 1.24 and 1.25].

1.3.1.1.A Thermoplastics

Thermoplastics polymers soften upon heating and could then be made to flow when stress is applied. These polymers would reversibly regain their solid or rubbery nature when they are cooled again, such as polyvinyl chloride (*PVC*), polymethyl methacrylate (*PMMA*), polyethylene (*PE*) and polypropylene (*PP*). Waste thermoplastics can be recovered and refabricated by application of heat and pressure.

1.3.1.1.B Thermoset

Thermosets polymers become soft and could also be made to flow as thermoplastics during their first heating. This heating process actually caused these polymers to undergo a curing reaction that makes them permanently hard. Subsequent heating will not soften thermosets polymers, in fact further heating finally lead only to degradation. Epoxies, vulcanized rubbers, phenolic and polyester resin are among the common thermosets polymers in many applications.

1.3.1.1.C Elastomer

An elastomer could be both thermoplastics or thermosets polymer, which can be stretched and then return to its original shape without permanent deformation. It is also defined as a rubber-like material with limited extensibility and incomplete retraction. On the other hand rubbers are known as polymers that can be stretched at least twice the original length and will retract rapidly upon stress removal. Among the common elastomer in applications are polybutadiene, polyisoprene and nitrile rubber.

1.3.1.2 Polymer Characteristics

The physical characteristic of polymers depends on their molecular weight (MW), shape and structure [1.23, 1.24, 1.25 and 1.26].

A. **Molecular weight -** Polymers with very long chains will show an extremely large molecular weight

B. **Molecular shape -** A great number of molecular chains within polymers may individually bend, coil and kink that leading to extensive inter-twining and the entanglement of adjacent chain molecules. These random coils and molecular entanglements contribute for several important characteristics of polymers.

C. **Molecular structure**

1. *Linear Polymers*: Linear polymers as illustrated in Figure 1.1(a) contain chains which their mer units are joined together end to end in single chain. These long chains are flexible and there may be extensive van der Waals bonding between these chains. Some of the common polymers that form with linear structures are polyethylene (*PE*)

2. *Branched Polymers*: Side chains on branched polymer backbone as shown in Figure 1.1(b) can reduce chains packing efficiency, which decrease the polymer density

3. *Network Polymers*: A polymer that is highly crosslinked may be classified as a network polymer. Schematic diagram in Figure 1.1(c) gives the illustration of such polymers. Strong covalent bonding involve the crosslinking make these polymers have distinctive mechanical and thermal properties

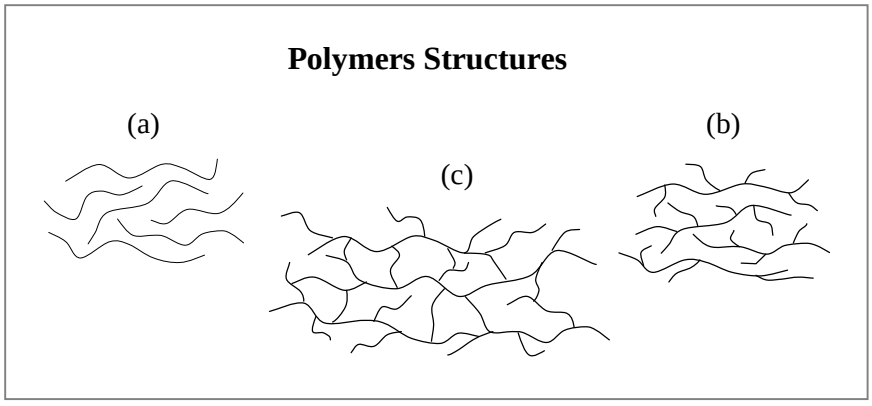

Figure 1.1: The schematic diagram of polymers chains show (a) the structure of linear polymers, (b) branched polymers.

1.3.1.3 Polymer Morphology

The structural arrangement of polymeric chains can cause significant effects on the bulk properties of polymers. Chains arrangements classify polymers into two groups, which are known as amorphous and semi-crystalline polymers.

a) Amorphous Polymers

On the molecular level, chains arrangements inside amorphous polymers are totally lack of positional order. Each molecular chain may bend, coil and kink in different ways that give a random structure to the amorphous polymers. Molecular motions in such structure can be categorize into four groups as follow [1.24].

i. Translational motion of entire molecules that permits flow

ii. Cooperative wriggling and jumping of segment molecules that involves about 40 to 50 carbon atom on polymeric backbone. It allows chain coiling and uncoiling that lead to elasticity

iii. The movement of a few atoms along the main chain (around five or six) or of side groups on the polymer backbone [1.27]

iv. The vibration of atoms about equilibrium positions that is similar to the vibration in crystal lattices, except that the atomic centers in amorphous polymers are not in a regular arrangement.

The motions described above are arranged in order of decreasing activation energy. The glassy state of amorphous polymers is when only motion **iii** and **iv** take place, while motion **i** and **ii** are considered frozen out. However, sufficient supplies of thermal energy then initiate motion **ii**, in which phase transition occurs at a glass transition temperature, T_g. Above the T_g, polymeric chains are in rubbery state that make amorphous polymers soft, flexible and rubbery, while below the T_g, these polymers are hard and rigid. Therefore, this glass transition temperature T_g affect the mechanical behaviors of polymers at particular temperature [1.23 and 1.24].

b) Semi-crystalline Polymers

This type of polymers contains both amorphous and crystalline structures in their system. Crystallite structure is formed when polymeric chains are regularly aligned and packed in ordered structures. The degree of crystallinity within polymers varies from 0 % for amorphous glasses to more than 90 % for highly crystalline polymers. Semi-crystalline polymers have true melting temperatures, T_m at which the ordered structures break up and become disordered. Fully amorphous polymers do not exhibit this T_m, but all polymers exhibit the glass transition temperature T_g that is lower than the melting temperatures T_m [1.28]. Above this temperature, polymers generally are in liquids form.

A series of natural rubbers used in this work will be useful to see various effects caused by polymers properties. For example, protein molecule and polar epoxide group within *DPNR* and *ENR-50* rubbers respectively. The works by Gan [1.29] on ENR rubbers have shown that the presence of such polar groups can change their glass transition temperature T_g, where it depends on the percentage of epoxide groups inside the modified rubber. The works also demonstrated that the T_g of *ENR-10*, *ENR-25* and *ENR-50* rubbers are around – 60 °C, – 45 °C and – 25 °C in that order. The effects of networks within natural rubbers can be studied by comparing them with another amorphous *pPVC* polymer. Crystallinity in *PE* polymer on the other hand offers good comparison for these amorphous polymers.

1.3.2 Montmorillonite, *Mon*

The term clay as described by Guggenheim and Martin [1.30 and 1.31] refers to a naturally occurring material composed primarily of fine grained minerals, which is generally plastic at appropriate water content and harden after drying and burning. Clay deposits are mostly composed of clay mineral, which is identified as minerals and phyllosilicate minerals that impart plasticity to clay and harden upon drying and burning. The majority of clay mineral however belongs to the class of layer silicates or phyllosilicates. Montmorillonite is a clay mineral in smectite group, which is one type of the phyllosilicates minerals [1.32].

1.3.2.1 The Common Structure of Phyllosilicates

In general, phyllosilicates is considered to be formed by superposed atomic planes that are parallel to d_{001} face [1.31]. These basic units of clay minerals, which are known as layers comprise of silica and alumina sheets. They are joined together in varying proportions and stacked on top of each other in a particular way. Silica sheet has two planes of oxygen and hydroxyl ions as illustrated in Figure 1.2, which are linked together to form Si(O, OH) tetrahedra. Likewise, alumina sheet has an upper and lower plane, which both consists of hydroxyl ions. In the middle of these planes, there is Al^{3+} ions plane that octahedrally coordinated to the hydroxyl groups. The layers of silica and alumina sheet in phyllosilicate are connected together by weak dipoles and van der Walls attraction forces. In that way, the interlayer or gallery structures as illustrated in Figure 1.2 are created within the clay mineral [1.32].

The types of cation occupy tetrahedral and octahedral site depend more on the coordination and ionic size than the cation valency. Therefore, there is a great potential for isomorphous replacement or substitution within the structures. This ionic replacement distinguishes the groups, series, species and varieties of the phyllosilicates, for example, partial substitution of Si^{4+} and Al^{3+} with cation of similar size and coordination but different valency (usually

lower) in tetrahedral and octahedral sites respectively [1.33]. Such replacements as a result raise the permanent negative net charge in the layered structure. This deficiency of positive charge is balanced by sorption of extraneous cations that may or may not be exchangeable.

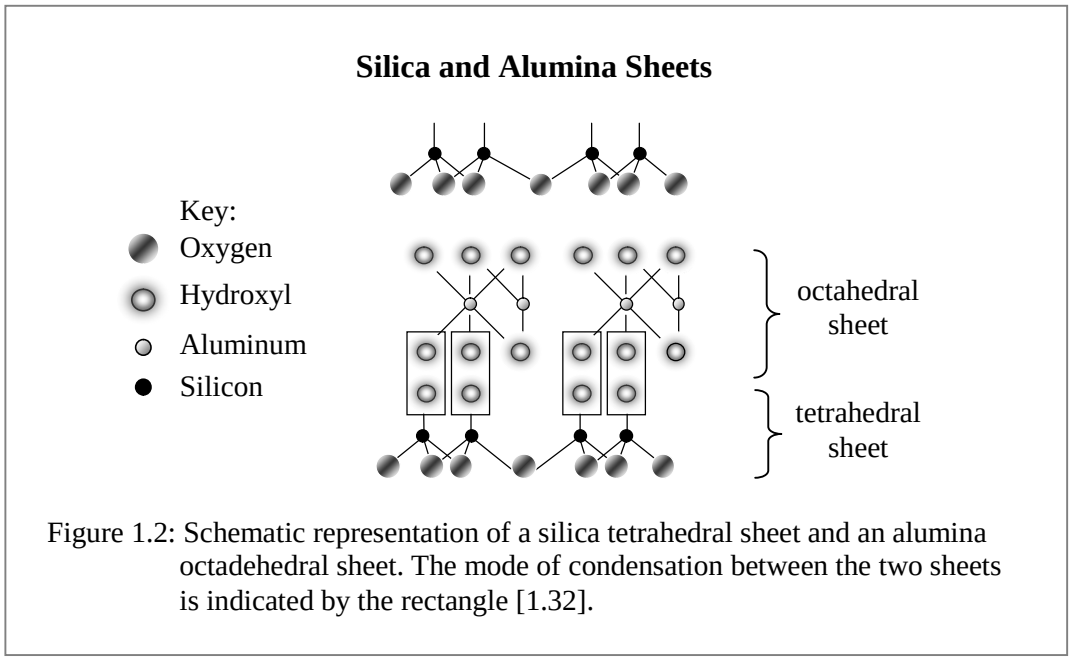

Figure 1.2: Schematic representation of a silica tetrahedral sheet and an alumina octadehedral sheet. The mode of condensation between the two sheets is indicated by the rectangle [1.32].

1.3.2.2 The Structure of Montmorillonite, *Mon*

Montmorillonite is called a 2:1 trimorphic or three-sheet mineral, where two silica sheets condense on an alumina sheet. The resultant layer structure cause the alumina sheet to be sandwiched between two sheets of silica sheet, as shown in Figure 1.3(a) for pyrophyllite mineral. In this structure, there is no isomorphous replacement, which balances the mineral charges. In Figure 1.3(b) however, the layer structure of *Mon* as suggested by Hofmann [1.34 and 1.32] indicate partial substitutions of Al^{3+} for other cations such as Mg^{2+}, Fe^{2+} and Fe^{3+} within the octahedral sites. While in the tetrahedral sheet, the substitution of Si^{4+} for Al^{3+} cation seldom happened. As a result, the increased negative net charges in this structure are balanced by extraneous cations. In case of *Mon* clay mineral, these charges are normally exchangeable.

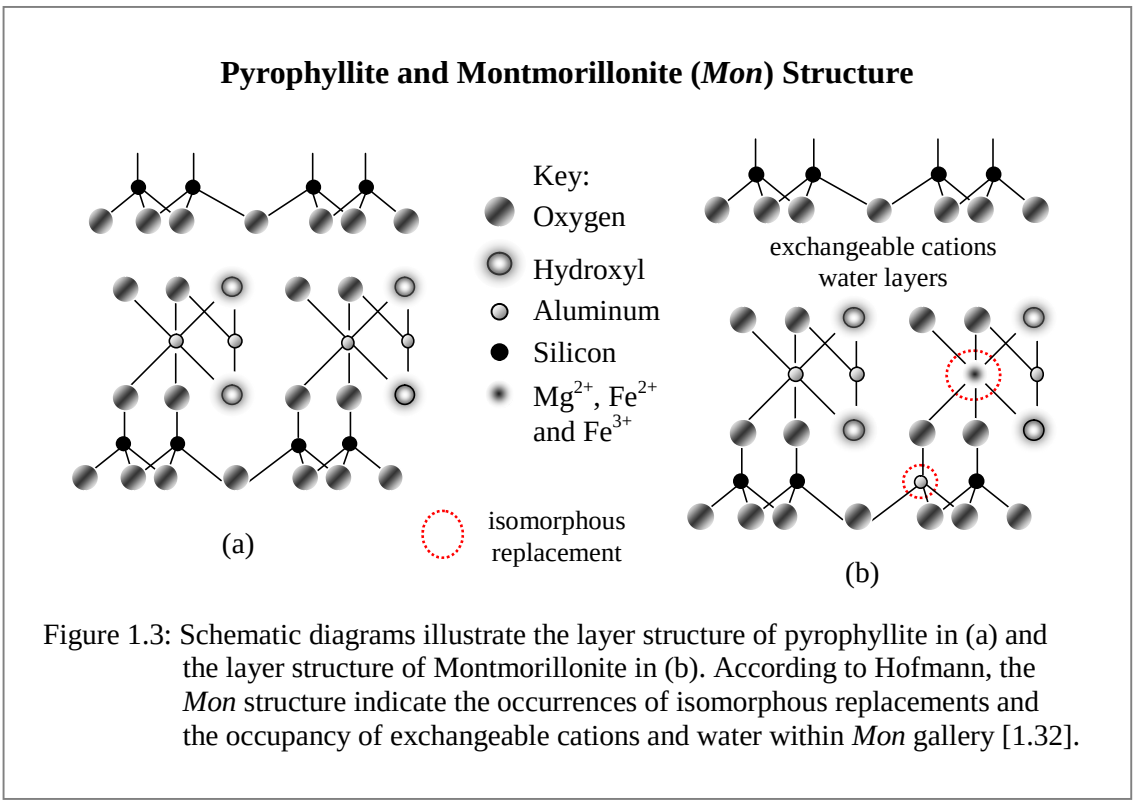

Figure 1.3: Schematic diagrams illustrate the layer structure of pyrophyllite in (a) and the layer structure of Montmorillonite in (b). According to Hofmann, the *Mon* structure indicate the occurrences of isomorphous replacements and the occupancy of exchangeable cations and water within *Mon* gallery [1.32].

In the 2:1 structure of pyrophyllite, just a small portion of the balancing cations is located at external crystal surface, while the majority cations reside within the interlayer spaces. Similarly, in the *Mon* structure where its gallery is occupied by exchangeable cations such as Na^+ and Ca^{2+}. Besides these charge-balancing cations, water is normally present inside the *Mon* gallery, where it tends to associate with the cations by forming hydration shell around them by means of cation-dipole bonding. The penetration of water molecules into *Mon* gallery depends on the relative humidity and the nature of exchangeable cations. The presence of exchangeable cations within *Mon* gallery therefore explains the good swelling property demonstrated by *Mon* minerals. For example, under optimum condition Li^+-*Mon* and Na^+-*Mon* in aqueous suspension may swell beyond basal spacing d_{001} 2.25 nm, where it can cause an interlayer separation of ten nanometers [1.35, 1.32 and 1.33].

From scanning electron microscopy SEM, *Mon* are found in the form of clusters with their sizes within the range of 0.1 to 1.0 μm. These clusters composed of primary particles,

which are formed of Mon layers as discussed in the previous section. According to Mering [1.36 and 1.37], the diameter of primary particle is less than 30 nm while its height is about 8 to 10 nm. The thickness of each layer on this particle is estimated around 0.96 to 1.0 nm. It is supposed that each particle consist of about 8 to 16 (001) silicate planes.

Water molecule interactions with exchangeable cations play important role in *Mon* reaction with small organic and uncharged organic substances. Since polar groups in such substance compete with water molecule for the same ligand site around these cations. This type of cation-dipole interaction is also expected to connect uncharged and polyfuntional organic polymer to the clay surfaces. However, it is true only in case of aqueous medium where in non-aqueous suspension *Mon* is hardly dispersed that leads to particle agglomeration. Such condition indicates that *Mon* clay mineral and organic compound generally is immiscible, which describes the organophobic property of the clay minerals. In order to make polymers composite with *Mon*, a proper compatiblizer has to be used to change the *Mon* property to organophylic.

1.4 Thesis Organization

This thesis has been divided into eight chapters and each chapter discusses specific areas. ***Chapter 1*** is an introduction chapter that presents the research background and the primary objective of this research work. The theoretical background and literature review for both thermo-electrical and mechanical studies are discussed in ***Chapter 2*****.** In ***Chapter* 3**, the methodology carried out in this work is explained. It covers both sample preparations and instrumentation, which involve the experimental method in the studies. The results of some basic characterization tests are discussed in ***Chapter 4***, they are the Differential Scanning Calorimetry (DSC), X-ray Diffraction (XRD) and Fourier Transform Infra-red (FTIR) spectroscopy.

Chapter 5 and ***Chapter 6*** give the results, analysis and discussion of Thermally Stimulated Current (TSC) measurement for the thermo-electrical studies. While the observations and analyses from tensile test for mechanical studies are discussed in ***Chapter 7***. The primary objective of this work is reviewed in ***Chapter 8***, together with the research findings and conclusions. This chapter also highlights several potential directions that can be considered as futures works.

References:

1.1 W. J. Work, K. Horie, M. Hess and R. F. T. Stepto, "Definitions of Terms related to Polymers Blends, Composites and Multiphase Polymeric Materials", *Pure Appl. Chem.*, **V 76(11)**, (2004), pg. 1985–2007

1.2 B. S. Mitchell, "An Introduction to Materials Engineering and Science for Chemical and Materials Engineers: For Chemical and Materials Engineers", *Wiley-IEEE*, US, (2004)

1.3 G. Akovali, "Handbook of Composite Fabrication", *Rapra Technology*, Billingham (2001)

1.4 J. C. Salamone, "Concise Polymeric Materials Encyclopedia", *CRC Press*, New York, (1998)

1.5 B. T Marouf, R. A. Pearson and R. Bagheri, "Anomalous fracture behavior in an epoxy-based hybrid composite", *Mat. Sci. Eng. A*, **V 515**, (2009), pg. 49 – 58

1.6 J. Kajtna and U.Šebenik, "Microsphere pressure sensitive adhesives-acrylicpolymer/montmorillonite clay nanocomposite materials", *Int. J. Adhesion & Adhesives*, **V 29**, (2009), pg. 543 – 550

1.7 J. M. Yeha, K. C. Changa, C. W. Penga, M. C. Lai, C. B. Hunga, S. C. Hsua, S. S. Hwang and H. R. Lin, "Effect of dispersion capability of organoclay on cellular structure and physical properties of PMMA/clay nanocomposite foams", *Mat. Chem. Phy.*, **V 115**, (2009), pg. 744 – 750

1.8 P. Li, N. H. Kim, Siddaramaiah, J. H. Lee, "Swelling behavior of polyacrylamide/laponite clay nanocomposite hydrogels: pH-sensitive property", *Composites B*, **V 40**, (2009), pg. 275 – 283

1.9 A. Martínez-Gómez, E. Pérez, C. Álvarez, "Effect of the intercalated/exfoliated nanostructure on the phase transformations of smectic polyester/layered silicate hybrids: Reinforcement of the liquid-crystalline matrix", *Polymer*, **V 50**, (2009), pg. 1447 – 1455

1.10 C. G. Martins, N. M. Larocca, D. R. Paul and L. A. Pessan, "Nanocomposites formed from polypropylene/EVA blends", *Polymer*, **V 50**, (2009), pg. 1743 – 1754

1.11 H. L. Lin, H. L. Chang, T. Y. Juang, R. H. Lee, S. A. Dai, Y. L. Liu and R. J. Jeng, "Nonlinear optical, poly(amide-imide)–clay nanocomposites comprising an azobenzene moiety synthesised via sequential self-repetitive reaction", *Dyes and Pigments*, **V 82**, (2009), pg. 76 – 83

1.12 D. Adame and G. W. Beall, "Direct measurement of the constrained polymer region in polyamide/clay nanocomposites and the implications for gas diffusion", *App. Clay Sci.*, **V 42,** (2009), pg. 545 – 552

1.13 H. M. C. de Azeredo, "Nanocomposites for food packaging applications", *Food Res. Int.*, (2009), in press

1.14 S. Pavlidou and C. D. Papaspyrides, "A review on polymer–layered silicate nanocomposites", *Prog. Poly. Sci.*, **V 33**, (2008), pg. 1119 – 1198

1.15 J. van Turnhout, "Thermally Stimulated Discharge of Electrets", Topics in Applied Physics: Electrets edited by G.M Sessler, **V 33**, *Springer-Verlag*, New York, (1980)

1.16 K. C. Kao, "Dielectric phenomena in solids: with emphasis on physical concepts of electronic processes", *Academic Press*, US, (2004)

1.17 S.W. Tkaczyk, "Manifestation of trapping border states in 1,4-cis-polybutadiene/SiC nanocomposite films", *Physica E*, (2009), in press

1.18 J. R. Davis, "Tensile Testing", 2nd. Edition, *ASM International-The Material Information Society*, New York, (2004)

1.19 R. L. Timings, "Mechanical Engineer's Pocket Book", 3rd Edition, *Newnes- Elsevier*, Amsterdam, (2005)

1.20 M. D. Antonijević, D. Q. M. Craig and S. A. Barker, "The role of space charge formation in the generation of thermally stimulated current (TSC) spectroscopy data for a model amorphous drug system", *Int. J. Pharm*., **V 353**, (2008), pg. 8 – 14

1.21 N. Wada, M. Nakamura, Y. Tanaka, K. Kanamura and K. Yamashita, "Formation of calcite thin films by cooperation of polyacrylic acid and self-generating electric field due to aligned dipoles of polarized", *J. Coll. Interface Sci*., **V 330**, (2009), pg. 374 – 379

1.22 W. Wang, S. Itoh, Y. Tanaka, A. Nagai and K. Yamashita, "Comparison of of bone ingrowth into hydroxyapatite ceramics with highly and lowly interconnected pores enhancement by Electrical Polarization", *Acta Biomaterialia*, (2009), in press

1.23 J.R. Fried, " Polymer Science and Technology",*Prentice Hall*, New Jersey, (1995)

1.24 S.L. Rosen, "Fundamental Principels of Polymeric Materials", 2nd Edition, *John Wiley& Sons*, New York, (1993)

1.25 F.W. Billmeyer Jr., "Textbook of Polymer Science", 3rd Edition, *John Wiley& Sons*, New York, (1984)

1.26 L. E. Nielsen, "Mechanical Properties of Polymers and Composites", **V 1**, *Marcel-Dekker*, New York, (1974

1.27 P. Hedvig, "Dielectric Spectroscopy of Polymers", *Adam Hilger Ltd*., Bristol, (1977)

1.28 M. Chanda and S. K. Roy, "Plastics technology handbook", *Marcel Dekker*, New York (1998)

1.29 A.H. Eng, Y. Tanaka and S.N. Gan, "Some Properties of Epoxidised Deproteinised Natural Rubber", *J. Natural Rubber Research*, **V 12(23)**, (1997), pg. 82-89

1.30 S. Guggenheim and R. T. Martin, "Definition of clay and clay mineral; joint report of the AIPEA nomenclature and CMS nomenclature committees", *Clays and Clay Minerals*, **V 43(2)**, (1995), pg. 255-256

1.31 B. B. Velde and A. Meunier, "The Origin of Clay Minerals in Soils and Weathered Rocks", *Springer*, New York, (2008)

1.32 B.K.G Theng, "Formation and Properties of Clay-Polymer Complexes", *Elsevier*, Amsterdam, (1979)

1.33 G. V. Middleton, M. J. Church, M. Coniglio, M. J. Church, M. Coniglio, "Encyclopedia of sediments and sedimentary rocks", *Springer*, New York, (2003)

1.34 U. Hofmann., K. Endell and D. Wilm, “Kristalstruktur und Quellung yon Montmorillonit”, *Z. Krist.*, **V 86**, (1933), pg. 340- 348

1.35 K. Norrish, “The Swelling of Montmorillonite”, *Disc. Faraday Soc*., **N 18**, (1954), pg. 120 - 134

1.36 J. Mering, “On the hydration of montmorillonite” , *Trans. Faraday Soc*., **V 42B**, (1946), pg. 205 - 219

1.37 A. Blumstein, “Polymerization of adsorbed monolayers: I. Preparation of clay-polymer complex”, *J. Poly. Sci Part A.: Poly Chem.*, **V 3**, (1965), pg. 2653 – 2664

Chapter 2

Theory

Chapter 2: THEORETICAL BACKGROUND AND LITERATURE REVIEW

Two major tests used in this work are Thermally Stimulated Current or TSC technique and tensile test for mechanical studies. Basic principles, classifications, theoretical background and some related formulations of the tests will be discussed throughout this chapter. These discussions also involve some basic standards for instrumentation as well as experimental procedures. Typical results of TSC and tensile tests will be given and briefly discussed in a few sections, which also highlights the influencing factors.

2.1 Thermally Stimulated Current, TSC Technique

Thermally Stimulated Current, TSC is a method to investigate electrical properties of high-resistivity solids or dielectrics, through the study of thermal relaxation effects. This method consists of measuring with definite heating scheme the current induced by thermal increase from an electrets. Where, the current are actually generated by the build-up and release of polarize state in the solid dielectrics that sandwiched between two electrodes. In that way, it contributes significantly to the current understanding of charge storage and charge decay in electrets. Relaxation effects revealed by TSC technique make it an attractive alternative to the conventional bridge methods or current-voltage-temperature measurements. It also offers a complimentary method to some isothermal tests; such as Dielectric Analysis, DEA and Dynamic Mechanical Analysis, DMA.

Besides, as far as electronic carriers are concerned TSC is considered closely related to the Thermally Stimulated Conductivity, TSCo technique. The mathematic in fact is similar to those found in the system, as well as from other non-isothermal methods such as Thermo luminescence, TL and Thermo-stimulated electronic emission, TSEE. Mathematically TSC is also related to other techniques of thermal analysis, which are not on charge decay basis.

For example, Differential Scanning Calorimetry (DSC) and Thermogravimetry (TGA) that based on energy different and loss of weight respectively [2.1, 2.2 and 2.3].

2.1.1 Basic Principles and Microscopic Mechanisms

In order to run TSC experiment it is very important to priory understand the fundamentals behind this technique. It involves basic principles for experimental procedures as well as the choice of sample to be used in the experiment. Likewise, attentions must also be given to identify potential microscopic mechanisms that are responsible for the relaxation process.The knowledge gathered about the processes in the studied sample will be useful in interpreting the TSC results.

2.1.1.1. Basic Principles of Electrets and TSC Technique

A part of TSC technique involves the formation of temporary thermoelectrets. By that means, basic nature of electrets has to be well understood to choose the right material for TSC measurement. Therefore, this section is dedicated to give brief ideas regarding electrets as well as procedures involved in the TSC technique.

2.1.1.1 A. Electrets

An electret is described as a piece of dielectric material having quasi-permanent electrical charges. The phrase quasi-permanent means that the time constant for the charges decay is much longer than the time which studies are performed with the electret. The sources for electret charges normally come from both dipole polarizations and space charges. These charges can be trapped within the material, or with time they may form layers of surface charges. This is illustrated in Figure 2.1 for an electret created in between two metallic electrodes. True polarization in this case is usually a frozen-in alignment dipoles. Electret charges however, may also comprise of carriers displaced within molecular or domain structures throughout the dielectric. It resembles a true dipole polarization, and referred to

as Maxwell–Wagner polarization if the charges are displaced to the domain borders. While trapped positive and negative carriers may formed layers of space charges, which often positioned near the two surfaces of the electrets [2.3 and 2.4].

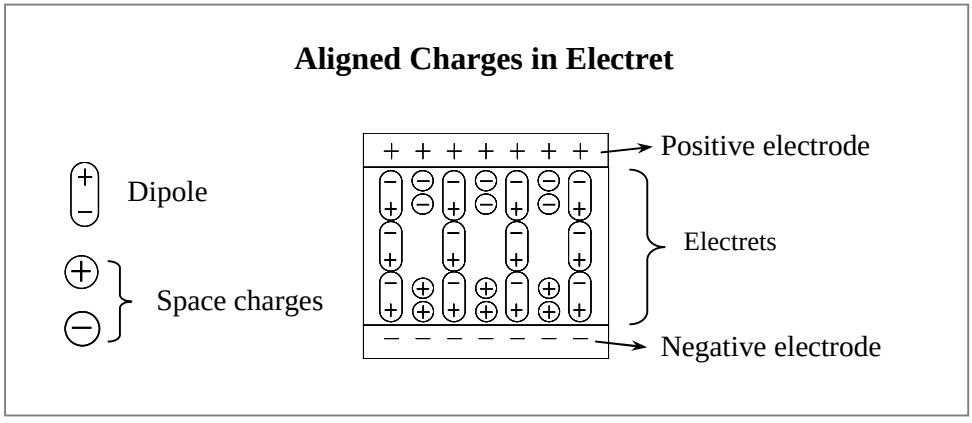

Figure 2.1: Schematic cross section of typical electrets shows aligned dipoles and space charges [2.9].

The above mention characteristics make polymers are among the good choice to create an electret. These materials contain a range of elements that can be polarized under electrical field. This is including various types of permanent dipoles, ions as well as electrons within the polymer molecular structures. Studies on polymeric materials tell that many interesting properties are owing to the molecular motions, which are usually very complex [2.5]. Therefore, the use of the TSC technique on polymer electrets seems reasonable to examine complex and overlapping dielectric relaxation effects. It may helps to understand more on thermo-electrical and structural characteristics of polymers.

2.1.1.1.B. TSC technique

Basic principles of this method are outlined in Figure 2.2. Where, the general experimental procedure usually involves four steps [2.4 and 2.6]:

1. *Polarization*

   An artificial thermoelectret can be formed by heating the sample well above its glass transition, T_g temperature. It follows with polarization by applying direct

current D.C electrical field F_p for t_p minutes. This procedure allows potential dipoles and charges to be polarized inside the sample.

2. *Quenching*

   Polarized charges are then frozen by cooling process on the tested sample under the polarization field, F_p to some lower temperature, T_o. These charges are supposed virtually immobile at this temperature.

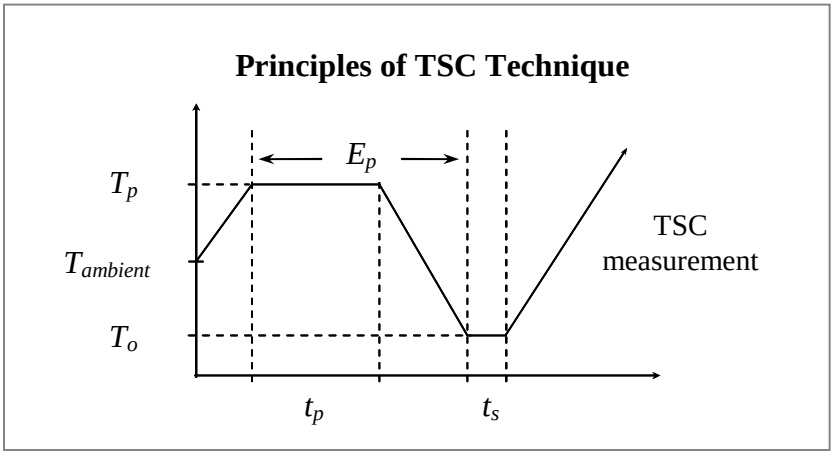

Figure 2.2: Schematic outlines for basic principles in TSC technique [2.4]

3. *Remove electrical field*

   The applied electrical field F_p at T_o is changed to a lower value, usually 0 Vm^{-1} as a preparation for the following step. The sample at that moment is stabilized at T_o temperature for t_s minutes. At this stage, electret charges developed within the sample turn it into a thermoelectret.

4. *Depolarization*

   The electrets sample is then short-circuited and reheated at a constant rate, such as at 1 °C/min. As a result the discharge current is generated by depolarization process of the activated electret charges. This thermally stimulated current, TSC is measured by an electrometer and recorded as a function of temperature by a computer.

Schematic outlines in Figure 2.3 give the illustrations of TSC results. It shows the plots of current, *I* versus temperature, *T* for the series of methacrylic polymers. Overall, the curves from this thermogram reveal three to four major relaxation peaks. These peaks that are known as the γ, β and α peaks are mainly related to dipoles inside the polymers. While ρ peaks observed at higher temperatures normally associated to space charges [2.3 and 2.7]. In order to produce good TSC results as shown in Figure 2.3, the choice of material to be used with TSC technique is very crucial. Conducting materials such as composite polymers with carbon black was found inappropriate to study via this method. Again, it tells that TSC technique practically should be used with dielectric materials.

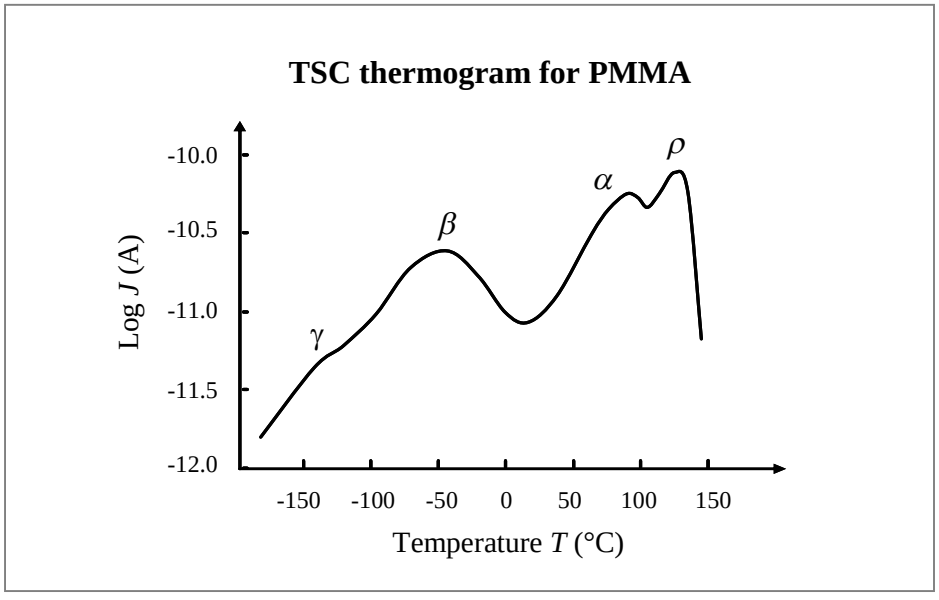

Figure 2.3: Schematic illustration shows typical TSC result for PMMA. This thermogram demonstrates several characteristic peaks that indicate relaxations processes in the polymer [2.3].

2.1.1.2. Microscopic Mechanisms

The knowledge about microscopic mechanism is important to investigate relaxation effects demonstrated by the TSC results. The origin for such effects detected in TSC thermogram comes from *polarization* processes that form a thermoelectret. It follows by *depolarization* processes on the electret charges, which are thermally activated. This section therefore will discuss possible mechanisms that are responsible for both processes.

2.1.1.2.A. Polarization

The polarization of a solid dielectric under high electric field may arise from different type of process [2.1 and 2.8]:

1. Displacement of electrons and nuclei, which is an instantaneous process:
   a) *Electronic polarization* – the fastest process that takes about 10^{-15} s resulted from electronic shell deformations.
   b) *Atomic polarization* – requiring about 10^{-14} to 10^{-12}s. This is the outcomes from atomic displacement in molecules with heteropolar bonds. It is also considered as deformation effects.
2. *Dipolar or orientational polarization* – electrical responses by both permanent molecular and ionic dipoles within dielectric materials, such as polymers. The time required for this process can be as low as 10^{-12}s depending upon frictional resistance of the dipoles medium. In which it can also take a long period that no relaxation is observed under the conditions of an experiment.
3. Migration of electrons, ions and ion vacancies, as well as their trapping sites close to the electrodes. For example:
   a) *Translational or space charge polarization* – this is owing to microscopic charge transfer towards electrodes, which then form total or partial barriers. This process can vary from millisecond to years, and normally detected in materials with intrinsic free charges. These charges can be either ions or electrons, or combination of both elements.
   b) *Interfacial polarization* – a process that is also known as *Maxwell- Wagner-Sillars* or *MWS* polarization. Normally this process takes place in a material with heterogeneous structures. Where, charge layers can be created by

charge depositions at interphases. This is owing to unequal conduction of electrical currents within various phases of such structures.

4. *A space charge polarization of extrinsic origin* – high electrical field, E_p used on a dielectric material can create homocharges. This is due to charge injection of excess electronic or ionic carriers from electrodes, known as *Schottky emission*. Such injection could also come from *Townsend breakdowns* in the surrounding atmosphere, for the case of imperfect electrode-dielectrics contacts.

Overall only the first type of polarizations occurs at any temperature immediately after the application of electric field E_p. While the other processes approach equilibrium with a characteristic relaxation time, which is temperature dependent.

2.1.1.2.B. Depolarization

Mechanisms responsible for TSC involve several processes that contribute to the discharge of electrets, in which restoration of charge neutrality is basically the driving force for all the processes. These processes can be classified into are two main categories [2.3, 2.9 and 2.10], they are:

1. *Disorientation of dipoles*

This process tends to destroy the persistent dipole polarization by redistributing all dipoles at random. It involves rotations by a couple pair of positive and negative charges, which takes certain amount of energy that is known as *activation energy*. For example, in solid dielectric it may amount to few eV per dipole. By this means, dipole disorientation is a thermally activated and can be accelerated by heating process. Activation energy for each dipole in electrets normally has some dissimilarity to one another. For that reason, current – temperature plots as shown in Figure 2.3 reveals several relaxation peaks. Dipoles with low activation energy will disorient at low

temperature. While those polarized dipoles with a high activation energy will disorient at relatively higher temperature. Among the peaks associated to dipoles are:

a) γ and β peaks

These peaks signify the disorientation of dipoles at low temperature region. Small differences in activation energy however, can cause individual peaks to overlap and merge into a broad peak. In polymers, such broad peak frequently referred to as β peak. This peak is the outcome of depolarization processes by polar side groups with continuous distribution activation energies.

b) α peak

This is another broad peak that is also a result of peaks overlapping. The origin however distinguishes this relaxation peak, where small variations in rotational mass of dipoles responsible for the peak emergence. Such as in polymers when heated to its softening temperature. Whereby, the dipoles are disoriented by the motion of main chains segments within the polymers. Disorientation by various dipoles thus produces the α peak in Figure 2.3, which are located at the glass-rubber transition temperatures T_g of the polymers.

2. *Space charges* - ρ peak

Immobilize space charges in electrets are non-uniformly stored and very often residing near electrodes. Heating process however give energy for these carriers to move and neutralize at the electrodes, as well as within the electrets. These neutralization processes involves the recombination of charges with opposite sign. While the driving force are their *drift* in local electric filed, and *diffusion* that tends to eliminate the charges concentration gradient. In Figure 2.3, the appearance of ρ peaks characterizes this relaxation effect. In which it appears at higher temperature compared to that of β and α peaks. This is due to the fact that the disorientation of dipole requires only

local rotation. On the other hand, the neutralization of space charges needs them to travel over many atomic distances. Hence, space charges should have sufficient energy that can be achieved at the relatively higher temperature.

Background information of a studied sample will useful to guess the type of mechanisms that may take place in the electret. For example, the compositions and elements that form the material as well as it's chemical and physical structures. Similarly, the history and pre-condition such as moisture contain of the sample also must be taken into consideration. Various microscopic mechanisms contribute to relaxation effects turn TSC technique into a sensitive tool to study materials. In fact, it adds more information such as ionic impurities that can be represented by additional ρ peak in TSC thermogram. In order to gain this high sensitivity however, right instrumentation must be carefully chose or designed.

2.1.2 Experimental Considerations

Previously in Section 2.2, the general principles of TSC technique were reviewed in details. It covers the basic experimental procedures of investigating thermally stimulated process, as well as data acquisition and interpretations. However, in order to produce good resolution peaks there are some issues that must be taken into account. They are:

1. *Sample*

   Generally, samples for TSC technique are used in the form of film; plate; single or polycrystalline compact and lightly compressed powder. The sample thickness is usually about 0.5 mm. However, it can be reduced to 25 μm if the sample contains polymeric substances, from which it can be transformed into thin foil.

2. *Electrodes*

   Various methods can be used to make a thermoelectret and normally the sample is placed in between two metallic electrodes. As in conventional electrical conducting

measurement, a guarded electrode should be used to avoid inhomogeneities on the polarizing field F_p and minimize surface conduction [2.1 and 2.8].

3. Thermostated sample holder [2.1 and 2.3]

   a) *Thermostat* – A thermostat is needed to ensure good thermal equilibrium between sample and heater. This thermostat can be either evacuated or filled with dry inert gas such as helium or nitrogen. The main purpose is to avoid water vapor that is known sensitive to the electrical properties of most materials.

   b) *Sample holder* – In order to reach highest possible sensitivity when investigating bulk process, a direct contact between sample and electrodes must be achieved and maintain during the whole experiment.

4. *Heater*

   An efficient heating unit is very important to conduct TSC measurement. It should be able to offer variable but linear heating rate over a wide range of temperature. Low heating rate is normally chosen to minimize temperature gradient across the studied sample, such as 1 °C/min, which is considered low enough to prevent the temperature lags and guarantee a good resolution peaks [2.1 and 2.3]. Previous studies [2.11, 2.12 and 2.13] demonstrate that most materials begin to produce current peaks at very low temperature, such as in Figure 2.3. For that reason, it is highly suggested that the TSC measurement should be started at a temperature of liquid nitrogen. It can be done by using liquid nitrogen to quench down the sample temperature, for example below −100 °C.

5. *Direct Current or dc generator*

   A stabilized dc generator is also important to maintain the applied electrical field on sample for certain period during polarization process.

6. *Current detector*

   Current measurements in TSC technique require a sensitive ammeter to sense small thermally induced current from depolarization processes. Typically it should be able to measure current in the range of 10^{-4} to 10^{-14} A [2.3].

7. *Data acquisition*

   A current – temperature recording unit must be designed to systematically collect TSC data through out the measurement process. This process can take about four hours; and data acquisition should be run automatically by this device for plotting as well as storage.

Preliminary analysis normally is done based on basic information regarding the studied material, such as the temperature of glass – rubber transition, T_g and softening or melting point temperature T_m. In case of polymers for example, the knowledge of T_g will be useful to identify an α peak, whereby both properties are known to have close connections with segmental motions of the polymers main chains. Further evaluations on TSC thermograms can be carried out then by utilizing some theoretical approach that will be discussed later in the next section.

2.1.3 Basic Equations for Dipolar Depolarization

Theoretical treatments in many cases of polarized materials are very often assumed free of charge carriers. By that means, the internal electrical field of a material as well as its dipolar polarization can be regarded as space independent. Practically however, both space charges and dipolar polarizations are frequently found coexisting in electrets, especially in thermoelectrets created at high temperature. Therefore, the electric field and polarization must then be considered as averaged over the thickness of a sample.

The first consistent theory on dipolar processes in TSC technique was developed by *Bucci* and *Fieschi* [2.1] in 1964. It was based on various studies carried out on some crystallite materials with dipolar ionic defects. They found that dipole reorientation in the materials is strictly obey the first order kinetic theory. It means that depolarizations within an electret system were dominated by charge recombination process, rather than retrapping.

In order to describe the system, *Bucci* and his co-worker used Debye relaxation model [2.1, 2.3, 2.8 and 2.14], which it assumed the electrets composed of non-interacting dipoles with a single relaxation time. Polarization process performed on these dipoles by the application electric field F_p at temperature T_p during time t build-up polarization density P in unit volume, which gives:

$$P(t) = P_e\left[1 - \mathbf{exp}\left(\frac{-t}{\tau}\right)\right] \tag{2.1}$$

Where τ is the dipolar relaxation time and P_e is the equilibrium or steady state polarization. According to *Langevin* for all cases except the lowest temperature and highest field,

$$P_e = \frac{sN_d\, p_\mu^2 \kappa F_p}{kT_p} \tag{2.2}$$

Geometrical factor s in this relation depends on the possible dipolar orientation. Where, for free rotating dipoles s =1/3 while for nearest-neighbor face-centered vacancy within ionic crystal s = 2/3. N_d represents the concentration of dipoles with p_μ is the electrical moment, k for Boltzmann's constant and κF_p for the local DC electrical field that operates on the dipoles. Assuming that relaxation times for both polarization and depolarization processes on the dipoles are identical, the decay of polarization following field removal at $t = \infty$ is given by

$$P(t) = P_e\ \mathbf{exp}\left(-\frac{t}{\tau}\right) \tag{2.3}$$

The first order kinetic equation that governs the process thus describes the corresponding depolarization current as follow,

$$J(t) = -\frac{dP(t)}{dt} = \frac{P(t)}{\tau} \tag{2.4}$$

Variations in both time and temperature however dictate the current density J from TSC measurement. Therefore, new variable parameter T was established with a presumption of linear temperature rise from temperature T_o. The relation puts temperature

$$T = T_o + ht \tag{2.5}$$

where $h = dT/dt$ is the heating rate; and rewriting equation (2.1) will give

$$P(t) = P_e\left[\mathbf{exp}\left(-\int_0^t \frac{dt}{\tau}\right)\right] \tag{2.6}$$

This equation is based on some postulate, which are:

a) this relation also hold s for varying temperature

b) the initially frozen-in polarization $P(T_o)$ is equal to the equilibrium polarization reach at the polarizing temperature $P_e(T_p)$

c) the temperature variation of τ is given by an Arrhenius-type equation

$$\tau = \tau_o\ \mathbf{exp}\left(\frac{E}{kT}\right), \tag{2.7}$$

where τ_o is the relaxation time at infinite temperature and E is the activation energy for dipolar orientation and disorientation.

It is to be noted that $f_o = 1/\tau_o$ is the characteristic frequency factor or natural frequency and normally associated to the vibrational frequency of a material. The current density J_D from TSC measurements thus, is given by

$$J_D(T) = \frac{P_e(T_P)}{\tau_o} \exp\left(-\frac{E}{kT}\right) \exp\left[-\frac{1}{h\tau_o}\int_{T_o}^{T} \exp\left(-\frac{E}{kT'}\right) dT'\right]. \qquad (2.8)$$

This expression represents an asymmetrical curve or peak in TSC thermogram [2.15, 2.16, and 2.17]. The first exponential dominates the low temperature range which is responsible for the initial rise of current with temperature, while the second exponential that dominates at high temperature gradually slows down the current increase. Subsequently, the induced current reduces very fast especially in the cases of high activation energy. It then generates a relaxation peak of which the shape is very much affected by the heating rate *h*, frequency factor *s* as well as activation energy *E*. Differentiating equation (2.8) will give an equation that shows their influences on the maximum temperature of a peak

$$T_m = \left[\frac{E}{k} h\tau_o \exp\left(\frac{E}{kT_m}\right)\right]^{1/2} \qquad (2.9)$$

The mathematical treatment on equation (2.8) can bring about various parameters that may describe relaxation effects from TSC results, such as the activation energy *E*, relaxation time τ, frequency factor f_o and the initial concentration of polarized charges, n_o. Moreover, information gathered from these parameters will be useful to make deductions on potential mechanisms behind the emergence of TSC peaks, for example high activation energy that is normally more than 4 eV suggests the involvement of space charge release for a ρ peak.

2.2 Tensile Test

Most engineering materials are used owing to desirable mechanical properties it offered at economical cost. In many material applications, the properties grow to be more important than the other physical and chemical properties. Therefore, the selection of a material for particular structural application requires good knowledge about its mechanical behaviors. For this reason it is important to study some standard test that can generate the mechanical properties. As well as the significant of each property produced from the tests. Mechanical properties generally are properties that determine the responses of a material to external mechanical influences. This is manifested in the ability of the material to create reversible and irreversible deformations, with its resistance to failure.

A number of standardized tests can be used to mechanically investigate material properties. For example tension and compression test, hardness, fatigue and creep test that capable to reveal mechanical behaviors under different conditions. Basic characterizations on material however usually determine by tests which resulting in various deformations versus stress dependencies. Examinations on such dependencies can readily bring out the characteristics of elasticity, plasticity and strength in a material. These features are expressed by several variables such as elasticity modulus, tensile strength and toughness.

2.2.1 Uniaxial Tensile Test

Tensile test is one of the most commonly used methods to evaluate mechanical properties of materials. A basic principle for this test is to pull a specimen to failure within a short period of time. It involves the specimen elongation under uniaxial tension that is applied at a constant rate, whereby the load needed to cause a given elongation is measured as a dependent variable.

2.2.1.1. Experimental Consideration

Even though the basic principle of tensile test is rather simple, numerous factors however can affect the results. Common resources for mechanical variations come from human error, methodology, ambient condition and equipments. Among the factors in methodology and also the effect of some parameters chosen are listed as follow [2.18 and 2.19].

1. *Shape of specimen* – A wide variety of specimen geometry may be employed in tensile test. Generally, it has a central segment of reduced area that is known as the gauge section. This section shown in Figure 2.4 is very critical part of a specimen, where it is designed to guarantee deformations and failure will be localized within this region. While at each end of the specimen there are enlarge section designed for gripping.

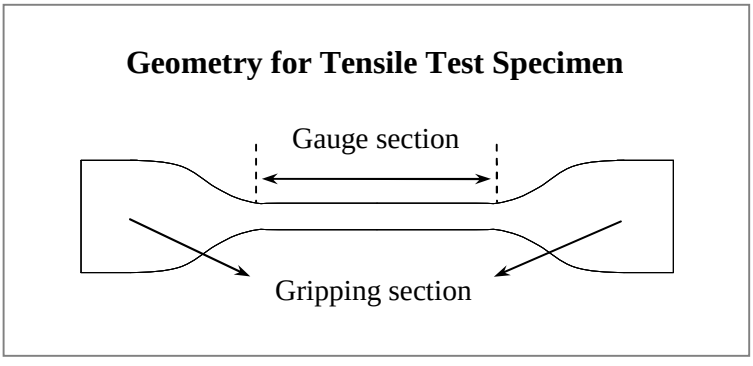

Figure 2.4: An illustration of typical geometry for tensile test specimen, which is known as dumbbell or dog-bone shape [2.18 and 2.19].

2. *Method of gripping* – There are various ways of gripping the tensile specimen, such as screwed into treated grip, pinned to a sample holder or held the grip section in between wedges plates. Above all, the concern is to ensure that specimen can be held at maximum load without slippage at the grip sections.
3. *Method of force application* – The load applied to specimen can be chosen either in static or dynamic manner, where the rate of load applied in dynamic load affects mechanical properties. [2.20]

4. *Determinations of strength properties* – There are a number of parameters that can describe the strength of a material. Such as Yield strength which has three common definition:
    a) Offset Yield strength – at which specimen exhibits plastic deformation
    b) Extension under load yield strength – at which specific amount of stretch has in the specimen
    c) Upper yield strength – the stress where measurable strain occurs without an increase in strain.
5. *Stress and strain rate* – The speed of force in dynamic load and strain elongation in static load application affect the stress-strain behaviors.
6. *Temperature* – Ambient temperature of a tested specimen can give great effect on final results.

High consideration should be given in test parameters selection, which depends very much on the type of material to be tested. For example, tensile test results for polymers strongly depend on its strain rate. This is owing to viscoplasticity property in polymers that exhibit time dependent deformation during stress loading. Temperature is another sensitive feature which easily affected mechanical properties of this material. Therefore, the control of both variables is more critical for polymers than other material.

2.2.1.2 General Procedure

Test set-up in general requires equipments that properly match to the type of mechanical test chosen. There are three basic requirements for a testing machine [2.18]:

1. Force capacity must sufficient to break a specimen to be tested.
2. Test speed either for load or strain as require by test specification

3. Sensitive sensor with good accuracy that can detect and record properly the load and extension data generated by the machine.

Many standard procedures can be employed to run a tensile test, which normally depends on the type of material used in the test. However, there are general rules in test procedures that may be applied in almost every tensile test. They are:

a. *Identification* – the identity of each specimen should be properly recorded

b. *Dimension* – the dimension for each specimen should be measured accurately especially for cross-sectional and strain calculation.

c. *Load and strain range* – maximum range must be sufficient to ensure that the test will fit within the range.

d. *Zeroes* – the load indicator and the plot-load axis should be set to zero before specimen is paced within the grips.

e. *Specimen mounting* – a specimen is placed in the grips and secured by closing the grips

f. *Parameters* – important parameters such as dimension, maximum ranges and test speed must be keyed-in into control software for tensile test before execute the test.

g. *Execute* – tensile test is ready to be carried out when pre-condition for this test is done, such as ambient temperature. An electromechanical machine will pull the specimen before automatically stop once it sense a break-off point. During the test, extensometer measure the extension while a sensor detects the amount of load used.

Computer based testing machine can simultaneously display graph while recording the raw data generated from the test. This system should also capable to permanently recode these data for further analysis. A proper tensile test needs each test to be repeated at lease five

times with same experimental conditions. For that reason, statistical values such as average and median values frequently used in analysis.

2.2.1.3 Stress-Strain Diagram

Raw data from tensile test normally in the form of applied force F and extension ΔL. These data that are measured and recorded at regular interval, create load-deformation curve for a specimen. These data pairs can also be converted into a stress-strain diagram as shown in Figure 2.5 for analysis. There some basic terms that are used to describe the mechanical behaviors of material in the diagram [2.18, 2.20, 2.21 and 2.22].

2.2.1.3.1. Stress **-** By definition, stress is simply the amount of force that act over a given cross-sectional area, A. It means that if the force is uniformly distributed, the stress can be calculated as the ratio force to area.

$$\text{Stress, } \boldsymbol{\sigma} = \frac{\text{Force, } \boldsymbol{F}}{\text{Area, } \boldsymbol{A}}$$

Engineering stress in metric unit typically is given in N/mm^2 or Pascal (Pa). The conversions among the unit are as follow:

$$1\ N/mm^2 = 1MN/m^2 = 1MPa$$

Where $1\ Pa = 1N/m^2$

2.2.1.3.2. Strain – Direct effect from application of stress on a body will be the change in size or shape. This change is known as deformation. Strain and elongation are two similar terms that describe the amount of deformation caused by a given quantity of applied stress. In general, strain is defined as change per unit length, ΔL in original linear dimension, L_o which gives

$$\text{Strain, } \boldsymbol{\Delta L} = \frac{\text{Extension, } \boldsymbol{\Delta L}}{\text{Original length, } \boldsymbol{L_o}}$$

2.2.1.3.3. ***Deformation*** in materials can be saparated into two groups. They are the elastic deformation from point *a* to *c* in Figure 2.5 While point *c* to *e* is the range for plastic deformation.

A. ***Elastic deformation*** is the ability of materials to change upon the applied force and return to original shape once the force is removed. This type of change occurs within the early segment of a stress-strain curve, where the stress-strain relationship is initially linear. There are two types of limits that characterize this elastic region:

i) Proportional Limit (PL) – A point where linear relationship between stress and strain begin to break down in elastic region. Point *b* in Figure 2.5 represents this *PL* point which also describe linear elasticity of a material.

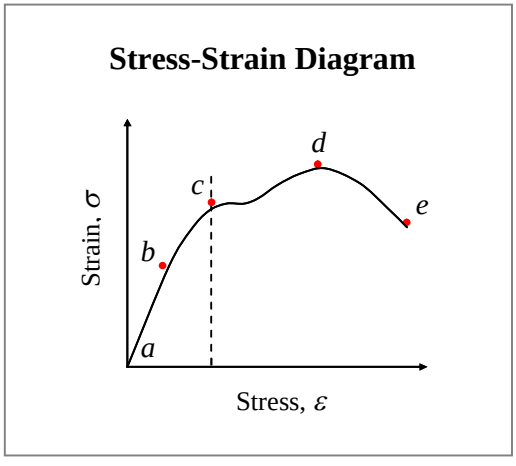

Figure 2.5: Typical illustration of stress-strain diagram from tensile test shows elastic and plastic deformations [2.20].

ii) Elastic Limit (EL) – Beyond the *PL* point, non-linear elasticity takes place where the strain increase unproportionally to the applied stress. *EL* as shown by point *c* indicates the border for elasticity behaviors in materials. In practical this point is also known as Yield point, where beyond this limit

permanent deformation will occurs. Yield stength is the stress at this point which is important property for a material.

B. Plastic deformation describe permanent changes on a specimen as a response towards further applied of external forces. It may involve structural changes such as dislocation atoms or molecules and broken chains in polymers. Plastic region on a stress-strain diagram covers the area beyond the yield point until a break-off point, which is represented by point *e* in Figure 2.5.Two important parameters characterize this region, they are:

i) Tensile strength, σ_{max} – The higest value of engineering stress at point *d* in Figure 2.5 is known as tensile strength. It tells the ultimate strength that a material can withstand when subjected to mechanical tension.

ii) Maximum elongation, ε_{max} – This parameter gives maximum strain at point *e,* the break-off point which marks material failure on the stress-strain diagram.

2.2.1.3.4. Beside the above mention ***mechanical parameters***, more information can be generated from a stress-strain curve. Among the important parameters are:

A.* Modulus of elasticity, *Y is a slope of the initially linear portion in elastic region which is also known as Young's Modulus. This modulus characterizes the proportionallity between stress and strain which is known as *Hooke's Law*. The relation gives modulus of elasticity

$$Y = \sigma/\varepsilon \qquad \text{or} \qquad \sigma = Y\varepsilon$$

Where σ = stress and ε = strain

Basically modulus of elasticity is determined by binding forces between atoms. These forces cannot be changed without changing the basic nature a

material. For that reason, modulus of elasticity is considered as the most structure - insensitive of all mechanical properties. [2.18]

B. **Toughness** is a parameter which involves both elastic and plastic regions. When load is applied on a body and cause certain deformation, work W is considered done. This relation gives $W = \int F dL$ with F and dL represent applied force and elongation respectively. In unit volume, this relation becomes

$$\frac{W}{A_o L_o} = \int \frac{F}{A_o L_o} \frac{\partial L}{L_o} = \int \sigma d\varepsilon$$

Where A_o = cross-section area and L_o = cross-section area

It means that work done perunit volume on a specimen during strectching can be estimated by the area under stress-strain curve. This mechanical work measures the amount of energy transfer, which is stored as strain energy in the specimen. It thus indicates the specimen toughness that describes the ability to absorb energy, throughout the elastic and plastic deformations. Toughness therefore is very much influenced by the tensile strength and elongation at break.

A lot of information can be generated from a simple tensile test. Analysis on stress-strain diagram for example brings out the basic knowledge about mechanical responses of a substance. This is very important in choosing the right material especially for engineering application. Such as high toughness, property is needed in materials used for gears, chains and crane hook.

2.2.2 Mechanical Properties of Polymers

Polymers are very important class of materials. Engineering polymers that are generally synthetic polymers found its uses in many applications. These synthetic materials in fact replace a number of conventional materials, such as wood and metals. It includes several natural fibers for example cotton and wool. A typical commercial synthetic polymer may consist of two or more polymers in addition to various additive and filler. Such inclusions necessitate in some cases to improve thermal and environmental stability, processability and mechanical properties of the final product.

2.2.2.1 Basic Principles

Polymer is believed consist of macromolecules, which composed of 10,000 or more atoms. Therefore, mechanical properties of polymers should be related to the basic characteristics of macromolecules. Among the important characteristics are [2.23]:

a) size of macromolecule such as molecular weight

b) flexibility such as segment size

c) characteristics of intermolecular interaction

Establishment of relationships between these features and mechanical properties helps to understand the appearance of many mechanical behaviors. Generally, any theory regarding mechanical responses of polymers was based on two main assumptions:

i. All polymeric body contains macromolecules

ii. Deformation and mechanical properties in polymers depends on macromolecules as well as their initial features, such as chemical structure, size and molecular bonding.

Polymeric materials in some cases normally regarded as continuous and homogeneous, for instance polymer solution and melt. However, there are also polymers with heterogeneous structures such as polyethylene, a semi-crystalline polymer.

2.2.2.2. Characteristic of Typical Mechanical Behaviors

Various structures in polymeric materials act differently towards the application of external loading. Stress-strain diagrams from tensile test for example, demonstrate a variety mode of mechanical behaviors. Typical stress-strain outlines for tensile test are given in Figure 2.6(a) to (e), represent different groups of polymers [2.24, 2.25 and 2.26].

A. *Rigid and brittle* – Figure 2.6(a) shows a polymer with high modulus of rigidity, low elongation and failure prior to yield point. As a result, it gives low toughness that is indicated by a small area under the curve. These are common behaviors in most thermoset polymers, such as *polystyrene (PS)*.

B. *Rigid and strong* – Both elasticity modulus and tensile strength for polymers which are represented by Figure 2.6(b) are high, while the elongation can be considered as medium, where it exceeds the yield point. A typical polymer from this group is *rigid polyvinyl chloride (PVC)*.

C. *Rigid and tough* – High modulus with reasonable elongation and tensile strength in Figure 2.6(c) are some common features frequently found in engineering polymers. It thus, explains high toughness in such polymers as shown by *nylon*.

D. *Soft and tough* – Low modulus in Figure 2.6(d) indicates the softness in polymers from this group. However, their great ability for extension increase the energy to break that turns them into a tough material. *Polyethylene (PE)* and *plasticized PVC* are among the good examples from this group.

E. *Elastomer* – The deformation in Figure 2.6(e) is elastic that explains the general feature of an elastomer. This is including the significantly high strain at break that contributes to the polymers toughness. Natural rubber is an example of

important elastomer in engineering application.

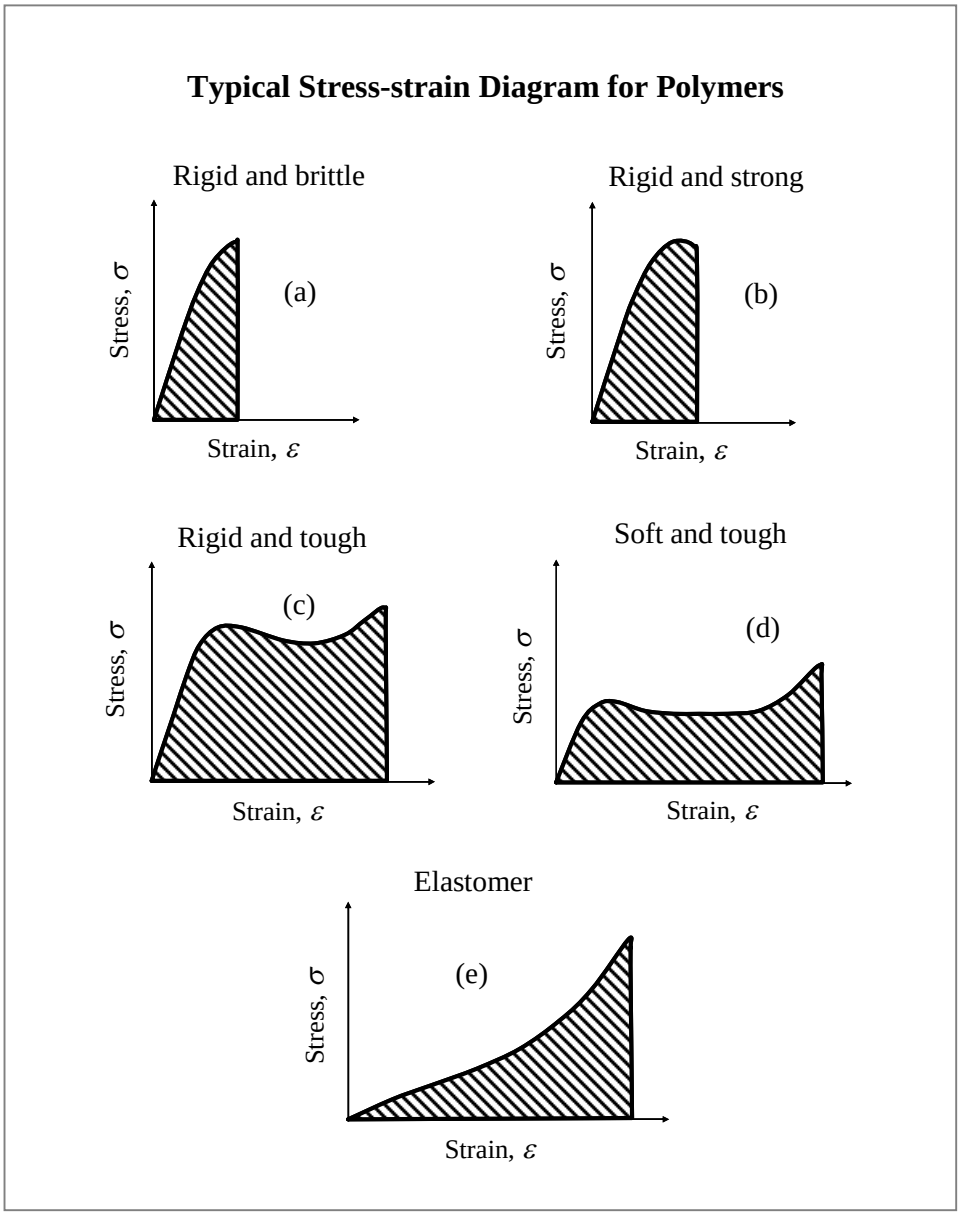

Figure 2.6: Schematic outlines of typical stress-strain diagrams for five major types of polymers [2.24].

These typical characteristics on stress-strain diagrams help to categorize a wide range of polymers into five major groups. Each polymer from the groups however demonstrates its own features. It depends very much on the structural effects bring about by chemical and physical organization of macromolecules in the polymers.

2.2.2.3 Influencing Factors

Many structural factors can affect the nature of stress-strain behaviors of polymers. They are listed as follow [2.27 and 2.28]:-

1. *Molecular weight (MW)* – Low molecular weight normally will give low strength to polymers. However, the increase in MW can give better strength that makes polymers useful for applications.

2. *Crosslinking and branching* – Both effects particularly crosslinking capable to lock together macromolecules in polymers. In this way, molecular motion becomes more restricted which improves chemical, physical and thermo-mechanical properties of polymers. This is including mechanical properties such as tensile strength.

3. *Crystallinity* – Uniform and repeatable molecular arrangements signify crystallinity in polymers, wherein good intermolecular reactions within such crystalline structures strongly bind their molecules. It thus explains the high modulus *Y* demonstrated by crystalline region in comparison to amorphous region.

4. *Copolymerization* – This is a way of improving mechanical properties, for example in a technique called rubber toughening.

5. *Plasticization* – The adding of plasticizer molecules into polymers is done to gain desired flexibility and durability for application. On the other hand, tensile strength and hardness in plasticized polymers will be reduced as a result of plasticization.

6. *Molecular orientation* – The orientation of polymeric chains can contribute for high strength and stiffness properties. Such as a biaxial oriented *PET* which has a typical Young's modulus about 5.4 GPa. While the unoriented *PET* gives just about 2.4 GPa [2.29].

7. *Filler* – Various substances normally added into polymers to get better mechanical properties. For example fibers, metallic and carbon powders are commonly used filler to improve tensile strength and hardness [2.30].

In addition to molecular and the above structural factors, there are some environmental and external variables, which also have great influences on mechanical properties. Among the major factors are temperature; time; pressure; ambient condition and type of deformation. Frequency and the rate of stress as well as the stress and strain amplitude are not less important in mechanical test. This is including the heat treatment or thermal history of a specimen.

A number of influence variables thus explain the individuality in each polymer. However, there are general properties showed by most polymers that make them important. Such as resistant to chemical that can be very high in certain polymers. They can also provide good insulation for thermal and electrical purposes. While in structural application, the growing interests on polymers arise due to their versatile mechanical properties, in which covers the range from soft elastomer to rigid plastic. For that reason, there is a great need to gather a lot of data in order to understand mechanical behavior of polymers.

2.2.3 Mechanical Response of Composites

Generally, composite is defined as material system composed of a mixture or combination of two or more micro or macro components, where the components are different in form and chemical composition. Composite materials must also have recognizable interface that distinguishes different phases formed by the components. Composite are created especially to optimize materials properties that have engineering importance. Polymer composites for example may give better chemical, physical and mechanical characteristic than its pristine polymers. By which it becomes more useful and expand its uses in many application.

2.2.3.1. Classification of Composites

Effective method to increase the strength and improve overall properties is by dispersion of reinforcing material into a binder substance. These elements create filler and matrix phases respectively, the two main regions that in general characterize a composite. A filler phase usually consists about 10% or more of structural component that can be used in composite classification. They are five general types of composite as illustrated by Figure 2.7, which represent three categories of reinforcements [2.31 and 2.32].

1. *Fiber reinforcement*: - Fiber is defined as a particle longer than 100 μm with aspect ratio greater than 10:1. **Fiber composites** are created using these particles either with or without the present of matrix phase.

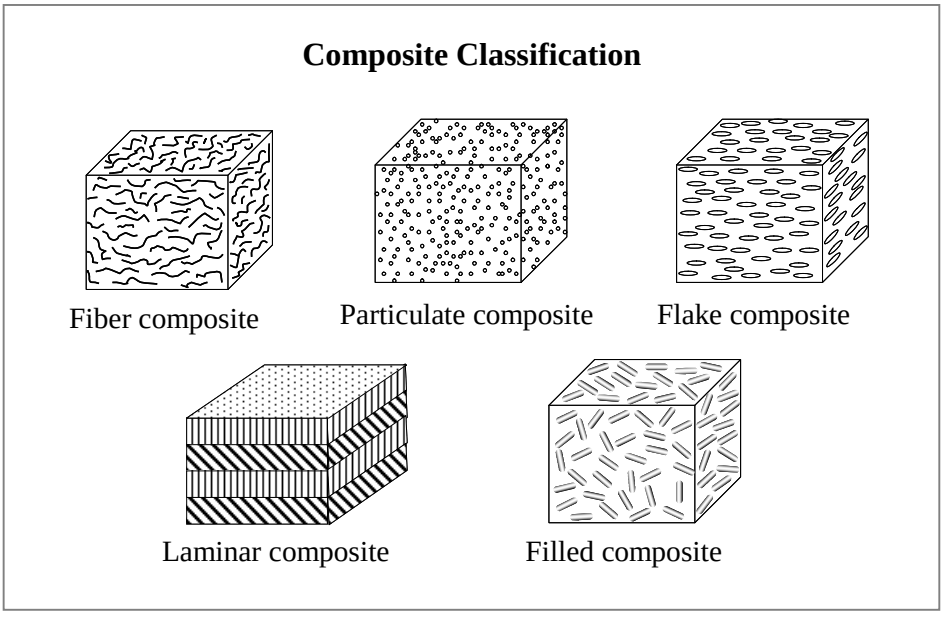

Figure 2.7: Illustrations for five major class of composites [2.31]

2. *Particle reinforcement*: -
   a) **Flake composite** consist of flake component as the filler, which is actually a flat and plate-like materials, such as mica flake
   b) **Particulate composite** is made of particulate materials which roughly spherical in shape in comparison to fiber and flake, for example, carbon and mineral powders.

3. *Structural reinforcement*: -
    a) **Filled composite** can be made of three dimensional fibrous or porous structured materials. This component is continuous and often considered as a primary phase. Second material is added via such process as chemical vapor infiltration (CVI).
    b) **Laminar composite** are composed of distinct layers, where it can be either from different materials or same material with different orientations. Laminated and sandwich panels are among the important laminar composites in application.

Reinforcement materials in these composites are embedded in matrix phase, which usually comprise about 30% to 40% of composite system. Polymers, ceramic and metal are among the widely used matrix material in composite fabrication. Matrix phase in composites has a number functions [2.32], it gives: -

1. *binding* – it binds the components together and gives thermo-stability for composite
2. *protection* – it protects the reinforcement materials from corrosion or abrasion and environment
3. *distribution* – it help to distribute applied load by acting as stress transfer medium
4. *strength* – it provide durability, interlaminar toughness and shear / compress / transverse strength to composite system;
5. *consistency* – it maintain desired fiber orientation and spacing in specific structure.

Matrix materials in composite usually are low in modulus. While reinforcing elements are typically 50 times stronger and 20 to 150 times stiffer than the matrix phase. Nevertheless, the matrix component still has roles in composite strength and toughness, where it is more subtle and complex compared to the filler phase. A good example is given by combination of brittle substances from both filler and matrix phases, which produce a tough material.

The toughness actually arises due to combination mechanisms that tend to keep cracks and flaws small and isolated. In that way, it disperses mechanical energy effectively.

2.2.3.2 Particulate Reinforced Composite

The need of composite in application is usually for their structural properties, for example improved strength and toughness. For that reason, particulate and fibrous form substances are the most commonly employed components for reinforcement. While for matrix phase, polymers are very popular in composite fabrication. Principally, stress-strain responses of particle reinforced composite is influenced by the features of both filler and matrix domain. The filler for example can give various effects that capable to influence elastic and plastic deformations in composite systems. The following factors are among important variables that must be considered in particulate composites [2.32, 2.33 and 2.34].

1. ***Modulus*** – rigid particle that is high in modulus will increase the strength and stiffness of particulate composites.

2. ***Volume fraction*** – the increase in volume fraction gives more contact area for filler-matrix interactions. In consequence it will improve composite strength as shown in Figure 2.8, illustrations of typical stress-strain outlines for particulate composites.

3. ***Size*** – the decrease in particles size will lead to the improvement in modulus *Y* and tensile strength of composites. This is due to the increase in surface area, which also increases surface energy of the particles. It thus can cause the increased absorption or particle-particle interaction, adherence and agglomeration. For example, silica and carbon black particles form chains and networks in their respective composites. Such formations can restrict matrix phase deformations, which then improved the modulus and strength. Most filler require particle smaller than 40 μm. However, fine particles which are less than 5 μm are needed if mechanical properties are important [2.35].

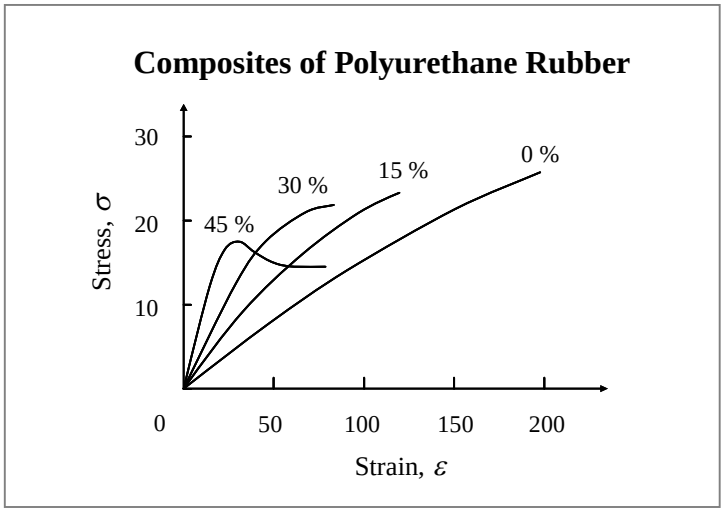

Figure 2.8: Schematic illustrations of stress-strain curves for polyurethane rubber composites with powder rock salt. Numbers on each curve refers to the volume fraction of the filler [2.34].

4. ***Shape*** – particle shape such as spherical, angular and cylindrical have great influence on mechanical behaviors of particulate composites. Shape factor normally is defined in term of *aspect ratio* which is a ratio of the largest and smallest dimensions [2.36],

$$\text{Aspect ratio, } A_R = d_{min} / d_{max}$$

Particles with high aspect ratio will raise elasticity modulus *Y*, elongation at failure and viscoplasticity of a composite. While low aspect ratio from angular particles for example will lead to early failure, where they can act as crack initiator in the system [2.37].

5. ***Dispersion*** – good particles dispersion is needed in order to get effective material strengthening. Particles agglomeration for example tends to reduce tensile strength, even tough the agglomeration is strong enough to increase composite modulus. This is because agglomerations create weak points that induce early failure in particulate composite [2.34].

6. ***Filler treatment*** – the nature of filler-matrix interface can be improved by prior treatment on filler particles with silane coupling agent and adhesion promoter. As a

result stress-strain behaviors will be changed, and treated fillers often increase tensile strength of particle reinforced composites [2.34 and 2.38].

These particulate composite can be categorized in two sub-classes based on reinforcement and strengthening systems. They are known as large-particle and dispersion strengthened composites. Particulate-matrix interaction in the large-particle composite can not be treated at atomic or molecular level, due to its large particle size (>0.1 mm). While in dispersion strengthened composite, relatively smaller particle size (0.01mm to 0.1mm) is used which improved filler-matrix interactions. The interaction in this case is believed to take place at the atomic or molecular level [2.32].

Modification on mechanical properties may be regarded as primary function of most filler in many composites. Even though reinforcement mechanism by the filler can take various ways, in general it causes restriction on matrix phase movements. This is the strengthening effect, which operates in the large-particle and dispersion strengthened composites. Right through the process, matrix domain transfers some of the applied stress to filler particles. Both mechanisms thus contribute to the improvement on composite mechanical properties.

2.3 Summary

Particulate reinforced composites in this work composed of non-conductive materials. For that reason, these composites as well as their pristine polymers can be used with the TSC technique. Relaxation phenomena reveals from TSC result can give lots of details about micro and macroscopic mechanisms within the materials. Besides, high sensitivity in TSC technique is an advantage to study the materials at molecular level.

In mechanical studies, tensile test was chose to bring out the basic mechanical properties of polymers and their respective composites. Such as elasticity modulus *Y*, tensile strength

σ_{max} and maximum elongation ε_{max} which are frequently used to characterize materials. These properties are useful to investigate the effects of fillers on mechanical responses in the composites.

Both types of tests apparently require proper instrumentations, especially in TSC technique to ensure good resolution peaks. While for tensile test, great attentions are needed in the gripping technique and sample preparations. Basic principles and experimental procedures discussed earlier can be used as guidelines in both cases.

References:

2.1. J. Vanderschueren and J. Gasiot, "Field-Induced Thermally Stimulated Current" Topics in Applied Physics: Thermally Stimulated Relaxation in Solids edited by P. Braunlich, **V 37**, *Springer-Verlag*, New York, (1979)

2.2. J. R. Saffell, A. Matthiesen, R. McIntyre and J.P. Ibar, "Comparing thermally stimulated current (TSC) with other thermal analytical methods to characterize the amorphous phase of polymers", *ThermochimicaActa*, **V 192**, (1991), pg 243 – 264

2.3. J. van Turnhout, "Thermally Stimulated Discharge of Electrets", Topics in Applied Physics: Electrets edited by G.M Sessler, **V 33**, *Springer-Verlag*, New York, (1980)

2.4. B. Hilczer and J Malecki, "Electrets" Studies in Electrical and Electronic Engineering, **V 14**, *Elsevier*, Amsterdam, (1986)

2.5. M. Zielinski and M. Kryszewski, "Theoretical Analysis of the Thermal Sampling Technique for TSD Measurement on Polymers" Thermally Stimulated Processes in Solids: New Prospects edited by J.P Fillard and J. van Turnhout, *Elsevier*, Amsterdam, (1977)

2.6. J. Belana, M. Mudarra, J. Calaf, J.C. Canadas and Menendez, " TSC Study of the Polar and Free Charges Peaks of Amorphous Polymers", *IEEE Trans. El. Ins.*, **V 28(2)**, (1993), pg. 287 – 293

2.7. C. C. Ku and R. Liepins, "Electrical Properties of Polymers – Chemical Principles", *Hanser Publisher*, Munich, (1987)

2.8. E. Riende and R. Diaz-Calleja, "Electrical Properties of Polymers", *CRC Press*, US, (2004)

2.9. J. van Turnhout, "Thermally Stimulated Discharge of Polymer Electrets" – A Study on Non-isothermal Dielectric Relaxation Phenomena, *Elsevier*, Amsterdam, (1975)

2.10. H. J. Wintle, "Conduction Processes in Polymer" Electrical Properties of Solid Insulating Materials: *Molecular Structure and Electrical Behaviors* edited by R. Bartnikas and R. M. Eichhorn, Engineering Dielectrics **V IIA** - ASTM Special Technical Publication No. 783, Philadelphia, (1983)

2.11. M. Fois, A. Lamure, P. Guuinic and C. Lacabane, "TSC Study of Secondary Dielectrics Relaxations in a Polyepoxy Matrix Composites", *J. App. Poly. Sci*., **V 66**, (1997), pg. 135 – 139

2.12. R. A. Vaia, B. B. Sauer, O. K. Tse and E. P. Giannelis, "Relaxations of Confined Chains in Polymer Nanocomposites: Glass Transition Properties of Poly (ethylene oxide) intercalated in Montmorillonite", *J. Poly. Sci.; Part B*, **V 35**, (1997), pg. 59 – 67

2.13. B. B. Sauer and P. Avakian, "Cooperative relaxation in amorphous polymers studied by thermally stimulated current depolarization", *Polymer*, **V 33(24),** (1992), pg. 5128 – 5142

2.14. R. Chen, Y. Kirsh, "Analysis of Thermally Stimulated Processes" – International Series on the Science of the Solid State, *Pergamon Press*, **V 15**, Oxford, (1981)

2.15. M. Mudarra, J. Belana, J.C. Canadas and J. A. Diego, "Polarization Time Effect on PMMA Space-Charge Relaxation by TSDC", *J. Poly. Sci.; Part B*, **V 36**, (1998), pg. 1971 – 1980

2.16. G. Kitis, J. M. Gomez-Ros and J. W. N. Tuyn, "Thermoluminescence glow-curve deconvolution function for first, second and general orders of kinetics", *J. Phy. D: Appl. Phys.*, **V 31**, (1998), pg. 2636 – 2641

2.17. N. S. Yuksek, N. M. Gasanly and H. Ozkan, "Thermally stimulated current analysis of shallow levels in TIGaS2 layered single crystals", *Semicond. Sci. Technol*., **V 18**, (2003), pg. 834 – 838

2.18. J. R. Davis, "Tensile Testing", 2nd. Edition, *ASM International-The Material Information Society*, New York, (2004)

2.19. W. F. Gale, C. J. Smithells, T. C. Totemeier - Contributor W. F. Gale and T. C. Totemeier, "Smithells Metals Reference Book", 8th Edition, *Butterworth-Heinemann* (*Elsevier*), Amsterdam, 2004

2.20. A. Mubeen, "Experimental Strength of Materials", 3rd. Edition, *Khanna Publishers*, Delhi, (1997)

2.21. W. Hayden, W. G. Moffatt and J. Wulff, "Mechanical Behavior", *John Wiley & Sons*, New York, (1965)

2.22. R. L. Timings, "Mechanical Engineer's Pocket Book", 3rd Edition, *Newnes- Elsevier*, Amsterdam, (2005)

2.23. N. M. Bikales, "Mechanical Properties of Polymers", *Wiley-Interscience*, New York, (1971)

2.24. D. M. Teegarden, "Polymer Chemistry: Introduction to an Indispensable Science", *NSTA Press*, Arlington, (2004)

2.25. A. Ram, "Fundamentals of Polymer Engineering", *Springer*, US (1997)

2.26. N. P. Cheremisinoff, "Polymer Mixing and Extrusion Technology", *CRC Press*, UK, (1987)

2.27. L. E. Nielsen, "Mechanical Properties of Polymers and Composites", **V 1**, *Marcel-Dekker*, New York, (1974)

2.28. L. H. van Vlack, "Elements of Materials Science", 2nd. Edition, *Addison Wesley Publishing Company*, Massachusetts, (1959)

2.29. B. Bhushan, "Mechanics and Reliability of Flexible Magnetic Media", *Springer*, Berlin, (2000)

2.30. S. Sulaiman, R. Yunus, N. A. Ibrahim and F. Rezaei, "Effect of Hardener on Mechanical Properties of Carbon Fiber Reinforced Phenolic Resin Composites", **V 3(1),** *J. of Eng. Sci. and Tech*., Taylor University College, (2008)

2.31. B. S. Mitchell, "An Introduction to Materials Engineering and Science for Chemical and Materials Engineers: For Chemical and Materials Engineers", *Wiley-IEEE*, US, (2004)

2.32. G. Akovali, "Handbook of Composite Fabrication", *Rapra Technology*, Billingham (2001)

2.33. ASM Handbook: Composites Volume 21 By Daniel B. Miracle, ASM International Handbook Committee, Steven L. Donaldson Contributor Daniel B. Miracle, Steven L. Donaldson Published by ASM International, (2001)

2.34. L. E. Nielsen and R.F. Landel, "Mechanical Properties of Polymers and Composites", 2nd Edition, *Marcel-Dekker*, New York, (1994)

2.35. J. C. Salamone, "Concise Polymeric Materials Encyclopedia", *CRC Press*, New York, (1998)

2.36. M. N. Rahaman, "Ceramic Processing", *CRC Press*, New York, (2006)

2.37. R. L. Oréfice, L. L. Hench, A. B. Brennan, "Effect of Particle Morphology on the Mechanical and Thermo-Mechanical Behavior of Polymer Composites", *J. Braz. Soc. Mech. Sci*., **V 23(1)**, Rio de Janeiro, (2001)

2.38. J. Leidner and R.T. Woodhams, "Strain Behavior of Particulate-Filled Composites", *J. App. Poly. Sci.*, **V 18**, (1974), pg. 2637 – 2651

Chapter 3

Methodology

Chapter 3: METHODOLOGY

Experimental works in this project, in general can be divided into two main sections. They are discussed through out this chapter under the heading of *Sample Preparations* and *Instrumentations & Experimental Methods*. Primary focus in *Sample Preparation* was on the Montmorillonite (*Mon*), smectite clay which is well recognized for its organophobic characteristic. In order to prepare composites with polymer matrix, the initial behavior of *Mon* had to be changed into organophylic. It means that *Mon* needs to go through some chemical modification before it can be used in composite preparations.

While in *Instrumentations*, the preliminary set-up of TSC [3.1] needed to be improved in order to improvise bigger ranges of temperature *T*, and also to have better controls for the heating process. Therefore, this task involved the modifications on some apparatus as well as development of new controlling and data acquisition software. Moreover, advanced work was carried out with the development of computer programs to help in analyzing the collected TSC data. While for the mechanical testing, an appropriate sample holder had to be designed to suit the thickness of prepared samples. For the same reason, a proper cutter that can give a clean cut and meets the ASTM standard was also customized

3.1 Sample Preparation

In order to prepare *polymer-OMON* composites, *OMON* was priory prepared by means of *Mon* modification. The process of organic modification needed montmorillonite *Mon* clay to go through some chemical processes. This organically modified *Mon* that is abbreviated as *OMON* were then used to produce *polymer-OMON* composites. In addition, composites polymer with pristine *Mon* were also prepared for comparison in this studies.

3.1.1 Organically modified Mon, *OMON*

3.1.1.1 Materials

Montmorillonite *Mon* used in this project is Swy-2 from University of Missouri clay repository and formulated as Na^{+}, Ca^{2+} - $(Al,Mg)_2Si_4O_{10}(OH)_2.nH_2O$. The given chemical compositions (see Appendix A) are SiO_2 (62.90%), Al_2O_3 (19.60%), Fe_2O_3 (3.35%), MgO (3.05%), CaO (1.68%), Na_2O (1.53%), K_2O (0.53%), FeO (0.32%), F (0.11%), TiO_2 (0.09%), S (0.050%) and P_2O_5 (0.049%). The cation exchange capacity, CEC of 76.4 meq/100g is estimated to occupy the space in between the *Mon* silicates layers. This value is referred to their primary ion exchanges, which are the sodium and calcium cations. While the surface area of *Mon* from the data sheet was estimated to be about 31.82 ± 0.22 m^2/g. Physical appearance of *Mon* clay mineral as received was a light gray grain with very fine particles that looked like powders. Generally, *Mon* is known for its good hydrophilic behavior that allows the mineral to absorb water even from the moisture its surroundings. Therefore, it is important to store *Mon* in a closed and dried container (28 ºC).

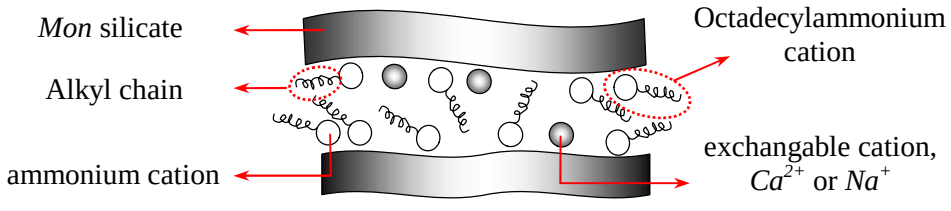

Figure 3.1: Exchangeable cations in *Mon* gallery are replaced by octadecylammonium cations via some chemical process. The ammonium cations are attached to *Mon* silicate while the alkyl chain is free to interact with organic substance.

The existence of cations exchange in smectite clay particularly *Mon*, provide a ground for chemical modification into organophylic material. The process involved the replacement of existing exchanged cations in *Mon* galleries with cations that have alkyl chains such as octadecylammonium. Schematic representation in Figure 3.1 illustrate the cation head as

attaches to silicates surface, while the alkyl chain which act as a tail is free to interact with any encounter organic substances [3.2 to 3.4]. Octadecyl amine $C_{18}H_{39}N$ that is a very important agent for the process was purchased from Fluka. This substance had to be treated earlier with hydrochloric acids in order to obtain the octadecylammonium cation, which was in the form of octadecylammonium chloride. Then, *Mon* and the octadecylammonium chloride had to be combined together for the chemical processes to take place as shown in

Mon* Modification into *OMON

$C_{18}H_{37}NH_2$ + HCl ⟶ $C_{18}H_{37}NH_3^+Cl^-$

Octadecylamine **hydrochloric acids** **octadecylammonium chloride**

$C_{18}H_{37}NH_3^+Cl^-$ + Na^+ - MON ⟶ $C_{18}H_{37}NH_3^+$ - MON + NaCl

Octadecylammonium chloride **montmorillonite *Mon*** ***OMON*** **sodium chloride**

Figure 3.2: Chemical reactions that involve in the process of *Mon* modification, which is abbreviated as *OMON*.

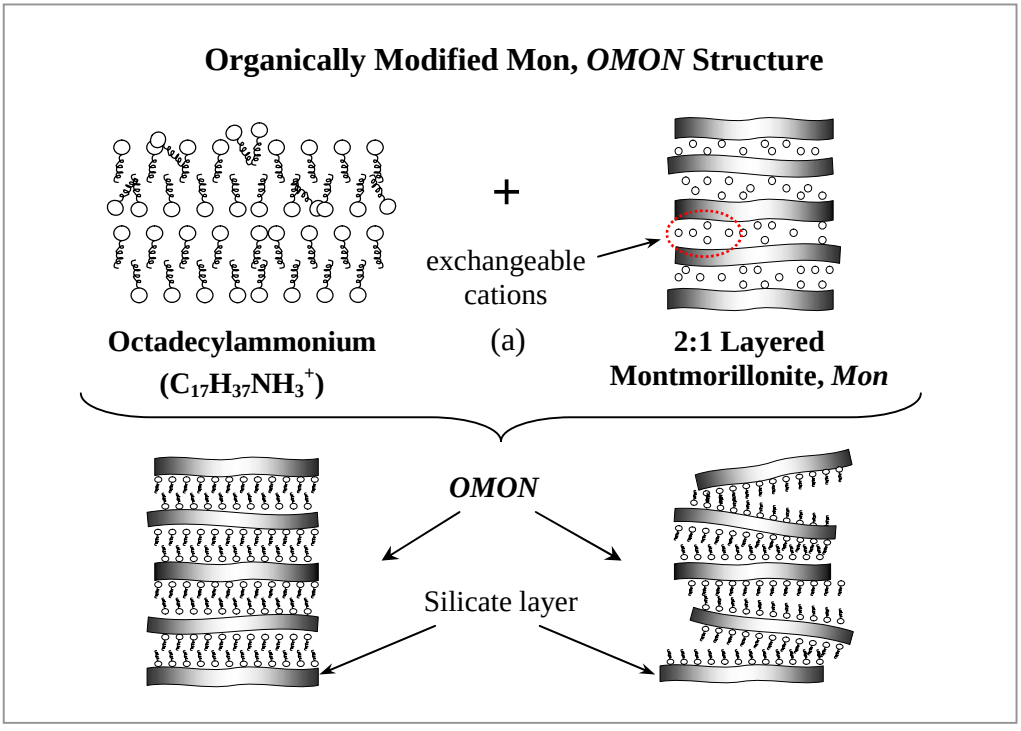

Figure 3.3: Schematic illustration of the cation replacement on *Mon* using the ammonium cations with alkyl tails (a) can cause the intercalation or exfoliation of *Mon* layers that give the organically modified *Mon* (*OMON*)

Figure 3.2. The process of cations replacement will drive the intercalation or exfoliation of *Mon* as illustrated in Figure 3.3(a) and 3.3(b) in that order.

3.1.1.2 Preparation of *OMON*

The process of *OMON* modification began with the dispersions of 8.0 g *Mon* into 500ml of distilled hot water at temperature 80 °C using a homogenizer. While another 200 ml of distilled hot water was used to dissolve 3.1 g octadecyl amine together with 1.2 ml of concentrated hydrochloric acid. In which, this solution went through a stirring process with a glass rod until all the octadecyl amine was dissolved. It was then slowly poured into the hot *Mon*-water solution before the stirring process was continued vigorously for about 5 minutes using a homogenizer to yield a white precipitate [3.5].

The precipitate was then collected on a white cloth filter, which was then followed with the washing process using hot distilled water (250 ml at 80 °C) repeatedly for five times. Finally, the organophyllic *Mon* precipitate was left to dry under room temperature for a few days. The out comes was a light gray and brittle chunk that needs to be crushed for further drying. After another one to two more weeks, these *OMON* granules were then ready to be grinded into smaller particles before kept it in a dry and close container. Figure 3.4(a) and 3.4(b) show the picture of pristine *Mon* and *OMON* clay minerals, respectively. The physical appearance of these clay minerals generally does not show much difference. However, the modifications had remarkably changed the organophobic property of *Mon* to organophylic in *OMON*.

X-ray diffraction, XRD test was performed on *Mon* and *OMON* samples to determine any changes in the gallery heights of their silicates. An increment in d_{001} spacing of *OMON* indicates the intercalation of octadecylammonium cations in the modification process. The observations proved the occurrence of intercalations in *OMON* and the detailed discussions will be carried out in Section 4.2.

Montmorillonite (*Mon*) and Organically modified *Mon* (*OMON*)

(a) (b)

Figure 3.4: Chemical modification on Montmorillonite, *Mon* in (a) produces renewed *OMON* clay mineral in (b). The modification does not affect their physical appearance, however it remarkably changes *Mon* organophobic property to organophylic.

3.1.2. Polymers and Polymers Composites with *OMON* and *Mon*

Three types of Malaysian natural rubbers (*NR*) were used in this project. They are the Standard Malaysian Rubber *SMRL*, Deproteinisied Natural Rubber *DPNR* and Epoxidised Natural Rubber *ENR-50*. These natural rubbers were supplied by Dr. Abu Amu from the Rubber Research Institute of Malaysia, *RRIM*.

According to the *RRIM*, *SMRL* is a *NR* with the latex grade. On the other hand, *DPNR* is a purified form of natural rubber with very low nitrogen and ash contents [3.6 and 3.7]. This modified rubber was prepared by treating *NR* latex with a proteinase to hydrolyze the protein in the latex, which makes it more water-soluble. Consequently, the protein can be washed away easier during processing.

ENR-50 is another type of modified *NR* that can give several improved properties, such as better oil resistance and lower gas permeation than the other form of *NR*. Epoxidation of *NR* in latex stage to high modification level can be readily carried out by peracid, which is generated from the reaction of formic acid and hydrogen peroxide [3.8]. This reaction will

change the unsaturated bonds in the *NR* into epoxide groups. The degree of epoxidation can be estimated, and as for the *ENR-50* it is about 50 % of its double bonds involve in the modification [3.9].

Commercial Polyethylene *PE* and plasticized Polyvinylchloride *pPVC* that are used in this project comes in the form of granule. In TSC technique and mechanical test however, the sample is required in sheet form. For that reason, the polymers and their composites in this study were prepared via solution casting, in order to get appropriate sample geometry for the tests. As many samples were needed particularly for the mechanical test, special glass containers with the dimension of 15 cm x 30 cm were designed for drying process.

Generally, the thicknesses of samples were prepared according to the nature of certain test. TSC technique for instance does not need a thick sample; the thickness around 0.04 mm to 2 mm is good enough depending on the amount of poling field, F_p chosen. On the other hand, in tensile test it depends on the type of material to be tested. For elastomeric material the thickness of 1 mm to 3 mm is needed for the chosen dimension of D 638-61T standard from ASTM. While for *pPVC*, *PE* and *polymer-OMON* composites, the thickness in the range of 0.2 mm to 0.7 mm was used in the mechanical test [3.10, 3.11 and 3.12].

3.1.2.1 *SMRL, DPNR, ENR-50* and Composites

Natural rubbers as received were in big chunk and they were then cut into smaller pieces (approximately 1 mm x 1 mm x 5 mm) for sample preparation. They were then weighted and combined with toluene solution in glass beakers, before it left to swell with constant stirrings using magnetic stirrer for 3 days at room temperature. Even though it was hard to dissolve the rubbers, but soaking for a few days in toluene will make them swell. However, for *SMRL* and *ENR-50* with the high gel contain they required the aid from acetic acids in order to swell.

Certain amount of *OMON* and *Mon* were also weighted and put into the rubber-toluene mixture to prepare *natural rubber-OMON* composites. The detail amount of *SMRL*, *DPNR*, *ENR-50*, *OMON*, *Mon*, toluene and acetic acids used are listed in Table 3.1, 3.2 and 3.3. This is including the weight percent for the natural rubbers and *OMON* in the composites. After three days, the rubbers and their composites were ready to be poured into glass containers; which were carefully balanced earlier on a flat surface. In fact, this procedure is very important in order to get consistence thickness for the samples. Subsequently, they were all left to dry for one week at room temperature. After one week, these samples were removed from their containers for further drying; especially for the bottom side of the samples. They were then left to dry at room temperature for another one to two weeks.

Table 3.1
DPNR and DPNR composites with *OMON* and *Mon*

No.	*DPNR*		*OMON*		Toluene (ml) ± 1
	Weight (gm) ± 0.1	(%)	Weight (gm) ± 0.1	(%)	
1.	50.0	100	0.0	0	700
2.	19.0	95	1.0	5	300
3.	18.0	90	2.0	10	300
4.	17.0	85	3.0	15	300
5.	16.0	80	4.0	20	150
6.	15.0	75	5.0	25	150
7.	14.0	70	6.0	30	150
8.	14.0	70	6.0 (*Mon*)	30	150

Table 3.1: Materials used to prepare *DPNR* samples and the composites of *DPNR–OMON* and *DPNR–Mon*.

Physical appearances for the rubber sheets are yellowish in color and easy to stick among themselves. While for the rubber-*OMON* composites, the color varied from light gray to dark gray depending on the weight percent of *OMON* constituted as shown in Figure 3.5. Similarly, the sticky behavior of these pristine natural rubbers seemed to decrease with the

Polymers and Composites Polymer with *OMON* and *Mon*

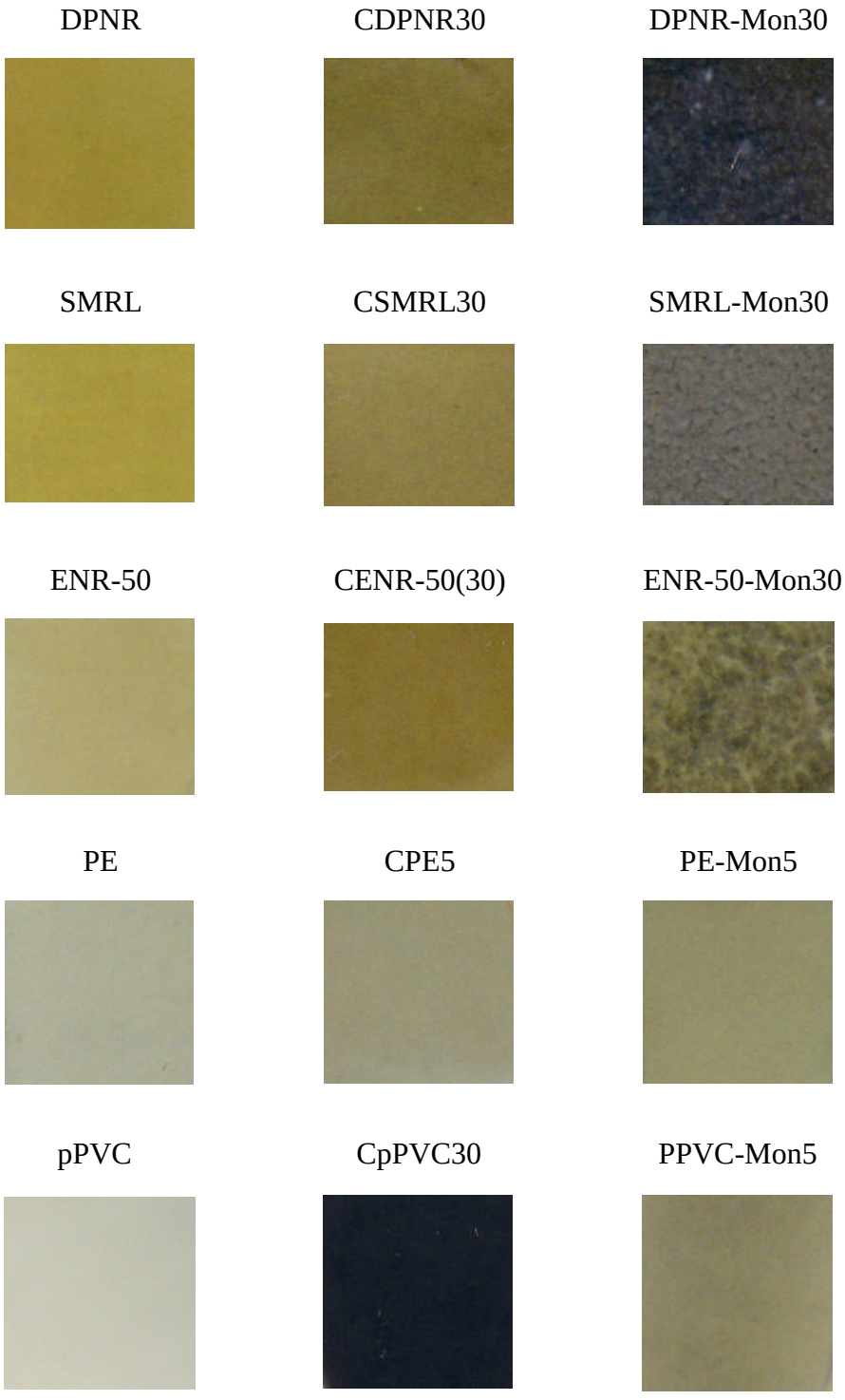

Figure 3.5: The samples of *DPNR, SMRL, ENR-50, pPVC, PE* and their respective composites with *OMON* and *Mon*.

Table 3.2
SMRL and SMRL composites with *OMON* and *Mon*

No.	*SMRL*		*OMON*		Toluene (ml) ± 1	Acetic Acids (ml) ± 0.25
	Weight (gm) ± 0.1	(%)	Weight (gm) ± 0.1	(%)		
1.	50.0	100	0.0	0	700	10.00
2.	19.0	95	1.0	5	300	2.00
3.	18.0	90	2.0	10	300	2.00
4.	17.0	85	3.0	15	300	2.00
5.	16.0	80	4.0	20	150	1.50
6.	15.0	75	5.0	25	150	1.50
7.	14.0	70	6.0	30	150	1.50
8.	14.0	70	6.0 (*Mon*)	30	150	1.50

Table 3.2: Materials used to prepare *SMRL* samples and the composites of *SMRL–OMON* and *SMRL–Mon*.

Table 3.3
ENR-50 and ENR-50 composites with *OMON* and *Mon*

No.	*ENR-50*		*OMON*		Toluene (ml) ± 1	Acetic Acids (ml) ± 0.25
	Weight (gm) ± 0.1	(%)	Weight (gm) ± 0.1	(%)		
1.	50.0	100	0.0	0	500	10.00
2.	19.0	95	1.0	5	240	2.00
3.	18.0	90	2.0	10	240	2.00
4.	17.0	85	3.0	15	240	2.00
5.	16.0	80	4.0	20	100	1.50
6.	15.0	75	5.0	25	100	1.50
7.	14.0	70	6.0	30	100	1.50
8.	14.0	70	6.0 (*Mon*)	30	100	1.50

Table 3.3: Materials used to prepare *ENR-50* samples and the composites of *ENR-50–OMON* and *ENR-50–Mon*.

increase amount of *OMON* inclusion. The appearance of natural-rubber composites overall look quite homogenous, without any obvious trace of *OMON* cluster as in the rubber-*Mon* composites. These samples gave various thicknesses, which were in the range of 0.2 mm to

3.0 mm depending on the amount of rubbers and *OMON* inclusion in the samples. *OMON* composites with *SMRL, DPNR* and *ENR-50* rubbers are abbreviated as *CSMRL, CDPNR* and *CENR-50* respectively.

3.1.2.2 Plasticized Polyvinyl Chloride, *pPVC* and Composites

The white granules of *pPVC* were weight and mixed with 150 ml of methyl ethyl ketone or *MEK* solution in a glass beaker. For the first few hours, heat was applied around 40 °C to 50 °C with consistence stirring by a magnetic stirrer. After two days of stirring at room temperature, the *pPVC* granules seemed to dissolve and ready to be poured in a glass container. *OMON* and *Mon* were then added accordingly as shown in Table 3.4 to make the composites of *pPVC-OMON* (*CpPVC*) and *pPVC-Mon* composites.

Table 3.4
pPVC and pPVC composites with *OMON* and *Mon*

No.	Plasticized PVC, *pPVC*		*OMON*		MEK (ml) ± 1
	Weight (gm) ± 0.1	(%)	Weight (gm) ± 0.1	(%)	
1.	20.0	100	0.0	0	150
2.	19.8	95	0.2	1	150
3.	19.6	90	0.4	2	150
4.	19.4	85	0.6	3	150
5.	19.2	80	0.8	4	150
6.	19.0	75	1.0	5	150
7.	14.0	70	6.0	30	150
8.	19.0	95	1.0 (Mon)	5	150

Table 3.4: Materials used to prepare samples of pPVC and the composites of *pPVC–OMON* (*CpPVC*) and *pPVC –Mon.*

The mixtures were left to dry at room temperature for three days, before a sheet of *pPVC* can be removed from the glass container. Thereafter the bottom side of the sample was let to dry for another week. *pPVC* sheet had a white color and by adding *Mon* it had turned into a dark gray at the bottom side. This is due to the aggregation of *Mon* that had formed

the dark cluster. On the other hand, *pPVC* composites with *OMON* varied in colors from pinkish to dark chocolate depending on the amount of *OMON* content. The thickness obtained for *pPVC* sheets as well as its composites were in the range of 0.6 mm to 0.8 mm. Therefore, these samples can be used for both TSC measurement and mechanical test.

3.1.2.3 Polyethylene, *PE* and Composites

Similarly to the *pPVC*, *PE* granules were carefully weighted before being mixed with 50 ml of toluene in a glass beaker. The mixture was then stirred with a magnetic stirrer at the temperature of 40 °C to 50 °C for one hour until the entire *PE* granules were dissolved. Thereafter, *OMON* and *Mon* were added in the mixture as listed in Table 3.5 accordingly to make the composites of *PE-OMON* (*CPE*) and *PE-Mon* composites. A glass container was balanced earlier in an oven before pouring the *PE* mixture. The drying process then took about two hours within a temperature range of 90 °C to 100 °C.

Table 3.5
PE and PE composites with *OMON* and *Mon*

No.	*PE*		*OMON*		Toluene (ml) ± 1
	Weight (gm) ± 0.01	(%)	Weight (gm) ± 0.01	(%)	
1.	6.00	100	0.00	0	150
2.	5.94	99	0.06	1	150
3.	5.88	98	0.12	2	150
4.	5.82	97	0.18	3	150
5.	5.76	96	0.24	4	150
6.	5.70	95	0.30	5	150
7.	5.70	95	0.30 (*Mon*)	5	150

Table 3.5: Materials used to prepare *PE* samples and the composites of *PE–OMON* and *PE–Mon*.

The hot sample was let to cool down in room temperature for about one hour, before a well formed sheet of *PE* can easily be removed from the container. Finally, this sample was left for further drying in a few days at room temperature. Since the thickness of *PE* sheets were

quite thin (0.04 mm to 0.4 mm), their white color were faded as can be seen in Figure 3.5. While the color of *PE-OMON* composites was light gray. In fact, they seemed to be more homogenous compared to the *PE* composite with *Mon*.

Throughout the process of sample preparation, a standard procedure for each set of sample were tried to be maintained. The significance was to produce similar samples from several batches of preparations. This is important for tensile test that required many samples as suggested by the ASTM standard. The obtained samples of pristine polymers and their respective composites were then kept in a desicator to avoid moistures. This effort is very important especially for TSC measurement, which is known sensitive to moisture content in a specimen.

3.2 Instrumentation and Experimental Methods

The instrumentation and experimental methods for both TSC measurement and tensile test followed the basic principles as previously discussed in Chapter 2. Some standards from *American Standard for Testing Materials* ASTM were also used as guide lines, especially for experimental set-up and apparatus to cut samples for tensile test. In order to give good controls and data acquisitions, a computer program was developed in TSC instrumentation. Another computer program was also developed to help the process of analyzing TSC data.

3.2.1 TSC Technique

Previously in Chapter 2, TSC measurement was described as a very sensitive technique in dielectric spectroscopy. However, it can generate valuable results for material studies. For example, the good control of heating rate (*h*) will allow this technique to detect dielectric relaxations of dipoles and space charges within a wide range of frequency. Therefore, the instrumentation and experimental method in TSC technique has to follow strict procedures to ensure good TSC results.

3.2.1.1 TSC Instrumentations

The good sensitivity of TSC technique actually depends on its instrumentation. Such as a TSC system with temperature controller that capable to handle a wide range of temperature *T* (-200 °C to 300 °C) and the good control of heating rate *h*. For that reason, a sensitive thermosensor and temperature controller are very important to give a stable heating rate and accurate readings. Moreover, it must be able to measure current, *I* within the range of pico (10^{-12}) to femto (10^{-15}) ampere. Overall, the whole TSC system must be robust enough to stand a long working time. In which for a global TSC test for example, it take about five to six hours to finish the whole experiment. Therefore, it is important to have a proper set-up for the TSC measurement. Figure 3.6 shows the schematic diagram of TSC system used in this work.

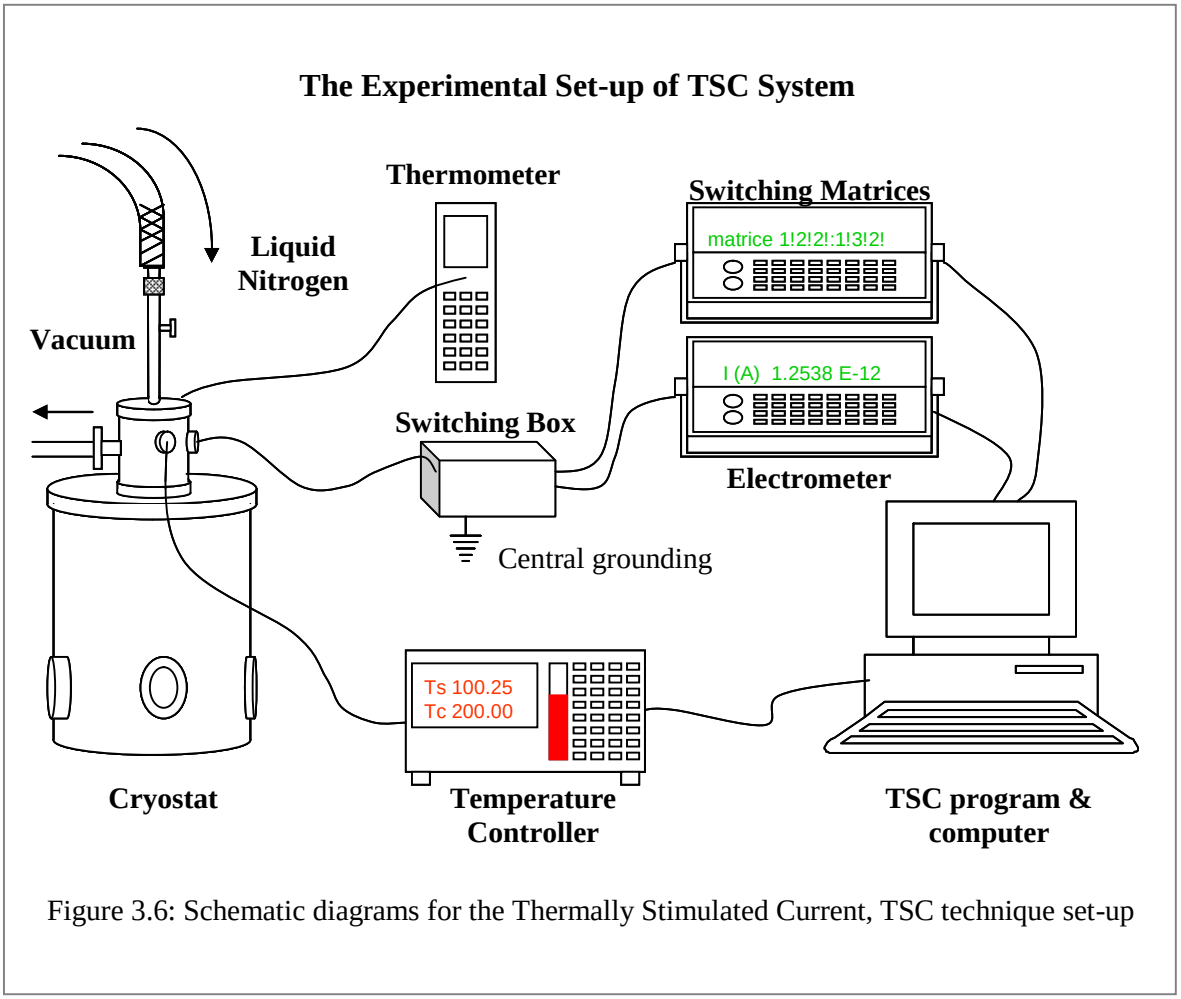

Figure 3.6: Schematic diagrams for the Thermally Stimulated Current, TSC technique set-up

3.2.1.1.A Cryostat

A cryostat from Janis Instrument was used in the set-up for sample mounting. This cryostat can be vacuumed through a special opening that can be connected directly to a vacuum pump. It was also designed with a nozzle on its top that can be connected to a liquid nitrogen tank. A special opening to release the pressure from liquid nitrogen was placed at the side of the nozzle. Moreover, this cryostat provides the grounds for sensor mounting as well as electrical connectors.

3.2.1.1.B Electrodes

The circular metallic-electrode system used in this TSC set-up was made of brass which is a common practice in dielectric measurements [3.13]. In fact, the electrode system was a three-terminal type with a guard-ring as illustrated in Figure 3.7. The significant of guard-

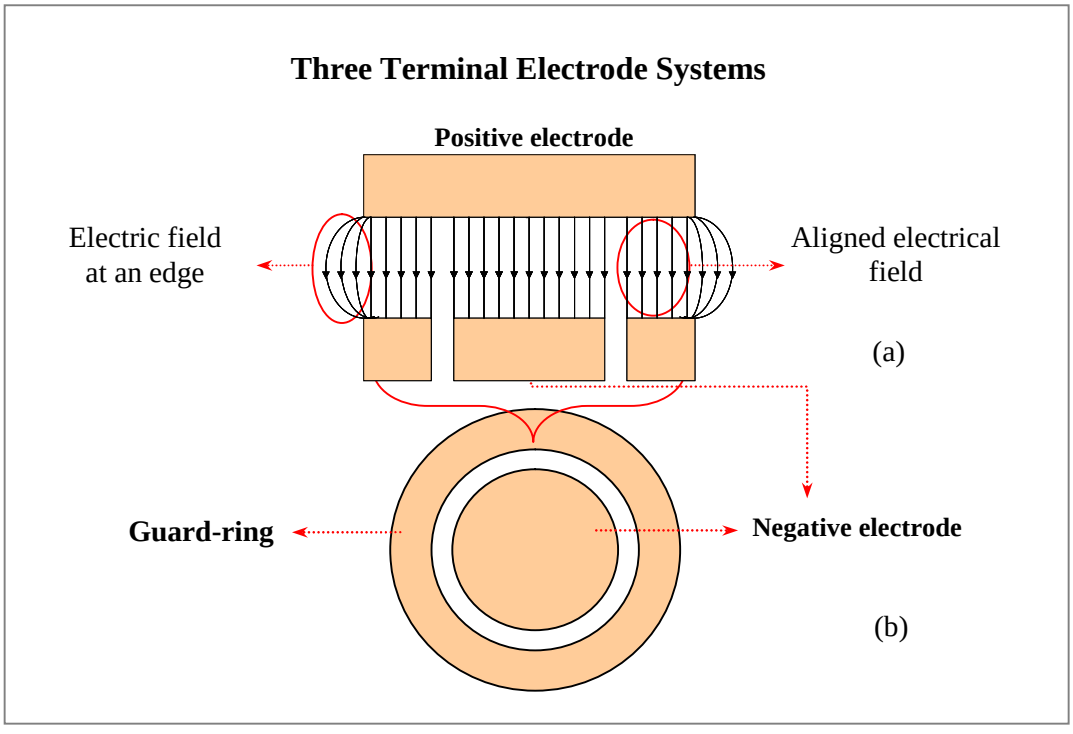

Figure 3.7: Schematic diagram for a cross section (a) of the 3-terminal electrode system which is comprised of circular guard-ring, positive and negative electrodes (b).

ring in TSC measurement is to avoid any inhomogeneous electrical field during the poling process [3.14]. The used of guard-ring actually is very important especially when dealing

with dielectric materials. The guard-ring can avoid or at least minimize surface conduction which may occur [3.15] during TSC measurement. In view of that, a guard-ring was placed around the negative electrode. There was also a suggestion to put the guard-ring around the positive electrode. In practice however, it had caused some charges to jump over from the positive electrode to guard-ring. As a result it created sparks and subsequently burnt the tested sample. For that reason, the guard-ring in this set-up was fixed around the negative electrode.

3.2.1.1.C Sample Holder

It was mentioned earlier in the introduction that TSC measurement involves an extreme temperature changes. For example, after the poling process at 100 °C the temperature of a sample has to be quenched down to −180 °C. It was then followed by a heating process up to 250 °C. This extreme conditions thus can make the sample and its holder to experience a sudden changes in temperature that causes them either expanding or shrinking alternately. As a result the contact area between the sample and electrodes were badly affected, which can contribute to the noises in measurements. Some sample holders made from insulators cannot stand this extreme condition. Normally, such holders will crack which then leads to the lost of current detections.

Sample holder as illustrated in Figure 3.8 is a combination of metal and Teflon polymer. It was created specifically to minimize the cracking problem. Even though the shrinking and expanding of the materials cannot be avoided, but the problem of contact stabilization can still be solved. The design of this sample holder utilized two springs, which were placed on top of the positive electrode and at the bottom of negative electrode. They had a function to push the electrodes towards sample, which can give a consistence contact through out TSC experiment.

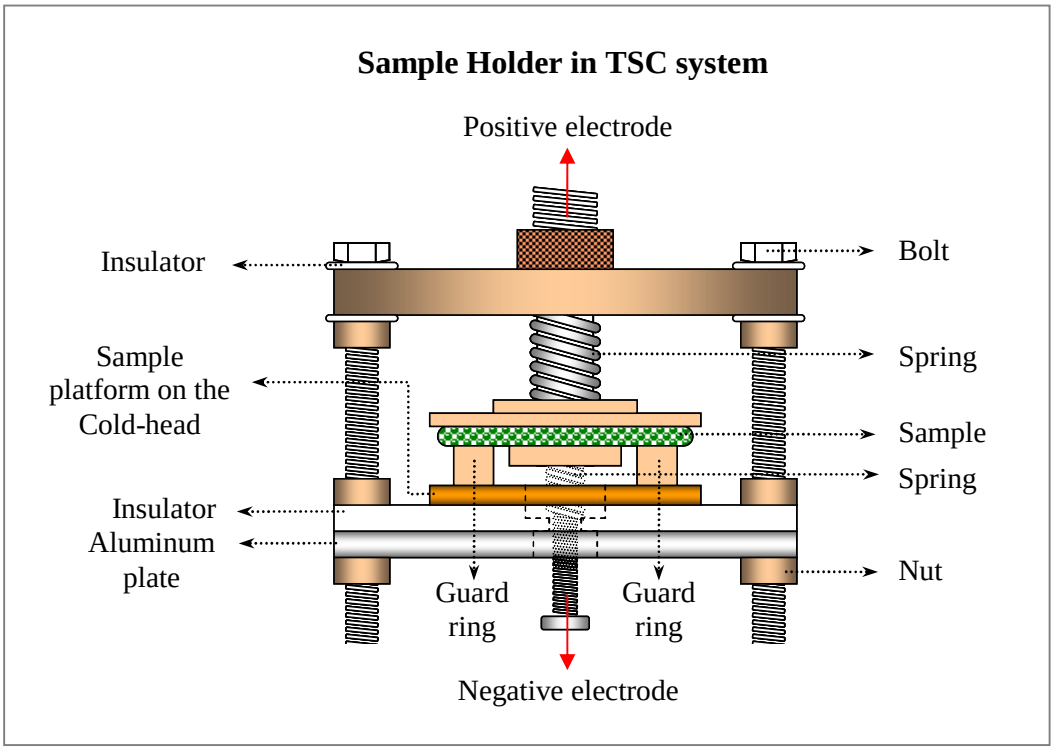

Figure 3.8: Illustration of the sample holder customized for the TSC technique. This metallic-polymer sample holder can stand extreme temperature changes and managed to maintain its contact with sample through out the experiment.

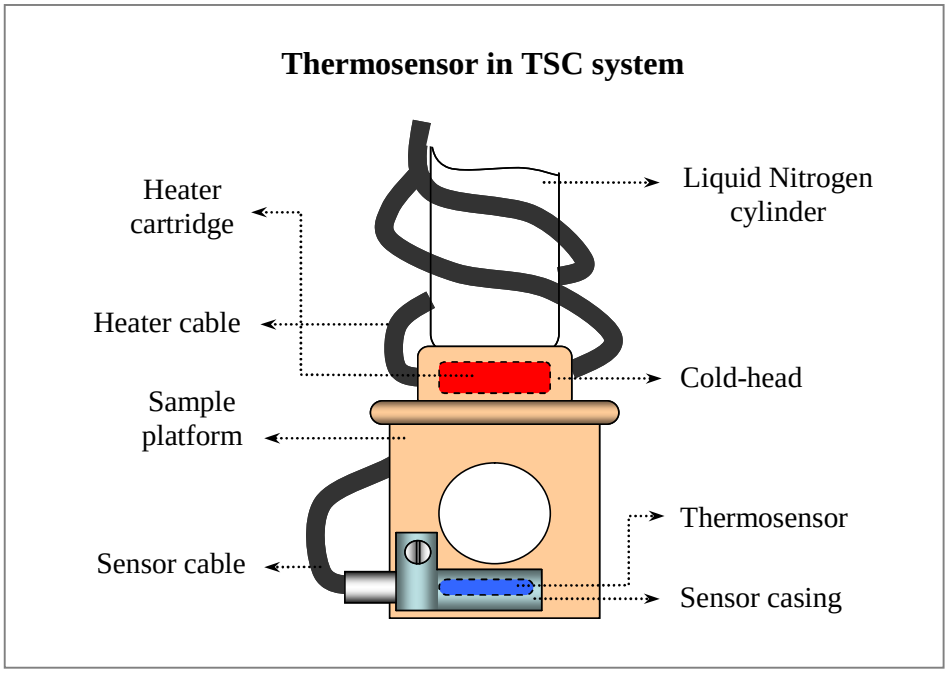

Figure 3.9: A schematic diagram for thermosensor mounting. The thermosensor and its casing is fixed on the sample platform.

3.2.1.1.D Temperature Controller

The temperature controller used in this TSC system is model TC330 of LakeShore. It is used to heat up and stabilizes the temperature of a sample at a given temperature. The heat is supplied by a heater cartridge that was placed at the cold head inside the cryostat. A platinum sensor RTD-PT103 was located at the sample platform to detect the temperature of tested sample. This temperature controller system can raise a sample temperature up to 600 °C, with the heating rate is in the range of 0.1 to 100 °C/min. The given accuracy for this temperature controller is ± 0.01 °C. The TC330 temperature controller also comes with IEEE-488 interface card that allows integrations with computerize system (Appendix B). The thermosensor in Figure 3.9 used to be located near the cold head by means of a special adhesive. However, it could not stand the extreme temperature changes that had made it cracked. This condition affected the thermosensor contact and the functions of temperature controller in the TSC system. Therefore, a metallic casing was designed to place the sensor firmly at a new location, which is closer to the sample position.

3.2.1.1.E Electrometer

An electrometer model EM6517 from Keithly was used to generate a direct current, DC voltage V_p during the poling process. This electrometer capable to generate voltage sources up to 100V at 10 mA and 1000V at 1mA. Besides, it comes with an option to measure electrical current, *I* without the presence of voltage source. Therefore, it gives an advantage for the TSC system which measures the thermally stimulated current of a tested sample. Moreover, this electrometer can make measurement within a range of $1x10^{-18}$ A to $2.1x10^{-3}$ *A* and these values are good enough for the TSC measurement. The accuracy of current *I* measurement as given by manufacturer in Appendix C is ± 1.0 % reading value, while for voltage source the accuracy is ± 0.15 % setting value.

3.2.1.1.F Switching Matrices

TSC measurement involves several processes, and some are very critical for the technique. Measuring small electrical current, *I* at a stable heating rate, *h* are only a part of the critical processes. There are some other procedures such as applying voltage for the poling process and short-circuit the electrodes to remove excess charges which are not less important. For that reason, a switching matrice machine Model SM770 from Keithly was used to make an automated TSC system. This switching machine operates as an intermediate ground for the electrode system in cryostat and electrometer. Illustration of the switching matrice can be seen in Figure 3.10. Any changes for the electrodes connections to the electrometer thereby can be controlled through a computer via IEEE-488 interface card (see Appendix D). This method practically reduces many noises and increases the efficiency of TSC system.

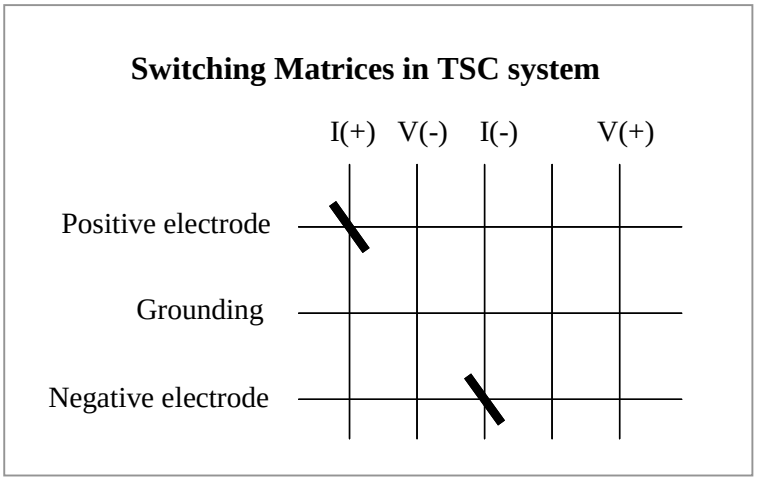

Figure 3.10: A matrice used in the switching matrices system for connections between the electrodes and electrometer.

3.2.1.1.G Switching Box

The switching box served as a base for the connections from switching system, electrodes, electrometer and groundings. It became the central groundings from all equipments in the TSC set-up. It is important to centralize the grounding in order to avoid any loop current that may arise if the equipments are grounded individually [3.16 and 3.17]. Loop current can cause noises in the TSC measurement.

3.2.1.1.H TSC software and Computer

Right through the discussion in this section, apparently, an automated system is needed for the TSC technique. Therefore, a special program was developed to organize the usage of electrometer, switching matrice and temperature controller. The efficiency of TSC system seemed to improve, especially when the important parameters such as poling temperature T_p, poling voltage V_p and poling time t_p are controlled simultaneously by the program.

A computer program for TSC measurement as shown in Section 3.2.1.2.B was developed using TestPoint V.2.0 software. This interactive program allows user to choose parameters to be measured accordingly to the tested sample. Despite the fact that this program makes the TSC measurement almost fully automated, it also gives an advantage for user to make interruptions during the experiment. This function is particularly important when it comes to the heating rate stabilization. Finally, the process of data acquisitions that may take several hours can be left to the program to operate. During this process, the colleted data can be used for graph plotting in the front panel display, and concurrently send to the Lotus 123 files as well as the file of back-up storage.

3.2.1.2 Experimental Method and Calibration of TSC system

The background study of a material to be tested is highly suggested in order to choose the right parameters for TSC measurement. Such as, the knowledge about the glass transition temperature T_g of a sample is very useful in choosing an appropriate poling temperature T_p. However, before any measurement can be conducted the TSC system has to be calibrated. Calibration is an important procedure in any system or tools for measurement. In this work it was done with some known polymers to see the performance of developed TSC system. Poly(methyl methacrylate) *PMMA* and Poly(ethylene terephthalate) *PET* are among the polymers which are frequently used for calibration.

3.2.1.2.A Physical set-up

Preliminary preparation for TSC measurement was carried out by polishing the electrodes as well as the metal parts of sample holder. This procedure was done to remove any dirt from the previous experiments. Moreover, it can remove any oxidations that might develop on the electrodes surfaces. The next step was washing these parts with detergent and water to take out any excess of polish paste. This process was performed repeatedly before the drying procedure with a hot air drier.

After the drying process, electrodes and sample holder were then ready to be fixed on a platform at the cryostat cold-head. Lastly, these parts were washed with acetone and left to dry at room temperature. As mentioned earlier, *PET* and *PMMA* polymers were used for the calibrations of TSC system, which represent the semi-crystalline and amorphous group respectively. These samples were cut into a rectangle shape with the dimension of 3 mm x 3 mm to cover the whole surface of positive electrode, as well as the guard ring.

A sample to be tested was then placed in a sandwich form between the electrodes as shown in Figure 3.11. After the sample holder was firmly fixed, they were then moved into the

Sample Mounting in TSC system

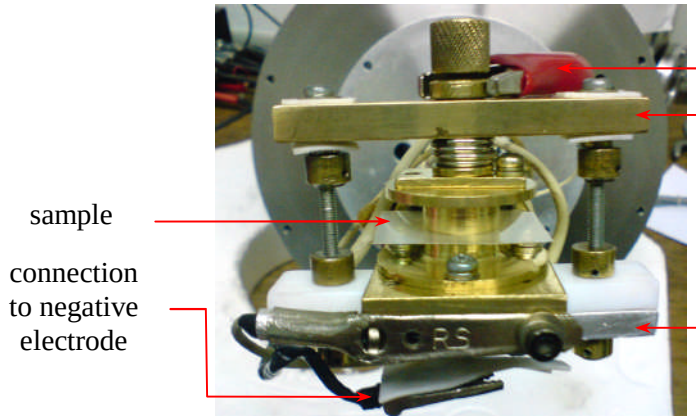

Figure 3.11: TSC sample is mounted in sandwich form arrangement between the positive and negative electrodes. It is firmly hold by the sample holder during TSC measurement.

cryostat. Some silicon grease had to be applied around the cryostat mouth before the cover mounting. This procedure is to avoid any leakage in the TSC system, and thus the cryostat can be pumped down at low pressure. Similarly, all joints with "O" rings were put on the same grease before being fitted.

3.2.1.2.B TSC Experiment for Calibration

Once the physical set-up was done, the TSC software as well as Lotus 123 was executed. The location for back-up storage file must be defined by user as instructed on the front panel in Figure 3.12(a). It is followed by pushing the button CONFIG that will bring users to the "Configuration" panel, where all parameters required to run the test have to be entered appropriately in each parameter boxes. While the "CONFIG2" button will bring user to "Cofigurasion2" panel where, information regarding the TSC test can be recorded. The equipments IP addresses are also kept in this panel. Finally, a TSC experiment will be started once the "Switch" toggle at the front panel is put into "On".

Figure 3.12(b) shows the parameters used for the calibration of TSC technique and set-up, where in this case *PET* polymer was used as the referenced sample. A poling temperature T_p at 100 °C was chosen since it was close to the T_g of *PET* that is around 90 °C to 110 °C. The test then started with TSC program instructed temperature controller to increase the sample temperature to T_p, with "RANG1: HIGH (3)" at a heating rate of 4 °C/min (HR 1). Shortly after the *PET* was stabilized at T_p for 5 minutes ($t_{stable1}$), 275 V of DC voltage (V_p) was applied on the sample to gain an electrical field of 5 MV/m. This poling process was performed on the sample for 45 minutes (t_p) before the quenching procedure took its place. At this stage, TSC program stopped any heating activity by the temperature controller and continuously monitored the temperature of *PET* sample.

The quenching process was carried out by letting the liquid nitrogen to drastically lowered the sample temperature to T_o, a minimum temperature that was about -100 °C for *PET*.

Thermally Stimulated Current, TSC Program

Front Panel

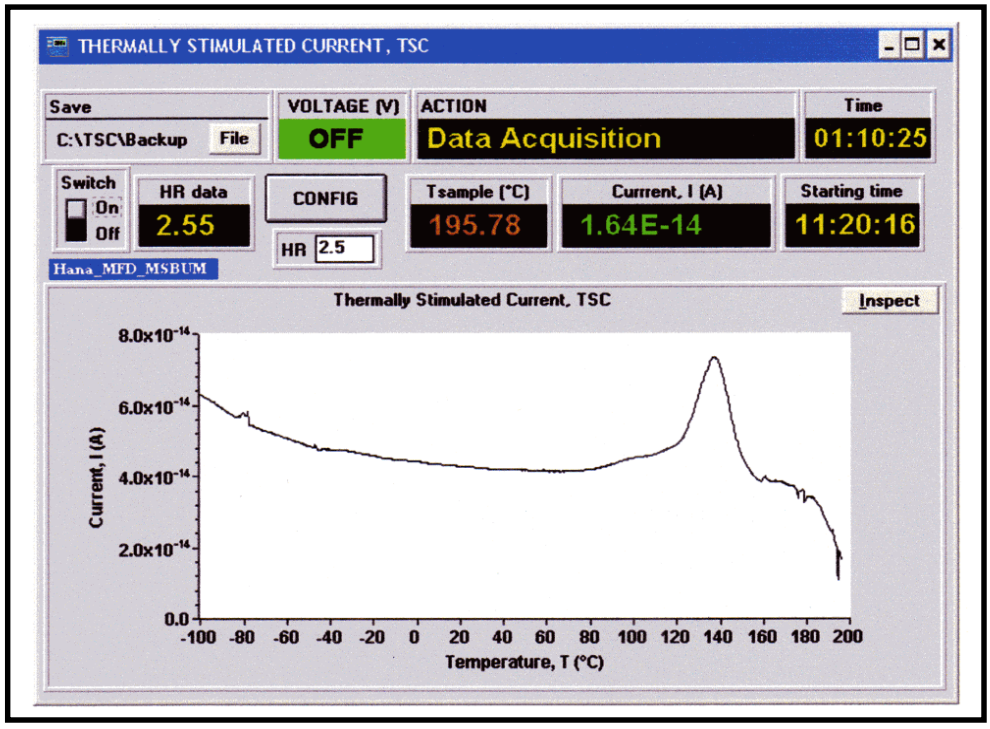

Figure 3.12(a): The front panel of TSC program for the calibration experiment using *PET* polymer. The panel shows the global TSC thermogram for this polymer.

Configuration Panel

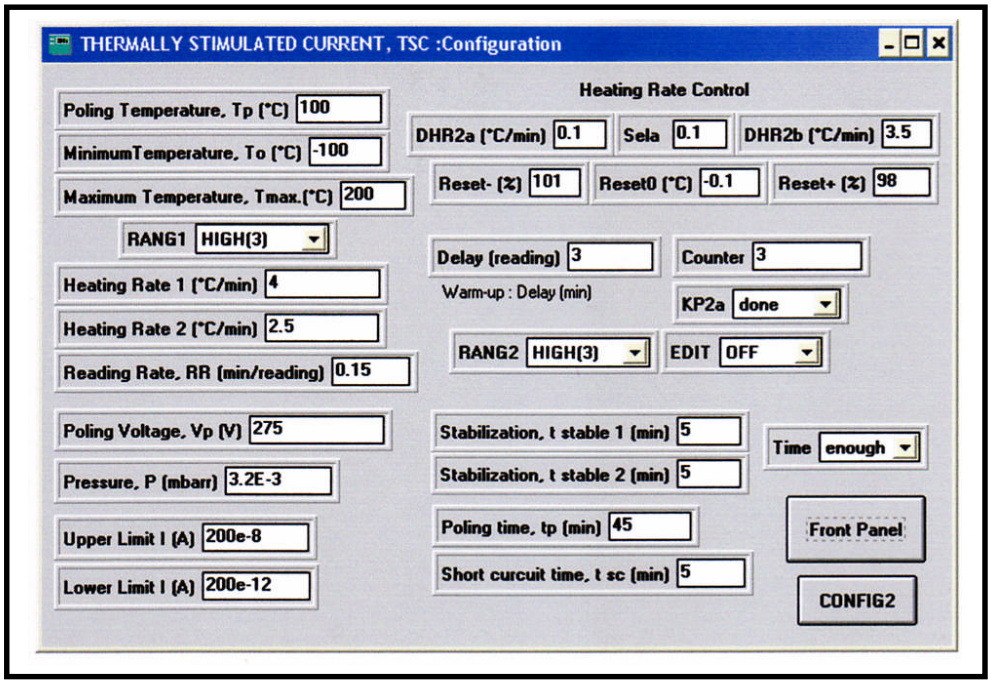

Figure 3.12(b): The configuration panel of TSC program shows the parameters used in the calibration experiment with *PET* polymer.

Actually, user can choose any value that is low enough to freeze dipoles and space charges inside the sample. Soon after the T_o was achieved and stabilized, the electrodes were then short-circuited for 5 minutes (t_{sc}) to remove any surface charges. During the stabilization period that took about 5 minutes ($t_{stabile2}$), the temperature was allowed to decrease slowly for stabilization.

After the stabilization period was finished, the temperature controller started to ramp again with "RANG2: HIGH(3)" and preliminary heating rate of 0.1 °C/min (DHR2a). TSC program continuously monitored the actual heating rate from its data acquisitions. When the heating rate was stable for "3 readings" (Delay and Counter), the program increased the rate with 0.2 °C/min (step) until the targeted rate of 2.5 °C/min (HR2) was achieved. However, an *over-shoot* condition may happen where the heating rate is increased beyond the given upper limit 3.5°C/min (DHR2b). A new cycle of ramping then will be executed with the preliminary heating rate. In this situation, user can interrupt the TSC program via the "Delay" parameter to assist the heating rate stabilization. The developed TSC system can also handle a low heating rate, such as 1 °C/min with a fluctuation about 0.05 °C/min within 9 second.

The data acquisitions process were carried out by the TSC program at the reading rate of 0.15 min/reading (RR) or 1 reading per 9 seconds. This rate can be chose by users and the rate of 0.15 to 0.25 min/reading were normally used in this study. The collected data were then used to plot a graph as displayed on the front panel. The heating rate value (HR data) which was calculated from the data is displayed above the graph. These data were sent to the "C:\TSC\Backup" file for default storage, which is saved in ASCII form. They were also sent to the "TSC1.WK4" and "TSC2.WK4" files which were priory opened in Lotus 123 program. This routine was continuously carried out until the sample temperature reached its maximum temperature T_{max} that was 250 °C for the *PET*. In another test, this

TSC system managed to handle a higher T_{max}, which was about 300 °C. The TSC program then stopped all the tasks carried out by the measurement units. It all released all the electrodes connections via the switching matrices units. Finally, the program showed a "FINISH" message on the "Action" display to mark the end of TSC measurement.

3.2.1.2.C Data Analyzing

For the purpose of data analyzing, a program named as *TSC Analysis* was developed using TestPoint Version 2.0. It was used to analyze the TSC thermogram of *PET* as shown in Figure 3.13. This program is very useful to locate the exact position of a peak, hump and trends that indicate the effects of relaxation processes. In addition, this computer program capable to calculate area under the curve of a peak and some important parameters. For example, the activation energy *E* and natural frequency, f_o.

TSC Analysis Program

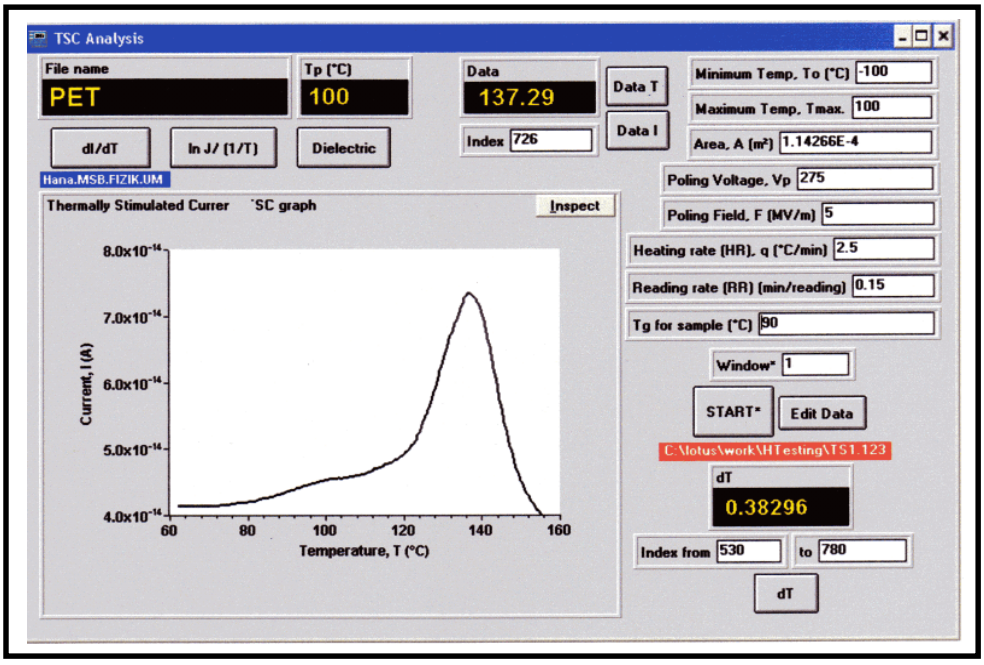

Figure 3.13: The TSC Analysis program used on the collected data of *PET*. This program helps to determine the location of a peak or hump and also and the maximum temperature T_{max}.

The thermograms of TSC calibrations using *PET* and *PMMA*

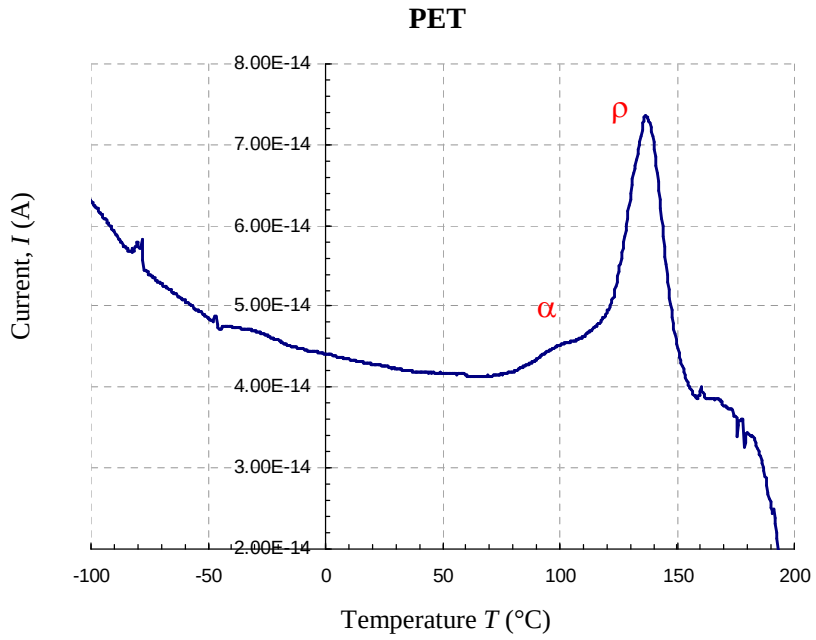

Figure 3.14(a): The TSC thermogram for *PET* shows a shoulder around 96.55 °C which arises from the α peak. The prominent peak at 126.38 °C is identified as ρ peak.

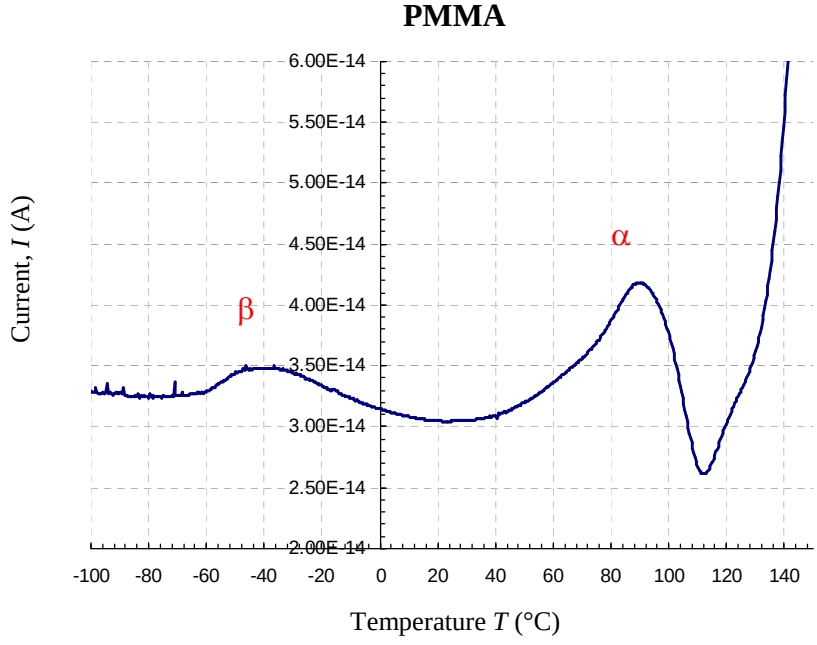

Figure 3.14b: The α peak for the TSC thermogram of *PMMA* can be clearly observed at 90 °C, while a hump around -40 °C is assigned as β peak.

The global TSC thermograms from TSC calibrations using *PET* and *PMMA* polymers are shown in Figure 3.14(a) and Figure 3.14(b) respectively. In Figure 3.14(a), the small hump around 91°C can be associated to the glass transition temperature, T_g which is referred as an α peak. The α peak however, can be clearly observed around 90 °C in case of *PMMA* in Figure 3.14(b). This maximum temperature T_{max} of the α peak is comparable with the T_g of *PMMA*. In case of *PET*, the prominent peak at 126 °C indicates space charge relaxation that is assigned as the ρ peak, whereas the peak around –40 °C in the thermogram of *PMMA* is recognized as the β peak which signifies the side chains relaxations.

The maximum temperatures T_{max} of these peaks as obtained from the TSC measurements are in the range reported by other researchers, which are listed in Table 3.6 for comparison.

Table 3.6
The Maximum Temperature T_{max} of some TSC Peaks

Sample	Peak	T_{max} Calibration (°C) ± 0.01	Previous value of T_{max} (°C)
PET	ρ	26.38	90 to 150 [3.18, 3.19 and 3.20]
	α	96.91	80 to 105 [3.18, 3.19 and 3.21]
PMMA	α	89.94	95 to 118 [3.22, 3.23 and 3.24]
	β	-37.50	-40 to -20 [3.22 and 3.24]

Table 3.6 lists the maximum temperature T_{max} of some TSC peaks from the calibration process using *PET* and *PMMA* polymers. The temperatures are comparable with those of previous researchers.

These observe thus indicates the reliability of the developed TSC measurement system in this work. From Table 3.6, the wide temperature range reported was due to some physical characteristics of individual tested polymers. Such as, even though *PET* is an amorphous polymer but if certain amount of stress is applied it will induce the formation of crystallite

structure within the *PET*. Such structures in the polymer affect its T_g, which can also shift the α peak position toward a higher temperature in the TSC plot.

There are a few precautions that must be taken into consideration in order to generate good TSC results. Direct contact with sample to be tested should be avoided, as the transferred moisture and impurities can be easily detected in TSC measurement. Throughout TSC test, ones should not get nearer to the TSC set-up. Observations showed that it may disturb the measurement of TSC current, which is significantly low around 10^{-15} to10^{-9} *A*. This effect perhaps can be associated with the generated electrical field in human body [3.25]. In spite of that the developed TSC system thus far manages to produce TSC thermograms with minimum noise, in both current and temperature measurements.

3.2.2 Mechanical Experiment

In any mechanical test it is very important to ensure that the right apparatus to be used with certain type of samples, as well as their geometries. Each type of material has its individual characteristics and limitations. In fact, they may respond differently in certain condition. Therefore, particular geometry and thickness must be put into considerations to study mechanical property effectively.

3.2.2.1 Tensile Test Instrumentations

Various standards for tensile test are mostly depending on the material and the mechanical property to be investigated. In this work, the D 638-61T, D412-62T and D881-61T of ASTM standard [3.9, 3.10 and 3.11] were used as guide lines to design proper instrumentations for tensile test. The instrumentation was carried out appropriate to the prepared samples of polymers and their respective composites, which are in the sheet form.

3.2.2.1.A Sample Geometry

According to the D 882-61T standards, polymers in general can be classified into two main categories. They are the *rigid plastics* and *non-rigid plastic* groups, such as *PMMA* and natural rubber respectively. Polymers and their composites in this study overall can be classified as the *non-rigid* group. The chosen geometry for the samples thus was based on the Type IV of D 638-62T *dumbbell* shape, as well as the D 412-62T of ASTM standards. Figure 3.15 illustrates the schematic drawing of the chosen shape and dimensions, which appropriate with the ranges of specimen thickness as listed in Table 3.7. A *dumbbell* mold in Figure 3.16(a) was made according to these dimensions to assist the cutting process.

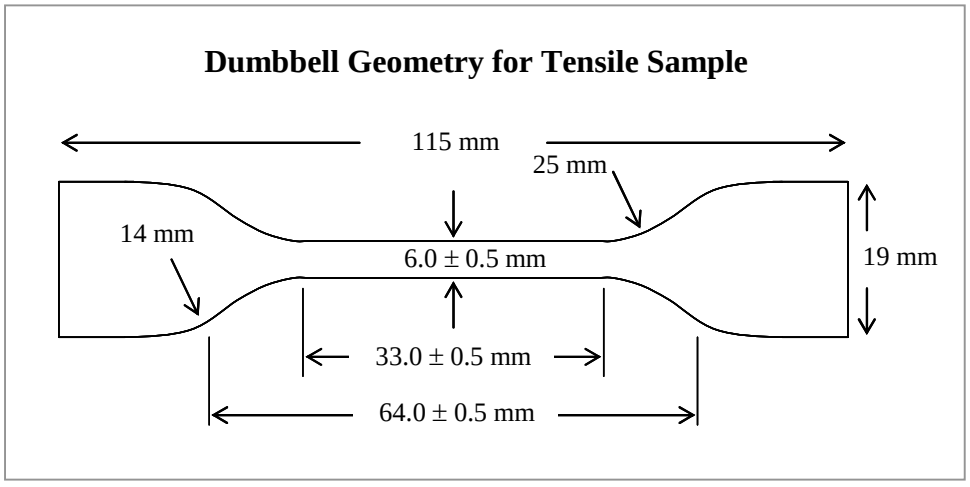

Figure 3.15: A dumbbell shape with dimensions according to the D638 of the ASTM standard

Table 3.7
The Thickness of Polymers and Respective Composites

No.	Polymers and their composites with *OMON* and *Mon*	Thickness, *d* (mm) ± 0.01
1	SMRL, DPNR and ENR-50	0.20 to 3.00
2	Plasticized PVC (pPVC)	0.60 to 0.80
3	Polyethylene (PE)	0.18 to 0.36

Table 3.7: The sample thicknesses of pristine polymers and their composites with *OMON* and *Mon* which were used in the tensile tests.

3.2.2.1.B Sample Cutter

Once the geometry for samples was decided, the attention was then focused on the cutting procedure. A sample to be tested in tensile test must have smooth and clean cut particularly around the *gauge length* up to its neck [3.9 and 3.26]. Any defect in this area, even a small slash will create a weak point to the sample. The effects can be seen when running a tensile test. The applied force distribution can be interrupted as it was centered on the defect point, which then resulted in premature sample failure.

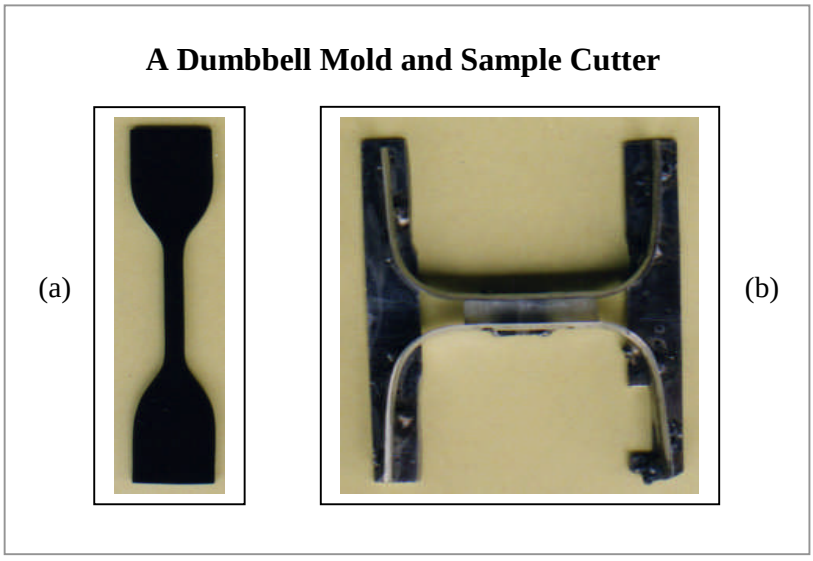

Figure 3.16: A dumbbell shape mold in (a) is used in the cutting process with the customized cutter in (b) for tensile test samples.

For that reason, a cutter was customized specifically for the chosen dimensions as shown in Figure 3.16(b). This cutter was made of two metal plates, which were grinded earlier on one side to sharpen them. It was then followed with the bending process on a rod with 25 mm radius for each end of the plates. Finally, the bended plates were aligned parallel to each other with a separation of 6 mm before being soldered together. The design of this customized cutter was focused on the critical areas, which are the *gauge length* and area around the neck. While for the upper part above the neck, a sharp scissor or a blade were used to cut the samples.

3.2.2.1.C Sample Holder

An appropriate sample holder to run the tensile test was customized to suit the specimen types and their dimension. The design of this sample holder as illustrated in Figure 3.17(a) and 3.17(b) follows the D 638-61T and D 412-62T of ASTM standards. This design also

Customized Sample Holders for Tensile Test

Moveable member

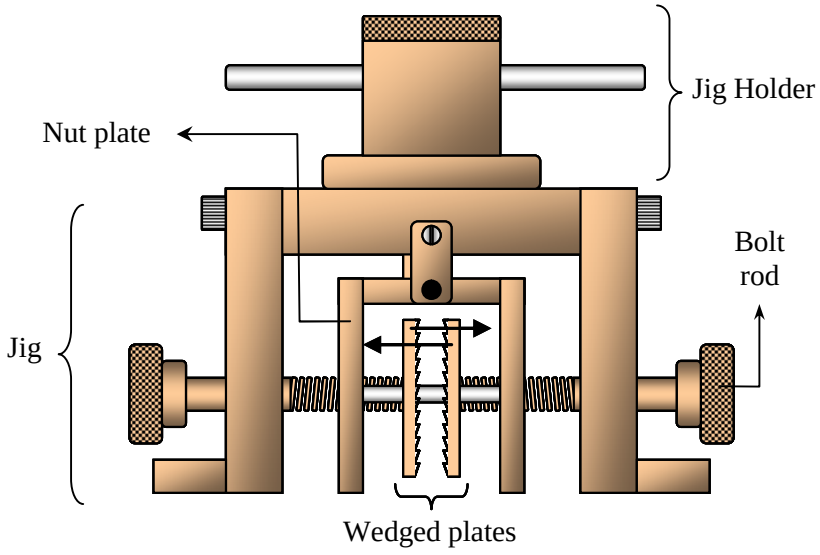

Figure 3.17(a): The *moveable member* which comprise of bolts and nut plates that can align itself when force is applied.

Fixed member

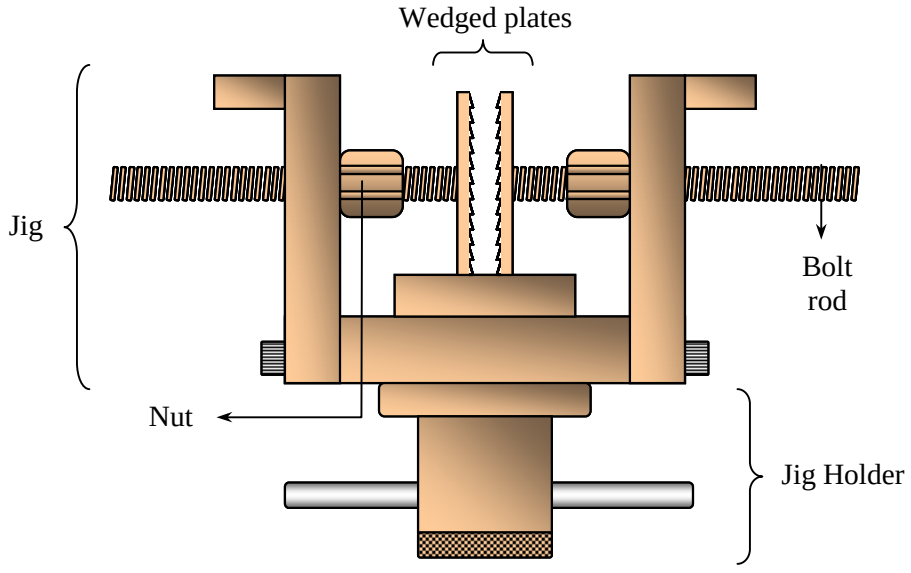

Figure 3.17(b): The *fixed member* is designed with wedged plates to firmly hold a sample during tensile experiment.

meets the basic principles, which were explained in Section 2.2.1.2. The ASTM standards give valuable guidelines, where they list the important characteristics for a tensile sample holder. They are:

1. *Fixed member* which means one side of the sample holder must be hold to static
2. *Moveable member* tells that the other side should be moveable
3. The sample holder has to self-align when forces are applied.
4. The vertical axis has to be in parallel with the force direction and positioned in the centre of the holder [3.26].
5. The holder can be tightened strong enough to avoid any slippage of the sample
6. The holder surfaces must be rough, such as with horizontal lines of small wedges [3.27].

The schematic drawing in Figure 3.17(a) shows the *movable member* of sample holder in this work, which comprise of wedged plates to firmly hold a sample during testing. This component is self-align when force is applied. Figure 3.17(b) illustrates the *fixed member* that also comes with the wedged plates. Both movable and fixed component has bolt rod and nut plates that can be used to tighten the sample gripping.

3.2.2.1.D Tensormeter

The machine used in this mechanical study was Zwick Z050, which is a Universal Testing Machine *UTM* that can be used for various types of mechanical testing. It comes with a heating chamber that can stabilize a sample temperature up to 200°C. This machine can be operated by means of special software that helps user to control the forces applied, as well as the tensile rate. This capability has widened the range of sample sizes that can be used with the machine.

Generally, the Zwick machine can be divided into three major components as shown in Figure 3.18. They are the *crosshead*, *sample holder* and *extensometer*. *Crosshead* is the

moveable component on this machine, where the *moveable member* of the customized sample holder was fixed. This *crosshead* can travel both ways, upward or downward with the chosen rate by user. *Sample holder* on the Zwick machine comprises of two parts. The lower part is fixed to the base of the machine, where the *fixed member* of the customized holder was fitted. The upper part is joined to the *crosshead*, where in this work it had been replaced with the *moveable member* of the customized sample holder.

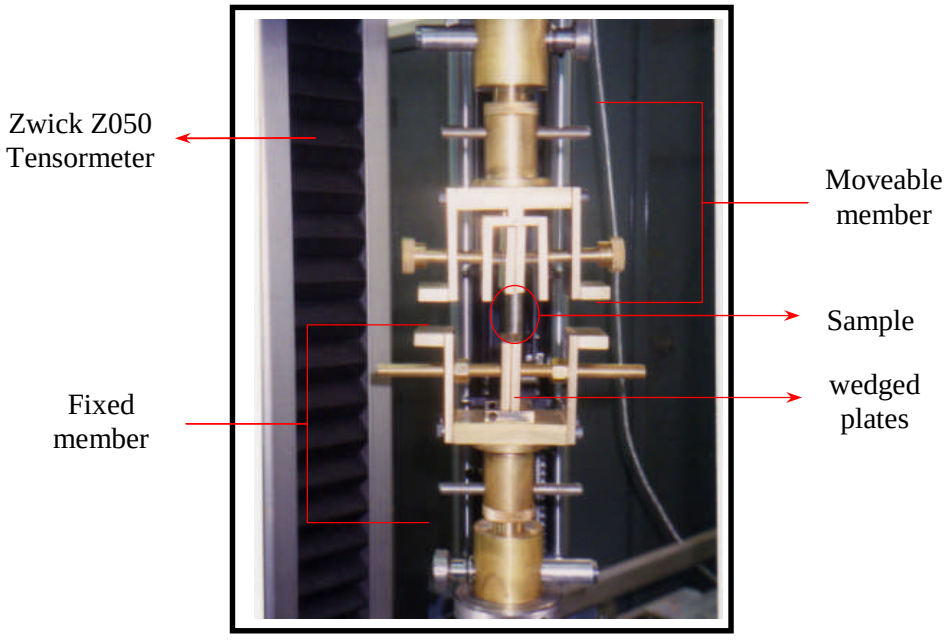

Figure 3.18: Sample mounting in the customized sample holder which had been fixed on the Zwick Z050 tensormeter.

3.2.2.2 Experimental method for Tensile Test

Proper instrumentation together with the right conduct in experimental method can be very helpful to produce reliable results. In this work, attentions were given in order to meet the standard procedures as suggested by the ASTM. Such as, the preparation of tensile samples which is extremely critical that forbids any defect within the sample *gauge length*. High consideration was also given in sample mounting, especially on the sample alignment and

gripping. The chose of testing parameter, for example the strain rate was done appropriate to the type of studied materials. Evaluation on the break-off conditions of a tested sample finally determined the reliability of tensile results.

3.2.2.2.A Sample cutting

Sample sheets were cut into smaller pieces about 120 mm (L) x 25mm (H) in dimension. The mold in Figure 3.16(a) was then used to draw a dumbbell shape on these samples. The customized cutter had to be carefully placed on the samples according to this drawn outline before it was pressed down using a hydraulic compressor. In order to get an even cutting, a solid block was placed on top of the cutter to distribute the applied pressure evenly. This procedure gave a smooth and clean cut around the critical area of a sample. A sharp scissor was then used to cut the grip area at both ends of the samples.

Figure 3.19 shows some of the cut specimens for tensile test. These samples were carefully checked before ready to be tested. This is important to make sure that they were free of any cutting defects, which will affect the tensile test result. In order to ensure smooth cutting, the sample cutter has to be sharpened after several usage depending on the type of material used in the cutting process.

Tensile Specimens

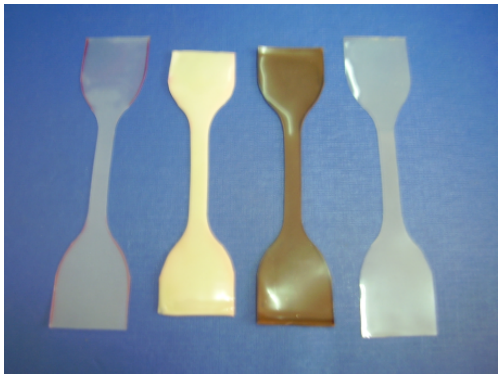

Figure 3.19: Some of the cut specimens for tensile test using the customized cutter in Figure 3.16(b).

3.2.2.2.B Tensile Test

Similarly as the apparatus, the experimental procedures for tensile test also followed some strict rules as recommended by the ASTM standards. In order to get reliable results, high considerations were stressed on the listed conditions to meet the standards [3.9 and 3.10].

1. A sample to be tested must be free from defects, which may arise from the sample itself or during the cutting process. Bubbles or lumps on the sample and cuts within the gauge length are among the unwanted defects.
2. A sample has to be stabilized at its testing temperature
3. Any results that come from a test which give a final break out side the gauge length should be rejected [3.28]
4. Five repeatable results from different samples were obtained and the average value was used as a result for one test [3.26]

Before mounting a specimen on its holder, the thickness was measured and recorded. This sample was then fitted on the *fixed member* of the holder. Afterward, the *movable member* was slowly moved towards the sample and they were then carefully aligned before being tightened. It is important to ensure that the wedged plates on these holder are in the right direction to avoid any slippage. These plates that were in fixed member must in downward direction and those of *movable member* must be directed upward. Figure 3.18 demonstrates the sample mounting in the customized sample holder, which had been fixed on the Zwick Z050 tensormeter.

The heating chamber was not employed for the tensile tests in room temperature. However, for experiments to study the effects of temperature on tensile properties, this chamber was used. The fitted sample and its holder were put inside the chamber before the temperature

was raised to a test temperature, T_t. A blower inside this heating chamber was used to stabilize the $T_{t,}$ and after five minutes of stabilization, the test can be carried out.

In order to run a test, some important parameters had to be keyed-in into the TestXpert program. They are the gauge length of 33 mm and the width within the gauge length that is 6 mm. These values are constants for the chosen shape and dimensions in this study. The thickness of each sample must be keyed-in, as well as the crosshead speed of 50 mm/min which was used for all samples in this work. This rate was referred to the ASTM standards, and appropriate to the type of studied materials.

Finally, the start button was pushed to initiate the tensile test and the data acquisition task was handled automatically by the program. User can also see the plotted stress-strain graph simultaneously on the computer screen, as well as the applied forces and elongations. The TestXpert program stopped this tensile experiment once it detected a failure on the sample, where the sample had been split into two pieces. This program also offered tools for data analyzing, which can calculate important parameters such as modulus Young Y and tensile strength σ_{max}. The reliability of tensile results however depends on the condition of break-off area on the tested sample. Result from sample with the final break was inside the *gauge length* was taken for analyses. In order to assist the process of analyses, *Tensile Analysis* that is a computer program was developed using commercial software TestPoint Version 2.0. This program in Appendix E gives better estimation for mechanical properties, such as the modulus Y and tensile strength σ_{max}. It is also useful to calculate certain properties, for example the sample toughness.

Good instrumentations with proper experimental procedures can avoid noises, especially in TSC measurement. For example, the smooth outlines from raw data as shown by the *PET* and *PMMA* thermogram in Figure 3.14(a) and 3.14(b) respectively may not be obtained in

the present of current noises. Consistency is important in experimental method. It can help to produce repeatable results, especially in tensile test that requires several results to be averaged. It is also important in order to compare various results from different samples.

3.4 Summary

- *OMON* was prepared via chemical modifications on the pristine *Mon* clay which is discussed in Section 3.1.1
- Section 3.1.2 gives the details on the preparation of *SMRL*, *DPNR*, *ENR-50*, *pPVC* and *PE* polymers, as well as their composites with *OMON* and *Mon*. They were prepared in sheet form for TSC measurement and tensile tests.
- Instrumentation for TSC system is explained in Section 3.2.1.1 which involved some physical set-up and computer programming. The developed TSC system was tested and calibrated with *PET* and *PMMA* polymers and discussed in Section 3.2.1.2.
- From the obtained results, the reliability of TSC system was proven within the range of -180 °C to 300 °C. This system can handle low heating rate such as 1 °C/min with a fluctuation about 0.05 °C/min for every 9 seconds. The system is capable to measure the small thermally stimulated current, which is within the range of 10^{-15} to 10^{-9} *A*.
- Instrumentation for tensile test focused on sample cutting and gripping. Section 3.2.2.1 explains the customized sample cutter for a dumbbell shape sample. The dimensions of this sample geometry are comparable with the type IV of D 638-61T standard.
- A set of sample holder with wedged gripping was also customized appropriate to the type and dimension of the studied materials. The design was done according to some basic standard as suggested by the D638- 61T and D 412-62T of ASTM standards.

- Experimental method in Section 3.2.2.2 explains the process of sample cutting which is very critical in tensile test. Repeatable tensile test on each type of samples were carried out to conform the results obtained.

- Computer programs to assist the process of data analyses were developed by means of TestPoint Version 2.0 software. Some of the programs are *TSC Analysis* and *Tensile Analysis*.

References:

3.1 M. F. Dimin, **"**Development of TSC and DC conductivity measuring system and its application to doped Chitosan", *Master Thesis*, University of Malaya, Kuala Lumpur, (2001)

3.2 A. R. MacLauchlin and N. L. Thomas, "Preparation and characterization of organoclays based on an amphoteric surfactant", *J. Coll. Interface Sci.*, **V 321**, (2008), pg. 39 - 43

3.3 L. B. de Paiva, A. R. Morales and F. R. V. Diaz, "Organoclays: Properties, preparation and application", *App. Clay Sci.*, **V 42**, (2008), pg. 8 - 24

3.4 Y. Dong and D. Bhattacharyya, "Effects of clay type, clay/compatibiliser content and matrix viscosity on the mechanical properties of polypropylene/organoclay nanocomposites", *Composites: A*, **V 39**, pg. 1177 – 1191

3.5 N. A. Halim, A. B. Ahmad and Z. A. Ibrahim, "Thermally Stimulated Current Measurements on Epoxidized Natural Rubber (ENR5O) - Organically Modified Montmorillonite Composite", *Jurnal Fizik Malaysia*, **V 23 (1 - 4)**, (2002), pg. 79 - 84

3.6 J. L. White, "Rubber processing: technology, materials, principles", *Hanser Verlag*, Munich New York, (1995)

3.7 K. T. Cheng, A. R. Rais and K. B. Basir, "Deproteinised Natural Rubber", *Rubb. Res. Inst. Malaysia Bull No. 11*, The Rubber Research Institute of Malaysia, Kuala Lumpur, (1996)

3.8 S.N. Gan and Z. A. Hamid, "Partial Convertion of Epoxidised Groups to Diols in Epoxidised Natural Rubber", *Polymer*, **V 38(8)**, (1997), pg.1953 – 1956

3.9 Rubber Research Institute of Malaysia, "Epoxidised Natural Rubber", The Rubber Research Institute of Malaysia, Kuala Lumpur, (1984)

3.10 ASTM Committee D20 on Plastics, "Tension Testing of Vulcanized Rubber: D 412-62T: ASTM Standards on Plastics", *American Society for Testing and Material*, Baltimore, (1962)

3.11 ASTM Committee D20 on Plastics, "Tensile Properties of Plastic: D 638-61T: ASTM Standards on Plastics", *American Society for Testing and Material*, Baltimore, (1962)

3.12 ASTM Committee D20 on Plastics, "Tensile Properties of Thin Plastic Sheeting: D 882-61T: ASTM Standards on Plastics", *American Society for Testing and Material*, Baltimore, (1962)

3.13 R. Bartnikas, E. J. McMahon and ASTM Committee D-9 on Electrical Insulating Materials, "Engineering Dielectrics: Electrical Properties of Solids Insulating Materials: Measurement Techniques", *ASTM International*, Baltimore, (1987)

3.14 P. L. Lewin, A. E. Davies, G. Chen, M. J. Ford, S. Swingler and D Patel, "The Measurement of Charge Trapping Characteristic in High Voltage Insulation Materials", Seventh Conference on Dielectric Materials Measurement & Application, **N 430**, (1996), pg. 46 - 49

3.15 V. Kazukauskas and J. V. Vaitkus, "Influence of defect traps and inhomogeneities of SiC crystals and radiation detectors on carrier transport", *Opto-electro. Rev*, **V 12(4)**, (2004), pg. 377 – 382

3.16 J. Stallcup and National Fire Protection Association, "Stallcup's Electrical Equipment Maintenance Simplified", *Jones & Bartlett Publishers*, Sudbury, (2007)

3.17 J. C. Whitaker, "The Electronics Handbook", 2nd. Edition, *CRC Press*, New York, (2005)

3.18 J. Belana, M. Pujal, P Colomer and S. Montserrat, "Cold Crystallization effect on α and ρ amorphous poly(ethylene teraphthalate) relaxations by thermally stimulated discharge currents", *Polymer*, **V 29**, (1988), pg. 1738 – 1744

3.19 A. Thielen, E. Hendrick, J. Niezette and J. Vanderschuaren, "Heat treatment effects on the metal-polymer interface and space charge formation in thin metallized polyethylene teraphthalate films", *J. App. Phy*., **V 75(8)**, (1994), pg. 4069 – 4076

3.20 N. Benrekaa, A. Gourari, M. Bendaoud, R. Saoud and C. Guerbi, " TSDC study of structural relaxation on polyethylene terephthalate", *J. Non-Crys. Sol*., **V 352**, (2006), pg. 4804 - 4808

3.21 M Ignatova, T. Yovcheva, A. Viraneva, G. Mekishev, N. Manolova and I. Rashkov, "Study of charge storage in nanofibrous poly(ethylene terephthalate) electrets prepared by electrospinning or by corona discharge method", *Euro. Poly. J.*, **V 44**, (2008), pg. 1962 – 1967

3.22 J. van Turnhout, "Thermally Stimulated Discharge of Electrets", Topics in Applied Physics: Electrets edited by G.M Sessler, **V 33**, *Springer-Verlag*, New York, (1980)

3.23 F. Namouchi, H. Smaoui, H. Guermazi, C. Zerrouki, N. Fourati, S. Agnel, A. Toureille and J. J. Bonnet, "Study of thermal aging effect on space charge in poly(methyl methacrylate)", *Euro. Poly. J.*, **V 43**, (2007), pg. 4821 – 4829

3.24 I. M. Kalogeras, F. Pallikari and A. Vassilikou-Dova, "The diverse effect of antiplasticizer in the molecular dynamics of an organic dye-doped polymer observed at different motional lengthscales", *Euro. Poly. J.*, **V 45**, (2009), pg. 1377 - 1384

3.25 X. Cai and G. T. Lines, "Enabling Numerical and Software Technologies for Studying the Electrical Activity in Human Heart", Advanced information systems engineering- 9th International Conference CAiSE 97 edited by A. Olivé and J. A. Pastor", Barcelona, (1997)

3.26 J. R. Davis, "Tensile Testing", 2nd. Edition, *ASM International-The Material Information Society*, New York, (2004)

3.27 W. F. Gale, C. J. Smithells, T. C. Totemeier - Contributor W. F. Gale and T. C. Totemeier, "Smithells Metals Reference Book", 8th Edition, *Butterworth-Heinemann* (*Elsevier*), Amsterdam, 2004

3.28 R. L. Timings, "Mechanical Engineer's Pocket Book", 3rd Edition, *Newnes- Elsevier*, Amsterdam, (2005)

Chapter 4

Characterization

Chapter 4: CHARACTERIZATION

In material sciences, basic characterizations for example Differential Scanning Calorimetry (DSC) technique is a necessitate to give important parameters. Such as the glass transition temperature, T_g and melting point, T_m. Together with measurement of specific properties for example basal spacing d_{001} and infra-red spectroscopy, they present strong support to the thermo-electrical and mechanical studies. For that reason, they become key elements in quest to understand the microscopic mechanisms.

4.1 Differential Scanning Calorimetry, DSC

As mention above, Differential scanning Calorimetry (DSC) is a basic and well-known technique to gain glass transition temperature T_g, melting point T_m and some other thermal properties. This technique utilizes measurements of energy necessary to establish a nearly zero temperature difference between a substance and an inert reference material, as the two specimens are subjected to identical temperature regimes in an environment [4.1].

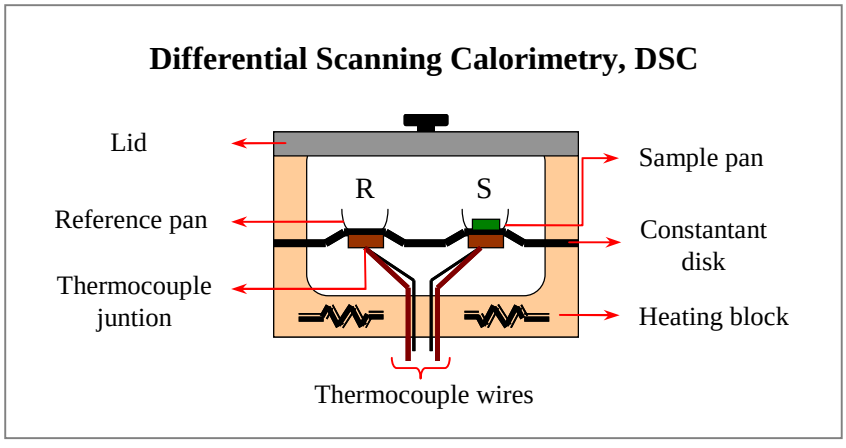

Figure 4.1: Schematic illustration of heat flux Differential Scanning Calorimetry, DSC [4.2]

The Rheometric Scientific DSC Gold used in this work is a heat flux DSC system, where a single furnace is used to heat both the sample and reference as illustrated in Figure 4.1. The sample and reference pans sit on raised platforms formed from a constantant disk, which allows heat transfer between the pans and the heating block. Thermocouples placed at the

bottom of these platforms measure the temperature differential between the sample and the reference as both are heated or cooled. The differential heat flow ΔQ is calculated using the following equation:

$$\Delta Q = \left(T_s - T_r\right) / R_d = \Delta T / R_d$$

where T_s and T_r is the temperature for sample and reference respectively, while ΔT is the differential temperature between the T_s and T_r. R_d is the thermal resistance of constantant disk [4.2].

In this work, the T_g and T_m are two DSC parameters that are highly focused particularly the glass transition temperature T_gs. This is due the fact that they are comparable to the α peak of relaxation process within Thermally Stimulated Current (TSC) thermograms. Thermal feature from DSC profile also provides information on amorphous and crystalline phases that may exist in samples [4.3 and 4.4]. DSC measurements were performed on samples at the heating rate of 10° C/min, after quenching their temperature down to -100 °C using liquid nitrogen.

4.1.1 Pristine Polymers

4.1.1.A *SMRL, DPNR* and *ENR-50*

Figure 4.2 exhibits the thermogram of *SMRL* and *DPNR*, while Figure 4.3 is for *ENR-50*. Thermal transitions in the low temperature region give the T_g of *SMRL* (-64.08 °C), *DPNR* (-64.13 °C) and *ENR-50* (-22.40 °C). These values are comparable with the T_g obtained by previous researchers [4.5 and 4.6]. In addition, the lack of any endothermic features in the scans suggests that amorphous phase dominate the microscopic structural of these samples. From the T_g values for *SMRL* (-64.08°C) and *DPNR* (-64.13 °C), it seems that the protein in natural rubber slightly influenced the transition temperature, even though it may affect the gel properties of the material. This assumption is based on qualitative observation, in which the *DPNR* was easily dissolved in *toluene* compared to *SMRL*.

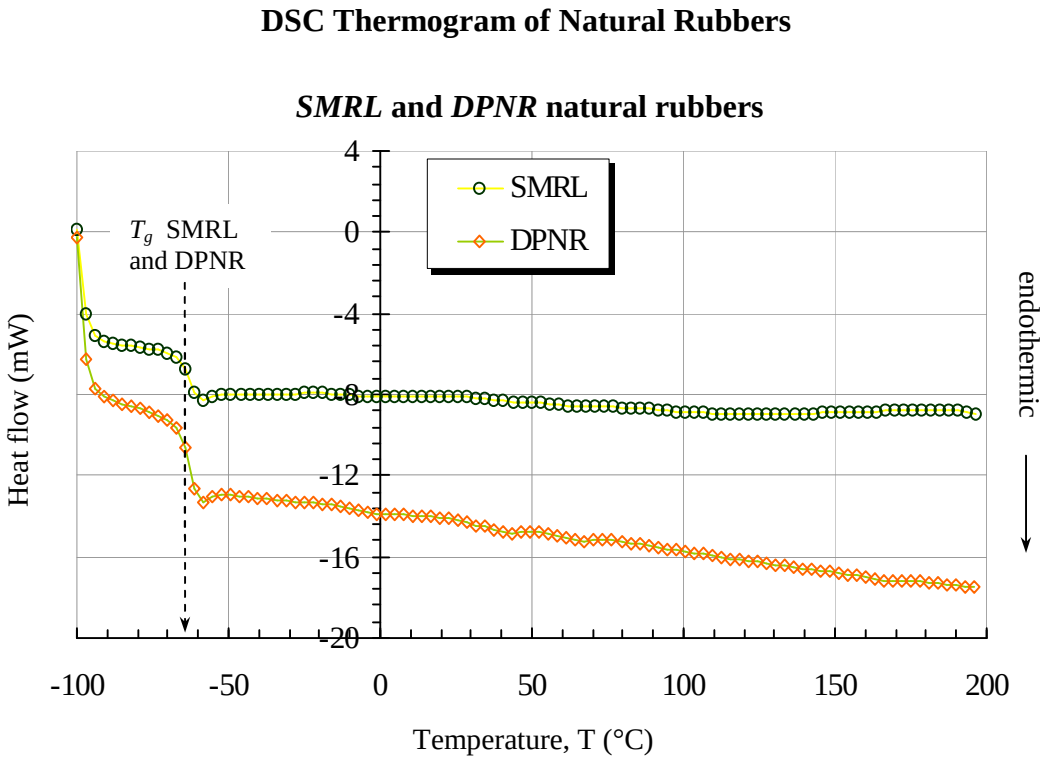

Figure 4.2: DSC thermograms for *SMRL* and *DPNR* shows the glass transition temperature, T_g around -64.08 °C and -64.13 °C, respectively.

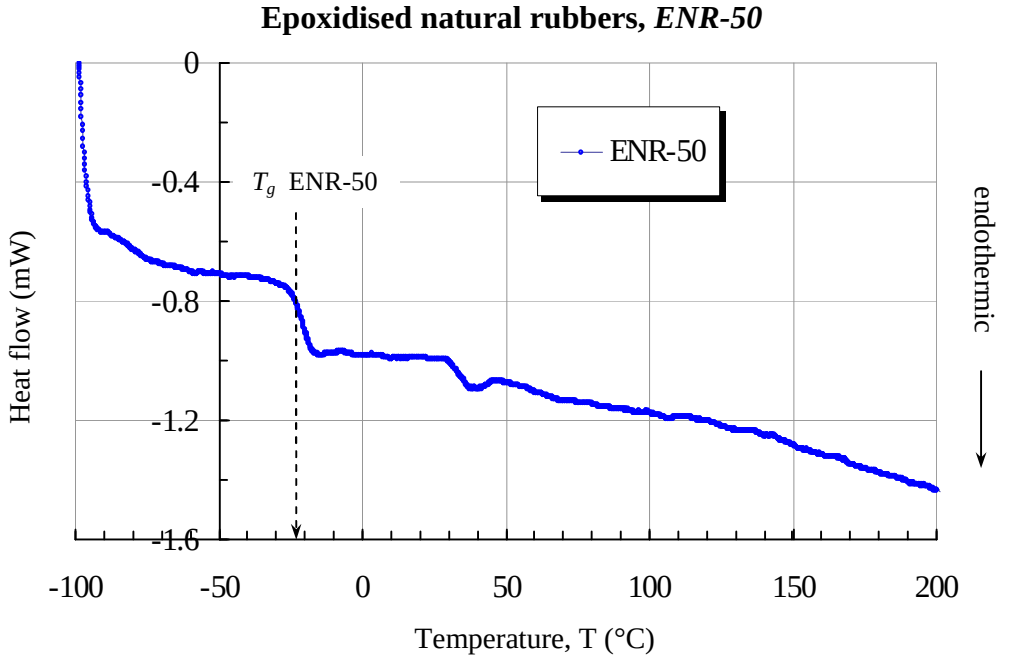

Figure 4.3: The DSC thermogram of *ENR-50* rubber shows the glass transition temperature T_g at -22.40 °C.

However, the situation is rather different when *SMRL* (-64.08 °C) is compared to *ENR-50* (-22.40 °C), where the variation in T_g is about 41.68 °C. This T_g increase in fact enlightens the effect of introducing epoxide group *–COC–* into cis-polyisoprene chains of *ENR-50* rubber. This polar group that covers about 50 % [4.7] of the double bond population on the chains drives stronger intermolecular bonding. For example, it can interact with the chains unsaturated bonds and protein molecules in this polymer [4.6, 4.7, 4.8 and 4.9]. As a result it modifies bonding energy and micro-structures within *ENR-50*, which then responsible for the increase in its T_g. The polar group also contributes to the increase in gel content, as *ENR-50* was found less dissolved in *toluene* compared to the *SMRL*. In Figure 4.3, its high temperature region shows that there is a thermal feature within the range of 30 °C to 40 °C. This feature however is not present in the other natural rubber cases, and thus far it remains unknown.

4.1.1.B *Polyethylene, PE*

PE is a well known non-polar polymer which is composed of organic crystallite structures, with a range of proportion that differentiates its properties. Such as the crystallite elements has been estimated to be just about 43% in Low Density PE (*LDPE*) (0.92g/cm^3). While in High Density PE (*HDPE*) (0.97g/cm^3) it was about 76% crystalline [4.10].

The DSC thermogram of *PE* in Figure 4.4 confirms the existence of crystalline phase in this polymer, especially with the obvious endothermic at T_m = 105.36 °C. Therefore, its temperature is assigned as the melting temperature or T_m for *PE* in this work. From chemical point of view, endothermic is actually demonstrating the dissociation processes of chemical bonds in aligned polymeric chains. By which, it will then lead to the melting of polymer [4.11]. Besides, there is no thermal transition observed in the scan that can be associated to the amorphous phase in *PE*. It thus tells that the crystallite component could be dominating the polymer microstructure.

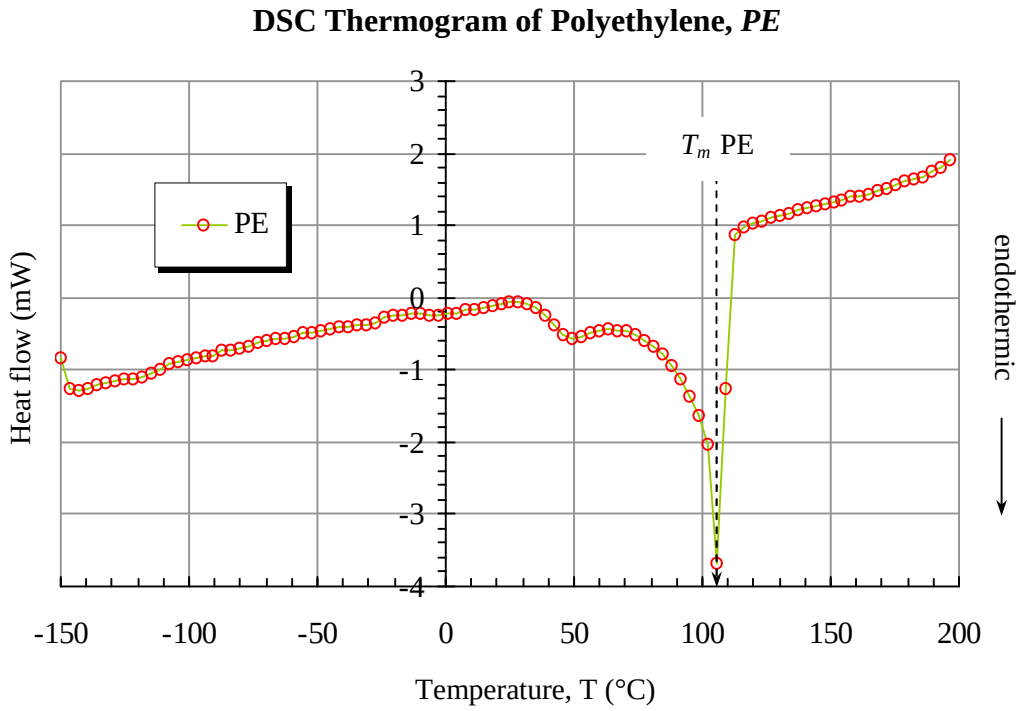

Figure 4.4: A big endothermic at 105.36 °C ascribed as T_m , this melting point shows the existence of crystalline phase in *PE*.

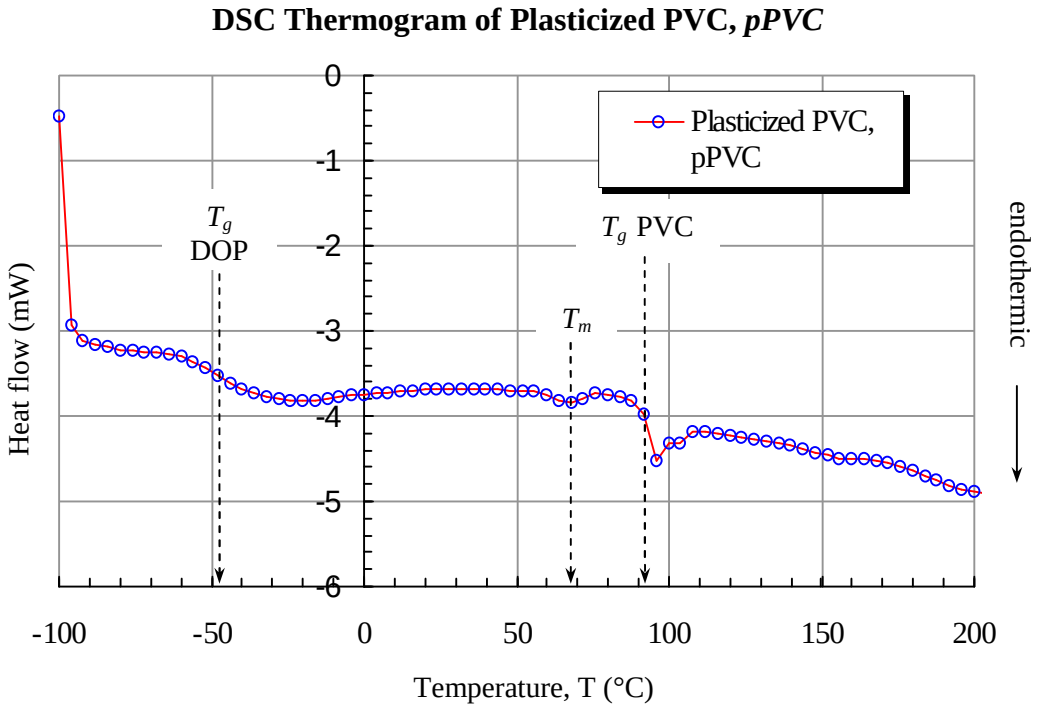

Figure 4.5: DSC thermogram shows the two glass transition temperatures in *plasticized PVC*. The original T_g is at 91.86 °C while the modified T_g is at -48.04 °C. The endorthermic for microcrystalite structures is located around 67.87 °C.

4.1.1.C *Plasticized Polyvinylchloride, pPVC*

Plasticized PVC is a modified polymer which utilizes small molecules as plasticizer agent. These molecules for instance, *Dioctylphthalate* (*DOP*) are frequently used to gain elasticity behaviors at ambient temperature. *DOP* is functioning to reduce intermolecular bonding, which then facilitates the movement of *PVC* chains [4.12]. Figure 4.5 of *pPVC* shows the new T_g at -48.04 °C that explained its elasticity at room temperature.

On the other hand, the original T_g of *PVC* is still observable at 91.86 °C which indicates that not all *PVC* chains were involved in the process. In Figure 4.5, it also reveals a small endothermic around 67.87 °C. This thermal feature could be related to a certain type of microcrystalline structures. Such structure might exist due to physical crosslink networks in the *plasticized PVC* [4.12 and 4.13]. Some researches performed by several authors, disclosed that the amount of *DOP* in *pPVC* will determined the position of T_g. Therefore, comparison between the observed T_g at -48.04 °C and the graph shown in Figure 4.6 gives an estimation of *DOP* content in the renewed polymer [4.14 and 4.15]. The plasticizer molecule is estimated to be about 50 wt% of the *pPVC* weight fraction.

The effect of DOP on T_g of plasticized PVC

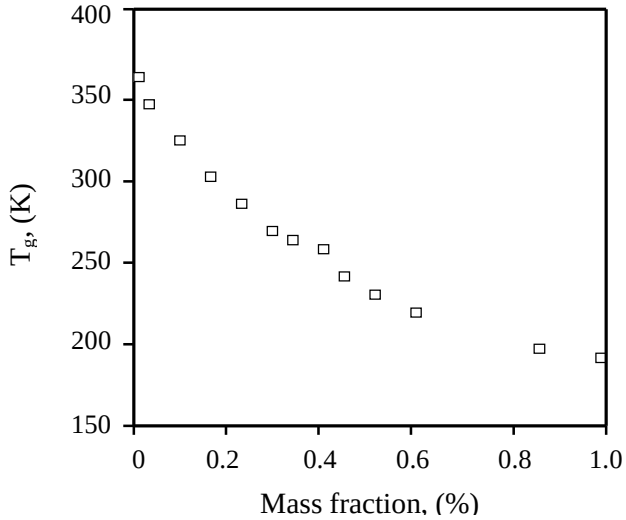

Figure 4.6: Glass transition temperature, T_g of *plasticized PVC* as a function of plasticizer (di(2-ethylhexyl)phthalate, *DOP*) [4.13]

4.1.2 Mon, ODA and OMON

In Figure 4.7(a), the thermogram of *Mon* demonstrates a big and wide endothermic around 57.92 °C. This thermal feature is expected seeing as *Mon* belongs to the class of layered silicates or *phyllosilicates* clay. It means that *Mon* must consist of crystalline structures. In addition, the appearence of such endothermic peak indicates the involvement of energy absorption during thermal process. In clay studies, the most common cause that may assist such process is dehydration due to the loss of water content [4.16 and 4.17].

In Figure 4.7(b) of *octadecylamine* (*ODA*), two endothermic around 62.77 °C and 89.53 °C are assigned as T_{m1} and T_{m2} respectively. These T_ms could be the indicator of a multi-stages mode during the melting process of *ODA* crystallites. Hence, the decompositions of *ODA* chains that were assisted by the dissociations of intermolecular and intramolecular bonds should be the main sources for these endothermics [4.11].

Figure 4.7(c) of *OMON* reveals an endothermic with some similarity to the *Mon* profile in Figure 4.7(a). However, the T_m is shifted to a lower temperature at 36.94 °C. The bigger weight ratio of *Mon* (72 %) compared to *ODA* (28 %) in *OMON* possibly the main reason behind this observation. Yet, there is another interesting reason that should be considered as well. The intercalation of *ODA* chains to a certain extent look as if the chains were hid inside the *Mon* interlayer space. Thereby, it may serve as an evidence for the occurrence of chemical modification within the interlayer of *OMON* structure.

4.1.3 Composites

4.1.3.A *CSMRL, CDPNR* and *CENR-50* Composites

Figure 4.8(a) shows DSC thermal features of *CSMRL*, a natural rubber-*OMON* composite. There is only a small thermal transition (T_g) around -64.01 °C that can be identified in this figure. *CDPNR* profile as shown in Figure 4.8(b) however demonstrates a shaper transition

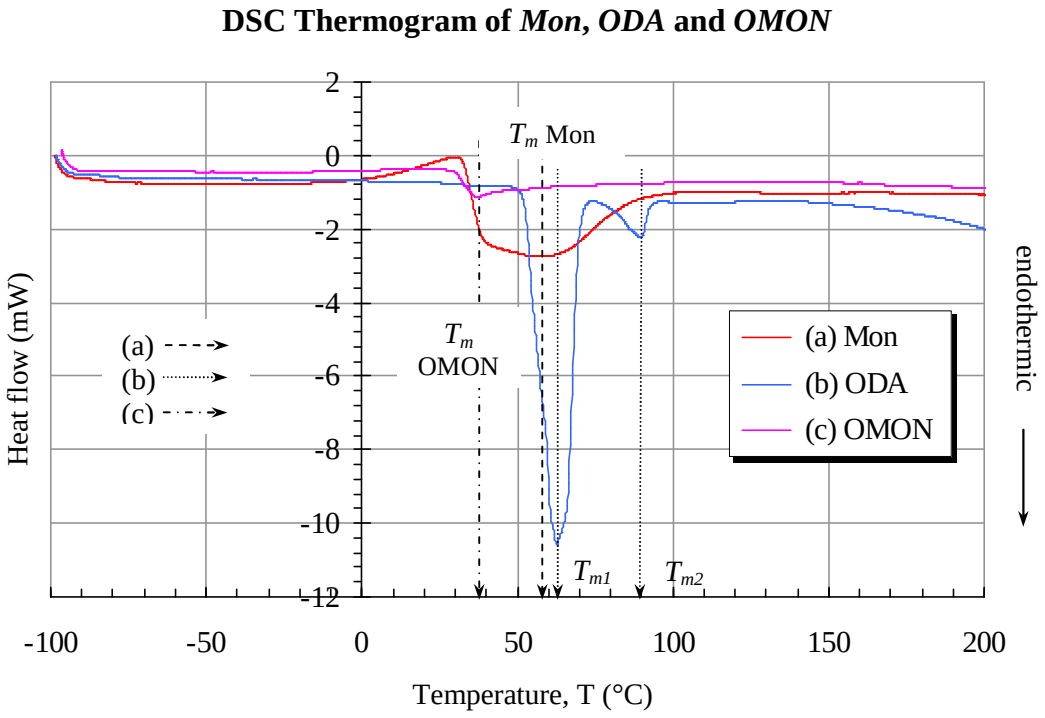

Figure 4.7: DSC thermogram shows endothermic in (a) *Mon* at 57.92 °C, (b) *ODA* at 62.77 °C and 89.53 °C and (c) *OMON*: 36.94 °C.

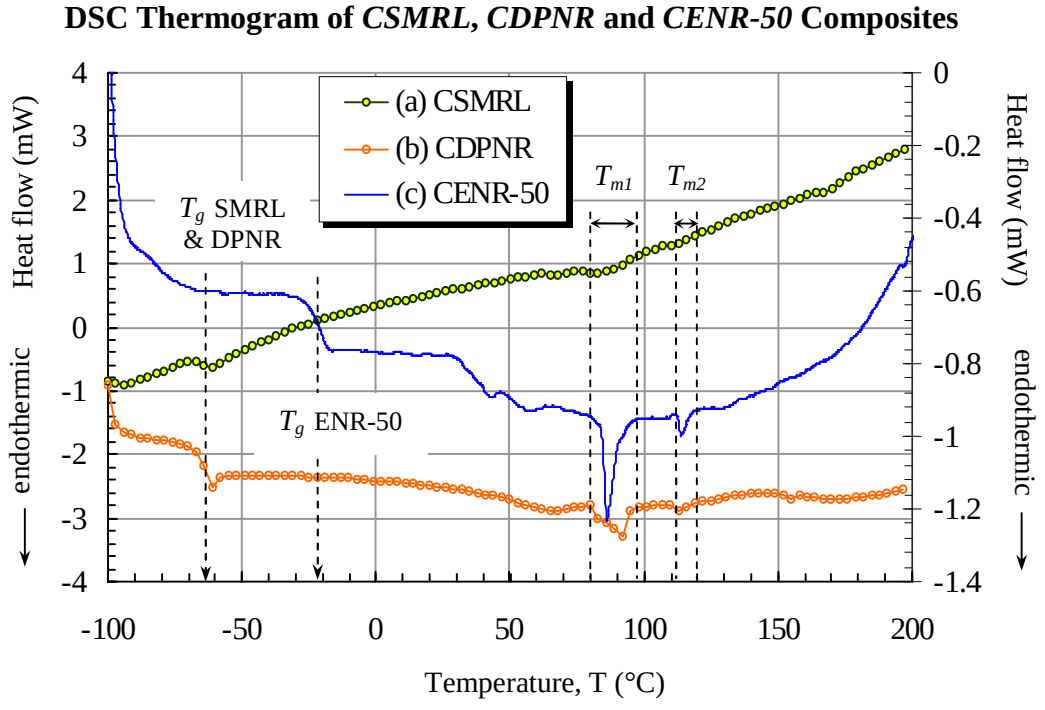

Figure 4.8: *Polymer-OMON* composites maintain their polymeric T_g at -64.01 °C in *CSMRL*, - 64.03 °C in *CDPNR* and -21.62 °C for *CENR-50*. T_{m1} which is originated from *ODA* appears around 80 to 98 °C while the T_{m2} are within the range of 112 to 119°C.

around -64.03 °C. There are two T_ms recognized in this figure that seem analogous to both *ODA* endothermics in Figure 4.7(b), except that they appear at higher temperatures. They are around 91.88 °C and 112.88 °C for T_{m1} and T_{m2} respectively.

Similar observations can be seen in Figure 4.8(c) for *CENR-50*, wherein T_{m1} is located at 86.24 °C while T_{m2} is recognized at 113.80 °C. These endothermic resemble those of *ODA* in Figure 4.7(b). Therefore, it can be suggested that the structures of alkyl chains in *OMON* could be the sole origin for such endothermic in the composites. In addition to the trace of *OMON*, analysis on *CENR-50* also indicates the existence of *ENR-50* where the T_g for *ENR-50* (see Fig. 4.3) appears around -21.62.0 °C in this composite.

4.1.3.B *CPE* Composite

DSC profile for *CPE* (5%) as shown in Figure 4.9 demonstrates a superimposed of T_ms at 105.37 °C. Where, it is expected to show two endothermics that is originated from *PE* and *ODA* at 105.36 °C (T_m *PE*) and 94.91 °C (T_{m1}) respectively. This finding is supported by the appearance of the small transition just about 73.95 °C. In which, it is also observed in *ODA* profile prior to its endothermic as revealed in Figure 4.7(b). However, the second endothermic (T_{m2}) that could be around 110.0 °C to 120.0 °C cannot be detected within the DSC thermogram of *CPE* composite.

4.1.3.C *CpPVC* Composite

Similar to case of *CDPNR* and *CENR-50* in Table 4.1, T_{m1} also appears on DSC profile of *CpPVC* (30%) at 95.86 °C as shown in Figure 4.10. However, this T_{m1} seems to overlap with the T_g from pristine *PVC* around 91.86 °C. In contrast, the T_{m2} that could be found within the range of 110 °C to 120.0 °C and the T_g of *DOP* just about -48.04 °C are missing in this DSC profile. However, there is an apparent endothermic emerges in *CpPVC (30%)* profile around 51.90 °C which is assigned as T_{m3}. There are a few reasons that may explain

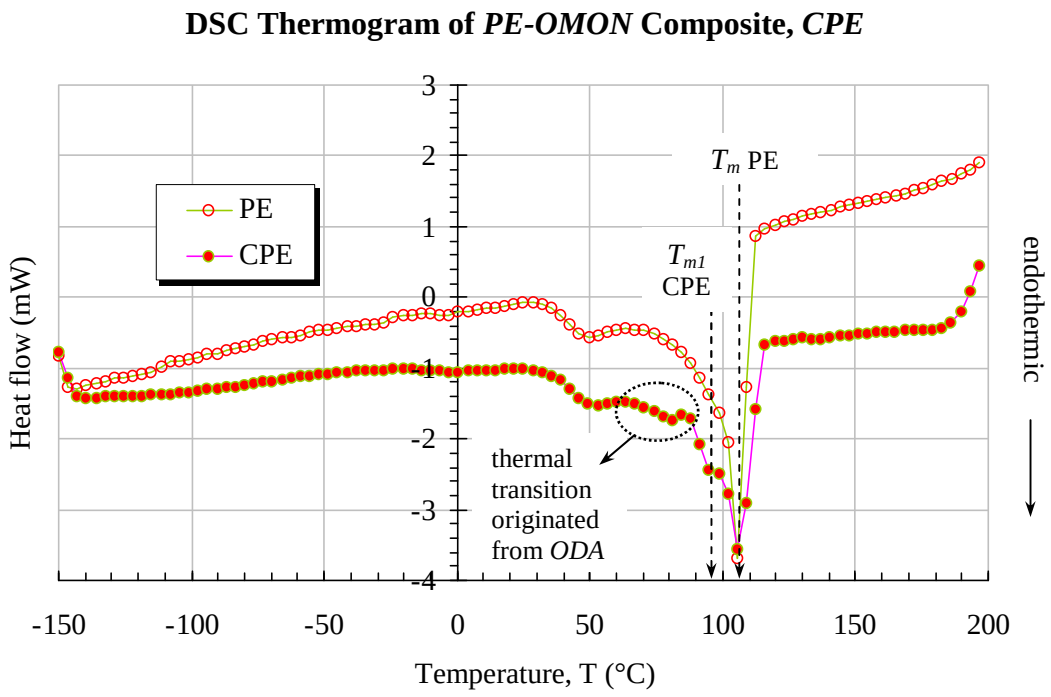

Figure 4.9: A big endothermic at 105.37 °C superimposed with the T_m from *OMON* around 94.91 °C. Small thermal transition around 73.95 °C proves the existence of *ODA*.

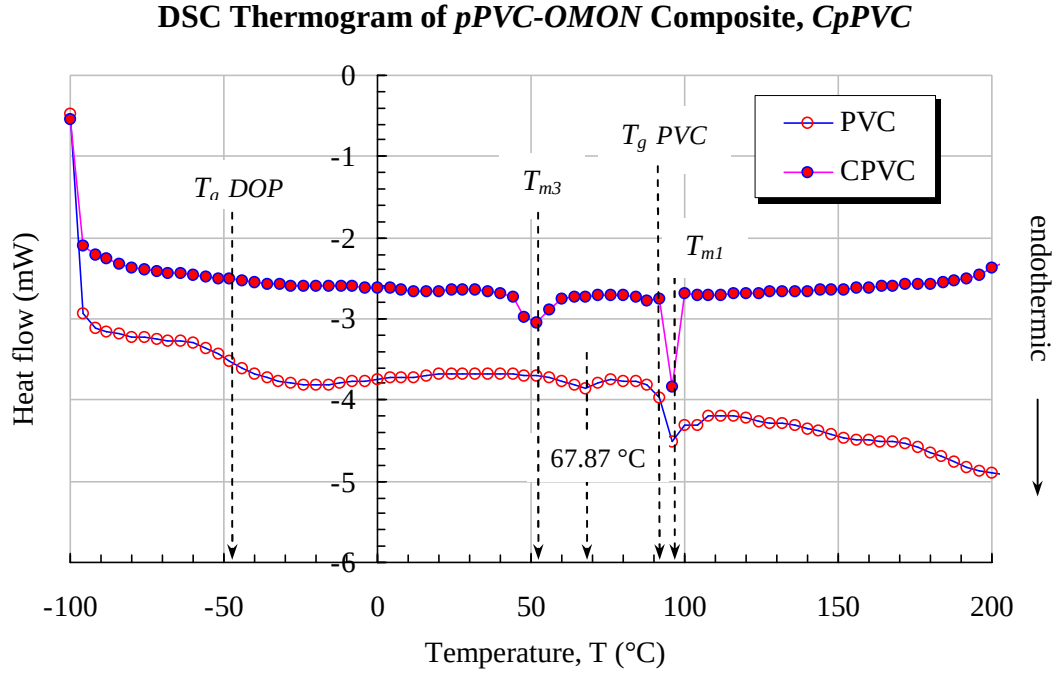

Figure 4.10: DSC profile shows the two glass transition temperatures in *plasticized PVC*. The original T_g *PVC* is at 91.86 °C while T_g *DOP* is due to the present of *DOP* molecules at -48.04° C. Traces of crystallite structures can be seen at 51.90 °C (T_{m3}) in *CpPVC* and at 67.87 °C in *pPVC*.

the source for the appearence of T_{m3} endothermic. It can be associated to the existence of pristine *OMON* as shown in Figure 4.8. Thereby, it can be concluded that blending of *pPVC* with *OMON* is incompatible, or the process of the intercalation itself could be incomplete. Therefore, there is some amount of unintercalated *OMON* left in the composite. However, this assumption can be confirmed only by XRD measurement. T_{m3} can also be related to some form of crystallite structure in *CpPVC (30%)* composite. The presence of *OMON* particle in this composite induces physical crosslinking among polymeric chains. As a result, new micro crystallites structures are formed in this material. The evidence is given by DSC profile in Figure 4.5 of *pPVC*. It shows that there is a small T_m at 67.87 °C compared to the new T_{m3} at comparatively lower temperature (52.0 °C) in *CpPVC*. By that means, matrix-*OMON* interaction had modified some of the existing crystallite chains in *pPVC* and created new crystalline structures in *CpPVC* (30%). This composite however, manage to maintain its elasticity behaviors at room temperature.

4.1.3 Summary

The knowledge on basic thermal properties has given some general ideas on the internal structure of the studied materials. Analysis on DSC results may serve as good foundation for thermo-electrical and mechanical studies carry out in this work. Table 4.1 lists several important thermal features observed on the polymer matrices and their related composites. From this table it can be concluded as follow.

- Glass transition temperature T_g and melting temperature T_m for pristine materials confirm the basic characteristics of the material.
- In composites profiles, thermal features prove the presence of *OMON* elements and related polymer matrix.

- The two endothermic that are identified as T_{m1} and T_{m2} become indicators for the alkyl chains of *octadecylammonium* cations within *OMON* gallery.
- Distorted endothermic in case of *CSMRL* and *CDPNR* indicate the modification on crystallite structure of alkyl chains.
- The lost of T_{m2} in *CpPVC* and *CPE* thermograms tells the disruption on certain arrangement of alkyl tails that contribute to its crystallinity.
- The shifted temperatures of T_{m1} and T_{m2} endothermic within polymer-*OMON* composites thermogram resulted from matrix-alkyl chains interactions.
- The absence of T_{m1} and T_{m2} in *OMON* thermogram shows that without interaction with polymeric matrix chains, alkyl tails remain isolated within *OMON* interlayer. Comparisons between the results of *ODA*, *OMON* and composite *OMON* therefore prove the intercalation of *octadecylammonium* cations in *OMON*.

Table 4. 1

DSC Results of Mon, ODA, OMON, Polymers and Polymer - OMON Composites

No.	Sample	Thermal Features at temperature T ± 0.01 (°C)					Remarks
		Polymers		OMON			
		T_g Polymer	T_m Polymer	T_m Mon	T_m ODA		
					T_{m1}	T_{m2}	
1.	Mon	—	—	57.92	—	—	T_m is related to water in *Mon*
2.	ODA	—	—	—	**62.77**	**89.53**	T_ms show crystallinity in *ODA*
3.	OMON	—	—	32.75* (T_g)	—	—	* endothermic in *Mon* is replaced by a thermal transition in *OMON*
4.	SMRL	-64.08	—	—	—	—	
5.	CSMRL	-64.01	—	—	80-90	110-120	traces for T_{m1} and T_{m2} are very weak and fade
6.	DPNR	-64.13	—	—	—	—	
7.	CDPNR	-64.03	—	—	91.88	112.88	shape of endothermic T_{m1} is distorted
8.	ENR-50	-22.40	—	—	—	—	
9.	CENR-50	-22.62	—	—	**86.24**	**113.80**	traces for T_{m1} and T_{m2} resemble those for *ODA*
10.	PE	—	105.36	—	—	—	
11.	CPE	—	105.37	—	**94..91**	nil	T_{m1} overlaps with T_m for *PE*; T_{m2} is missing
12.	pPVC	-48.04 *DOP* / 91.86 *PVC*	67.87	—	—	—	
13.	CpPVC	nil / 87.90 *PVC*	51.90	—	**95.86**	nil	T_{m1} overlaps with T_g for *PVC*; T_{m2} is missing $T_{m\,PVC}$ shows micro crystallites induced by *OMON*

4.2 X-ray Diffraction, XRD

One of the main goals in this work is to prepare polymer-clay composites. The preparation is carried out through intercalation processes of polymeric chains into the *OMON* silicates layers. Thus, the changes in basal spacing, d_{001} of the silicates layers become the primary focus in the measurements and analyzing of XRD graphs.

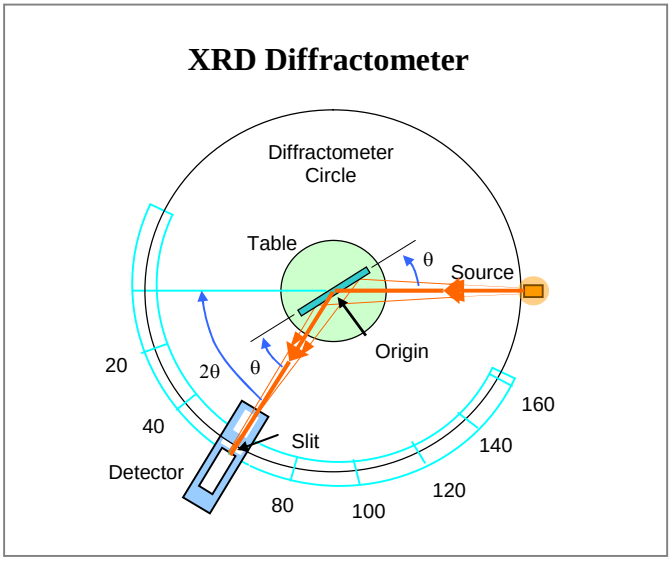

Figure 4.11: A Schematic diagram for X-Ray Diffraction, XRD spectrometry [4.17].

XRD measurement utilize X-ray beam that will be projected onto sample. It is followed by the collection of diffracted beam through a narrow slit illustrated in Figure 4.11. The beam is then passed through a nickel filter in order to ensure that only one wavelength of X-rays reaches the counter. The gearing of the counter arm has a function to make rotation in scale of 2θ to collect the entire diffracted beam. Bragg's Law combined the parameters involve in the X-ray scan as shown below [4.16 and 4.18]:

Braggs's Law $n\lambda = 2d\sin\theta$

where:

n = an integer 1,2,3….

k = constant (the value is generally = 0.9)

λ = wavelength (0.1541 nm)

d (d-spacing) = basal spacing (nm)

θ = the diffraction angle (°)

In this work, Siemens XRD diffractometer model D5000 with a copper anode was used to produce X-ray beams with λ = 0.1541 nm. The scan covered the angle of 2θ = 2° to 50°.

4.2.1 *Mon, ODA* and *OMON*

XRD scan for *Mon* in Figure 4.12 shows a profile between 2θ = 2° to 37°. There are two sharp and strong peaks observed in the graph at 2θ = 26.68° and 27.72°, whereas three other peaks around 6.04°, 19.80° and 28.40° are comparatively wide and weak. Important characteristic peak however is given by the (*001*) surface of *Mon* at 2θ = 6.04°. This peak gives the basal spacing, d_{001} = 1.462 ± 0.001 nm of *Mon* layers.

According to K. Jesmund and J. Mering, the d_{001} spacing for *Mon* is about (1.50 ± 0.30) nm [4.19]. While the basal spacing d_{001} given by Hendricks at relative humidity of 50%, regarding to the three different exchangeable cations Na^{+}, Mg^{2+} and Ca^{2+} are about 1.23 nm, 1.41 nm and 1.45 nm respectively [4.20]. Hence, it is most likely that the observed basal spacing indicates the presence of Ca^{2+} as the exchangeable cation.

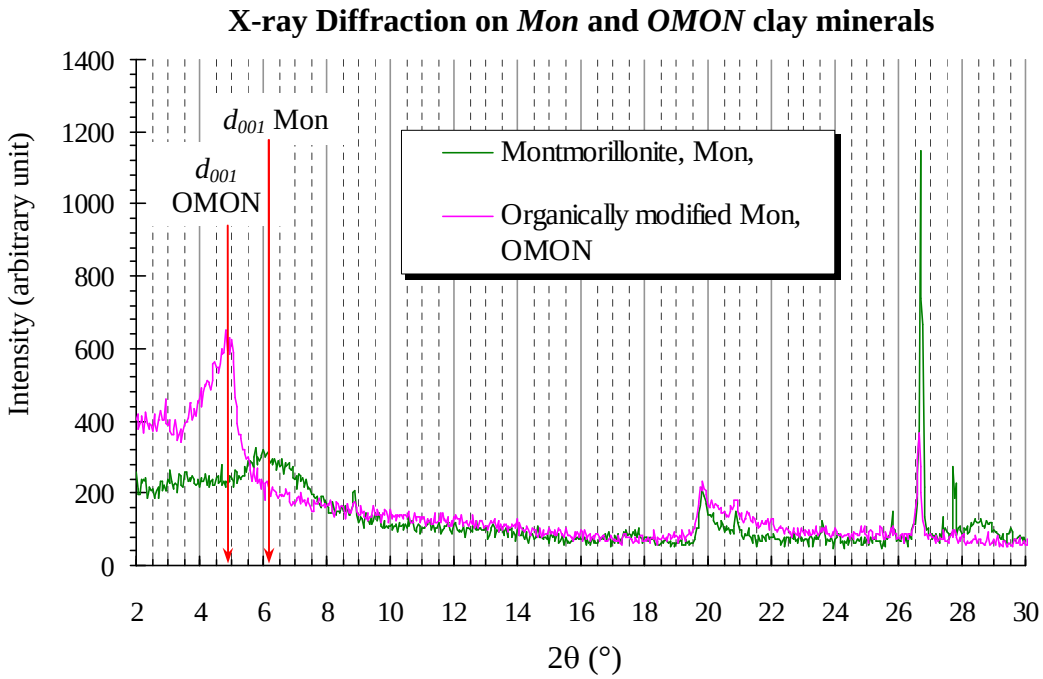

Figure 4.12: XRD profiles for *Mon* and *OMON* showing the position of d_{001} at 2θ = 6.04 ° and 4.80 ° for *Mon* and *OMON* respectively.

The d_{001} spacing depends very much on the humidity condition of the tested *Mon* sample. This is due to the fact that water is normally present in the interlayer gallery together with the exchangeable cation. The occupied water in such confine space thus, tends to associate with the cations and then form hydration shells around them [4.21]. It means that the type of exchangeable cations play a very significant role, since they have different hydration energy depending on their valency. For example, with monovalent exchangeable cations such as Na^+, the d_{001} will increase from the non-hydrated thickness of 0.96 nm [4.22] to 1.25 nm forming one molecular water layer. While in the presence of polyvalent cations such as Ca^{2+}, two layers of molecular water are formed that give the thickness around 1.45 nm to 1.55 nm [4.23].

This phenomena explained by Mering with evidences suggest that at low relative humidity (<30% *R.H*) a *Ca-Mon* does not form a single water layer as in case of *Na-Mon*. Instead, a skeletal double layers is created corresponding to the octahedral coordination of hydration water around Ca^{2+}. The thickness of such water layer is about 0.44 nm and as the relative humidity is raised from 30% to 80%, two complete water layers are created. The thickness of water layers therefore increase to 0.59 nm. Further study by Mering and Glaeser reveals that the saturation about 30% of the exchangeable cations with Ca^{2+} is sufficient enough to generate the hydration characteristic of a *Ca-Mon* [4.22 and 4.23].

This analysis reveals that the studied *Mon* clay contain at least 30 % of the base-exchange capacity with Ca^{2+} cation. While the rest must be Na^+ cation because they are the principal exchange cations as stated by SWy2 data sheet. The thickness of water layer about 0.502 ± 0.001 nm in the *Mon* gallery signifies a relative humidity around 50 %, which was the *R.H* for such basal spacing as observed by Hendrick [4.23]. Therefore, the d_{001} = 1.462 ± 0.001 nm obtained, agreed well with the value he gave for Ca^{2+} as the exchangeable cations.

This knowledge in addition brought us to the actual location of *Mon*'s origin in Wyoming, as stated in the data sheet. The finding shows that *Mon* is originated from Crook County in Wyoming. This is due the fact that it is the only site which producing *Ca-Mon* in that area. Moreover, it confirmed that the content of Ca^{2+} cation is more than 30% in the fraction of exchangeable cations. This is shown in an increasing order: K^{+}(3%) < Mg^{2+}(20%) < Na^{+}(27%) < Ca^{2+}(50%) [4.20].

As a result to the intercalation process, the (*001*) peak is shifted to the left in *OMON*'s XRD profile, where it gave a new basal spacing, d_{001} about 1.840 ± 0.001 nm at 2θ = 4.80°. This increment in d_{001} spacing about 0.378 ± 0.001 nm reveals the intercalation process of *octadecylammonium*, $C_{18}H_{37}NH_3^{+}$ cation into *Mon* interlayer structure. During the process, Ca^{2+} and Na^{+} cations which occupied *Mon* gallery were replaced by the ammonium cation in the presence of Cl^{-} anions [4.24, 4.25, 4.26 and 4.27]. A model frequently used to describe the mechanism views the ammonium ion (NH_3^{+}) head from *octadecylammonium* (*ODA* cations) to be bonded on silicate surface. Its aliphatic tails from methylene chains in contrast are free to coil and entangle with any hydrocarbon chains [4.28, 4.29, 4.30 and 4.31]. This intercalation process subsequently rendered the initial organophobic property of *Mon* into organophylic. In this work, this *organically modified Mon* is abbreviated to *OMON*.

However, the increment in basal spacing d_{001} of about 0.378 nm is not a satisfactory result in comparison to the works by some previous researchers. They managed to produce better expansions in O*MON*, which were around 0.56 nm to 1.21 nm [4.32, 4.33 and 4.34]. The basal spacing about 1.840 nm in *OMON* again appear as a sign of Ca^{2+} existence in *Mon* gallery, which controlled the clay hydration characteristic. Despite having high hydration energy, as a polyvalent cation Ca^{2+} does experience ion-ion correlation effects within the interlayer which can restrain the gallery expansion beyond d_{001} = 1.9 nm in water medium

[4.35, 4.36 and 4.37]. Therefore, the limited ability of *Ca-Mon* to swell should then restrict extensive expansion as in case of *Na-Mon*, which was used by the researchers. Therefore, it explains the small increase in basal spacing d_{001} for *OMON* in this work. It was due to limited expansion of *Ca-Mon* particles, which had to be dispersed in water prior to the chemical modification that gave the increase in gallery height.

Besides the characteristic peak, there are two other peaks at 2θ = 27.72 ° (d_{001} = 0.321 ± 0.001 nm) and 2θ = 28.40° (d_{001} = 0.314 ± 0.001 nm), which are quite important in Mon's profile. However, they are almost disappearing in the case of *OMON* as shown in Figure 4.12. These peaks represent feldspar mineral, particularly *albite* that is known rich with the Na^+ cation [4.19]. This mineral contains crystallite structures that give the two typical d_{001} spacing. The first intensity peak is supposed to give about 0.321 nm to 0.322 nm, while its second peak should be around 0.317 nm to 0.319 nm that are analogous with the observed peaks in this work. This remark thus proves the reduction of Na^+ cations in *OMON* follows the expected chemical reactions that took place between Na^+ and Cl^- ions. There are also another two peaks at 2θ = 19.84 ° and 2θ = 26.68 ° that signify the silicates (SiO_2) group, a primary component (62.9%) in the *Mon* clay mineral [4.19]. Therefore, these peaks are still observables in the *OMON*'s diffractogram.

Figure 4.13 compares the XRD profiles between *ODA* and *OMON*. In the scan of *ODA*, many sharp peaks indicate the crystalline structures within the material. This observation seems is in agreement with the two endothermic peaks as shown earlier in Figure 4.9 for the DSC thermogram of *ODA*. Again, the whole XRD profile of *OMON* resembles the one for *Mon* as in case of DSC thermogram in Figure 4.10. Recall the remark in Section 4.1.2, which assumed that *Mon* particles hide the *ODA* molecules within its silicates interlayer during the intercalation processes inside *OMON*. Now, it appears to be proven with the

increase in basal spacing, d_{001} of about 0.378 nm, which marks the expansion of *OMON*'s gallery height due to the penetration of *ODA* cations.

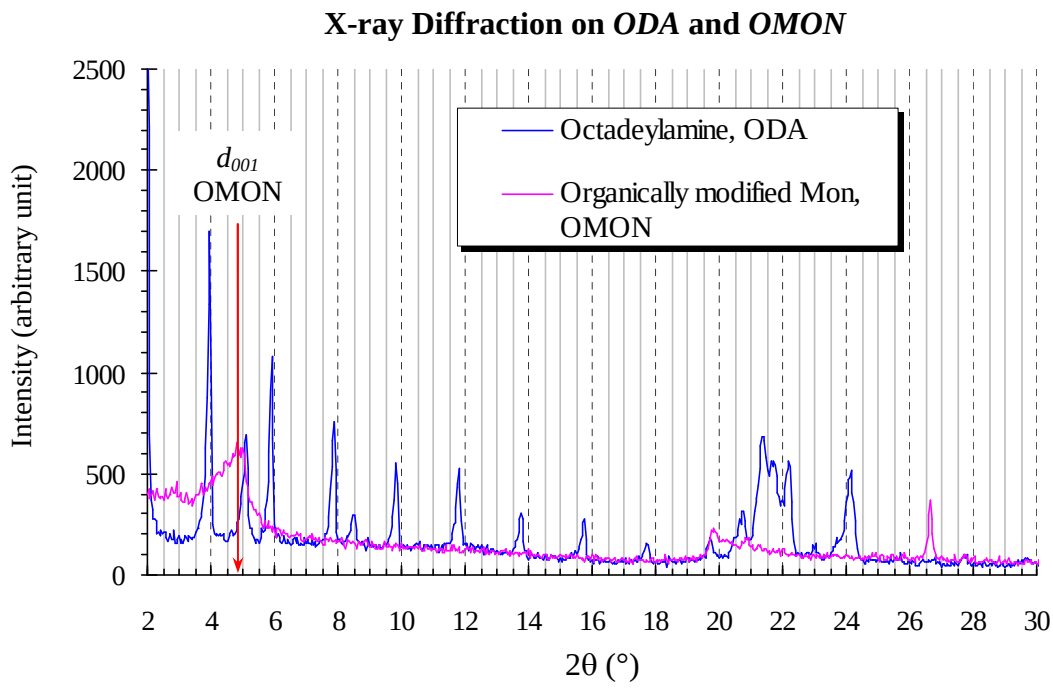

Figure 4.13: Sharp peaks shown in this XRD diffraction profile demonstrate the crystallinity within octadecylamine (*ODA*)

4.2.2 Composites

4.2.2.1 Intercalation and Exfoliation

OMON with its organophylic property is not just capable of absorbing organic substances but it also provides wide surface area for further intercalations. Small organic *ODA* cations (*octadecylammonium*) which are bonded to the silicates surface had made *OMON* became more miscible with large polymeric molecules. *OMON* intercalation that was facilitated by chain coiling and entanglement between the aliphatic tails and matrix chains can be seen within the XRD profiles, especially on the evolution of d_{001} peak positions.

4.2.2.1.A CSMRL, CDPNR and CENR-50

In Figure 4.14 of *CSMRL* (30%), the shifted peak of *OMON* reveals the expansions of *OMON* galleries from the average basal spacing d_{001} about 1.840 nm to 2.582 ± 0.001 nm

(3.42°). Similarly in *CDPNR* (30%), where the peak relocation give new basal spacing d_{001} = 2.439 ± 0.001 nm (3.62°). Hence, the increases in basal spacing about 0.742 ± 0.001 nm for *CSMRL* and 0.599 ± 0.001 nm for *CDPNR* prove the intercalations of matrix chains in the composites. It means that alkyl tails had helped the sorption of these polymeric chains into *OMON* galleries.

The expansion from d_{001} = 1.840 nm to 1.954 ± 0.001 nm (4.52°) in Figure 4.14 gives just a small increase about 0.114 ± 0.001 nm for *CENR-50* (30%), in comparison to the other two rubbers composites. This value actually is irrational since around 50% of the *ENR-50* double bonds were converted into epoxide groups. Such high content of polar components should promote good intercalation process [4.21]. The XRD result in contrast shows that the process took place insignificantly. This finding perhaps can be explained better from another point of view. Polar epoxide groups on *ENR-50* backbone probably had driven the intercalation process extensively thereby, responsible for exfoliation process. In that case, the interlayer structure of *OMON* was disrupted following such process in the *CENR-50*. The disrupted structure however cannot be detected by the XRD diffractometer [4.29 and 4.38]. *CENR-50* (30%) diffractogram in Figure 4.14 thus could only show the effects of intercalation process in the composite. This prediction is also based on the possibility that the detected peak is a second order diffraction profile (d_{002}) that indicates the intercalated component of *OMON*. The estimated basal spacing d_{001} is about 3.864 ± 0.001 nm. Further explanations on this matter will be discussed on the next section.

The absence of any peak emergence either at 2θ = 4.80° from *OMON* or at 2θ = 6.04° as of *Mon* (see Figure 4.12) within composites profiles, in general indicates that *OMON* was homogenously dispersed and well miscible with polymers matrix. In contrast, composite of S*MRL-Mon* as well as *DPNR-Mon* as shown in Figure 4.15, exhibiting characteristic peaks

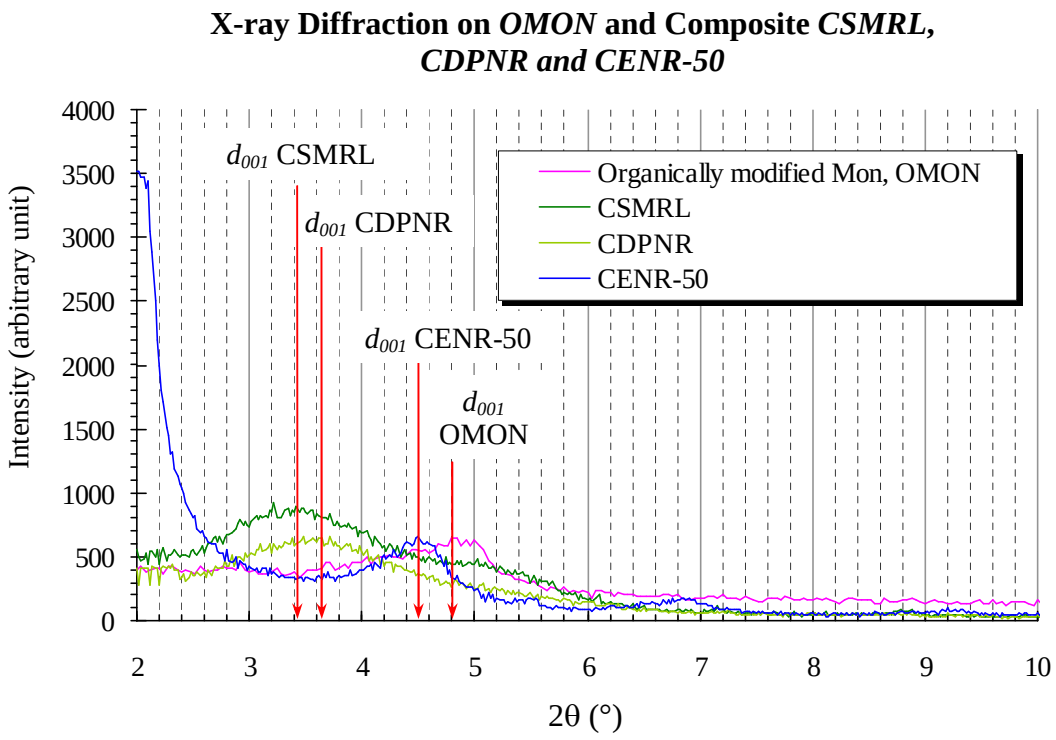

Figure 4.14: XRD profiles for *OMON* and its composites with *SMRL*, *DPNR* and *ENR-50*. The d_{001} peaks are shifted from 4.80 ° to 4.52 ° (*CENR-50*), 3.42 ° (*CSMRL*) and 3.62 ° (*CDPNR*).

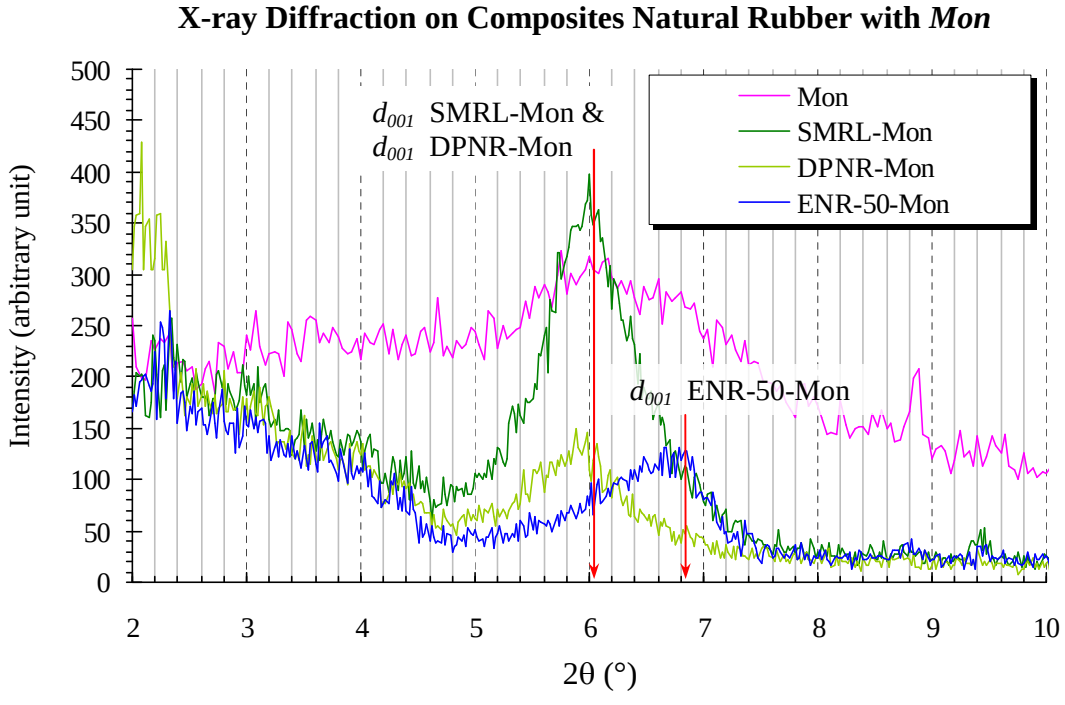

Figure 4.15: Composites *SMRL-Mon* and *DPNR-Mon* maintain their d_{001} peaks of *Mon* around 6.04 ° while in *ENR-50-Mon* the peak is shifted towards 6.84 °.

from *Mon* around 2θ = 6.04°. These peaks thus are not only demonstrating the lack of intercalation processes, but they also provide evidences for the organophobic property of *Mon*. Nevertheless, the shifted peak towards smaller d_{001} spacing at 6.84° in case of *ENR-50-Mon* will be discussed later in Section 4.2.2.2.A.

Previously, Section 4.1.1 (A) discusses gel property where it was qualitatively observed in the studied natural rubbers. It was observed that high gel content in the rubbers reduced its capability to swell in *toluene* solvent. The trend for gel content in the rubbers displayed as follow: *DPNR* < *SMRL* < *ENR-50*. The significant of this sequence has to be taken into account, as it seems to appear again within the XRD profiles as shown in Figure 4.16(a). Except now it is representing the growth of wide peak intensity and crystallite size.

From region 2θ = 12 ° to 26 ° as shown in Figure 4.16(b), it can be seen that the diffraction peaks for *CDPNR*, *CSMRL* and *CENR-50* give just a small but wide hump. These humps obviously analogous to the wide peak of *SMRL* at average d_{001} spacing = 0.472 ± 0.001 nm, as well as for *DPNR* shows in Figure 4.16a. While in *ENR-50*, the basal spacing for such peaks is about 0.582 ± 0.001 nm and 0.421 ± 0.001 nm. These diffraction profiles of *DPNR*, *SMRL and ENR-50* reveal the existence of organic crystalline structures in the elastomers. Therefore, the humps observed in Figure 4.16(b) become an indicator for the presence of natural rubber component within the composites.

According to Scherrer equation,

$$D = \frac{k\lambda}{\beta \cos\theta}$$

Where D = crystallite size (nm)

k = constant (the value is generally = 0.9)

λ = wave length (0.1541 nm)

β = width of XRD peak at half peak maximum (radian)

θ = XRD peak position (°)

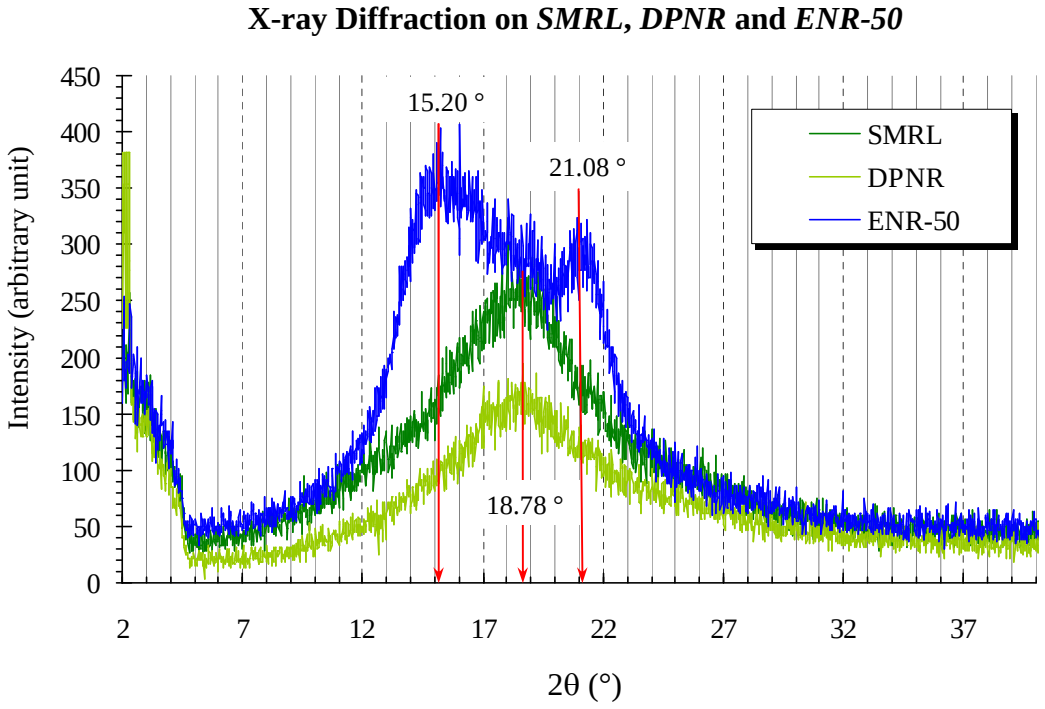

Figure 4.16(a): XRD profiles reveal crystalline structure in *SMRL* and *DPNR* around 18.78 ° while in *ENR-50* they appear at 15.20 ° and 21.08 °.

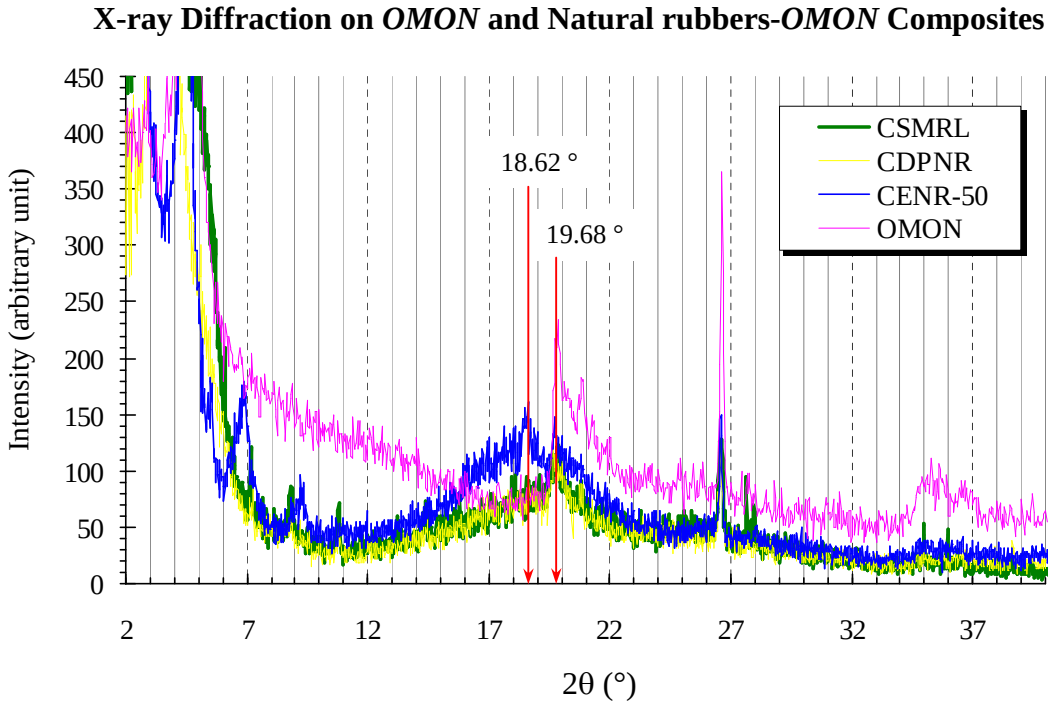

Figure 4.16(b): Wide humps in *CSMRL* and *CDPNR* (19.68 °) as well as in *CENR-50* (18.62 °) are analogous to the peaks, which represent crystallinity in the matrix natural rubbers.

Using this Scherrer equation, size of crystallite structures in the natural rubbers can be estimated [4.39 and 4.40] and is listed in Table 4.2. Apparently, the growth of crystallite sizes in this table is comparable to the trend showed by gel property. It reveals the order of

Table 4.2
Basal Spacing d_{001} and Crystallite Size *D* of Natural Rubber

Sample	**2θ (°)** ± 0.02	**Basal spacing, d_{001} (nm)** ± 0.001	**Half peak width, β (°)** ± 0.02	**Crystallite size, *D* (nm)** ± 0.01
DPNR	18.78	0.472	9.26	0.87
SMRL	18.78	0.472	7.60	1.06
ENR-50	15.20	0.582	4.04	1.98
	21.08	0.421	3.52	2.29

Table 4.2 lists basal spacing d_{001} and crystallite size *D* of *DPNR*, *SMRL* and *ENR-50*.

average diameters for natural rubbers are as follow: *DPNR* (0.87 nm) < *SMRL* (1.06 nm) < *ENR-50* (1.98 nm and 2.29 nm). Crystallinity in polymers comes from regular and ordered packing of some polymeric chains with regularity and ordered structures. These chains are strongly held by secondary forces, which are responsible for the formation of polymer crystal lattices. These crystal lattices produce the diffraction patterns during XRD scan [4.10] as shown in Figure 4.16(a). Therefore, it seems that the gel effect observed could be the indicator of crystalline phase within the natural rubbers. It is generally known that any polymeric structure is a mixture of organic crystalline and amorphous phases [4.3]. Hence, the findings may serve as complementary observations to the DSC results in Figure 4.2 and Figure 4.3. Where, thermal transitions in these figures demonstrated the amorphous phase of the polymers.

This knowledge leads to further analysis on the elastomer-clay composite, especially in the increment of *OMON* gallery heights. Likewise, the crystallite sizes in pristine elastomers, the growth of the d_{001} increments reveals a similar pattern: 0.599 nm (*CDPNR*) < 0.742 nm

(*CSMRL*) < exfoliation (*CENR-50*). It thus, draws attention to the effect of crystallinity on intercalation and exfoliation processes in these composites.

In order to rationalize this idea, it is important to understand the origin of crystallinity in elastomer, which is supposed attributable to the crosslinking effects. Chains crosslink is a type of covalent bonding that is important in elastomer, particularly to establish a three dimensional (*3-D*) network among the elastomeric chains [4.1 and 4.10]. A number of factors might contribute to the formation of crosslinking in elastomers. Such as unsaturated double bond and polar group that exist in the materials. In this case, the last factor seems to be more appropriate as natural rubbers can be differentiated by the presence of certain polar group, for example epoxide and amino acid groups. Our finding thus indicates that the ability of polar groups within natural rubbers to assist chains crosslink determines its crystallite size, which subsequently influences the increment in d_{001} spacing of *OMON* due to the intercalation or exfoliation processes in the *OMON-natural rubber* composites.

4.2.2.1.B CPE

The gel content-crystallinity relation discussed above however are not applicable for *CPE* (5%) as shown in Figure 4.17. The significant peak at d_{001} spacing = 0.414 ± 0.001 nm (21.42°) in the *PE* diffractogram for example, does not indicate the existence of any gel feature. On the other hand, it gives additional proof for the DSC result on the crystallinity in this non-polar semi crystalline polymer. On the contrary to the discussed elastomer, *PE* looks as if it comprised a range of crystalline components with different sizes ($D_{20.14\ °C}$ = 1.69 nm; $D_{21.42\ °C}$ = 16.80 nm and $D_{23.68\ °C}$ = 6.63 nm), and more definite structures. These structures have manifested themselves with the prominent diffraction intensities on the XRD scans. From DSC profile in addition, the big endothermic at 105.36 °C also proved the crystallinity of *PE* as shown in Figure 4.4.

From diffraction profile of *CPE* (5%), it seems that *PE* chains penetration into *OMON*'s galleries had caused the relocation of *OMON* characteristic peak to the new position at 2θ = 3.16 °. The new d_{001} spacing gives about 2.794 ± 0.001 nm, which means that the *PE* hydrocarbon chains had occupied *OMON* interlayer spaces of about 0.954 ± 0.001 nm in height. This increment is much better compare to that of *CSMRL* composite, which is about 0.742 nm. In fact, it is quite satisfactory for a non-polar polymer as the *PE*.

4.2.2.1.C CpPVC

Polarity effects on intercalation process can be seen in the case of *CpPVC* (30%) as shown in Figure 4.18, where a new peak emerges at 2θ = 2.36 ° gives basal spacing d_{001} = 3.741 ± 0.001 nm. This peak shows extensive increment in *OMON*'s gallery height, which is about 1.901 ± 0.001 nm. In previous discussion on *OMON-natural rubbers* composites, it has been suggested that the degree of intercalation was influenced by polymer crystallite size, in which it may be induced by polar groups on the polymer backbone. Analyses on Figure 4.18 in additions, confirms that polar groups itself had played a significant role to promote advanced intercalation in *CpPVC*. For example, oxygen atoms from the *DOP* molecules in *pPVC* can induce hydrogen bonding [4.41] between this plasticized polymer and *OMON* silicates. Subsequently, it assisted more chains of the matrix polymer to penetrate *OMON* galleries. The argument above can be used to explain the ability of bulky polyisoprene chains within natural rubbers to participate in intercalation process, regardless its crystallite sizes [4.10]. In that case, the driving force for this process possibly came from unsaturated double bonds in the matrix chains, which might have provided the potential reaction sites with *OMON* components. The effect of polar group was also important in the intercalation of natural rubber chains. Particularly, when there is a co-existence of several polar groups, such as amino acid and epoxide group within C*SMRL* and C*ENR-50* composites.

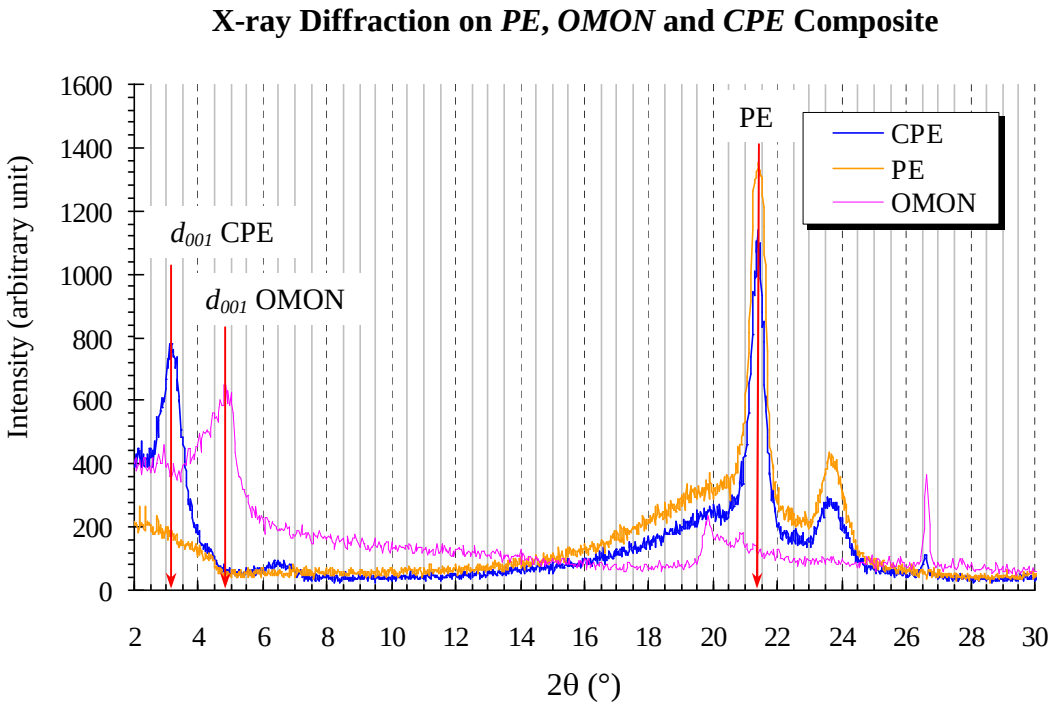

Figure 4.17: The crystallinity in *PE* is proven by the appearance of peak at 21.42 °. The shifted peak for *CPE* appears at 3.16 °.

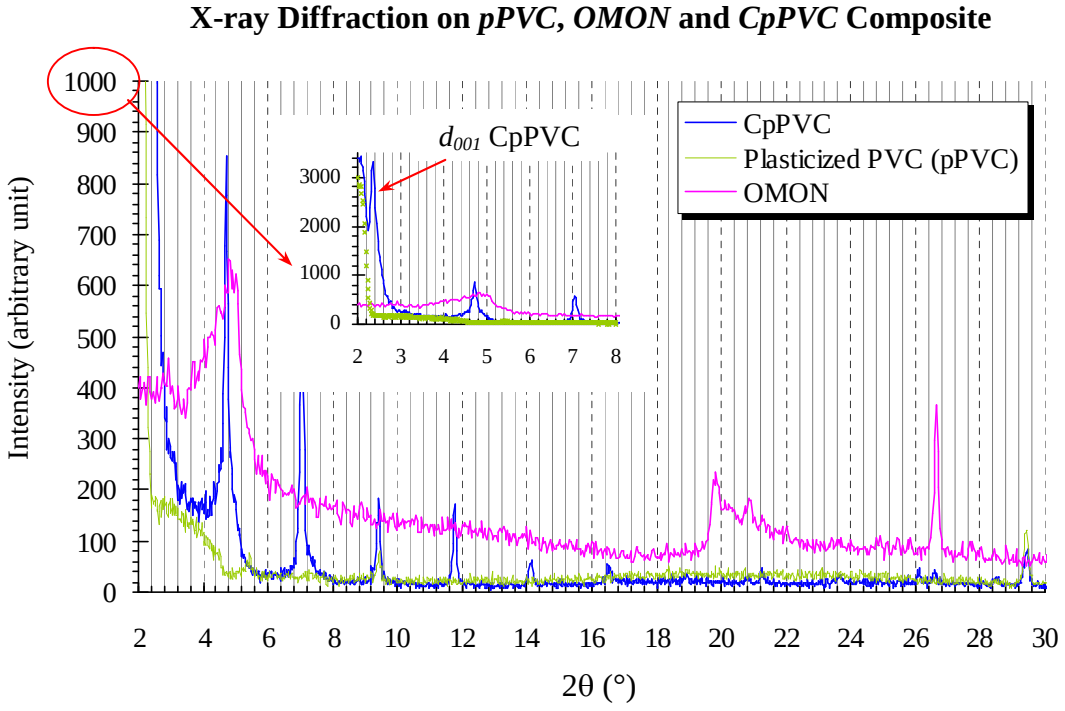

Figure 4.18: Sharp peaks shown in this diffraction profile resemble the high degree of crsytallinity in *CpPVC*. Inset shows that the d_{001} peak for *CpPVC* at 2.36 ° is about 3.741 nm.

From these analyses, the studied composites can be divided into two main categories. They are assigned as the polar and non-polar groups depending on their polymer matrices. Table 4.3 illustrates the evolution of basal spacing d_{001} from *Mon* to *OMON* and to the *polymer-OMON* composites.

Table 4.3

Basal Spacing d_{001} of *Polymer-OMON* Composites

Filler		**XRD parameter, 2θ (°)** ± 0.02		**Basal spacing, d_{001} (nm)** ± 0.001		d_{001}***OMON -*** d_{001}***Mon*** **= ∂d_{001} (nm)** ± 0.001	
Mon		6.04		1.462		—	
OMON		4.80		1.840		0.378	
Polar				**Non-Polar**			
Composite	**2θ (°)** ± 0.02	d_{001} **(nm)** ± 0.001	∂d_{001} **(nm)** ± 0.001	Composite	**2θ (°)** ± 0.02	d_{001} **(nm)** ± 0.001	$\partial_c d_{001}$ **(nm)** ± 0.001
CENR-50	2.28 *	3.864 *	2.024 exfoliation	**CDPNR**	3.62	2.439	0.599
				CSMRL	3.42	2.582	0.742
CpPVC	2.36	3.741	1.901	**CPE**	3.16	2.794	0.954

* Undetectable; $\partial_c d_{001}$ = d_{001}***Composite -*** d_{001}***OMON***

Table 4.3 summarizes all the discussed basal spacing d_{001} and the increments involve within the composites.

From the table, it can be seen that polar polymers have better chance to intercalate compare to those from the non-polar polymers group. In this non-polar group, the growths in gallery height ∂d_{001} for *CSMRL* and *CDPNR* are small compared to that of *CPE*. Since similar solvent (*toluene*) was used to prepare these composites, the increase in basal spacing ∂d_{001} could be influenced by the crystallite size of the polymers. The smallest crystallite size *D* in *PE* for example was estimated to be around 1.69 nm that is bigger than those in *SMRL* (*D* = 1.06 nm) and *DPNR* (*D* = 0.87 nm). The differences are consistent with the variation in d_{001} spacing as shown in Table 4.3 for *CPE, CSMRL* and *CDPNR*.

4.2.2.2 Further Analysis on XRD profiles

Previous XRD analyses on *polymer-OMON* composites discuss mainly on the d_{001} peaks that revealed a lot of information on compatibility of these composites, which involve the intercalation and exfoliation processes. More facts however are needed to understand the clay material composites, especially when they involved -different groups of polymers.

4.2.2.2.A Bridging Flocculation

Figure 4.19 shows the effect of polar as well as non-polar polymers on their composites with *Mon*. For example in the non-polar *polymer-Mon* composites, typical peak of *Mon* that give the d_{001} spacing about 1.462 nm still appear at the same angle 2θ = 6.04 °. In case of polar polymer matrix however, these peaks are shifted towards higher diffraction angles. They can be seen at 2θ = 6.84 ° (d_{001} = 1.291 ± 0.001 nm) for *ENR-50–Mon* and at 2θ = 6.60 ° (d_{001} = 1.338 ± 0.001 nm) for *pPVC–Mon*. These drops in d_{001} spacing demonstrate the reduction in gallery heights of *Mon* particles within the composites.

The effect is most likely due to the bridging flocculation process. Polar groups within the polymeric chains interact with oxygen or hydrogen on silicates surfaces to form hydrogen bonding. This interaction can also improve van der Waals forces between the materials. A part of the process involves the removing of water layer at the interface where the chains are about to form the bonding. A schematic diagram in Figure 4.20 illustrates the matrix-silicate interaction at interface. In case where the polymeric chain is long enough then the other end will form a similar bonding with another surface from the other layers, especially with the adjacent layer. The movements on segmental chain as a result will draw the both layers closer to one another. It thus reduces the interlayer height d_{001} and gives the higher 2θ values as shown in Figure 4.19 [4.42 and 4.43]

According to Smalley [4.42], this phenomenon is commonly found in many polar systems such as a mixture of *PEO* and *vermiculite* in water. Likewise, the effect took place when

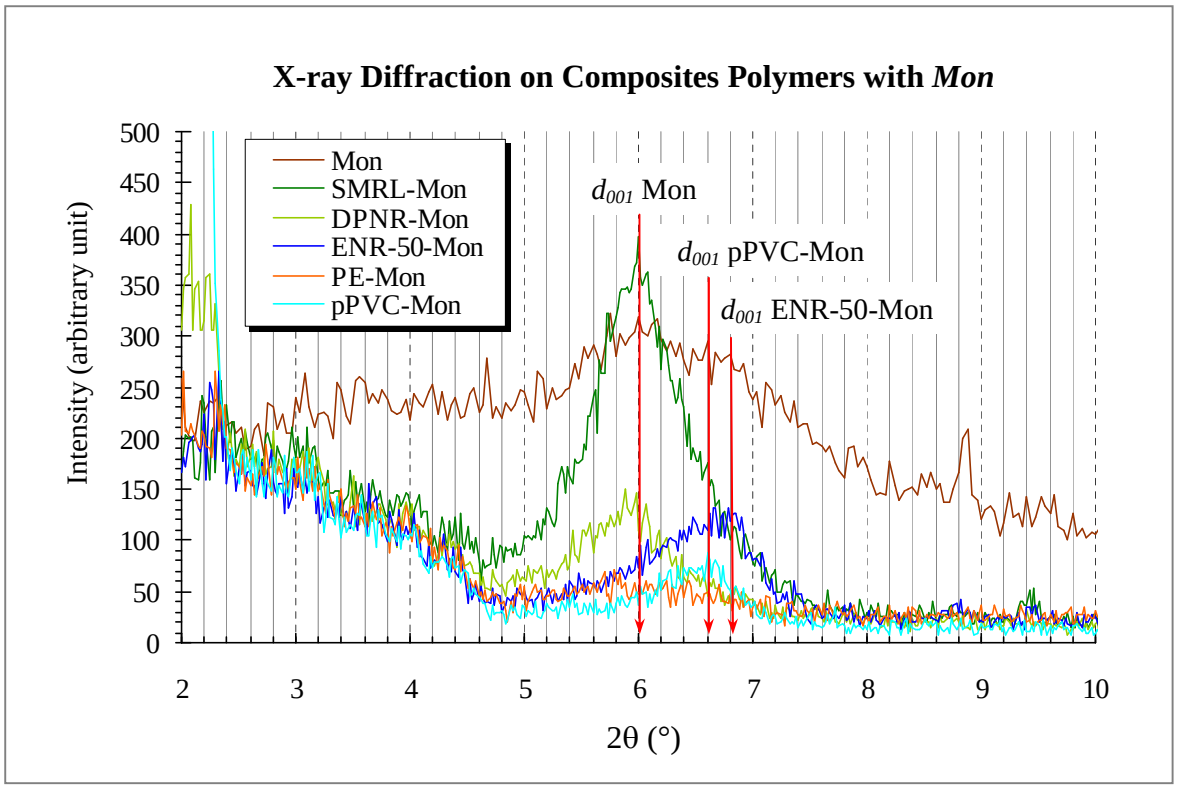

Figure 4.19: XRD profiles shows that the d_{001} peak of Mon around 6 ° is preserved in *SMRL-Mon*, *DPNR-Mon* and *PE-Mon*. In case of *pPVC-Mon* and *ENR-50-Mon*, the peak is shifted to 6.60 ° and 6.84 ° respectively.

Bridging Flocculation in *Polymer-Mon* Composite

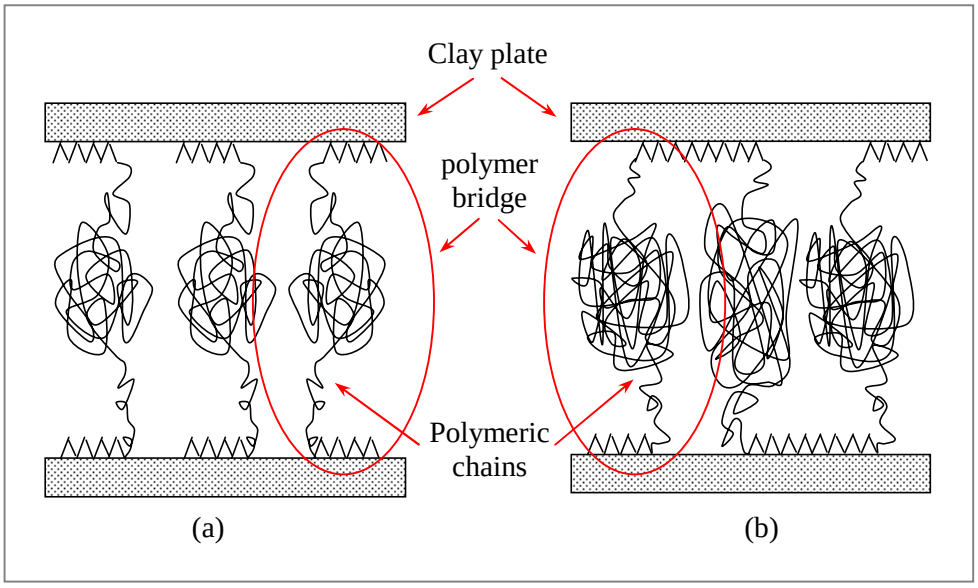

Figure 4.20: Schematic illustration of the bridging flocculation by polymers in clay gallery shows the case: (a) for a polymeric chain that is just large enough to form a single bridge while (b) multiple bridge is formed by a larger polymeric chain [4.40].

blending polar *pPVC* with *Mon* in *methyl ethyl ketons* (*MEK*). As a result, it had shrunk the silicates interlayer height. However, this argument cannot be used to explain the decrease in gallery height of *ENR-50–Mon* system. Since a non-polar organic solution, *toluene* was used as the solvent [4.44] for the mixture.

Previous works by some authors in the study of clay swelling [4.45, 4.46, 4.47 and 4.48] revealed that polarity of solution is given by the dielectric constant, ε. This parameter plays important role to determine the layers expansions. There were evidences that demonstrated solution with high ε value was well desorbed, which had caused the clay plates to swell better then those in solution with low ε values. This remark seems reasonable for *MEK* with ε = 18.30 [4.45], which was used as a solution in the *pPVC-Mon* system. Moreover, it is generally known that whether in aqueous or non-aqueous system a large number of solvent is desorbed into silicates interlayer to facilitate the sorption of a single polymeric molecule [4.21]. However, the relatively low dielectric constant ε about 2.38 of the non-polar *toluene* [4.48 and 4.49] may not give the same effect in *ENR-50–Mon* system, as the polar *MEK* in *pPVC-Mon* composite.

However, there are recent evidences that suggested the potential for *cation-*π bonding to be formed in a system with restricted geometries, such as in the *Mon* interlayer spaces. It is highly believed that the interaction that is importance in protein can also occur between the exchangeable cations in *Mon* gallery and the π *electron* of aromatic guest molecules [4.50, 4.51 and 4.52]. The fundamental nature of this interaction is a weak attraction that occurs between a cation and the electron-rich π orbital of an aromatic or any other simple π system. The double bonds in benzene for instance, produce electron cloud that can attract positive ions to form a non-covalent binding force. This force is comparatively strong with an approximation of five times bigger than the force for hydrogen bond.

For that reason, aromatic rings in *toluene* may have served as the source of π electrons that formed temporary bonding with the exchangeable cations, Ca^{2+} or Na^{+} in *Mon* galleries. In that way it allowed the adsorption of *toluene* into *Mon* interlayer, where it then induced organic substances to penetrate into the spaces. At the same time, *toluene* also interacted with the *ENR-50* chains. In which, it induced the rubber chains to swell and thus, loosens its 3D network structures. By this means, *toluene* turned out to be the solvent for both materials. Together with the assistance from epoxide groups, *ENR-50* was then capable to penetrate the *Mon* galleries.

As a result, bridging flocculation as in *pPVC-Mon* is supposed to take place in the *ENR-50-Mon* system as well. In addition, it seems reasonable to believe that multiple bridging flocculations as illustrates in Figure 4.20(b) occurred in this composite. Particularly, when the long polymeric chains and 3D network structure in the *ENR-50* is considered. In which it can assist a much higher degree of bridging flocculation in this system. Consequently the *Mon* gallery shrunk even better in *ENR-50-Mon*, where it gives a bigger decrease in basal spacing, ∂d_{001} = 0.171 ± 0.001 nm compared that of *pPVC-Mon* ∂d_{001} = 0.124 ± 0.001 nm as shown by XRD result in Figure 4.19.

This special ability of *toluene* solvent as illustrated in Figure 4.21 is much more significant

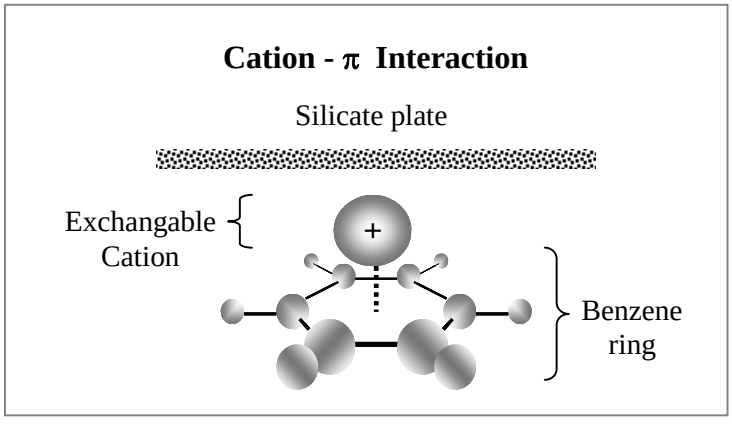

Figure 4.21: Schematic diagram of the cation-π interaction [4.49], between exchangeable cation in *Mon* interlayer and benzene ring from *toluene*.

in *polymer-OMON* composites. In which, it helped non-polar polymers such as *PE, SMRL* and *DPNR* to intercalate into *OMON* interlayer. This effect should be more prominent in case of *CENR-50*, wherein it promoted extensive intercalation that eventually may lead to the exfoliation of silicate plates in this composite.

4.2.2.2.B Ordering Effect

Bridging flocculation is not a simple suggestion to describe several peaks observed above the characteristic of *OMON* at 2θ = 4.80 ° in Figure 4.22(a) and 4.22(b). Analyses on the peaks must also take into account the trend that they have developed on the XRD results. From XRD diffraction principle, a unit cell dimension is given as follow:

$$a = \frac{\lambda}{2}\frac{\sqrt{h^2 + k^2 + l^2}}{Sin\theta}$$

and from Bragg's law, $$d = \frac{k\lambda}{2Sin\theta}$$

thus, $$a = d\sqrt{h^2 + k^2 + l^2}$$

for d_{00l}, $$a = d\sqrt{l^2}\ , \qquad [4.53 \text{ and } 4.54]$$

so at (0,0,1) unit cell dimension, $a = d_{001}$

where $k\lambda$ = wave length (0.9 x 0.1541 nm) d = basal spacing (nm)

θ = XRD peak position (°) h,k,l = Miller indices (h,k,l)

Table 4.4(a) shows that the obtained ***l*** values of *CpPVC* are tolerable with small standard deviations percentages (0.31 % to 0.57 %). Therefore, it confirms that *CpPVC* peaks in the XRD profile indicate ordering effect on diffractions pattern. The effect which is caused by internal structure of a material is represented in the form of *Miller* indices (h,k,l).

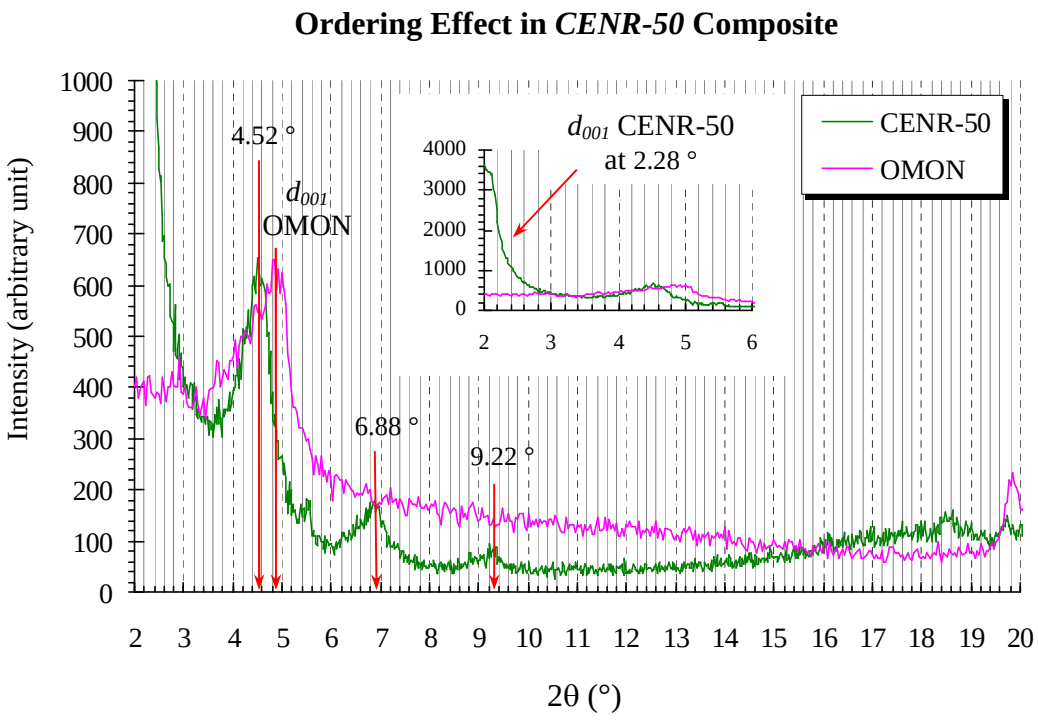

Figure 4.22(a): The ordering effects as appear in *CENR-50*: at 4.52 ° (002), 6.88 ° (003) and 9.22° (004). While the inset shows the calculated d_{001} at 2.28 °.

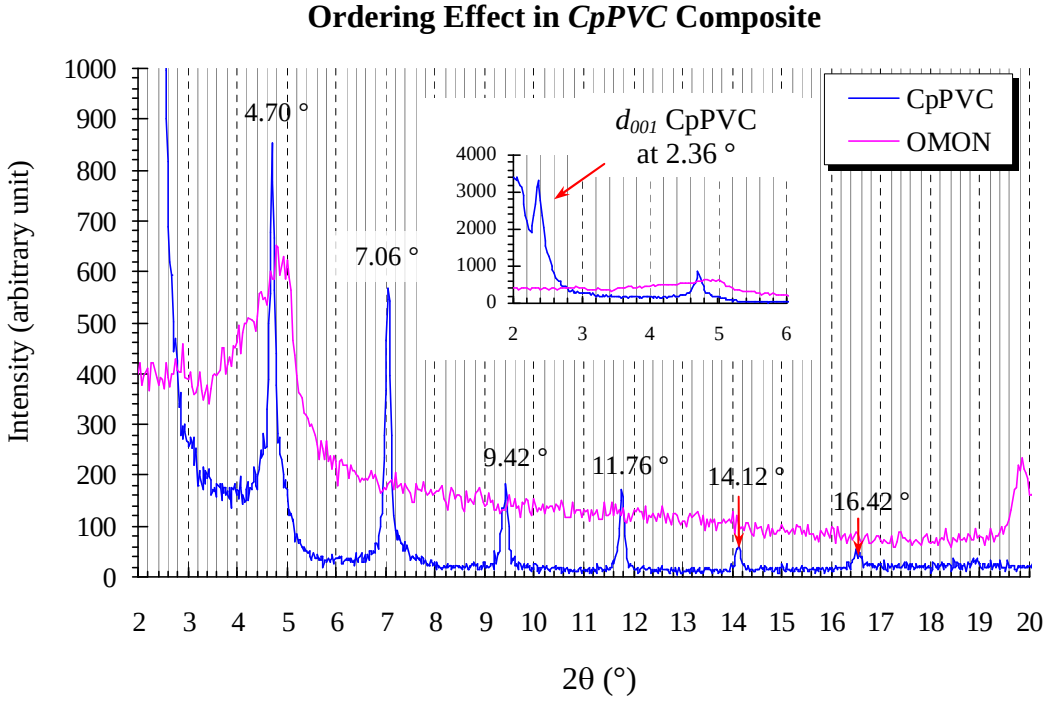

Figure 4.22(b): These sharp peaks indicate the ordering effect in *CpPVC*: 2.36 ° (001), 4.70 ° (002), 7.06 ° (003), 9.42 ° (004), 11.76 ° (005), 14.12 ° (006) and 16.42 ° (007).

Similarly in *CENR-50*, by assuming the same ordering effect the unit cell dimension (*a*) of each peak can be estimated which is equivalent to the basal spacing d_{001}. From the mean value of a_n, 2θ for the first order peak can be calculated using the Bragg's law. The value is recorded in Table 4.4(b), where the 2θ angle is approximately 2.285 ± 0.001° with its basal spacing d_{001} = 3.864 ± 0.001 nm. Perhaps, limitation at small angle measurement in XRD scan was the main reason behind the failure to detect this peak earlier.

Besides the advantage of forming bond with silicate surfaces, chain length factor is also very important in bridging flocculation process [4.42], especially in *OMON*. These factors become more significant due to bigger gallery height in *OMON* compared in pristine *Mon*. In addition, the present of *octadecylammonium* molecules act as chains entanglement and coiling sites for polymeric chains. These molecules consequently may trap some part of the chains, and thus reduce the length of free-chain that can form bridging flocculation on the silicate surfaces. These remarks thus, justify the irrelevant of considering the bridging flocculation effect in the cases of *CENR50* and *CpPVC* composites.

Some studies on *Mon* revealed that its thickness is approximately 1 nm, while the range for diameters could be around 500 to 2000 nm. Therefore, this high aspect ratio tells that *Mon* is not composed of rigid silicate plates, but plates with some flexibility [4.16, 4.20, 4.23 and 4.55]. This behavior influenced the order of layered structure as graphically illustrated in Figure 4.23(a). In fact, this feature look as if it was preserved even after undergoes some chemical modification in order to make it organophylic (*OMON*). The intercalations of polymeric chains had caused the *Mon* clay plates to be consistently spaced, and thereby it became uniform. This effect can be seen in the transition of *Mon* to *OMON* and lastly the *OMON* composites, where XRD peaks intensity as well as their shape are progressively improved as shown in Figure 4.12, 4.14, 4.17 and 4.18. Moreover, the contribution of polar

groups in polymer intercalation could have helped silicate layers to be parallel, which gives a more coherent structure compared to the initial arrangement [4.42 and 4.56].

Table 4.4(a)
Ordering Effect in *CpPVC* Composite

CpPVC						
Peak n	**2θ (°)** ± 0.02	d_{00n} (nm) n = 1, 2, .. ± 0.001	$l = \frac{d_{001}}{d_{00n}}$, n = 1, 2, ... ± 0.001	$\boldsymbol{l}$	$\frac{\lvert \boldsymbol{l} - l \rvert}{\boldsymbol{l}} \times 100\,(\%)$ ± 0.01	*Miller index* **(*h,k,l*)**
1	**2.36**	3.741	1.000	1	0.00	**(*0,0,1*)**
2	**4.70**	1.879	1.991	2	0.45	**(*0,0,2*)**
3	**7.06**	1.251	2.990	3	0.33	**(*0,0,3*)**
4	**9.42**	0.938	3.988	4	0.30	**(*0,0,4*)**
5	**11.76**	0.752	4.975	5	0.50	**(*0,0,5*)**
6	**14.12**	0.627	5.966	6	0.57	**(*0,0,6*)**
7	**16.48**	0.537	6.966	7	0.49	**(*0,0,7*)**

Table 4.4(b)
Ordering Effect in *CENR-50* Composite

CENR-50						
Peak n	**2θ (°)** ± 0.02	d_{00n} (nm) n = 1, 2, .. ± 0.001	$l = \frac{d_{001}}{d_{00n}}$, n = 1, 2, ... ± 0.001	$\boldsymbol{l}$	$\frac{\lvert \boldsymbol{l} - l \rvert}{\boldsymbol{l}} \times 100\,(\%)$ ± 0.01	*Miller index* **(*h,k,l*)**
1	~ **2.28**	3.864 *	1.000	1	0.00	**(*0,0,1*)**
2	**4.52**	1.954	1.978	2	1.10	**(*0,0,2*)**
3	**6.88**	1.284	3.010	3	0.33	**(*0,0,3*)**
4	**9.22**	0.958	4.032	4	0.80	**(*0,0,4*)**

* the mean value from a_2, a_3 and a_4 where $a_n = d_n\sqrt{\boldsymbol{l}_n^{\,2}}$

Table 4a and 4b list the results from analyses on XRD peaks of *CpPVC* and *CENR-50*, which reveal the ordering effects within these composites.

Such structure as shown in Figure 4.23(b) can cause the ordering effects on XRD profile of composite with polar matrix. In this work, the effects are seen in Figure 4.22(a) and Figure 4.22(b) for *CENR-50* and *CpPVC* composite, respectively.

The emergences of repeatable peaks above *Mon* characteristic peak ($2\theta > 6.04$ °) in these composites also indicate the ordering effect. It means that these peaks are not indicating the shrinked *OMON* interlayer or the unintercalated portion of both *Mon* and *OMON* in the composites. This remark also confirms the earlier assumption in Section 4.1.3.C. In which the formation of crystallites structures in *CpPVC* was induced by intercalation process, as shown by T_{m3} in Figure 4.10 of DSC thermogram.

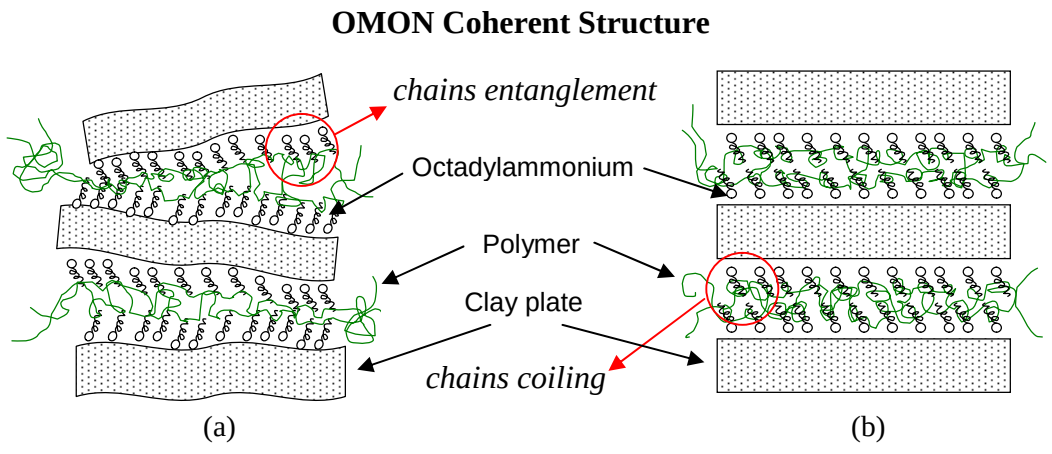

Figure 4.23: Schematic illustrations of *OMON* particle shows (a) a less ordered structure and (b) a coherent structure with consistently spaced and more uniform arrangement which can produce ordering effect on XRD profile.

4.2.2.2.C Stacking Order, *N*

The idea of bridging flocculation structure discussed earlier involves successive silicates layers within the single structure of *Mon* particle. However, it may also take place between silicate layers from several Mon particles. As a result, it promotes more aggregation in the *ENR-50-Mon* and *pPVC-Mon* systems compare to the particles within non-polar *polymer-Mon* composites. The effect however is much more significant in *OMON* composites, since

it can improve the stacking order as listed in Table 4.5. Base on the theory of multiple slit diffractions and Scherrer equation, the number of layers in a single *Mon* or *OMON* particle can be estimated. Compare the equation for multiple slits diffractions,

$$Nd = \frac{k\lambda}{\nabla\theta \ cos\theta} \qquad [4.57 \text{ and } 4.58]$$

with the crystallite size equation, $D = \frac{k\lambda}{\beta \cos\theta}$

where

D = crystallite size (nm) N = number of slits

k = constant (the value is generally = 0.9) d = basal spacing (nm)

λ = wave length (0.1541 nm) $\nabla\theta$ = line width

β = width of XRD peak at half peak maximum (radian) θ = XRD peak position (°)

and taking $\nabla\theta = \beta$, it can be seen that $\boldsymbol{Nd = D}$

Table 4.5 shows additional contribution by the polarity of polymer matrix. It is understood that the great tendency of polar groups in polymers to interact with *OMON* polar elements encourage extensive intercalations. This interaction either within *OMON*'s gallery or on its silicate surfaces in fact, may also enhance the stacking orders of *OMON* silicates layers. For example in *CpPVC*, the stacking order *N* value about 21 layers is relatively greater than that of non-polar *CPE*. Likewise, *CENR-50* showed an improved staking order in comparison to those of less polar *CSMRL* and *CDPNR*. In fact, the estimated *N* value about 3 layers from *CSMRL* and *CDPNR* are smaller than the 4 layers structure obtained from pristine *OMON*. It thus tells that clay delamination had occurred in *OMON* structure within these composites. Despite the stacked structure, under certain condition *OMON* layers can also be delaminated.

Table 4.5 shows that natural rubbers overall are weak in its ability to stack *OMON* silicates layers. Even though *CPE* involve the non-polar *PE*, it has bigger *N* value about 6.19 than

that of polar elastomer *CENR-50* (*N* = 5.71). This effect on *OMON* structure is illustrated in Figure 4.43 of Section 4.2.3. This analysis distinguishes the outcomes produced by different mode of interaction between matrix and alkyl chains in *OMON* gallery. It seems that coiling between these chains in *CpPVC* and *CPE* helps *OMON* to stack more silicate layers on its structure. While entanglement by bulky polyisoprene chains in natural rubbers create weak interaction, which insufficient to promote the stacking process.

Table 4.5
Stacking Order *N* in *Mon*, *OMON* and *Polymer-OMON* Composites

Sample	**2θ (°)** ± 0.02	**Half peak width, β (°)** ± 0.02	**Basal spacing, d_{001} (nm)** ± 0.001	**Crystallite size, *D* (nm)** ± 0.001	***N* = *D*/d_{001}** ± 0.01
Mon	6.04	1.44	1.462	5.527	3.78
OMON	4.8	1.12	1.840	7.103	3.86
CDPNR	3.62	1.14	2.439	6.975	2.86
CSMRL	3.42	1.06	2.582	7.501	2.91
CENR-50	2.28	0.36	3.864	22.082	5.71
CPE	3.16	0.46	2.794	17.285	6.19
CpPVC	2.36	0.10	3.741	79.495	21.25

Table 4.5 shows the effect of *OMON* in the composites with the increment in basal spacing, d_{001}; crystallite sizes, *D* and stacking order, *N*.

4.2.3 Summary

- In section 4.2.1, XRD analysis on *Mon* gives basal spacing d_{001} about 1.462 ± 0.001 nm (2θ = 6.04 °), which in aggrement with the present of Ca^{2+} cation in *Mon* from Crook County in Wyoming,US. This primary cation created at least 30 % of the exchangeable cations population within the *Mon* intelayer.
- Chemical modification on *Mon* produced *OMON* with new basal spacing d_{001} around 1.840 ± 0.001 nm (2θ = 4.80°). The growth approximately 0.378 ± 0.001 nm in gallery height confirms the intercalation of *ODA* cations within silicate interlayer. The increase however is quite small due to limited swelling ability of *Mon*, which is controlled by Ca^{2+} cation system.
- The drop in diffraction intensity of *albite* mineral at 2θ = 27.7° and 28.4° prove the reducing of Na^{+} cation due to chemical reaction, during modification process on *Mon*.
- In Section 4.2.2.1, intercalation of polymers matrix had increased *OMON* basal spacing in *polymer-OMON* composites. In case of *CENR-50*, it is believed that exfoliation had occurred in this composite.
- *Polymer-OMON* composite are separated into two category based on their respective polymer matrix. They are listed in Table 4.3 as *Polar group* which consists of *CpPVC* and *CENR-50*, and *Non-polar group* with *CPE*, *CSMRL* and *CDPNR* composites.
- Polarity of polymers matrix and their crystallite size promote intercalation process and the increase of *OMON* basal spacing.
- The increment in basal spacing d_{001} can be used as an indicator for *polymer-OMON* compatibility.In *polymer-Mon* system its incompatibility had caused the d_{001} spacing remains unchanged.

- In Section 4.2.2.2.A, *polar polymer-Mon* composites show the decrease in d_{001} spacing of *Mon* particle. It was due to *bridging flocculation* process by polar chain that brought successive *Mon* layers closer to one another. Polarity of a solvent is very important to assist the process, such as *MEK* in *pPVC-Mon* system. While in non-polar *toluene* for *ENR-50-Mon* system, the process was assisted by *cation-*π interaction.

- XRD peaks greater than *Mon* characteristic peak ($2\theta > 6.04°$) in polar *CENR-50* and *CpPVC* profiles reveal *ordering effect* on XRD diffraction patterns. Polar matrix chains had helped to realign silicates layers, and gave coherent structure that contributes to the effect as shown in Section 4.2.2.2.B.

- Matrix chains interactions with alkyl chains have great effect on *OMON stacking order N* which is discussed in Section 4.2.2.2.C. Chains coiling in *CpPVC* for example, gives *N* about 21 layers. While chains entanglement within less polar *CSMRL* contributed to the delaminating of *OMON* silicate layers. The polarity of matrix chains also helped to improve the stacked layer on *OMON* particles. Such as in case of polar *CENR-50* with 6 silicate layers structure in the composite.

4.3 Fourier Transform Infra-Red, FTIR

Infrared spectroscopy detects the vibration characteristics of chemical functional groups in a sample. When IR radiation is passed through a sample as shown in Figure 4.24, it will interact with the matter thereby causes chemical bonds to stretch, contract and bend. Therefore, a chemical functional group usually tends to adsorb IR radiation in a specific wave number range regardless of the structure formed in the rest of a molecule.

The essential fact about FTIR is its consistency in the wave number position, portrayed by individual functional groups. It is despite the effect of temperature, pressure, sampling and structural changes in the neighboring part of the molecule. Hence, it is very useful in this work as the composites involve the incorporation of materials from different origins. FTIR technique offers a way to conform the pristine component via their characteristics bonds [4.59 and 4.60].

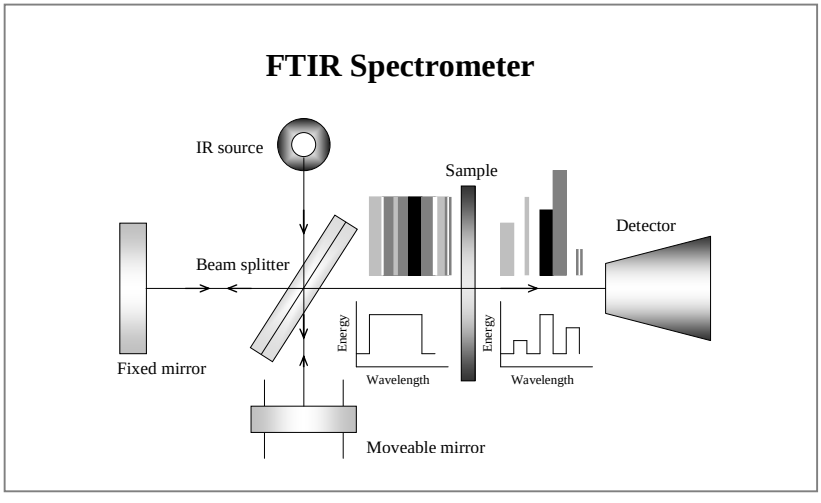

Figure 4.24: A schematic diagram for Fourier Transform Infra-Red, FTIR spectroscopy [4.58].

Any elements that chemically took part in the interaction between *OMON* and polymeric chains can be detected. Besides, this technique is very helpful to identify the formations of new entities, following any chemical or physical processes occurred in the composites. In this work, a FTIR machine Nicollet Magna-IR 5508 was used to take the transmittance spectrums in the mid infrared region which is in between 400cm^{-1} to 4000 cm^{-1}.

4.3.1 Pristine Polymers

4.3.1.A *SMRL, DPNR* and *ENR-50*

Table 4.6 summarizes major characteristic absorption bands for *DPNR*, *SMRL* and *ENR-50*. It is confirmed then that the rubbers are actually composed of polyisoprene chains with the *cis* structure on double bond (*C=C*) isomerism. The configuration for this isomer is illustrated in Figure 4.25, wherein the trace is presented by the 1664 cm^{-1} absorption band as shown in Figure 4.26. The stretching mode for *C–H* bond (ν*CH*) from (=*CH*) element is shown by the strong and sharp band at 3035 cm^{-1}, while the out of plane bending mode (*∂CH*) appears around 837 cm^{-1}.

Cis 1, 4 polyisoprene

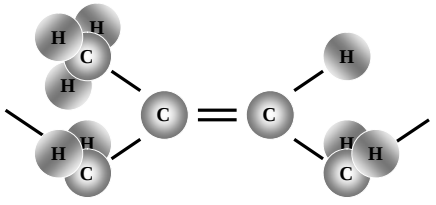

Figure 4.25: The isomer structural of cis 1, 4 polyisoprene [4.10]

Strong absorption around 1375 cm^{-1} demonstrates peaks overlapping. It involves methyl symmetry bending mode ($\partial_s CH_3$) and *C–H* bending mode (*∂CH*) from methyl group on the (*–CO-*CH_3 *–*) component. Likewise, the trace of asymmetry bending vibration ($\partial_{as} CH_3$) at 1448 cm^{-1} superimposes with *C–H* bending band (*∂CH*) of methylene on the *cis* structure (*–*CH_2*-C=C–*). Methylene bands in natural rubbers can be seen within the absorption range of 2850 cm^{-1} to 3000 cm^{-1} as shown in Figure 4.26. The trace around 2850 to 2860 cm^{-1} for example demonstrates the symmetry stretching bands ($\nu_s CH_2$) of methylene, whereas it's asymmetry stretching vibration ($\nu_{as} CH_2$) appears within the range of 2918 to 2927 cm^{-1}. Absorption band observed at 2962 cm^{-1} is another result of bands overlapping. It involves the asymmetry stretching mode ($\nu_{as} CH_3$) of methyl group, and methylene stretching band

($\nu_s CH_2$) from ($=CH_2$) element around 2975 cm^{-1}. Actually, most of the bands can be found in many polymers and functioning as basic identification for the materials.

Table 4.6
Characteristic Bands for *SMRL*, *DPNR* and *ENR-50*

No.	Group/type	Band (cm^{-1}) ± 1	Assignment
1.	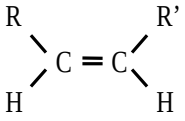	1664 (ref.: 1660)	Cis isomerism of alkenes
2.	=C-H	3035 (ref.: 3020)	ν *CH*
3.	=CH	837 (ref.: 800 - 840)	∂ *CH* out of plane
4.	Overlap $-CH_3$ and $CO-CH_3$	(ref.: 1375) 1375 (ref.: 1360-1355)	∂_s CH_3
			∂ *CH*
5.	Overlap $-CH_3$ and $CH_2C=C$	(ref.: 1450) 1448 (ref.: 1445-1430)	∂_{as} CH_3
			∂ *CH*
6.	$-CH_2$	2850-2860 (ref.:2853)	ν_s CH_2
7.	$-CH_2-$	2918-2927 (ref.: 2925)	ν_{as} CH_2
8.	Overlap $-CH_3$ and $=CH_2$	(ref.: 2962) 2960 – 2970 (ref.: 2975)	ν_{as} CH_3
			ν_s CH_2
9.	Sodium salt of amino acid, $CO_2^-Na^+R-NH_2$	3280 (ref.: 3200 - 3400)	ν *NH*
10.	$-NH_2$	1541	∂ (*N-H*) from -NH-
		1630	∂ (*N-H*) from $-NH_2$-
11.	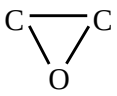	798, 876 and 1252	epoxy ring: 12μ , 11μ and 8μ

Table 4.6 is continued in the next page

From previous page

No.	Group/type	Band (cm^{-1}) ± 1	Assignment
12.	R– C-O-C	1064	ν_{as} *C-O-C*
13.	C-O-C	1113, 1150 and 1174	*C-O-C* band splitting
14.	Polymeric	3488	Intermolecular hydrogen bonding
15.	Carbonyl of aldehydes –C=O	1732 – 1734 (ref.: 1740-1720)	ν *C=O*

Table 4.6 lists some of the characteristic absorption bands for the identification of *SMRL*, *DPNR* and *ENR-50*. [4.59, 4.60 and 4.61]

The source for elastomers used in this work is natural rubbers, which mean it is a naturally produced polyisoprene. Therefore, it may come with some impurities for instance, a certain amount of protein that can be observed through its amino acid related bands. Such as the wave number at 3280 cm^{-1} shows a *N-H* stretching band (νNH) from sodium salt of amino acid. While the bending mode (∂NH) can be seen at 1541 cm^{-1} and 1630 cm^{-1} for *–NH-* and *–NH_2-* groups respectively. However, these bands are missing in FTIR of spectrum *DPNR*. This is expected as *DPNR* had undergone some chemical processes to remove its protein components.

ENR-50 is another member in the invention of modified natural rubbers. It was modified in such a way that about 50% of its unsaturated double bonds were changed into epoxide groups. The existence of this group is confirmed by the emergence of 12μ, 11μ and 8μ bands at 798 cm^{-1}, 876 cm^{-1} and 1252 cm^{-1} accordingly. These bands represent epoxy ring as shown in Table 4.6. In addition, an absorption band of asymmetric stretching vibration (ν_{as}*C–O–C*) at 1064 cm^{-1} from *R–C–O–C* group supports these observations. According to Silverstein [4.59], branching on carbon atom adjacent to the oxygen usually leads to the splitting of *C–O–C* band within the region of 1114 cm^{-1} to 1170 cm^{-1}. It thus, explains a

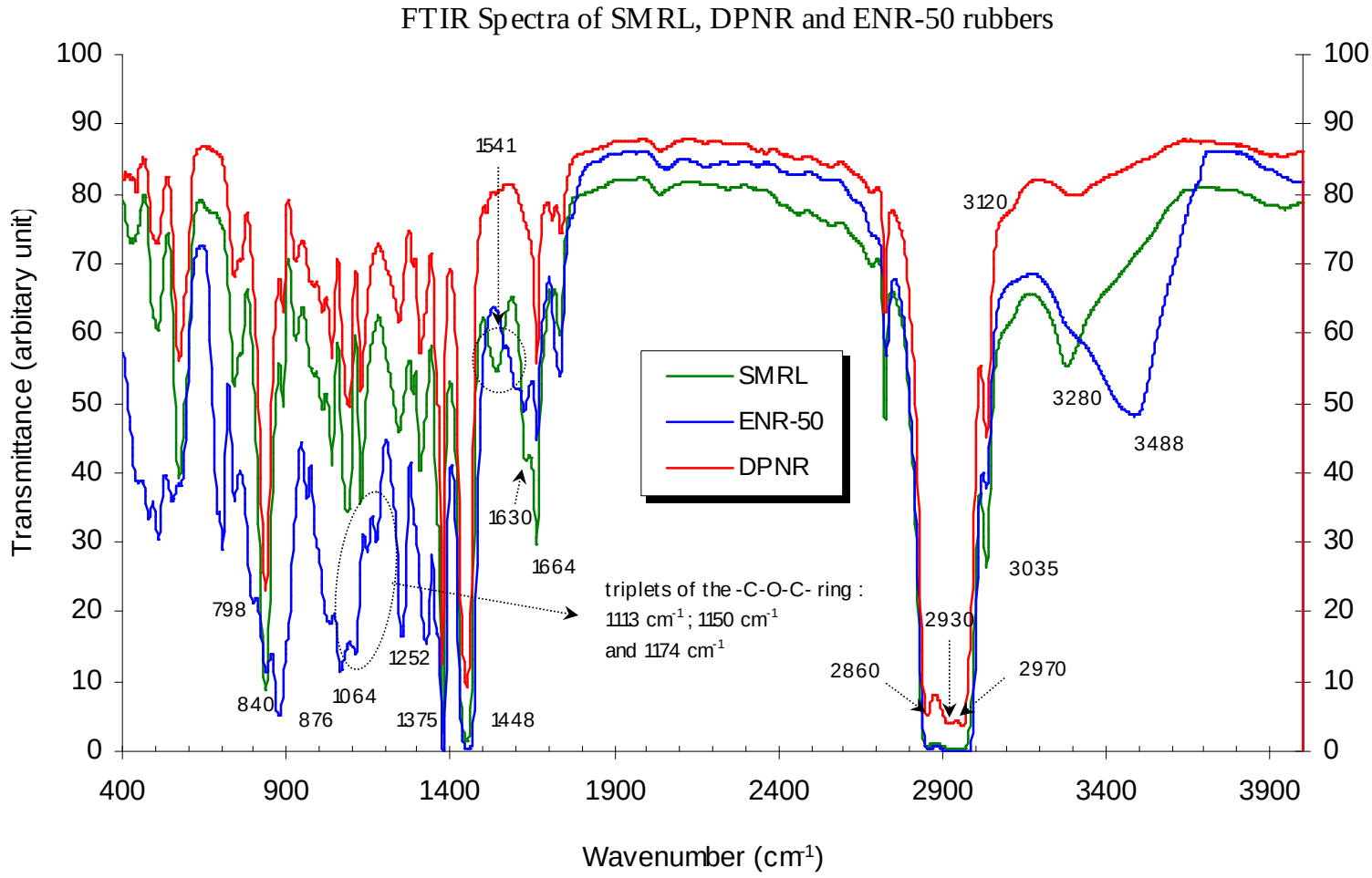

Figure 4.26: FTIR spectra of SMRL, DPNR and ENR-50 rubbers show some of the major characteristic bands.

triplets bands found around 1113 cm^{-1}, 1150 cm^{-1} and 1174 cm^{-1}. The presence of oxygen atom in polyisoprene chains is very important, as it can promote the formation of hydrogen bonds among the polymeric chains. Therefore, it contributes for the emergence of band around 3488 cm^{-1} that indicates the intermolecular hydrogen bond.

Previously in Section 4.2, it was suggested that crosslink reactions among the polyisoprene chains produced 3D physical network structures within the natural rubbers. From FTIR analysis, the source for this reaction to take place is confirmed that is the double bonds on the elastomers backbones. These electron-rich unsaturated double bonds are functioning as nucleophiles, which provide the potential sites for crosslink reaction. The resulted covalent bonds from such reaction connect the rubber chains together. Hence, this primary bonding responsible for the 3D network structure that contributes to the gel formation in the natural rubbers [4.62 and 4.63]. The effect became more prominent in case of *ENR-50* rubber that is manifested with the high gel content. Particularly, since this rubber contained the three member-ring of epoxy element as proven earlier via FTIR analysis. These polar groups are very reactive towards nucleophile substitution. They can also provide more potential sites for the formation of intermolecular hydrogen bonds, which subsequently can increase the gel content.

Moreover, the non-rubber elements present in natural rubbers especially protein had been reported to play significant role behind the gel formation in both *SMRL* and *ENR-50* [4.64 and 4.65]. It means that polar components from protein molecules should also participate in the crosslink reaction. This is shown with the missing of amino band (*∂NH*) at 1541 cm^{-1} in *ENR-50* profile, whereas at 3280 cm^{-1} a rather fade band of amino salt from protein molecules arise in the spectrum. However, it is overlapped by the bigger band at 3488 cm^{-1} of intermolecular hydrogen bond. This finding explains the effect of protein removal from natural rubber that can reduce the chances for intermolecular crosslinking. The gel effect

thus is minimized as demonstrated by the deproteinised natural rubber (*DPNR*) after being soaked in *toluene* solvent.

According to Gan [4.8], natural rubbers composed of at least 97 % cis -1, 4 polyisoprene. It means that about 3 % of natural rubber content could be in other forms of isomerism and structures. Therefore, it explains the bands related to ($=CH_2$) group around 2975 cm^{-1} that may represents 3, 4 polyisoprene. Oxidation on unsaturated double bonds can lead to chain scissoring, which then produces carbonyl group. Such effect is detected within the natural rubbers as the carbonyl stretching band ($\nu C=O$) from aldehydes appears around 1732 cm^{-1} to 1734 cm^{-1}. Likewise, the trace for *C-H* bending mode (∂CH) from ($–CO\text{-}CH_3–$) groups add more evidence for the effect of oxidation. This band is believed overlaps at 1375 cm^{-1} with the bending band ($\partial_s CH_3$) of methyl group. Similarly as in case of *ENR-50*, epoxide group can also be detected within the spectra of *DPNR* and *SMRL*. It is represented by the 8μ band from epoxy ring around 1245 to 1250 cm^{-1}.

4.3.1.B Polyethylene, *PE*

Polyethylene is a widely used polymer created through polymerization of ethane C_2H_4. It composed of long polymeric chains that are rich with methyl and methylene groups. The FTIR spectrum for *PE* is shown in Figure 4.27 with the biggest trace placed itself within the band range of 2800 cm^{-1} to 3000 cm^{-1}. The observable bands for methylene group are identified at 2850 cm^{-1} for its symmetric stretching mode ($\nu_s CH_2$). While the asymmetric vibration ($\nu_{as} CH_2$) at 2920 cm^{-1} overlaps with the asymmetric stretching mode ($\nu_{as} CH_3$) of methyl group at 2960 cm^{-1}. The absorption band found at 719 cm^{-1} is an indicative of the rocking vibration mode ($\rho(CH_2)_n$) for methylene chains, whereas it's scissoring vibration band ($\partial_{as} CH_3$) is located at 1464 cm^{-1}. Both peaks are very prominent and sharp compared to the weak absorption band at 1377 cm^{-1}. This band represents the symmetrical bending

vibration of methyl groups ($\partial_s CH_3$) and can be used as an indicator for chain branches in *PE* [4.66]. The result therefore tells that the studied *PE* is lack of branching structure in its system. It means that the polymer has high crystallinity with compact chains arrangements. The polymer thus can be classified as a high-density polyethylene or *HDPE*.

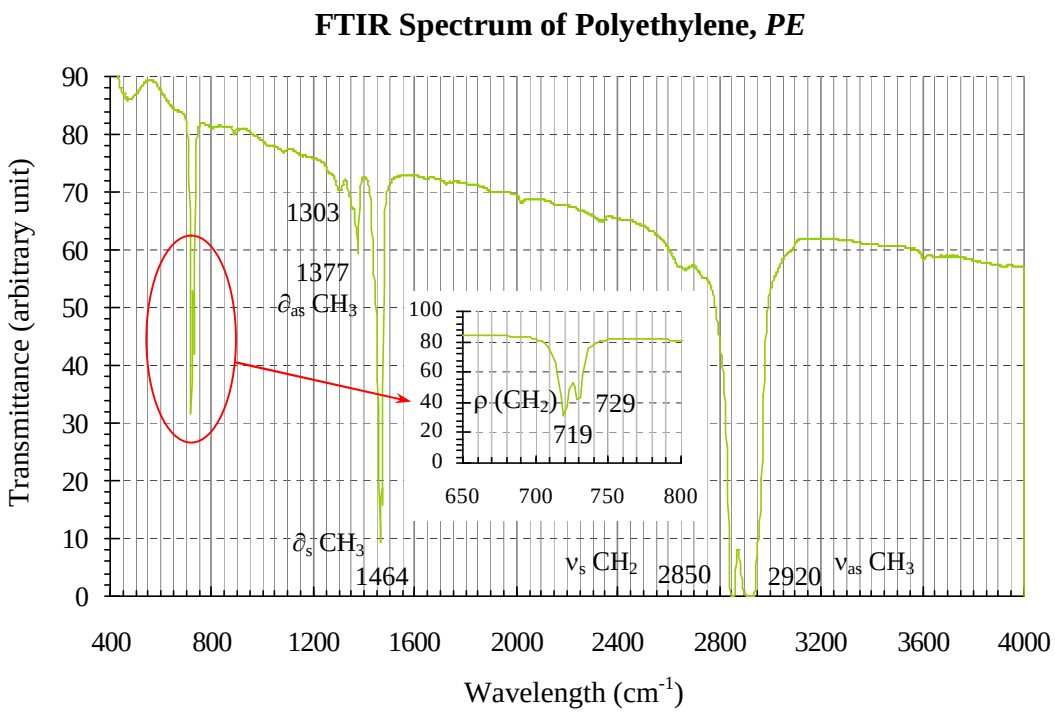

Figure 4.27: FTIR spectrum for *PE* shows the characteristic methyl and methylene bands for stretching and bending vibrations modes.

The assumption is based on the comparison with Wang and co-author [4.66] works on various type of *PE*. It is learned that the absorption intensity of methyl bending vibration ($\partial_s CH_3$) at 1377 cm^{-1} is about a quarter of methylene band ($\partial_s CH_2$) at 1464 cm^{-1} in *HDPE*. This fact is comparable with the *PE* spectrum as shown in Figure 4.27. Besides, the idea is supported with the adsorption band at 1303 cm^{-1} that signifies the amorphous phase in *PE*. This band arises as a small hump, in contrast to the sharp trace detected at 729 cm^{-1} for *PE* crystalline region. The observations thus are consistent with the findings in DSC and XRD analysis that also demonstrate the crystallinity in *PE*.

4.3.1.C Plasticized Polyvinyl chloride, *pPVC*

Figure 4.28 demonstrates the absorption spectrum for plasticized *PVC* or *pPVC*. Typical absorption band for this polymer emerges within the range of 850 cm^{-1} to 550 cm^{-1}, which represent the aliphatic halogen (*RC–Cl*) group. They are normally found in the form of triplets as detected around 617 cm^{-1}, 636 cm^{-1} and 706 cm^{-1} in the spectrum. Another band that is also related to the chlorine atom could come from the (CH_2Cl) molecule. It appears as a wide and strong absorption trace from 1230 cm^{-1} to 1300 cm^{-1}. This band is recognized as the effect of wagging vibration (ωCH_2) by methylene group. The characteristic methylene stretching bands for polymers can be seen at 2930 cm^{-1} ($\nu_{as}CH_2$) and 2860 cm^{-1} ($\nu_s CH_2$). While the stretching bands for methyl groups appear at 2960 cm^{-1} and 2874 cm^{-1} reveals the asymmetric ($\nu_{as}CH_3$) and symmetric ($\nu_s CH_3$) mode in that order.

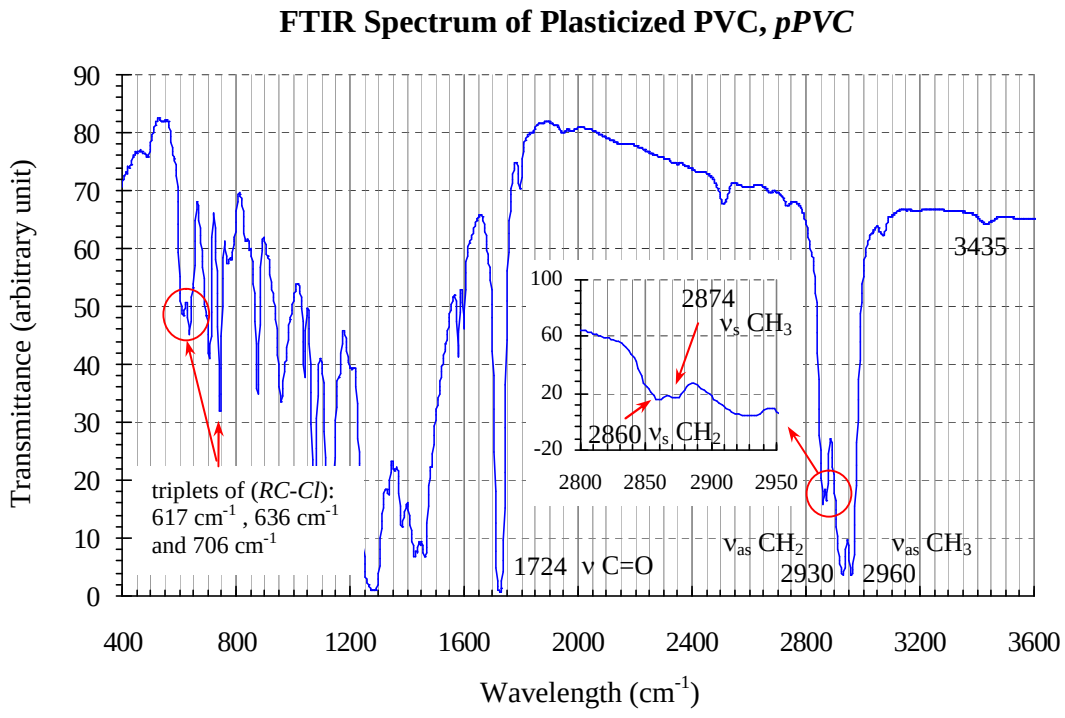

Figure 4.28: Besides the characteristic bands, this spectrum for *pPVC* shows the existence of dioctylphthlate, *DOP*. This plasticizer is represented by the *C=O* stretching band at 1742 cm^{-1}.

Previously in Section 4.1.1.C, the function of *dioctyl phthalate* (*DOP*) plasticizer molecules on *pPVC* chains was discussed. It was including the new T_g in DSC profile that explained the polymer elasticity behavior at room temperature. FTIR spectrum additionally, presents more proof on the existence of *DOP* molecule. The *DOP* related band can be seen in *pPVC* spectrum around 1724 cm^{-1} with strong absorption intensity. This band was generated by carbon-oxygen symmetrical stretching mode ($\nu_s C=O$), from ester group ($R\text{–}O\text{-}\overset{\overset{O}{\|}}{C}\text{–}R'$) within *DOP* molecules [4.67]. These molecules promoted hydrogen bond formation inside *pPVC*, which is represented by a band at 3435 cm^{-1} of intermolecular hydrogen bonding.

4.3.2 OMON and Polymer-OMON Composites

OMON is a renewed *Mon* that had been organically modified via some chemical processes. Major characteristic bands of the pristine *Mon* nevertheless are still observable in *OMON*'s spectrum as shown in Figure 4.29, and listed in Table 4.7. The stretching vibration mode of silicate (νSiO) for example, can be detected at 1045 cm^{-1} while it's bending mode (∂SiO) appears around 523 cm^{-1}. The two bands at 796 cm^{-1} and 467 cm^{-1} represent silica (SiO_2) and alumina (Al_2O_3) molecules respectively, which are the major elements of *Mon* particle. From XRD analyses, it has been discussed earlier that *Mon* is capable of absorbing some layers of water molecules into its gallery. This fact is in agreement with the FTIR analysis, where the absorption bands for hydroxyl stretching (νOH) from hydration and hydroxyl bending (∂HOH) mode appear at 3438 cm^{-1} and 1651 cm^{-1} respectively.

As a result to the intercalation of *octadecylammonium* cations, some traces that are related to the methylene group and ammonium ion become observerable within *OMON* spectrum. They are at 719 cm^{-1} signifies the rocking mode of methylene chains vibration ($\rho(CH_2)_n$), while the bands at 2848 cm^{-1} and 2918 cm^{-1} represent its symmetry ($\nu_s CH_2$) and asymmetry

Table 4.7
Characteristic Bands for *OMON* and *Polymer-OMON* Composites

No.	Group/type	Band (cm^{-1}) ± 1	Assignment
1.	SiO	1045	ν *SiO*
		629	∂ *SiO*
		523	∂ *SiO*
2.	SiO_2	796	SiO_2
3.	Al_2O_3	467	ν *AlO*
4.	OH	920	∂ *OH* linked to $2Al^{3+}$
5.	H_2O	3438	ν *OH*
		1651	∂ *HOH*
6.	$–CH_2–$	2918	ν_{as} CH_2
		2848	ν_s CH_2
		719	ρ $(CH_2)n$
		1472	∂_s CH_2
7.	$–NH_3^+$	1504	∂_s NH_3^+
		1614	∂_{as} NH_3^+
		2048	(~2000) overtones
		2505	
		2530	
8.	Si–O–R	1000 - 1100	R, aliphatic
9.	Si–H	920	∂ *Si–H*
		2100 - 2360	ν *Si–H* — 2189 cm^{-1} (*CENR-50*)
			ν *Si–H* — 2210 cm^{-1} (*CpPVC*)

Table 4.7 list the important absorption bands found in the FTIR spectra of *OMON* and polymer-*OMON* composites. [4.18, 4.58, 4.59, and 4.67]

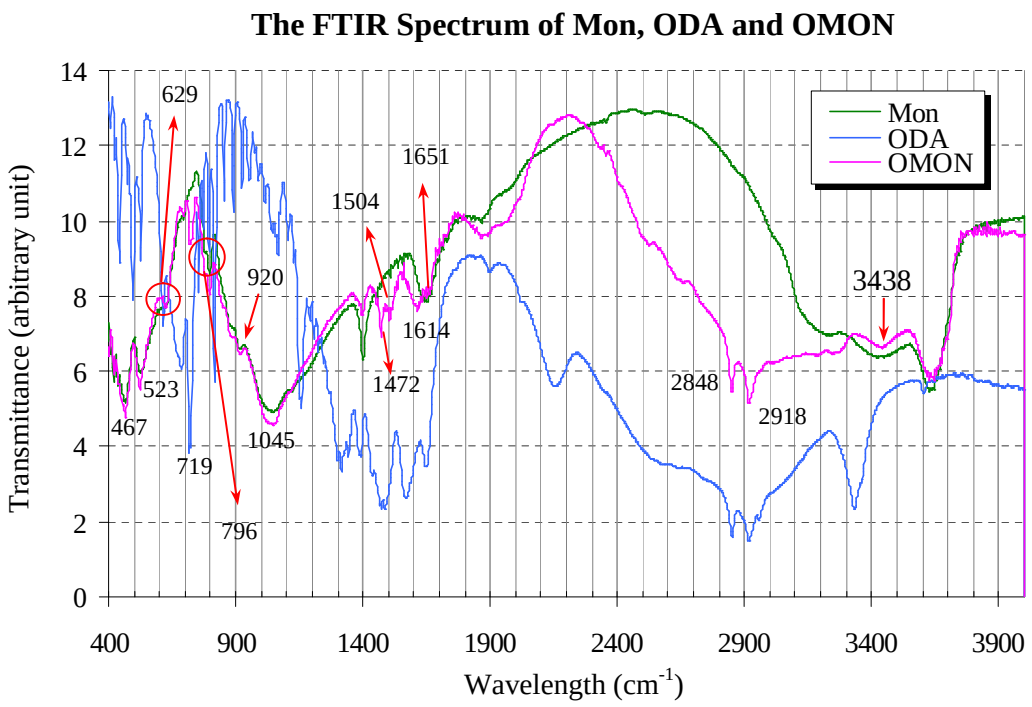

Figure 4.29: Some major characteristic bands from *Mon* and *ODA* appear in *OMON* spectrum. They are listed in Table 4.7, which proves the chemical modification carried out on *Mon*.

($\nu_{as}CH_2$) stretching vibration in that order. The band for symmetrical bending mode of ammonium ions ($\partial_s NH^{3+}$) is detected at 1504 cm^{-1}. It is followed by the trace at 1614 cm^{-1} that characterizes its asymmetrical bending ($\partial_{as} NH^{3+}$) mode. This absorption band overlaps with the band for hydration bending vibration (∂HOH) at 1651 cm^{-1}.

The purpose of FTIR analysis in this work is to examine microscopically the effects of intercalation and exfoliation processes within *polymer-OMON* composites. Hence, primary focus is on some bands in Table 4.7 that may serve as the evidences for such processes. The observations can be divided into four main groups that demonstrate various interaction and effects on *OMON* particle and matrix chains. They are the *Matrix and Alkyl chains interaction*, *Matrix chains and OMON silicate interaction*, *Effects on OMON silicate* and *Effects on matrix chains*.

4.3.2.1 Matrix and Alkyl Chains Interaction

4.3.2.1.A. ($\partial_s CH_2$) band

Figure 4.30(a) shows the bending mode of methylene vibration ($\partial_s CH_2$) at 1472 cm^{-1}. This band manages to maintain its appearance only within *ODA* and *OMON* spectra. The band actually reveals the intermolecular interaction within the crystallite structures [4.69 and 4.70] of alkyl tails inside *OMON* galleries. From the spectra however, it seems that matrix-alkyl chains reaction had caused disruptions on the intermolecular interactions. Therefore, the absence of this methylene band proves chain interaction between matrix chains and the alkyl tails of *ODA* cations within *polymer-OMON* composites. In case of *CPE* composite, careful analysis shows that the band is attributable to the ethylene groups from *PE* matrix chains as shown in Figure 4.27.

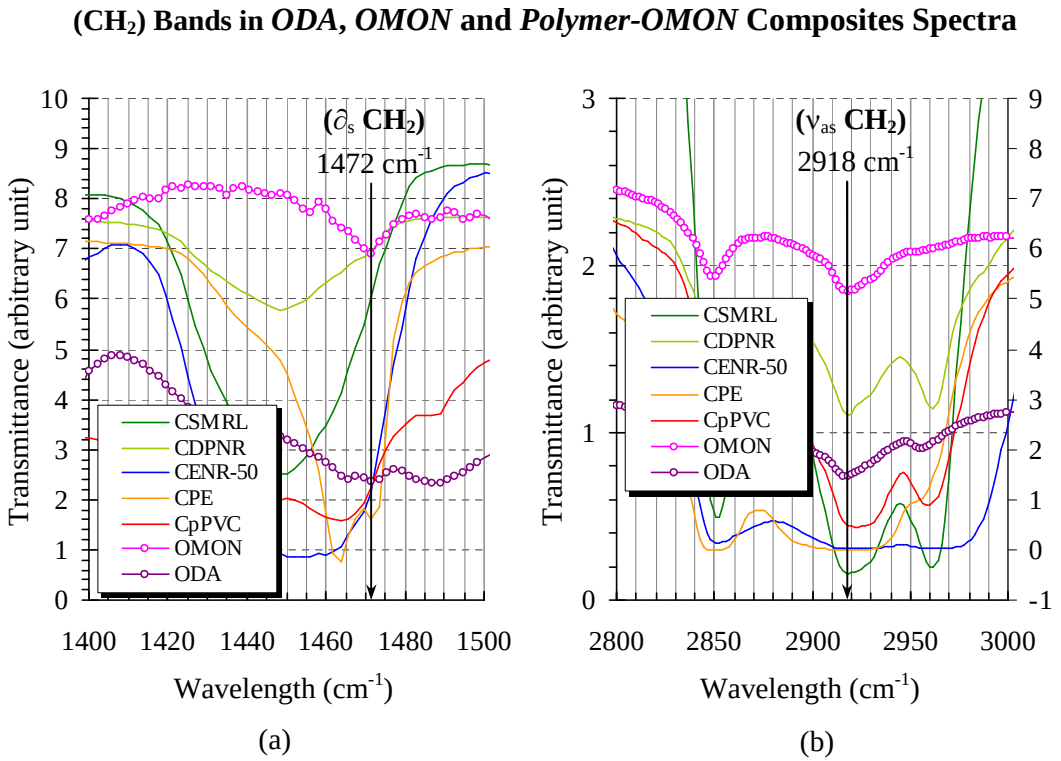

Figure 4.30: Methylene symmetrical bending in (a) proves the intermolecular interaction in crystalline structure while the stretching mode in (b) reveal the all-trans conformation in methylene chains which is also related to crystallinity of the chains.

Trans/gauche Conformers in Methylene Chains

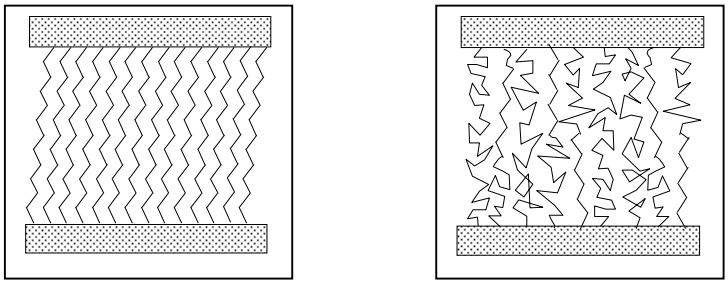

(a) (b)

Figure 4.31: Schematic illustrations of methylene chains conformation in *OMON* and *OMON* composites show: (a) all-trans conformation and (b) gauche conformation [4.68, 4.69 and 4.70]

4.3.2.1.B. ($\nu_{as}CH_2$) band

Absorption band in Figure 4.30 for the asymmetry stretching of methylene group, ($\nu_{as}CH_2$) at 2918 cm^{-1} is recognized to represent the highly ordered all trans–conformations of the methylene chains. It indicates the crystallite structures as shown in Figure 4.31(a) [4.69, 4.70 and 4.71]. This band can be observed clearly in *ODA*, *OMON*, *CSMRL* and *CDPNR* spectra, where they appear just about the same wave number. In case of *CENR-50*, *CpPVC* and *CPE* spectra however, the band is slightly shifted toward higher wave numbers. They actually reveal the increased ratio of gauche conformation on the alkyl chains in *OMON* gallery, as schematic illustrated in Figure 4.31(b).

This finding perhaps distinguishes the effect from chains entanglement and chains coiling reactions within *polymer-OMON* composites, as suggested earlier in the XRD analyses. The coiling of polymeric chains with the alkyl tails seems to dominate the chain interaction inside *CpPVC* and *CPE* composites. Such interaction as a result increased the ratio of less ordered or gauche conformation on the methylene tails in *OMON* gallery. The 3D network structure of natural rubber matrix however, might restrict this chain coiling reaction. On the other hand, it can promote chains entanglements with the alkyl tails at certain entangled points. Such as, at the end of alkyl tails that saved the highly order all trans-conformation.

In case of *CENR-50* composite, such chain entanglement can take place progressively and further towards silicates surfaces. This is due to the polarity effect caused by polar epoxide groups on the *ENR-50* backbone. It thus, affects the highly ordered conformation and shifts the methylene band to a higher wave number as shown in the *CENR-50* spectrum.

4.3.2.1.C. ($\rho(CH_2)_n$) band

More evidence on the effect of chains coiling and entanglement is given by the rocking vibration mode of methylene chains ($\rho(CH_2)_n$) at 719 cm^{-1}. From Figure 4.32, it seems that the band consistently appears within *ODA*, *OMON* and all of *OMON* composites spectra, except for *CpPVC* composite. Previously in the discussion on chain interaction by rubbers matrix chains, it was believed that the rubber chains entangled to the methylene tails at certain entanglement points. In that way, it may provide some freedom for the aliphatic tails to vibrate especially in the rocking mode. In case of *CpPVC* however, the methylene tail is supposed to coil with the plasticized *PVC* chains as pictured in Figure 4.23. The tails movement in that way is most likely restricted. As a consequent, the rocking mode of methylene ($\rho(CH_2)_n$) chains is diminished from the *CpPVC* spectrum.

From *CPE* spectrum, the rocking band ($\rho(CH_2)_n$) could be the result of bands overlapping by methylene tails within *OMON* gallery and *PE* matrix chains. However, careful analyses suggested that the absorption band at 719 cm^{-1} is most likely representing only methylene chains from *PE* polymer. This belief is based on typical behavior shown by many bands overlapping or superimpose within FTIR spectrum, where each original band normally will reveal its existence in the new formed trace. The situation however is different in case of *CPE* where no clear evident of band overlapping that can be related to such effect. For that reason, the superimpose of methylene in-plane bending bands ($\rho(CH_2)_n$) as of *OMON* and *PE* is inappropriate to describe the band in *CPE*. The rocking mode of methylene chains from *OMON* thereafter is considered absent in *CPE* as in *CpPVC* spectrum.

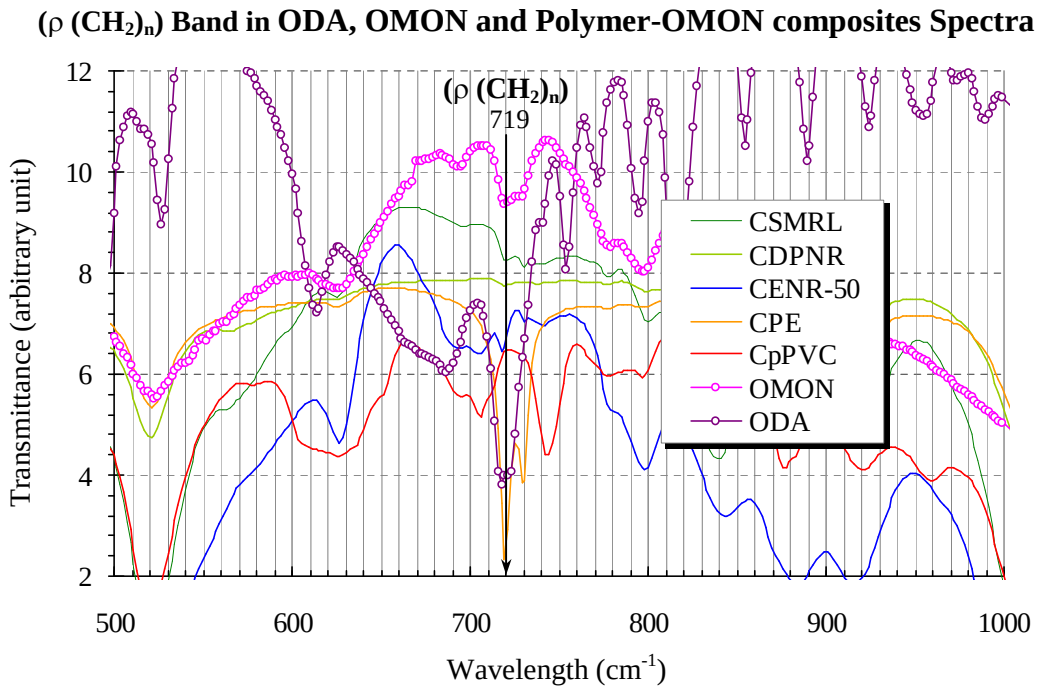

Figure 4.32: Rocking vibration of methylene chains at 719 cm^{-1} disappear from *CpPVC* spectrum, while in *CPE* it comes from *PE* as the polymer matrices.

Recall the missing second endothermic (T_{m2}) in *CpPVC* and *CPE* thermograms, as shown in Figure 4.9 and 4.10 respectively. On the contrary, the T_{m2} can be clearly detected in case of *CDPNR* (Figure 4.8(b)) and *CENR-50* (Figure 4.8(c)) around 110 °C to 120 °C. Such thermal behavior found in *CpPVC* and *CPE* should have some connections with the lost band of methylene rocking vibration ($\rho(CH_2)_n$). It is believed that chains coiling between matrix chain and *octadecylammonium* tail had affected not only the vibration mode of *C-H* bond on the methylene tail, but its structures as well. Hence, it may have caused the lost of T_{m2} endothermic, since the crystalline structure that is related to *C-H* bond on the alkyl tails changed to such an extent that they cannot be detected via the DSC scan.

4.3.2.1.D. ($\partial_s NH_3^+$) band

The idea of chain coiling reaction is strengthened with the symmetry bending vibration of ammonium ion at 1510 cm^{-1}. The absorption intensity is quite strong within both *OMON*

(1504 cm^{-1}) and *CENR-50* (1510 cm^{-1}) spectra. In fact, Figure 4.33(a) demonstrates that the absorption band also appears in the *CSMRL* (1519 cm^{-1}) and *CDPNR* (1510 cm^{-1}) spectra. This band however is missing in case of *CPE* and *CpPVC* composites. Again, reasonable explanation could be related to the effect of chain coiling, where it might have restricted the hydrogen bonds (*N–H*) in NH_3^+ cation from in-phase vibration as illustrated in Figure 4.34(a). The hydrogen bonds however are free to vibrate in different phases or the out-of-phase mode as shown in Figure 4.34(b). In that way, *CPE* and *CpPVC* composites lost the symmetrical bending band in their spectrum.

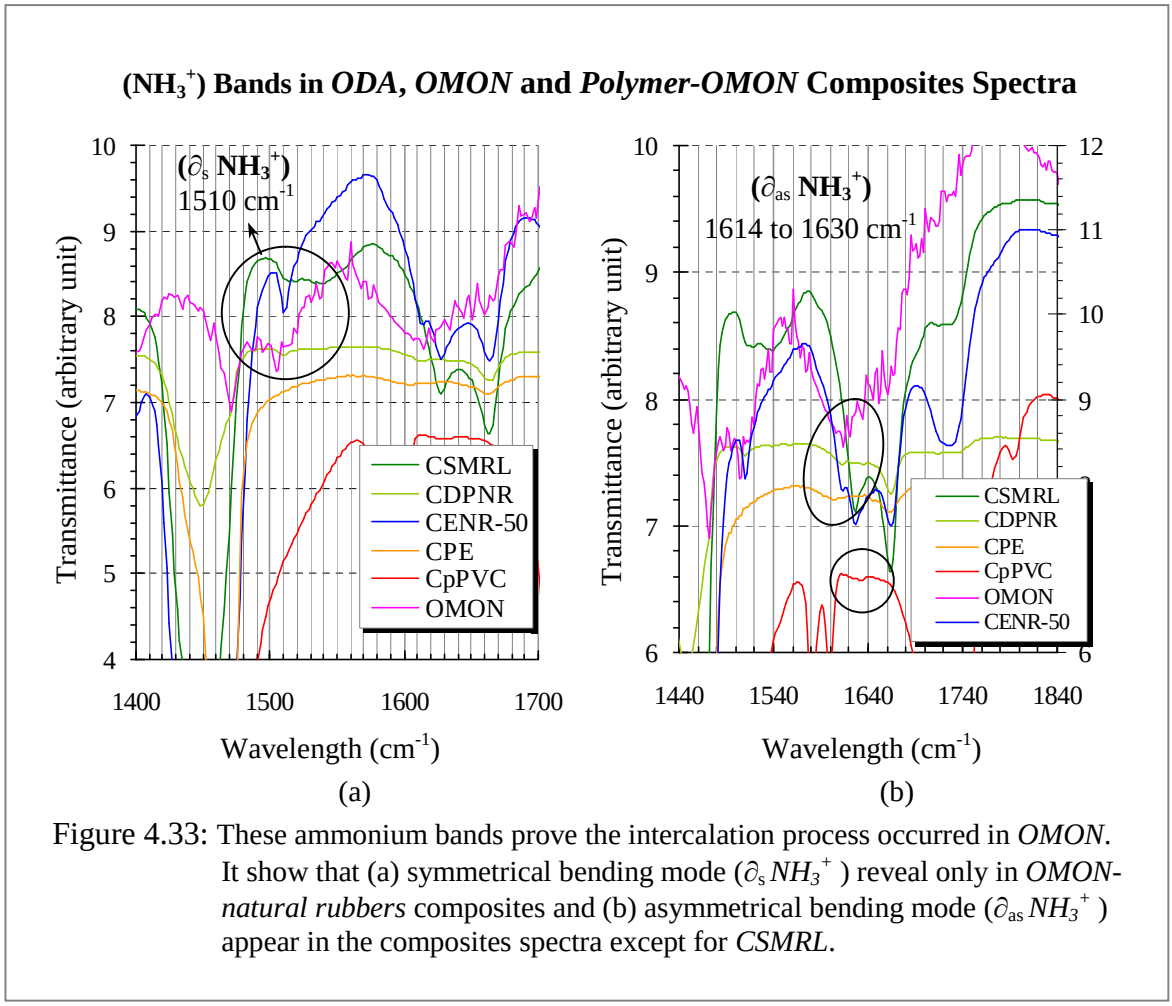

Figure 4.33: These ammonium bands prove the intercalation process occurred in *OMON*. It show that (a) symmetrical bending mode ($\partial_s NH_3^+$) reveal only in *OMON-natural rubbers* composites and (b) asymmetrical bending mode ($\partial_{as} NH_3^+$) appear in the composites spectra except for *CSMRL*.

There are some connections between these findings and the effects of *stacking order* from XRD analysis. Stacking parameter *N* about 21.25 and 6.19 had been estimated for *CpPVC* and *CPE* composite respectively, in which it is supposed that chain coiling dominates the

matrix-alkyl chain interaction inside the composites. Comparatively, they also have better staking order than *CENR-50* (5.71), *CSMRL* (2.91) and *CDPNR* (2.86) composite, where entanglement is believed to play the major role in chains interaction in these composites. It thus adds more proof that the coiling of matrix-alkyl chains in *OMON* gives strong chain-chain interaction.

Bending Vibrations of ammonium ion, NH_3^+

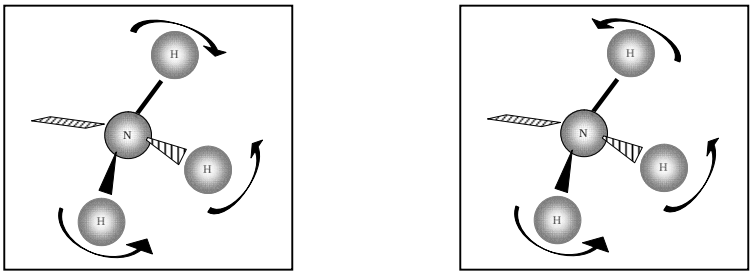

(a). Symmetrical, ∂_s (b). Asymmetrical, ∂_{as}

Figure 4.34: The illustrations of ammonium ion bending mode: (a) symmetrical vibration involves the in-phase bending of the *N–H* bond and (b) the asymmetrical involve the out-of-phase bending of the *N–H* bond. [4.58]

4.3.2.1.E. ($\partial_{as} NH_3^+$) band

Despite the fact of losing symmetrical bending band from the ammonium cation, *CPE* and *CpPVC* maintain their asymmetry mode ($\partial_{as} NH_3^+$) within the range of 1614 to 1630 cm^{-1} as shown in Figure 4.33(b). This band appears within *OMON* and all of *OMON* composites spectra except for *CSMRL* composite. From the DSC thermogram of *CSMRL* in Figure 4.8(a), the two endothermics (T_m) that demonstrate the crystallinity of methylene chains in *OMON* are almost disappearing. In contrast, these T_m appear in the DSC thermogram of *CDPNR*. However, there are some deformations on their outline as shown in Figure 4.8(b). Based on the remark it is believed that the crystallite structure of methylene tails on *ODA* cation (*octadecylammonium*) to a certain extent had been modified.

In previous Figure 4.20, the bridging flocculation in *Mon* composites was visualized as an intra-unit process, where it involved successive silicates plates in a single *Mon* particle.

Additionally, this process could actually happen among plates from different particles as graphically illustrated in Figure 4.35. Entanglements by some polyisoprene chains with several *OMON* particles can induce the inter-unit process, which generate the interparticle bridging flocculation structure within *OMON* composite. Chains movements from various directions within *OMON* galleries produce stresses on the alkyl chains that can shift their positions as a result. This relocation of alkyl molecules affects their crystallite structures as shown by the distorted endothermic of *CSMRL* and *CDPNR* in DSC profile.

From FTIR analysis, it seems that alkyl chain relocation gives insignificant effect on the all–trans conformation and rocking mode vibrations. However, it had restricted the out-of-phase mode ($\partial_{as}NH_3^+$) in *CSMRL* spectrum where it had caused the hydrogen bonds (*N–H*) on NH_3^+ cations to vibrate only in-phase or symmetrical mode as shown in Figure 4.34(a). The alkyl chain relocation gives impact not only on the arrangement of *ODA* cations, but also on the motion of hydrogen bonds on the cations.

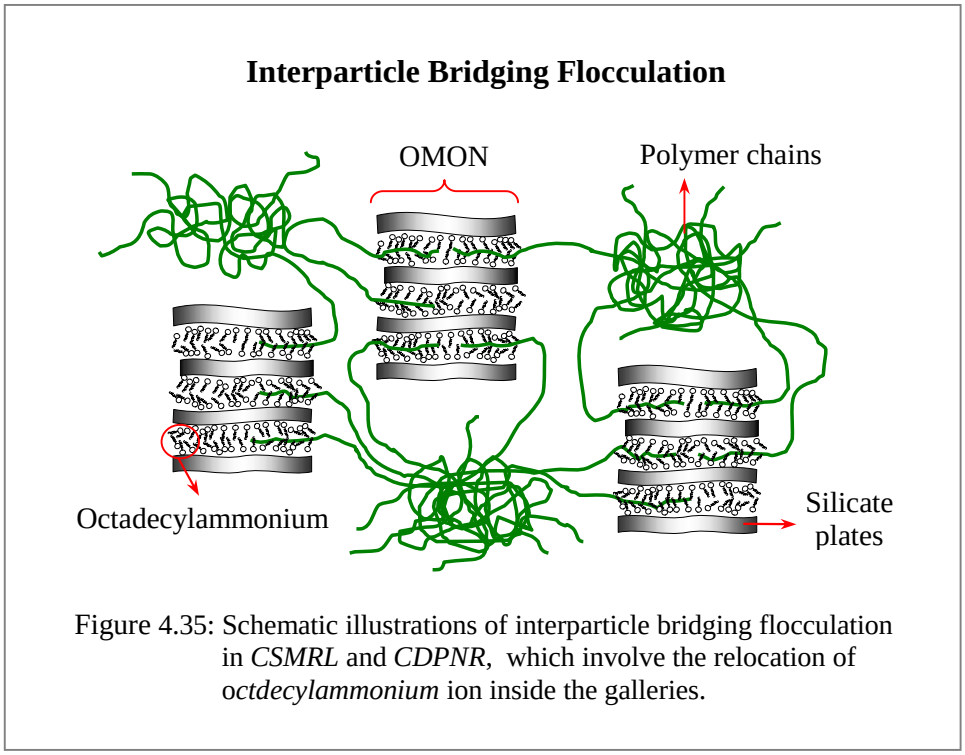

Figure 4.35: Schematic illustrations of interparticle bridging flocculation in *CSMRL* and *CDPNR*, which involve the relocation of o*ctdecylammonium* ion inside the galleries.

4.3.2.2 Matrix Chains and *OMON* Silicate Interaction

(*Si-O-R*), (ν*Si–H*), (∂*Si–H*) and **(*–NH$_3^+$*)** of amine salt

Along with the silicate stretching band (ν*SiO*) at 1044 cm^{-1}, it is seems that the (*Si–O–R*) band appears within the range of 1000 cm^{-1} to 1100 cm^{-1} as shown in Figure 4.36(a). This band represents the stretching vibration of silicates, except that it involves aliphatic chains. It thus, proves the interactions between *OMON* silicate surfaces and polymeric chains by means of van der Waals force and hydrogen bonding. This trace actually is very prominent in case of *CENR-50*, suggesting a close encounter by the rubber chains to silicate surfaces. Moreover, the appearance of multiple ammonium vibration (*–NH$_3^+$*) bands at 2048 cm^{-1}, 2505 cm^{-1} and 2530 cm^{-1} in Figure 4.36(b) are attributed to the exfoliation of *OMON* layer structures. These findings confirm the earlier prediction on exfoliation as revealed in XRD analyses. From Table 4.2, it shows that the big polymeric crystallite size of *ENR-50* gives an advantage for the elastomer to occupy bigger space within *OMON* interlayer.

Figure 4.19 in addition reveals the great ability of polar components in the *ENR-50* rubber to assist chains penetration into the organophobic *Mon* gallery. The polar matrix chains in effect capable to stimulate water replacement for their inhabitation at *Mon* surface, during bridging flocculation process inside the clay interlayer. Similarly, in case of *OMON* it was believed that great amount of *ENR-50* chains managed to reach the clay surfaces especially with the assistance of alkyl tails from *ODA* cations (*octadeclammonium*). In that way, they had interrupted the interaction between *OMON* layers and *ODA* cations. On the contrary to the bridging flocculation, the effect leads to the exfoliation of *OMON* silicate layers. This process of silicate delaminating is very important as it responsible for the exposure of more silicate surfaces. As a result, the amount of contact surface within *CENR-50* composite was improved, which then increased the chances to progressively interact with the elastomer chains.

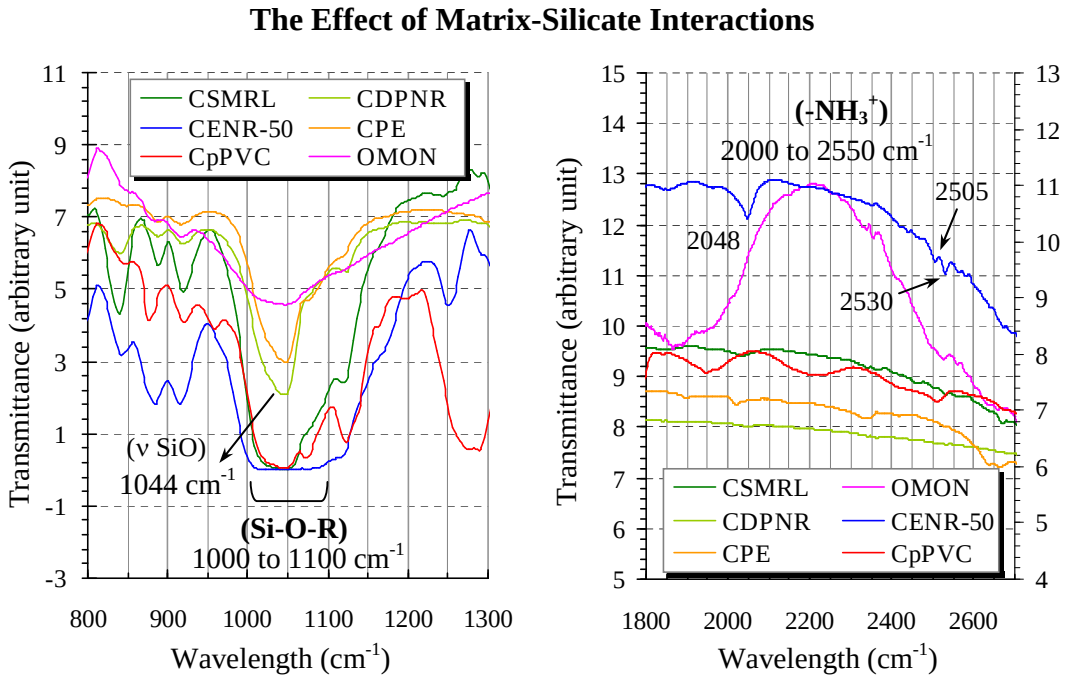

Figure 4.36: The evidences of *polymer-OMON* interactions as shown by (a) the growth In band absorption within 1000 to 1100 cm^{-1} from silicate interaction with aliphatic chains (*Si-O-R*). This band is overlapped by *SiO* band at 1044 cm^{-1}. Ammonium ion bands in (b) reveal the effect of exfoliation in *CENR-50*.

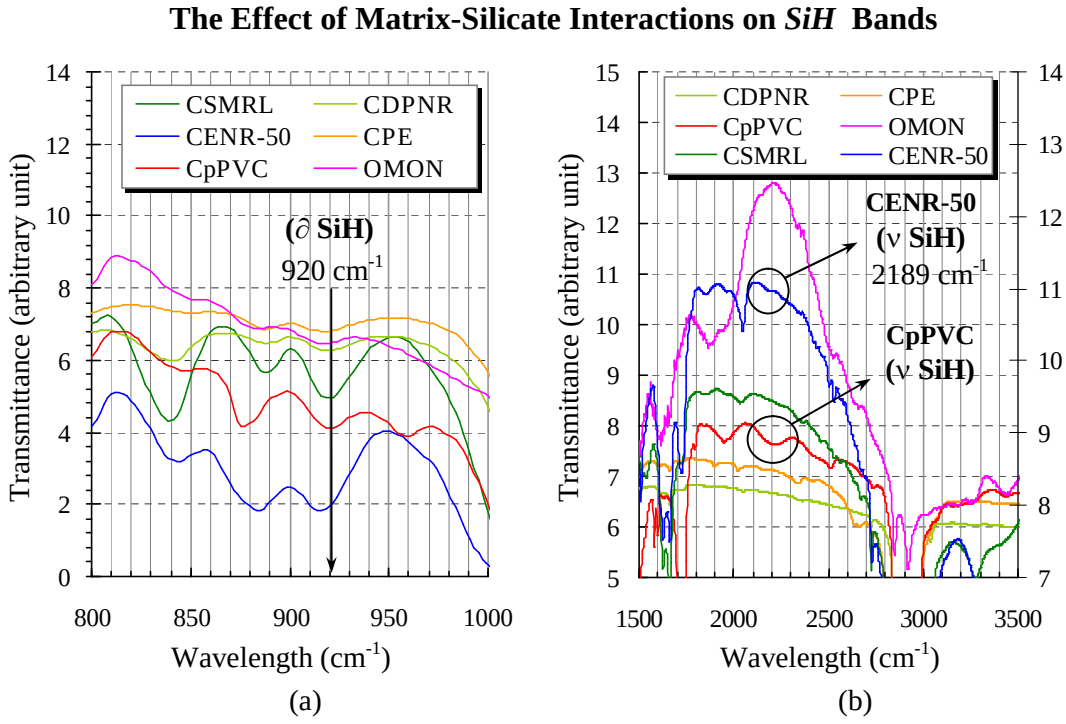

Figure 4.37: Weak bands appear in (a) around 920 cm^{-1} indicates the *SiH* bending vibration (*∂ SiH*), while in (b) the stretching mode (*ν SiH*) can only be seen in *CENR-50* and *CpPVC*.

Another band that should also be considered is the bending vibration mode of *SiH*, (*∂SiH*) at 920 cm^{-1}. In which, it superimposes with the hydroxyl band (*∂OH* in Fig. 4.38(a)) as shown in Figure 4.37(a). This is supported with the bands at 2189 cm^{-1} for *CENR-50* and at 2210 cm^{-1} of the *CpPVC* in Figure 4.37(b), which demonstrate the stretching mode of *SiH* group (ν*SiH*). These observations thus add more proofs for the interaction among polymers and *OMON* particles.

4.3.2.3 The Effects on OMON Silicate – Water Removal

(*∂HOH*) and **(ν*OH*)** of hydration, **(ν*AlO*), (ν*SiO*), (*∂SiO*),** and **(*∂OH*)**

Investigation on the hydration effects reveals the removal of water molecules from *OMON* structure. This is due to the lost of bending vibration at 1615 cm^{-1} (*∂HOH*), as well as the stretching mode (ν*OH*) at 3438 cm^{-1} from water molecule as shown in Figure 4.38(a). It is supposed that the effect took place within *OMON* composites, even though the trace is still observable within *CENR-50* and *CpPVC* spectra. Careful analyses on FTIR spectrum for *ENR-50* and *pPVC* however suggested that the trace was contributed by the intermolecular hydrogen bond from these polar polymers in the composites. The intermolecular hydrogen band can be observed in Figure 4.26 and Figure 4.28.

Despite the missing of hydration related bands, there are some typical bands from *Mon* appear in the composites spectra with a comparatively bigger and shaper out lines. These bands can be detected in Figure 4.38(b) at 467 cm^{-1} (ν*AlO*), 526 cm^{-1} (*∂SiO*) and 1044 cm^{-1} (ν*SiO*), which represents the aluminates and silicate groups. Broad band is also observed around the *SiO* trace within *CpPVC, CENR-50* and *CSMRL* spectra. This effect is due to superimpose between the band of *SiO* and *Si-O-R* groups. While the improved absorption bands for (ν*AlO*), (*∂SiO*) and (ν*SiO*) groups could be the result of water replacement by matrix chains. The process of water replacement can take place on the loosely held water

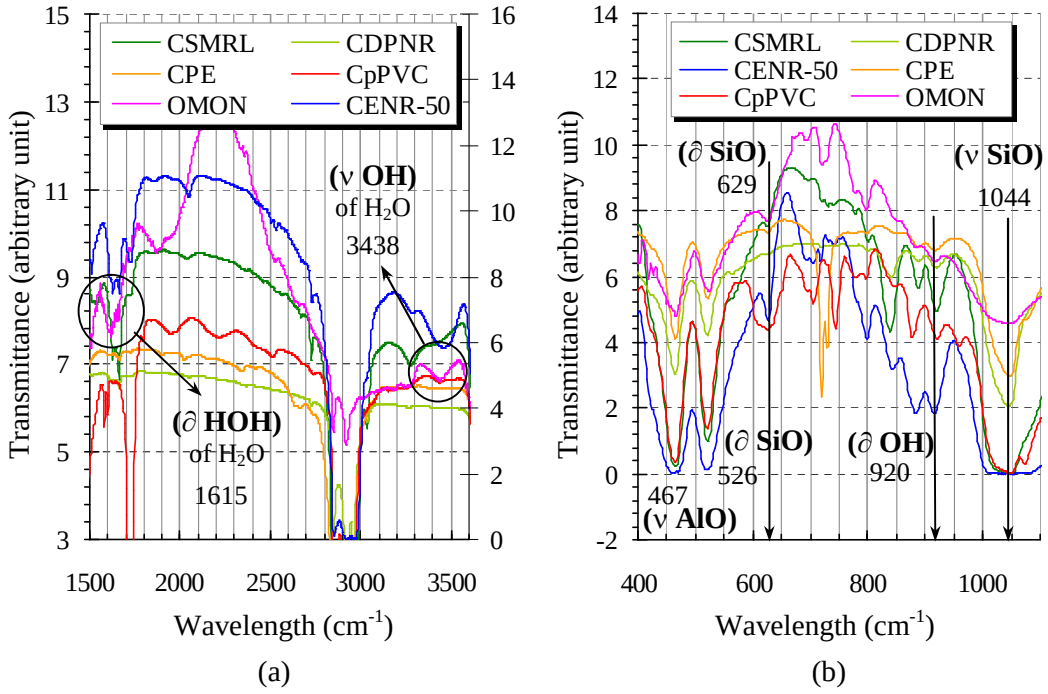

Figure 4.38: The effects of water removal from *OMON* are confirmed in (a) as the sign of water ((ν *OH*) and (∂ *HOH*)) are gone in the composites spectra. In case of *CENR-50* and C*pPVC*, the appeared traces around the hydroxyl band signifies intermolecular hydrogen bonds in the polymers matrix. The growth in some of *Mon* characteristic bands in (b) add more proofs on the water removal.

molecules within *OMON* interlayer [4.72 and 4.73]. Water removal in effect had reduced the potential extended hydrogen bond between the water molecules and (*AlO*) and (*SiO*) groups. This hydrogen bonding is responsible to shadow the groups' existence within the clay spectrum. The lack of such extended hydrogen bonds in *OMON* composites thus had caused the improvements on adsorption band for the clay components.

Similar effects can be seen at 920 cm^{-1}, with a tremendous growth in absorptions band by the hydroxyl bending vibration (∂*OH*) of *Mon* sheet within *CENR50*, *CpPVC*, *CSMRL* and *CDPNR* spectra. The developed trend is considered as the influence of polar groups from the polymers matrix, especially at the edge of *OMON*'s sheet. Since the possibility for the hydroxyl group to be exposed occurs only at the broken edge of clay sheet.

Another interesting finding is at 629 cm^{-1} that can be associated to the bending mode of silicate (*∂SiO*) vibration. This trace demonstrates an improved absorption band only in the case of *CENR-50* and *CpPVC* spectra. Again, similar effect that is water replacement at the clay edge can be used to explain these observations. It means that polar groups from *ENR-50* and *pPVC* chains are able to facilitate water removal on both types of broken edges, the hydroxyl (*OH*) and silicate (*SiO*) sites as schematic illustrated in Figure 4.39.

Montmorillonite, *Mon* Layered Structure

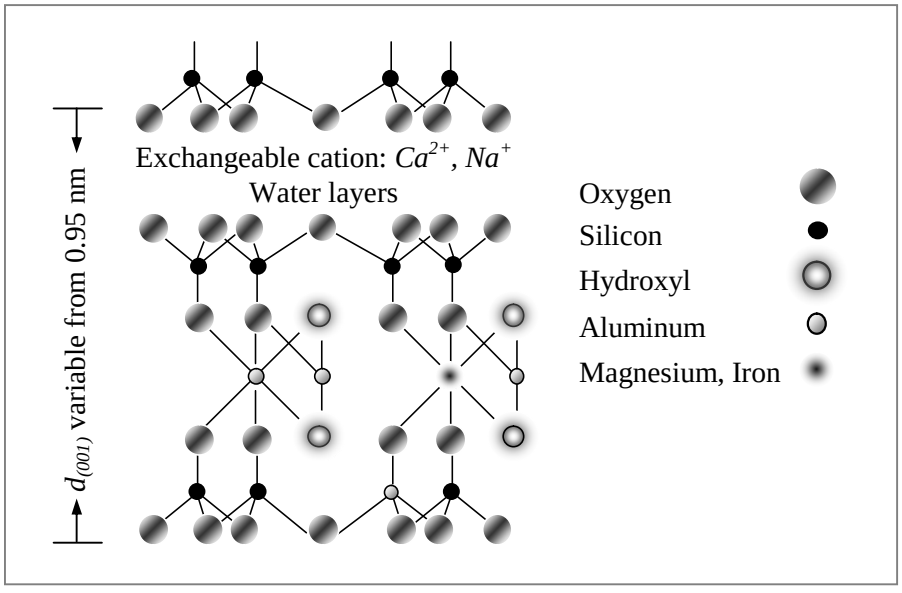

Figure 4.39: The layered structure of *Mon* according to Hoffmann, Endell, Wilm and Marshall [4.20]. It shows the possible broken edges either hydroxyl (*OH*) or silicate (*SiO*) group.

It can also be associated to the ability of *CpPVC* and *CENR-50* to improve their stacking orders, *N*. Particularly in the *CENR-50*, where it is believed that the inter-chains reactions for this composite were dominated by chain entanglements. Hence, the lack of inter-chain coiling in *CENR-50* should reduce its potential to stack more silicate layers. It turned out differently however, with the improvement of staking layers from *N* about 3.86 (*OMON*) to 5.71 (*CENR-50*). It seems that the ability to react at both type of broken edges (*OH* and *SiO*) had helped *ENR-50* chains to gather more silicate layers into *OMON* structure within

the composite. Similarly, this reaction gave an advantage for *pPVC* to stacke more layers inside *CpPVC* compared to that of *CPE* with their *N* is about 21.25 and 6.19, respectively.

In case of *CSMRL* and *CDPNR*, the interactions between polymeric chains and clay edges were limited only to the sites with hydroxyl groups. It thus did not improve the staking order *N*. On the contrary, Table 4.5 shows that *OMON* had lost their silicate layers that reduced the *N* value for the composites. Such matrix-silicate interaction might also induce the polyisoprene chains to further intercalate with several units of *OMON* particles, where it causes the relocation of alkyl chains as pictured earlier in Figure 4.35. Polymer-silicate interactions within *CENR-50* on the other hand, hold some parts of *ENR-50* chains at the silicates edges. This condition can reduce the effect of external chains movements on the intercalated *ENR-50* chains, which are entangled to the alkyl chains within *OMON* gallery. Therefore, it prevents the alkyl chains relocation within *CENR-50* that had saved the chains crytallinity as shown by the DSC profile in Figure 4.8(c).

4.3.2.4. The Effects on Matrix Chains

4.3.2.4.A. Crosslink Reaction

The intensity drop of several characteristic bands can be observed within *OMON-natural rubber* composites spectra in Figure 4.40(a), (b) and (c). The bands are around 1664 cm^{-1} of *cis* 1, 4 polyisoprene (–CH_2-C=C–), 837 cm^{-1} (*∂CH* from =*CH*), 1448 cm^{-1} (*∂CH* from –CH_2-C=C–) and 3035 cm^{-1} (ν*CH* from =*CH*). It also involve the band at 2970 cm^{-1} from =CH_2 group ($\nu_s CH_2$) in 3, 4 polyisoprene. These bands that are related to double bonds on the polyisoprene backbone show a clear drop compare to their counterparts within pristine natural rubber. Analyses on Figure 4.40 (a) show that the drops more pronounce in case of *CDPNR* compare to that of *CSMRL* and the stronger bands within *CENR-50* spectrum. In addition, the *CDPNR* spectrum in Figure 4.40(b) shows a band at 3269 cm^{-1} that indicates the *N-H* stretching vibration (ν*NH*) from secondary amine (*RNHR'*) [4.59].

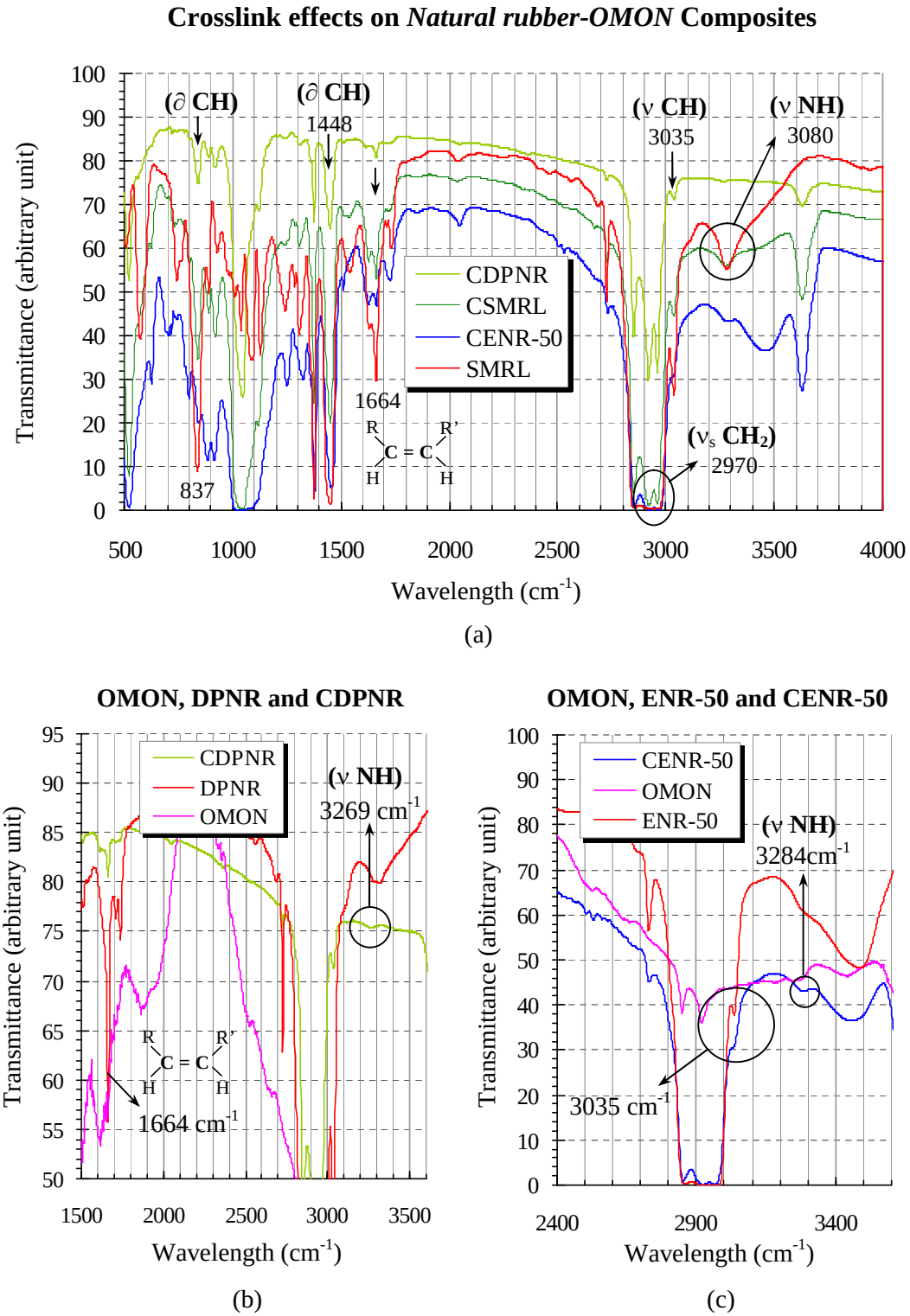

Figure 4.40: Intensity drop of absorption bands in (a) which are related to double bond on polyisoprene chains indicate crosslink effect in *natural rubbers-OMON* composites. It is supported with the appearance of *NH* stretching (ν *NH*) band at 3269 cm^{-1} in (b) from secondary amine. This band is overlapped around 3280 cm^{-1} in case of *CSMRL* and 3284 cm^{-1} in *CENR-50*.

The observations therefore, suggest that crosslink reaction might have occurred in these composites. Even though the actual mechanism is not really understood, but the results indicate the involvement of *ODA* cation in the crosslink reaction. Perhaps, being trapped in such confine space of *OMON* interlayer induced ammonium head (NH_3^+) from the cation to react with unsaturated bonds on the matrix chains. This reaction thus crosslinked the intercalated polyisoprene chains in *OMON* gallery. It is believed that the crosslink reaction also took place within *CSMRL* and *CENR-50* composites.

In *CSMRL* however, the trace for secondary amine seems to overlap with the broad band around 3280 cm^{-1} from salt of amino acids. Likewise, the *N-H* stretching band in *CENR-50* is overlapped at 3284 cm^{-1} by a band from hydroxyl groups as shown in Figure 4.40(c). In case of *CSMRL* and *CDPNR* composites, the crosslink reaction within *OMON* gallery can induce better interparticle bridging flocculation structure. However, good matrix-silicate interaction in *CENR-50* can make the intercalated matrix chains apart from each other. For that reason, it may have restricted the crosslinking process in this composite.

4.3.2.4.B. Anti-oxidation

The reduction in absorption intensity of several oxygen related bands are also detected in *OMON-natural rubbers* composites. Figure 4.41 shows that the bands can be seen around 1250 cm^{-1} for the epoxide (-*COC*-) group and within the range of 1732 to 1734 cm^{-1} for carbonyl (-*C=O*) group. While the *C-H* bending vibration (∂CH) of (-CO-CH_3) component around 1380 cm^{-1} is overlapped by a bending band ($\partial_s CH$) from methyl (CH_3) groups. Again, the ammonium head (NH_3^+) from *ODA* cation within *OMON* gallery is supposed responsible for these results. According to the previous works by some researchers [4.9 and 4.74], amine groups can act as anti-oxidation agent in natural rubbers. The suggested reactions are as follow:

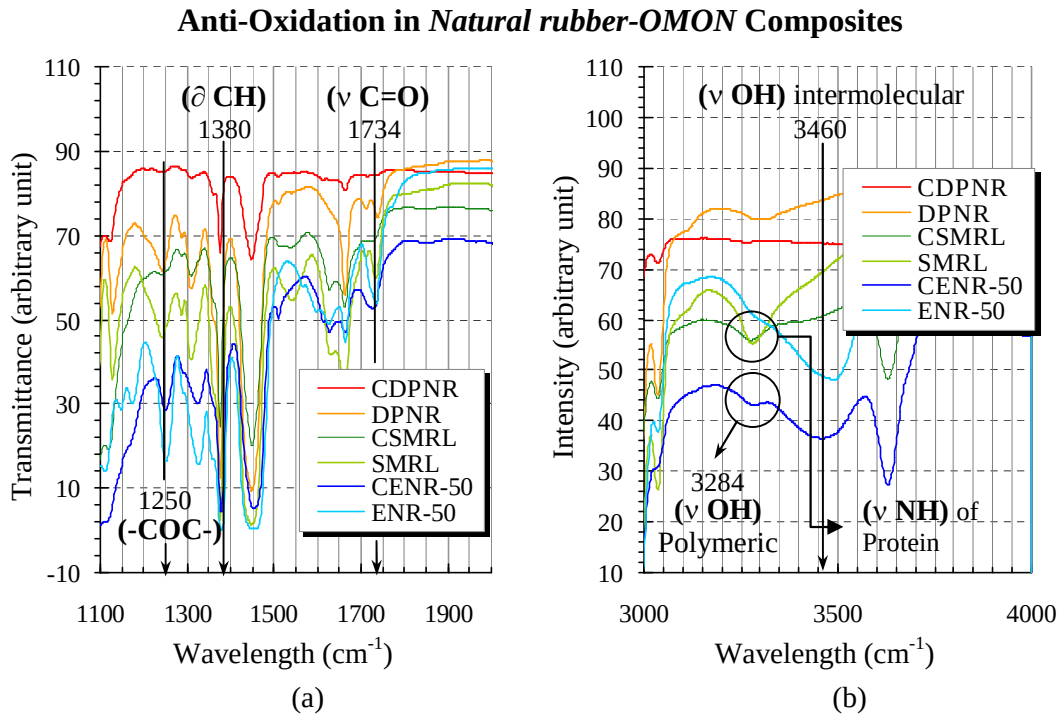

Figure 4.41: The effect of anti-oxidation reaction in *natural rubber-OMON* composites causes the intensity drop of several absorption bands in (a), for oxygen related component. This is supported by the growth in hydroxyl stretching (ν *OH*) bands as shown in (b), especially in case of *CENR-50*.

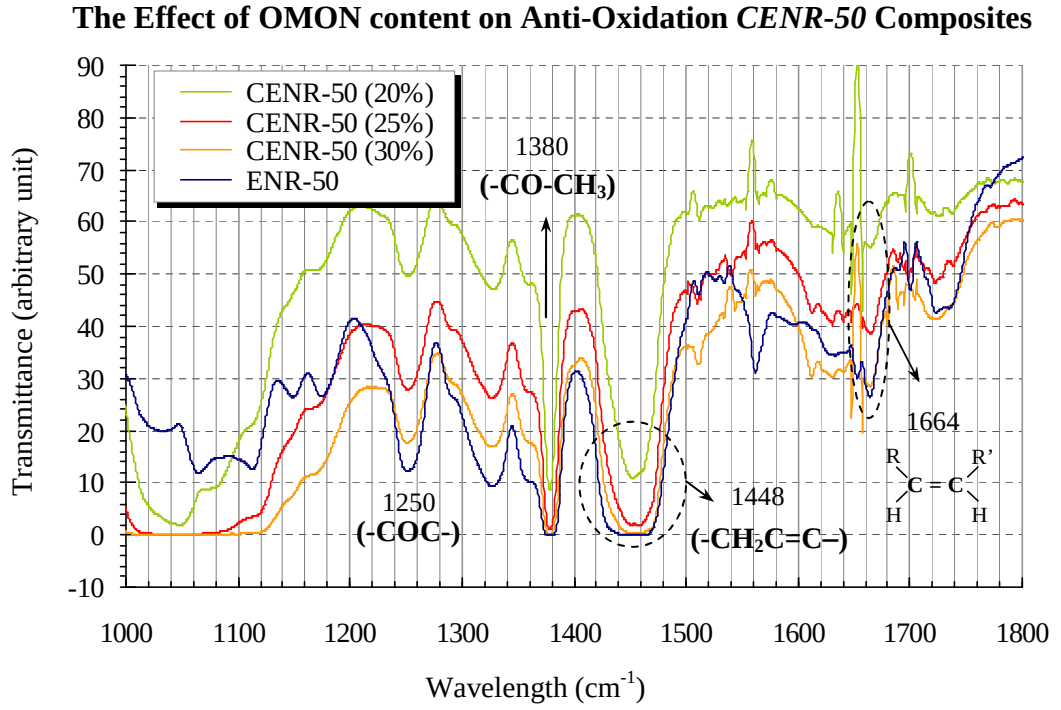

Figure 4.42: The increase of absorption bands in *CENR-50* spectra due to *OMON* increase in the composites. These bands are related to the effect of crosslink reaction and anti-oxidation in *OMON* gallery.

Anti-Oxidation Reaction

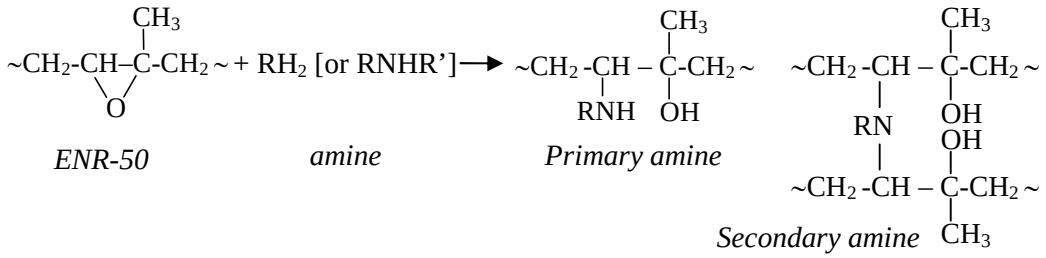

Anti-oxidation reaction by amine group on epoxidised natural rubber, *ENR-50* [4.9]

These reactions thus explain the increase in absorption intensity of several bands. Such as, the band around 3284 cm^{-1} due to hydroxyl stretching mode (ν*OH*) in polymeric chains and at 3460 cm^{-1} that indicates the intermolecular hydrogen bonds. Analyses show that reaction with other oxygen related elements such as protein molecules could also take place within the composites. *ODA* cation thus can be regarded as anti-oxidation agent for polyisoprene chains inside *OMON* gallery. The anti-oxidation reaction as a result increases the interchain reaction among matrix chains [4.8 and 4.9], and between the matrix and alkyl chains within *natural rubbers-OMON* composites. From FTIR spectra in Figure 4.42, the effects of anti-oxidation seem as reducing with the increase of *OMON* content in *CENR-50* composites. It involves the absorption bands around 1250 cm^{-1} (-*COC*-) and 1380 cm^{-1} (*∂CH*) from (-*CO-CH*$_3$) group. Similar reduction can also be seen for the effects of crosslink reactions on *ENR-50* double bond. They are around 1664 cm^{-1} (–*CH*$_2$-*C=C*–) and 1448 cm^{-1} (*∂CH*) from (–*CH*$_2$-*C=C*–) groups. Further discussions on these observations will be carried out in Section 7.2.2.1.A.

4.3.2.4.C. Hydrolysis

Besides *ODA* cations, water molecules in *OMON* particles also contribute to matrix chains reactions. According to Gan *et.al* [4.7], epoxide group within natural rubbers chains can be hydrolyzed under mildly acidic condition with the present of water and heat. The reaction he proposed is as follow:

Hydrolysis Reaction

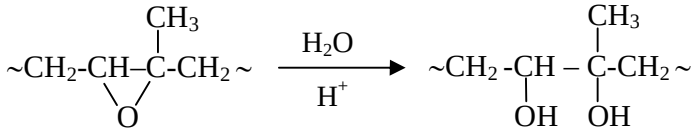

ENR-50 *hydrolysis* *diol group*

Hydrolysis reaction on epoxidised natural rubber, *ENR-50* as suggested by Gan [4.7]

In case of *CENR-50*, certain amount of organic acid was added to assist the *ENR-50* chains to swell in *toluene* solvent. It also involved the applied of heat to promote the swelling process. Hence, this condition might have induced the hydrolysis process especially with the present of water molecules from *OMON* particles. Figure 4.43(a) shows the evidences

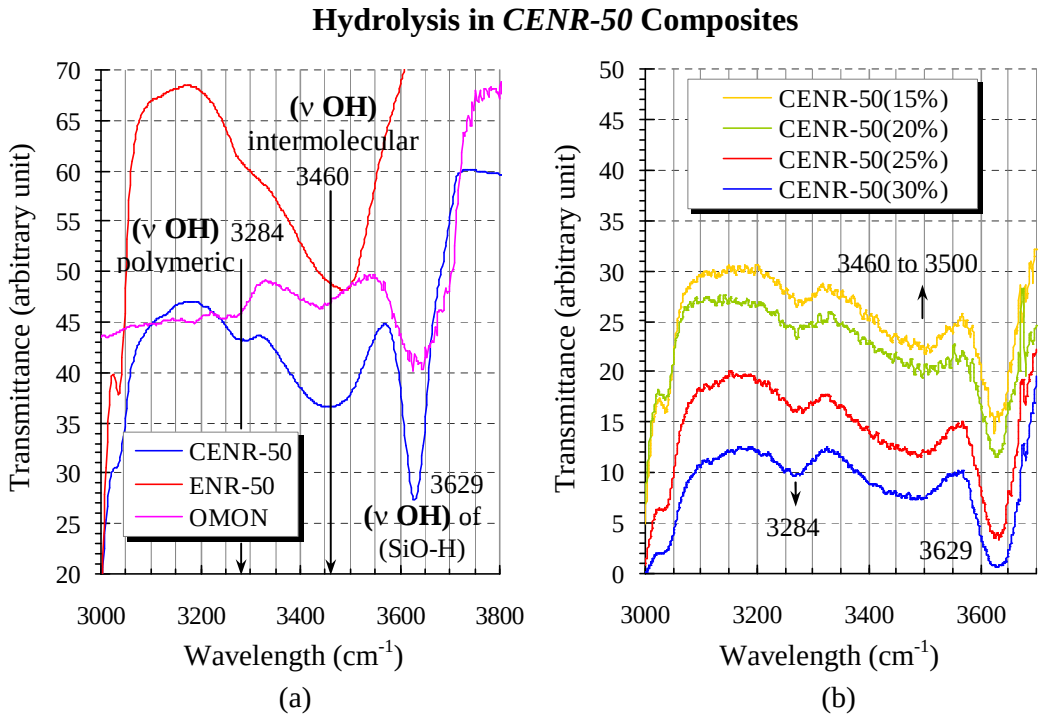

Figure 4.43: Hydrolysis within *CENR-50* can be observed in (a) via hydroxyl bands that indicate the improved hydrogen bonding among polymeric chains, as well as for matrix-silicate interaction. These bands seems to be improved in (b) as *OMON* content increases within the *CENR-50* composites.

with the growths in absorption band around 3284 cm^{-1} from hydroxyl stretching vibration (ν*OH*) in polymeric chains. It is confirmed with the band at 3629 cm^{-1} of hydrogen bond

(ν*OH*) from polymer-silicate interaction (*SiO-H*). More proof is given by intermolecular hydrogen bonding band at 3460 cm^{-1}, which is overlapped by the hydroxyl (ν*OH*) band from hydration in *OMON* particles.

From *CENR-50* spectra in Figure 4.43(b), it seems that the absorption intensity of these bands is increased as *OMON* content raises in the composites. The developed trends tell that water content in *OMON* had played significant role to promote the hydrolysis process within the *CENR-50* composites. The formed hydroxyl groups from this process induced more hydrogen bonding between *ENR-50* matrix chains and *OMON* particles. This finding thus reveals the additional source that can give strong interfacial adhesion in the *CENR-50* composite.

FTIR analyses manage to support the earlier predictions suggested in DSC as well as XRD studies. They are mainly regarding the effects of intercalation and exfoliation on *Mon*, *OMON* and *polymer-OMON* composites. Table 4.8 lists all the major adsorption bands that can be related to these effects. Analyses on FTIR spectra also gathered more information on the internal structures of *OMON* particles. Some processes such as alkyl chains relocation, interparticle bridging flocculation and polymer-silicate interaction on both silicate surfaces and edges are supposed to influence the particle structure within *polymer-OMON* composites.

Table 4.8

FTIR Bands of ODA, OMON and Polymer-OMON Composites

No	Band (± 1 cm^{-1})	Sample							Remark
		ODA	OMON	CSMRL	CDPNR	CENR-50	CPE	CpPVC	
1	$\partial_s CH_2$ (2918)	√	√						- Intermolecular int. of cryst. str. - prove the entanglement & coiling in composites
2	$\nu_{as} CH_2$ (1472)	√	√	√	√				- all-trans conformation - differentiates the entanglement & coiling - CENR-50 – polar – entanglements deeper
3	$\rho(CH_2)_n$ (719)	√	√	√	√	√			-effect of coiling -in DSC – the lost of T_{m2} -in XRD – better stacking layers (*N*) -prove chemical modification on *OMON* - in DSC the lost of T_{m1} and T_{m2} in *CSMRL*
4	$\partial_s NH_3^+$ (1504 – 1510)		√	√	√	√			
5	$\partial_{as} NH_3^+$ (1614 – 1630)		√		√	√	√	√	
6	*Si–O–R* (1000 – 1100)			√	√	√	√	√	- int. with aliphatic chains, *R*
7	$-NH_3^+$ (2000 – 2550)					√			- from octadecylammonium cation - prove the exfoliation in *CENR-50*
8	The growth in *∂SiH* (920)		origin	√	√	√		√	- overlaps with *∂OH* at 920 cm^{-1} - prove the int. of clay with polymers - *CENR-50* at 2189cm^{-1} and *CpPVC* at 2210cm^{-1}
9	*νSiH* (2189 – 2210)					√		√	
10	(H_2O): *νOH* (1615) *∂HOH* (3438)		√						- water replacement in composites
11	The growth in *νAlO* (467), *νSiO* (1044) and *∂SiO* (526)		origin	√	√	√	√	√	- water replacement reduce the ability to form extended *H* bonds which bring about the enhancement - polar groups assist water replacement at the edges of clay plate which is related to hydroxyl (*OH*)
12	The growth in *∂OH* (920)		origin	√	√	√		√	

Table 4.8 is continued in the next page

Table 4.8
FTIR Bands of ODA, OMON and Polymer-OMON Composites

From previous page

No	Band (± 1 cm^{-1})	Sample							Remark
		ODA	OMON	CSMRL	CDPNR	CENR-50	CPE	CpPVC	
13	The drop in cis *C=C* (1664), *∂CH* (=CH) (837), *νCH* (=CH) (3035), *νCH₂* (=CH₂) (2970) and *∂CH* (–CH₂–C=C–) (1448)			√	√	√			- the effect of crosslink reaction within *OMON* gallery in *natural rubber-OMON* composites - the reaction which is assisted by *ODA* cation attack double bond on the matrix chains
14	*νNH* (RNHR')			√	√	√			- appear in *CDPNR* at 3269 cm^{-1}, - overlapped in *CSMRL* at 3280 cm^{-1} and in *CENR-50* at 3300 cm^{-1}
15	The drop in *C-O-C* (1250), *νC=O* (=CO) (1732) and *∂CH* (–CO–CH₃) (1380)			√	√	√			- *ODA* cations acted as anti-oxidation agent within *OMON* gallery - the reaction involved oxygen related elements
16	The growth in *νOH* in polymeric (3284) and *νOH* of intermolecular bond (3460)			√	√	√			- reaction on epoxide group produce hydroxyl component which increase hydrogen bonding in composite especially *CENR-50*.
17	The growth in *νOH* from SiO-H (3629)					√			- hydrolysis on epoxide groups in *CENR-50* produce more hydroxyl group which induce the hydrogen bonding

Table 4.8 lists the discussed absorption bands which describe *polymer matrix-OMON* interaction. This is including the effects on both elements especially within *OMON* gallery in *polymer-OMON* composites.

Natural rubber-OMON composite *Polymer-OMON* composite Polar group Non-polar group

4.3.3 Summary

- Analyses on FTIR spectra in Section 4.3.1 had identified the characteristic absorption bands of each pristine polymer. Table 4.6 lists these bands for *SMRL*, *DPNR* and *ENR-50* natural rubber.
- Polyethylene (*PE*) is characterized by strong stretching and bending vibration bands from methyl and methylene groups. A sharp trace of methylene at 729 cm^{-1} compared to the small hump of methyl at 1303 cm^{-1} confirms the semi crystalline structure of *PE* chains.
- A triplet at 617 cm^{-1}, 636 cm^{-1} and 706 cm^{-1} represent aliphatic halogen group (*RC-Cl*) in *pPVC*. While *C-O* vibration $\nu(C=O)$ at 1724 cm^{-1} which is from ester group in *DOP* (*dioctylphthalate*) confirms the present of plasticizer molecules in *pPVC*.
- Table 4.7 in Section 4.3.2.1 and also Table 4.8 list important bands in *OMON* and its composites. The trend shows by methylene bending vibration (∂CH_2) around 1472 cm^{-1} proves the intercalation and interaction of polymer with alkyl chains from *ODA* cation. While its stretching (νCH_2) and rocking mode ($\rho(CH_2)_n$) reveal the effect of matrix chains on *ODA* crystallinity in *OMON* gallery. These bands also help to distinguish the effect of entanglement and coiling in matrix-alkyl chains interactions. Similarly, bands at 1540 cm^{-1} ($\partial_s NH_3^+$) and 1614 cm^{-1} ($\partial_{as} NH_3^+$) which represent the ammonium head on *ODA* cations add more proof on this effect. In case of *CSMRL*, the lost of ($\partial_{as} NH_3^+$) band is believed a result of *interparticle bridging flocculation* process in the composite.
- Interaction between matrix chains and *OMON* silicates is revealed by the appearance of broad band around 1000 to 1100 cm^{-1} from (*Si-O-R*) vibrations. The *Si-H* stretching band (νSiH) at 2189 cm^{-1} and 2210 cm^{-1} provide more evidence. This is including the bending mode (∂SiH) at 920 cm^{-1} as shown in Section 4.3.2.2.

- Exfoliation in *CENR-50* composite had caused *OMON* layer to delaminate and released the trapped *ODA* cations. The effect is recognized by the appearance of ammonium (NH_3^+) triplets' bands around 2048 to 2530 cm^{-1}.

- Intercalation and exfoliation induced *water removal* from *OMON* structure. Section 4.3.2.3 discussed the effect that can be seen with the lost of hydroxyl band (ν*OH*) from hydration at 3438 cm^{-1}. Likewise, the growth in intensity of (ν*AlO*), (ν*SiO*), (∂*SiO*) and (∂*OH*) bands from silicate components prove this effect in composites.

- Polar matrix chains in *CENR-50* and *CpPVC* composites have the capablity to facilitate water removal at both hydroxyls (*OH*) and silicate (*SiO*) broken edges on *OMON* clay plates.

- *OMON* addition into natural rubber composite is recognized to cause several effects on the rubber matrix chains, which is discussed in Section 4.3.2.4. Such as, *ODA* cation is believed had induced crosslink reaction among the intercalated polyisoprene chains in *OMON* gallery. This effect can be seen on the intensity drop of bands which are related to double bonds on the matrix chains.

- *ODA* cation is also believed to act as anti-oxidation agent in the rubber composites. It had caused reduction in absorption intensity of some oxygen related bands.

- In case of *CENR-50* the present of acid, heat and water molecule from *OMON* particles had induced hydrolysis process. This process had changed a number of epoxide groups on *ENR-50* chains into hydroxyl groups, which then promoted matrix-silicate reaction via hydrogen bonding.

4.4 The Structure of *OMON* and *Polymer-OMON* Composites

From DSC, XRD and FTIR studies, the basic structure of *OMON* particle can be suggested as the schematic illustrations in Figure 4.44. Important findings and information regarding *OMON* structures that were gathered from the studies are summarized in this section. The structure of pristine *OMON* particle is briefly discussed, which includes the filler particle in *polymer-OMON* composites and their effect on the composites structure.

4.4.1 *OMON* Particle

The intercalation of *ODA* cation (*octadecylammonium*) within *OMON* gallery as shown in Figure 4.44(a) is confirmed via some DSC and XRD studies. XRD analysis for example, reveals the improved gallery height as the basal spacing d_{001} is increased from 1.462 nm of *Mon* to 1.840 nm in *OMON*. It was also estimated that *OMON* structure composed of 4 successive silicate layers as in the pristine *Mon*. The interaction of ammonium head (NH_3^+) with the silicate surface did not render the crystallite structure of methylene chains on *ODA* cations. In fact, the crystallinity of the alkyl tails within *OMON* gallery was proven in the DSC and FTIR analyses.

4.4.2 *Polymer -OMON* Composites

4.4.2.1 CpPVC Composite

The intercalation of polar *pPVC* chains into *OMON* gallery gives the new basal spacing around d_{001} = 3.741 nm for *CpPVC* composite. The increase about 1.901 nm was assisted by chains coiling between alkyl tails and the matrix chains. The interactions among polar elements on *pPVC* chains with *OMON* components induced extensive chains coiling, as shown in inset of Figure 4.44(b). Chains coiling as a result interrupted the interchains reaction in the crystallite structure of *ODA* cations. However, it generated good matrix-alkyl chains reactions as well as matrix-silicate interactions that give strong interfacial adhesion to the *CpPVC* composite. In that way, the stacked structure of *OMON* was greatly

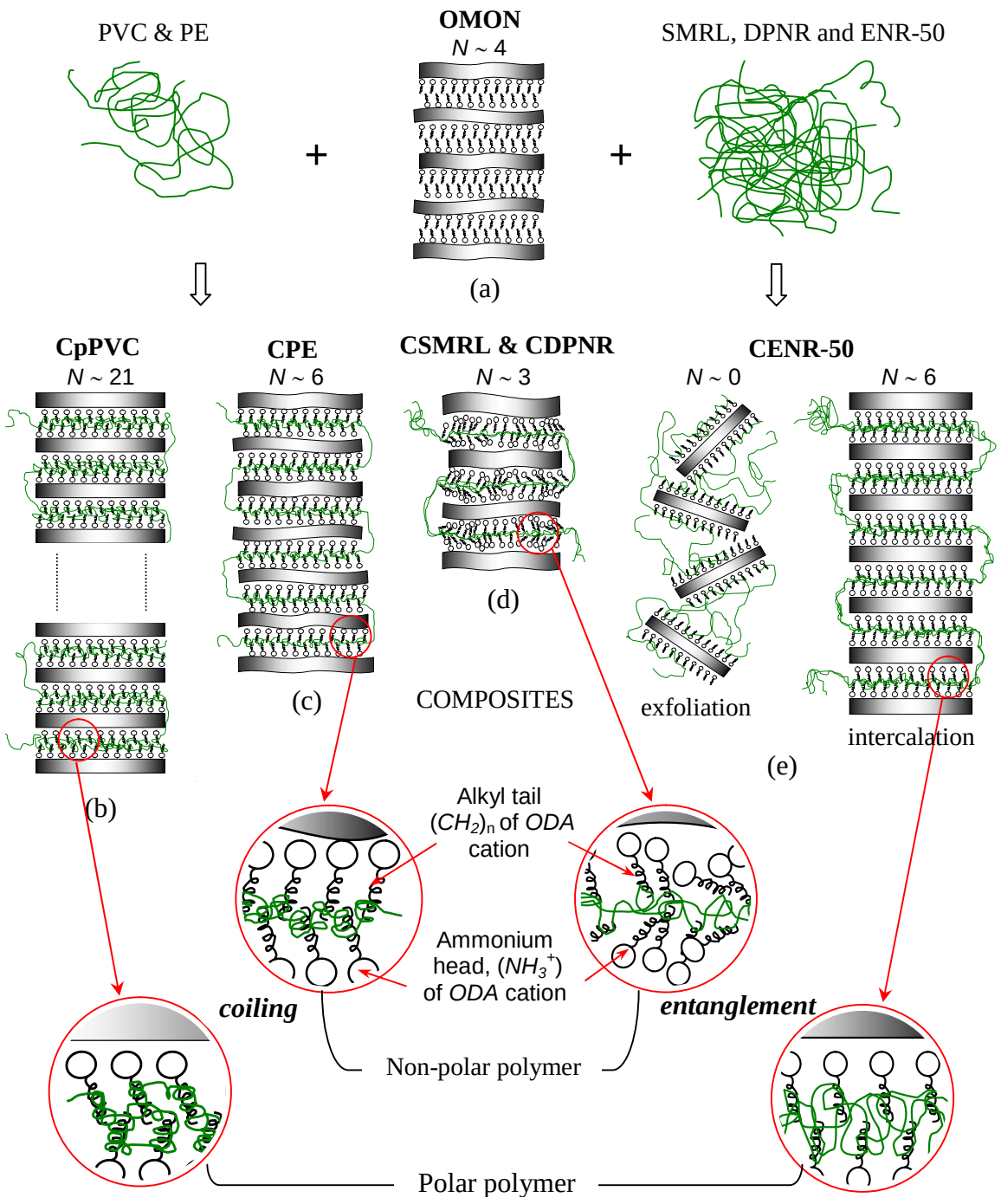

Figure 4.44: Graphical illustrations of *OMON* particle show various effects from polymer-*OMON* interaction. Intercalation and exfoliation on this particle are very much influence by polarity of the polymer matrix chains, and their mode of interaction either coiling or entanglement with alkyl tails in *OMON* gallery. This is highlighted in the insets to distinguish several effects from different polymers. The effect of polar polymer can be seen on the improved stacked layers (*N*), and the coherent structure it caused on *OMON* particles within the studied *CpPVC* and *CENR-50* composites.

improved in the composite, from 4 layers to 21 layers structure as shown in Figure 4.44(b). This figure also illustrates the coherent structure of silicates, which is due to the silicates interaction with polar *pPVC* chains. Such interaction can help *OMON* silicate plates to align uniformly toward one another.

4.4.2.2. CPE Composite

OMON basal spacing d_{001} in *CPE* was increased to 2.794 nm by the intercalation of non-polar *PE* chains. As in *CpPVC*, chains coiling had helped these matrix chains to penetrate *OMON* gallery and raised its height about 0.954 nm. Various sizes of polymeric crystallite (*D* is about 1.69 to 16.79 nm) in *PE* also contributed to the increase in *CPE*. Good matrix-alkyl tails interactions generated by the chains coiling helped to improve *OMON* stacked structure in the composite. Figure 4.44 (c) shows a schematic diagram for *OMON* particle within *CPE* that is composed of 6 stacked layers structure. This finding thus proves the strong interfacial adhesion produced by the chains coiling, where it was able to assist the non-polar chains in stacking new silicate layers on *OMON* particle. The coiled chains as shown in the inset of Figure 4.44 (c) however distorted the interchain reaction among alkyl tails in the crystallite structure of *ODA* cations.

4.4.2.3. CSMRL Composite

The penetration of polyisoprene chains from *SMRL* rubber into *OMON* gallery had raised its height with the basal spacing d_{001} is about 2.582 nm for *CSMRL* composite. Chain entanglement assisted the *SMRL* chains to intercalate that caused the rise about 0.742 nm. This increment is small compared in case of *CPE* that is about 0.954 nm, which could be due to the bigger crystallite size of *PE* (*D* ~1.69 to 16.79 nm) compared in *SMRL* (*D* ~1.06 nm). Analyses however, revealed that it was most likely owing to weak matrix-alkyl chains interaction produced by chain entanglements. The delimitating of silicate layers as pictured in Figure 4.44(d) provides the evidence. It shows that *OMON* particle in *CSMRL* consist of

3 silicate layers, which is less than the 4 layers structure of pristine *OMON*. Such weak interactions as illustrated in inset of Figure 4.44(d) also leaved interchain reactions among the alkyl tails from *ODA* cations remain unchanged.

ODA cation is believed responsible for crosslink reaction on the intercalated polyisoprene chains. This reaction together with the lack of matrix-silicate interaction promotes better *interparticle bridging flocculation* process within *CSMRL*. *ODA* cation also reacted with oxygen related components in *SMRL* as anti-oxidation agent. Such chemical reaction that involved epoxide group and protein molecule improved matrix-alkyl chains interaction in *OMON* gallery. This condition then contributed to distortation of *ODA* crystallinity (T_{m1} & T_{m2}) as shown in Figure 4.8. It shows the effect of alkyl chains relocation caused by matrix chains motions in the *interparticle bridging flocculation* structure.

4.4.2.4 CDPNR

Intercalated polyisoprene chains from *DPNR* in *OMON* gallery increased the basal spacing d_{001} to 2.329 nm. The increase about 0.599 nm in *CDPNR* is more or less the same in case of *CSMRL*. Likewise, chain entanglement dominated matrix-alkyl chain interactions in this rubber composite. Weak interfacial adhesion by the entanglement led the delaminating of silicate layers, as illustrated in Figure 4.44 (d) with the 3 layers structure. It also helped the alkyl tails to keep their interchains reaction in *ODA* crystalline structure.

DPNR comparatively is a less polar elastomer than *SMRL* due to protein removal from this rubber. The lack of polar components thus reduced potential matrix-silicate interactions in *CDPNR*. Such condition can improve the crosslink reaction by *ODA* cations on the trapped polyisoprene chains. By this means, it promoted better *interparticle bridging flocculation* process within *CDPNR* compared to *CSMRL*. On the other hand, anti-oxidation reaction by *ODA* cation was lessened in *CDPNR* due to the small content of polar elements in the matrix *DPNR* chains. The rubber matrix and alkyl chains then became less interacted

and alkyl chain relocation due to matrix chains motion could be reduced. It thus explains the distortion of T_{m1} and T_{m2} endothermics compared to that of *CSMRL* in Figure 4.8.

4.4.2.5. CENR-50

ENR-50 is a polar natural rubber with epoxide groups on the polyisoprene backbone. These chains intercalation into *OMON* interlayer gives d_{001} spacing about 3.864 nm in *CENR-50* composite. Polar groups in the *ENR-50* promoted extensive chains entanglement with alkyl tails, as shown in inset of Figure 4.44(e). This interaction contributed to the increase about 2.024 nm in *OMON* gallery height. Extensive entanglements however did not interrupt the alkyl interchain reaction within crystalline structure of *ODA* cations. Such entanglement together with polar matrix-*OMON* interaction generated strong interfacial adhesion, which promoted stacking layer process in *CENR-50*. *OMON* particles in this composite managed to stack about 6 silicates layers on its structure, as shown in Figure 4.44(e).

It is believed that strong interfacial adhesion also contributes for the intercalation of bulky *ENR-50* chains. In fact, it had caused the exfoliation on *OMON* structures as illustrated in Figure 4.44(e). Polar elements from *ENR-50* can promote good matrix-silicate interactions within the *CENR-50*. Such interactions facilitated silicate layers to align uniformly and give a coherent structure to *OMON* particles. The good interaction however distanced the trapped polyisoprene chains in *OMON* gallery. In that way, it can reduce the chances for crosslink reaction on the matrix chains. This remark thus explains the lack of *interparticle bridging flocculation* structure in the *CENR-50* composite. Hydrolysis on epoxide groups produced hydroxyl groups, which can stimulate more hydrogen bondings. By this means, it improved matrix-silicate interactions in the rubber composite. Anti-oxidation reaction on the epoxide group in fact created more hydroxyl group for the interaction. These reactions are the additional source for strong interfacial adhesion, which is caused by the intercalated and exfoliated *OMON* particles in the *CENR-50* composite.

References:

4.1 F.W. Billmeyer Jr., "Textbook of Polymer Science", 3rd Edition, *John Wiley& Sons*, New York, (1984)

4.2 J. D. Menczel and B. Prime, "Thermal Analysis of Polymers, Fundamentals and Applications", *Wiley*, New York, (2009)

4.3 J.R. Fried, " Polymer Science and Technology",*Prentice Hall*, New Jersey, (1995)

4.4 W. L. Oliani, D. F. Parra, H. Otaguro and A. B. Lugão, "Study of High Strength Polypropylene (HMS-PP) under Thermal Aging", *Procc. Poly. Process. Soc. 24th Ann. Meet. ~ PPS-24*, Salerno (Italy), (2008)

4.5 D.R. Burfield and K.L. Lim, "Diffrential Scanning Calorimetry Analysis of Natural Rubber and Related Polyisoprene. Measurement of the Glass Transition Temperature", *Macromolecules*, **16**, (1983), pg.1170 – 1175

4.6 A.H. Eng, Y. Tanaka and S.N. Gan, "Some Properties of Epoxidised Deproteinised Natural Rubber", *J. Natural Rubber Research*, **V 12(23)**, (1997), pg. 82 – 89

4.7 S.N. Gan and Z. A. Hamid, "Partial Convertion of Epoxidised Groups to Diols in Epoxidised Natural Rubber", *Polymer*, **V 38(8)**, (1997), pg.1953 – 1956

4.8 S.N. Gan, "Crosslinking Reactions Responsible for the Storage Hardening in Natural Rubber", *Curr. Trend in Poly. Sci.*, **V 2**, (1997), pg. 70 – 82

4.9 D.R Burfield, "Epoxy groups responsible for crosslinking in natural rubber", *Nature*, **V 249**,(1974), pg.29 – 30

4.10 S.L. Rosen, "Fundamental Principels of Polymeric Materials", 2nd Edition, *John Wiley & Sons*, New York, (1993)

4.11 F. Bonfils, J.C. Laigneu, S. Sylla and J.S. Beuve, "DSC Valuation of PRI of Natural Rubber", *J. App. Poly. Sci.*, **V 79**, (2001), pg. 2354 – 2359

4.12 W. Coaker, "Flexible PVC: PVC Handbook – editors: C. E. Wilkes, C. A. Daniels and J. W. Summers", *Hanser*, Cincinnati, OH, (2005)

4.13 B.Y. Zhong, W.Z. Xue, H.Z. Ming and P.Z. Ren, "Effect of Physical Crosslinking on Properties of Plasticized High Molecular Weigh PVC", *J. Zhejiang Uni. Scie.*,**V 1(2)**, (2000), pg. 171 – 177

4.14 M. Scandola, G. Ceccorulli, M. Pizzoli and G. Pezzin, "Further Evidence of an Unusual T_g-Concentration Dependence for Plasticized Polyvinylchloride", *Polymer Bull.*, **6**, (1982), pg. 653 – 660

4.15 T.M. Martin, D.M Young, "Correlation of the glass transition temperature of plasticized PVC using a lattice fluid model", *Polymer*, **44**, (2003), pg. 4747 – 4754

4.16 C.I. Rich and G.W. Kunze, "Soil Clay Mineralogy (A Symposium)", *Uni. Carolina Press*, North Carolina, (1964), pg. 227

4.17 M. Kharroubi, S. Balme, F. Henn, J.C. Giuntini, H. Belarbi and A. Haouzi, "Dehydration enthalpy of alkali-cations-exchanged montmorillonite from thermogravimetric analysis", *J. Coll. & Interface Sci.*, **329(2)**, (2009), pg. 339 – 345

4.18 H.S. Peiser, H.P. Rooksby and A.J.C Wilson, "X-Ray Diffraction by Polycrystalline Materials", *The Institute of Physics – Chapman and Hall*, London, (1960)

4.19 H. Van Olphen and J.J. Fripiat, "Data Handbook for Clay Minerals and Other Non-Metalic Minerals- X-Ray diffraction", *Pergamon Press*, Oxford, (1979)

4.20 R.E. Grim and N. Güven, "Developments in Sedimentology 24: Bentonites", *Elsevier*, Amsterdam, (1978)

4.21 B.K.G Theng, "Formation and Properties of Clay-Polymer Complexes", *Elsevier*, Amsterdam, (1979)

4.22 J. Mering, " On the Hydration of Montmorillonite", *Trans. Faraday Soc.*, **V 42B**, (1946), pg.205 – 219

4.23 R.E. Grim, "Clay Mineralogy", 2nd edition, *McGraw-Hill*, New York, 1968

4.24 A. Leszczyńskaa, J. Njugunab, K. Pielichowskia and J. R. Banerjeec, "Polymer/montmorillonite nanocomposites with improved thermal properties. Part I: Factors influencing thermal stability and mechanisms of thermal stability improvement", Thermchimica Acta, V 453(1), (2007), pg. 75 – 96

4.25 H. L. Lin, H. L. Chang, T. Y. Juang, R. H. Lee, S. A. Dai, Y. L. Liu and R. J. Jeng, "Nonlinear optical, poly(amide-imide)–clay nanocomposites comprising an azobenzene moiety synthesised via sequential self-repetitive reaction", *Dyes and Pigments*, **V 82**, (2009), pg. 76 – 83

4.26 M. Huskić, E. Žagar, M. Žigon, I. Brnardić, J. Macan and M. Ivanković, "Modification of montmorillonite by cationic polyesters", *App. Clay Sci*., **V 43**, (2009), pg. 420 – 424

4.27 A. M. F. Guimarães, V. S. T. Ciminelli and W. L. Vasconcelos, "Smectite organofunctionalized with thiol groups for adsorption of heavy metal ions", *App. Clay Sci*., **V 42**, (2009), pg. 410 – 414

4.28 J. Zhang, E. Manias and C. A. Wilkie, "Polymerically Modified Layered Silicates: An Effective Route to Nanocomposites", *J. Nanosci. Nanotech*., **V 8**, (2008), pg. 1 – 19

4.29 S. Pavlidou and C. D. Papaspyrides, "A review on polymer–layered silicate nanocomposites", *Prog. Poly. Sci*., **V 33**, (2008), pg. 1119 – 1198

4.30 P. Bordes, E. Pollet and Luc Avérous, "Nano-biocomposites: Biodegradable polyester/nanoclay systems", *Prog. Poly. Sci.*, **V 34**, (2009), pg. 125 – 155

4.31 A. Martínez-Gómez, E. Pérez, C. Álvarez, "Effect of the intercalated/exfoliated nanostructure on the phase transformations of smectic polyester/layered silicate hybrids: Reinforcement of the liquid-crystalline matrix", *Polymer*, **V 50**, (2009), pg. 1447 – 1455

4.32 P. Zapata, R. Quijada, J. Retuert and E. Moncada, "Preparation of Nanocomposites by In Situ Polymerization", *J. Chil. Chem. Soc.,* **V 53(1)**, (2008), pg. 1369 - 1371

4.33 S. B. Bae, C. K. Kim, K. Kim and I. J. Chung, "The effect of organic modifiers with different chain lengths on the dispersion of clay layers in HTPB (hydroxyl terminated polybutadiene)", *Eur. Poly. J.*, **V 44**, (2008), pg. 3385 – 3392

4.34 L. B. de Paiva, A. R. Morales and F. R. V. Díaz, "Organoclays: Properties, preparation and applications", *App. Clay Sci.*, **V 42**, (2008), pg. 8 – 24

4.35 M. B. McBride, "A critique of diffuse double layer models applied to colloid and surface chemistry", *Clays Clay Miner*., **V 45**, (1997), pg. 598 – 608

4.36 M. B. McBride and P. Baveye, "Diffuse Double-Layer Models, Long-Range Forces, and Ordering in Clay Colloids", *Soil. Sci. Soc. Am. J.*, **V 66**, (2002), pg.1207 – 1217

4.37 M. B. McBride and P. Baveye, "Respond to "Comments on 'Diffuse double-layer models, long-range forces, and ordering of clay colloids", *Soil. Sci. Soc. Am. J.*, **V 67**, (2003), pg. 1961– 1963

4.38 F. Ciardelli, S. Coiai, E. Passaglia, A. Pucci and G. Ruggeri, "Nanocomposites based on polyolefins and functional thermoplastic materials", *Polym Int*, **V 57**, (2008), pg. 805 – 836

4.39 S. Sinha Ray, K. Okamoto and M. Okamoto, "Structure-Property Relashonship in Biodegradable Poly(butylenesuccinate)/Layered Silicate nanocomposites", *Macromolecules*, **36**, (2003), pg. 2355 – 2367

4.40 E.W. Nuffield, "X-ray Diffraction Methods", *John Wiley & Sons*, New York, (1966)

4.41 A. Yebra-Rodríguez, P. Alvarez-Lloret, A. B. Rodríguez-Navarro, J. D. Martín-Ramos and C. Cardell, "Thermo-XRD and differential scanning calorimetry to trace epitaxial crystallization in PA6/montmorillonite nanocomposites", *Mat. Lett*., **V 63**, (2009), pg. 1159 – 1161

4.42 M. V. Smalley, "Clay Swelling and Colloid Stability", *CRC Press- Taylor and Francis Group*, New York, (2006)

4.43 N. Guven, "Book Review on Clay Swelling and Colloid Stability", *Clays and Clay Minerals*, **V 54 (6)**, (2006), pg. 773 – 775

4.44 P. Opaprakasit and P. C. Painter, " Swelling of Clays in N-Methyl-2-pyrrolidinone/Carbon disulfide Mixed solvent", *Energy & Fuels*, **18**, (2004), pg. 1704 – 1708

4.45 R. S. Murray and J. P. Quirk, "The Physical Swelling of Clays in Solvent", *Soil. Sci. Soc. Am. J.*, **V 46**, (1982), pg. 865 – 868

4.46 I. Barshad, "Factor Affecting the Interlayer Expansion of Vermiculite and Montmorillonite with organic Substances", *Soil. Sci. Soc. Proc.*, (1952), pg. 176 – 182

4.47 C. D. Maio, L. Santoli and P. Schiavone, "Volume change behavior of clays: the influence of mineral composition, pore fluid composition and stress state", *Mechanics of Materials*, **36**,(2004), pg. 435 – 451

4.48 S. M. Rao and A. Sridharan, "Mechanism Controlling the Volume change Behavior of Kaolinite", *Clays and Clay Minerals*, **V 33 (4)**, (1985), pg. 323 – 328

4.49 http://www.sigmaaldrich.com/chemistry/solvents/toluene-center/physical-properties.html

4.50 D. Zhu, B. E. Herbert, M. A. Schlautman, E. R Carraway and J. Hur, "Cation-π Bonding: A New Perspective on the Sorption of Polycyclic Aromatic Hydrocarbon to Mineral Surfaces", *J. Environ. Qual*., **V 33**, (2004), pg. 1322 – 1330

4.51 P. D. Clark, S. T. E. Mesher, A. Primak and H. Yao, "C-S bond formation in aromatic substrate using Mn(II)-promoted montmorillonite clays.", *Catalysis Lett.*, **48**, (1997), pg. 79 – 82

4.52 J. C. Ma and D. A. Dougherty, "The Cation-π Interaction", *Chem. Rev.*, **97**, (1997), pg. 1303 – 1324

4.53 H. P Klug and L. E. Alexander, "X-ray Diffraction Procedures for Polycrystalline and Amorphous Materials", *John Wiley & Sons*, New York, (1974)

4.54 L. H. Van Vlack (Zainal Arifin Ahmad), "Seramik Fizik untuk Jurutera", *Dewan Bahasa dan Pustaka* (Kuala Lumpur) *& USM* (Pulau Pinang), (1991)

4.55 C. Pizzey, S. Klein, E. Leach, J. S. van Duijneveldt and R. M. Richardson, "Suspensions of Colloidal Plates in a Nematic Liquid Crystal: A small angle x-ray scattering study", *J. Phy. Condens. Matter*, **16**, (2004), pg. 2479 – 2495

4.56 N. Hasegawa, A. Tsukigase and A. Usuki, "Silicate Layer Dispersion in Copolymer/Clay Nanocomposites", *J. App. Poly. Sci.*, **V 98**, (2005), pg. 1554 – 1557

4.57 E. Hecht, "Optics", 2nd. Edition., *Addison-Wesley Publishing*, USA, (1987), pg.427

4.58 D. Halliday, R. Resnick and J. Walker, "Fundamentals of Physics – Extended, with Modern Physics", *John Wiley & Sons*, New York, (1993), pg. 1089

4.59 R. M. Silverstein, F. X. Webster, "Spectrometric Identification of Organic Compounds", 6th. Edition., *John Wiley & Sons*, New York, (1998)

4.60 K. Nakanishi, "Infrared Absorption Spectroscopy", 2nd. Edition, *Holden-Day Inc.*, San Francisco, (1977)

4.61 N. P. G. Roeges, "A Guide to the Complete Interpretation of Infrared Spectra of Organic Structures", *John Wiley & Sons*, New York, (1994)

4.62 A. Subramaniam, "Molecular weight and other properties of natural rubber: A study of colonial variation", *Procc. Int. Rubber Conf.*, **V 4**, (1975), pg. 3

4.63 J. Tangpakdee and Y. Tanaka, " The gel phase in Natural Rubber", *Rubber Chem Technol.*, **70**, (1997), pg. 707 – 713

4.64 D. R. Burfield and S. N. Gan, "Nonoxidative crosslinking Reactions in Natural Rubber. I Determination of Crosslinking Groups", *J. Poly. Sci.*, **V 13**, (1975), pg. 2725 – 2734

4.65 K. S. Tan and A. Yusof, "Some studies on the effect of solvents in ENR-60 gel content measurements", *J. Rubber Res.*, **V 6 (4)**, (2003), pg. 189 – 194

4.66 X. Wang, N. Yoshimura, D. Tu, Y. Tanaka and T. Takada, "Distribution Characteristics and Formation Mechanism of Space Charge in PE Materials", *Procc. Int. Symp. Elec. Ins. Mat.*, **A3-5**, (1998), pg. 109 – 12

4.67 U.K Mandal, "Ionic elastomer based on carboxylated nitrile rubber: infrared spectra analysis", *Polym. Int.*, **49**, (2000), pg. 1653 – 1657

4.68 M. J. Wilson (editor), "Clay Mineralogy: Spectroscopic and Chemical Determinative Methods", *Chapman & Hall, London*, (1994)

4.69 R. A. Via, R. K. Teukolsky and E. P. Giannelis, "Interlayer Structure and Molecular Environment of Alkylammonium Layered Silicates", *Chem. Mater*., **6**, (1994), pg. 1017 – 1022

4.70 W. Wang, L. Li and S. Xi, "A Fourier Infrared Study of the Coagel to Micelle Transition of Ctyltrimethylammonium Bromide", *J. Coll. & Interface Sci.,* **155**, (1993), pg. 369 – 373

4.71 H. R. Kricheldorf, N. Probst, G. Schwarz and C. Wutz, "Layer Structures. 4. Role of Long Alkane Spacers in Poly(esterimide)s Derived from *N*-(4¢-Hydroxyphenyl)-4-hydroxyphthalimide", *Macromolecules*, **V 29**, (1996), pg. 4234 – 4240

4.72 A. Nisha, M. K. Rajeswari and R. Dhamodharan, "Intercalative Redox Polymerization and Characterization of Poly(*N*-vinyl-2-pyrrolidinone) in the Gallery of Vermiculite: A novel Inorganic-Organic Hybrid Material", *J. App. Poly. Sci.,* **V 76**, (2000), pg. 1825 – 1830

4.73 A. M. F. Guimarães, V. S. T. Ciminelli and W. L. Vasconcelos, "Surface modification of synthetic clay aimed at biomolecule adsorption: synthesis and characterization", *Mat. Res.*, **V 10 (1)**, (2007)

4.74 P. H Lye and H. K. Toh, "Incorporation of Amine Antioxidants into Natural Rubber Network via Epoxide Groups", *J. Poly. Sci.: Poly. Ltt. Edt.*, **V 22**, (1984), pg. 327 – 334

Chapter 5

Thermoelectric Properties
- Thermally Stimulated Current (TSC)

Chapter 5: THERMO-ELECTRICAL PROPERTIES – THERMALLY STIMULATED CURRENT, TSC

Results and observations from Thermally Stimulated Current, TSC experiments carried out on polymers, *ODA* (*octadecylamine*), *Mon* (*Montmorillonite*), *OMON* and *polymer-OMON* composites are discussed through out this chapter. Basic evaluations on TSC thermograms are done by comparing the results with those from DSC technique. This is very important to identify TSC peaks and other thermal feature observed in the thermogram. For example, the relaxation α peak that is comparable with the glass transition temperature, T_g from DSC scan. Information obtained from the α peak is useful to assist the search for other possible relaxation effects. Such as the location of β and ρ peaks that represent the dipole group and space charges relaxations respectively. Preliminary analysis within this chapter is also very important to demonstrate the sensitivity and reliability of TSC technique, as well as the developed TSC system in this project.

5.1 Analysis on Elementary Components

Each peak within the TSC thermogram indicates the relaxation effect of certain polarized group or species in a material. Its appearance is unique and can be used to characterize the material. This characteristic peak in fact may appear whenever its polarized species exist, even in a mixture that involve the material. Hence, it is very important to priory recognize each peak from pristine materials in this studies, such as polymers, *ODA* and *Mon*.

5.1.1 Pristine Polymers - *SMRL, DPNR ENR-50, PE and pPVC*

5.1.1.1 *α Peak*

Figure 5.1 and 5.2 show the TSC and DSC thermograms of *SMRL* and *DPNR* respectively. In current-temperature plot as shown in Figure 5.1(a), a TSC peak can be clearly observed around −65.48 °C, which is around the T_g for *SMRL* about −64.08 °C as shown in the DSC

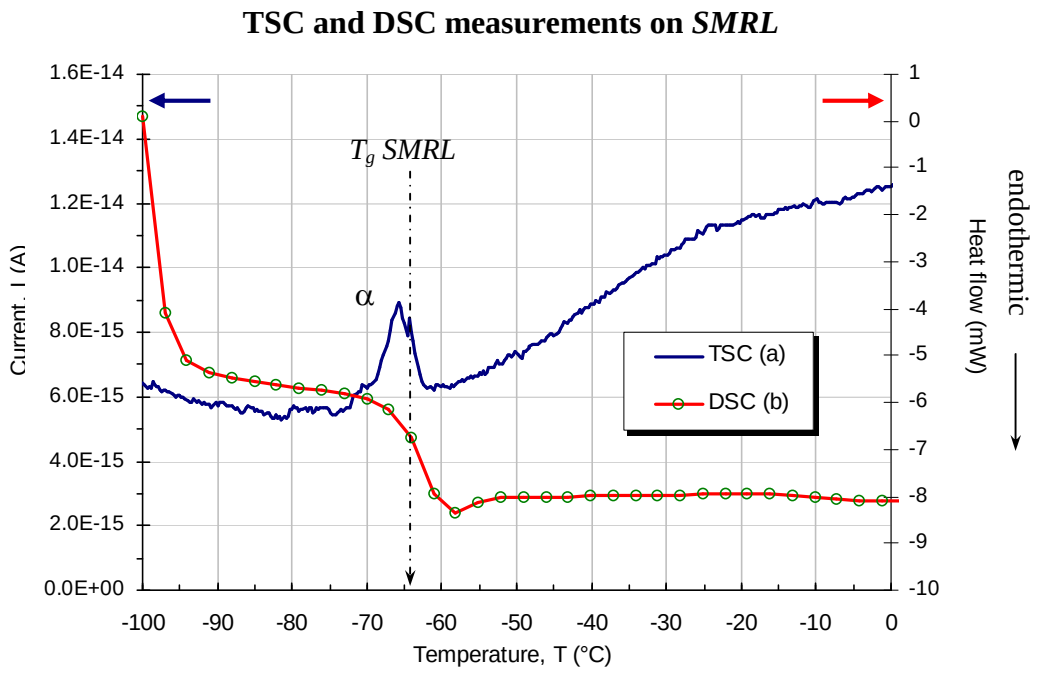

Figure 5.1: TSC thermogram for *SMRL* in (a) shows the α peak at -65.48 °C, while in (b) the glass transition temperature, T_g from DSC scan can be seen at -64.08 °C.

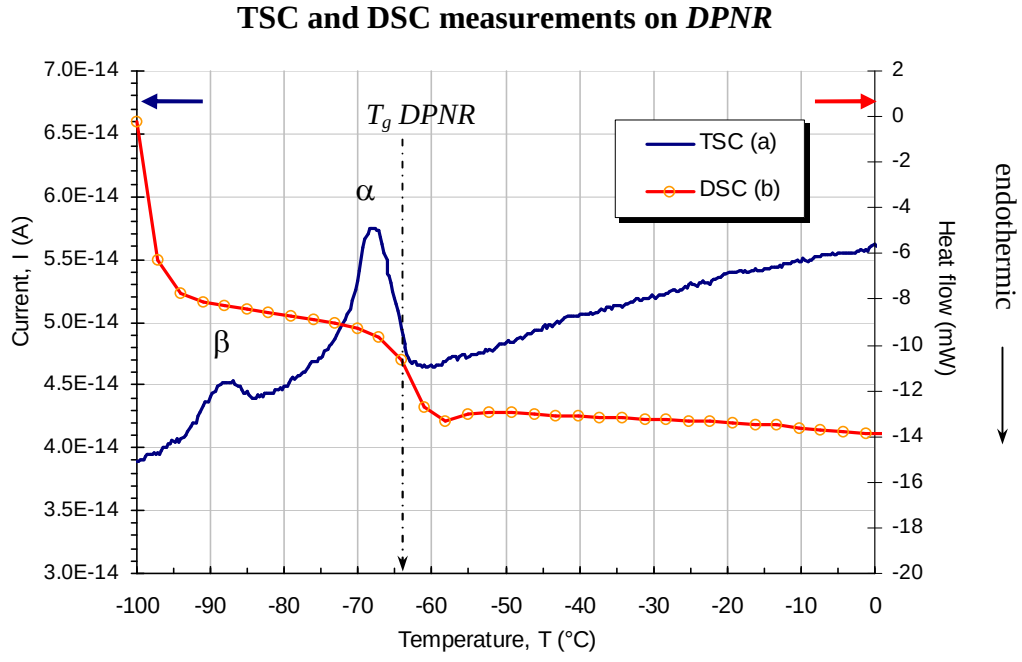

Figure 5.2: The α peak for *DPNR* that is located at -67.76 °C is comparable to the T_g at -64.13 °C. Besides, there is a β peak at -86.87 °C which is not detected in the TSC thermogram for *SMRL*.

scan in Figure 5.1(b). The peak thus is referred as the α peak of *SMRL* rubber. This α peak arises from the dielectric relaxations of polarized segments on polyisoprene backbone [5.1, 5.2 and 5.3] in *SMRL*, as well as in the *DPNR* and *ENR-50* rubbers. Therefore, similar peak is also found within the TSC plot of *DPNR* in Figure 5.2(a) that is around −67.76 °C (T_g = −64.13 °C). While in case of *ENR-50* in Figure 5.3(a), the α peak is found at −62.58 °C. In addition, there is another peak observed around −25.02 °C within the TSC thermogram of *ENR-50*. It seemed that the maximum temperature T_{max} of this peak is similar with the thermal transition at −22.40 °C [5.4], which is known as the characteristic T_g for *ENR-50* as shown in Figure 5.3(b). The TSC peak is then ascribed as the α_{ENR50} peak for *ENR-50*. This TSC peak and the thermal transition at T_g from DSC scan apparently share similar origin. Both thermal features are due to the presence of epoxide groups on the polyisoprene molecules. The existence of such polar groups responsible for the increased T_g in *ENR-50* rubber as discussed earlier in Section 4.1.1.A.

On the other hand, the DSC thermogram of *ENR-50* reveals only one thermal transition that indicates the effect of epoxide group. Despite the T_g, it does not provide any obvious indication for the existence of unepoxidised polyisoprene chains within the rubber, where it should be around −60 °C to −70 °C (see Fig. 5.3(b)) as shown by the α peak within TSC thermogram. However, thermal transition that is related to the polyisoprene chains can be clearly observed around −64.10 °C in Figure 5.1(b) and 5.2(b) for *SMRL* and *DPNR* in that order. The temperatures are comparable with the α peak of *SMRL* (−65.48 °C) and *DPNR* (−67.76 °C) rubber as discussed earlier.

The emergence of α peak in Figure 5.3(a) thus proves that TSC technique is sufficiently sensitive in detecting the amorphous characteristic of polymers. This α peak can also be observed within the TSC thermogram of *PE* around −103.55 °C, as shown in Figure 5.4(a).

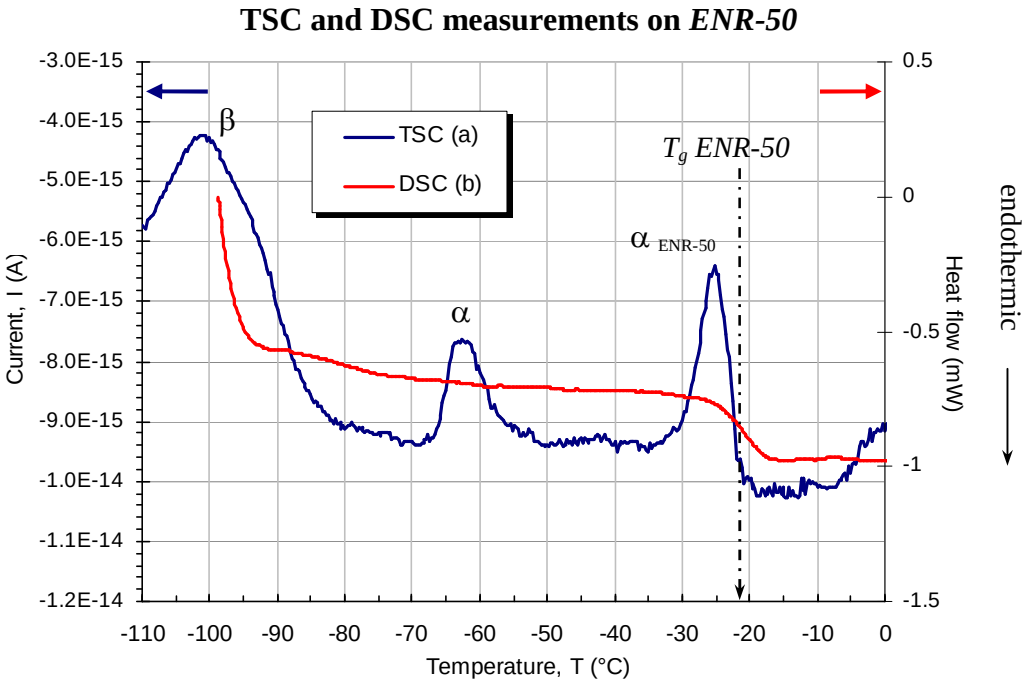

Figure 5.3: TSC scan for *ENR-50* shows two α peaks: $\alpha_{\text{ENR-50}}$ at -25.02 °C which is analogous to the T_g at -22.40 °C, and α peak around -62.58 °C represents polyisoprene chains in *ENR-50*. A β peak for this polymer can be seen at -101.24 °C.

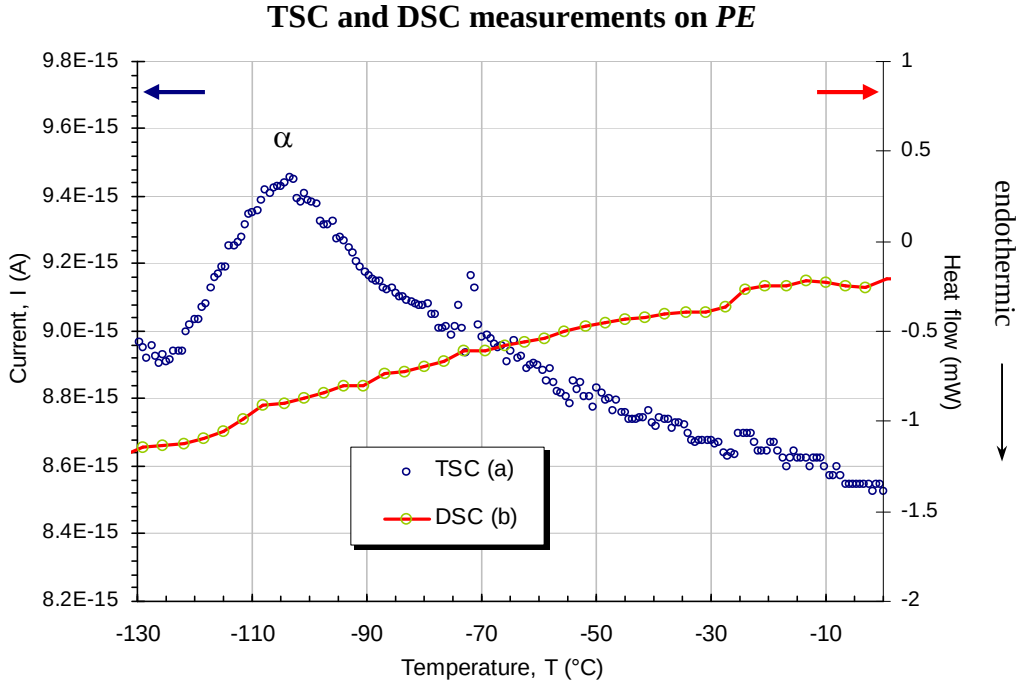

Figure 5.4: DSC scan for semi-crystalline *PE* does not show any trace of T_g. However, TSC thermogram manages to present the α peak at -103.55 °C which proved the existence of amorphous region in the studied *PE*.

The DSC thermogram in Figure 5.4(b) in contrast does not show any thermal transition within the range of known T_g (−120 °C to −100 °C), which can be related to the amorphous region in *PE* as depicted by the α peak.

From current-temperature plots in Figure 5.5(Ia) and Figure 5.5(IIa) for TSC measurement on *pPVC*, similar observations as shown earlier by the *ENR-50* can be observed. There are the two α peaks appear at − 37.46 °C and 79.76 °C, which is assigned as α_{DOP} and α_{PVC} respectively. The former peak is associated to the effect of plasticizer molecules (*DOP*) on *PVC* chains, while the later peak indicates the presence of *PVC* chains within *pPVC*. These deductions arise as the peaks are analogous to DSC thermal transitions found in Figure 5.5(Ib) and 5.5(IIb) for *pPVC*. The first T_g taking place around −48 °C is comparable to the α_{DOP} peak, which is due to the effect of plasticizer molecules as previously explained in Section 4.1.1.C. While the second thermal transition (T_g) at 91.86 °C [5.5 and 5.6] is related to the emergence of α_{PVC} peak in the TSC plot. The T_{max} for α_{PVC} peak actually lies in between the T_g and an endothermic, T_m at 67.87 °C. Previously in Section 4.1.1.C, it was believed that the T_m indicates some microcrystallite structures in *pPVC.* It means that the melting of such crystallite structures stimulated chains movements, which then assisted segmental chains relaxation for the α_{PVC} peak. The mobility as a result led the *pPVC* chains to phase transition at the T_g.

Basically, the movement of segmental molecules contributes for these observations from TSC or DSC thermograms as discussed above. It involves the motion of about 40 to 50 carbon atoms on the polymers backbones [5.7]. As the polymers temperature crosses their T_g during TSC measurements, the segmental molecules gradually receive enough thermal energy to facilitate the mobility of polarized and frozen main chains to depolarize and then randomize. This depolarization process within a material is known as dielectric relaxation in TSC technique, which is represented by the α peaks [5.1, 5.8, 5.9, 5.10 and 5.11].

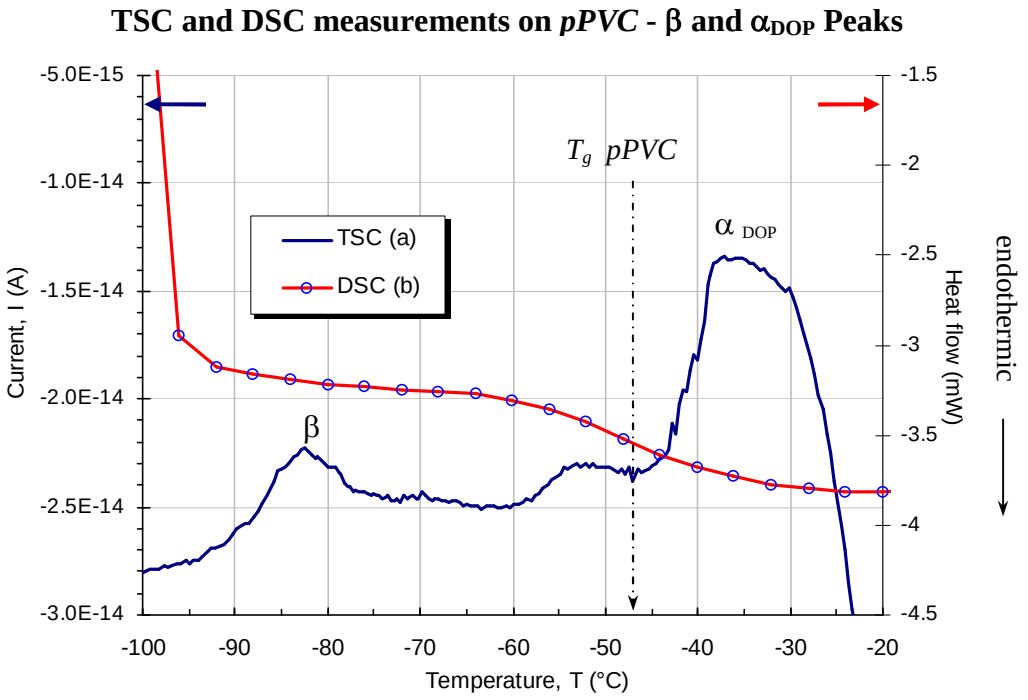

Figure 5.5(I): The effect of plasticizer in *pPVC* can be seen within TSC plot with the α_{DOP} peak at -37.46 °C, which is comparable to the T_g at -48.0 °C. There is also a β peak observed at -82.56 °C in the thermogram.

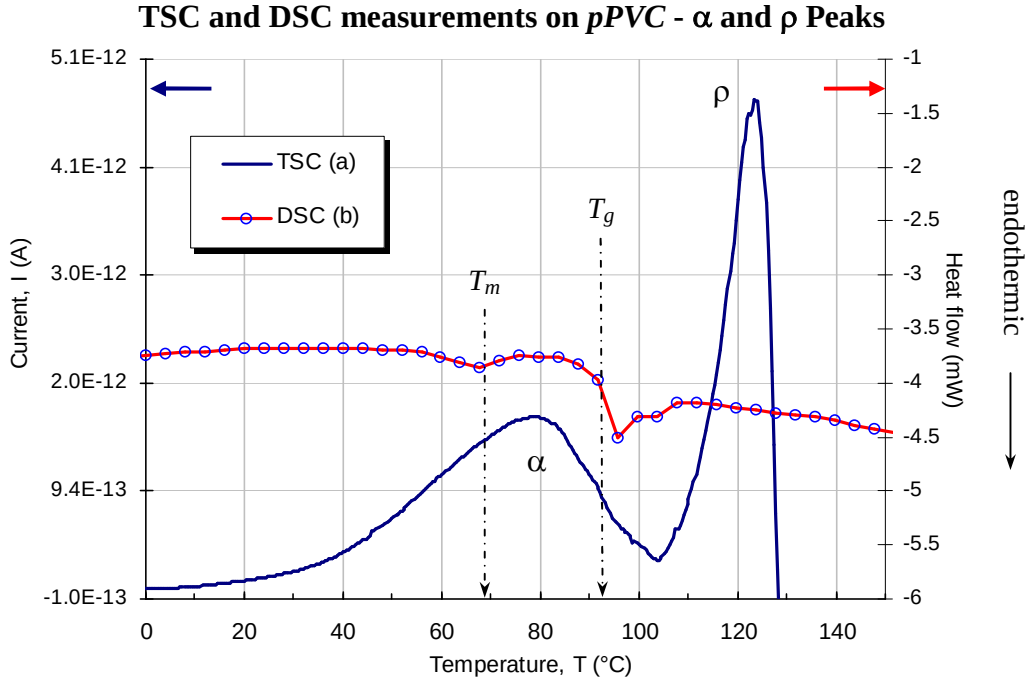

Figure 5.5(II): The α peak for pristine *PVC* chains appear at 79.76 °C which is in between a small endothermic T_m at 67.87 °C and the T_g at 91.86 °C in DSC scan. It is followed by the ρ peak at 123.89 °C.

Table 5.1
The Maximum Temperature T_{max} of Polymers α Peaks

No.	Sample	Maximum Temperature, T_{max} (°C)			
		TSC α peaks (± 0.01)		T_g (± 0.01)	Known T_g
1.	SMRL	– 65.48		– 64.08	– 60 to – 70 [5.12 and 5.13]
2.	DPNR	– 67.76		– 64.13	
3.	ENR-50	– 25.02		– 22.40	– 20 to – 25 [5.14 and 5.15]
4.	PE	– 103.55		Not detected	– 120 to – 100 [5.16, 5.17 and 5.18]
5.	pPVC	–37.46	79.76	91.86	79 to 97 [5.19 and 5.20]

Table 5.1: The maximum temperature T_{max} of α peak for each polymer in this work compared with their T_g from DSC thermogram and the known T_g from some previous authors.

However, there are some variations in the maximum temperature T_{max} of these α peaks and their related thermal transitions T_g within DSC thermograms. Table 5.1 lists the T_{max} and T_g of the α peaks together with some known T_g from previous researcher for comparison. The differences in value given by both DSC and TSC techniques may be explained by the fact that DSC is a non-isothermal method of testing. TSC method however is closely reaching the isothermal condition due to the small heating rate employed in this study, which was about 1 °C/min. This rate is relatively small than 10 °C/min that is frequently used in the DSC technique. Such high heating rate can shift the T_g to a higher temperature, which may explain the variation in the T_{max} and T_g temperatures. Similarly, high heating rate can also shift the T_{max} of a TSC peak. Therefore, it is recommended to choose a small heating rate such as 1°C/min for the TSC technique.

5.1.1.2 β Peak

The knowledge of α peak is useful to investigate some other TSC peaks, which normally appear in most of the TSC thermogram. For example, there is a prominent peak observed around – 86.87 °C that is around 21 °C below the temperature of α *DPNR* peak in Figure

5.2(a). This peak is identified as β peak and associated to the relaxation of side chains on the polymer backbone [5.21, 5.22 and 5.23]. Similar observation can also be seen in Figure 5.3(a) of *ENR-50* rubber, where the β peak is located at – 101.24 °C. In both cases, the β peaks could also be related to the impurities in these rubbers [5.24]. Such impurity may come from chemical residue after went through some modifications to get the *DPNR* and *ENR-50* rubbers. In case of *pPVC*, the β peak is located at – 82.56 °C as shown in Figure 5.5(Ia). The maximum temperature, T_{max} of these β peaks is listed in Table 5.2.

Table 5.2
The Maximum Temperature T_{max} of Polymers β and ρ Peaks

	Sample	Maximum Temperature, T_{max} (°C)	
		β peaks (± 0.01)	**ρ peaks (± 0.01)**
1.	SMRL	not detected	68.54
2.	DPNR	– 86.87	145.87
3.	ENR-50	– 101.24	70.00 to 100.00
4.	PE	not detected	51.33
5.	Plasticized PVC	– 82.56	123.89

Table 5.2: Maximum temperature, T_{max} for the observed β and ρ peaks within the TSC thermogram of each pristine polymer in this work.

5.1.1.3 ρ Peak

Beside the β peaks, there is also a ρ peak that can be seen at 123.89 °C for *pPVC* in Figure 5.5(IIa), at 145.87 °C for *DPNR* (Figure 5.7(a)) and around 90.00 °C for *ENR-50* in Figure 5.8(a). It seems that these peaks appear far above the temperature of α peak in each case of the polymers. It is due the fact that the peaks represent the depolarization of space charges [5.25, 5.26 and 5.27], which are trapped within localized traps in the polymers. Once the polymers temperature crossed their T_g, the polymeric chains that created the localized traps became loosen. The chains movement therefore assists the depolarization process of space charge from the traps. The increase in heat supply in fact give sufficient activation energy for the polarize space charges to be released in the process.

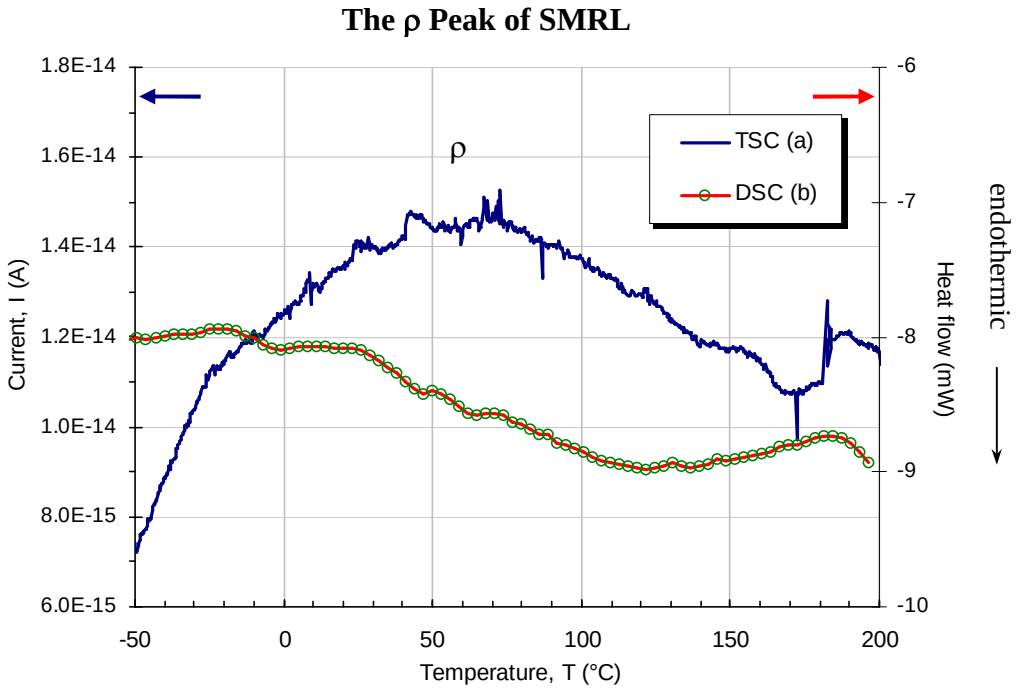

Figure 5.6: The big and wide peak at 68.54 °C within the TSC plot of *SMRL* is most likely indicating the ρ peak, which falls within the range of softening temperature, T_s for the natural rubber.

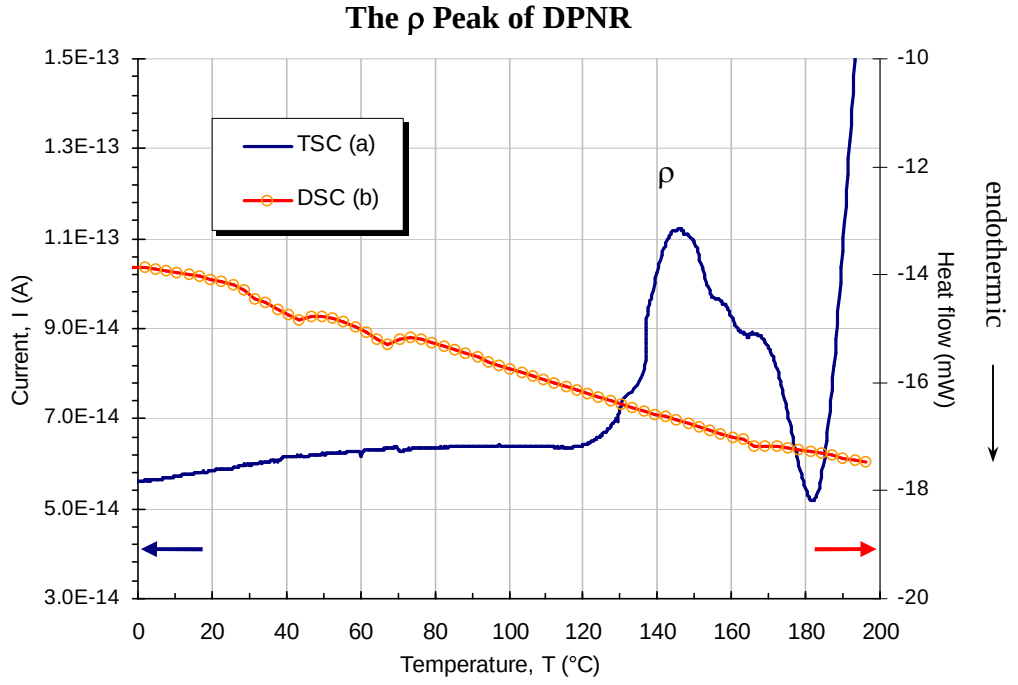

Figure 5.7: Similarly as in *SMRL*, the ρ peak of *DPNR* is also hardly observed. However, there is a prominent ρ peak at 145.87 °C which probably demonstrates the space charges relaxation.

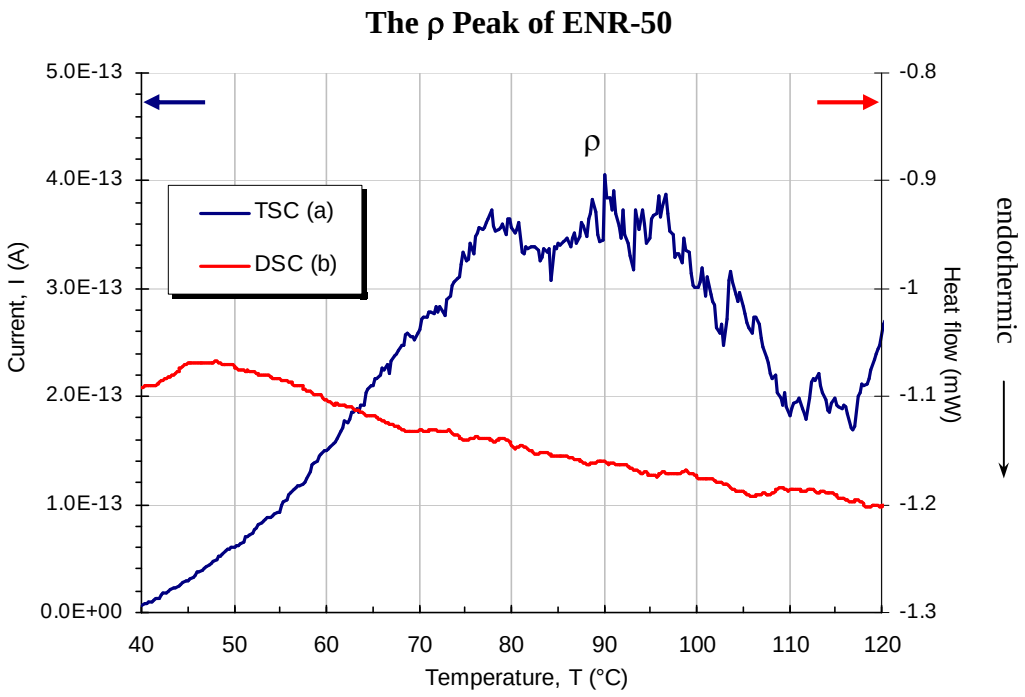

Figure 5.8: Besides the β and α peaks, there are big and wide peaks within 70.00 °C to 100.00 °C within the TSC plot of *ENR-50*, which possibly indicates the ρ peak relaxation.

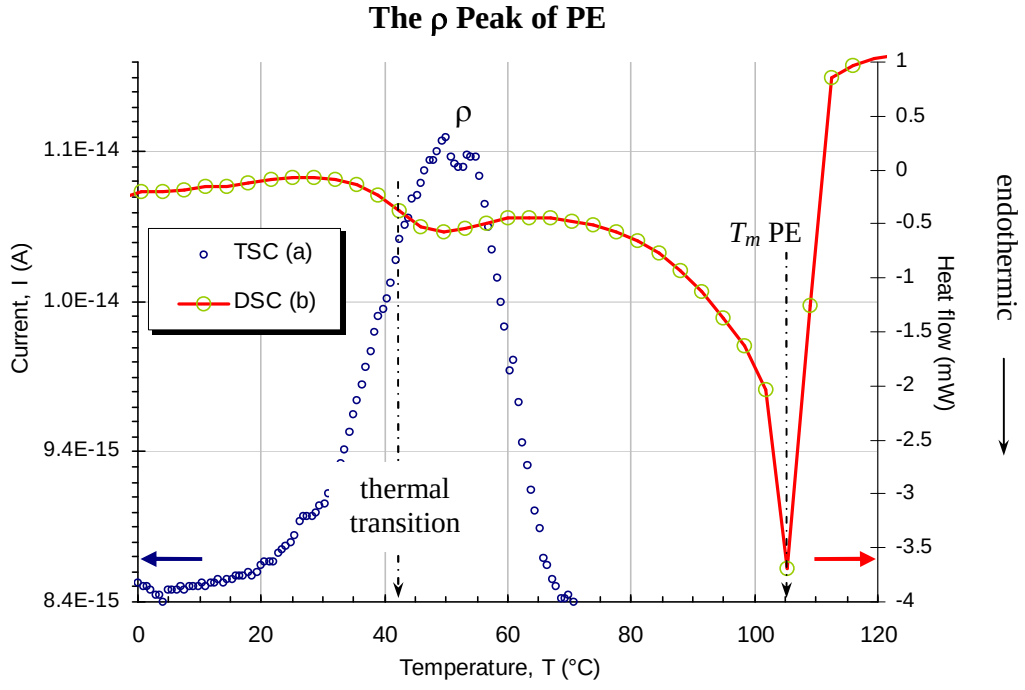

Figure 5.9: TSC thermogram for *PE* reveals a ρ peak at 51.33 °C, where it falls near a thermal transition at 42.49 °C in the DSC thermogram. This transition appears before the big endothermic that give the T_m at 105.36 °C for *PE*.

Broad peaks at 68.54 °C in Figure 5.6(a) of *SMRL* and at 51.33 °C in Figure 5.9(a) for *PE* probably reveal similar relaxation effects. Natural rubbers are known to have a softening temperature, T_s within the range of 60 °C to 70 °C wherein the polymeric chains start to loosen extensively after passing the T_s. As the ρ peak of *SMRL* falls within the temperature range, the softening process thus might have assisted the depolarization of space charges in the *SMRL* rubber. In the DSC thermogram of *PE*, a thermal transition appears at 42.49 °C prior to the big endothermic (T_m) at 105.36 °C. It indicates the movement of alkyl chains that subsequently contribute to the appearence of *PE* ρ peak in the TSC plot. Maximum temperature, T_{max} for these ρ peaks are listed in Table 5.2.

5.1.2 Montmorillonite, *Mon*

Figure 5.10(a) shows the TSC thermogram of *Mon* with a small shoulder around 25.17 °C. The next observation is the peak at 74.70 °C that is the only peak observed in the current - temperature plot. In fact, there is no clear indication of other relaxation effects that can be identified for the clay mineral. From the DSC plot of *Mon* as shown in Figure 5.10(b), a big and wide endothermic can be seen with the minimum at 57.92 °C. As suggested earlier in Section 4.1.2, the endothermic comes from dehydration process due to the loss of water content in *Mon* gallery during heating. As a result, the process possibly had released some polarized charges that were detected via the TSC measurement. Hence, the observed peak within the TSC thermogram is referred as the ρ peak of *Mon*.

5.1.3 Octadecylamine, *ODA*

Figure 5.11(a) shows the current-temperature plot of TSC and Figure 5.11(b) demonstrates the thermogram of DSC for *octadecylamine* (*ODA*). The observed peaks in Figure 5.11(a) are located at 28.03 °C, 55.07 °C and 75.66 °C, where the fist peak is much smaller than the last two peaks. In Figure 5.11(b), the DSC profile reveals one small thermal transition

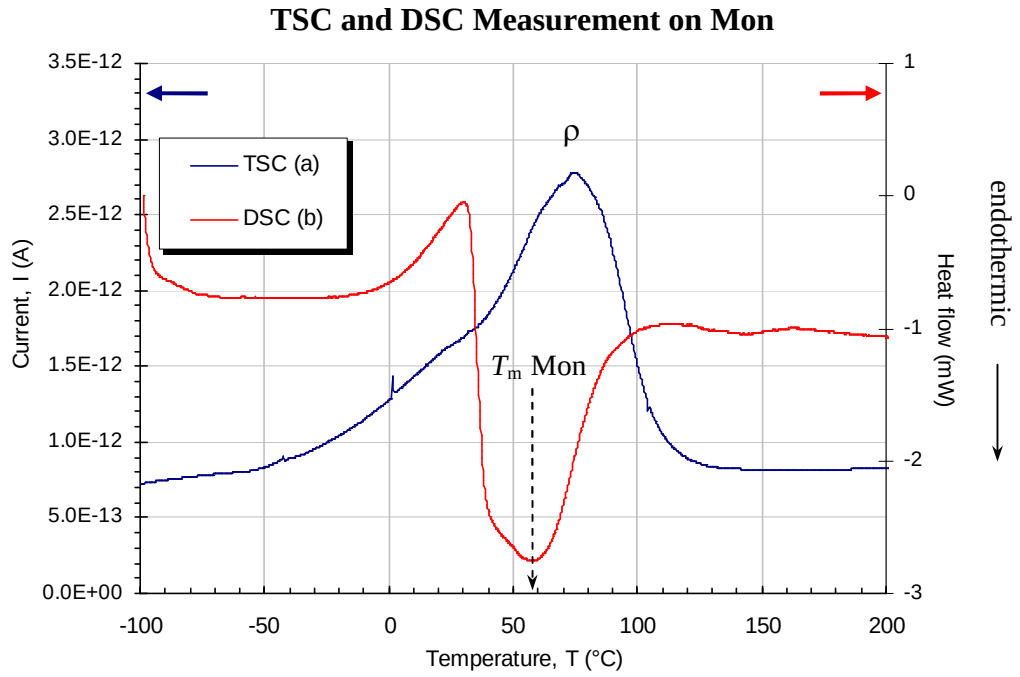

Figure 5.10: There is only one peak from TSC thermogram observed for *Mon* at 74.70 °C. The peak is recognized as ρ peak since it appears within the temperature region of the big endothermic (57.92 °C) within DSC thermogram.

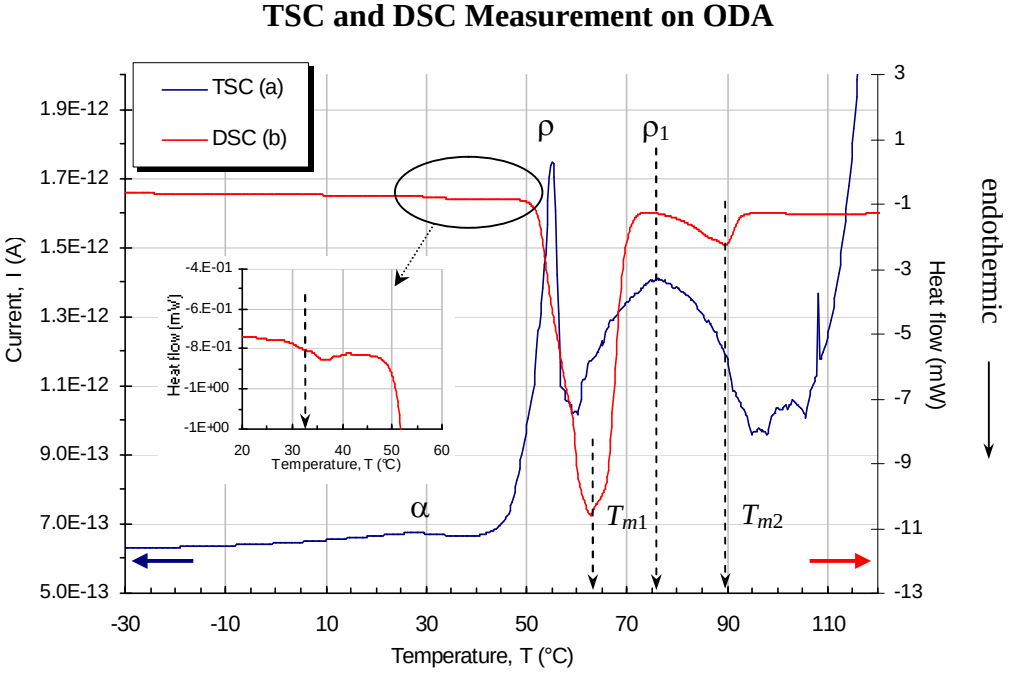

Figure 5.11: The ρ peaks at 55.07 °C and 75.66 °C in the TSC plot of *ODA* are analogous to the T_ms at 6.77 °C and 89.53 °C in the DSC thermogram. The first peak at 28.03 °C is referred as α peak and comparable with the small transition around 33.55 °C in the inset.

around 33.55 °C and two endothermic. These endothermics are associated to the melting process of *ODA* chains around 62.77 °C (T_{m1}) and 89.53 °C (T_{m2}).

DSC thermal transition, T_g at 33.55 °C is comparable to the peak at 28.03 °C in the TSC plot. Therefore, the peak is assigned as the α peak of *ODA* material. The differences in temperatures that separate the TSC peaks (~21 °C) and the endothermic (~27 °C) are also comparable. The second TSC peak at 55.07 °C thus is associated to the T_{m1} at 62.77 °C and ascribed as the ρ peak of *ODA*. The endothermic T_{m2} at 89.53 °C however is much smaller and difficult to interpret compared to the first endothermic. A few interpretations can be used to explain the existence of T_{m2} endothermic. It could be representing the second stage of melting processes for T_{m1}. However, there is no sign of exothermic peak that can prove the suggestion [5.28]. Second opinion suggests that *ODA* does not consist of single crystal system. It means that the T_{m2} arose from the melting process of some other crystal systems. This idea allows ones to relate the T_{m2} endothermic with the third TSC peak at 75.66 °C. Hence, this peak is assigned as the ρ_1 peak for *ODA*. This peak is also associated to the space charges relaxations as the ρ peak.

Analyses on TSC thermograms for the pristine polymers and *ODA* identify the relaxation α peak. This peak with comparable temperature to that of the T_g from DSC test demonstrates the reliability of the developed TSC system. The α peak also confirms the contribution of segmental motion in the thermal reactions of polymeric materials. Relaxation process by the side chain components on polymeric backbone bring about the β peak in some cases of the material. This peak shows that the TSC technique is sufficiently sensitive to distinguish various thermal responses of elements in a material. More proof is given by the emergence of ρ peak that appears next to the α peak. Where, space charge relaxation process produces the observed ρ peaks in the pristine polymers, *Mon* and *ODA* thermograms.

5.2 Analysis on OMON and Polymer-OMON Composites

OMON is a renewed clay mineral that is composed primarily of *Mon* particles and *ODA* cations. Structural modification due to interactions between the two components may have some effects on their relaxation processes. Therefore, prior analysis on TSC thermogram for pristine *Mon* and *ODA* will be useful to investigate *OMON* thermogram. In the same way, the identified *OMON* characteristic peaks can assist the analysis process on several relaxation effects in *polymer-OMON* composites.

5.2.1 Organically modified Montmorillonite, *OMON*

The TSC profile in Figure 5.12(Ia) demonstrates a small hump around −23.14 °C, which is assigned as the β peak of *OMON*. While the next prominent peak observed at 34.87 °C is referred as an α peak. Following the peak, there are two other peaks appear closely to each other. They are at 85.96 °C and 105.35 °C that are respectively ascribed as the ρ and ρ_1 peaks of *OMON*. These peaks are comparable with the ρ peaks of *ODA*, as shown by the TSC plot in Figure 5.11(a). The interpretations are also supported by the DSC thermogram in Figure 5.12(Ib), where it demonstrates only one thermal transition at 32.75 °C that is analogous to the α peak of *OMON*. Previously in Section 4.1.2, it was suggested that the missing *ODA* endothermics within *OMON* thermogram can be regarded as an evidence for the intercalation of *ODA* cations. Moreover, from FTIR analysis in Section 4.3.2.1.A it was shown that the alkyl chains of *ODA* cations capable to maintain their crystallite structures inside *OMON* gallery. The melting of such structures as a result leads to the depolarization of space charges, which are represented as the ρ peaks.

Generally, the α and ρ peaks observed in Figure 5.12 (IIa) are very much alike and similar in shapes with the *ODA* peaks in Figure 5.11(a). However, the positions of the peaks are shifted towards higher temperatures from their initial T_m in *ODA*. This could be the effects

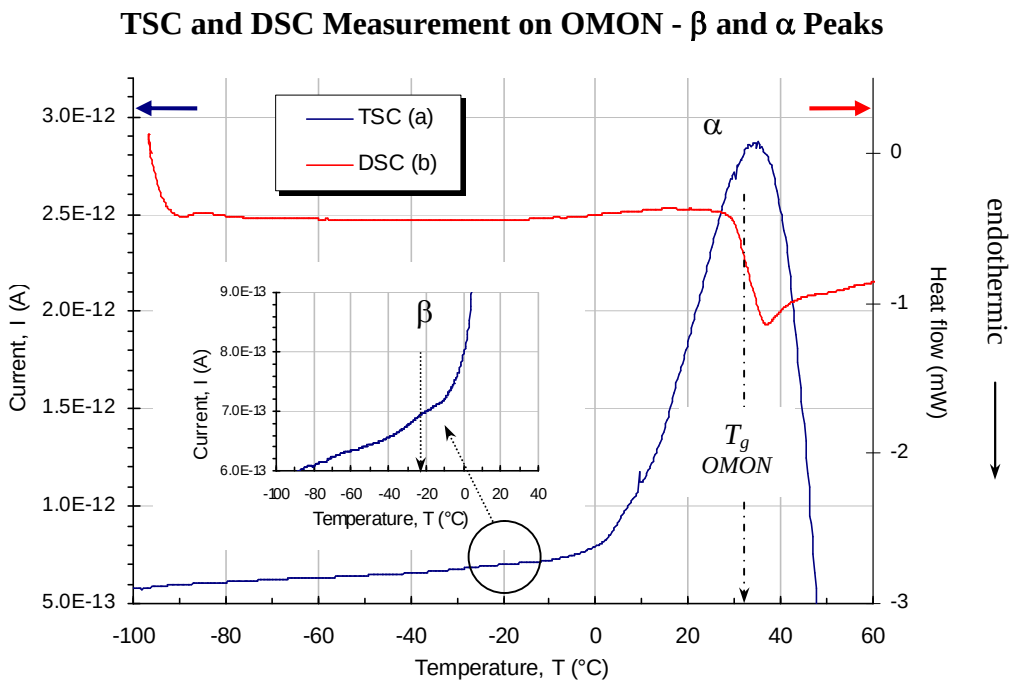

Figure 5.12 (I): A small hump at -23.14 °C in inset is assigned as the β peak. It appears prior to the α peak at 34.87 °C which is analogous to the thermal transition at 32.75 °C in the DSC thermogram.

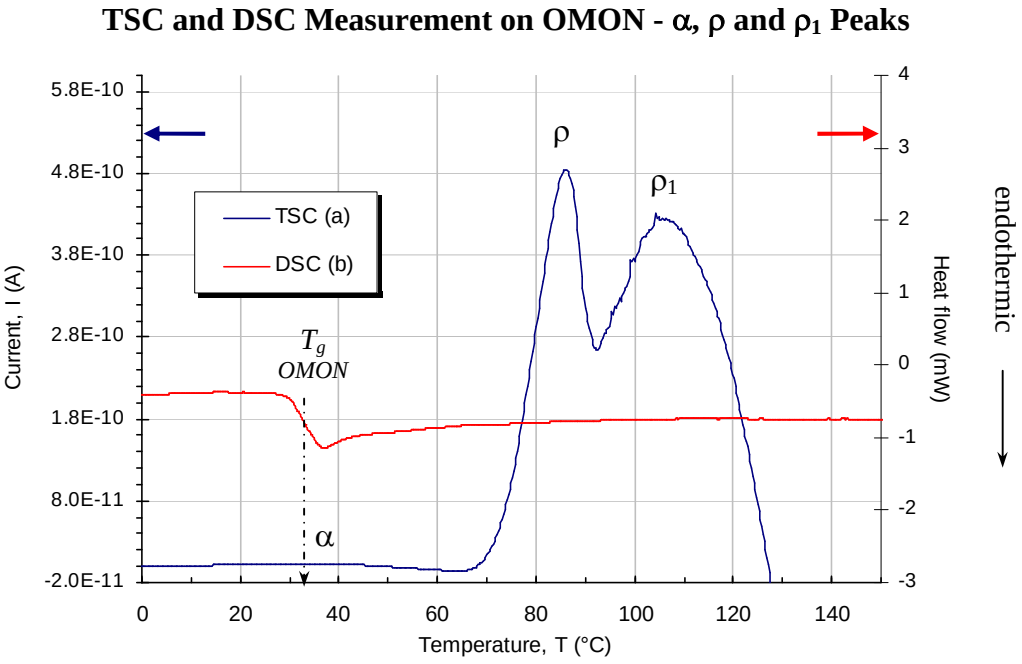

Figure 5.12 (II): The two ρ peaks of *ODA* can be seen within the TSC plot of *OMON*. They appear around 85.96 °C and 105.35 °C for the ρ and ρ_1 peaks, respectively.

of *ODA* cations inside *OMON* gallery, which are more electropositive compared to that of *ODA* molecules. In that way, these ionic molecules had played significant role to generate good physical contact with *OMON* silicates. More energy however was needed to facilitate the relaxation process of such ionic molecules, which subsequently shifted the maximum temperatures of TSC peaks.

From the TSC thermogram, the intercalation of *ODA* cations into *OMON* galley is proven. The appearance of α and ρ peaks confirm the presence of alkyl chains from *ODA* cations. In the DSC thermogram however, no thermal feature is identified that can be associated to *ODA* existence inside *OMON* particles. Therefore, it is believed that the intercalated *ODA* cations within *OMON* gallery cannot be detected via the DSC technique. The observations also confirm that the TSC system built in this work is sufficiently sensitive to demonstrate the effect of *OMON* intercalation.

5.2.2 *Polymer-OMON* Composites

TSC thermograms for the studied *polymer-OMON* composites in general demonstrate the presence of main components within the materials, such as the inset in Figure 5.13 of TSC current-temperature plot for *CDPNR* composite. This plot reveals the α peak at −59.49 °C, which indicates the existence of polyisoprene chains from *DPNR* rubber in the composite. Likewise, the peak is detected within the TSC plot of *CENR-50* at −64.26 °C as shown in the inset of Figure 5.15(I). From this plot, the typical α peak for the *ENR-50* rubber can be observed at −20.48 °C. The existence of polyisoprene chains in the *natural rubber-OMON* composites can also be observed within their DSC plots. The glass transition temperature, T_g of the unepoxidised polyisoprene chains in *CENR-50* however cannot be detected using the DSC technique, which is shown in Figure 5.15(Ib).

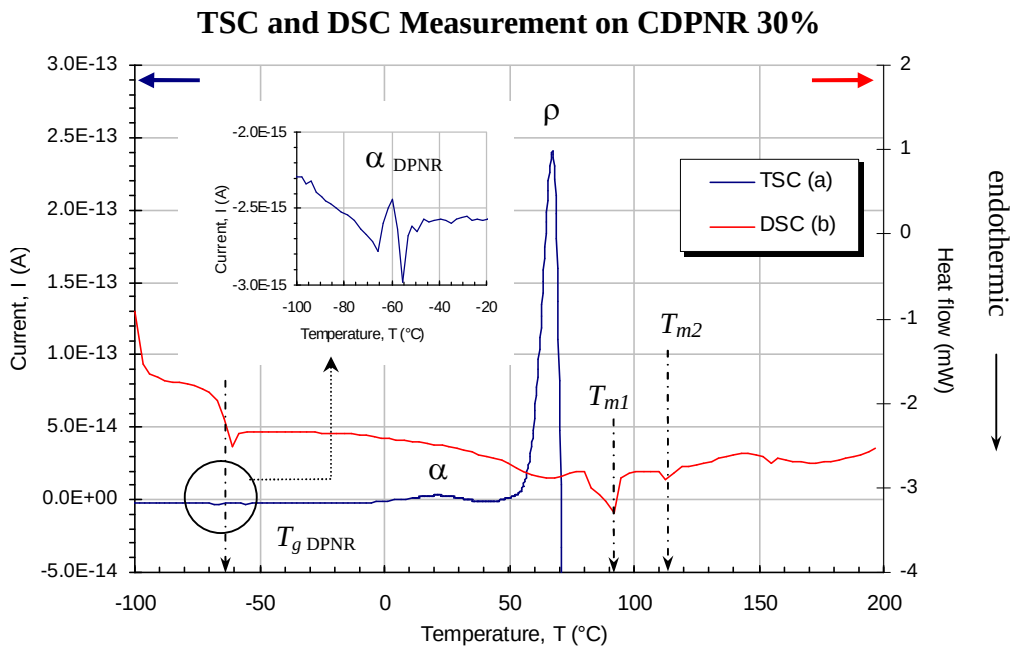

Figure 5.13: A small α peak from *DPNR* is detected at -59.49 °C. While a pair of α and ρ peak at 21.43 °C and 67.33 °C respectively, resemble similar peaks within *OMON* thermogram. DSC plot also indicate the presence of *OMON* with the T_{m1} and T_{m2} endothermic. Polymer matrix component in this composite is represented by the T_g DPNR at -64.03 °C.

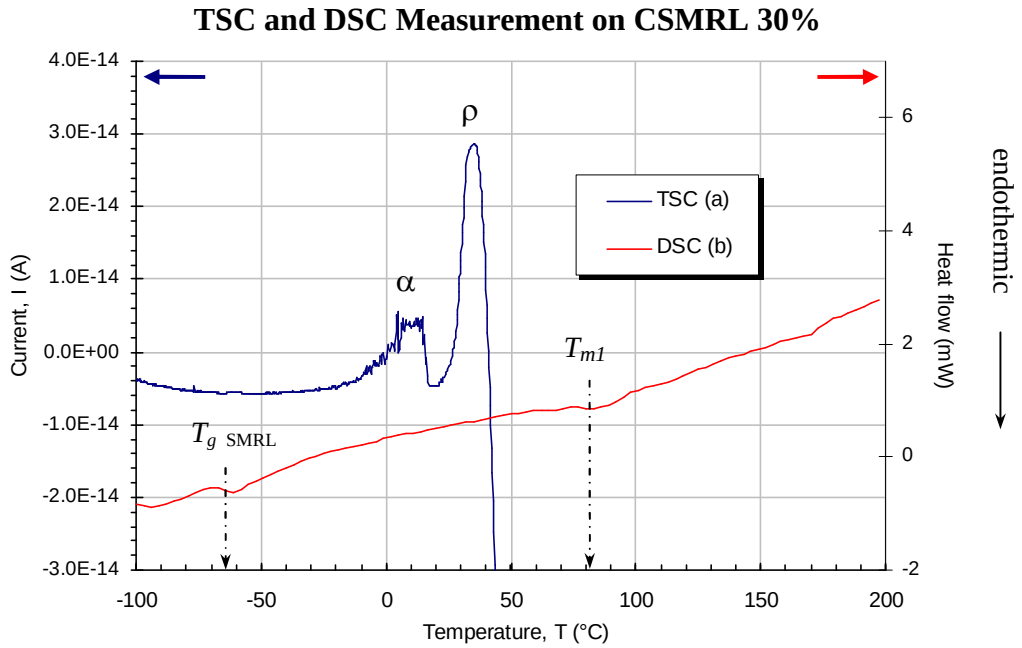

Figure 5.14: TSC plot for *CSMRL* shows the α peak of *SMRL* at -60.19 °C and a pair of α and ρ peak at 7.58 °C and 34.54 °C respectively. DSC thermogram however, does not show clear trend that indicates *OMON* existence in the composite.

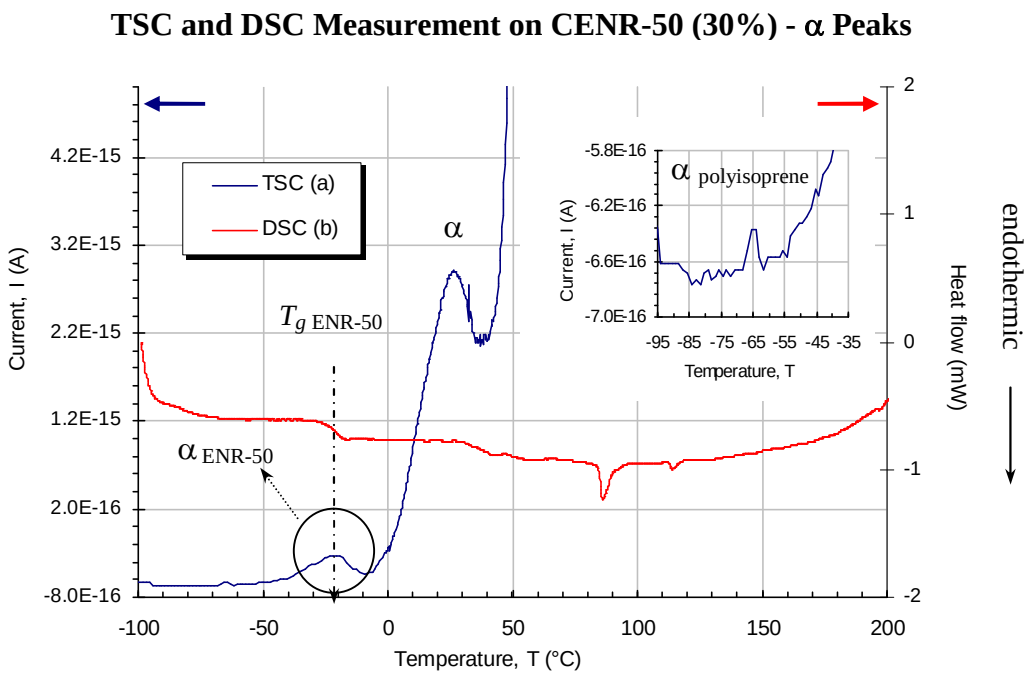

Figure 5.15 (I): The presence of polyisoprene and epoxidised polyisoprene chains within *CENR-50* is confirmed with the $\alpha_{\text{polyisoprene}}$ at -64.26 °C in the inset, and $\alpha_{\text{ENR-50}}$ at -20.48 °C. While the α peak of *OMON* is observed at 26.55 °C. From the DSC plot, the temperature for $T_{g\ \text{ENR-50}}$ at -21.62 °C is comparable to that of $\alpha_{\text{ENR-50}}$.

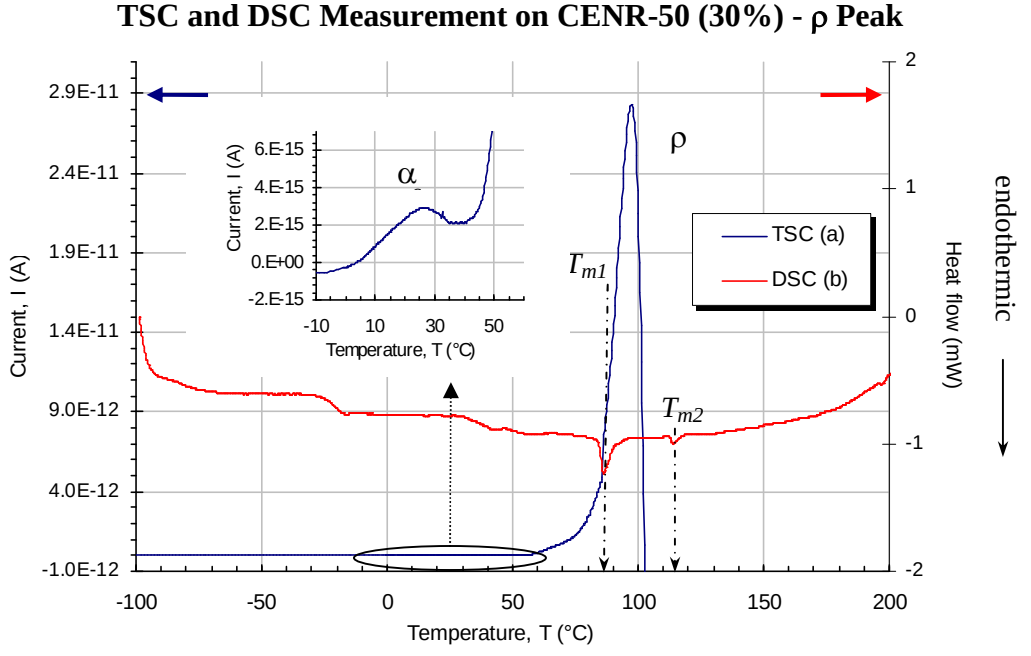

Figure 5.15 (II): The ρ peak of *OMON* peak arises at 97.22 °C, next the α peak in TSC plot for *CENR-50*. From the DSC thermogram, T_{m1} and T_{m2} of *OMON* appear at 86.24 °C and 113.80 °C in that order.

TSC characteristic peaks for *pPVC* matrix can be detected within the *CpPVC* thermogram in Figure 5.16(a). They are the shifted α_{DOP} peak at −24.81 °C ($\alpha_{DOP} \sim -48$ °C) and a hump around 54.24 °C that is assigned as α_{pPVC}. Careful analysis suggests that the hump looks like a combination of some peaks, which are originated from the *pPVC* as can be seen in Figure 5.5. This is supported by the DSC plot for *CpPVC* in Figure 5.16(b), which reveals the T_{m3} endothermic at 51.91 °C as discussed earlier in Section 4.1.3.C. This T_{m3} indicates the presence of *pPVC* microcrystallite structures in the composite.

In case of *CPE* composite in Figure 5.17(a), a ρ peak arises in the TSC plot at 54.07 °C. It confirms the presence of *PE* matrix chains in the composite. This ρ_{PE} peak can be related to the release of space charges caused by alkyl chains mobility, prior to the melting process (T_{m1}) in *PE*. The effect of chains mobility is confirmed with the appearance of thermal transition at 42.46 °C, as shown in Figure 5.17(b).

Some typical peaks of *OMON* particularly the α and ρ peaks are also arise in the TSC plots of *polymer-OMON* composites. They mark *OMON* existence that acts as filler components inside the composites. Table 5.3 lists the maximum temperature T_{max} of the α and ρ peaks, which highlights *OMON* and *ODA* as the origin of these peaks. It also shows that in most cases the peaks consistently appear even though their T_{max} show temperature variations. For example, the T_{max} for both peaks in *CSMRL* and *CDPNR* are lowered from their initial T_{max} in *OMON*. In case of *CENR-50*, the T_{max} for α peak is reduced to 26.55 °C. The T_{max} of *OMON* ρ peak however is increased to 97.22 °C as shown in Figure 5.15(II), where it is relatively bigger than those in the *CSMRL* and *CDPNR* plots. The emergence of TSC peaks generally is analogous to the T_ms in DSC thermogram of the composites. They also mark the presence of *OMON* particles within the natural rubber composites. In case of *CSMRL* however, the endothermic T_m of *OMON* is difficult to detect as shown in Figure 5.14(b).

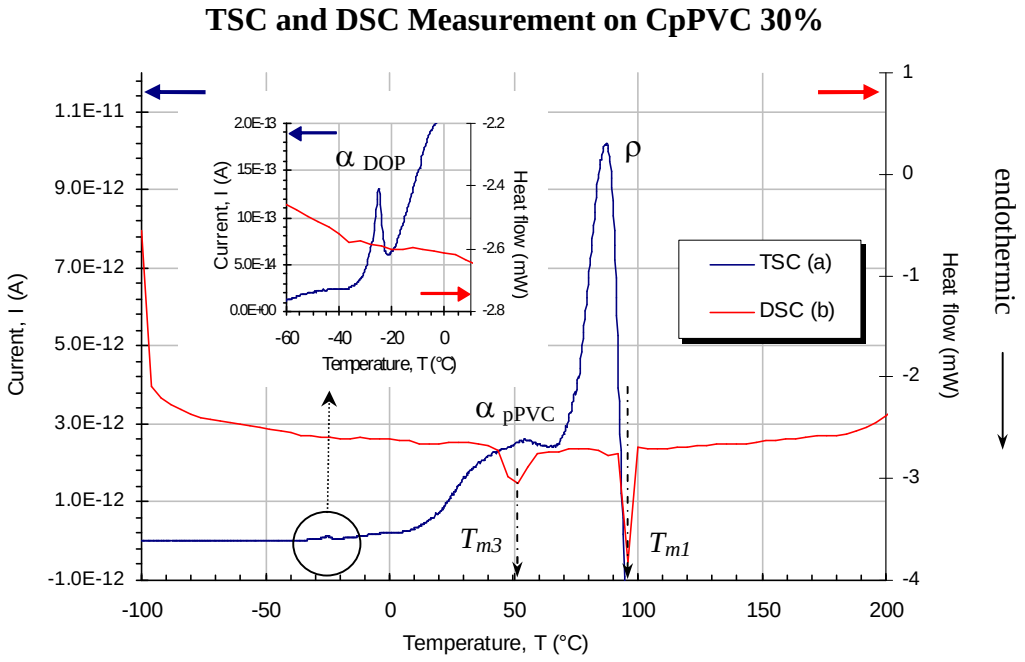

Figure 5.16: The effect of plasticizer appears within *CpPVC* plot at -24.81 °C (α_{DOP}). The ρ peak which is located at 87.00 °C is comparable with the T_{m3} at 95.86 °C of *OMON*. A big hump at 54.24 °C is assigned as α_{pPVC} and related to the T_{m3} at 51.91 °C.

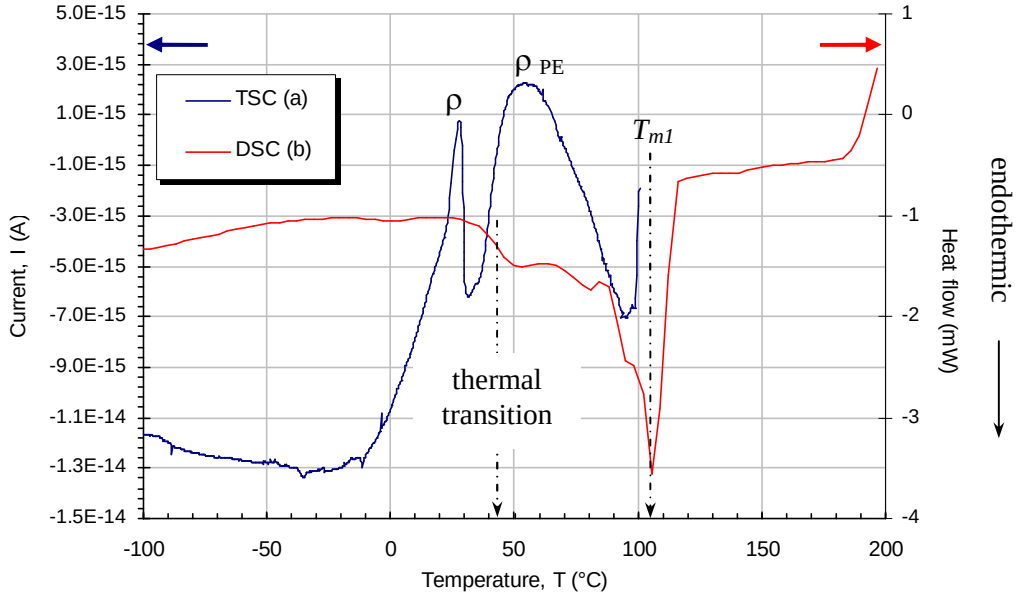

Figure 5.17: There are only ρ peaks that can be clearly observed within the TSC plot of *CPE*. They are at 27.66 °C represents the ρ of *OMON*, and at 54.07 °C which proves the presence of *PE* chains. The ρ_{PE} peak is related to chains mobility as shown by a thermal transition at 42.46 °C, before the melting process T_{m1} at 105.37 °C.

Table 5.3

The Maximum Temperature T_{max} of *OMON* α, ρ and ρ_1 Peaks

Sample	Maximum Temperature, T_{max} (°C) ± 0.01					
	α polymer		α	ρ	ρ_1	ρ polymer
ODA			28.03	55.07	75.66	
OMON			34.87	85.96	105.35	
CDPNR	-59.49		21.43	67.33		
CSMRL	-60.19		7.58	34.54		
CENR-50	-64.26	-20.48	26.55	97.22		
CPE				27.66		54.07
CpPVC	-24.81	54.24		87.00		

Table 5.3 lists the characteristic α and ρ peaks identified in within *polymer-OMON* composites thermograms. The peaks origin is from either polymer matrix or *OMON* content in the composites.

TSC plots in Figure 5.16 of *CPE* and Figure 5.17 of *CpPVC* show that the α peak from *OMON* is hardly observed, it thus considered absent within the thermograms. The ρ peak of *OMON* however is seen at 27.66 °C and 87.00 °C for the *CPE* and *CpPVC* composites, respectively. The absence of α peaks can be related with chains coiling in the composites, which involve the interaction between polymers matrix and alkyl chains inside *OMON* interlayer. However, more discussion on this issue will be carried out in Section 6.2.2.2.B. From DSC graphs for the composites, only T_{m1} endothermic can be detected that indicates *OMON* existence. The lost of T_{m2} endothermic on the other hand is related to the matrix-alkyl chains interaction inside *OMON* gallery.

Perhaps the lost of ρ_1 peak in the composite thermograms can also be associated with the matrix-alkyl chains interactions. This assumption is based on the lost of methylene bending vibration ($\partial_s CH_2$) at 1472 cm^{-1} within the FTIR spectra of *polymer-OMON* composites. This band signifies molecular interaction among the methylene groups in crystalline phase. Matrix-alkyl chains interactions however had interrupted such intermolecular reactions, which could be offering sites for the formation of localized traps. As a result, the relaxation

effects that are represented by the ρ_1 peak cannot be generated in the TSC measurement of *CpPVC* and *CPE* composites. The missing ρ_1 peak thus indicates the lack of space charge relaxation from localized traps in the intermolecular structure of methylene groups, which also prove the effect of matrix-alkyl chains interaction.

From the graphs generally, it seems that physical interactions between the alkyl tails and matrix chains have significant effects on the TSC results. For example, in case of *CSMRL* and *CDPNR* composites with similar polyisoprene matrix chains, except the small content of protein component in *CDPNR*. They were given the same experimental conditions with $F_{p\ \mathrm{CSMRL}} = 0.466\ \mathrm{MVm^{-1}}$ and $F_{p\ \mathrm{CDPNR}} = 0.466\ \mathrm{MVm^{-1}}$. However, the relaxation peaks from TSC measurement on *CDPNR* in Figure 5.13 seems more prominent than that of *CSMRL* in Figure 5.14, which are mostly shadowed by the current noises. The maximum current, I_{max} values of *CSMRL* peaks in fact are much lower compared to that of *CDPNR*. These observations are comparable with their DSC results in Figure 5.13(b) and 5.14(b) for *CSMRL* and *CDPNR* in that order. The findings indicate the distortion of methylene chains structure, which is possibly due to their interactions with the rubber matrix chains. Any logical explanation thus should point out the differences in matrix-alkyl chains interaction within these natural rubber composites. It is believed that such interaction can give great influence on the trend of thermally stimulated current, TSC.

Analyses on the relaxation effects of *OMON* reveal the characteristic α, ρ and ρ_1 peaks, which are originated from *ODA* components in the modified clay. These peaks can be also detected within the TSC plots of *polymer-OMON* composites, except for the ρ_1 peak which prove the effects of matrix-alkyl chains interactions. In fact, the lost of α peak within *CPE* and *CpPVC* plots is associated with chains coiling in such interactions. The observations show that different interactions with various types of polymers had caused the variations in T_{max} for *OMON* peaks in the studied composites.

TSC analyses on thus far capable to demonstrate the good sensitivity and reliability of TSC method, as well as the system developed. However, more information is needed to relate the trends observed with the *polymer-OMON* interaction. It is very important to understand the mechanisms and effects behind the intercalation or exfoliation processes. For example, the effects of chains coiling and entanglement on *OMON* structures as suggested earlier in Chapter 4. Structural modifications on *OMON* particles may result in certain effects on the relaxation behavior of *polymer-OMON* composites.

5.3 Summary

- Analyses on TSC thermograms in Section 5.1.1 identify the relaxation α peaks of the pristine polymers. These peaks maximum temperatures T_{max} are comparable with the polymers T_g as shown in Table 5.1.
- β peak from side chains relaxation is detected prior to the α peak in case of *DPNR*, *ENR-50* and *pPVC* polymers. Table 5.2 lists the T_{max} for these peaks.
- Space charge relaxation that is represented by the ρ peak can be observed next to the α peak in most of the polymers TSC thermograms. The maximum peak temperature, T_{max} of the ρ peaks can be seen in Table 5.2.
- The ρ peaks at 74.70 °C within TSC plot of *Mon* in Section 5.1.2 is analogous to the clay T_m around 57.92 °C which appears as an endothermic in DSC thermogram.
- The relaxation processes of *ODA* created three peaks in TSC thermogram, as shown in Section 5.1.3. These peaks are assigned as α, ρ and ρ_1 peak at 28.03 °C, 55.07 °C and 75.66 °C respectively.

- *OMON* thermogram in Section 5.2.1 reveals the characteristic *ODA* peaks. The T_{max} of these peaks however are shifted to 34.87 °C, 85.96 °C and 105.35 °C in that order.
- *OMON* characteristic peaks appear in the TSC plots of *polymer-OMON* composites. These *OMON* α and ρ peaks appearance indicate the presence of *OMON* particles, which is discussed in Section 5.2.2.
- The characteristic α and ρ peaks from *OMON* appear in most cases of *polymer-OMON* composites, except for the ρ_1 peak. The missing peak reveals the involvement of space charge relaxations from methylene group structure. It also confirms matrix-alkyl chain interactions within *OMON* gallery.
- The lack of α peak in case of *CPE* and *CpPVC* composites is associated with chains coiling in matrix-alkyl chains interactions.
- The variations in T_{max} for α and ρ peaks as shown in Table 5.3 indicate various effects from matrix chains interactions with *OMON* silicates and alkyl chains.

References

5.1 D. Fragiadakis and P. Pissis, "Glass transition end segmental dynamics in poly(dimethylsiloxane)/silica nanocomposites studies by various technique", *J. Non-Cryst. Sol.*, **V 353**, (2007), pg. 4344 – 4352

5.2 M. Arous, H. Hammami, M. Lagache and A. Kallel, "Interfacial polarization in piezoelectric fibre-polymer composites", *J. Non-Cryst. Sol.*, **V 353**, (2007), pg. 4428 – 4431

5.3 S. Hikosaka H. Ishikawa and Y. Ohki, "Effects of Crsytallinity on Thermally Stimulated Current and Complex Permittivity of Poly(L-lactide)", *Ann. Rep. Conf. Elec. Ins. Diel. Phenom.*, (2008), pg. 497 – 500

5.4 B. T. Poh, P. G. Lee and S. C. Chuah, "Adhesion property of epoxidized natural rubber (ENR)-based adhesive containing calcium carbonate", *eXpress Poly. Lett.*, **V 2(6)**, (2008), pg. 398 – 403

5.5 A. Nogales and B.B Sauer, "Cooperative Motions in PVC Studies by Thermally Stimulated Currents: Comparison with A.C. Dielectric Derivative Analysis", *J. Poly. Sci. Part B:Poly Phy.*, **36**, (1998), pg. 913 – 918

5.6 N. Doulache A. Gourari and M. Bendaoud, " TSC Study of Liquid-Liquid transition in Polyvinylchloride", Electrets, *8th International Symposium, (ISE 8*) on 7-9 Sep, (1994), pg. 523 – 527

5.7 S.L. Rosen, "Fundamental Principles of Polymeric Materials", 2nd. Edition., *John Wiley & Sons*, New York, (1993)

5.8 F. Henn, J. C Giuntini, J. Bisquert and G. Garcia-Belmonte, "An Explanation of the Peculiar Behavior of TSDC Peaks at T_g: a Simple Model of Entropy Relaxation", *IEEE Tran. Diel. Elec. Ins.*, **V 13(5)**, (2006), pg. 1042 – 1048

5.9 I. M. Kalogeras, A. Stathopoulos, A. Vassilikou-Dova, "Nanoscale Confinement Effects on the Relaxation Dynamics in Networks of Diglycidyl Ether of Bisphenol-A and Low-Molecular-Weight Poly(ethylene oxide)", *J. Phys. Chem. B*, **V 111**, (2007), pg. 2774 – 2782

5.10 M. Arous, I. B. Amor, A. Kallel, Z. Fakhfakh and G. Perrier, "Crystallinity and dielectric relaxations in semi-crystalline poly(ether ether ketone)", *J. Phys. Chem. Sol.*, **V 68**, (2007), pg. 1405 – 1414

5.11 E. Passaglia, M. Bertoldo, F. Ciardelli, D. Prevosto and M. Lucchesi, "Evidences of macromolecular chains confinement of ethylene-propylene copolymer in organophilic montmorillonite nanocomposites", *Euro. Poly. J.*, **V 44**, (2008), pg. 1296 – 1308

5.12 L. M. Robeson, "Polymer Blends: A Comprehensive Review", *Hanser Verlag*, New York, (2007)

5.13 S.K. De and A. K. Bhowmick, "Thermoplastic Elastomers from Rubber-plastic Blends", *Ellis Horwood- Original from the University of California*, West Sussex, (1990)

5.14 J.A. Brydson, "Speciality Rubbers - Report 74", **Vol 7 (No.2),** *iSmithers Rapra*, (1994)

5.15 A.H. Eng, Y. Tanaka and S.N. Gan, "Some Properties of Epoxidised Deproteinised Natural Rubber", *J. Natural RubberResearch*, **V 12(23)**, (1997), pg. 82 – 89

5.16 A. J. Peacock, "Handbook of Polyethylene: Structures, Properties, and Applications", *CRC Press - Taylor and Francis Group*, New York, (2000)

5.17 L. H. Sperling, "Introduction to Physical Polymer Science", 4th. edition, *Wiley-Interscience*, New York, (2006)

5.18 Y.H. Hui, "Handbook of Food Science, Technology, and Engineering", **Vol. 3**, *CRC Press - Taylor and Francis Group*, New York, (2006)

5.19 B.Y. Zhong, W.Z. Xue, H.Z. Ming and P.Z. Ren, "Effect of Physical Crosslinking on Properties of Plasticized High Molecular Weigh PVC", *J. Zhejiang Uni. Scie.*,**V 1(2)**, (2000), pg. 171 – 177

5.20 M. Scandola, G. Ceccorulli, M. Pizzoli and G. Pezzin, "Further Evidence of an Unusual T_g-Concentration Dependence for Plasticized Polyvinylchloride", *Polymer Bull*., **6**, (1982), pg.653 – 660

5.21 H. P. Diogo and J. J. M. Ramos, "Slow molecular mobility in the crystalline and amorphous solid states of glucose as studied by thermally stimulated depolarization currents (TSDC)", *Carbohyd. Res.*, **V 343**, (2008), pg. 2797 – 2803

5.22 N. A. Nikonorova, E. B. Barmatov, M. V. Barmatova, D. A. Pebalk and R. Diaz-Calleja, "Local modes of molecular mobility in comb-shaped liquid crystalline ionomers containing alkaline metal ions", *Euro. Poly. J.*, **V 44**, (2008), pg. 3806 – 3816

5.23 N. Mzabi, H. Smaoui, H. Guermazi, Y. Mlik, S. Agnel and A. Toureille, "Heating Effects on Structural and Electrical Properties of Polyetherimide", *Amer. J. Eng. App. Sci*., **V 2(1)**, (2009), pg. 120 – 126

5.24 B. Hilczer and J. Malecki, "Electrets" - Studies in Electrical and Electronic Engineering, **V14**, *Elsevier PWN-Polish Scientific Publishers*, Warszawa, (1986)

5.25 M. D. Antonijevic, D. Q. M. Craig and S. A. Baker, "The role of space charge formation in the generation of thermally stimulated current (TSC) spectroscopy data for a model amorphous drug system", *Inter. J. Pharm*., **V 353**, (2008), pg. 8 – 14

5.26 Z. An, M. Zhao, J. Yao, Y. Zhang and Z Xia, "Influence of fluorination on piezoelectric properties of cellular polypropylene ferroelectrets", J. Phys. D: App. Phys., V 42, (2009), in press

5.27 K. Ikezaki and Y. Murata, "Electret properties of ethylene–propylene random co-polymer", *J. Electrostatics*, **V 67**, (2009), pg. 407 – 411

5.28 B.F. Mathot, "Calorimetry and Thermal Analysis of Polymers", *Hanser*, Munich New York, (2000)

Chapter 6

Thermally Stimulated Current (TSC) - Data Evaluation

Chapter 6: THERMALLY STIMULATED CURRENT, TSC - DATA EVALUATION

In quest to understand the technique, data evaluations was carried out on the TSC results. This effort is very important to produce activation energy, *E* values and several other parameters that might reveal the natures of TSC peaks. The existence of molecular-ion by charge deposition or injection for instance, can also be established here. It thus, helps to understand more on the source of the observed relaxations within polymers, as well as in their respective composites. However, this is not enough to explain the irregularity of some trends shown in the composites thermograms.

Further analyses are needed to find parameters that may assist the analysis, particularly in recognizing the effect of intercalation by polymeric chains into *OMON* galleries. Through out the investigation process, an improved method of fitting the TSC data was developed as an alternative to the known *William-Landel-Ferry* (*WLF*) formulation. This *N-Fitting* formulation seems to suit well with the mathematically decomposed peaks, as well as the experimental data. Generally, it is capable to fit more than 90 % of data populations, where they have less than 5 % ($\leq$ 5 %) deviation from each targeted data.

This fitting method is also capable to give reasonable values for the pre-exponential factor, which also known as characteristic relaxation time τ_o for both below and above the glass transition temperature, T_g. The generated values in fact can be associated with some known relaxation phenomena such as space charge, dipole group and segmental relaxations. It also involves the cooperative relaxation, particularly around and above a T_g as described by the *WLF* theory [6.1, 6.2 and 6.3]. The knowledge on the τ_o helps in making some deductions on the *ODA*-polymers chains interactions within *OMON* interlayer. It can give reasonable explanations for the absence of certain peaks within the TSC plot of some *polymer-OMON* composites. The details will be discussed extensively in Section 6.2

6.1 Data Evaluation - Activation Energy, *E*

In the earlier analyses of Chapter 5, the observed peaks or thermal trends were recognized by priory identified the position of α peak. However, the nature of these trends can only be predicted by knowing some important parameters, such as the activation energy, *E* and pre-exponential factor, τ_o. The knowledge about *E* for instance, will leads to the understanding of energy level and the type of traps involved in relaxation process. Hence, the origin of certain relaxations that are responsible for the formation of TSC peaks or any thermal trend can be suggested.

6.1.1. Determination of Activation Energy, *E* via the Initial Rise Method.

Previously in Chapter 2, "TSC Analysis" which is a developed computer program has been introduced as a tool to locate the exact position of a TSC peak. The program was also designed to calculate some related TSC parameters, such as the value of activation energy *E* that can be estimated via a technique known as *initial rise method*.

The current density, J_D during TSC measurement is given by the equation (2.8),

$$J_D(T) = \frac{P_e(T_p)}{\tau_o}\exp\left(\frac{-E}{kT}\right)\exp\left[\frac{-1}{h\tau_o}\int_{T_o}^{T}\exp\left(\frac{-E}{kT'}\right)dT'\right]$$

The initial rise method which was introduced by Garlick and Gibson [6.4 and 6.5] focus on the initial currents that form a TSC peak. It is based on the fact that the integrals term in the $J_D(T)$ function is being negligible at $T << T_{max}$. The first exponential thus dominates the temperature rise of the initial current, so that at the beginning of a peak the TSC current becomes

$$J_D(T) = \frac{P_e(T_p)}{\tau_o}\exp\left(\frac{-E}{kT}\right) \qquad \text{or} \qquad \ln J_D(T) \approx const. - \frac{E}{kT}$$

Therefore, the activation energy *E* values can be estimated by plotting the Arrhenius type equation with the $\ln J_D(T)$ against $(1/T)$. A straight line should be obtained with a slope that gives $-E/k$ as shown in Figure 6.1. The *E* values of α peaks for some polar and non-polar polymers obtained from this method are listed in Table 6.1. This table also shows the

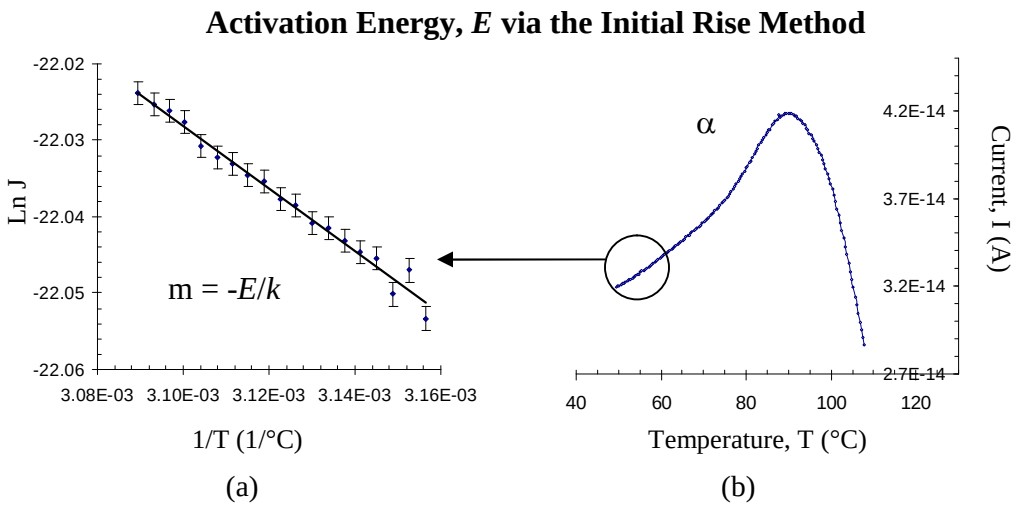

Figure 6.1: The Arrhenius plot (a) for the initial current (circled) of the α peak on the TSC thermogram of *PET* in (b).

Table 6.1
Activation Energy *E* for the α Peak of Some Polymers

Type	Sample	Activation Energy, *E* (eV)		$\frac{E_1}{E_2} = \partial E$ (%)
		Initial rise, E_1	Pre. author, E_2	
Non-polar	PET	0.07	0.62 to 0.72 [6.6 to 6.8]	10.4
	PE	0.07	0.50 to 1.1 [6.6 and 6. 9]	12.7
polar	PMMA	0.03	1.20 [6.10]	2.5
	pPVC	0.65	1.90 to 2.90 [6.11 to 6.13]	27.1

Table 6.1 list the activation energy, *E* for α peaks in polar and non-polar polymers, which are obtained via the initial rise method and compared with the values by previous authors.

comparisons with some values from previous researchers. The differences between the obtained values and that of previous researcher are generally big, with the accuracy (∂E) varies from 2 to 27 %. Moreover, the given value for *PE* (0.07 eV) and *PMMA* (0.03 eV)

(0.03 eV) are not reasonable, if considering the fact that *PMMA* is more polar compare to the non-polar *PE*. It seems that the initial rise method is suitable only for the case of non-distributed relaxation process. In other word, a number of distributed relaxation processes with variable activation energy (*E*) generate the analyzed α peaks. Therefore, an alternative technique must be used to find the *E* values for these peaks.

6.1.2 Decomposition of TSC Peak

Suppose the α peaks follow the non-Debye model with distribution of relaxation processes. It means that these peaks have to be decomposed in order to know the type of relaxation processes involved during TSC measurement. Each of the decomposed peaks will reveal its individual characteristics, which adds more information on the localized depolarization processes that participated in the formation of TSC peaks.

Decomposition actually can be done both ways, either experimentally for example via the "Windowing Polarization" (*WP*) technique, or theoretically by using the first-order kinetic theory. In order to study the collected TSC data, the first-order kinetic theory therefore was used in a fitting procedure carried out in this work. First-order kinetic theory gives the TSC current as follow [6.14, 6.15, 6.16 and 6.17] (see appendix F),

$$I(T) = I_m \exp\left[1 + \frac{E}{kT}\frac{T - T_{\max}}{T_{\max}} - \frac{T^2}{T_{\max}^2} \times \exp\left(\frac{E}{kT}\frac{T - T_{\max}}{T_{\max}}\right)(1 - \Delta) - \Delta_{\max}\right] \qquad (6.1)$$

where I_m = current at maximum peak
T_{max} = temperature at maximum peak
k = Boltzmann constant
T = temperature
E = activation energy
$\Delta = 2kT/E$
$\Delta_{\max} = 2kT_{\max}/E$

This fitting method needs to utilize the temperature (*T*) from TSC experimental data along with appropriate values for the activation energy (*E*), maximum current (I_m) and maximum

temperature (T_{max}) to generate a peak. The data fitting was carried out by adjusting the E, I_m and T_{max} values for a number of decomposed peaks. Simultaneously monitoring the sum of current, $I(T)$ values from the peaks to fit the TSC current, I. The processes were repeated until all the summation falls on the targeted current, I of experimental data, which formed the original TSC peak.

Several peaks may be needed to fit an experimental TSC peak, as shown in Figure 6.2(a) for the decomposition of α peak from *PMMA*. Table 6.2 in (b) lists the used E, I_m and T_{max} values in the fitting procedure. The values exhibit the distribution of relaxation processes as mentioned earlier, which also reveal the characteristics of each decomposed peaks. Each decomposed peak represents certain relaxation process, which contributes to the creation of the experimental α peak.

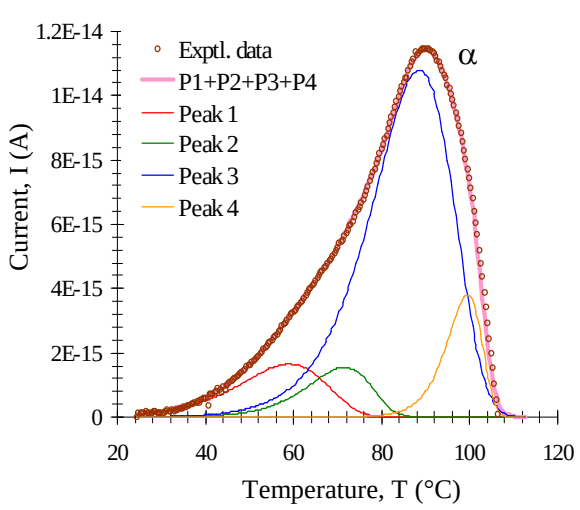

(a)

Table 6.2
Decomposed α Peaks of PMMA

Peak	T_{max} (°C) ± 0.01	I_m (A)	E_{fitt} (eV)
1	59.00	1.65E-15	0.95
2	71.50	1.55E-15	1.40
3	88.50	1.08E-14	1.20
4	99.5	3.80E-15	3.00

(b)

Figure 6.2: Data fitting on the α peak of *PMMA* (a) shows the experimental peak, decomposed peaks and summation of the peaks. The values used for the fitting are listed in Table 6.2 as shown in (b).

Table 6.3 lists the energy E values for the closest decomposed peaks to the maximum temperature, T_{max} of their σ original TSC peaks. The obtained E values from these fitting

are generally quite satisfactory compare to those from the initial rise method. In fact, their accuracies are improved such as in case of *pPVC*, where its accuracy is increased from about 27 % via the initial rise method to 77 % in this technique. For that reason, the data fitting method was used on the important peaks in this TSC studies.

Table 6.3
The Activation Energy *E* of Decomposed α Peaks

Type	Sample	T_{max} for α peak (°C) ± 0.01	T_{max} for the closest peak (°C)	Activation Energy, *E* (eV)	
				Closest peak	Previous authors
Non-polar	PET	96.55	91.50	0.76	0.62 to 0.72[6.6 to 6.8]
	PE	-103.55	-104.60	0.63	0.5 to 1.1 [6.6 and6. 9]
polar	PMMA	89.94	88.50	1.20	1.2 [6.10]
	pPVC	79.62	80.00	1.85	1.9 to 2.9 [6.11 to 6.13]

Table 6.3: Activation energy *E* from decomposed peaks with the closest T_{max} to the T_{max} of original peaks are compared with the *E* values from some previous authors.

Peak Decomposition on TSC results of SMRL

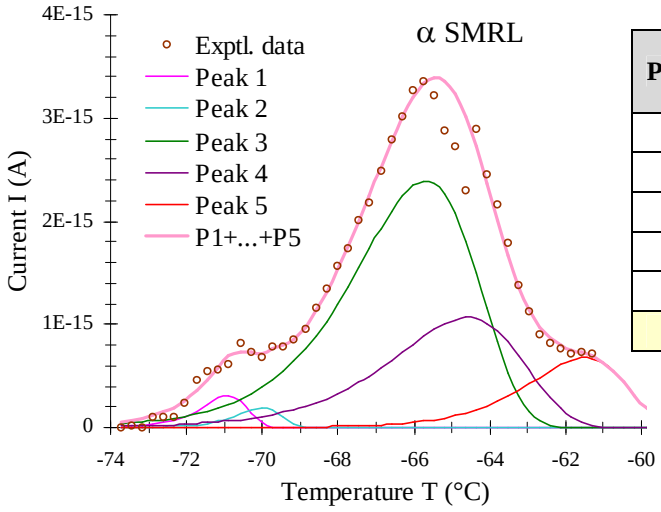

Table 6.4
Decomposed α Peaks of SMRL

Peak	T_{max} (°C) ± 0.01*	I_m (A) ± 0.01	E_{fitt} (eV)
1	-70.90	3.09E-16	6.00
2	-70.00	1.86E-16	6.00
3	-65.70	2.39E-15	2.30
4	-64.60	1.06E-15	2.20
5	-61.50	6.77E-16	3.00
α	-65.48*	3.39E-15*	

* measured

Figure 6.3: Decomposition on the pristine α *SMRL* peak give five decomposed peaks with the fitting parameters are listed in the Table 6.4 next to graph.

Peak Decomposition on TSC Results of DPNR

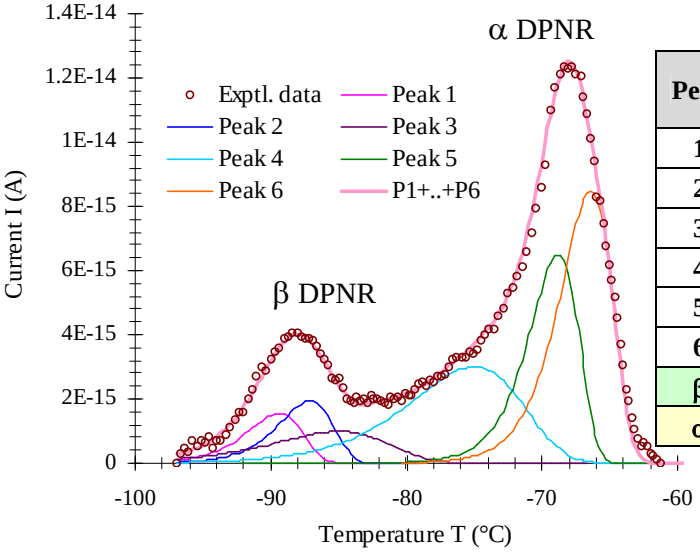

Table 6.5
Decomposed Peaks of DPNR

Peak	T_{max} (°C) ± 0.01*	I_m (A) ± 0.01*	E_{fitt} (eV)
1	-89.40	1.55E-15	1.40
2	-87.10	1.95E-15	1.50
3	-85.00	9.80E-16	0.70
4	-75.00	3.00E-15	0.80
5	-68.80	6.50E-15	1.96
6	-66.40	8.50E-15	1.90
β	-86.87*	3.85E-15*	
α	-67.76*	1.24E-14*	

* measured

Figure 6.4: Both β and α peaks of *DPNR* are decomposed together as they are in the same current, *I* range. Table 6.5 lists the fitting parameter for these peaks.

Peak Decomposition on α Peaks of ENR-50

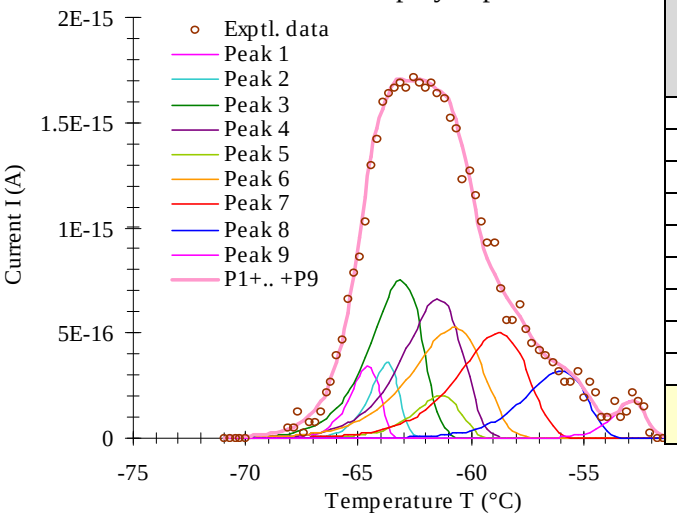

(a)

Table 6.6(a)
Decomposed $\alpha_{polyisoprene}$ of ENR-50

Peak	T_{max} (°C) ± 0.01*	I_m (A) ± 0.01*	E_{fitt} (eV)
1	-64.55	3.45E-16	6.00
2	-63.70	3.58E-16	6.00
3	-63.10	7.50E-16	3.40
4	-61.45	6.60E-16	3.00
5	-61.30	2.00E-16	3.80
6	-60.75	5.25E-16	2.50
7	-58.75	5.00E-16	2.60
8	-56.00	3.19E-16	3.10
9	-52.80	1.78E-16	6.00
α rubber	-62.58*	1.72E-15*	

* measured

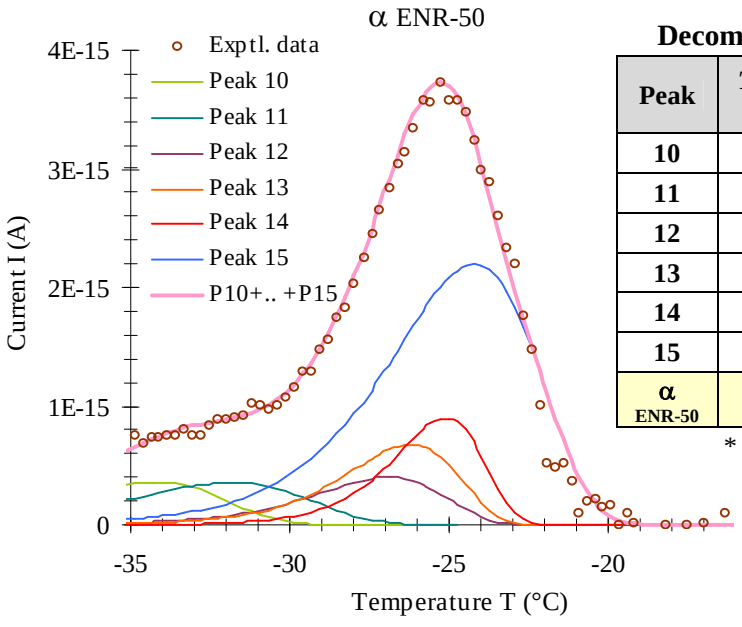

(b)

Table 6.6(b)
Decomposed α_{ENR-50} of ENR-50

Peak	T_{max} (°C) ± 0.01*	I_m (A) ± 0.01*	E_{fitt} (eV)
10	-34.20	3.60E-16	2.00
11	-31.80	3.55E-16	1.80
12	-26.90	4.00E-16	2.60
13	-26.20	6.80E-16	3.00
14	-25.10	9.00E-16	3.80
15	-24.20	2.20E-15	2.30
α ENR-50	-25.02*	3.58E-15*	2.42

* measured

Figure 6.5(I): Decomposition on *ENR-50* peaks were carried out on both α peaks from polyisoprene chains in (a) and the epoxidised chains in (b). The activation energy *E* and other related parameters are listed in Table 6.6(a) and 6.6(b).

Peak Decomposition on ρ Peaks of ENR-50

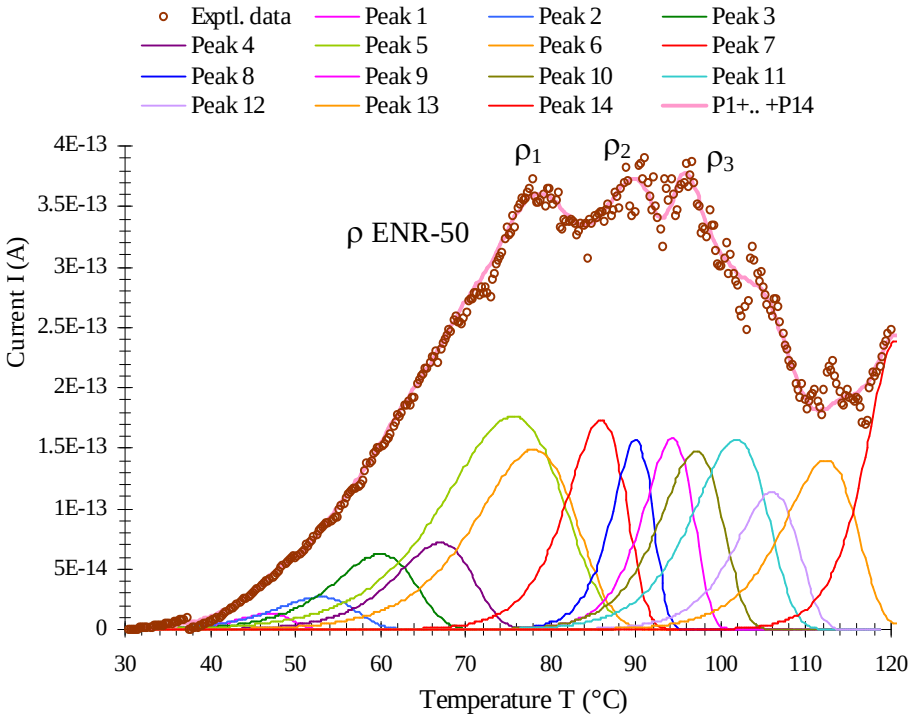

(c)

Table 6.6(c)
Decomposed ρ Peaks of ENR-50

Peak	T_{max} (°C) ± 0.01	I_m (A) ± 0.01	E_{fitt} (eV)
1	47.00	1.31E-14	3.00
2	53.00	2.67E-14	2.00
3	60.00	6.21E-14	2.00
4	67.00	7.14E-14	2.20
5	75.50	1.76E-13	1.50
6	78.00	1.49E-13	1.80
7	85.90	1.74E-13	3.20
8	90.00	1.57E-13	4.80
9	94.30	1.58E-13	4.00
10	97.10	1.47E-13	3.20

Peak	T_{max} (°C) ± 0.01*	I_m (A) ± 0.01*	E_{fitt} (eV)
11	101.80	1.57E-13	2.80
12	106.00	1.14E-13	3.40
13	112.30	1.40E-13	3.00
14	120.50	2.40E-13	4.50
ρ_1	78.83*	3.61E-13*	
ρ_2	89.84*	3.73E-13*	
ρ_3	95.90*	3.77E-13*	

* measured

Figure 6.5(II): Decomposition of the big ρ peak in *ENR-50* reveals 14 decomposed peaks. They could be representing various relaxation effects around the rubber softening temperature. Table 6.6c lists the fitting parameters for the decomposed peaks.

Peak Decomposition on TSC Results of PE

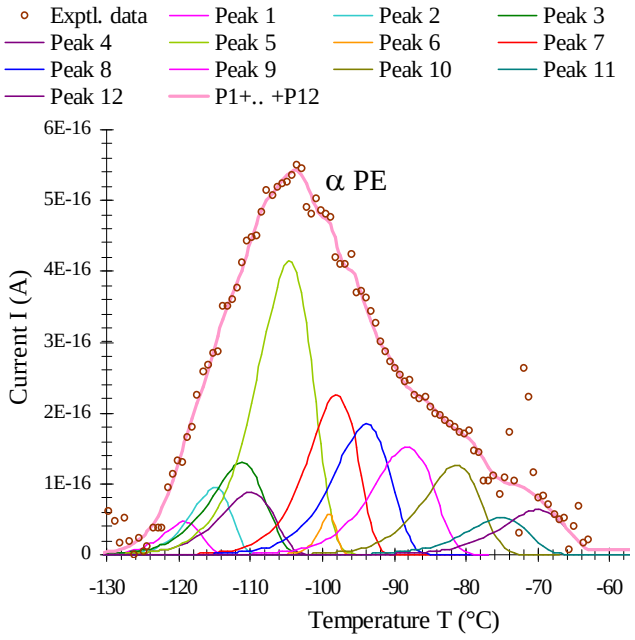

(a)

Table 6.7(a)
Decomposed α Peaks of PE

Peak	T_{max} (°C) ± 0.01*	I_m (A) ± 0.01*	E_{fitt} (eV)
1	-119.10	4.68E-17	0.80
2	-115.00	9.57E-17	0.80
3	-111.20	1.30E-16	0.60
4	-109.90	8.86E-17	0.62
5	-104.60	4.14E-16	0.63
6	-99.00	5.62E-17	2.20
7	-98.00	2.27E-16	0.77
8	-93.80	1.85E-16	0.70
9	-88.10	1.52E-16	0.70
10	-81.30	1.36E-16	0.30
11	-75.00	5.20E-17	0.80
12	-70.00	6.80E-17	0.30
α	-103.55*	2.84E-11*	

* measured

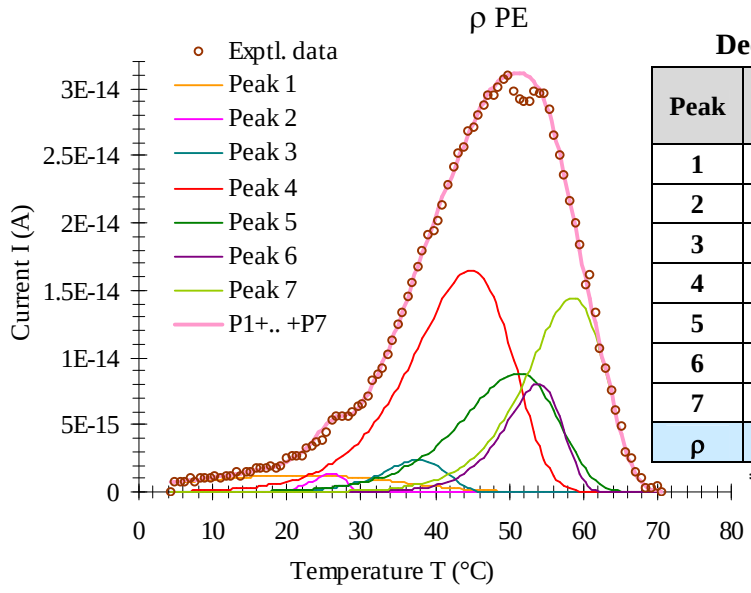

(b)

Table 6.7(b)
Decomposed ρ Peaks of PE

Peak	T_{max} (°C) ± 0.01*	I_m (A) ± 0.01*	E_{fitt} (eV)
1	22.00	1.22E-15	0.50
2	26.10	1.39E-15	4.00
3	38.00	2.37E-15	2.00
4	44.80	1.65E-14	1.30
5	51.20	8.80E-15	1.40
6	54.00	8.04E-15	2.40
7	58.60	1.44E-14	1.80
ρ	51.33*	3.11E-14*	1.58

* measured

Figure 6.6: Decomposition on α *PE* peak in (a) produce twelve decomposed peaks which is almost half of those from ρ peak in (b). The fitting parameters for the peaks are listed in Table 6.7(a) and 6.7(b) for decomposed α and ρ peaks in that order.

Peak Decomposition on TSC Results of pPVC

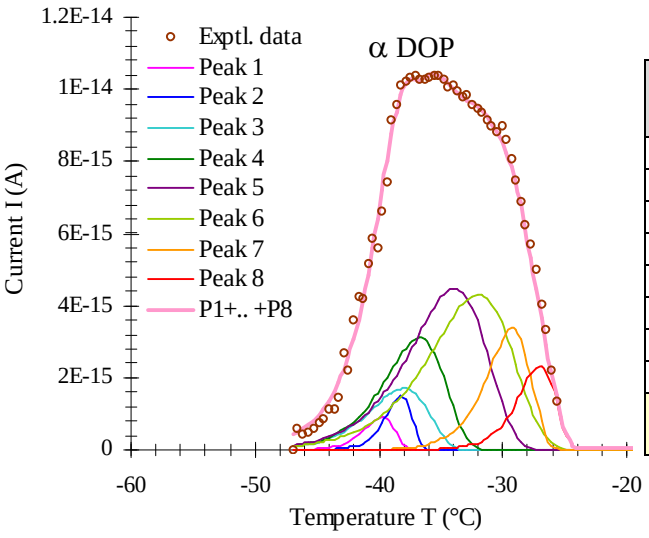

(a)

Table 6.8(a)
Decomposed α_{DOP} Peaks of pPVC

Peak	T_{max} (°C) ± 0.01*	I_m (A) ± 0.01*	E_{fitt} (eV)
1	-39.73	9.00E-16	3.80
2	-38.20	1.50E-15	4.60
3	-38.00	1.70E-15	2.00
4	-36.70	3.10E-15	2.00
5	-33.90	4.46E-15	1.60
6	-32.00	4.30E-15	1.50
7	-29.20	3.38E-15	3.00
8	-27.00	2.30E-15	3.50
α DOP	-37.46*	3.11E-14*	

* measured

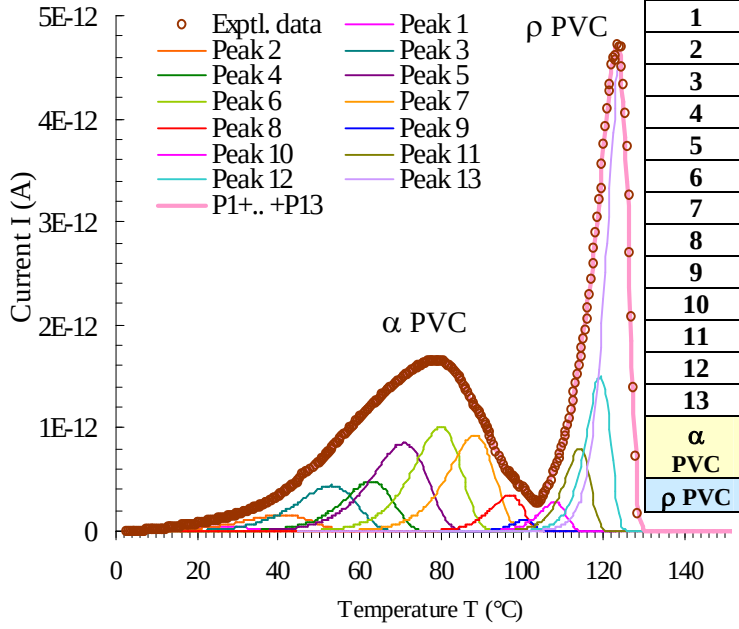

(b)

Table 6.8(b)
Decomposed α and ρ Peaks of pPVC

Peak	T_{max} (°C) ± 0.01	I_m (A) ± 0.01	E_{fitt} (eV)
1	25.50	5.00E-14	0.90
2	41.00	1.50E-13	1.00
3	53.00	3.70E-13	1.20
4	63.00	6.60E-13	1.40
5	70.90	7.30E-13	1.70
6	80.00	1.03E-12	1.85
7	88.40	9.30E-13	2.00
8	97.00	3.50E-13	3.00
9	100.70	1.10E-13	4.80
10	108.00	2.80E-13	4.00
11	114.20	8.00E-13	4.20
12	119.30	1.50E-12	4.50
13	124.00	4.50E-12	5.00
α PVC	79.76*	1.65E-12	
ρ PVC	123.89*	4.70E-12	

* measured

Figure 6.7: Decomposition on α peak can be seen in (a) for α *DOP* and in (b) for α *PVC* . In (b) it also shows the decomposed ρ peaks of plasticized *PVC* (*pPVC*). The activation energy *E* and related fitting parameters are tabulated in Table 6.8(a) for α *DOP* peak and Table 6.8(b) for α and ρ *PVC* peaks.

Data fitting via the peak decomposition on some typical peaks of the studied polymers are shown in Figure 6.3 to 6.7, with their respective fitting parameters. In Chapter 2 previously, the mechanisms that are responsible for TSC current were briefly explained. The current in general is merely described as the results of polarized chains mobility and space charges released.

From electrical point of view basically, the current is generated from the flows of initially induced image charges by both homocharges (injected charge) and heterocharges (dipole and space charge) in an electret. These induced charges leave both electrodes towards an electrometer as schematic illustrated in Figure 6.8. The flows actually take place due to the released of image charges. It occurs following the trapped charge release or disorientation of dipoles that took place in order to restore charges neutrality within the electrets [6.18].

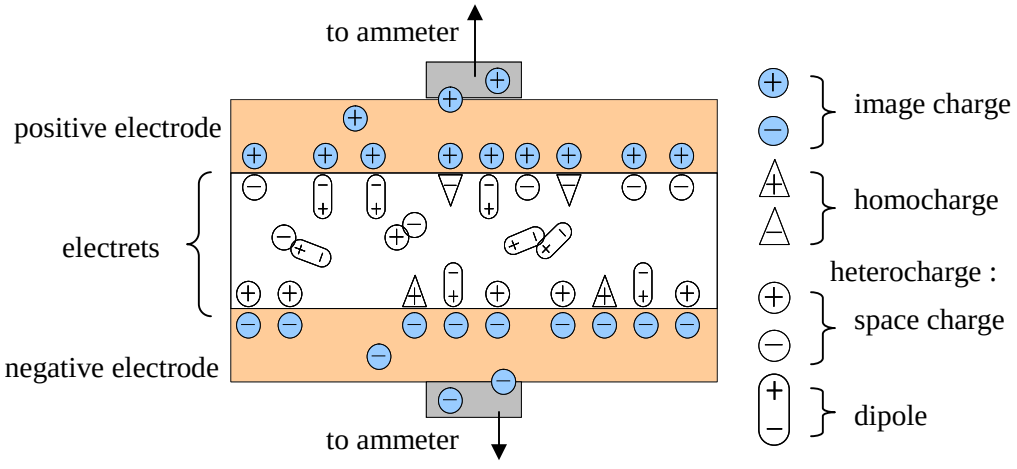

Figure 6.8: Schematic illustration for the mechanisms that generate TSC current, where image charges on electrodes are released due to depolarization of dipoles, space charges and homocharges within the electrets.[6.17]

The dipoles reorientation is believed to involve the rotations of a coupled pair of positive and negative charges. It thus, required certain energy to depolarize wherein for solid it may

amount up to a few eV [6.2]. This remark is comparable with the ranges of activation energy *E* as shown in Table 6.4 to Table 6.8, which is about 0.3 eV to 3.0 eV. The data fitting also demonstrates that dipoles with relatively low activation energy depolarized at low temperature. Such as, the peaks at low temperature range – 130 °C to – 60 °C in Table 6.7a of *PE* that have the energy *E* values just around 0.3 eV to 0.8 eV. On the other hand, the relaxation effects from dipoles in *PVC* chains appear at higher temperature range (0 °C to 100 °C) with relatively higher values of energy *E* around 0.9 eV to 3.0 eV, as shown in Table 6.8b.

These findings explain the comparatively high glass transition temperature, T_g of the *PVC* chains that is about 80 °C in comparison to that of *PE*, which is about – 100 °C. It means that more energy was needed by these *pPVC* chains to overcome energy barrier before its segmental main chains started to move progressively. As an effect to the phase changing from glassy to rubbery state (T_g) in the polymers, their polymeric chains became loosen and thereby it may lead to release of trapped space charges. The decompositions of TSC ρ peaks prove the space charge relaxations as shown in Figure 6.4 to 6.7. It is demonstrated by the high-energy *E* values for decomposed ρ peaks that is around 3 eV to 5 eV, compare to that of decomposed peaks for α relaxation within the range of 0.3 eV to 3 eV. This is reasonable indeed, when consider the fact that depolarization of dipoles involves only local rotations. The neutralization of space charges on the other hand requires these charges to travel over many atomic distances [6.2].

It is generally accepted that besides the dipoles, heterocharges within polymer electrets is believed to consist of immobilized space charges as well. These charges can be either ionic which comes from impurities within a polymer, or electrons and holes [6.2, 6.19, 6.20 and 6.21]. On the contrary to the schematic diagram in Figure 6.8, these electronic charges are

distributed non-uniformly and often residing near the electrodes. They are all viewed to be trapped in localized traps that are formed by intrinsic structural defects.

Normally in polymer electrets, the intrinsic defects can be provided by many sources. Such as chain branching, chain entanglement, chain end and pendant group [6.2 and 6.19]. These structures in fact can be found within the studied polymers. Such as the branching in *PE*, chain entanglements in *ENR-50* and pendant groups in *pPVC*. By that means, the variations in energy *E* values for the decomposed ρ peaks give a reasonable picture on the nature of localized traps. It tells that each localized trap has energy barrier, which is equivalent to the activation energy *E*. Comparison with energy related model would be useful to relate the decomposed peaks with the origin of ρ peak relaxations.

6.1.2.1 Band Model

The energy level as shown by the decomposed ρ peaks in Table 6.7b of *PE* and Table 6.8b of *pPVC* varies from 0.5 eV for a shallow trap, up to 5 eV for a deep trap. According to the band theory for polymeric insulating material, the shallow traps in *PE* could come from its carbon chains [6.19]. In this situation, electron is imagined to jump from one molecule to the neighboring molecule in an activated manner along the chains.

Figure 6.9(b) gives the schematic representation of energy level within amorphous or semi crystalline dielectric materials, such as the studied polymers. The splitting of energy band into several levels (0.1 eV to 0.5 eV) makes the movement of electron waves impossible. This wave motion responsible for charge transfers in the band model of macromolecular crystal as illustrated in Figure 6.9(a). Therefore, it is assumed that electrical conductivity in the polymer band model has a hopping mode [6.19 and 6.22]. Charge carrier transport in this hopping mode takes place mainly between the energy level of least bound electrons. Such as, within the carbon chains of *PE* that has been pointed out earlier as a shallow trap.

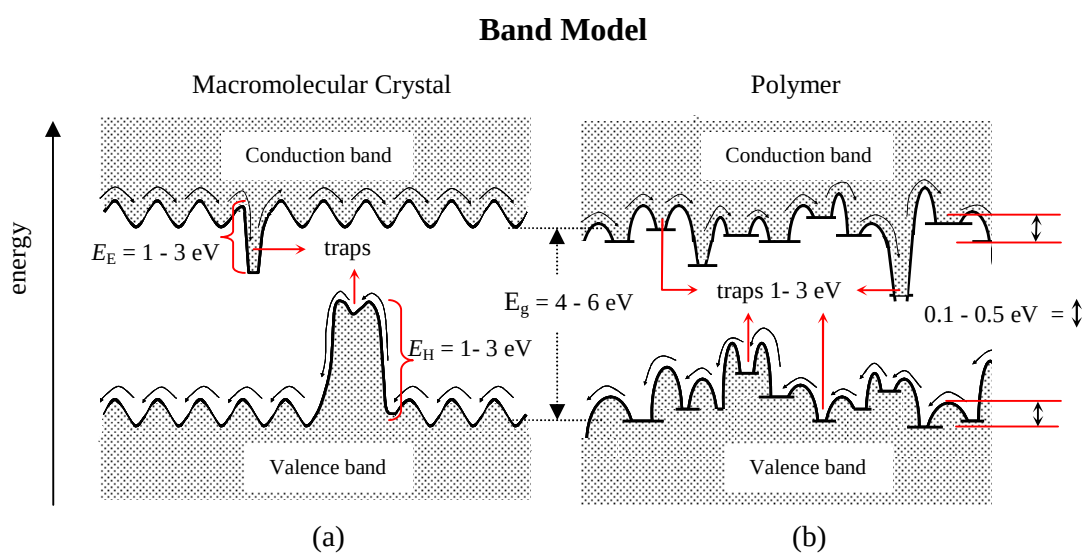

Figure 6.9: Schematic representation of band models for macromolecular crystal in (a) and polymers in (b) with the traps within both conduction and valence bands in these materials [2 and 15].

The intrinsic structural defects inside polymer electrets give significant effects on the local values of electron energies. Subsequently, the rendered local levels play the role as current carrier traps in the dielectric materials. It is characterized in the band model as local energy levels that are located within the forbidden gap. The range of energy given is about 1 eV to 3 eV, which is comparable with the values revealed by most of decomposed ρ peaks in this work. However, there are some decomposed peaks with activation energies *E* beyond the energy range that is around 4 eV to 5 eV. They can be seen in case of *ENR-50* and *pPVC* as shown in Table 6.6(c) and 6.8(b). In fact, such high energy range is equivalent to the energy gap for forbidden area about 4 eV to 6 eV as illustrated in Figure 6.9. This energy gap E_g gives the minimal energy for electron removal from a valence band, which is also referred as ionization energy. There is no clear evidence however for the ionization process to take place during the TSC measurements. The high activation energy *E* values are also considered as too big for a localized trap.

6.1.2.2 Molecular–Ion Model

Molecular-ion model however can support the occurrence of high-energy traps. The model was proposed by *Duke* and *Fabish* [6.23 and 6.24], as they managed to demonstrate the presence of electronic acceptor (or donor) state in polymers. The obtained energy E were analogous to the work function of various metals that is around 4 eV to 8 eV [6.2, 6.23 to 6.26]. The energies that are comparable to the ionization energy E_g can be also detected in some cases of the decomposed ρ peaks of *ENR-50* and *pPVC*.

This model explains that the existence of such deep traps may be attributable to atomic and electronic relaxation process, which can be induced by charge injections. It thus, draws attention to the significant effects of homocharges in electrets. Typical polarizing field, F_p employed during TSC experiment in this work was about 0.015 MVm^{-1} to 0.263 MVm^{-1}. The used F_p however is too small if compares to the required polarizing field for charge injections. At elevated temperature, the F_p should be at least 80 MVm^{-1} while at ambient temperature it can increase up to 400 MVm^{-1} [6.2]. The actual conditions of electrodes – sample interface apparently must be taken into consideration.

6.1.2.2.A Charge Injection

According to Gross [6.27], when the contact surface between electrodes and a sample is imperfect, there will be air-gaps develop at the interface. Such imperfection can come from defects on the electrodes surfaces for example small points, scratches and furrows. If the strength of local electrical field is high enough, it is believed that localized discharges will happen within those air cavities [6.18, 6.27 and 6.28]. Therefore, these localized discharges can also take place at electrodes-sample interfaces in the TSC measurement. Since small scratches that are beyond the normal eye view could happen during the polishing process on the electrode surfaces. Irregularity on the electrode surfaces as schematic illustrated in Figure 6.10(a) can create micron scale air-gaps, which could be within a range of 0.2 μm to

40 μm in depth. The air-gaps might happen especially at electrodes-sample interfaces that involve flexible sample, for example natural rubbers. The elastomeric samples can create such a tiny gap following the applied pressure during sample mounting. Moreover, the compressed sample itself acts as a sealer around the electrodes edges and in that way, it manages to preserve the trapped air throughout vacuum process.

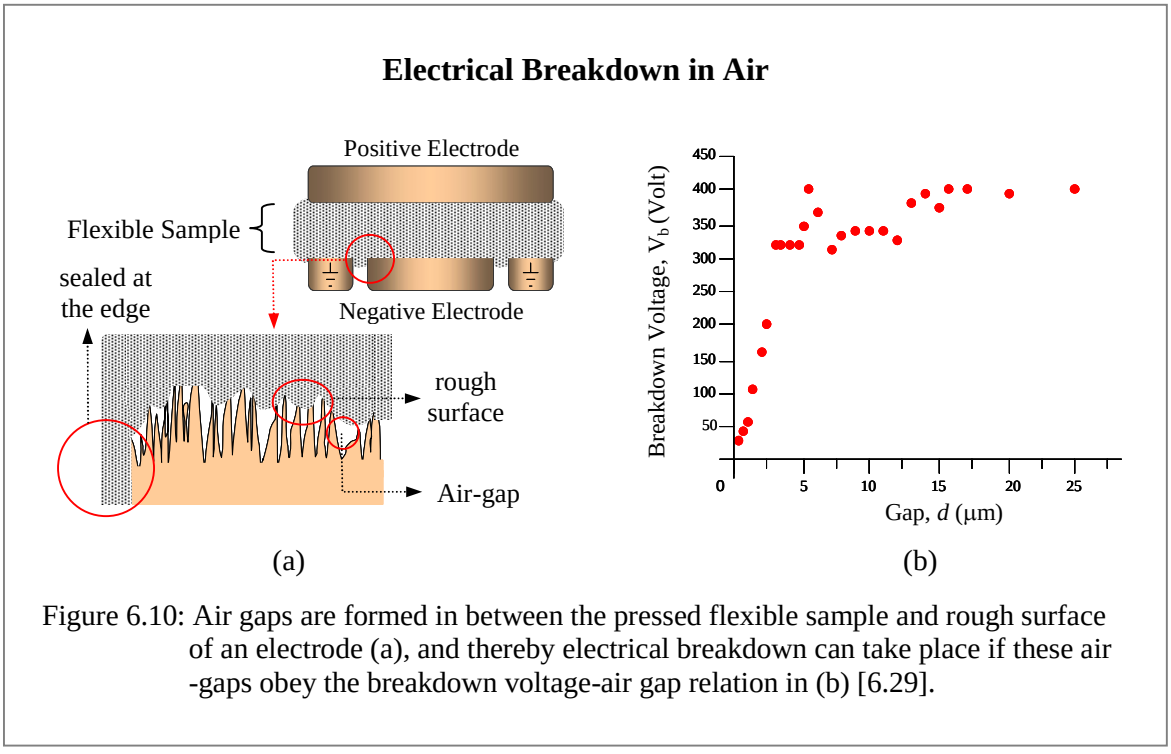

Figure 6.10: Air gaps are formed in between the pressed flexible sample and rough surface of an electrode (a), and thereby electrical breakdown can take place if these air -gaps obey the breakdown voltage-air gap relation in (b) [6.29].

According to Slade *et.al* [6.29], even a small air-gap will allow Townsend breakdown to take place if the localized breakdown voltage V_b of air is achieved. The breakdown voltage versus air-gap plot in Figure 6.10(b) demonstrates the correlation. From the graph, it can be deduced that for air-gaps of about 0.5 μm in depth, the needed breakdown voltage is approximately 30 V. Therefore, the smallest polarization voltage V_p around 28 V applied on *ENR-50* sample probably had induced the air-breakdown process. The process in effect injected ions or electrons from air into the polymer electrets, concurrently with the dipole and space charges polarization processes. From this observation, the air-gaps formed at the interface between electrodes and *ENR-50* sample were estimated of about 0.5 μm.

Return to the discussion on *molecular-ions* model. The model suggested that if there were proper acceptors or donors present within a polymer, then the injected electronic carriers can create *molecular-ions* with them [6.23 to 6.26]. The charge acceptors or donors could be in the form of polar and pendant groups, such as the epoxide groups in *ENR-50* and vinyl chloride in *pPVC* chains, respectively. This remark explains the high-energy deep traps that can be observed in case of several decomposed α and ρ peaks for *ODA*, *OMON*, *ENR-50*, *pPVC* and some *polymer-OMON* composites. Such deep traps with their high energy E is equivalent to the ionization energy E_g indicate the formations of *molecular-ions* within the materials during polarization process. These *molecular-ions* could have trapped charge carriers, which turned them into localized traps with high activation energy E inside the electret materials.

The trace of *molecular-ion* however can not be detected in case of decomposed α peaks for polar *PMMA* as in shown Figure 6.2. Even though it had been polarized at a high electrical field, F_p = 2 MVm^{-1} with the applied voltage V_p up to 500V. *PMMA* is a rigid polymer, similarly when it was fixed to the TSC system at room temperature. The cryostat was then vacuumed to remove the air that surrounded the *PMMA* specimen. This process created a vacuumed environment to the specimen including at its interfaces with electrodes, where the air-gaps were connected directly or indirectly to the opening at the edges as shown in Figure 6.11(a). These air-gaps are supposed to be bigger than those in Figure 6.10(a) of *ENR-50* due to the high rigidity of *PMMA*.

Air breakdown in this situation has to follow the breakdown voltage, V_b – vacuumed gap, d relation as shown in Figure 6.11(b). From the graph, the required voltage V_b for electrical breakdown to take place in a vacuumed-gap is comparatively higher to similar event in air-gap as given by the graph in Figure 6.10(b). Therefore, *PMMA* with the vacuumed-gaps has higher V_b compares to that of *ENR-50* with air-gaps at electrodes-sample interfaces.

This is supported with thought that the vacuumed gaps (in Figure 6.11(a)) were relatively bigger than the air-gaps of *ENR-50* (in Figure 6.10(b)). The bigger gaps in effect require higher voltage V_b to induce the breakdown. Hence, it is assumed that the applied voltage V_p = 500V on the *PMMA* was insufficient to stimulate the electrical breakdown within the vacuumed gaps. Charge injections can not take place without such breakdown, which then lessened the potential for *molecular-ion* states formation in the *PMMA* electrets. It thus explains the lack of decomposed peaks with high activation energy *E*, as shown in Table 6.2 for this rigid polymer.

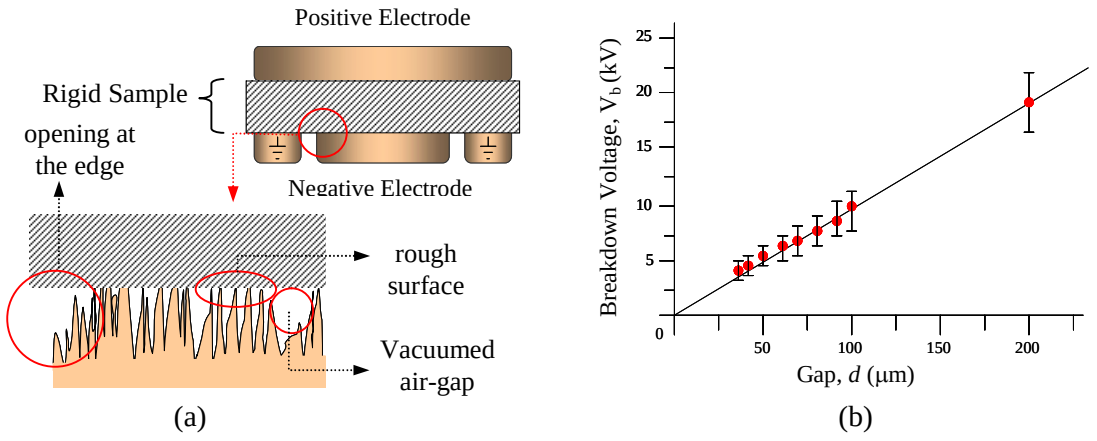

Figure 6.11: The opening at electrode edges due to sample rigidity produce the small air-gaps at the interface which then turn into vacuumed gap in (a), therefore air breakdown follows the relation for electrical breakdown voltage V_b versus vacuumed gap *d* in (b) [6.29].

6.1.2.2.B Charge masking

The effect of charge injection was not only on the formations of deep traps, but it is also believed that the injected charge become homocharges within electrets. The significant of homocharges arise as they normally responsible for charge neutralization and masking on heterocharges [6.2]. The effects can be seen in Figure 6.12 and 6.13 for *ENR-50* and *pPVC* respectively. These TSC plots reveal the lost of certain peaks with the increasing electrical polarization field F_p.

The increments of polarizing field F_p in Figure 6.12 seemed to enhance the $\alpha_{ENR\text{-}50}$ peaks, which indicate the epoxidised polyisoprene chains in *ENR-50*. However, at the same time the $\alpha_{polyisoprene}$ peak that is related to polyisoprene chains vanishes from the TSC plot. Similar situation is also detected in case of *pPVC* as shown in Figure 6.13(a). The α_{DOP} peak that signifies the effect of plasticizer molecules around – 32 °C vanishes due to the increase in F_p from 0.125 MV/m to 0.597 MV/m. In the intermediate case as shown in Figure 6.13(b), the applied field F_p is about 0.250 MV/m where a downward peak appears prominently next to the α_{DOP}. The peak indicates the presence of localized deep traps due to the increase of applied field F_p. This observation is supported with the fitting parameter in Table 6.9, which is the activation energy E for decomposed peaks. From the table it can be seen that there are three peaks with *molecular-ion* state energy, where their energy E is within the range of 4 eV to 4.7 eV.

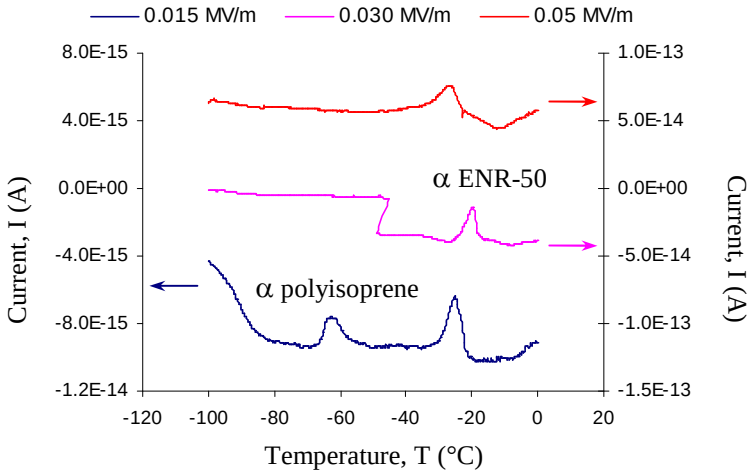

Figure 6.12: The effect of increasing the polarizing field, F_p had caused the lost of $\alpha_{polyisoprene}$ peak in *ENR-50* plots. It was due to charge masking or charge neutralization in the *ENR-50* electrets.

Further increase on the applied field F_p means more injections or depositions of electrical charge carriers. Despite the *molecular-ion* formation, these homocharges can also mask or

neutralize the heterocharges within the *pPVC* electrets. The effect involves the *molecular-ion* deep traps as well. Therefore, both α and *molecular-ion* peaks are absent within the TSC plot in Figure 6.13(a) with the F_p is about 0.597 MV/m.

The Effect of Polarizing Field, F_p on some TSC results for Plasticized PVC (pPVC)

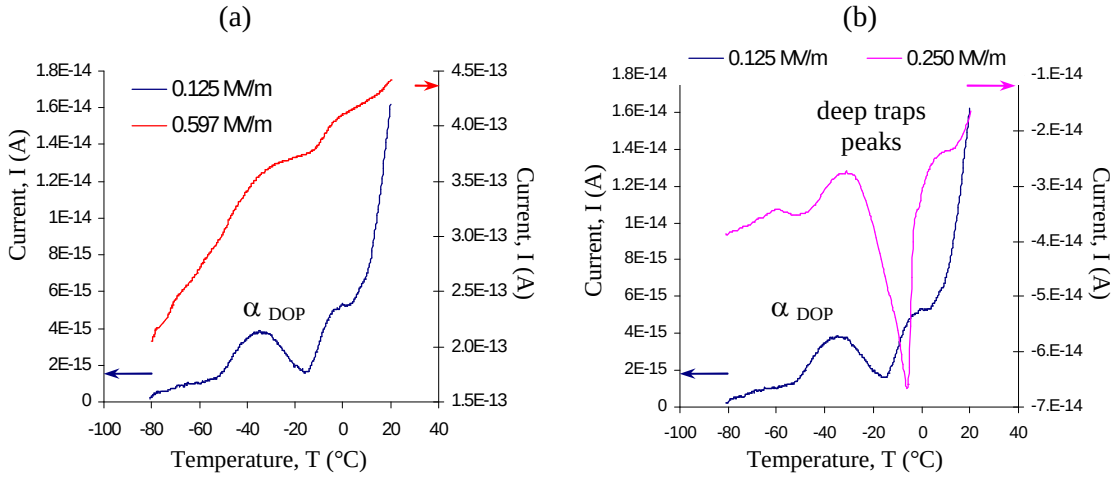

Table 6.9
Activation Energy *E* for decomposed pPVC Peaks

Peak	T_{max} (°C)	*E* (eV)
1	-22.00	1.6
2	-18.20	2.5
3	-15.30	4.0
4	-13.50	4.1
5	-11.60	4.7
6	-9.90	3.2

Figure 6.13: The effect of increasing the polarizing field, F_p vanish the α_{DOP} peak in (a), which indicate charge neutralization and masking. While in (b) it is most likely showing the deep traps depolarization following a moderate increment in F_p. Table 6.9 in (c) lists the activation energy for the decomposed deep trap peaks.

Analyses on activation energy, *E* for decomposed peaks thus far manage to gather valuable information, such as the origin of relaxation processes that generated TSC peaks. There are cases however, where similar peaks consistently appear in some of the TSC plots with the variations in their maximum temperature T_{max} as shown in Table 5.3. From Figure 5.11 to 5.17, some similarities can be seen in the shape of ρ peaks within the TSC plots of *ODA*,

OMON and *polymer-OMON* composites. Despite that decompositions on the ρ peaks show variations in activation energy *E*. Table 6.10 lists the energy *E* of the decomposed ρ peaks. The energy *E* variations in case of *ODA* and *OMON* are related to *ODA* cation interactions with silicates inside *OMON* gallery. While the differences in energy *E* among *OMON* and *polymer-OMON* composites support previous prediction in Chapter 4. They present more proof to the belief that *OMON* act differently in each case of the composite, depending on the polymers physical and chemical structures. However, more information is needed to relate the internal structures of *OMON* with the observed relaxation behaviors.

Table 6.10

Activation Energy *E* for decomposed OMON ρ Peaks

Sample	Fitted Activation Energy *E* for decomposed ρ peak (eV)			
	Peak 1	**Peak 2**	**Peak 3**	**Peak 4**
ODA	2.70	4.70	5.70	4.50
OMON	3.70	4.40	5.40	4.60
CDPNR		1.95	3.65	5.40
CSMRL	5.00	3.00	3.30	
CENR-50	2.30	2.55	3.80	
CPE		1.80	3.30	9.50
CpPVC		2.50	3.30	

Table 6.10: The variation in activation energies *E* of decomposed ρ peaks for *OMON* that are observed in *ODA*, *OMON* and *polymer-OMON* composites.

6.2 Data Evaluation – Pre-exponential Factor, τ_o

According to Lushcheikin and Migahed [6.30], pre-exponential factor, τ_o that is the inverse of natural frequency f_o is a characteristic time for a relaxation process to take place. The knowledge on this characteristic relaxation time τ_o can be very helpful to differentiate the type of localized relaxation processes. This is important when the activation energies E for dipoles and space charges relaxations fall within the same energy range from 1eV to 3eV. The authors suggested that the range of τ_o from 10^{-13} to 10^{-10} s is attributed to dipole group relaxations. While τ_o within the range of 10^{-18} s to 10^{-25} s is for the relaxation process by segmental dipole in polymers. These values add more information on the origin of certain relaxation process, which are responsible for the observed current-temperature trends within TSC plot.

From the characteristic parameters of TSC peaks that are based on the first order kinetic theory, the value for τ_o can be calculated. This theory gives the equation (2.9) that involves the τ_o as previously shown in Chapter 2. Rewrite the equation will give the characteristic relaxation time, [6.2, 6.4, 6.5 and 6.14]

$$\tau_o = \frac{kT_{\mathbf{max}}^2}{hE}\,\mathbf{exp}\left(-\frac{E}{kT_{\mathbf{max}}}\right) \tag{6.2}$$

where E = activation energy
h = heating rate
T_{max} = maximum temperature of a peak
k = Boltzmann constant

The formula was then used with the fitting parameters for each decomposed α and ρ peaks of *pPVC* as shown in Figure 6.14(a). Table 6.11(a) lists the calculated values for $\tau_{o,}$ which show that several peaks represent dipole group and dipole segmental relaxation processes. None of the calculated τ_o however seems to indicate the cooperative mode as expected for

relaxation processes around and above a glass transition temperature T_g, especially within polymers. In fact, the smallest calculated τ_o is just about $2x10^{-13}$ s that can only be related with the relaxation of dipole groups. The significant of cooperative relaxation mode within polymer will be discussed in the next Section 6.2.1.

Decomposed α and ρ Peaks of *pPVC*

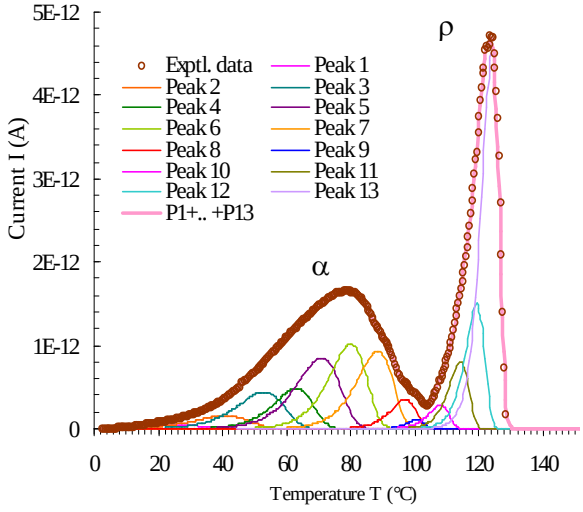

(a)

Table 6.11(a)
τ_o of decomposed α and ρ pPVC Peaks

Peak	T_{max} (°C)	E_{fitt} (eV)	τ_o (s)
1	25.50	0.90	**2.06E-13**
2	41.00	1.00	**2.86E-14**
3	53.00	1.25	**1.32E-17**
4	63.00	1.60	**2.33E-22**
5	70.90	1.50	**2.74E-20**
6	80.00	1.85	**8.93E-25**
7	88.40	2.00	**2.84E-26**
8	97.00	3.00	**2.11E-39**
9	100.70	4.80	**1.81E-63**
10	108.00	4.00	**1.50E-51**
11	114.20	4.20	**2.59E-53**
12	119.30	4.50	**1.78E-56**
13	124.00	5.00	**3.59E-62**

(b)

Figure 6.14: The fitted peaks for α and ρ peaks of *pPVC* in (a), while in (b) Table 6.11(a) lists the calculated pre-exponential factor from their respective fitting parameters which also involve the heating rate of 1.5 °C/min.

6.2.1 William-Landel-Ferry, WLF Fitting

Above the range for dipole group relaxations, the τ_o is described by a relation known as *Vogel-Fulcher-Tamman* or *VFT* equation that is comparable to the *William-Landel-Ferry*, *WLF* theory. The theory basically explains that relaxation occurs within the temperature region around and above a T_g is in a cooperative manner [6.2, 6.3, 6.32 and 6.33]. This is analogous to the idea of distributed relaxation processes, which normally take longer time than those in a single relaxation mode. It also consistent with the compensation relaxation

times τ_c produced by some previous researchers. They showed that the characteristic time that is related to the cooperative processes is within the range of 10^{-7} s to 10^{1} s [6.11, 6.12, 6.34, 6.35 and 6.36].

The theory also emphasize that when polymer temperature reaches the T_g, the motions of bulky main chains depend on the unoccupied or free volume [6.2 and 6.3] in the material. The relaxation involved therefore obeys the *WLF* equation, which gives the relaxation frequency as follow:

$$\alpha_v(T) = \alpha_g \exp\left\{\frac{c_1(T - T_g)}{(c_2 + T - T_g)}\right\}, \qquad T > T_g \tag{6.3}$$

or in Arrhenius form $$\alpha_v(T) = \alpha_w \exp\left(-\frac{A_w}{k(T - T_\infty)}\right), \tag{6.4}$$

which give the *VFT* equation,

where $\alpha_g = 7 \times 10^{-3}\ s^{-1}$ (for most amorphous polymer);

$c_1 = 40$ and $c_2 = 52$ °C.

$$\alpha_w = \alpha_g \exp c_1 \approx 1.6 \times 10^{15} \tag{6.5}$$

$A_w = c_1 c_2 k = 0.18$ eV

$T_\infty = T_g - c_2$.

At $T = T_{max}$ $$\alpha_w = \alpha(T_{\max}) \exp\left(\frac{c_1 c_2 k}{k(T_{\max} - T_g + c_2)}\right) \tag{6.6}$$

if $T_{max} = T_g$ $$\alpha_w = \alpha(T_{\max}) \exp c_1 \tag{6.7}$$

and compare with equation (6.5), $$\alpha(T_{\max}) = \alpha_g \tag{6.8}$$

From Arrhenius relation as shown by the equations (2.7), the relaxation frequency at the peak maximum is $$\alpha(T_{\max}) = \alpha_o \exp\left(-\frac{E}{kT_{\max}}\right),$$

and with the $\alpha_o = \frac{qE}{kT_{\max}^2}\exp\left(\frac{E}{kT_{\max}}\right)$ from equation (6.2), the relaxation frequency becomes $\alpha(T_{\max}) = \frac{qE}{kT_{\max}^2} = \alpha_g$ (6.9)

Where it then gives the relaxation frequency $\alpha_w = \frac{qE}{kT_{\max}^2}\exp c_1$ (6.10)

Hence, the relaxation characteristic time τ_{wlf} that is comparable to the τ_o is derived as

$$\tau_{wlf} = \frac{kT_{\max}^2}{qE}\exp(-c_1) \quad (6.11)$$

Using the given equation (6.10), a new fitting method was used on numerical data from decomposed peaks. The effort was done in order to calculate the *WLF* characteristic time, τ_{wlf} that may reveal the cooperative mode of relaxation processes for TSC peaks. The data fitting was employed on TSC decomposed peaks, such as in Figure 6.15(a) and 6.15(b) for the decomposed α peak of *pPVC*. These figures show the fitted data around and above the T_g, which indicate that the data fitting are consistent with the *WLF* theory.

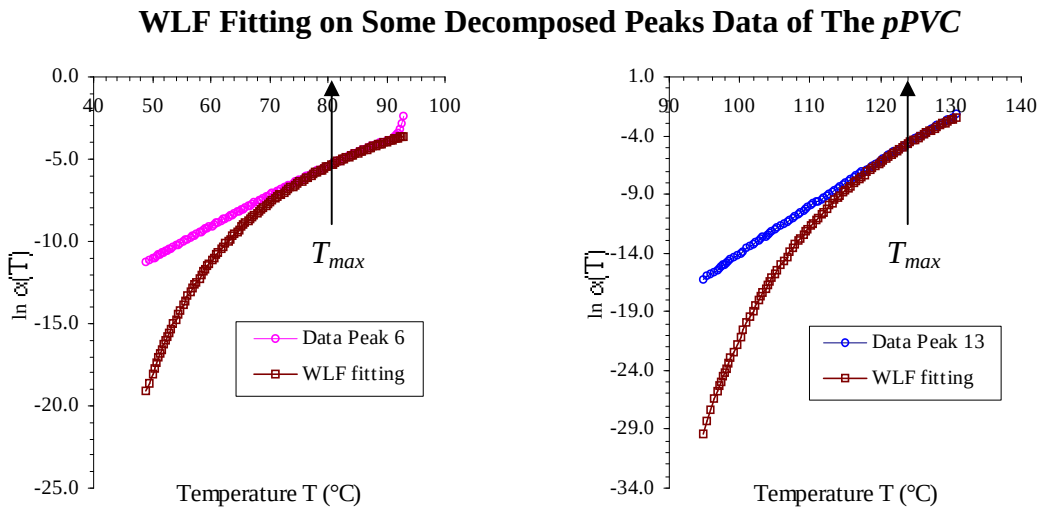

Figure 6.15: *WLF* fitting on data from decomposed Peak 6 in (a) and Peak 13 in (b) for the α peak of *pPVC*. The data are well fitted around and above the T_g of *PVC*, which is about 80 °C.

It is to be noted that it is impossible to fit the data by using the *WLF* equation if the actual T_g is used in the equation. Therefore in these cases, T_{max} was considered as the T_g for each peak, thereby the values of τ_{wlf} came out as listed in Table 6.11(b). From the table, it seems that the characteristic times τ_{wlf} slightly vary within the range of 10^{-15} to 10^{-16} s. They can be associated to either dipole group or dipole-segmental relaxations. However, they are not indicating the cooperative relaxation process as expected for the decomposed α peaks.

Table 6.11(b)
The τ_{wlf} of α and ρ pPVC Peaks from *WLF* Fitting

Peak	T_{max} (°C) ± 0.01*	E_{fitt} (eV)	τ_o (s)	τ_{wlf} (s) ± 0.01**
1	25.50	0.90	2.06E-13	**1.40E-15**
2	41.00	1.00	2.86E-14	**1.35E-15**
3	53.00	1.25	1.32E-17	**1.20E-15**
4	63.00	1.60	2.33E-22	**1.00E-15**
5	70.90	1.50	2.74E-20	**1.15E-15**
6	80.00	1.85	8.93E-25	**9.86E-16**
7	88.40	2.00	2.84E-26	**9.56E-16**
8	97.00	3.00	2.11E-39	**6.68E-16**
9	100.70	4.80	1.81E-63	**4.26E-16**
10	108.00	4.00	1.50E-51	**5.31E-16**
11	114.20	4.20	2.59E-53	**5.23E-16**
12	119.30	4.50	1.78E-56	**5.01E-16**
13	124.00	5.00	3.59E-62	**4.62E-16**
α	79.76*	0.61		**2.36E-15****
ρ	123.89*	2.28		**6.31E-16****

* measured ** calculated

Table 6.11(b): The values of pre-exponential factor t_{wlf} produced via *WLF* fitting on data from decomposed α peaks and experimental peaks from the TSC plot of *pPVC*.

The effort was continued by using the Arrhenius and *VTF* relation as shown by equation (2.7) and (6.4), respectively. In case where the plot of $ln\ \alpha(T)$ versus $1/T$ shows good linearity as shown in Figure 6.16(a), the τ_o can be estimated by means of the Arrhenius equation. The *VTF* relation on the other hand is used when the frequency-temperature plot give a curve. The curve had to be tuned into a linear line in as shown in Figure 6.16(b) and 6.16(c) by adjusting the variable temperature T_∞. In fact, this variable is supposed to be the same for all decomposed peaks as it may represents the origin temperature of cooperative

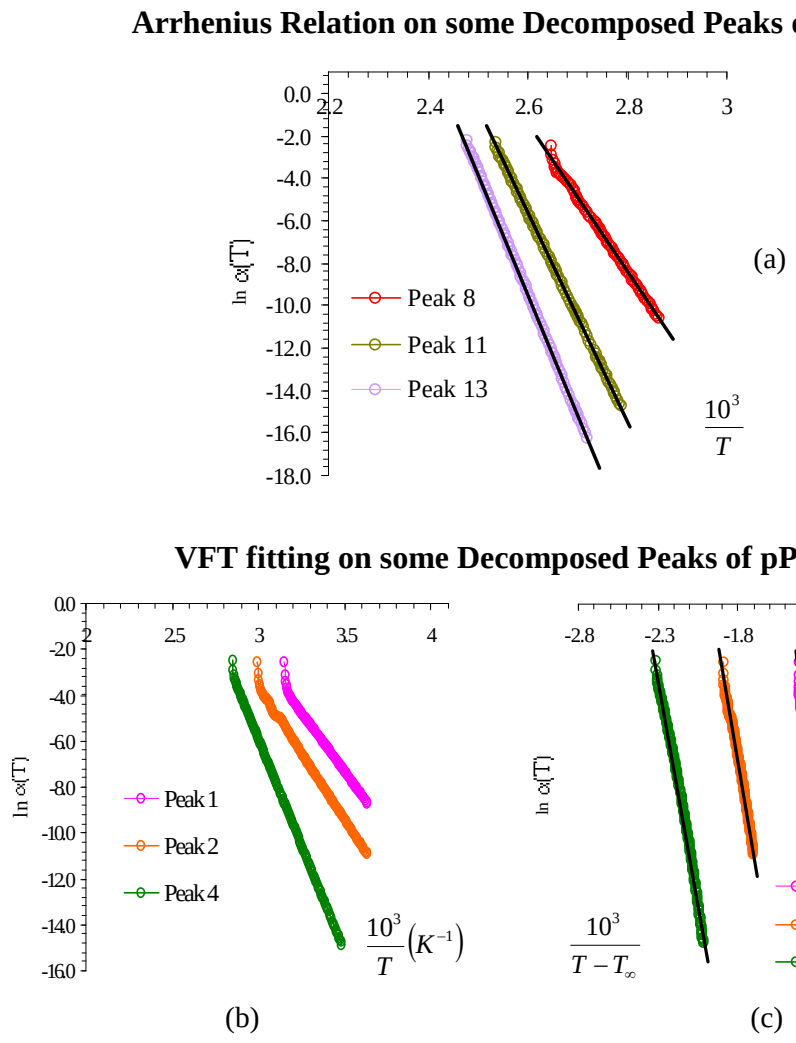

Figure 6.16: The plots of *ln α(T)* verses 1/*T* for decomposed Peak 8, 11 and 13 in (a) give straight lines which indicate Arrhenius relation. Similar plot on decomposed Peak 1, 2 and 4 in (b) give curve lines that can be straightened via VTF fitting as shown in (c).

relaxations [6.12]. From Table 6.11(c) however, the fitting temperature T_∞ varies except for decomposed peak 4 and 5. The *VTF* fitting also produced characteristic relaxation times τ_{VTF}, which are within the range of 10^6 s to 10^{40} s as listed in the table. This range relatively is much bigger than that of previous authors [6.11, 6.12, 6.34, 6.35 and 6.36] around 10^{-7} s to 10^1 s, which indicates the cooperative relaxation. Decomposed peak 8 to 13 with their T_{max} above the T_g (~80 °C) on the other hand give τ_o Arrhenius within the range of 10^{-15} s

to 10^{-8} s. The values are inconsistent with the *WLF* theory, which anticipate that τ_o around and above a T_g should demonstrate the cooperative relaxation mode. Therefore, the attempt to use the *VTF* as well as *WLF* equation was not proceeded.

Table 6.11(c)

The τ_{VTF} of α and ρ pPVC Peaks from *VTF* Fitting

Peak	T_{max} (°C) ± 0.01*	E_{fitt} (eV)	T_∞ (°C)	τ_o (s)	τ_{wlf} (s) ± 0.01**	τ_o *graph* (s)	
						$\tau_{Arrhenius}$	τ_{VFT} ± 0.01**
1	25.5	0.90	**750**	2.06E-13	1.40E-15		**4.93E+40**
2	41.0	1.00	**590**	2.86E-14	1.35E-15		**4.40E+33**
3	53.0	1.25	**660**	1.32E-17	1.20E-15		**4.46E+44**
4	63.0	1.60	**510**	2.33E-22	1.00E-15		**4.04E+40**
5	70.9	1.50	**310**	2.74E-20	1.15E-15		**2.33E+19**
6	80.0	1.85	**327**	8.93E-25	9.86E-16		**1.56E+23**
7	88.4	2.00	**320**	2.84E-26	9.56E-16		**5.40E+22**
8	97.0	3.00	-	2.11E-39	6.68E-16	**4.32E-08**	
9	100.7	4.80	-	1.81E-63	4.26E-16	**7.28E-15**	
10	108.0	4.00	-	1.50E-51	5.31E-16	**1.73E-11**	
11	114.2	4.20	-	2.59E-53	5.23E-16	**2.39E-12**	
12	119.3	4.50	-	1.78E-56	5.01E-16	**1.19E-13**	
13	124.0	5.00	-	3.59E-62	4.62E-16	**1.09E-15**	
α	79.76*	0.61	**288**		2.36E-15**		**2.48E+09****
ρ	123.89*	2.28	**153**		6.31E-16**		**2.91E+06****

* measured ** calculated

Table 6.11(c): The values of pre-exponential factor, t_{VFT} from the *VFT* fitting on the decomposed peaks data of the *pPVC*.

A good reason that may explain these observations can be associated with the source of the fitted data. Normally, previous researchers [6.26, 6.37 and 6.38] used the *Relaxation Map Analysis*, *RMA* method to decompose the pristine α and ρ TSC peaks. The *RMA* procedure as shown by the schematic diagram in Figure 6.17 is another type of TSC technique. This procedure allows ones to choose a series of signals via the method known as windowing technique. In this technique, each signal or peak correspond to a specific group of dipoles [6.32 and 6.34]. The researchers employed the *VFT* equation on the experimental data from *RMA* decomposed peaks, which are able to reveal the occurrence of cooperative relaxation in polymers.

The reason for the mathematical generated data is inappropriate to be used with the *WLF* and *VFT* relations can be explained. The numerical data to be fitted in this analysis were obtained from decomposed TSC peaks using the first order kinetic theory. This theory assumes the involvement of Debye relaxation in the depolarization process. Hence, each decomposed TSC peak represents a localize relaxation in the process. It is in contradiction with the *WLF* theory, which predicts the cooperative relaxation mode. The differences in approach by these two theories could be the cause for the failure.

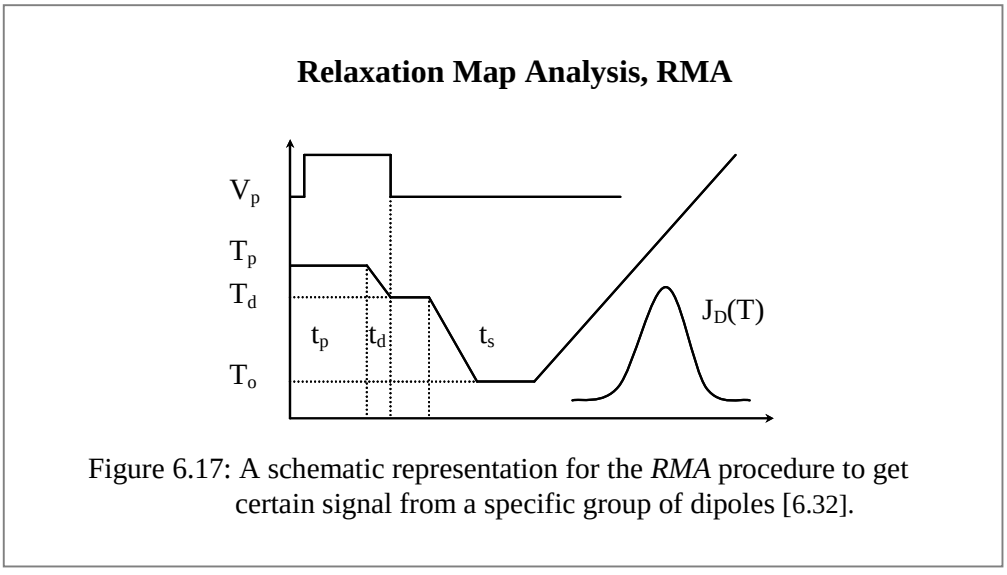

Figure 6.17: A schematic representation for the *RMA* procedure to get certain signal from a specific group of dipoles [6.32].

In addition, the frequency – temperature plot from each elementary peak itself shows good linearity regardless the small curvature at the edge as shown in Figure 6.16(b). It confirms that they follow the Arrhenius law, which proves the single relaxation Debye model. On the other hand, the trends of activation energy E and characteristic time τ_o in Table 6.11(a) seem to establish the condition of Compensation law, where the increase in energy E is followed with the decrease of τ_o. These observations show that the decompositions of TSC peaks that are based on the first order kinetic theory manage to demonstrate the existence of elementary relaxations.

6.2.2 The N-Fitting Method

Even though the attempt to employ the *WLF* fitting was not satisfactory, however it gave the idea of fitting the whole data from a peak. It means that the *WLF* formulation had to be modified by introducing some new parameters. The modification thus affects the values of existing parameters such as pre-exponential factor, τ_o. Preliminary attempt was carried out on the decomposed α and ρ peaks of *pPVC* using this new formulation,

$$\alpha_n = \alpha_g \exp\left(\frac{C_{n1}(T - T_m)}{C_{n2}(T) + (T - T_m)}\right)$$

where the C_{n1} and $C_{n2}(T)$ are the fitting parameters. This formula is analogous to the *WLF* equation and it can also be written as follow,

$$\alpha_n = \alpha_{on} \exp\left(-\frac{A_n(T)}{k(T - T_n(T))}\right)$$

with $\alpha_{on} = \alpha_g \exp C_{n1}$; $A_n = kC_{n1}C_{n2}(T)$ and $T_n = T_m - C_{n2}(T)$

therefore, $\tau_n = \tau_g \exp(-C_{n1})$ or $\tau_n = \frac{kT_m^2}{\beta E}\exp(-C_{n1})$.

Table 6.11(d)
The τ_n of α and ρ pPVC Peaks from *N-Fitting*

Peak	T_{max} (°C) ± 0.01*	E_{fitt} (eV)	τ_o (s)	τ_{wlf} (s) ± 0.01**	τ_o *graph* (s) ± 0.01**		τ_n (s) ± 0.01**
					$\tau_{Arrhenius}$	τ_{VTF}	
1	25.50	0.90	2.06E-13	1.40E-15		4.93E+40	**7.48E-12**
2	41.00	1.00	2.86E-14	1.35E-15		4.40E+33	**4.93E-12**
3	53.00	1.25	1.32E-17	1.20E-15		4.46E+44	**6.66E-14**
4	63.00	1.60	2.33E-22	1.00E-15		4.04E+40	**2.48E-17**
5	70.90	1.50	2.74E-20	1.15E-15		2.33E+19	**2.91E-15**
6	80.00	1.85	8.93E-25	9.86E-16		1.56E+23	**3.44E-18**
7	88.40	2.00	2.84E-26	9.56E-16		5.40E+22	**7.43E-19**
8	97.00	3.00	2.11E-39	6.68E-16	4.32E-08		**7.17E-28**
9	100.70	4.80	1.81E-63	4.26E-16	7.28E-15		**4.36E-45**
10	108.00	4.00	1.50E-51	5.31E-16	1.73E-11		**1.79E-35**
11	114.20	4.20	2.59E-53	5.23E-16	2.39E-12		**4.98E-36**
12	119.30	4.50	1.78E-56	5.01E-16	1.19E-13		**1.11E-37**
13	124.00	5.00	3.59E-62	4.62E-16	1.09E-15		**6.65E-41**
α	79.76*	0.61	-	2.36E-15**		2.48E+09**	**1.41E-04****
ρ	123.89*	2.28	-	6.31E-16**		2.91E+06**	**6.09E-20****

* measured ** calculated

Table 6.11(d): The values of pre-exponential factor, τ_n as obtained from the *N-fitting* on the decomposed peaks data of *pPVC*, as well as the pristine α and ρ peaks.

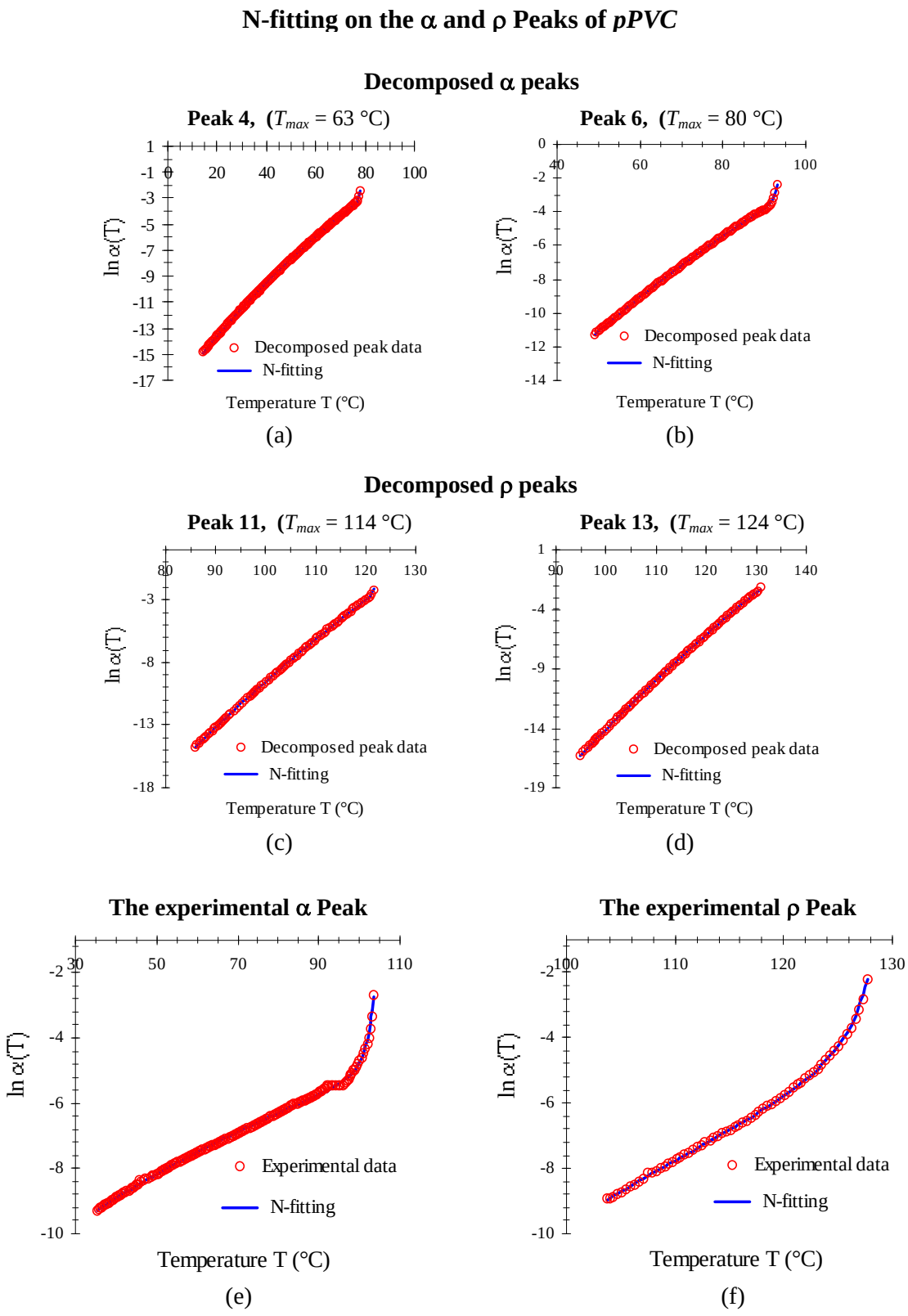

Figure 6.18: The results from *N-fitting* method on TSC data from the α and ρ peaks of *pPVC*, including some of their decomposed peaks.

The results demonstrate that the new fitting which is from now referred as *N-fitting* appear to work quite well. It managed to fit all the data from decomposed peaks, which presents a range of 90 % to 100 % of data population with a deviation ≤ 5 % from each targeted data. Figures 6.18(a) to 6.18(d) show some of the results from *N-fitting* on the α and ρ peaks of *pPVC*, as well as on their decomposed peaks. The characteristic times, τ_n that are listed in Table 6.11(d) can be estimated from the calculation with some fitting constants.

From the table, the trend for τ_n values seems quite similar to that of the calculated τ_o from the earlier data fitting that produced the decomposed peaks, even though there are great variations in their values. The ability of this fitting procedure to fit the experimental data was very motivating. Figure 6.18(e) and 6.18(f) show the fitting on the experimental α and ρ peaks of *pPVC* in that order, where 100 % of its data populations are fitted with less than 5 % (≤ 5 %) deviation from the targeted data. The calculated characteristic time τ_n for the α peak as listed in Table 6.11(d) is just about 1.4×10^{-4} s. This value is within the range of cooperative characteristic relaxation time (10^{-9} s to 10^{0} s) as stated earlier in Section 6.2.1. Obviously, the τ_n of α peak indicates the occurance of cooperative relaxation around the T_g of *pPVC* polymer. The *N-fitting* method is applicable for both experimental and numerical data. This fitting method thus was employed on the polymers α peaks to see its reliability in demonstrating the cooperative mode, as proposed by the *WLF* theory.

6.2.2.1 Polymers

The results of applying *N-fitting* method on the α peaks of *SMRL*, *DPNR*, *ENR-50* and *PE* are shown in Figures 6.19 to 6.22 respectively. From the graphs and tables, the consistency of the method is rather good. This is demonstrated by the high percentage that is constantly depicted by the data population, *P* parameter. The smallest *P* with deviation less than 5 % is about 90 % is observed on the α_{DPNR} fitting as shown in Figure 6.20(c). The fitted line to

N-fitting on The α Peak of *SMRL*

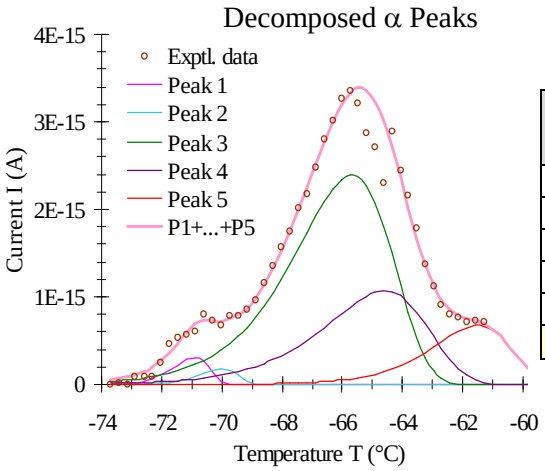

Table 6.12
τ_n of α *SMRL* Peaks

Peak	T_{max} (°C) ± 0.01*	E_{fitt} (eV)	τ_n (s) ± 0.01**	P (%)
1	-70.90	6.00	4.92E-20	100
2	-70.00	6.00	1.90E-26	100
3	-65.70	2.30	2.66E-19	100
4	-64.60	2.20	1.35E-33	100
5	-61.50	3.00	1.02E-41	100
α	-65.48*	2.09	2.17E-02**	100

* measured ** calculated

P is a population of the fitted data with a deviation ≤5% from its counterpart

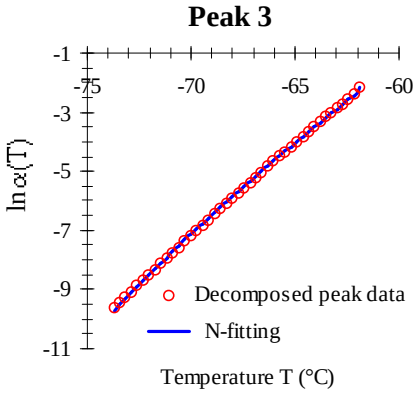

(a)

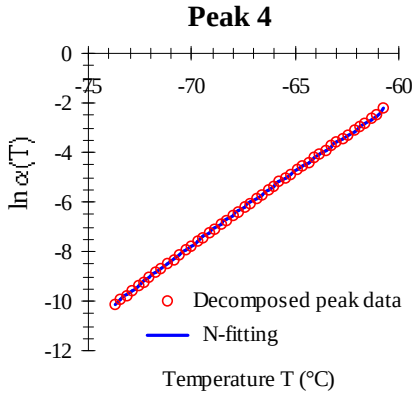

(b)

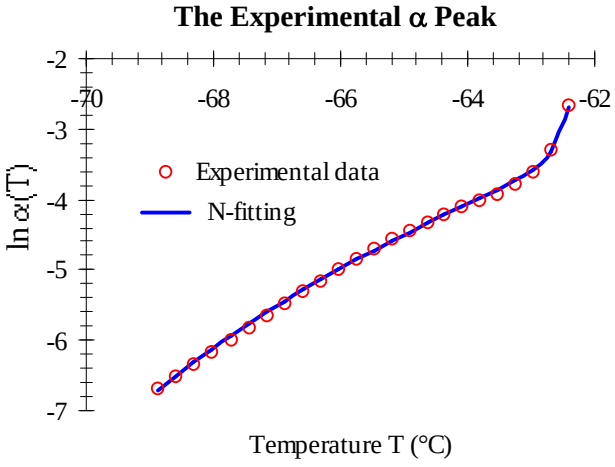

(c)

Figure 6.19: The results of *N-fitting* method on the α peaks of *SMR,L* as well as on the decomposed α peaks.

N-fitting on The α Peak of *DPNR*

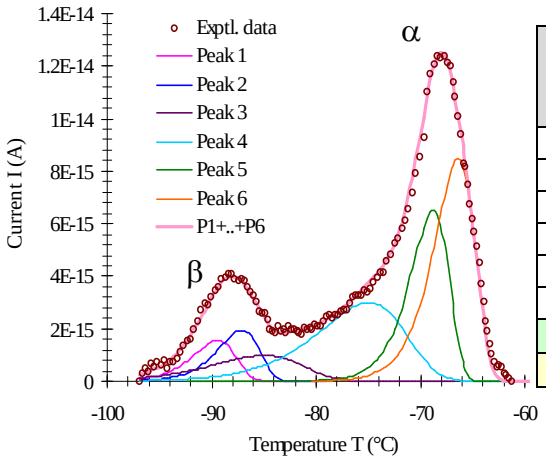

Table 6.13
τ_n of β and α *DPNR* Peaks

Peak	T_{max} (°C) ± 0.01*	E_{fitt} (eV)	τ_n (s) ± 0.01**	*P* (%)
1	-89.40	1.40	2.10E-14	100
2	-87.10	1.50	3.35E-18	100
3	-85.00	0.70	1.52E-25	100
4	-75.00	0.80	1.44E-14	100
5	-68.80	1.96	4.25E-12	100
6	-66.40	1.90	3.21E-19	98
β	-86.87*	0.06	7.52E+01**	100
α	-67.76*	0.10	8.98E-01**	90

* measured ** calculated

P is a population of the fitted data with a deviation ≤5% from its counterpart

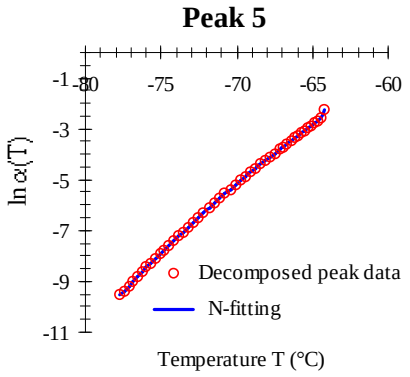

(a)

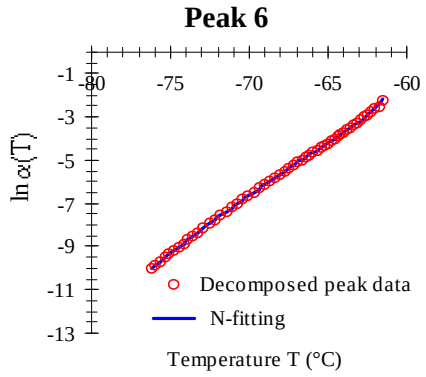

(b)

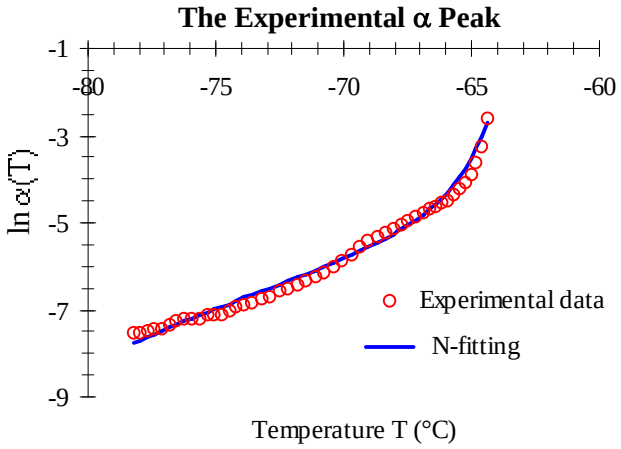

(c)

Figure 6.20: *N fitting* on the α peaks of *DPNR* in (c) gives the fitted data population *P* in Table 6.13 about 90 %. However, the *P* for decomposed peaks reaches 100 % which indicate good accuracy of the fitting procedure.

N-fitting on The $\alpha_{polyisoprene}$ Peak of *ENR-50*

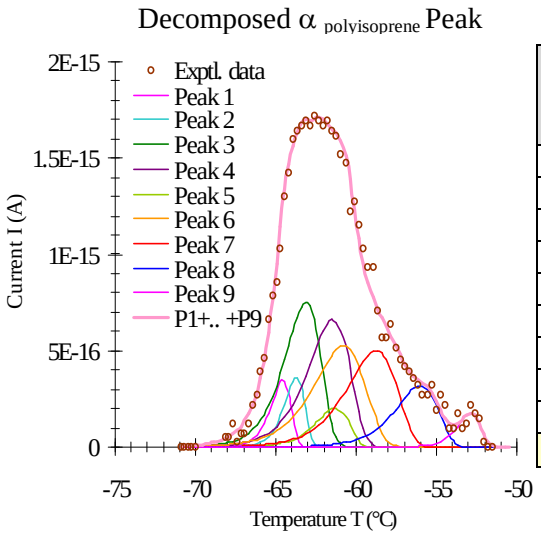

Table 6.14(a)

τ_n of $\alpha_{polyisoprene}$ *ENR-50* Peaks

Peak	T_{max} (°C) ± 0.01*	E_{fitt} (eV)	τ_n (s) ± 0.01**	*P* (%)
1	-64.55	6.00	2.93E-39	100
2	-63.70	6.00	2.43E-38	100
3	-63.10	3.40	4.37E-32	100
4	-61.45	3.00	7.63E-28	100
5	-61.30	3.80	2.53E-40	100
6	-60.75	2.50	2.14E-28	100
7	-58.75	2.60	3.66E-35	100
8	-56.00	3.10	5.03E-34	100
9	-52.80	6.00	3.92E-28	100
α	-62.58*	0.60	4.00E+01**	94

* measured ** calculated

P is a population of the fitted data with a deviation ≤5% from its counterpart

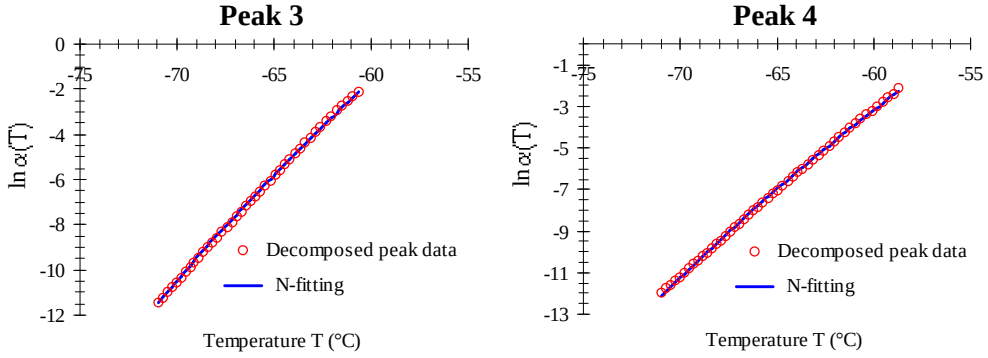

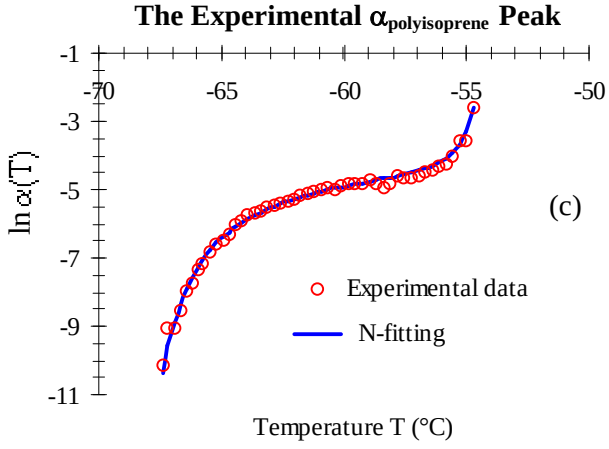

Figure 6.21(a): The results of *N-fitting* method on $\alpha_{polyisoprene}$ peak at -62.58 °C which indicates the presence of polyisoprene chains in *ENR-50* rubber. Table 6.14(a) lists the fitting parameters for $\alpha_{polyisoprene}$ peak.

N-fitting on The α_{ENR-50} Peak of *ENR-50*

Decomposed α_{ENR-50} Peak

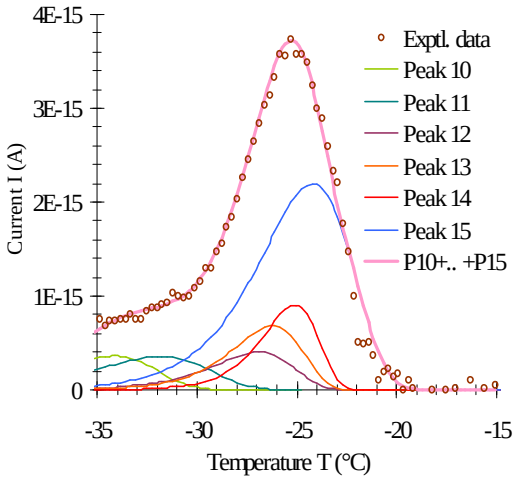

Table 6.14(b)
τ_n of α *ENR-50* Peaks

Peak	T_{max} (°C) ± 0.01*	E_{fitt} (eV)	τ_n (s) ± 0.01**	P (%)
10	-34.20	2.00	6.40E-20	100
11	-31.80	1.80	5.56E-17	100
12	-26.90	2.60	1.14E-22	100
13	-26.20	3.00	3.23E-26	100
14	-25.10	3.80	6.39E-33	100
15	-24.20	2.30	5.61E-22	100
α_{ENR-50}	-25.02*	2.42	2.85E-11**	100

* measured ** calculated

P is a population of the fitted data with a deviation ≤5% from its counterpart

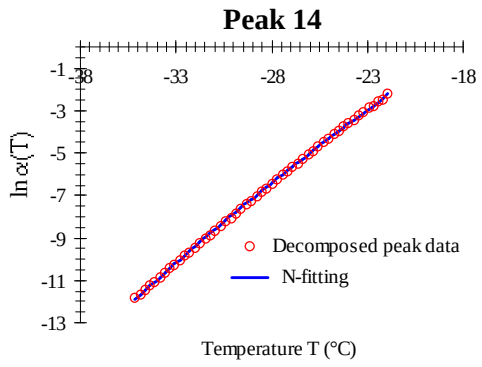

(a)

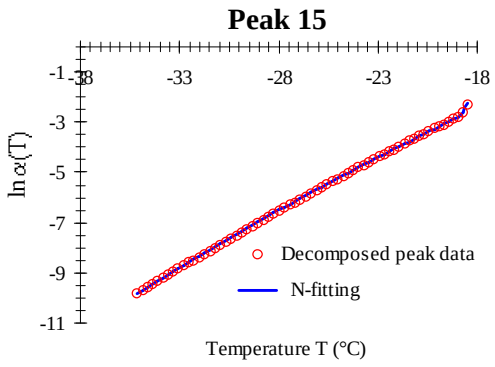

(b)

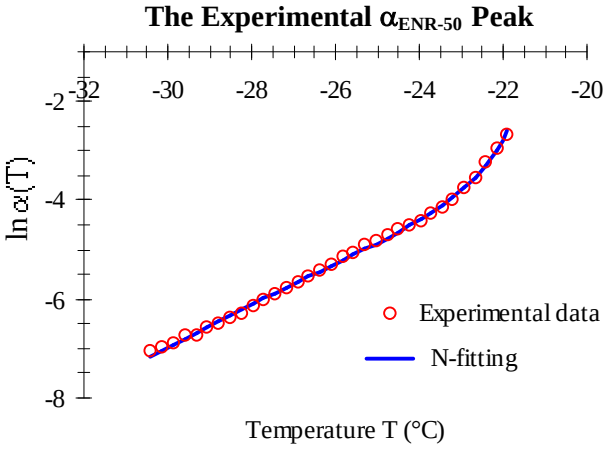

(c)

Figure 6.21(b): The results of *N-fitting* method on α_{ENR-50} peak at -25.02 °C which is a characteristic peak for *ENR-50* rubber. Table 6.14(b) lists the fitting parameters for α_{ENR-50} peak.

N-fitting on The α Peak of *PE*

Decomposed α Peaks

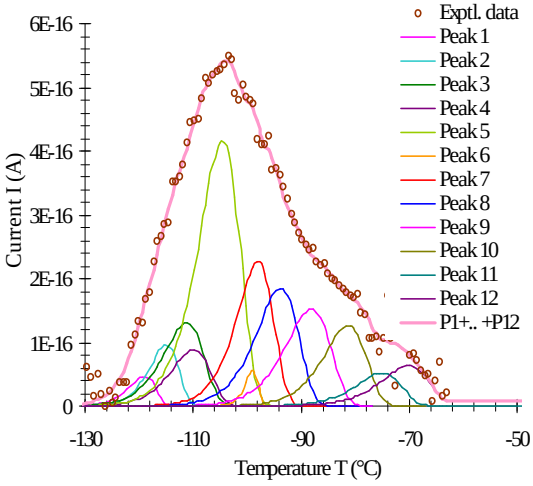

Table 6.15
τ_n of α *PE* Peaks

Peak	T_{max} (°C) ± 0.01*	E_{fitt} (eV)	τ_n (s) ± 0.01**	*P* (%)
1	-119.10	0.80	2.13E-15	100
2	-115.00	0.80	1.13E-17	100
3	-111.20	0.60	3.58E-12	100
4	-109.90	0.62	2.87E-12	100
5	-104.60	0.63	1.72E-16	100
6	-99.00	2.20	9.23E-57	96
7	-98.00	0.77	5.80E-18	100
8	-93.80	0.70	3.79E-17	100
9	-88.10	0.70	6.40E-16	100
10	-81.30	0.30	1.31E-19	100
11	-75.00	0.80	4.76E-18	100
12	-70.00	0.30	3.58E-18	99
α	-103.55*	1.62	7.88E+01**	100

* measured ** calculated

P is a population of the fitted data with a deviation ≤5% from its counterpart

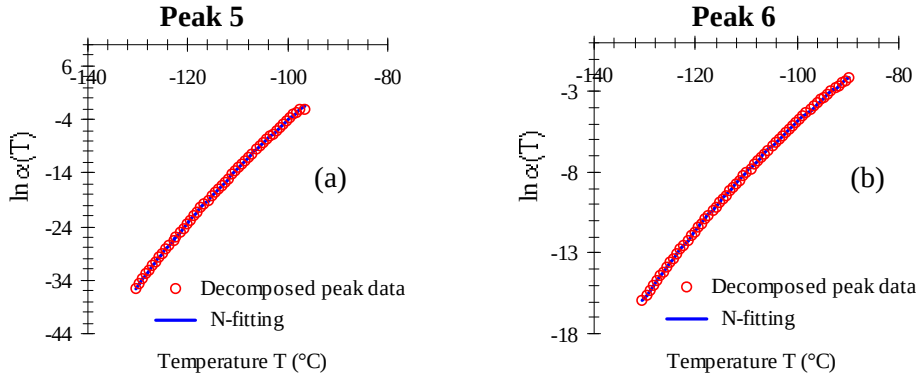

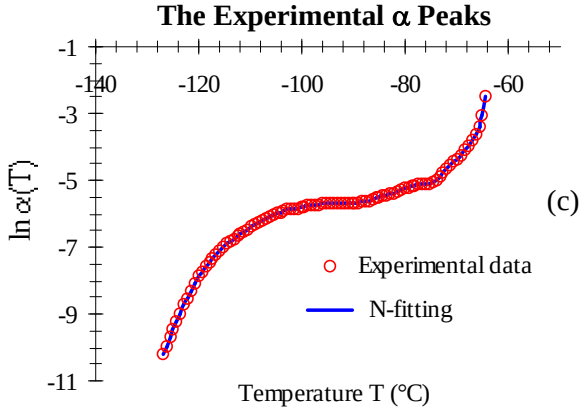

Figure 6.22: The experimental data of α peaks for *PE* in (c) are well fitted via the *N-fitting* method with the *P* parameter is about 100 %, similarly as the decomposed peaks in (a) and (b).

certain point capable to trace the trend of relaxation frequency for the α peaks. Likewise, the graphs of decomposed peaks can also be accurately fitted by using the *N-fitting* method as demonstrated in Figure 6.20(a) and 6.20(b). Primary focus in this discussion is on the characteristic time τ_n values tabulate in Table 6.16. This table lists the results for TSC α peaks of the polymer electrets. Overall, it gives the τ_n within the range of 10^{-4} s to 10^{+1} s for all the experimental α peaks except that of *ENR-50* rubber. From the table, the τ_n is about 2.8 x 10^{-11} s for $\alpha_{ENR\text{-}50}$ (– 25.02 °C) that is around the glass transition temperature T_g at – 25 °C. The comparatively smaller value of τ_n is most likely representing the dipole group relaxations around the T_g. This is reasonable if considering the existence of epoxide side group in *ENR-50* as the source for such relaxations. Since they are also responsible for the high T_g in *ENR-50* compares to the unmodified natural rubbers, such as *SMRL* with the T_g is just about – 64 °C. In general, the characteristic times τ_n of α peaks fall within the range that indicates the cooperative relaxations in polymers. The *N-fitting* method thus far shows that it can be used to fit the experimental data accurately. The calculated τ_n from this procedure in addition remarkably demonstrate the occurrence of dielectric relaxations in cooperative mode, as described by the *WLF* theory.

Table 6.16
The Pre-exponential factor τ_n of *N-Fitting* on some α Peaks

Sample	T_{max} **(°C)** ± 0.01	E_{fitt} **(eV)**	τ_n **(s)** ± 0.01	***P*** **(%)** *
SMRL	-65.48	2.09	2.17E-02	100
DPNR	-67.76	0.10	8.98E-01	90
ENR-50	-62.58	0.60	4.00E+01	94
	-25.02	2.42	2.85E-11	100
PE	-103.55	1.62	7.88E+01	100
pPVC	79.76	0.61	1.41E-04	100

* *P is a population of the fitted data with a deviation ≤ 5% from its counterpart*

Table 6.16: The values of pre-exponential factor, τ_n that is calculated from the *N-fitting* parameters for some α peaks of the studied polymers.

The same fitting method on the decomposed peaks reveals relaxations that may contribute to the cooperative relaxations of α peaks. This assumption is based on their characteristic relaxation time τ_n values in Table 6.12 to 6.15, where the values are comparable to those for dipole group (10^{-10} to 10^{-13} s) and dipole-segmental (10^{-18} to 10^{-25} s) relaxations [6.30]. Hence, it seems that the ability of *N-fitting* method is more than fitting the data from both numerical and experimental data. In fact, the fitting procedure is useful to differentiate the types of relaxation processes that take place behind each TSC peak.

From the tables, it can be suggested that characteristic relaxation time smaller than 10^{-30} s ($\tau_n \leq 10^{-30}$ s) indicates the space charge relaxation. Since decomposed TSC peak with such small characteristic time is normally associated with deep trap inside the polymers. This is due to their high-energy *E* level, which is beyond 3 eV ($E \geq 3$eV). Although the physical meaning for such small characteristic time is still irrelavent, but it suggests the contribution of relaxation process that is in high frequency. This is consistent with the belief that a trapped charge should have high natural frequency f_o, which is also known as an attempt to escape frequency in order to get sufficient energy to escape. This energy is very important for the space charge to overcome the energy barrier of intrinsic trap that is equivalent to the activation energy, *E*.

There are also cases where the characteristic time of space charge is demonstrated by peaks with relatively small energy. For example, Peak 4 in Table 6.12 gives the $\tau_n = 1.4 \times 10^{-33}$ s with the energy *E* is just about 2.2 eV. This is possible since the depth of trap energy can vary from 1 eV up to 3 eV as shown in Figure 6.9. The energy depth depends on various sources, such as the intrinsic structural defects as explained earlier in Section 6.1.2.1 It also involves chemical defects such as the residue of catalyst, solvent and monomer.

6.2.2.2 *OMON* and *Polymer – OMON* Composites

Analyses on the α peaks of polymers via *N-fitting* method add more knowledge regarding the correlations between the origin and nature of certain dielectric relaxation processes. It thus may assist the study on TSC peaks of *polymer-OMON* composites. This is primarily important to understand the variations of energy depth, as shown by some similar peaks in different composites. Therefore, the *N-fitting* technique is also employed on the composites peaks including those for the pristine *OMON*.

Figures 6.23 to 6.28 show the results for *OMON*, *CDPNR*, *CSMRL*, *CENR-50*, *CPE* and *CpPVC* in that order. From these results, the populations *P* parameter in some cases seem less consistence in comparison with those of the pristine polymers. The smallest *P* is about 76 % for the α_{DOP} peak of *CpPVC* composite as listed in Table 6.22. Some of the fitted decomposed data are demonstrated in Figure 6.25(a), 6.25(b), 6.26(II) (b), 6.26(II) (c) and 6.26(II) (d).

Primary focus in this study is to examine the α and ρ peaks of *OMON* as shown in Figure 6.23. The peaks that are believed to have the origin from ODA appear in most cases of the *polymer-OMON* composites plots. These peaks look as if mark the existence of *OMON* particles in the composites. Analysis by means of the *N-fitting* method on the peaks gives a range of characteristic time τ_n that are listed in Table 6.17 to 6.23. They can be related to the dipole group, dipole-segmental and space charge relaxations, as well as the cooperative relaxation mode.

N-fitting on the α and ρ Peaks of *OMON*

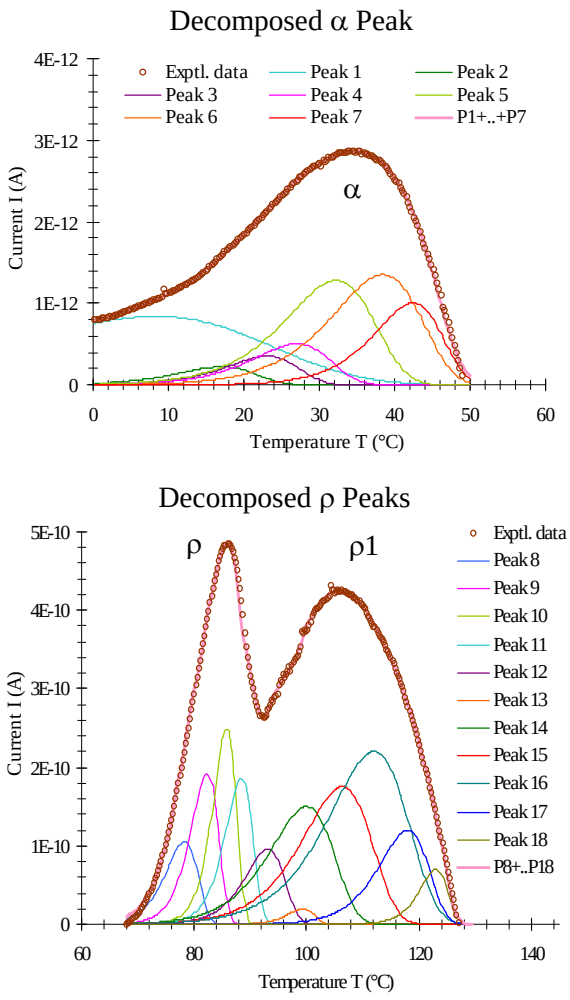

Table 6.17
τ_n of α, ρ and ρ_1 *OMON* Peaks

Peak	T_{max} (°C) ± 0.01*	E_{fitt} (eV)	τ_n (s) ± 0.01**	P (%)
1	8.00	0.40	8.48E-05	100
2	17.00	1.40	4.78E-21	100
3	23.10	1.60	4.42E-23	100
4	27.00	1.50	8.30E-21	100
5	32.20	1.35	6.26E-18	100
6	38.40	1.40	1.30E-17	100
7	42.40	1.90	6.35E-24	100
α	34.87*	0.30	2.24E-01**	93
8	78.25	3.70	2.07E-39	100
9	82.28	4.40	1.59E-45	99
10	85.80	5.40	9.34E-55	97
11	88.40	4.60	6.61E-46	97
12	93.10	3.30	2.79E-31	100
13	99.40	5.20	2.32E-48	100
14	100.00	2.10	2.44E-18	98
15	106.35	2.00	9.64E-17	100
16	112.00	1.80	4.64E-14	100
17	118.00	3.00	9.94E-24	100
18	123.00	5.50	1.62E-45	100
ρ	85.96*	3.45	4.07E-03**	100
ρ1	105.35*	1.02	5.42E-06**	96

* measured ** calculated

P is a population of the fitted data with a deviation ≤5% from its counterpart

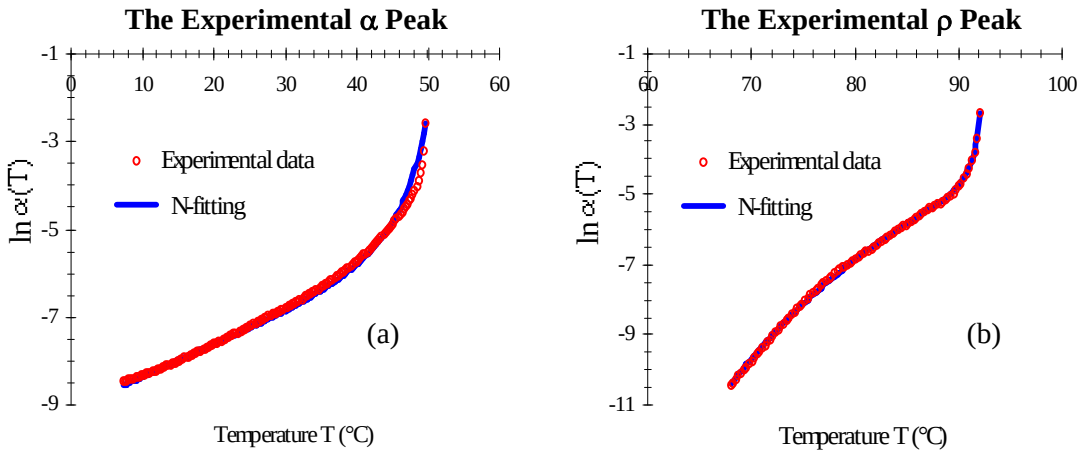

Figure 6.23: Results from *N-fitting* method on the α and ρ peaks of *OMON*, as well as their decomposed peaks in Table 6.17. The fitted experimental data are shown in (a) and (b) for the α and ρ peak respectively.

N-fitting on the α and ρ Peaks of *CDPNR*

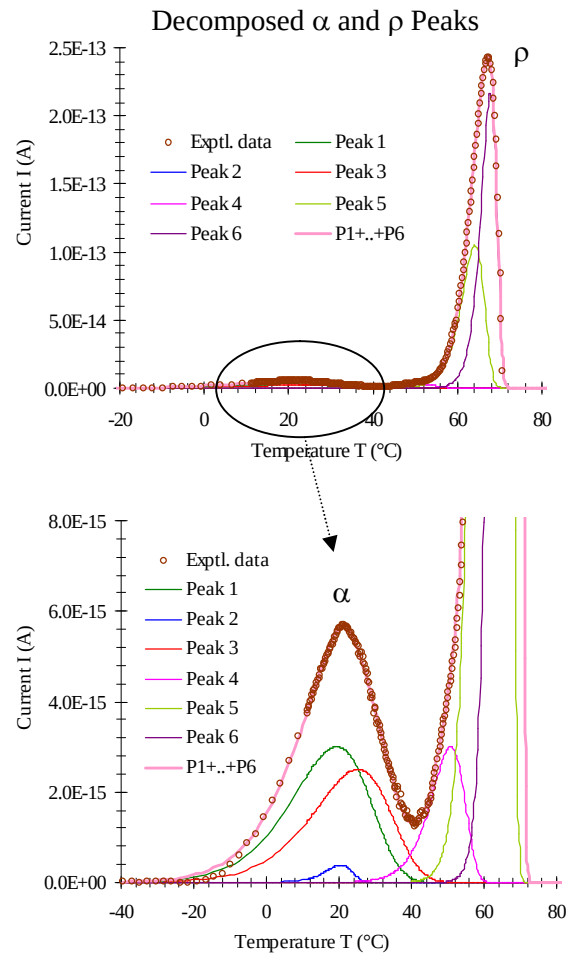

Table 6.18
τ_n of α and ρ *CDPNR* Peaks

Peak	T_{max} (°C) ± 0.01*	E_{fitt} (eV)	τ_n (s) ± 0.01**	P (%)
1	19.30	0.67	3.41E-08	100
2	20.50	2.00	8.53E-30	100
3	25.10	0.70	3.29E-08	100
4	50.80	1.95	2.95E-23	100
5	64.10	3.65	4.76E-42	100
6	67.80	5.40	3.85E-62	100
α	21.43*	0.75	5.24E+00**	100
ρ	67.33*	3.70	1.23E-03**	100

* measured ** calculated

P is a population of the fitted data with a deviation ≤5% from its counterpart

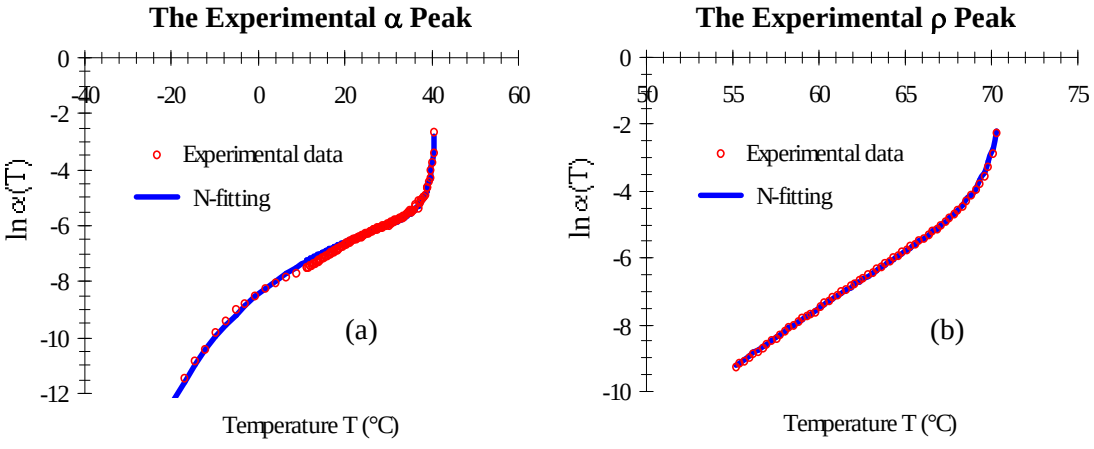

Figure 6.24: The α and ρ peaks of *OMON* can be detected within *CDPNR* plots. Results from the N-fitting method on these peaks, as well as on their decomposed peaks are listed in Table 6.18. The fitted experimental data are shown in (a) and (b) for the α and ρ peak respectively.

N-fitting on the α and ρ Peaks of *CSMRL*

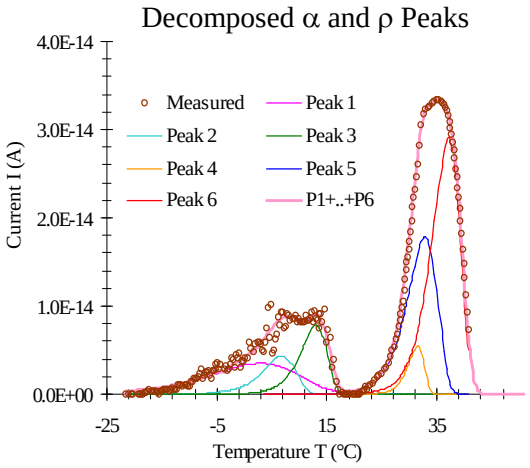

Table 6.19
τ_n of α and ρ *CSMRL* Peaks

Peak	T_{max} (°C) ± 0.01*	E_{fitt} (eV)	τ_n (s) ± 0.01**	P (%)
1	3.00	0.80	1.64E-12	100
2	6.80	2.30	9.98E-39	100
3	13.00	3.00	7.87E-45	99
4	31.30	5.00	9.39E-30	100
5	32.80	3.00	1.35E-25	84
6	37.10	3.30	2.44E-36	99
α	7.58*	0.78	1.13E-01**	99
ρ	34.54*	3.27	1.94E-02**	81

* measured ** calculated

P is a population of the fitted data with a deviation ≤5% from its counterpart

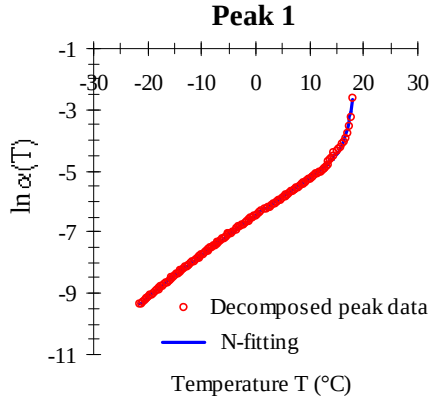

(a)

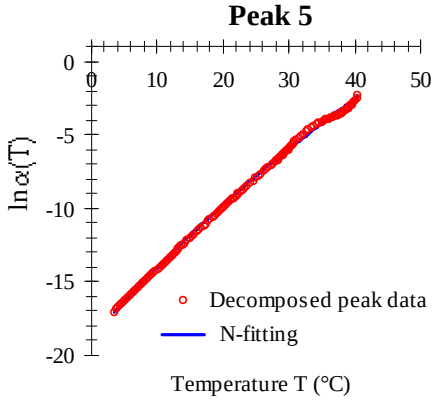

(b)

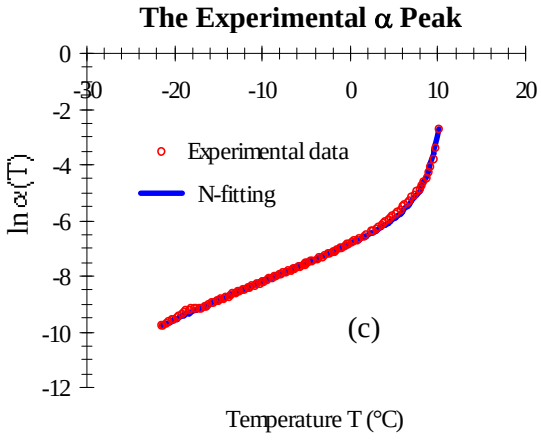

(c)

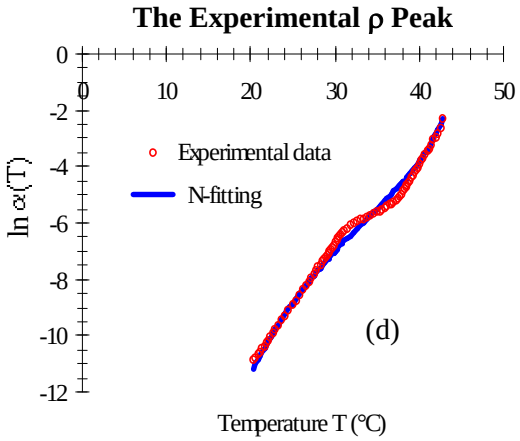

(d)

Figure 6.25: Results from the *N-fitting* method on *OMON* peaks in *CSMRL* plot are listed in Table 6.19, together with their decomposed peaks. The fitted data for decomposed Peak 1 and 5 are shown in (a) and (b) respectively. While those for the experimental α and ρ peaks can be seen in (c) and (e) in that order.

N-fitting on the α and ρ Peaks of *CENR-50*

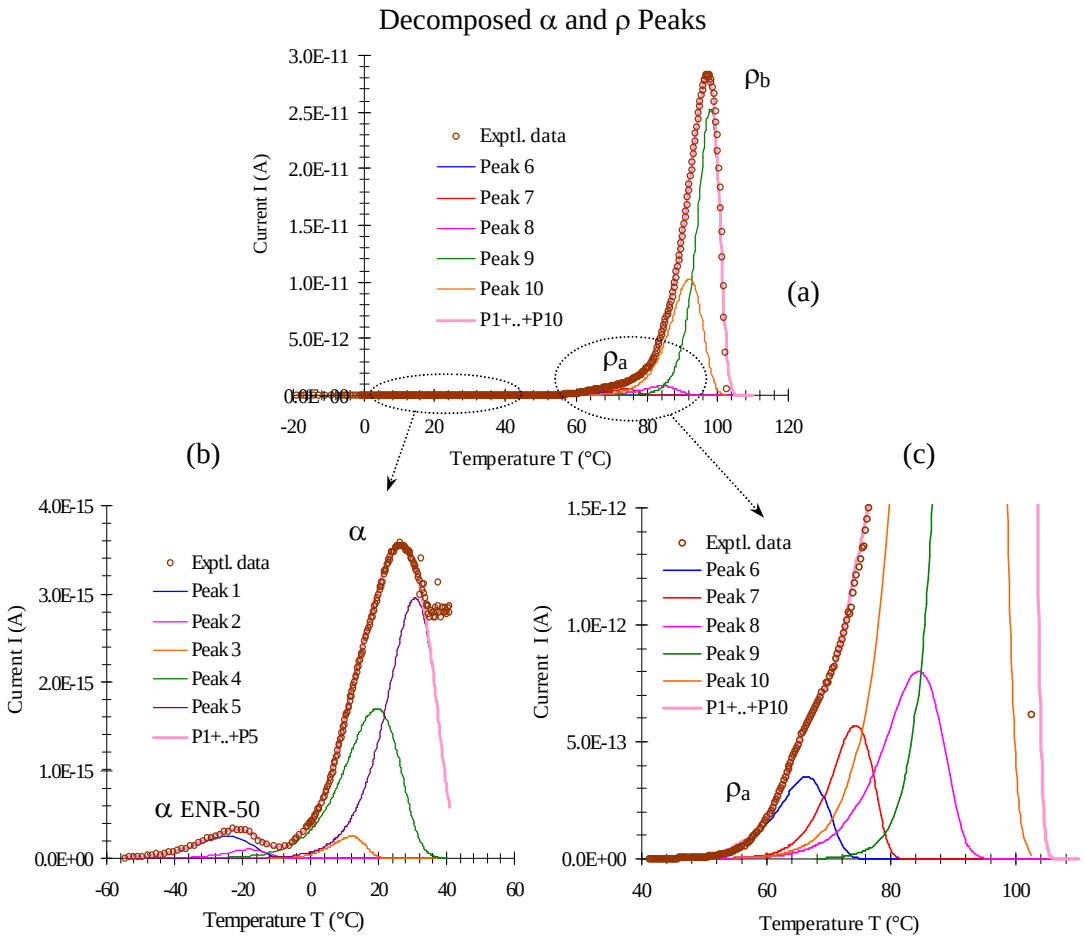

Table 6.20(a)
τ_n of α *CENR-50* Peaks

Peak	T_{max} (°C) ± 0.01*	E_{fitt} (eV)	τ_n (s) ± 0.01**	P (%)
1	-24.30	0.65	2.71E-13	100
2	-18.00	1.00	5.10E-21	100
3	12.00	1.50	2.40E-23	100
4	19.50	0.90	3.75E-12	100
5	30.80	1.10	3.88E-14	100
α ENR-50	-20.48*	0.63	3.29E-12**	100
α	26.55*	0.92	1.05E-02**	100

Table 6.20(b)
τ_n of ρ *CENR-50* Peaks

Peak	T_{max} (°C) ± 0.01*	E_{fitt} (eV)	τ_n (s) ± 0.01**	P (%)
6	66.50	0.65	1.21E-27	100
7	74.30	1.00	4.04E-33	100
8	84.40	1.50	4.49E-22	100
9	92.00	0.90	7.65E-24	100
10	98.00	1.10	1.33E-35	100
ρ_b	97.22*	0.92	1.32E-16**	100

* measured ** calculated

P is a population of the fitted data with a deviation ≤5% from its counterpart

Figure 6.26-I: Beside the α_{ENR-50} peak, the α and ρ peaks of *OMON* can also be detected as shown in (a) and (b). The ρ_b peak in (a) is associated to the exfoliation in *CENR-50*, while the ρ_a peak is believed superimposes with the big ρ_b peak as shown in (c). The *N-fitting* parameters for the α_{ENR-50}, α and ρ_b peaks are listed is Table 6.20(a) and 6.20(b).

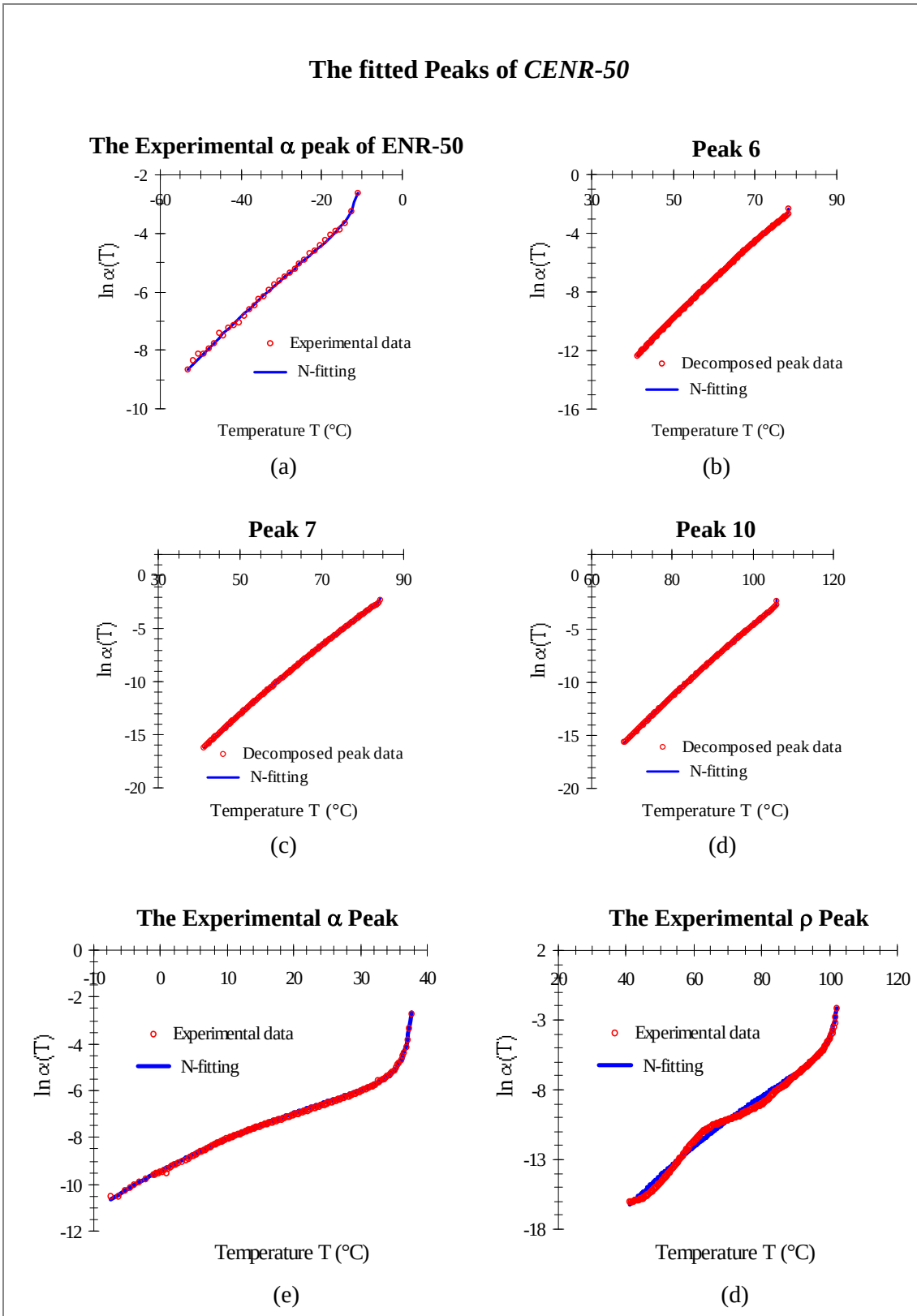

Figure 6.26-II: The plots of frequency-temperature relation from N-fitting technique on the decomposed peaks of *CENR-50*, as well as also on the $\alpha_{ENR-50,}$ α and ρ peaks.

N-fitting on the ρ Peaks of *CPE*

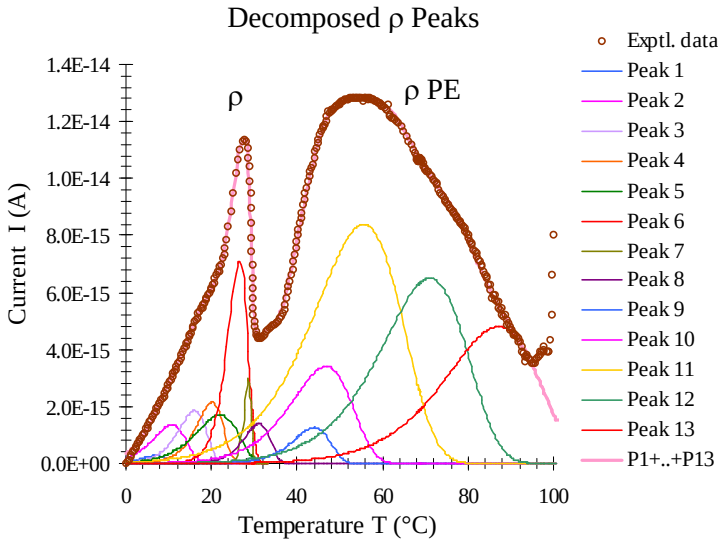

Table 6.21(a)
τ_n of ρ *CPE* Peaks

Peak	T_{max} (°C) ± 0.01*	E_{fitt} (eV)	τ_n (s) ± 0.01**	P (%)
1	7.00	2.60	7.64E-44	100
2	10.70	1.80	4.52E-29	100
3	15.80	2.20	1.22E-34	100
4	20.00	2.60	1.56E-39	100
5	21.00	1.80	1.07E-27	99
6	26.50	3.30	1.99E-48	89
7	28.60	9.50	1.79E-109	100
ρ	27.66*	3.28	3.60E-02**	86

Table 6.21(a)
τ_n of ρ_{PE} *CPE* Peaks

Peak	T_{max} (°C) ± 0.01*	E_{fitt} (eV)	τ_n (s) ± 0.01**	P (%)
8	31.10	2.60	6.06E-37	82
9	44.00	2.00	2.25E-25	100
10	46.70	1.22	3.39E-14	100
11	55.50	0.88	6.31E-09	96
12	71.00	1.00	8.58E-09	97
13	87.00	1.00	1.44E-07	98
ρ PE	54.07*	0.92	3.25E+02**	96

* measured ** calculated

P is a population of the fitted data with a deviation ≤ 5% from its counterpart

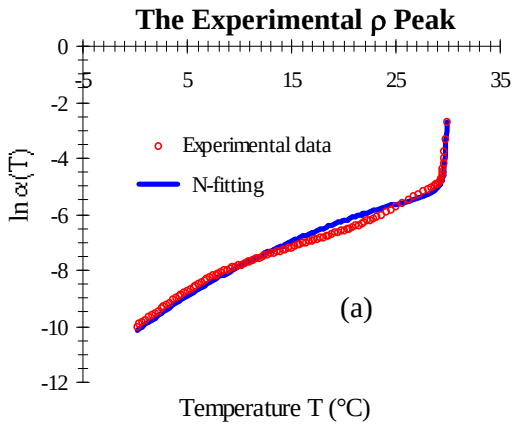

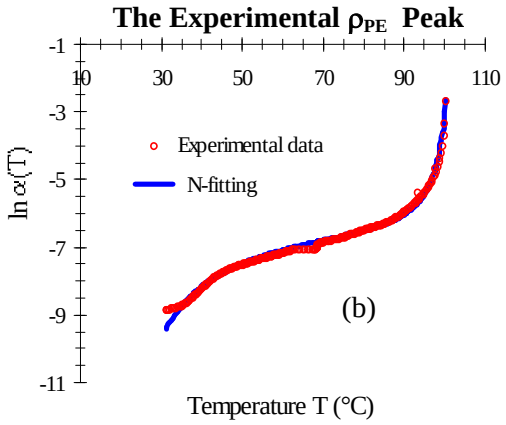

Figure 6.27: Only the ρ peak of *OMON* can be detected within *CPE* plot, which appears prior to the ρ_{PE} peak. Fitting parameters for these peaks and their decomposed peaks are listed in Table 6.21a and 6.21b. The fitted experimental data for the ρ and ρ_{PE} peaks are shown in (a) and (b) respectively.

N-fitting on the α and ρ Peaks of *CpPVC*

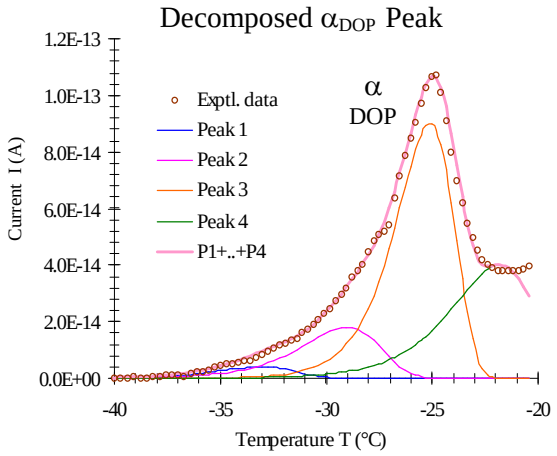

Table 6.22(a)
τ_n of α_{DOP} *CpPVC* Peaks

Peak	T_{max} (°C) ± 0.01*	E_{fitt} (eV)	τ_n (s) ± 0.01**	*P* (%)
1	-33.00	2.80	3.51E-32	100
2	-29.00	2.80	1.85E-30	100
3	-25.10	3.90	6.00E-39	100
4	-21.80	2.80	1.90E-63	98
α DOP	-24.81*	0.69	1.05E-24**	76

* measured ** calculated

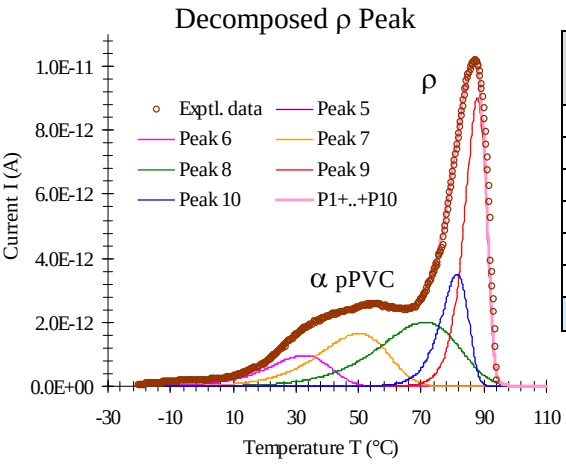

Table 6.22(b)
τ_n of ρ *CpPVC* Peaks

Peak	T_{max} (°C) ± 0.01*	E_{fitt} (eV)	τ_n (s) ± 0.01**	*P* (%)
5	-4.50	0.62	5.75E-10	95
6	32.50	0.80	5.35E-10	99
7	50.00	0.80	4.99E-08	100
8	71.00	0.78	5.01E-06	99
9	81.50	2.50	5.61E-25	100
10	88.00	3.30	2.69E-32	100
ρ	87.00*	0.64	4.39E-17**	100

* measured ** calculated

P is a population of the fitted data with a deviation ≤5% from its counterpart

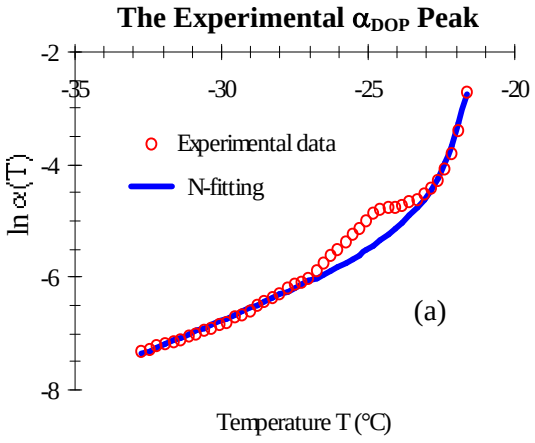

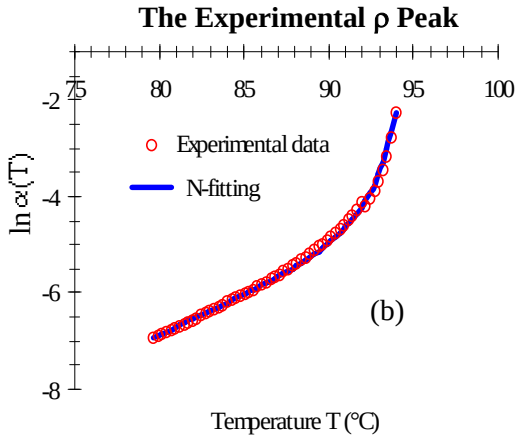

Figure 6.28: Similarly as in *CPE*, only the ρ peak of *OMON* can be detected within C*pPVC* plot. While the appearance of α_{DOP} and α_{pPVC} peaks represent *pPVC* component in the composite. The *N-Fitting* parameters for α_{DOP} and ρ peaks are listed in Table 6.22a and 6.22b in that order. The frequency-temperature plots in (a) and (b) show the fitted data in for the α_{DOP} and ρ peaks respectively.

Table 6.23
The Results of N-fitting on the α and ρ Peaks of *OMON*

Sample	*Peak*	T_{max} (°C) ± 0.01	*E fitt* (eV)	τ_n (s) ± 0.01	*Peak*	T_{max} (°C) ± 0.01	*E fitt* (eV)	τ_n (s) ± 0.01
OMON	α	34.87	0.30	2.24E-01	ρ	85.96	3.45	4.07E-03
	1	8.00	0.40	8.48E-05	8	78.25	3.70	2.07E-39
	2	17.00	1.40	4.78E-21	9	82.28	4.40	1.59E-45
	3	23.10	1.60	4.42E-23	10	85.80	5.40	9.34E-55
	4	27.00	1.50	8.30E-21	11	88.40	4.60	6.61E-46
	5	32.20	1.35	6.26E-18				
	6	38.40	1.40	1.30E-17				
	7	42.40	1.90	6.35E-24				
CDPNR	α	21.43	0.75	5.24E+00	ρ	67.33	3.70	1.23E-03
	1	19.30	0.67	3.41E-08	4	50.80	1.95	2.95E-23
	2	20.50	2.00	8.53E-30	5	64.10	3.65	4.76E-42
	3	25.10	0.70	3.29E-08	6	67.80	5.40	3.85E-62
CSMRL	α	7.58	0.78	1.13E-01	ρ	34.54	3.27	1.94E-02
	1	3.00	0.80	1.64E-12	4	31.30	5.00	9.39E-30
	2	6.80	2.30	9.98E-39	5	32.80	3.00	1.35E-25
	3	13.00	3.00	7.87E-45	6	37.10	3.30	2.44E-36
CER-50	α	26.55	0.92	1.05E-02	ρ_a	superposition		
	3	12.00	1.50	2.40E-23	6	66.50	2.50	1.21E-27
	4	19.50	0.90	3.75E-12	7	74.30	3.10	4.04E-33
	5	30.80	1.10	3.88E-14				
	α				ρ_b	97.22	1.62	1.32E-16
					9	92.00	2.55	7.65E-24
					10	98.00	3.80	1.33E-35
CPE	α				ρ	27.66	3.28	3.60E-02
					5	21.00	1.80	1.07E-27
					6	26.50	3.30	1.99E-48
					7	28.60	9.50	1.79E-109
CpPVC	α				ρ	87.00	0.64	4.39E-17
					9	81.50	2.50	5.61E-25
					10	88.00	3.30	2.69E-32

experimental α *OMON* □ experimental ρ *OMON* □ deep trap peak [xx]

Table 6.23 lists the relaxation times τ_n from *N fitting* technique on the α and ρ peaks of *OMON* and their decomposed peaks. It also involves similar peaks that can be detected within the TSC plots of *polymer-OMON* composites.

6.2.2.2.A The ρ Peak Relaxation

Even though the ρ peak of *OMON* consistently appears within *polymer-OMON* composites plots, but the activation energy *E* varies each case of the *OMON* composites. Likewise, the variation in energy *E* is seen for the decomposed ρ peaks. Similar trend is also detected on the characteristic time τ_n values in Table 6.23, which are within the range of 10^{-2} to 10^{-17} s. From these values, it looks like the ρ peak of *OMON*, *CDPNR*, *CSMRL* and *CPE* has the cooperative relaxation mode with their τ_n is in the range of 10^{-2} to 10^{-3} s. While the τ_n around 10^{-16} to 10^{-17} s for the ρ peaks of *CpPVC* and *CENR-50* (ρ_b) perhaps indicates the dipole-segmental relaxation. These observation are analogous to different effects caused by polar and non-polar polymers matrix, for example the polarity of polymeric chains that is recognized to influence the degree of intercalation within *polymer-OMON* composites. In Chapter 4 earlier, analysis carried out on the XRD results revealed that non-polar polymers were less intercalated compared to the polar polymers, as shown in Table 4.3. The results tell that less interaction took place between the matrix chains of non-polar polymers and alkyl chains inside *OMON* gallery.

The same reason is supposed responsible for the trend develops by the characteristic times τ_n of ρ peaks in the non-polar polymer composites. Intermolecular reactions among alkyl chains within *OMON* gallery as pictured in Figure 6.29(a) generate cooperative relaxation during depolarization processes. The lack of matrix-alkyl chains interactions within the non-polar composites preserves the interchains reactions of alkyl chains on *ODA* cations (*octadecylammonium*). In that way, alkyl chains in these composites were able to maintain their cooperative relaxations for the ρ peak as in *OMON*. Figure 6.29(b) gives the graphical illustration of such effect within *CSMRL* and *CDPNR* composites, which is due to matrix-alkyl chains entanglement. Figure 6.29(c) illustrates similar effects caused by matrix-alkyl chains coiling within *CPE*. This suggestion is supported by the energy *E* from decomposed

Peak 6 of *CDPNR*, Peak 4 of *CSMRL*, Peak 7 of *CPE* and most of decomposed ρ peaks from *OMON*. The energies that are in the range of 4 eV to 9.5 eV indicate the formation of *molecular-ion* deep traps due to charge injections. They also depend on the intermolecular condition of *ODA* cations, which serve as potential site for the creation of such deep trap. The signs of *molecular-ion* existence in the non-polar polymer composites add more proof that matrix-alkyl chain interactions in the composites give less effect on the intermolecular reactions of alkyl chains, as well as on the *ammonium* cations.

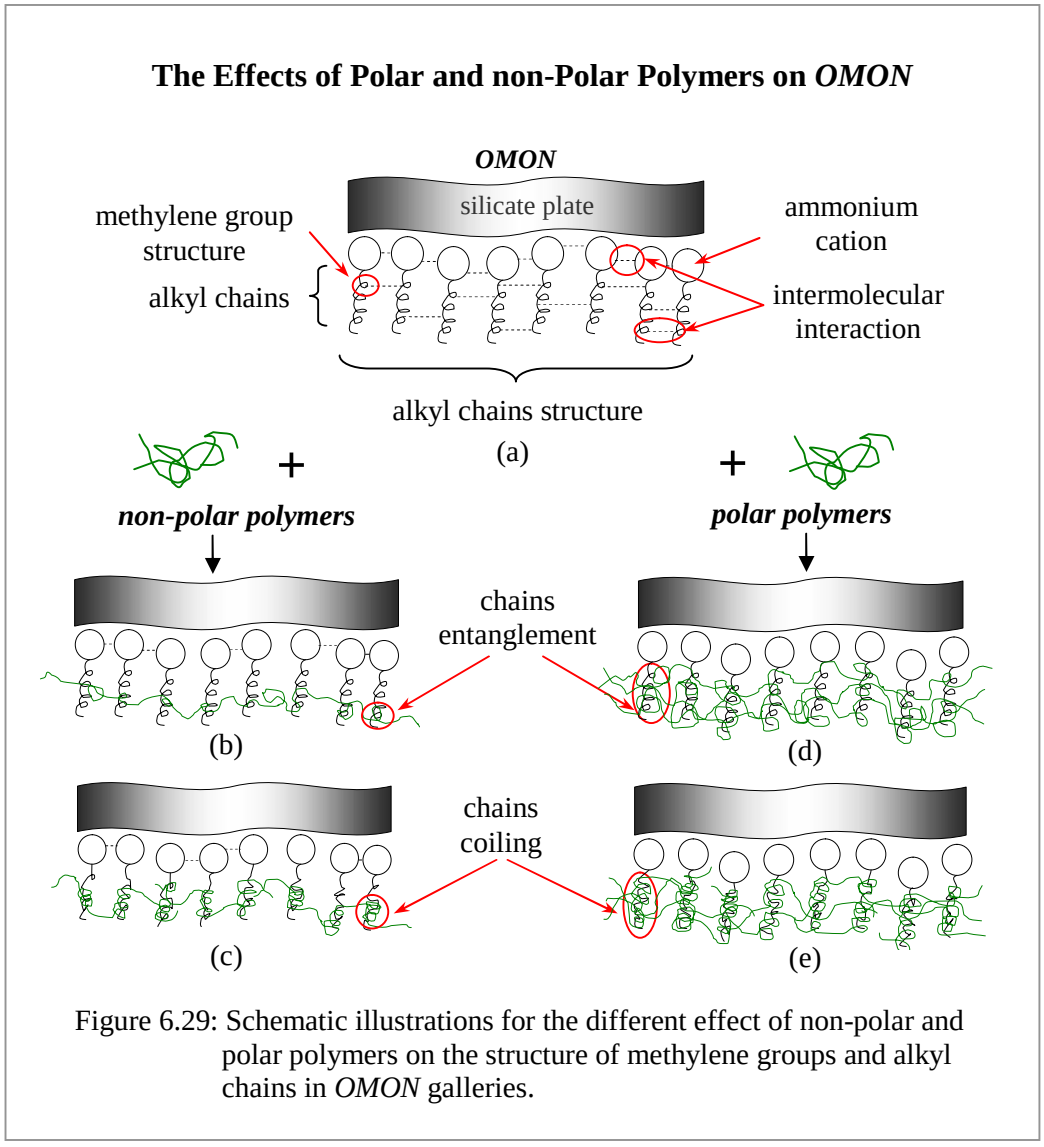

Figure 6.29: Schematic illustrations for the different effect of non-polar and polar polymers on the structure of methylene groups and alkyl chains in *OMON* galleries.

From Table 6.23, decomposed ρ peak with the deep trap energy however is absent in case of *CENR-50* and *CpPVC* composites. Extensive matrix-alkyl chains interaction in the polar

polymer composites interrupted the intermolecular reaction of *ODA* cations. As a result, it disturbs the potential of *molecular-ion* formation for the deep traps in the composites. This is probably explains the lack of decomposed ρ peak with high-energy *E*. Figure 6.29(d) illustrates the effect of extensive interaction by chains entanglement inside the *CENR-50* composite. While similar effect in case of *CpPVC*, which is due to extensive chain coiling is illustrated in Figure 6.29(e). Such interruptions on the structure of *ODA* cations can also restrict the alkyl chains from moving cooperatively. In that way, the motion of alkyl chains become distinct and subsequently induces the combination of segmental and dipole group relaxations. Therefore, the τ_n of experimental *OMON* ρ peak for *CpPVC* and *CENR-50* (ρ_b) is believed indicating the dipole-segmental relaxation of alkyl chains.

6.2.2.2.B The α Peak Relaxation

Another interesting thermal feature that attracts attention in this study is the α peak. Even though its appearance within the TSC plots of *polymer-OMON* composites is inconsistent. Table 6.23 lists the peak that can be found within the plot of *OMON* and natural rubbers composites. While in case of *CPE* and *CpPVC* the α peak is hardly detected. This observes highlight the effects of alkyl chains reactions with different types of polymers. It has been suggested in Chapter 4 that the physical characteristics of polymer matrix can influence the mode of matrix-alkyl chain interaction. Such as crosslinking within natural rubbers induces chain entanglement in the elastomer reactions with alkyl chains. Chain coiling on the other hand was viewed as the mode of interaction between the alkyl tails and polymeric chains. These ideas were based on the *FTIR* analyses in Section 4.3.2, which revealed the effect of chains coiling within the *CPE* and *CpPVC* spectra. They are the shifted band of methylene asymmetry stretching mode ($\nu_{as}CH_2$), and the lost band of rocking vibration on methylene chain ($\rho(CH_2)_n$). The findings indicate structural modifications on the methylene groups of alkyl chains inside *OMON* gallery.

Besides the alkyl chains structure, schematic diagram in Figure 6.29(a) also illustrates the structure of methylene groups on these chains inside *OMON*. Perhaps, such structure play a role behind the cooperative relaxation of α peak with the τ_n in Table 6.23 is around 10^{-5} s. Entanglement within the matrix-alkyl chains interaction as shown in Figure 6.29(b) and (d) gives insignificant effects on the methylene structures. As a result, the methylene groups in *natural rubber-OMON* composites preserved their original structures as in pristine *OMON*. This probably explains the appearance of *OMON* α peaks, where their τ_n within the range of 10^0 to 10^{-4} s also indicate the cooperative relaxation mode.

Chains coiling as illustrated in Figure 6.30(c) and 6.30(e) however promote better matrix-alkyl chains reaction within *CPE* and *CpPVC* composites. Previously in Section 4.2.3.2, the strong interaction from chains coiling was proven with the increased layer of *OMON* silicates in these composites. Such interaction however restricts the motion of methylene groups, which then affect their responses towards polarization field F_p. This condition thus can lead to the lost of α peak within the *CPE* and *CpPVC* plots.

6.2.2.2.C Partial Relaxation

Localized motion of alkyl chains and methylene groups are believed responsible for partial relaxations throughout depolarization processes. Decomposed peaks in Table 6.23 are most likely representing the localized relaxations, which responsible for the appearance of TSC peaks. Consider the case of non-polar polymer composites in the table, where *CSMRL* and *CDPNR* demonstrate a pair of α and ρ peaks. While in case of *CPE*, only the ρ peak can be detected. It is also important to highlight that decomposed α peaks within the table involve relatively small energy *E* compare to those of decomposed ρ peaks. The energy variations indicate that different set of partial relaxations contribute to the α and ρ peaks emergences. Each set demonstrates the combination of localized dipole group, dipole-segmental, space

charge and also cooperative relaxations depending on their τ_n values. For that reason, it is possible for the ρ peak to appear alone as it arises from partial relaxations that are related to alkyl chains on *ODA* cations. The α peak on the other hand is related to the relaxations of methylene groups on these alkyl chains.

I. Decomposed ρ Peak

Generally, each ρ peak within both polar and non-polar polymer composites in Table 6.23 seems to contain at least a pair of decomposed peaks. The characteristic relaxation time τ_n of these peaks which are within the range of 10^{-23} s to 10^{-48} s demonstrate a coupled of segmental–space charge relaxations. The decomposed ρ peaks of *OMON* however show relatively small characteristic times, with their τ_n are in the range of 10^{-37} to 10^{-55} s. These peaks indicate partial relaxations due to the release of localized space charges. They come from molecular-ion deep traps within the structure of *ODA* cations as illustrated in Figure 6.30(a). Matrix-alkyl chains interaction in *OMON* interlayer can interrupt such structure as shown in Figure 6.30(b) and 6.30(c). The interruptions therefore distanced the alkyl chains, where it also ruined the intermolecular interactions of methylene groups within crystalline structure as discussed earlier in Section 5.2.2. This condition as a result promoted partial dipole-segmental relaxations. Previously in Section 6.2.2.2.A it has been suggested that the interruption also reduced the number of deep trap formation. However, matrix-alkyl chains reactions generated intrinsic defects, which then created new charge traps at the interaction sites. For example, the entanglement and coiling points in Figure 6.30(b) and 6.30(c). This belief is consistent with some of the decomposed ρ peaks in Table 6.18 to 6.22, where their characteristic time τ_n ($<10^{-30}$ s) and energy E (< 4eV) indicate that they were generated by partial space charge relaxations.

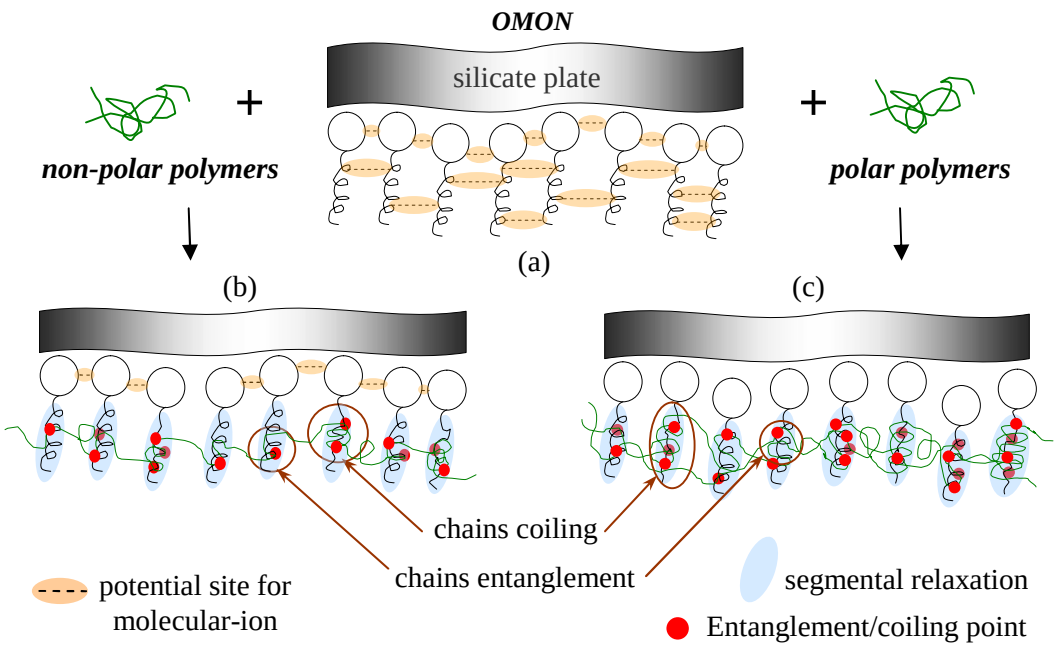

Figure 6.30: Graphical illustration in (a) shows the potential sites for molecular-ion formation in *OMON* , which are the source for localize space charge relaxation. Interaction with non-polar and polar polymeric chains as shown in (b) and (c) can induce partial segmental relaxations and localize space charge relaxations from intrinsic defects at the entanglement/coiling points.

II. Decomposed ρ Peak - Exfoliation

Analyses on *CENR-50* suggest that the presence of ρ_a peak is superimposed by a relatively bigger peak that arises around it. However, the maximum temperature T_{max} of this peak can be traced by means of the decomposed peaks. From Figure 6.26-I(c), the T_{max} for the peak is estimated to be around 74 °C. Therefore, this is one good case to illustrate the advantage of applying the decomposition method on experimental peaks. There is also a prominent ρ_b peak around 97.22 °C in Figure 6.26-II(a), which probably appears alone as those of *CPE* and *CpPVC*. This ρ_b peak is most likely signifying the exfoliation component that can be found only in case of *CENR-50*. Schematic illustration in Figure 6.31 shows the extensive entanglements by matrix-alkyl chains interaction in the exfoliated *OMON*. The extensive

interactions perhaps restrict the polarization of methylene group, which then responsible for the lost of α_b peak. Similarly as in *CpPVC* and *CPE*, this belief is supported by the shifted band of methylene asymmetry stretching vibration ($\nu_{as}CH_2$) in *CENR-50* spectrum. The shifted band indicates the increased ratio of gauche conformation, which proves the changes in the original structures of methylene groups.

The Sources of Partial Relaxations from the Exfoliated Layer of *OMON*

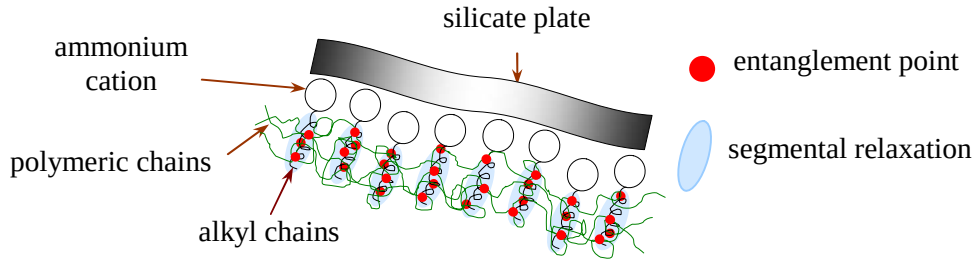

Figure 6.31: Schematic diagram for the exfoliated layer of *OMON* silicates shows the source for partial segmental dipole and space charge relaxations. The charge release may come from intrinsic defects at the entanglement points.

III. Decomposed α Peak

Figure 6.32(a) shows the illustration for methylene group structure in *OMON* gallery. Such structure perhaps contributes to localized motions that are mostly in segmental mode. By that means the characteristic time τ_n of decomposed α peaks in Table 6.23 indicate partial segmental relaxation, where are in the range of 10^{-17} s to 10^{-24} s. It has been highlighted that the restriction on methylene group motions is suppose to responsible for the lost of α peaks within *CPE* and *CpPVC* plots. These observe possibly demonstrate the outcome of chains coiling in matrix-alkyl chains reaction as shown in Figure 6.32(b). The restriction which is induced by chain coiling in effect reduce the potential for partial relaxations by methylene groups, which then contribute to the missing α peaks. A schematic diagram in Figure 6.32(c) illustrates the entanglements in matrix-alkyl chains reactions for natural

rubber composites. Chain-chain interactions in this case allow the methylene groups to be polarized, which then lead to partial relaxations as in *OMON*. This is shown by the τ_n of decomposed *OMON* α peaks in Table 6.23. From the τ_n values, it can be imagined that chains entanglements also generate structural changes, which can induce additional partial relaxations. For example, the entanglement points in Figure 6.32(c) that can act as charge traps [6.2 and 6.19]. Such trap contributes to localized space charge relaxations inside the rubber composites as shown by their characteristic times τ_n, which are within the range of 10^{-30} to 10^{-45} s. While some polarized methylene groups that are close to the entanglement points can stimulate localized dipole group relaxations. From Table 6.23, the τ_n for these partial relaxations are around 10^{-12} to 10^{-14} s.

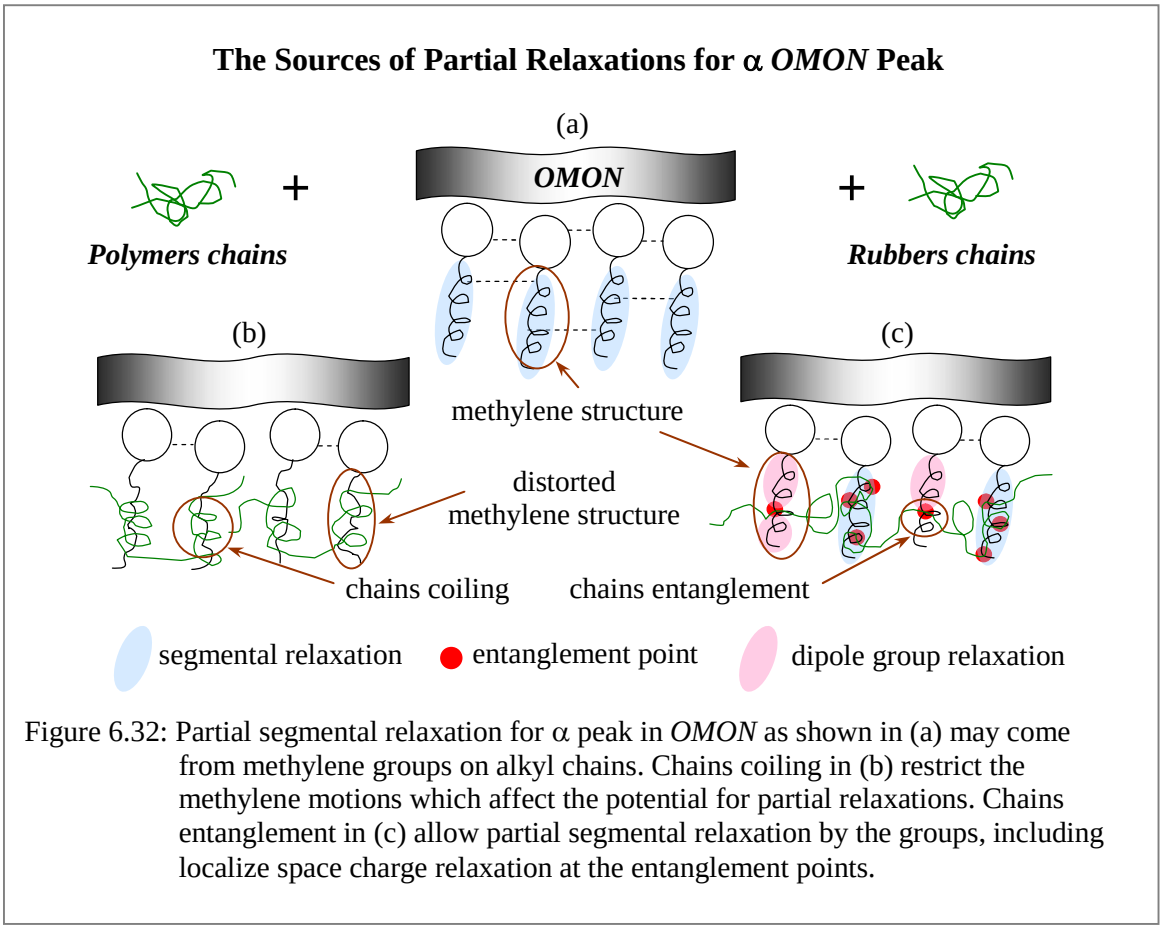

Figure 6.32: Partial segmental relaxation for α peak in *OMON* as shown in (a) may come from methylene groups on alkyl chains. Chains coiling in (b) restrict the methylene motions which affect the potential for partial relaxations. Chains entanglement in (c) allow partial segmental relaxation by the groups, including localize space charge relaxation at the entanglement points.

6.2.2.2.D Discussion

The results obtained from the *N-fitting* procedure indicate that experimental peaks in this study overall demonstrate the cooperative relaxation mode, except for a few peaks which indicate dipole-segmental relaxations as shown in Table 6.23. These observations appear to contradict with previous prediction in Chapter 5. From preliminary analyses on TSC peaks within this chapter, it was believed that ρ peak indicates space charge relaxation processes. This is however consistent with the results of *N-fitting* method on several decomposed ρ peaks. Even though the experimental TSC peaks demonstrate either cooperative or dipole segmental relaxation, a number of characteristic time τ_n from their decomposed peaks on the other hand indicate the space charges relaxation mode.

N-fitting technique thus far generates results that bring another perspective on the dielectric relaxation processes of polymeric materials. Practically, it could be describing the actual situation in a major depolarization process. It can be imagined that various types of partial relaxations can take place concurrently with the process, which involves the motions of the whole molecular structure. Localized motions from different sources within the structure on the other hand induce these partial relaxations, which are also responsible for the major relaxation process. For that reason, the characteristic relaxation time τ_n of experimental peaks are believed to illustrate the way of polarized structure respond in consequence to adequate energy supply. While the τ_n from decomposed peaks appears to characterize the relaxation processes of some localized mass within the primary structure. In this work, the experimental and decomposed α peaks are related to methylene groups. While those for ρ peaks are associated with the alkyl chains on *ODA* cations.

Perhaps, previous TSC studies on *PVC* by some researchers can be used for comparison. It is to be noted here that in plasticized *PVC* (*pPVC*) polymer the original features of *PVC* chains remain significant, even though the plasticizer molecules had affected its physical

characteristic. Typical peaks for the *PVC* chains as a result can be detected within the TSC plot of *pPVC*. Therefore, results from previous studies on *PVC* polymers by some authors are used for comparison, as summarized in Table 6.24 (a) and (b).

Some Results from Analyses on the TSC Peaks of PVC and pPVC

Table 6.24(a)
VTF Fitting by Doulache

Peak	T_{max} (°C)	E_{fitt} (eV)	τ_o (s)	*Note*
1	45	1.07	9.37E-16	Arrhenius
2	55	1.25	3.92E-18	
3	65	1.39	6.53E-20	
4	75	1.91	1.02E-16	
5	85	2.24	6.92E-31	
6	95	1.28	3.90E-16	
7	105		3.80E-01	VTF
8	115		4.70E-01	
9	125		1.03E+01	
10	135		1.28E+01	

Table 6.24(b)
Interation Method by Migahed

Peak	T_{max} (°C)	E_{fitt} (eV)	τ_o (s)	*Note*
1	72	1.26	1.41E-17	Iterative method
2	74	1.27	1.00E-17	
3	78	1.53	2.93E-21	
4	84	1.58	1.00E-21	
5	88	2.01	1.00E-28	
6	90	2.03	5.12E-28	
7	92	1.99	3.70E-27	
8	92	1.92	3.12E-26	
9	106	1.12	7.74E-14	

Table 6.24(c)
N-Fitting on the α and ρ Peaks of *pPVC*

Peak	T_{max} (°C) ± 0.01*	E_{fitt} (eV)	τ_n (s) ± 0.01**	Note
1	25.50	0.90	**7.48E-12**	dipole
2	41.00	1.00	**4.93E-12**	
3	53.00	1.25	**6.66E-14**	dipole-segmental
4	63.00	1.60	**2.48E-17**	
5	70.90	1.50	**2.91E-15**	
6	80.00	1.85	**3.44E-18**	segmental
7	88.40	2.00	**7.43E-19**	
8	97.00	3.00	**7.17E-28**	
9	100.70	4.80	**4.36E-45**	space charge
α	79.76*	0.61	**1.41E-04****	cooperative
10	108.00	4.00	**1.79E-35**	space charge
11	114.20	4.20	**4.98E-36**	
12	119.30	4.50	**1.11E-37**	
13	124.00	5.00	**6.65E-41**	
ρ	123.89*	2.28	**6.09E-20****	segmental

* measured ** calculated

Table 6.24: Results from some previous authors on the decomposed peaks of *PVC*. Table 6.24(a) lists the characteristic time τ_o obtained by Doulache using the Arrhenius and *VTF* theory [6.12]. While Table 6.24(b) comes from Migahed works on the iteration method [6.32]. These results are comparable to those in Table 6.24(c) which are the results from *N-fitting* method.

It is generally accepted that space charges can be initiated to neutralization by extensive movements in an electrets. The high mobility of charges that is induced by thermal energy is experienced by large parts of polymeric chains during the phase transitions at a T_g. The chains movements as a result promote space charge relaxations that generate a ρ peak, next to the α peak within TSC thermogram. However, Doulache's works by means of the *WLF* / *VTF* theory revealed characteristic time τ_o that are in the range of 3.8×10^{-1} s to $1.3 \times 10^{+1}$ s. These τ_o values from decomposed α and ρ peaks as are listed in Table 6.24(a) indicate the cooperative relaxation mode. In that case, they believed that the τ_o for ρ peaks was actually generated by dipolar relaxations instead of space charge relaxations. Based on this idea, they claimed that the τ_o signifies the liquid-liquid transition processes within *PVC* electrets. According to Boyer, such transition process can take place in polymers at a temperature above the T_g which he estimated to be about $(1.20 \pm 0.05)T_g$ [6.12].

On the other hand, Migahed and his group [6.38] work on *PVC* polymer managed to show the existence of dipolar relaxation by means of iteration method. The idea was based on the characteristic time τ_o of decomposed peaks in Table 6.24(b), which are within the range of 10^{-14} s to 10^{-28} s. They believed that the effect from dipole-dipole interactions had affected the mode of relaxation process within *PVC* electret [6.30, 6.38 and 6.39]. Such interactions as a result induced dipole-segmental relaxations as shown by the characteristic times τ_o in the table.

Table 6.24(c) tabulates the characteristic relaxation time, τ_n for *pPVC* using the *N-fitting* method, which was discussed in details all through Section 6.2.2. From these discussions, the advantage of *N-fitting* was recognized as it is able to fit the experimental data of TSC peaks. This fitting method also managed to confirm the *WLF* theory on the *pPVC* electrets, where the τ_n of experimental α peak in the table reveals the cooperative relaxation mode.

Decomposed α and ρ peaks on the other hand give a range of characteristic times τ_n which are in the range of 10^{-12} s to 10^{-45} s. Comparison with the growths in maximum temperature T_{max} of decomposed peaks suggests that the trend developed by the τ_n is comparable with the thermal energy transfer within the electrets. These partial characteristic times seems to evolve from dipole to dipole-segmental, segmental and lastly space charge relaxation. The characteristic time of dipole-segmental are shown by the τ_n of Peak 3, Peak 4 and Peak 5 around 10^{-14} s to 10^{-17} s in the table. This range is analogous to the characteristic time τ_n in Section 6.2.2.2.A (10^{-16} to 10^{-17} s) that suggests the dipole-segmental relaxation mode for *OMON* ρ peak. In addition, the τ_n prove the occurrence of dipole-dipole interactions as proposed by Migahed and co-authors [6.30]. The τ_n of Peak 6, Peak 7, Peak 8 and Peak 9 around 10^{-18} s to 10^{-28} s reveal segmental relaxations, which dominate the depolarization processes during glass-rubber transition T_g in *pPVC* electret. The movements of segmental chains in the polymer induced this mode of relaxation. Similarly, such movement by alkyl chains responsible for the localized segmental relaxation of decomposed *OMON* α peaks. These peaks with their characteristic time, τ_n is around 10^{-17} s to 10^{-24} s were discussed at length in Section 6.2.2.2.C.

Previous works by Doulache and his group [6.12] on *PVC* proved the existence of sub-T_g relaxation mode at temperature *T* around 55 °C. In that case, the polymeric chains of *PVC* were thought to start moving progressively at the sub-T_g towards its phase transition at the T_g. This belief is consistent by the τ_n from Peak 3 (53 °C) and Peak 4 (63 °C) in this work, where their T_{max} are within similar temperature region. The dipole-segmental relaxation mode as indicated by the τ_n of these peaks therefore indicate that segmental chains were initiated around the sub-T_g to move together with the dipole groups on the *pPVC* backbone.

The basis behind the *WLF* theory emphasizes the cooperative movement around and above a glass transition temperature, T_g, and for the *pPVC* it was about 80 °C. The experimental ρ peak with the T_{max} about 123.89 °C in Table 6.24(c) however does not seem to confirm the theory. This ρ peak with its τ_n is around 10^{-20} s on the other hand demonstrates segmental relaxation mode on the whole structure of *pPVC*.

According to Frankel [6.12], the intermolecular segment-segment interactions in a material create three dimensional, 3D physical networks. These networks in consequence can melt at the liquid-liquid transition temperature, T_{ll} when the material is heated to a state where the entire macromolecule could move. It means that segmental motions from segment-segment interactions either within a chain or with the neighboring counterparts dominate the state transition process. Therefore, it appears that the ρ peak is actually demonstrating the effects of liquid-liquid transition process. It involves extensive segmental motions and thereby induced the major relaxation on the whole structure. The segmental movements and disruption of 3D network structures promote localized space charge relaxations, which take place simultaneously with the main relaxation. This is demonstrated by the τ_n from decomposed Peak 10, 11, 12 and 13 in Table 6.24(c), which are within the range of 10^{-35} s to 10^{-41} s. It thus proved the generally accepted belief that space charges release plays a role behind the emergence of ρ peak.

Right through this analysis, the inconsistency of T_{max} from *OMON* peaks within the TSC plots for *polymer-OMON* composites can be understood. The variation shows that diverse effects may arise from reactions by different polymeric chains with the alkyl tails. It also depends on the chains thermal features, as well as the degree of intercalation involved in the composites. From XRD analysis for example, polyisoprene chains within *CDPNR* were recognized as less intercalate compared to those in *CSMRL*. The lack of matrix-alkyl chain

interactions thus explains the α and ρ *OMON* peaks in *CSMRL* (7 °C to 35 °C) plot, which appear at relatively lower temperature than those in *CDPNR* (20 °C to 70 °C).

On the other hand, even though *CSMRL* was less intercalated than *CpPVC* however, the T_{max} for *OMON* peaks in *CSMRL* plot are much lower than those of *CpPVC*. Therefore, it is believed that thermal feature of polymeric chains had a role in this case. The motions of rigid *PVC* chains were initiated at higher temperature than the flexible polyisoprene within the *CSMRL*. The ρ peak of *OMON* as a result appeared at higher temperature around 87 °C within *CpPVC* plot compare to those of *CSMRL* about 35 °C. This observation thus, proves the interactions between alkyl chains on *ODA* cations with the polymer matrix of *polymer-OMON* composites. More evidence is demonstrated by the variation of activation energy *E* from decomposed *OMON* peaks. The energy variations actually indicate the differences in reactions by various polymers with the alkyl chains. As a result, various effects may arise following the chains interactions such as, chains entanglement and chains coiling that can create intrinsic defects with a range of energy depths.

6.3 Summary

- Activation energy *E* is calculated by means of initial rise method in Section 6.1.1. However, comparison between the obtained *E* of α peak for *PET*, *PE*, *PMMA* and *pPVC* with that of previous researchers show big divergence as shown in Table 6.1.
- The differences in *E* values indicate that the α peaks of these pristine polymers involve distributed relaxation processes. Therefore, the initial rise method that is formulated for single relaxation process is inappropriate to be used in that case.

- Decomposition on the α peaks reveals several decomposed peaks that may represent the distributed relaxation processes. Table 6.3 in Section 6.1.2 lists the energy *E* of these peaks which are comparable with those of previous researchers.
- The variation in energy *E* from decomposed peaks is consistent with the energy range of dipole relaxation within 0.3 eV to 3.0 eV.
- In Section 6.1.2.1, the energy *E* of decomposed ρ peak are within the range of charge carrier trap around 1 to 3 eV. It proves the involvement of space charge relaxations behind the appearance of ρ peak, and perhaps diffusion impurities.
- Decomposed peak with activation energy *E* around 4 to 8 eV indicates the presence of molecular-ion deep trap. Section 6.1.2.2 discusses the existence of such deep traps in electrets, which were also responsible for the ρ peak emergence.
- Discussions in Section 6.1.2.2A suggest that defects at sample-electrodes interfaces contribute to charge injections, which are important for the molecular-ion formations.
- Charge injections can also generate homocharge that may lead to charge masking and neutralization. The evidence is given in Section 6.1.2.2B which show the lost of TSC peak due to the increase in polarization field, F_p.
- The knowledge on characteristic relaxation time that is also known as pre-exponential factor τ_o helps to predict the origin of certain relaxation process. However, the τ_o of decomposed peaks in Table 6.11(a) does not demonstrate the cooperative relaxation as expected in *WLF* theory for peaks around and above a T_g.
- The attempt to establish the cooperative relaxation via *WLF* and *VTF* fitting in Section 6.2.1 also give unsatisfactory results, as listed in Table 6.11(b) and 6.11(c).

- Section 6.2.2 introduces the *N-fitting* method, which is capable to fit data from both decomposed and experimental peaks as shown in Figure 6.18.

- Characteristic relaxation time τ_n generated from the *N-fitting* method in Table 6.11(d) demonstrates the cooperative relaxation, as well as dipole group, dipole segmental and space charge relaxations.

- Even though the physical meaning of $\tau_n \leq 10^{-30}$ s is unknown, but decomposed peaks with such low characteristic relaxation time show high energy E ($\geq$ 3eV). Such energy can be associated with intrinsic defects and also deep traps, which contribute to space charge relaxations in electrets.

- The expected cooperative relaxation on α peak from polymers is confirmed via the *N-fitting* procedure with their τ_n are around 10^{-4} to 10^{+1} s as shown in Table 6.16.

- The cooperative mode is also demonstrated by the experimental *OMON* α and ρ peaks in Table 6.23. These *OMON* α and ρ peaks are associated with the methylene groups and alkyl chains on *ODA* cations, respectively.

- However, the τ_n of experimental *OMON* ρ peaks around 10^{-16} to 10^{-17} s from *CENR-50* and *CpPVC* composites indicate the dipole-segmental relaxation. Discussion in Section 6.2.2.2.A relates this observes with the extensive matrix-alkyl chain reactions, which were induced by the polar matrix chains.

- In Section 6.2.2.2.B, the lost of α peak within *CPE* and *CpPCV* plots is due to matrix-alkyl chains coiling that had restricted the mobility of methylene groups. In case of *natural rubber-OMON* composites, entanglements among the chains allow cooperative relaxation by these groups, which is manifested with the α peak emergence.

- A number of relaxation processes show by the τ_n of decomposed peaks in Table 6.23 represent partial relaxations that contribute for the appearance of TSC peaks. Such as local segmental movements by alkyl chains responsible for partial segmental relaxation in decomposed *OMON* α peaks (τ_n ~10^{-17} to 10^{-24} s)

- Discussion on the localized relaxations in Section 6.2.2.2.C also highlight the effects of matrix-alkyl chains interactions that add more sources for partial relaxations.

- From the studies, it is suggested that the τ_n from experimental *OMON* α and ρ peaks describe the relaxation processes that involves the structure of methylene groups and alkyl chains, respectively. The τ_n of decomposed *OMON* α and ρ peaks on the other hand represent the partial or localized relaxations, which occur within the structure of alkyl chains and methylene groups.

- Comparison with some previous *PVC* results in Section 6.2.2.2.D highlights that the τ_n of α peak (10^{-4} s) prove the cooperative relaxation around a T_g. Segmental relaxation as shown by the τ_n of ρ peak (10^{-20} s) demonstrates the process of liquid-liquid transition around a T_{ll} temperature. This process stimulated localized space charge to be released, which is indicated by the τ_n from decomposed ρ peaks around 10^{-35} s to 10^{-41} s. It thus proves that the appearance of TSC ρ peak can be related to space charge relaxations processes in electrets.

References

6.1 D.I. Bower, "An Introduction to Polymer Physics", *Cambridge Uni. Press*, Cambridge UK, (2002)

6.2 J. van Turnhout, "Thermally Stimulated Discharge of Electrets", Topics in Applied Physics: Electrets edited by G.M Sessler, **V 33**, *Springer-Verlag*, New York, (1980)

6.3 P. Hedvig, "Dielectric Spectroscopy of Polymers", *Adam Hilger Ltd*., Bristol, (1977)

6.4 R. Chen, Y. Kirsh, "Analysis of Thermally Stimulated Processes" – International Series on the Science of the Solid State, *Pergamon Press*, **V 15**, Oxford, (1981)

6.5 V. M. Gunko, V. I. Zarko, E. V. Goncharuk, L. S. Adriyko, V. V. Turov, Y. M. Nychiporuk, R. Leboda, J. Skubiszewska-Zieba, A. L. Gabehak, V. D Osovskii, Y. G. Ptushinskii, G. R. Yurchenko, O. A. Mishehuk, P.P Gorbik, P. Pissis and J. P. Blitz, " TSDC spectroscopy of relaxation and interfacial phenomena", *Adv. Coll. Interface Sci.*, **V 131**, (2007), pg. 1 – 89

6.6 W.K.Sakamoto, "Dilectric spectroscopy and thermally stimulated discharge current in PEEK film", *Ecletica Quimica*, **V 28(2)**, (2003)

6.7 Y. Gorokhovatsky, D. Temnov, J.N. Marat-Mendes, C.J. Dias and D.K. Gupta, "On the energy Spectrum of Electrically Active Defects in Polyethylene Terephthalate (PET) Films ", *10th. International Symposium on Electrets, IEEE* (1999), pg. 339 – 342

6.8 Y. Asano and T. Suzuki, "Characteristic of Polyethylene Terephthalate Electrets", *Jap. J. app. Phys.* , **V 11(6)**, (1972), pg. 1139 – 1141

6.9 P. Fischer and P. Röhl, "Thermally Stimulated and Isothermal Depolarisation Currents in Low-density Polyethylene", *J. Poly. Sci. Poly. Pyhs*., **V 14**, (1976), pg. 531 – 542

6.10 K. Mazol, "More data about dielectric and electret properties of poly(methyl methacrylate", *J. Phys. D: Appl. Phys.*, **30**, (1997), pg. 1383 – 1398

6.11 J.J. del Val, A. Alergria and J. Colmenero, "Study of the α and β relaxation on a commercial poly(vinyl chloride) by thermally stimulated creep and depolarization current tehniques", *J.Appl. Pyhs*., **59(11),** (1986), pg. 3829 – 3834

6.12 N Doulache, A.Gourari and M. Bendaoud, "TSC Study of Liquid-Liquid Transition in Polyvinyl Chloride", Electrets, *8th International Symposium, (ISE 8*) on 7-9 Sep, (1994), pg. 523 – 527

6.13 K. Marossy, "Thermally stimulated depolarization (TSD) current study of plasticized PVC", *Poly. Bull.*, **41**,(1998), pg. 729 – 736

6.14 G. Kitis, J. M. Gomez-Ros and J. W. N. Tyun, " Thermoluminescence glow-curve deconvolution functions for first, second and general order of kinetics", *J. Phys. D: App. Phys*., **V 31**, (1998), pg. 2636 – 2641

6.15 F. O. Ogundare and M. L. Chitambo, "Thermo luminescence kinetic analysis of quartz with a glow peak that shifts in an unusual manner with irradiation dose", *J. Phys. D: App. Phy*., **V 40**, (2007), pg. 247 – 253

6.16 S. K. Sharma, S. S. Pitale, M. Manzar, R. N. Dubey and M. S. Qureshi, "Luminescence studies on the blue-green emitting $Sr_4Al_{14}O_{25}:Ce^{3+}$ phosphor

synthesized through solution combustion route", *J. Lumines*., **V 129**, (2009), pg. 140 – 147

6.17 B. A. Sharma, A. N. Singh, S. N. Singh and O. B. Singh, "Application of computerized glow curve deconvolution to determine the spectroscopy of traps in colorless microcline", *Rad. Measure*., **V 44**, (2009), pg. 32 – 37

6.18 J. van Turnhout, "Thermally Stimulated Discharge of Polymer Electrets" – A Study on Non-isothermal Dielectric Relaxation Phenomena, *Elsevier*, Amsterdam, (1975)

6.19 B. Hilczer and J. Malecki, "Electrets" - Studies in Electrical and Electronic Engineering, **V14**, *Elsevier PWN-Polish Scientific Publishers*, Warszawa, (1986)

6.20 S. N. Taraskin and F. Henn, "Depolarization current density within the symmetric double-well potential model for solid ionic conductors", *Phys. Rev. B*, **V 77**, (2008), pg. 134306-1 – 134306-11

6.21 K. Ikezaki and Y. Murata, " Electret properties of ethylene-propylene random co-polymer", *J. Electrostat*., **V 67**, (2009), pg. 407 – 411

6.22 V. Kazukauskas, "Investigation of carrier transport and trapping by oxygen-related defects in MEH-PPV diodes", *Semicond. Sci. Technol*., **V 19**, (2004), pg. 1373 – 1380

6.23 C.B. Duke and T.J. Fabish, "Charge Induced Relaxation in Polymers", *Phy. Rev. Lett.*, **V 37(16)**, (1976), pg. 1075 – 1078

6.24 T.J. Fabish and C.B. Duke, "Molecular charge state and contact charge exchange in polymers", *J. App. Phy.*, **V 48(10)**, (1977), pg. 4256 – 4266

6.25 A. Mellinger, F. C. Gonzalez and R. G. Multhaupt, "Photostimulated Discharge in Electret Polymers: an Alternative Approach for Investigating Deep Traps", *IEEE Trans. Diel. Elec. Ins.*, **V 11(2)**, (2004), pg. 218 – 226

6.26 L.L. Cui, M. H. Song, Y. X. Kong, D. Wang, Y. H. Xiao and J. Jiang, "The comparative studies of charge storage stabilities among three PP/poros PTFE/PP electret", *J. Electrostatics*, **V 67**, (2009), pg. 412 – 416

6.27 B. Gross, "Static Charges on Dielectrics", *Brit. J. App. Phy*., **V 1**, (1950), pg. 259 – 267

6.28 E. Hourdakis, B. J. Simonds and N. M. Zimmerman, "Submicron gap capacitor for measurement breakdown voltage in air", *Rev. Sci. Instrm.*, **V 77**, (2006)

6.29 P. G. Slade, "Electrical Breakdown in Atmospheric Air between Closely Spaced (0.2 μm) Electrical Contacts", *IEEE Tran. Comp. & Pack. Tech.*, **V 25(3)**, (2002), pg. 390 – 396

6.30 M.D. Migahed, M.T. Ahmed and A.E. Kotp, "Thermally stimulated depolarization current studies on the relaxation in poly(methyl methacrylate)-poly(vinyl chloride) blends and its relation to compensation laws", *J. Phys. D: App. Phys*., **V 33**, (2000), pg. 2108 – 2116

6.31 R. Chen," On the Calculation of Activation Energies and Frequency Factors from Glow Curve", *J. App. Phys*., **V 40(2)**, (1969), pg. 570 – 585

6.32 M. Mudarra and J. Belana, " Study of poly(methyl methacrylate) space charge relaxation by TSDC", *Polymer*, **V 38 N(23)**, (1997), pg. 5815 – 5821

6.33 B. B. Sauer and P. Avakian, "Cooperative relaxation in amorphous polymers studied by thermally stimulated current depolarization", *Polymer*, **V 33(24),** (1992), pg. 5128 – 5142

6.34 B. B. Sauer, "Comment on compensation analysis as applied to thermally stimulated current thermal sampling", *Polymer*, **V 38(16),** (1997), pg. 4065 – 4069

6.35 M. Fois, A. Lamure, P. Guuinic and C. Lacabane, "TSC Study of Secondary Dielectrics Relaxations in a Polyepoxy Matrix Composites", *J. App. Poly. Sci*., **V 66**, (1997), pg. 135 – 139

6.36 H. E. Feki, A. B. Salah, A. Daoud, A. Lamure and C. Lacabanne, "Studies by thermally stimulated current (TSC) of hydroxy- and fluro-carbonated apatites containing sodium ions", *J. Phy. Condens. Matter*., **V 12**, (2000), pg. 8331 – 8343

6.37 A. Nogales and B.B Sauer, "Cooperative Motions in PVC Studies by Thermally Stimulated Currents: Comparison with A.C. Dielectric Derivative Analysis", *J. Poly. Sci. Part B:Poly Phy*., **36**, (1998), pg. 913 – 918

6.38 M.D. Migahed, M.T. Ahmed and A.E. Kotp, "Iterative evaluation of thermally stimulated depolarization current peak parameters in polymers: A dipolar interaction approach to molecular dipole relaxation", *J. App. Phys*., **V 78(8)**, (1995), pg. 5079 – 5083

6.39 M. D. Migahed, M. Ishra and T. Fahmy, " Rate theory and cooperative structural relaxation in amorphous polymer blends as revealed by a thermal sampling study", *J. Phys. D: App. Phys*., **V 27**, (1994), pg. 2216 – 2222

Chapter 7

Mechanical Properties

Chapter 7: MECHANICAL PROPERTIES

Basic characterizations on mechanical properties of solid are usually determined by tests resulting in various deformations-versus-stress dependencies. Stress-strain diagrams used in this work provide good example for such dependency where they demonstrate material elongations in response towards tensile stress, which is a commonly studied behavior in polymeric materials. Series of tensile tests were done on *SMRL*, *DPNR*, *ENR-50*, *PE* and *pPVC*, as well as their related composites in order to generate the diagrams.

Investigations perform on such correlation readily reveal important features of elasticity, plasticity and strength of the materials. Such as elasticity modulus or modulus Young *Y*, PL strength PL_{st}, PL strain PL_{sn}, Tensile strength σ_{max} and strain at break or Maximum elongation ε_{max}. Area under the stress-strain curve in addition, shows the energy absorbed before failure takes place on a tested sample at its break off point. This energy is identified as strain energy density, *U* that indicates the sample toughness [7.1 and 7.2]. The above-mentioned mechanical properties generally are very much influenced by the inner structure of a tested material. By this means, these properties can be used to learn different effects caused by *OMON* addition within various types of polymer composites. Polymer-*OMON* interactions and the initial structures of polymers are equally important to understand these composites mechanical behaviors. For that reason, analysis on pristine polymers as well as their corresponding composites will be discussed in this chapter.

7.1 Polymers

Preliminary analysis for mechanical studies was carried out on the stress-strain diagrams of pristine polymers. The significant was to identify the behaviors of each polymer under the applied tensile forces. In which, the observed characteristic either in the elastic or plastic

region could be related to the physical features of polymers such as crystallinity, branching and cross-linking.

7.1.1 Polymers Deformation

Both Figure 7.1(a) and 7.1(b) show the stress-strain diagrams for *SMRL*, *DPNR*, *ENR-50*, *PE* and plasticized *PVC* (*pPVC*). These diagrams can be separated into two main sections, which are identified as the elastic and plastic region. Linear correlation of the stress- strain outlines up to the EL points as shown in Figure 7.1(b) cover the elastic region. While the trace beyond this point until it reaches the break off point in Figure 7.1(a) is recognized as the plastic region [7.1, 7.2 and 7.3]. These deformation regions represent the mechanical response of the polymers subsequent to the developed stress loading by tensile forces. The inner structure of these polymers in fact can give great influence on both elastic and plastic deformations; such as the crystallization in *PE*, stereoisomerism in natural rubbers and the effect of plasticizer in *pPVC*.

Deformation mechanisms probably began when the applied stress initiated covalent bonds in polymeric molecules to stretch out. This condition can stimulate bond straightening and bond lengthening as illustrated in Figure 7.2(a) and 7.2(b), respectively. In that way, this process of elastic deformation responsible for the strain increase within the elastic region. However, this temporary extension recovered once the stress was removed [7.4].

Further application of external stresses can cause permanent or plastic deformation [7.5] on the polymers. Primarily, it was due to the slippage occurred between adjacent molecules as illustrated Figure 7.3(a). It could also happen when the uncoiling polymeric chains failed to coil up again after the removal of external forces as shown in Figure 7.3(b). Basically, this permanent deformation occurs since the intermolecular attractive forces of polymeric molecules are weaker than the intramolecular forces. This condition thus allows molecules

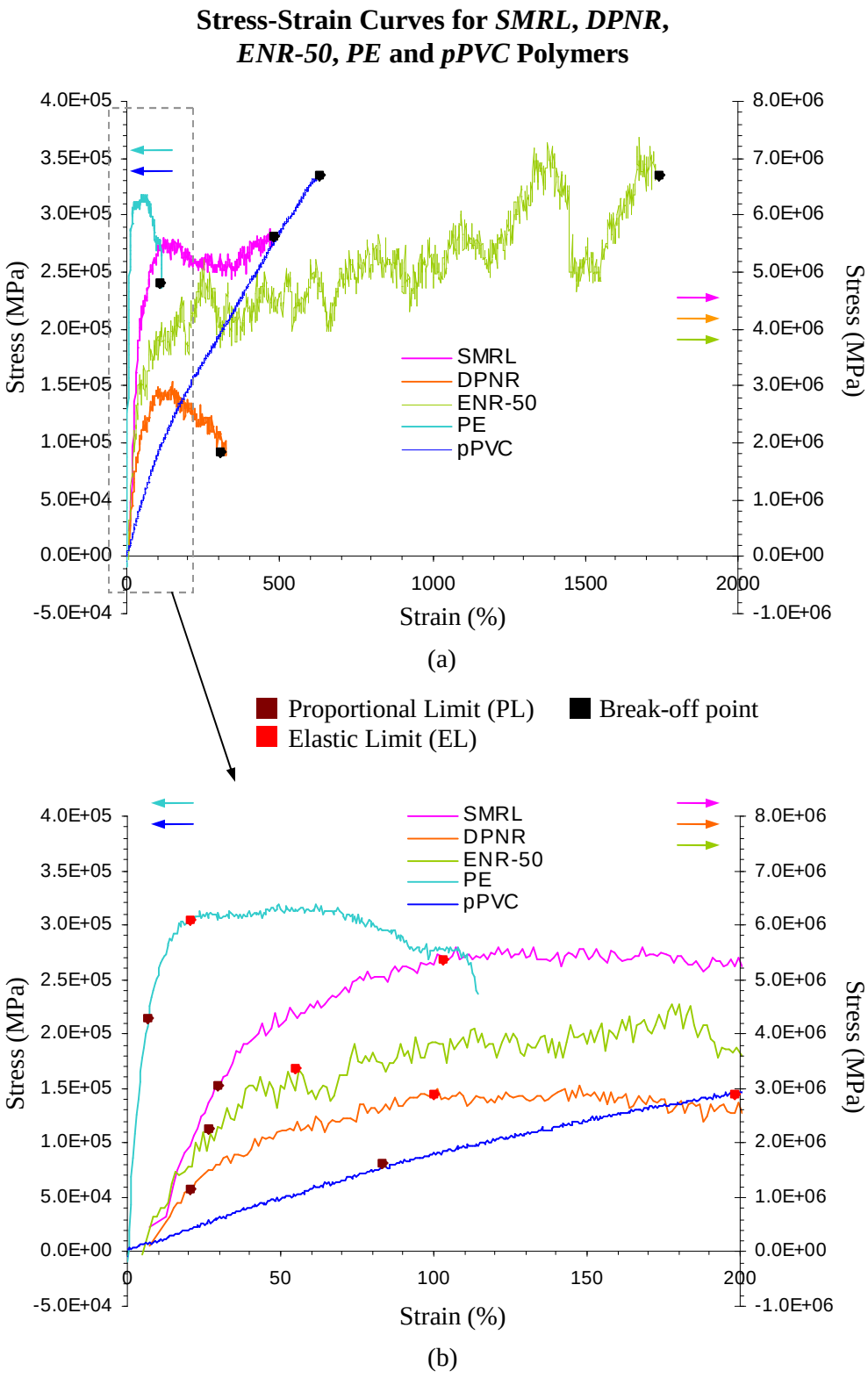

Figure 7.1: Stress-strain curves from tensile tests in (a) for *SMRL*, *DPNR*, *ENR-50*, *PE* and plasticized *PVC* (*pPVC*) with the intersect in (b).

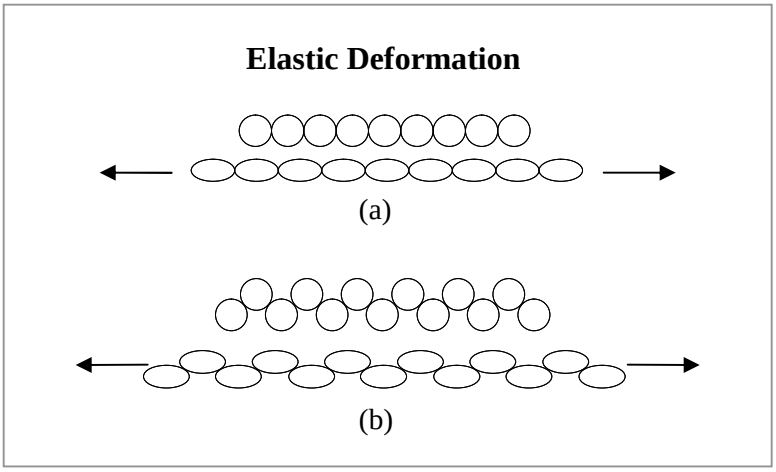

Figure 7.2: Elastic deformation on polymeric chains produces strains (a) by bond lengthening, (b) by bond straightening [7.4].

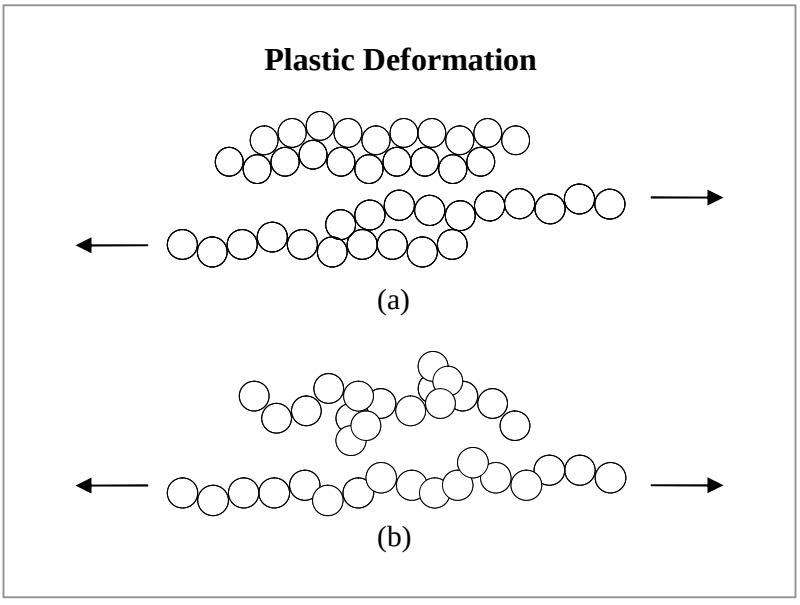

Figure 7.3: Plastic deformation on polymeric chains caused by (a) chains slippage and (b) main chains uncoiling [7.5].

to pass each other by the breaking and remaking of secondary bonding force [7.4 and 7.5]. From these stress-strain diagrams, some mechanical parameters were generated for each polymer and they are listed in Table 7.1. Mechanical properties that represent the elastic deformations are the Young modulus *Y*, PL strength PL_{st} and PL strain PL_{sn}. On the other hand, Tensile strength σ_{max} and Maximum elongation ε_{max} at the break-off point describe deformations within the plastic region.

7.1.2 Mechanical Properties of Polymers

7.1.2.1 *SMRL, DPNR* and *ENR-50*

Table 7.1 shows that elasticity modulus *Y* for natural rubbers (*SMRL*, *DPNR* and *ENR-50*) lies within the range of 0.35 MPa to 0.55 MPa. This range is considerably small compares with the obtained modulus *Y* for *PE* (180 MPa) and *pPVC* (2 MPa). These results might have some connection to the linear structure of polyisoprene chains. This chain of natural rubbers as illustrated in Figure 7.4(a) is known for its cis-type structure. Stereoisomerism turn cis-polyisoprene chains in the rubbers into a highly kinked structure as illustrated in Figure 7.4(b). It is believed that the unbalanced structure adjacent to the double bond in the chain induces this kinked structure [7.4].

The application of external stresses caused the chain-kinking structure in natural rubbers to gradually unkinked, before the bond-straightening process took place. It is followed by the process of bond-lengthening that gave the PL strain, PL_{sn} around 26% to 34%. The values

Table 7.1
Tensile Properties of Polymers

Sample	**SMRL**	**DPNR**	**ENR-50**	**PE**	**pPVC**
Elastic Modulus *Y*, (MPa)	0.35	0.57	0.55	179.94	2.10
PL Strength, PL_{st} (MPa)	0.09	0.14	0.12	1.71	0.85
PL Strain, PL_{sn} (%)	34.05	26.14	25.83	1.85	41.78
Tensile Strength, σ_{max} (MPa)	0.16	0.30	0.38	6.84	6.74
Maximum elongation, ε_{max} (%)	333.97	485.83	1737.05	117.36	635.78

Table 7.1: Tensile properties for *SMRL*, *DPNR*, *ENR-50*, *PE* and *pPVC* that are calculated from their stress-strain curves.

are quite high compared to that of *PE* which is just about 2 %. In fact, these high PL strains PL_{sn} perhaps contribute to the reduced elasticity modulus *Y* of the rubbers. In addition, the inner structures of natural rubbers do not seem to have much contribution to generate high PL strengths PL_{st}, which can balance the elastic elongations PL_{sn} of the rubbers.

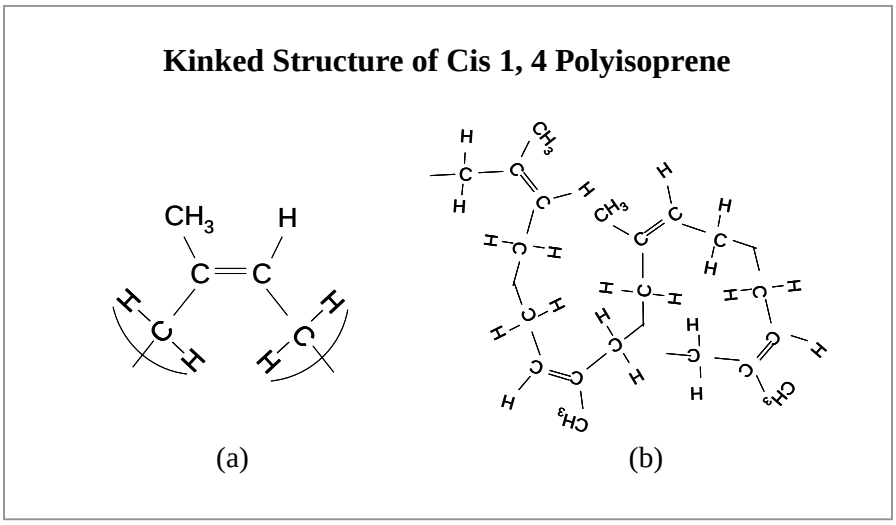

Figure 7.4: Schematic diagrams for cis 1, 4 polyisoprene show (a) elementary structure and (b) kinked structure due to the isomerism [7.4].

The stretching process may not be possible without the help from the crosslinked structures in natural rubbers. This is very important since each rubber molecule can perform elastic extension. However, they may also slide by one another rather than deforming elastically. Chain crosslink therefore is functioning to tie the rubber molecules together. During stress application however, chain crosslinking in natural rubbers still allows the chains to slide on their neighboring chains towards the area without the crosslink effect. This condition will recover once the stress is removed [7.6]. In that way, the natural rubbers can maintain their good elasticity property even at high PL strain PL_{sn}.

This special ability of rubbers however has its limitation beyond their PL points. Extensive elongations restricted the chains to recover its initial structures and thence gave permanent deformation on a tested sample. Figure 7.5 shows the physical changes on natural rubbers, which is due to various modes of deformation from elastic to plastic region. In the plastic region, cross-linking structures again play its role to control chains slippage as the applied force is increased. Even though the tensile strengths σ_{max} of the rubbers are relatively low, good force distribution however gave them remarkable maximum elongation ε_{max} with the percentage increase varies within the range of 333 % to 1737%.

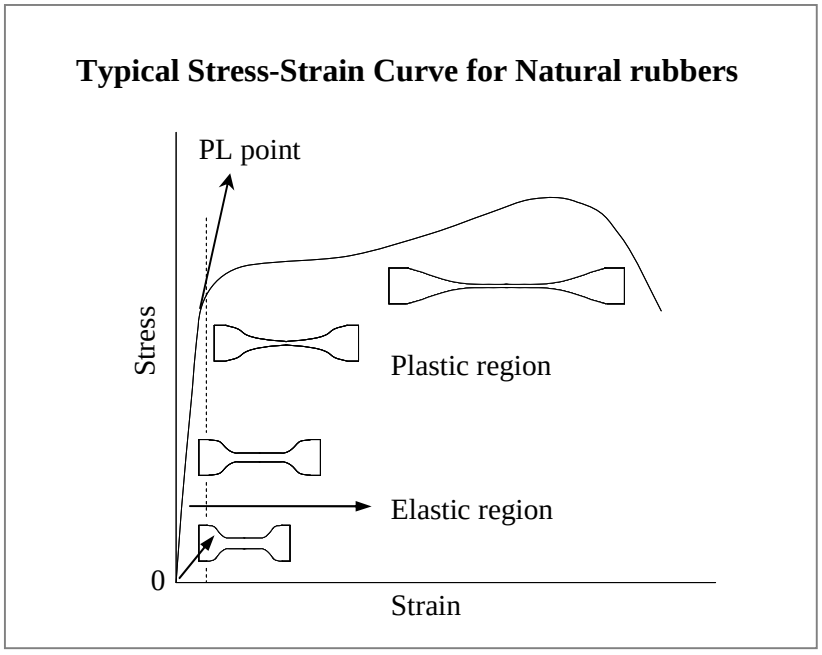

Figure 7.5: Sketches show modes of specimen deformation within elastic and plastic region on stress-strain curve of natural rubbers. [7.5]

7.1.2.2 Polyethylene, *PE*

From Table 7.1, it shows that *PE* polymer has the highest elastic modulus *Y* that is around 179 MPa. This observation must be related to the crystalline structures of *PE* [7.7 and 7.8], which is known as a semi-crystalline polymer. Previously in Chapter 4, crystallinity in *PE* was confirmed via the XRD and DSC analysis. Crystallinity in non-polar polymers such as *PE* is believed to arise from chains regular arrangement as schematically illustrated in Figure 7.6(a). The adjacent molecules coordinate their position with each other, which then produced better packing for these chains. In fact, this structure can create stronger van der Waals attraction forces that give the high modulus *Y* for *PE*.

Another aspect that should also be considered is the existence of bifurcated chains or chain branching. It was proven in this work via the FTIR spectroscopy on *PE* in Section 4.3.1B. This source of amorphous region in *PE* can actually formed three-dimensional molecular structure as the effect of cross-linking in natural rubbers. In *PE* however, it occurs by the simple mechanism of intertangling [7.4] that binds the polymers chains into such structure.

Therefore, extensive branching can effectively restricts movements between the adjacent molecules in *PE*. In that way, both crystalline and amorphous phases within the polymer contributed for its mechanical behavior. The relatively high PL strength PL_{st} and low PL strain PL_{nt} of *PE* in Table 7.1 thus explain its high elasticity modulus *Y*.

The Structure of Polyethylene, *PE* chains

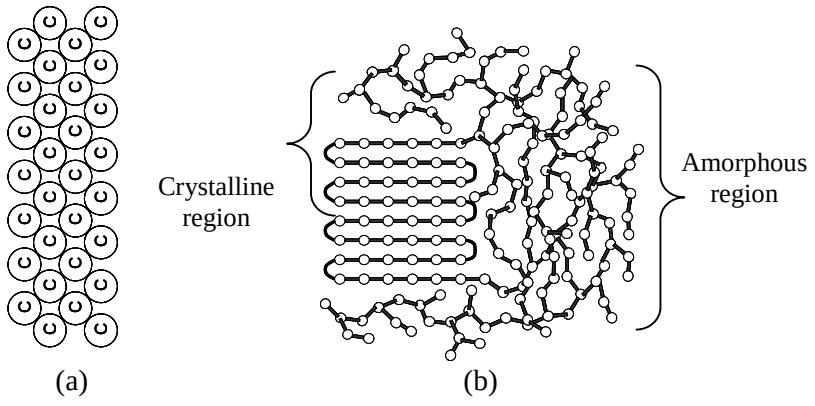

Figure 7.6: Schematic representations of polyethylene (*PE*) show molecular chains in (a) crystalline and (b) amorphous regions. [7.4 and 7.9]

The chain branching and crystallinity in *PE* should have some contributions on its Tensile strength σ_{max} as well. The strength about 6.8 MPa is relatively higher than those for natural rubbers in Table 7.1. Structural effects however had limited the chains elongation in *PE* for plastic deformation. In fact, it gave the smallest percentage of Maximum elongation ε_{max} compared to that of other polymers. In spite of that *PE* sample was able to reach 117 % on the ε_{max} before it breaks-off. This is primarily because crystallization is seldom perfect in polymers, especially in *PE* where only the weak van der Waals forces is available to align its molecules. Besides, a large number of atoms must be maneuvered into position in order to form *PE* crystalline structures. It thus tells that slippage could also take place in *PE* with the increase of applied stresses. The condition for randomly oriented molecules in *PE* is comparable with the aligned model as illustrated in Figure 7.6(b). It shows that as long as

the molecules are bonded only by the van der Waals forces, deformation can take place at the weaker point between the molecules, rather than breaking the intramolecular bonding.

7.1.2.3 Plasticized Polyvinylchloride, *pPVC*

From Table 7.1, the low modulus *Y* of about 2.1 MPa (Y_{PE}: 179 MPa) and high strain at break ε_{max} of around 635 % (ε_{max} *PE*: 117%) suggest the presence of three dimensional 3D networks inside *pPVC*. Besides, Figure 7.1(a) shows that the stress-strain curve of *pPVC* actually resembles those of the natural rubbers. The observation shows significant changes on the mechanical properties of rigid *PVC*, where the elasticity modulus *Y* can give around 2730 MPa [7.10]. This is attributable to the presence of small *DOP* molecules in between *PVC* chains within the plasticized polymer [7.11 and 7.12]. In order to understand the role of the plasticizer molecules, physical features of rigid *PVC* must also be considered.

The Structure of Plasticized PVC, *pPVC* Molecules

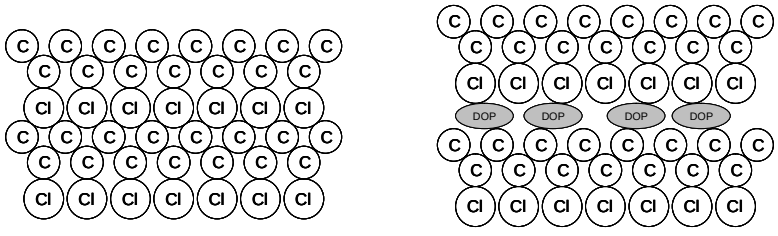

(a) (b)

Figure 7.7: Illustrations on structural effect for (a) Polyvinyl chloride, *PVC* and (b) plasticized *PVC* with the plasticizer molecules, *DOP*. [7.4 and 7.11]

Figure 7.6(a) and 7.7(a) give the illustrations of molecular shape effect on *PE* and *pPVC* mechanical behaviors, respectively. *PE* molecules in Figure 7.6(a) comparatively had a simpler and more uniform shape than those of *PVC* chains in Figure 7.7(a), especially with the large lump of chlorine atoms periodically along its chains. These structures thus make the movements between neighboring molecules likely restricted. Polarizations among *PVC* molecules in addition increased the strength of van der Waals attraction forces, which can

also contribute to the polymer rigidity. The present of plasticizer molecules within *pPVC* is functioning to reduce the attractive forces, as illustrated in Figure 7.7(b). This is including any electrostatic repulsion that may arise among the *PVC* chains. Such condition therefore creates more flexibility for the polar polymeric chains, which renders its initial mechanical properties.

7.1.3 Discussion

Previously from the XRD analysis in Chapter 4, crystallinity was detected in both *PE* and *ENR-50*. However, the nature of their crystallite structures gave different outcomes on the responses towards external stresses. For example, the close pack nature of *PE* chains that created its crystalline phase effectively limited its Maximum elongation ε_{max} to only around 117 %. While chains cross-linking that is responsible for the crystallinity of *ENR-50* gives higher Maximum elongation due to the better mechanism of force distributions. Polymeric crystallinity that is originated from 3D networks structure inside the *ENR-50* also helps to sustain the applied forces. The effect can be seen on the remarkably increase of Maximum elongation ε_{max}, which is about 1737 % as listed in Table 7.1

Plasticized *PVC* or *pPVC* with the Maximum elongation ε_{max} of about 636 % is also very much influenced by the cross-linking structures. Physical cross-linking within the polymer could come from physically cross-linked chains by hydrogen bonds, chain entanglements and micro-crystallites structure. In fact, chains cross-linking in *pPVC* is frequently related to such crystallinity by most researchers [7.13]. On the other hand, *SMRL* (ε_{max} = 334 %) and *DPNR* (ε_{max} = 485 %) that comprise of cross-linked polyisoprene chains as in *ENR-50* show lower percentages in their ultimate elongations. From these observations therefore, it seem that polar groups within the *ENR-50* and *pPVC* polymers had played significant role to induce extensive cross-linking among their chains.

Molecular weight (MW) is another important factor that determines the elongation at break ε_{max} of the polymers. For example, the known MW for *PE* is within the range of 28 000 to 40 000 g/mol [7.5], less than the average value for *pPVC* from 50 000 to 150 000 g/mol [7.10]. The values are actually smaller when compared to the average MW for the natural rubbers, which is about 5 x 10^5 g/mol [7.5] The developed trend for molecular weight in *PE*, *pPVC* and *ENR-50* thus is in increasing manner and analogous to their Maximum elongation ε_{max} in Table 7.1.

The values from *pPVC* mechanical properties consistently show that it is a highly flexible *PVC*. Table 7.2(a) lists these values for comparison with some typical values of *pPVC*. In case of *PE*, the measured properties as shown in Table 7.2(b) fall within the range for low and medium density *PE*. From Table 7.2(c) for natural rubbers, the calculated elasticity modulus *Y* is much lower than their typical values. This is possibly due to the process of sample preparation that may reduce these values. Above it all, primary focus in this work is to study the effect of *OMON* within these polymers composites. Therefore, the measured values will be used as references in the *polymer-OMON* composites analyses.

Table 7.2
Some Typical Values of Polymers Tensile Properties

Table 7.2(a)
Tensile Properties of Plasticized PVC, *pPVC*

Sample	**pPVC**	
	measured	typical value
Elastic Modulus *Y*, (MPa)	2.1	2.7 – 12.6 [7.8 and 7.11]
Maximum elongation, ε_{max} (%)	635	250 – 450 [7.11]

Table 7.2(b)
Tensile Properties of Polyethylene, *PE*

Sample	**PE**	
	measured	typical value
Elastic Modulus *Y*, (MPa)	179	170 – 280 [7.12]
Maximum elongation, ε_{max} (%)	117	100 – 650 [7.5 and 7.12]

Table 7.2(c)
Tensile Properties of Natural Rubbers

Sample	**SMRL**		**DPNR**		**ENR-50**	
	measured	typical value	measured	typical value	measured	typical value
Elastic Modulus *Y*, (MPa)	0.35	2.40 [7.13]	0.57	1.82 [7.13]	0.55	1.80 [7.14]
Maximum elongation, ε_{max} (%)	333.97	523.00 [7.13]	485.83	544.00 [7.13]	1737.05	565.00 [7.14]

Table 7.2: Comparison with typical value for some mechanical properties from (a) *pPVC*, (b) *PE* and (c) *SMRL*, *DPNR* and *ENR-50*.

7.2 *Polymer - OMON* Composites

7.2.1 Stress-Strain Diagrams of *Polymer - OMON* Composites

Nanocomposites composed of polymers and layered silicates such as *OMON* frequently exhibiting improved mechanical properties. Hence, such improvement is also expected for *polymer-OMON* composite system in this work. *OMON* may change to a certain extent the initial curve of stress-strain diagram for polymer matrix. As a result, the elasticity modulus *Y*, Tensile strength σ_{max} and Maximum elongation ε_{max} of polymer matrix could be either increasing or experience a reduction. Relative values of the properties will be useful to see *OMON* effect on the mechanical behavior of *polymer-OMON* composite.

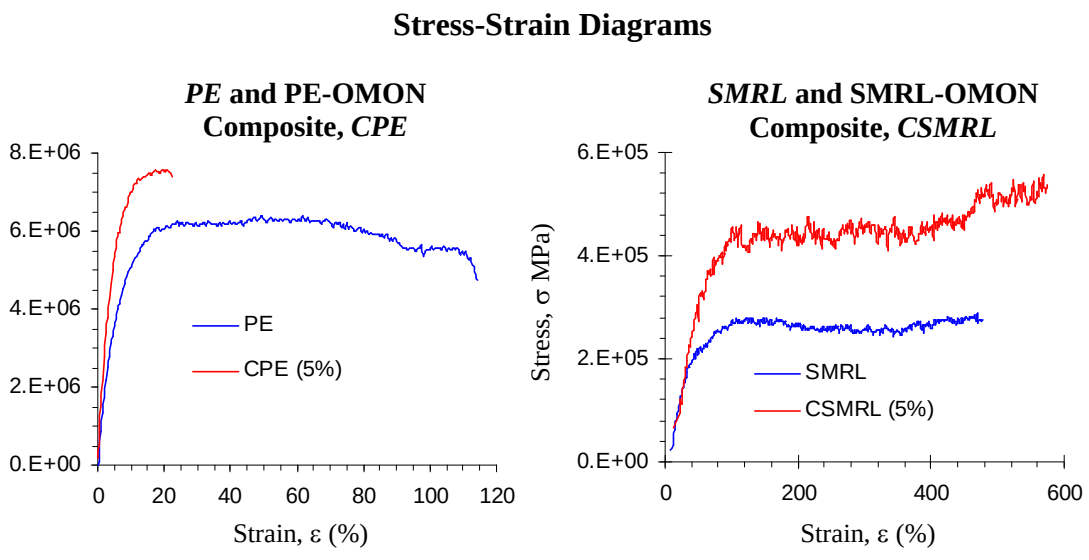

Figure 7.8: Stress-strain curves show (a) typical effect of filler incorporation in *CPE* that reduce composite strain at break; while in (b) similar amount of *OMON* content increase the strain in *CSMRL*.

Figure 7.8(a) and 7.8(b) shows the stress-strain diagram for *PE* and *SMRL* respectively. In each graph, the stress-strain plots for their corresponding composites with 5 % of *OMON* loading (*CPE* and *CSMRL*) are plotted together. Elasticity modulus *Y* for these composites seems as relatively increased compared to that of pristine polymers. The estimated increase

is about 17 % for *CPE*, and 116 % in case of *CSMRL*. On the other hand, the elongation at break ε_{max} in *CPE* is reduced about 78 % from the initial value for *PE*. These are actually some typical effects of discontinuous filler on composite mechanical properties. However, ε_{max} in *CSMRL* demonstrates a remarkable increase around 20 %, which is rarely happened within a conventional composites system. These behaviors thus reveal the differences in *OMON* interaction with various types of polymeric chains. In order to study the effects, stress-strain curves from polymers are plotted together with those for their composites, in increasing amount of *OMON* loading.

7.2.2 Effective Filler-based Micromechanical Model

Composite material is defined as a material system that contains two or more constituent materials with significant different physical and chemical properties. These micro or macro scale materials are essentially insoluble in each other and creating phases in the composite materials. Various phases generated however in general can be separated into two major groups. They are *continuous phase* that represents the matrix element and *reinforcement phases*, which is comprised of filler or particle elements [7.5, 7.18 and 7.19]. Mechanical behaviors of composites thus reflect the interactions between these phases. By the above definition, *continuous phase* within polymer-clay composite is represented by the polymer matrix. *OMON* particles in that case create the *discontinuous phase*, which is functioning to modify the mechanical properties of the pristine polymers.

In composite macroscopic model, the total spatial volume is viewed as well portioned by the particle domain and matrix domain as shown in Figure 7.9(a). Both domains are treated as homogeneous materials with certain elasticity properties. However, such clearly defined particle domain does not exist in the system of intercalated polymer-clay composites. The idea of *effective particle* therefore is utilized to model the micromechanical properties of

discontinuous reinforcement within a composite system. A well-defined spatial volume as illustrated in Figure 7.9(b) distinguishes the *effective particle*. The volume is occupied by both silicate layers and interlayer galleries, which form a spatial domain that is analogous to the particle domain [7.20, 7.21 and 7.22].

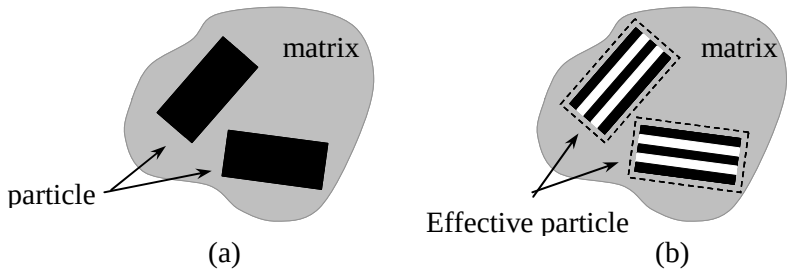

Figure 7.9: Illustration of the particle and matrix domain in (a) conventional composites and (b) nanocomposite. The dash-lined boxes in (b) indicate spatial domain of the effective particle [7.20].

In conventional micromechanical models, various parameters have been used to create the connections between the mechanical properties of filler and composite. Among them are the volume fraction, f_p; particle aspect ratio, L/t and particle/matrix stiffness ratio, Y_p/Y_m. For example in case of Halpin-Tsai equation, these parameters have important effects on the normalized modulus Y_{11}/Y_m. Halpin-Tsai equation is one of the micromechanical model that give formulation for reasonable stiffness estimation [7.20, 7.21, 7.22 and 7.23]. This model is based on the equation

$$\frac{Y_{11}}{Y_m} = \frac{1+2(L/t)f_p\eta}{1-f_p\eta} \qquad \ldots (7.1)$$

where

$$\eta = \frac{(Y_p/Y_m)-1}{(Y_p/Y_m)+2(L/t)} \qquad \ldots (7.2)$$

with L = length of particle

t = thickness of particle

Y_p = elasticity modulus of particle

Y_m= elasticity modulus of matrix

Equation 7.1 can be linearized as

$$\frac{Y_{11}}{Y_m} = 1 + Bf_p \qquad \ldots (7.3)$$

where B is a positive factor that depends on particle/matrix stiffness ratio, as well as the particle aspect ratio.

However, this model has a major weakness when it comes to the case of polymer-clay composite. Typical idea of particle thickness, *t* is certainly inappropriate to describe the thickness of intercalated *OMON* particles. Especially with the occupied gallery spaces by polymeric matrix that increased the interlayer spacing of 1 to 4 nm. Here, the significance of *effective particle* concept can be seen in case of an intercalated smectite clay composite system. The thickness of effective particle is expressed as follow [7.20 and 7.21]:

$$t_{eff} = (N-1)d_{001} + t_{sheet}$$

Where t_{eff} = effective thickness

N = number of platelets per stacked clay

d_{001} = basal spacing

t_{sheet} = silica sheet thickness

Thereby, the effective aspect ratio becomes

$$\alpha_{eff} = \frac{L}{t_{eff}} = \frac{L}{(N-1)d_{001} + t_{sheet}} \qquad \ldots (7.4)$$

and effective particle stiffness can be estimated as

$$Y_p^{eff} = \frac{Nt_{sheet}Y_p}{(N-1)d_{001} + t_{sheet}} \qquad \ldots (7.5)$$

Other important parameters for clay structure are the number of silicate platelet per unit particle thickness:

$$\chi_N = \frac{N}{t_{eff}} = \frac{N}{(N-1)d_{001} + t_{sheet}} \quad \ldots (7.6)$$

which can alternatively express as the volume fraction of silicate in the effective particle:

$$\chi = \frac{V_{silicate}}{V_p} = \frac{Nt_{sheet}}{(N-1)d_{001} + t_{sheet}} \quad \ldots (7.7)$$

This equation thus is very useful to make a conversion from clay weight fraction, W_c to particle volume fraction, f_p for the effective particles. According to Sheng *et.al* [7.20] (see Appendix G):

$$f_p = \left(\frac{\rho_m}{\rho_{silicate}} \frac{1}{\chi} \right) W_c \quad \ldots (7.8)$$

with ρ_m = density of matrix

$\rho_{silicate}$ = density of silicate sheet

The density $\rho_{silicate}$ can be calculated from montmorillonite, *Mon* lattice parameters [7.21],

$$\rho_{silicate} = \rho_{lattice} = \frac{M_o}{A_o t_{sheet}} = \left(\frac{2.44}{t_{sheet}} \right) \text{nm g/cm}^3 \quad \ldots (7.9)$$

where M_o = molecular weight = 720 g/mol

A_o = planar area = 0.49 nm^2

t_{sheet} = sheet thickness = 0.615 nm

From these equations, the Halpin-Tsai micromechanical model can now be coupled with the concept of *effective particle*. The outcomes then will be useful to see the crucial effect of intercalated *OMON* parameters. The comparison of normalized modulus Y_{11}/Y_m from the measured and theoretical fitted data is another interesting angle to study. It will show the validity of the Halpin-Tsai model on various types of *polymer-OMON* composites.

7.2.3 Mechanical Properties

Systematic evaluation will be carried out in this section to generate mechanical properties of the *polymer-OMON* composites. Stress-strain plots for each composite with the different weight ratio of *OMON* content will be analyzed. It also involves the plot of *polymer–Mon* composites for comparison, and also to distinguish the organophobic effects. Mechanical properties such as the elasticity modulus, Y; tensile strength, σ_{max}; elongation at break, ε_{max}; PL strength, PL_{st}; PL strain, PL_{sn} and strain energy density, U that defines the toughness of a material are then listed in the increasing manner of *OMON* loading. This is very useful to study the developed trend caused by *polymer-OMON* interactions.

In quest to study the actual effects from such interactions however, a normalized value is more appropriate to be used in the analysis. For that reason, the properties are normalized in the form of ratio percentage, relative to their counterparts for the pristine polymers. The influence of *OMON* loading on certain mechanical properties will be discussed based on some graphs of these normalized values. The values of certain *OMON* weight fraction (5 % and 30 %) are compared in order to understand the differences in *OMON* effects on various polymer matrixes.

7.2.2.1 *Natural Rubber- OMON* Composites

The stress-strain diagrams of composites natural rubbers with *OMON* loading of 5%, 10%, 15%, 20%, 25%, 30% will be analyzed, as well as their composite with 30% of Mon. The wide range of filler constituent was used since the natural rubbers are basically composed of bulky polyisoprene elastomer chains. Normally elastomeric chains can take such high filler inclusion better than a lower molecular weight (MW) polymer [7.25 and 7.26]. Such as in case of *polystyrene-OMON* (*CPS*) composite, where even a small loading can easily lead to brittleness. The results for *CPS* however are not presented in this thesis.

7.2.2.1.A. Composite OMON-ENR-50, (CENR-50)

Typical effects of filler in a composite system can be seen on the stress-strain behaviors of *CENR-50* samples as shown in Figure 7.10. Reinforcement mechanism induced by *OMON*

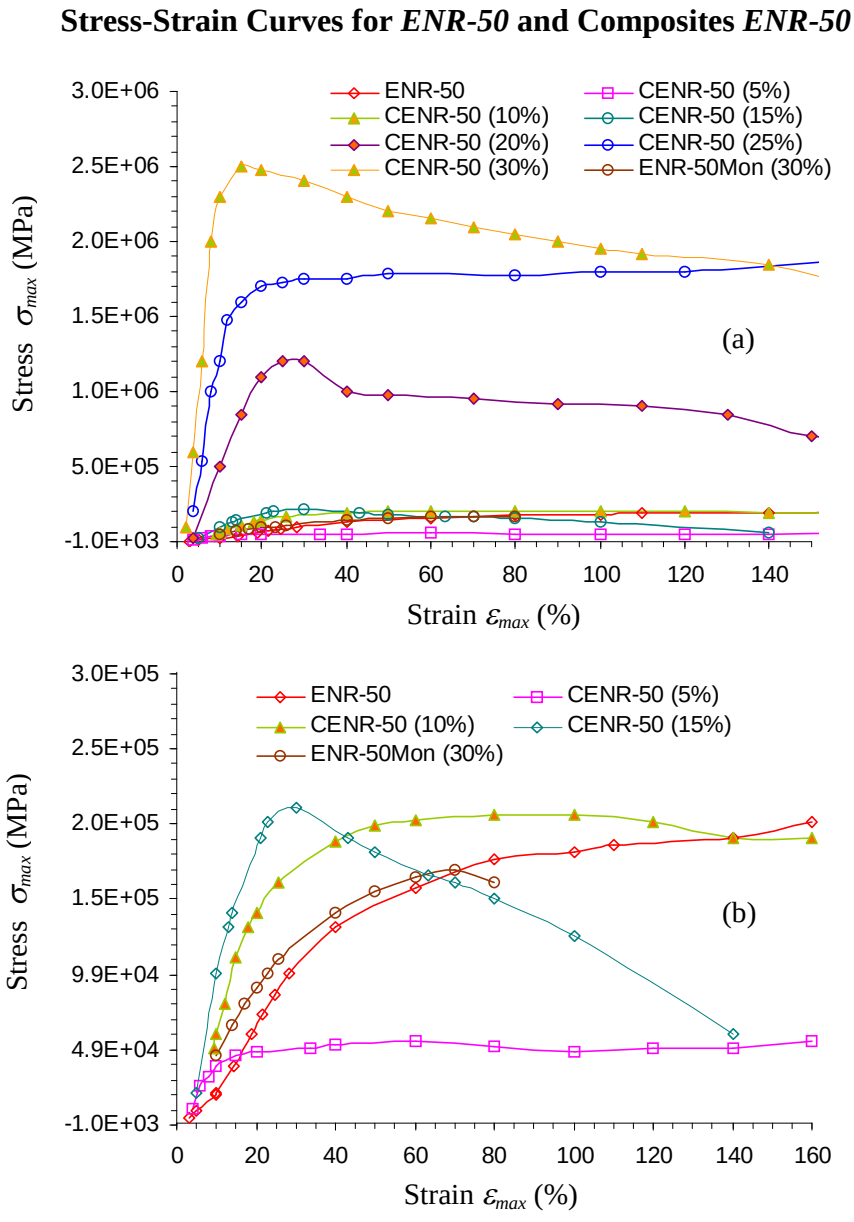

Figure 7.10: Stress-strain curves for (a) *ENR-50* and *composites ENR-50* with 5%, 10%, 15%, 20%, 25% and 30% of *OMON* content. It is including the composite *ENR-50Mon* as shown in (b) with 30% of *Mon* weight fraction.

effectively had helped the composites to undergo stress loading. However, simultaneously they are losing their elastomeric characteristics with the significant drops in strains. Similar observation can be seen in the case of *ENR-50-Mon* composite.

Table 7.3(a)
Mechanical Properties of *ENR-50* and Composite *CENR-50*

Sample	ENR-50	CENR-50 (5%)	CENR-50 (10%)	CENR-50 (15%)	CENR-50 (20%)	CENR-50 (25%)	CENR-50 (30%)	ENR-50 Mon (30%)
Modulus, *Y* (MPa) (± 0.01)	0.55	0.76	2.31	2.58	31.31	63.19	85.41	1.79
PL Strength, *PLst* (MPa) (± 0.01)	0.12	0.01	0.11	0.17	0.78	0.85	1.28	0.12
PL Strain, PL_{sn} (%) (± 0.01)	25.83	18.76	3.28	4.42	7.24	1.75	1.11	3.23
Tensile Strength, σ_{max} (MPa) (± 0.01)	0.38	0.38	0.61	0.25	1.21	2.36	2.78	0.24
Max elongation, ε_{max} (%) (± 0.01)	1737.05	1797.14	1619.91	422.47	337.85	340.61	176.74	83.27
Strain energy density, *U* (MN/m²) (± 0.01)	4.36	2.60	5.12	0.23	2.63	6.50	3.56	0.11

Table 7.3(a): Mechanical properties for *ENR-50*, composite *CENR-50* with 5%, 10%, 15%, 20%, 25% and 30% of *OMON*. As well as composite with 30% of *Mon* content *ENR-50Mon* (30%) for comparison.

Table 7.3(b)
Relative Percentage for Mechanical Properties in *CENR-50* and *ENR-50Mon*

Sample	CENR-50 (5%)	CENR-50 (10%)	CENR-50 (15%)	CENR-50 (20%)	CENR-50 (25%)	CENR-50 (30%)	ENR-50 Mon (30%)
Modulus, *Y* (%) (± 0.01)	38.35	320.12	368.60	5589.43	11381.23	15420.21	225.89
PL Strength, PL_{st} (%) (± 0.01)	-91.87	-3.61	42.73	551.13	612.46	976.21	-0.92
PL Strain, PL_{sn} (%) (± 0.01)	-27.37	-87.29	-82.90	-71.96	-93.24	-95.72	-87.50
Tensile Strength, σ_{max} (%) (± 0.01)	0.88	59.88	-32.92	219.28	522.81	632.72	-37.66
Max elongation, ε_{max} (%) (± 0.01)	3.46	-6.74	-75.68	-80.55	-80.39	-89.83	-95.21
Strain energy density, *U* (%) (± 0.01)	-40.28	17.48	-94.71	-39.71	49.11	-18.40	-97.50

Table 7.3(b): Relative percentage for mechanical properties from composite *ENR-50* with *OMON* (*CENR-50*) and *Mon* (*ENR-50Mon*) in comparison with the counterparts in pristine *ENR-50*.

Elasticity modulus *Y* for *CENR-50* in Table 7.3(a) shows remarkable improvements with the presence of *OMON* component within the material. Figure 7.11(a) demonstrates that the modulus relative percentage increases exponentially with the filler weight fraction, W_c. In which from Table 7.3(b), it reveals that the enhancement had reached up to 15420 % for *CENR-50*(30%) with 30 % of *OMON* inclusion. This result indicates the great reinforcing mechanism in the composite that operates at polymer-filler interface.

Numerous factors can contribute to generate interfacial adhesion in *CENR-50*. Intercalation of *ENR-50* chains into *OMON* interlayer for instance, gives wide surface contact for the rubber matrix chains to form both physical and chemical bonding with silicates. This effect became more important when exfoliation took place within the composite system. The delamination of *OMON* silicate layer can give large contact area for extensive interactions. Strong bonding forces that operated at the matrix-filler interface thus, responsible for such high increase in the modulus *Y*. This structural effect on normalized modulus Y_{11}/Y_m can be seen in Figure 7.11(b). Comparison with the Halpin-Tsai model shows that it can fit the experimental results, up to 15 % of *OMON* weight fraction W_c or approximately 0.18 in volume fraction, f_p. Away from this threshold the measured values continue to increase rapidly. Therefore, deviation from the predicted rate for an intercalated system suggesting that exfoliation was the main reason behind the great improvement on modulus *Y*.

A wide surface contact will be meaningless without good binding forces at interface. *Mon* silicate platelets for instance, provide potential grounds for hydrogen bond formations with oxygen atoms and hydroxyl groups on its structures. Thus, it is a great advantage for the *CENR-50* with matrix chains that are known rich of epoxide groups. These polar groups can give oxygen atoms to form hydrogen bonding with *OMON* silicate. Besides, hydrolysis on epoxide groups can bring out hydroxyl molecules that effectively generated hydrogen bonding with the silicates. In fact, more hydroxyl molecules were created as anti-oxidation

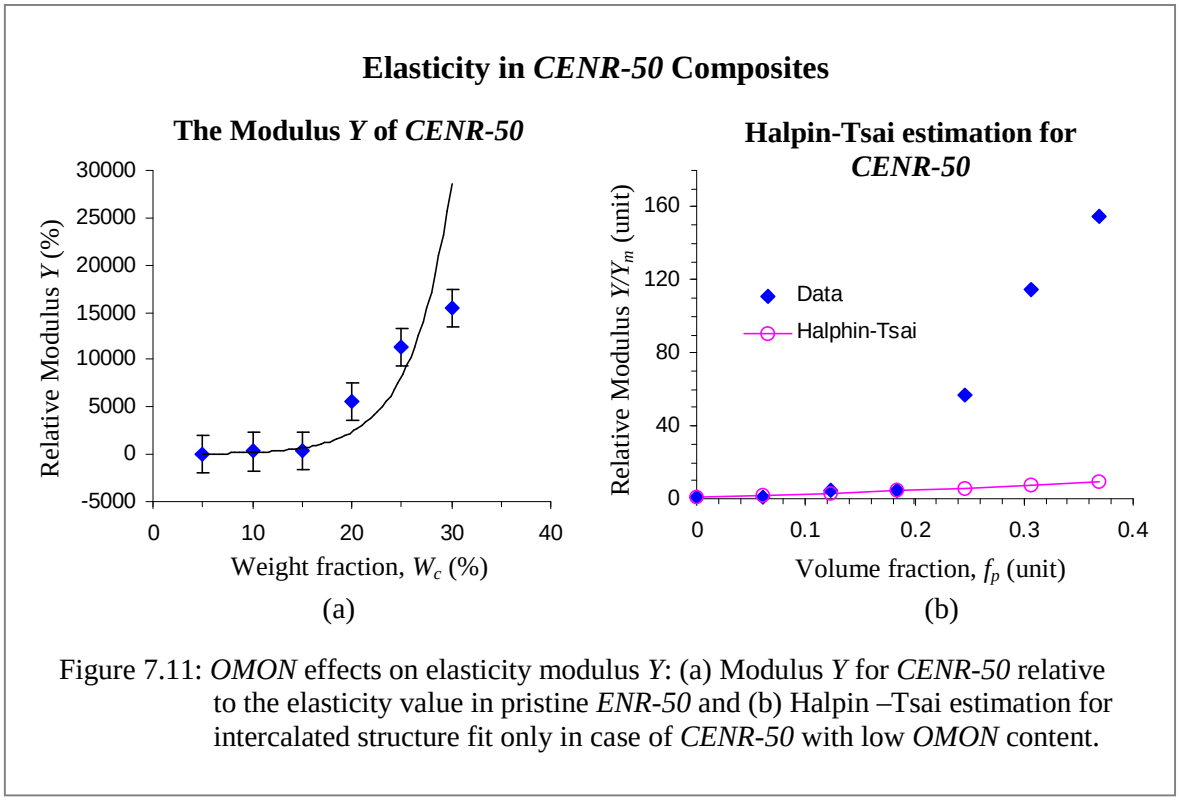

Figure 7.11: *OMON* effects on elasticity modulus *Y*: (a) Modulus *Y* for *CENR-50* relative to the elasticity value in pristine *ENR-50* and (b) Halpin –Tsai estimation for intercalated structure fit only in case of *CENR-50* with low *OMON* content.

reaction on epoxide group took place in the composite system. This amine-assisted process as a result promotes more chemical crosslinking among *ENR-50* chains in *OMON* gallery. The potential hydrogen bonding due to the process of anti-oxidation and hydrolysis, which was discussed earlier in Section 4.3.2.4.C and 4.3.2.4.B could be the sources for the strong interfacial adhesion in *CENR-50*.

The intercalation of *ENR-50* chains led to two major processes in *OMON* gallery, they are the matrix-filler bonding and chains crosslinking. From previous analyses on FTIR spectra in 4.3.2.4.B, the indication of chain crosslinking in *CENR-50* became more obvious with the decreasing amount of *OMON* content. This is reasonable since *ENR-50* chains have great tendency to interact with the filler silicates. Limited number of *OMON* particle within the composite can attract many chains to enter each *OMON* gallery. In that way, the *ENR-50* chains easily occupied the inner surface of *OMON* silicate. Hence, it left the remainder chains to be crosslinked with one another within the filler gallery. On the other hand, high *OMON* loading increased the chances of *ENR-50* chains to be intercalated. However, it can

reduce the chains population within *OMON* gallery, as well as on the silicate surfaces. The intercalated chains in this case thus had better chances to interact with the silicates, where the number of potential chains left for the crosslinking processes were lessened (Section 4.3.2.4A). Schematic diagram in Figure 7.12(a) and 7.12(b) illustrate the effects of *OMON* addition on chains crosslinking in *CENR-50* composites.

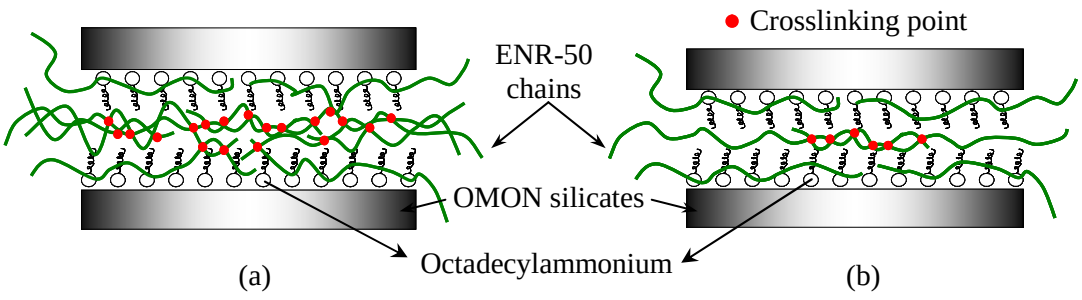

Figure 7.12: Intercalation in *CENR-50* with (a) low and (b) high *OMON* content. Chains crosslinking due to crosslink reaction and anti-oxidation effect are more pronounce in *OMON* gallery which is full of *ENR-50* chains.

Hydroxyl groups produced from anti-oxidation and hydrolysis processes stimulated good interactions between the crosslinked chains and *OMON* silicates. Physical network thereby can be developed in *CENR-50*, especially when the *ENR-50* chains continue to intercalate and crosslink within several *OMON* galleries. Further increase of *OMON* content promoted this network to expand widely in the rubber composite. Schematic diagram for the physical network is given in Figure 7.13. This belief is consistent with the growing effect on PL strength PL_{st} as *OMON* contents increased in the *CENR-50* composites. The trend of PL_{st} in Table 7.3(b) indicates the improved stress distribution mechanism in these composites.

The increase of *OMON* inclusion can also offer more contact surfaces for *ENR-50* and the crosslinked chains to interact with *OMON* silicates. The interactions that were assisted by binding forces at interphase promote stress sharing inside the *CENR-50*. It thus highlights

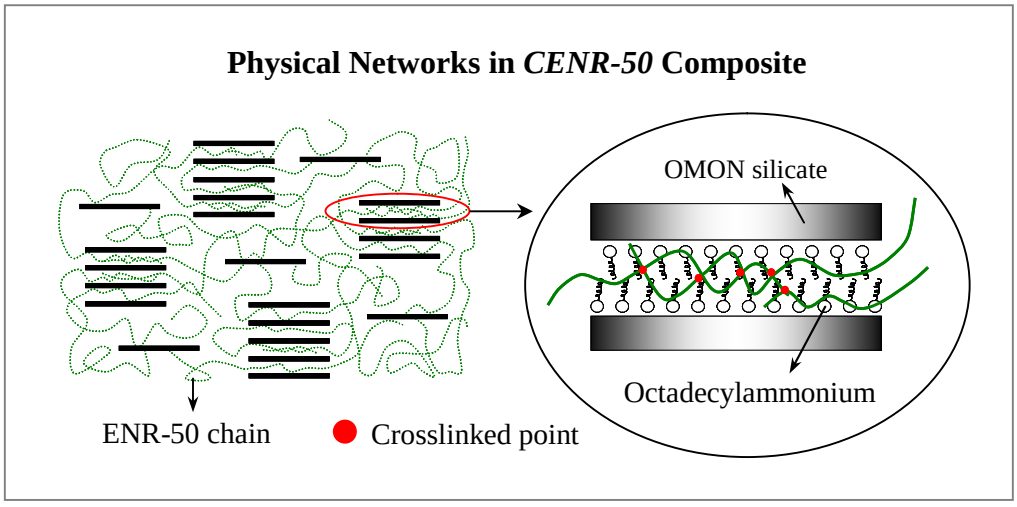

Figure 7.13: Crosslink reaction on matrix chains and good interactions with *OMON* silicate together formed physical network in *CENR-50*, which link both matrix and the filler domain in the composite system.

the benefit of good interfacial adhesion, which can easily facilitate stress transfer across a phase boundary [7.18]. In that way, it allowed *OMON* particles to share external stresses that in response stimulated strong reaction forces. As a result, more energy was needed to uncoil and straighten the matrix chains in *CENR-50*. The growing effect of stress sharing had some contributions on the mechanical properties of a composite. Such as the growth in PL strength PL_{st} for *CENR-50* with more than 15 % (> 15 %) of *OMON* content. The sudden increase of PL_{st} as shown in Table 7.3(b) for these cases provides the evidences. However, PL strains PL_{sn} from the table demonstrate notable reductions in the strain at proportional limit, PL. The drops could be indicating the increased amount of matrix chain that involved in *polymer-OMON* interactions, which can reduce the ability of these chains to uncoil elastically in the *CENR-50* composites.

The effects caused by stress distribution and stress sharing appear again within the plastic region of *CENR-50*. It is manifested on the increments of Tensile strength σ_{max} in Figure 7.14 with the increased loading of *OMON* particles. This observes confirms that physical networks managed to disperse applied stresses through out composites system. In response toward the stresses, both reinforcing mechanisms generated reaction forces. In which, it

requires great tensile strength to overcome the forces and cause permanent deformation in the *CENR-50* composites.

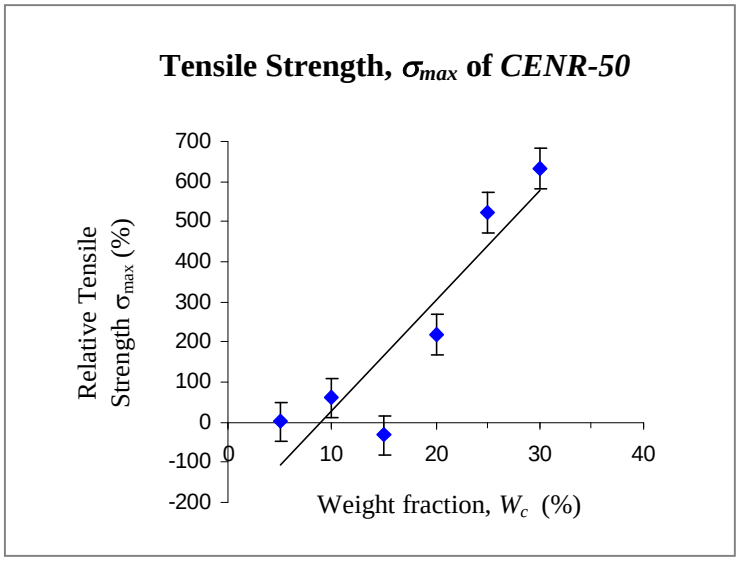

Figure 7.14: Relative tensile strength reveals structural effects caused by *OMON* particles on the ultimate strength in *CENR-50*.

The increased amount of *OMON* particle in *CENR-50* on the contrary led to the decrease in relative Maximum elongation, ε_{max} as shown in Figure 7.15. Typically, these results reveal the disadvantage of good adhesion that operates at the interphases in these composites. The growing number of *ENR-50* chains bonded to *OMON* silicates, at the same time weakened the linkage among matrix chains. Even though chains crosslinking from crosslink reaction process can generate more linkage for the intercalated chains, but the increase of *OMON* content discourage this process to take place effectively. The number of potential slippage among neighboring chains therefore was reduced in the composites. It affected the ability for extension within *CENR-50*, which reduced its Maximum elongation ε_{max}. The distortion on polymeric networks in *CENR-50* thus explains the ultimate elongation drops.

The significant of crosslink reaction is manifested on the growth of Maximum elongation, ε_{max} as listed in Table 7.3(b). Even though it had caused just a small increase about 3.5 %, but such increment can be seen only in case of *CENR-50* (5%). This finding is consistent

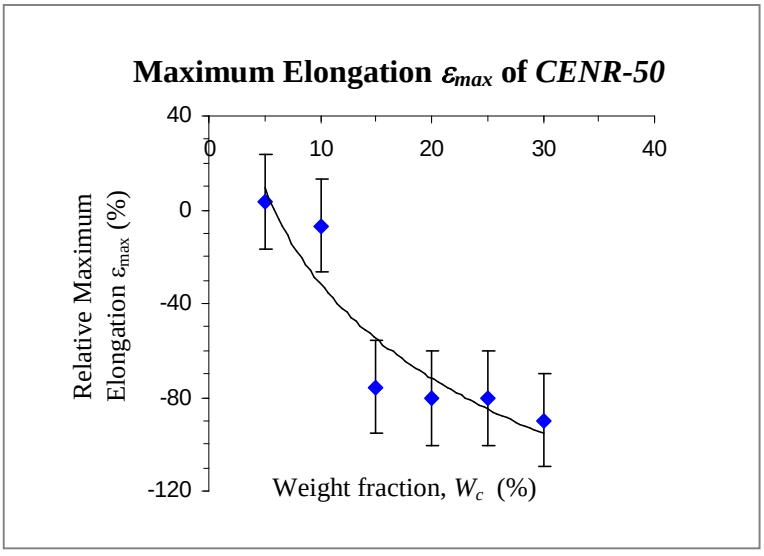

Figure 7.15: Relative maximum elongation shows that strain at break reduce logarithmically as *OMON* content increase in *CENR-50*.

with the earlier idea, which stated that low *OMON* content can stimulate extensive chains crosslinking inside *CENR-50*. Limited contact surface offered by *OMON* particles in such composite promotes more crosslink reaction process on intercalated chains. Even though intercalation had caused interruptions on the polymeric network of matrix chains, chemical crosslinking however managed to create new chain-linkages inside the composite. It thus, explains the growth in strain at break for *CENR-50* (5%).

Good distribution in low *OMON* content composite can cause the filler particles to distant from each other. A schematic diagram in Figure 7.16 illustrates possible condition for this case, which might have affected the inner structure of *CENR-50* (5%). This model suggests that matrix-filler interaction in the composite possibly had developed some local networks, which link a few adjacent particles together. These isolated networks however can hardly create effective physical network for stress dispersion mechanism. Small increment about 0.8 % in Tensile strength σ_{max} in Table 7.3(b) gives the proof for weak stress distribution in the composite. Mechanical behavior within the elastic region reveals more support for this finding. In fact, apparent drops about 91.8 % in PL strength PL_{st} and 23.4 % in PL strain PL_{sn} also highlight the effect of weak stress sharing at composite interfaces. The isolated

networks also weakened stress distribution within the elastic region. Combination of both effects actually had changed *OMON* particles into a stress concentrator during the elastic deformation. As a result, it induced early failure in the elastic region of *CENR-50* (5%) that contribute for the PL_{st} and PL_{sn} drops in this composite.

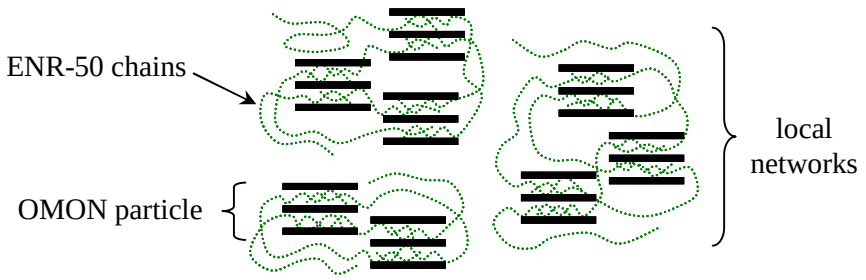

Figure 7.16: Small local networks in *CENR-50* with low *OMON* content.

Stacked layers structure of *OMON* is another effect from good interfacial adhesion within *CENR-50*. Analyses on XRD data revealed that five layers of *Mon* silicate platelets were neatly arranged within this structure. Though it was just a small increment, but it can be considered as an improvement in comparison with the original four layers structure from pristine *OMON*. In fact, *OMON* in less polar rubber composites (*CSMRL* and *CDPNR*) were losing their initial stacked layers during matrix-filler interactions. In polymer-clay composite, this arrangement has great potential to create mechanical friction that can add more elements into reinforcement mechanism. Nevertheless, this type of structure is also likely to act as a stress concentrator and creates weak points in composite system. By this means, its crucial effect should be on the reduction of ultimate elongation and maximum strength in *CENR-50*.Table 7.3(b) provides the evidence with the sudden drops in Tensile strength σ_{max} about 33 % for *CENR-50* (15%). It is including the 76 % drop in Maximum elongation ε_{max} of the same composite. These results therefore tell that the weak points that

were created by *OMON* particles had effectively induced the premature break within the *CENR-50* (15%) composite.

Excellent improvement on the elastic modulus *Y* in *CENR-50* was not an indication for its toughness. In fact, there is no clear trend developed as shown in Figure 7.17 except for its elastic toughness in Table 7.3(b). The toughness of materials describes the ability to absorb energy during elastic as well as plastic deformations. Under a stress-strain curve, energy is the works done as applied stress produce deformations on a body [7.1 and 7.3]. Therefore, it should be related to physical networks within the *CENR-50*. The increase in both stress distribution and stress sharing by such networks can produce growing effect on the energy absorption. Reduction in ultimate elongation ε_{max} however affected the amount of absorbed energy, especially with the improved stacking order ($N \sim 5$ layers) that may induce early failure in the composite. In that way, stress distributions can be distorted and then reduced the composite toughness. Moreover, the presence of stacked structure within the tested area of each sample could also dictated the *CENR-50* toughness.

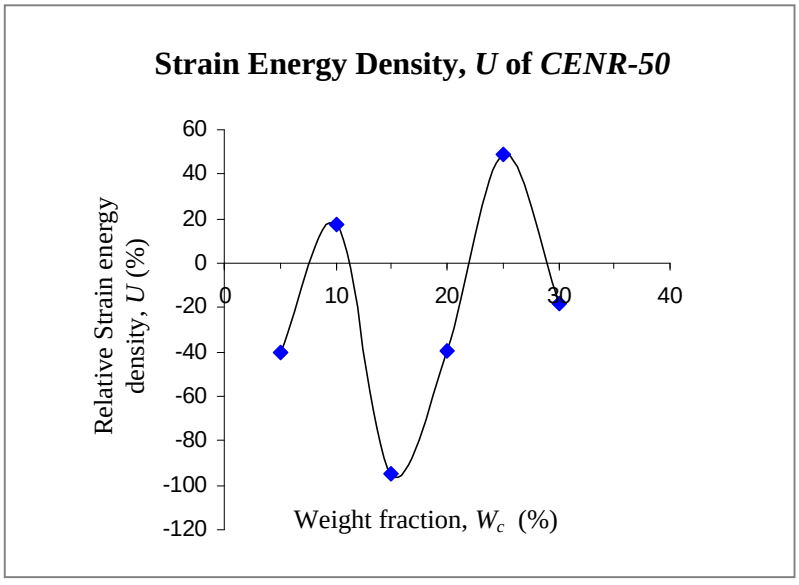

Figure 7.17: Relative strain energy density shows uncertain trend for *CENR-50* toughness as *OMON* particles increase in the composites.

7.2.2.1.B. Composite OMON-SMRL, CSMRL

Mechanical reactions toward external forces by *CSMRL* with 5 %, 10 %, 15 %, 20 %, 25 % and 30 % of *OMON* weight fractions are shown in Figure 7.18. These stress-strain curves demonstrate unusual effect of rigid filler interaction with polymeric matrix. Practically, it should be associated with *OMON* dispersion within the *CSMRL* composites. Typical result however, can be seen in *SMRL-Mon* (30 %) composite with a drop in Maximum elongation ε_{max}. The effects caused by *OMON* and *Mon* particles are reflected on several mechanical properties of these composites in Table 7.4(a). While Table 7.4(b) presents their relative percentage, which demonstrates that the clay particles as reinforcing agents had operated differently in the composites.

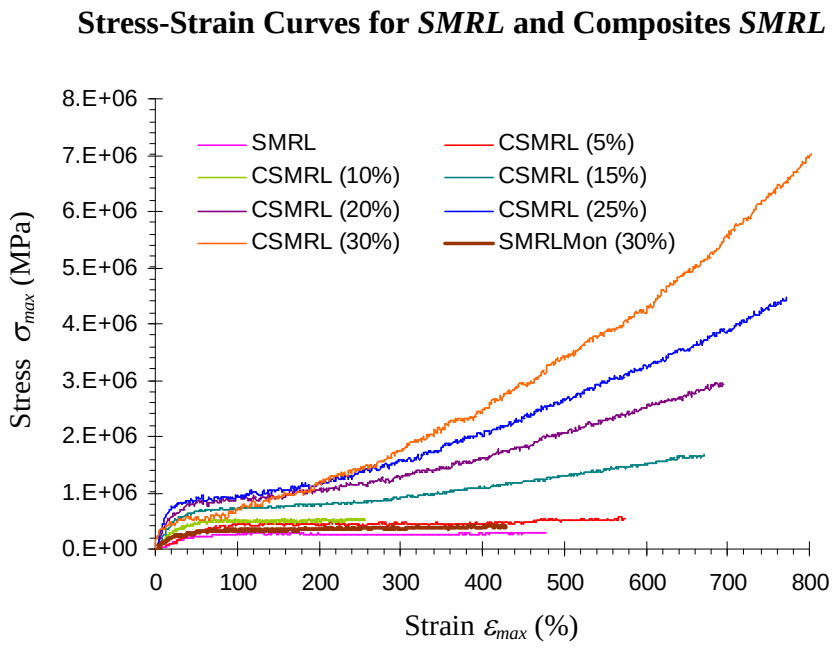

Figure 7.18: Stress-strain diagrams from tensile test on *SMRL* and composites *SMRL* with 5%, 10%, 15%, 20%, 25 % and 30% of *OMON* content. While *SMRLMon* (30%) represents composite with 30% of *Mon* for comparison.

The growths in the elasticity modulus, *Y* for *CSMRL* samples give good example. It seems that they are increased linearly with *OMON* contents as shown in Figure 7.19(a). In which the highest percentage increase is about 1258 % with 30 % of *OMON* inclusion. This is

Table 7.4(a)
Mechanical Properties of *SMRL* and Composite *CSMRL*

Sample	SMRL	CSMRL (5%)	CSMRL (10%)	CSMRL (15%)	CSMRL (20%)	CSMRL (25%)	CSMRL (30%)	SMRL Mon (30%)
Modulus, *Y* (MPa) (± 0.01)	0.57	1.23	2.07	4.15	4.78	6.75	7.72	0.68
PL Strength, *PLst* (MPa) (± 0.01)	0.14	0.31	0.34	0.39	0.47	0.44	0.33	0.18
PL Strain, PL_{sn} (%) (± 0.01)	26.14	46.44	25.81	15.25	13.59	9.35	6.06	16.87
Tensile Strength, σ_{max} (MPa) (± 0.01)	0.30	0.57	0.76	1.68	2.98	4.58	7.45	0.44
Max elongation, ε_{max} (%) (± 0.01)	485.83	583.21	638.82	680.47	704.39	780.86	824.76	437.10
Strain energy density, *U* (MN/m²) (± 0.01)	1.20	2.50	3.47	7.03	11.23	17.22	24.68	1.48

Table 7.4(a): Mechanical properties for *SMRL*, composite *CSMRL* with 5%, 10%, 15%, 20%, 25% and 30% of *OMON*. As well as composite with 30% of *Mon* content *SMRLMon* (30%).

Table 7.4(b)
Relative Percentage for Mechanical Properties in *CSMRL* and *SMRLMon*

Sample	CSMRL (5%)	CSMRL (10%)	CSMRL (15%)	CSMRL (20%)	CSMRL (25%)	CSMRL (30%)	SMRL Mon (30%)
Modulus, *Y* (%) (± 0.01)	116.54	264.08	630.09	740.76	1088.11	1257.78	20.17
PL Strength, PL_{st} (%) (± 0.01)	125.97	145.85	182.40	235.45	213.62	135.21	30.58
PL Strain, PL_{sn} (%) (± 0.01)	77.68	-1.25	-41.66	-48.00	-64.24	-76.81	-35.44
Tensile Strength, σ_{max} (%) (± 0.01)	90.40	156.57	467.17	902.81	1442.94	2407.76	47.40
Max elongation, ε_{max} (%) (± 0.01)	20.04	31.49	40.06	44.99	60.73	69.76	-10.03
Strain energy density, *U* (%) (± 0.01)	107.72	188.45	484.81	834.16	1331.96	1951.98	23.37

Table 7.4(b): Relative percentage for mechanical properties from composite *SMRL* with *OMON* (*CSMRL*) and Mon (*SMRLMon*) in comparison with the counterparts in *SMRL*.

way too big compared to the 20 % increase for the same amount of filler in *SMRL-Mon* system, as listed in Table 7.4(b). Intercalation inside *CSMRL* therefore, should have played significant role that differentiate the effects from both *OMON* and *Mon* particles. Chains penetration into *OMON* interlayer was not just widen its chances to interact with the filler silicates. In fact, the trapped polyisoprene chains in such a confine space could also lead to some correlated processes that also contribute to the reinforcement in *CSMRL* composites.

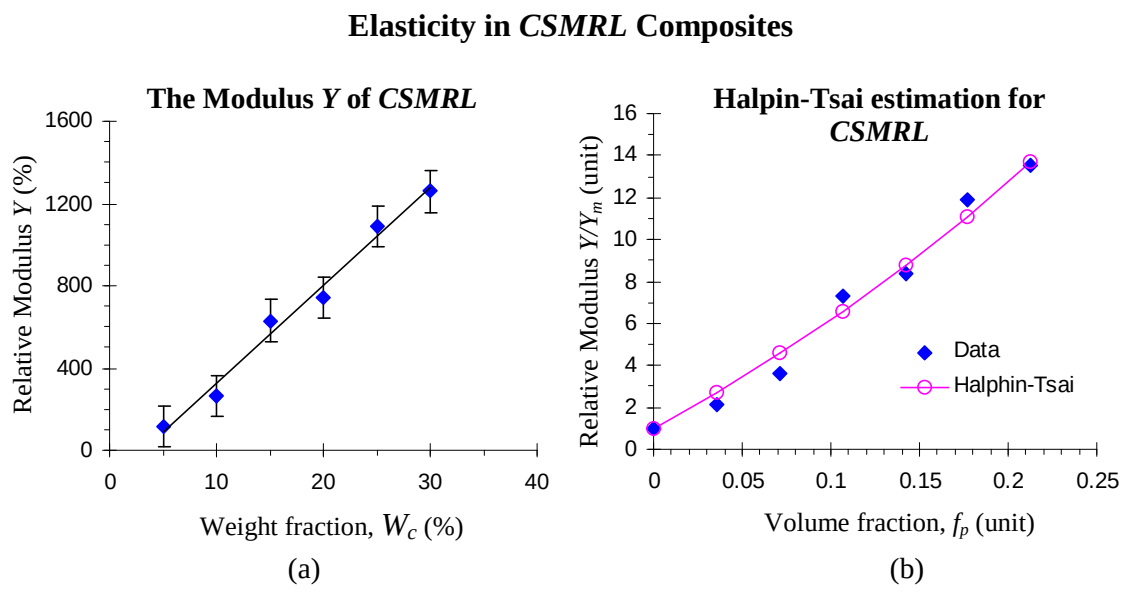

Figure 7.19: *OMON* effects on elasticity modulus *Y*: (a) Modulus *Y* for *CSMRL* relative to the elasticity value in pristine *SMRL* and (b) Halpin –Tsai estimation for intercalated structure fit the relative modulus *Y* of *CSMRL*.

SMRL is a type of natural rubber composed of cis 1, 4 polyisoprene chains with limited amount of polar component, such as the epoxidised double bonds and protein molecules. Practically these polar components are not enough to promote extensive hydrogen bonding as in case of *CENR-50*. However, the created hydrogen bonds together with van der Waals forces managed to bring the bulky matrix chains into close contact with *OMON* silicate surfaces. Physical interactions thereby can be generated at phase boundaries, which then became a part of the reinforcing mechanism within *CSMRL* composites.

The lack of physical linkage between polyisoprene chains and *OMON* silicates gave an advantage to the *CSMRL* composite. Weak attraction forces that operated at the materials interphase had slightly affected the matrix interchains reactions. In consequence, it left most of the polyisoprene chains still intact to one another. Such condition promotes better crosslink reaction to take place, which were assisted by the amine cations within *OMON* gallery. This chemical reaction on double bonds of the matrix chains would easily facilitate chemical crosslinking among the adjacent chains of *SMRL*. Section 4.3.2.4.A discussed the effects of this reaction on the double bonds in *SMRL* chain. The intercalation and crosslink processes continued to work on more galleries of several *OMON* particles. As a result, they formed *interparticle bridging flocculated* structures inside the *CSMRL* composites. The long elastomeric chains of *SMRL* matrix effectively promoted this *interparticle bridging flocculation* process, where it turned out to be the important source for chemical networks within the flocculated structures. Illustration for such structures within the *CSMRL* is given in Figure 7.20.

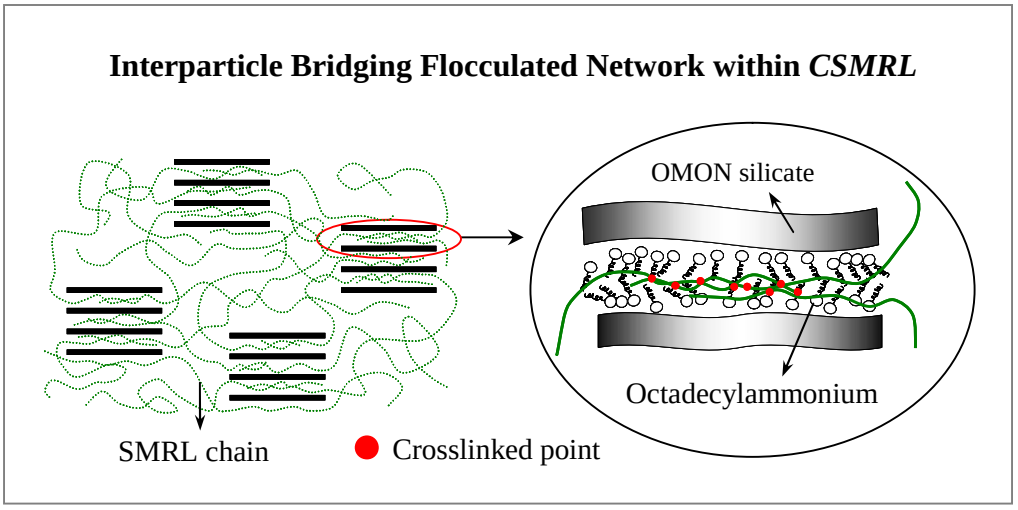

Figure 7.20: Chains crosslinking simultaneously within several *OMON* galleries connect both matrix chains and *OMON* particles into a big interparticle bridging flocculated network in *CSMRL*.

Both physical and chemical interactions actually had strong effect on the strength behavior of *CSMRL*. The strength increase at PL points, PL_{st} in Table 7.4(b) provides the evidence.

It shows that the percentage increases of PL_{st} strength are analogous to the values in Table 7.3(b) for *CENR-50* composites, which had strong interfacial adhesion. However, similar physical adhesion is not a dominant in *CSMRL* composites. From the earlier discussions on reaction force, it was believed that the generated force during stress loading is important to assist matrix chains to uncoil elastically. This observation thus tells that chemical networks within the *CSMRL* composites could also generate such reaction force. Despite the lack of strong interfacial adhesion, *CSMRL* network therefore was able to cause the growing effect in elastic strength PL_{st} as the *CENR-50* composites.

High external stress that were needed to overcome the reaction forces, in return affected the normalized modulus Y/Y_m. Figure 7.19(b) shows that the modulus Y increases almost linearly with the volume fractions, f_p. The trend developed can be fitted by the estimation values from the Halpin–Tsai equation. Where, it covers a wide range of weight fractions W_c from 0 % up to 30 % that is about 0.0 to 0.2 in the volume fraction f_p. This fitting apparently is consistent with the theory that predicts the Y/Y_m values for an intercalated system, as in case of *CSMRL*. However, the fitted curve within such big range of volume fraction ($f_p > 0.1$) thus far is not clearly understood. The Halpin–Tsai model is normally used to describe the cases for small filler loading ($W \leq 10$ %). This finding perhaps can be associated to the unique flocculated network structure in the *CSMRL* composites.

The real benefits of *interparticle bridging* based networks can be seen within the plastic region of *CSMRL* stress-strain diagrams. The growth in Tensile strength σ_{max} as shown in Figure 7.21 for instance demonstrates an exponential increase with *OMON* addition. This observes could be an indicator for excellent stress distribution mechanisms, which can effectively weaken stress intensity at a point within the composite system. In that way, it encouraged more external stresses to be absorbed before chains slippages took place among the matrix chains. For example, it had caused about 2408 % increment in σ_{max} for

CSMRL with 30 % of *OMON* weight fraction. While in case of *CENR-50* with deteriorated matrix networks, similar amount of filler generated just about 633 % increment on the ultimate strength. Hence, it proves that flocculated networks within *CSMRL* had improved stress distribution mechanism within the composite.

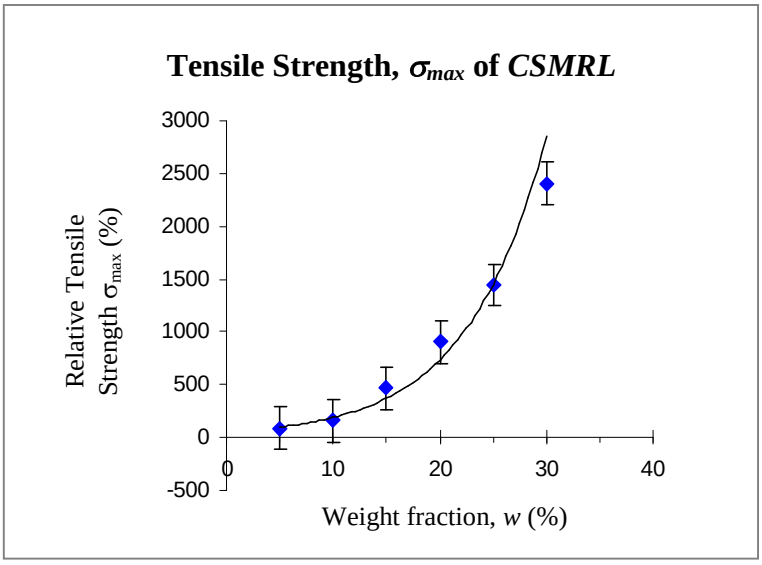

Figure 7.21: Relative tensile strength reveals good stress dispersion by interparticle bridging flocculated network in *CSMRL*.

Prominent effect produced by the modified structure actually was on Maximum elongation ε_{max} as shown in Figure 7.22, where *OMON* inclusion had caused the linear growth on the

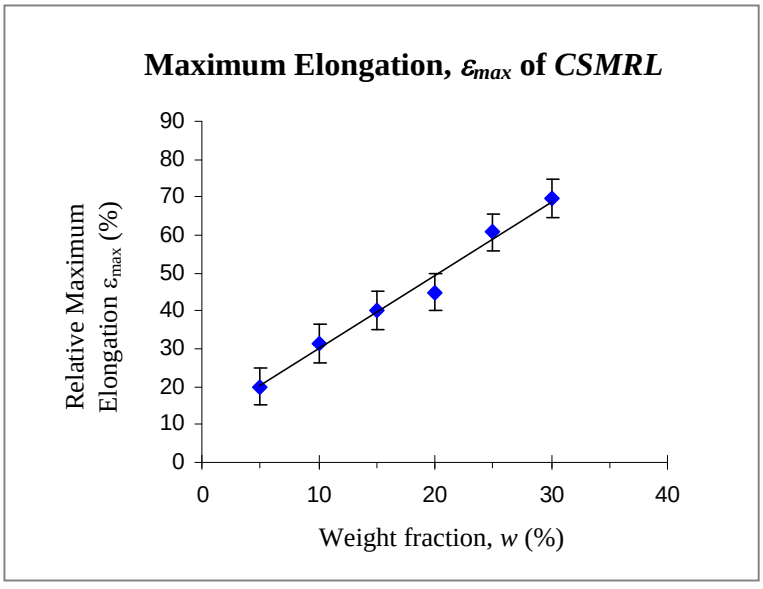

Figure 7.22: Relative maximum elongation shows notable growths that indicate the growing effect from vulcanization process within *OMON* interlayer in *CSMRL* composites.

elongation at break ε_{max} of *CSMRL* composites. This unique mechanical behavior should have some connections to the chemical networks of *interparticle bridging* structures in the composites. Intercalation generally leads to disruption on the polymeric network of matrix chains. Amine assisted crosslinking reaction however had helped to reorganize and create new polymeric linkage among the rubber matrix chains inside *OMON* galleries. Therefore, chains slippage was more pronounced within *CSMRL* composites in comparison to that of pristine *SMRL*.

The growths in Tensile strength σ_{max} together with Maximum elongation ε_{max} produced the growing effects on *CSMRL* toughness. Strain energy density *U* plot in Figure 7.23 reveals the exponential increase of *CSMRL* toughness, which is caused by *OMON* inclusion in the composites. Table 7.4(b) shows that the energy density *U* for *CSMRL* can reach more than 100 % increment, with just about 5 % of *OMON* addition. Again, good stress distribution via the *bridging flocculated networks* in effect had allowed the *CSMRL* composites to absorb more energy before mechanical failure took place.

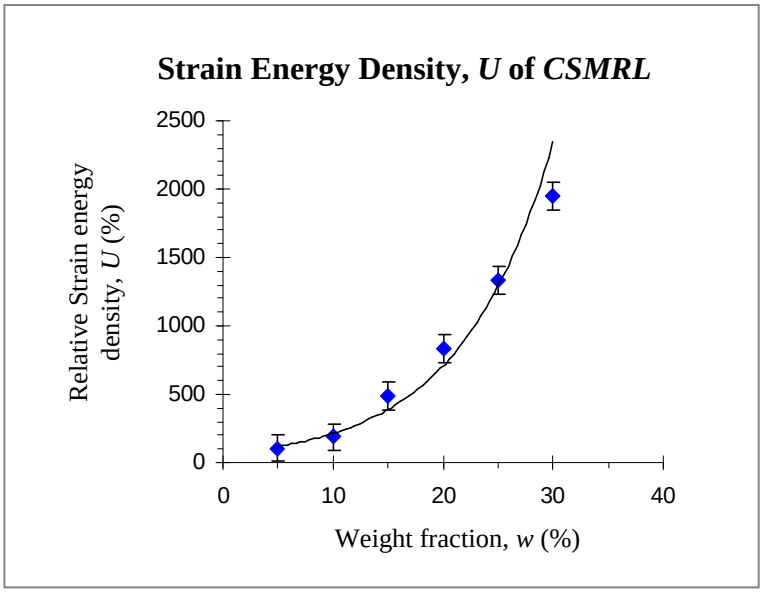

Figure 7.23: Relative strain energy density shows that *CSMRL* toughness increase due to the rise in both ultimate strength and strain within the composites.

7.2.2.1.C. Composite OMON-DPNR, CDPNR

Trends developed by mechanical properties for *CDPNR* in Table 7.5(a) are comparable to their counterparts in the previously discussed *CSMRL* composites. Figure 7.24 shows the stress-strain plots of *CDPNR* with 5 %, 10 %, 15 %, 20 %, 25 % and 30 % of *OMON* inclusions. Similarly as the *CSMRL*, these plots reveal the unique coupled improvements in the Tensile strength σ_{max} and Maximum elongation ε_{max} of *CDPNR* composites. However, different scenario is observed on the influence of *Mon* loading on *DPNR* and *SMRL* matrix chains. Composite *DPNR* with 30 % of *Mon* in Figure 7.24 for example shows a growth on the maximum strain ε_{max}, which is about 6 % as shown in Table 7.5(b). From Table 7.4(b) however, the same amount of *Mon* had caused about 10 % reduction in the strain at break ε_{max} of *SMRL-Mon* system.

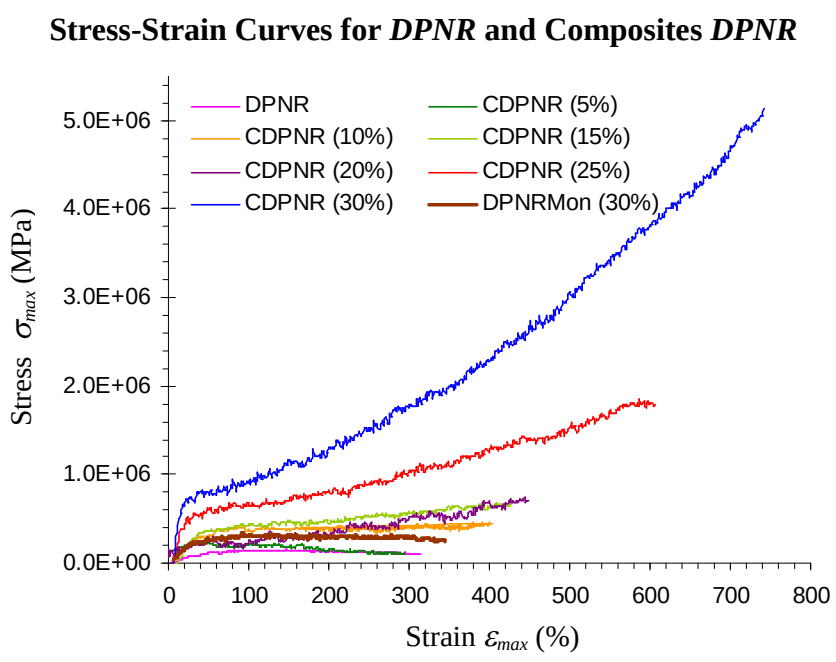

Figure 7.24: Stress-strain diagrams from tensile test on *DPNR* and composites *DPNR* with 5%, 10%, 15%, 20%, 25% and 30% of OMON content. While *DPNRMon* (30%) represents composite with 30% of *Mon* for comparison.

Both increment and reduction can actually take place in *DPNR-Mon* as well as *SMRL-Mon* composites. However, the outcomes depend on *Mon* dispersions within the tested area of a

Table 7.5(a)
Mechanical Properties of *DPNR* and Composite *CDPNR*

Sample	DPNR	CDPNR (5%)	CDPNR (10%)	CDPNR (15%)	CDPNR (20%)	CDPNR (25%)	CDPNR (30%)	DPNR Mon (30%)
Modulus, *Y* (MPa) (± 0.01)	0.24	0.43	1.37	1.51	2.22	2.83	3.31	0.24
PL Strength, *PLst* (MPa) (± 0.01)	0.08	0.22	0.24	0.25	0.14	0.42	0.34	0.08
PL Strain, PL_{sn} (%) (± 0.01)	25.46	25.61	26.75	26.28	5.41	18.65	10.71	25.46
Tensile Strength, σ_{max} (MPa) (± 0.01)	0.16	0.25	0.47	0.71	0.87	1.97	5.33	0.16
Max elongation, ε_{max} (%) (± 0.01)	333.97	399.78	405.52	436.30	457.78	615.15	751.44	333.97
Strain energy density, *U* (MN/m²) (± 0.01)	0.38	0.58	1.49	2.10	1.86	6.60	18.13	0.38

Table 7.5(a): Mechanical properties for *DPNR*, composite *CDPNR* with 5%, 10%, 15%, 20%, 25% and 30% of *OMON*. As well as composite with 30% of *Mon* content *DPNRMon* (30%).

Table 7.5(b)
Relative Percentage for Mechanical Properties in *CDPNR* and *DPNRMon*

Sample	CDPNR (5%)	CDPNR (10%)	CDPNR (15%)	CDPNR (20%)	CDPNR (25%)	CDPNR (30%)	DPNR Mon (30%)
Modulus, *Y* (%) (± 0.01)	77.66	465.32	523.26	820.04	1069.66	1268.13	167.87
PL Strength, PL_{st} (%) (± 0.01)	163.86	185.45	196.97	68.35	404.09	310.77	136.76
PL Strain, PL_{sn} (%) (± 0.01)	0.60	5.07	3.21	-78.77	-26.73	-57.94	4.59
Tensile Strength, σ_{max} (%) (± 0.01)	64.15	203.47	356.50	457.54	1170.94	3332.00	123.01
Max elongation, ε_{max} (%) (± 0.01)	19.70	21.42	30.64	37.07	84.19	125.00	5.85
Strain energy density, *U* (%) (± 0.01)	51.50	287.10	446.39	384.12	1616.38	4614.83	150.45

Table 7.5(b): Relative percentage for mechanical properties from composite *DPNR* with *OMON* (*CDPNR*) and Mon (*DPNRMon*) in comparison with the counterparts in pristine *DPNR*.

sample. Good dispersion in effect will widely spread the tiny *Mon* particles among the rubber matrix chains. These particles increased interchains distance, and thereby produced the *plasticizer effect* on matrix chains. The effect allowed the chains to further extent and then produced the ε_{max} growth in *DPNR-Mon*. This effect can actually take place without the involvement of intercalation process inside the composite. However, *agglomeration* of *Mon* particles created clusters, which can act as a stress concentrator. Even a small cluster of *Mon* within the tested area will easily induced premature failure on a sample. This effect possibly had caused the ε_{max} reduction in the *SMRL-Mon* composite.

OMON effects on *CDPNR* mechanical properties within elastic region are more or less the same with those for *CSMRL* composites. The growths on elastic modulus Y in Table 7.5(b) are among the good examples. It reveals that for 30 % of *OMON* content in *CDPNR*, the modulus Y is increased about 1268 %. This value is close to the 1258 % increment in *CSMRL* with the same amount of *OMON* content. In fact, both *CDPNR* and *CSMRL* in Figure 7.19(a) and Figure 7.25(a) respectively had linear improvement on their modulus *Y*.

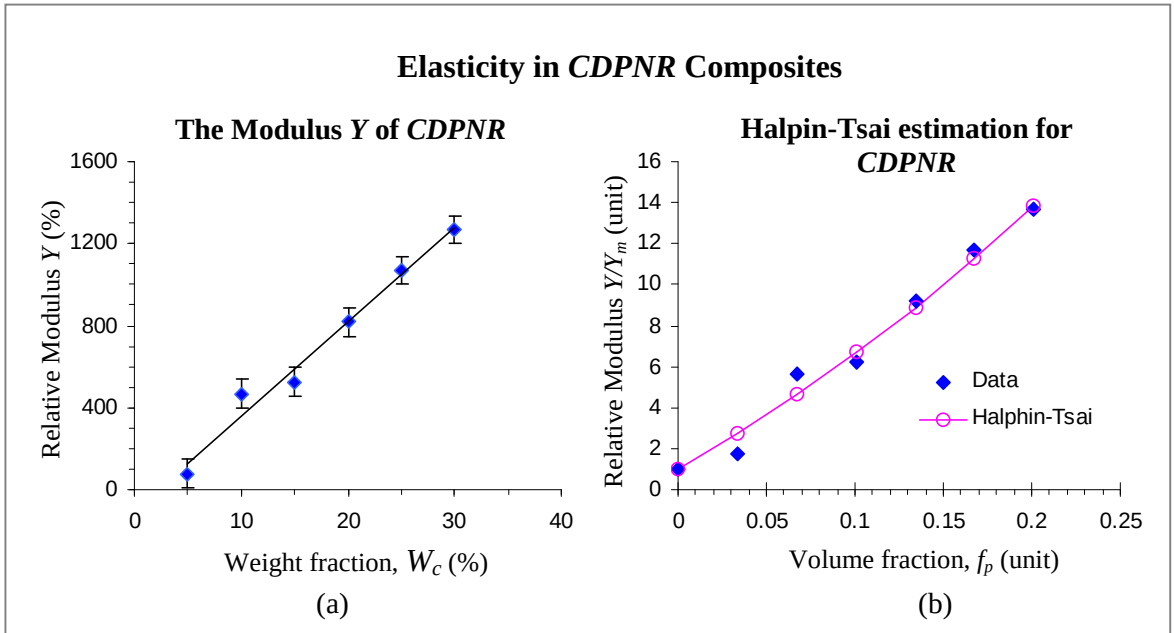

Figure 7.25: *OMON* effects on elasticity modulus *Y*: (a) Modulus *Y* for *CDPNR* relative to the elasticity value in pristine *DPNR* and (b) Halpin –Tsai estimation for intercalated structure fit the relative modulus from *CDPNR*.

More similarity can be observed on the normalized modulus Y/Y_m for *CDPNR* composites in Figure 7.25(b). Where, the curve of experimental data is also well fitted by the Halpin-Tsai estimation as that of *CSMRL* in Figure 7.19(b).

Despite the fact that protein components in *DPNR* are removed, the internal structures of *DPNR* and *SMRL* are not so distinct. They are basically comprised of similar polyisoprene chains and thereby it may explain the observations. However, advanced crosslink reaction was detected in case of *CDPNR* composite via FTIR analyses in Section 4.3.2.4.A. By that means, the developed interparticle *bridging flocculated* structures in this composite should be improved as well. The improved crosslink reaction also demonstrates the lack of *DPNR* interaction with *OMON* silicates. Small deviation on the increase of modulus *Y* for *CDPNR* and *CSMRL* highlights the important of both effects. It tells that flocculated network and reinforcement by the filler silicates are equally important to create reaction forces in elastic region. This reaction force is believed to give great influence on the elastic properties of *natural rubber-OMON* composites. Schematic illustrations in Figure 7.26 differentiate the inner structure of *CDPNR* from its counterpart in *CSMRL*, as shown in Figure 7.20.

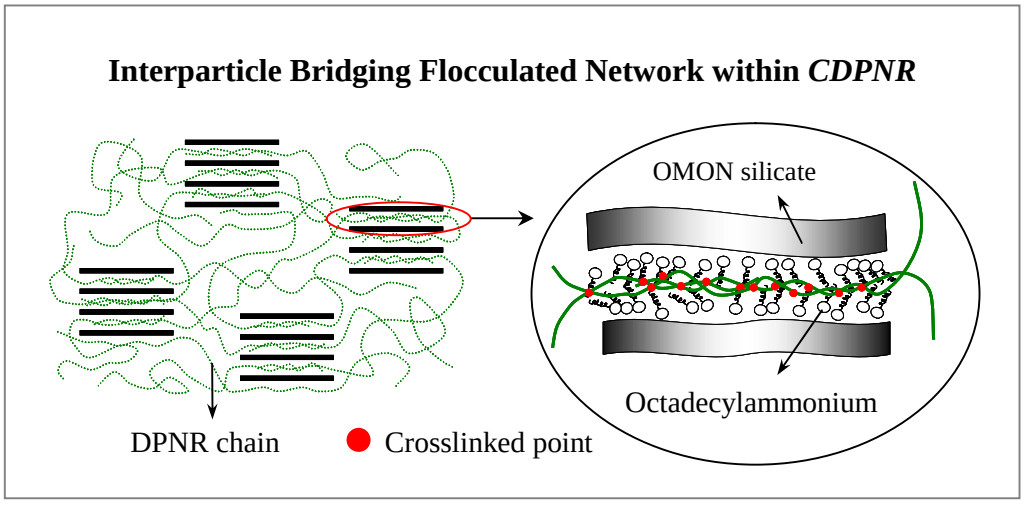

Figure 7.26: The lack of interaction with silicates encourages better crossliking on *DPNR* chains within *OMON* galleries. It also improve the interparticle bridging process that develop the flocculated networks in *CDPNR*.

Nevertheless, the improved networks had caused strong effects on the mechanical behavior within plastic region, mostly in *CDPNR* samples with high *OMON* constituent. Consider the exponential growth of Tensile strength, σ_{max} for *CDPNR* and *CSMRL* in Figure 7.27 and 7.21, respectively. The growths are comparable in both types of composites with less than 20 % of *OMON* content. However, greater than this percentage the increments had large difference. For example with 30 % of *OMON* addition, the Tensile strength σ_{max} of *CDPNR* gives about 3232 % increment. While in case of *CSMRL*, it is just about 2408 %. These observe show that stress distribution was actually more efficient in *CDPNR* (30%) system compare to that of *CSMRL* (30%). The lack of polar components caused by protein removal from *DPNR* chains may explain the results. Polar component in matrix chains is known to promote matrix-silicate interactions [7.27, 7.28 and 7.29] within *polymer-OMON* composite. The lack of polar components in *DPNR* therefore effectively reduced the close interactions between the *DPNR* chains and *OMON* silicates. In that way, the rubber matrix chains had better chances to intercalate into more *OMON* particles, which subsequently led to bigger interparticle bridging network structures.

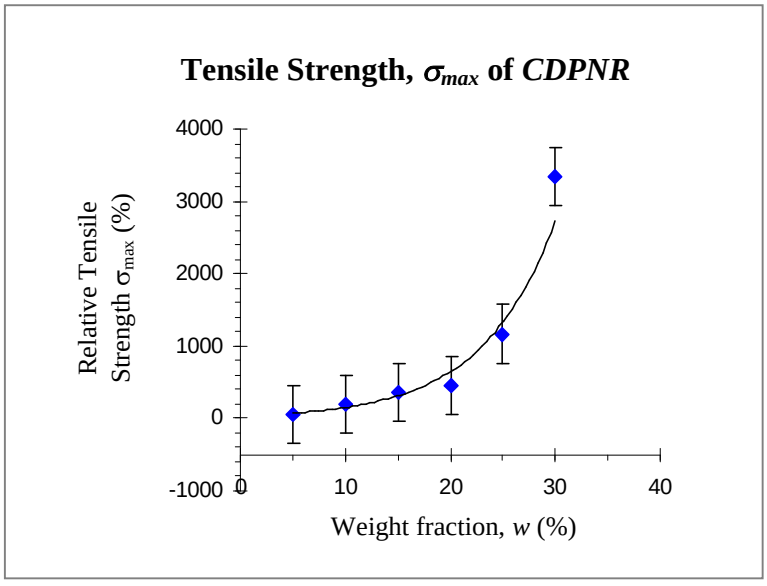

Figure 7.27: Relative tensile strength in *CDPNR* adds more proof on excellent effect of interparticle bridging flocculated networks toward stress distribution mechanism in composite.

This idea is in agreement with the results demonstrated by Maximum elongation ε_{max} in Figure 7.28 The exponential growth by *CDPNR* had caused about 125 % increment on a specimen with 30 % of *OMON* weight fraction. This is about 79 % higher for similar effect in case of *CSMRL* with the same amount of *OMON* content. These observations actually indicate that the improved crosslink reactions within *CDPNR* had effectively linked up the matrix chains in *OMON* gallery. Subsequently, the advanced chains crosslinking promoted extensive *interparticle bridging flocculation* process in the *CDPNR* composites. Therefore, more chain slippage can take place as reflected on the improved Maximum elongation ε_{max} of *CDPNR* (30%) compare to that of *CSMRL* (30%).

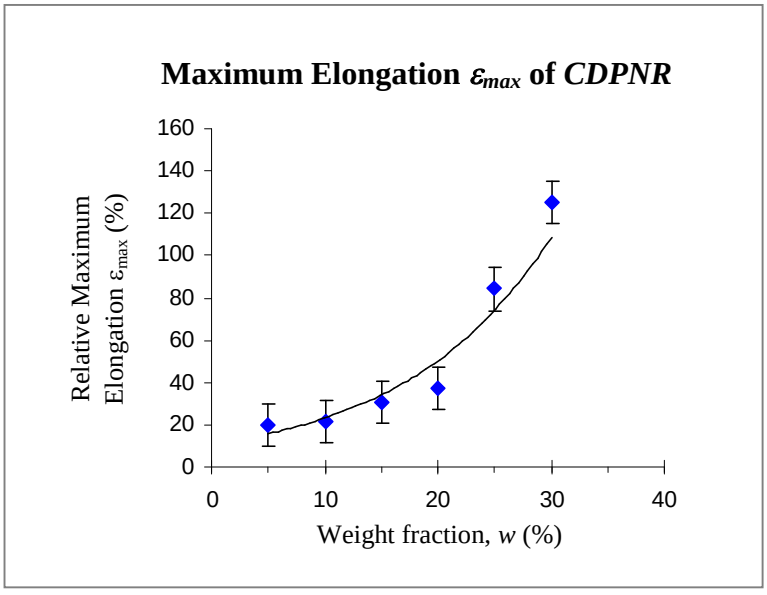

Figure 7.28: Relative maximum elongation shows notable growths that indicate more chains crosslink from vulcanization process in *CDPNR*.

Likewise, the toughness of *CDPNR* was increased where it rise exponentially with *OMON* content as shown in Figure 7.29. Extensive *bridging networks* in *CDPNR* seemed as given great advantage for the toughness. For example, about 30 % of *OMON* particles had caused the toughness to rise around 4146 % in *CDPNR* (30%). It is a big growth in comparison with the similar effect within *CSMRL* (30%), where its flocculated structures generated just about 1952 % increment. The growth in *CDPNR* (30 %) can be considered as a remarkable

improvement, especially when compare to the toughness drop in Table 7.3(b). It reveals that the toughness of *CENR-50* (30%) was decreased approximately 0.34 %, despite the strong interfacial adhesions in the composite.

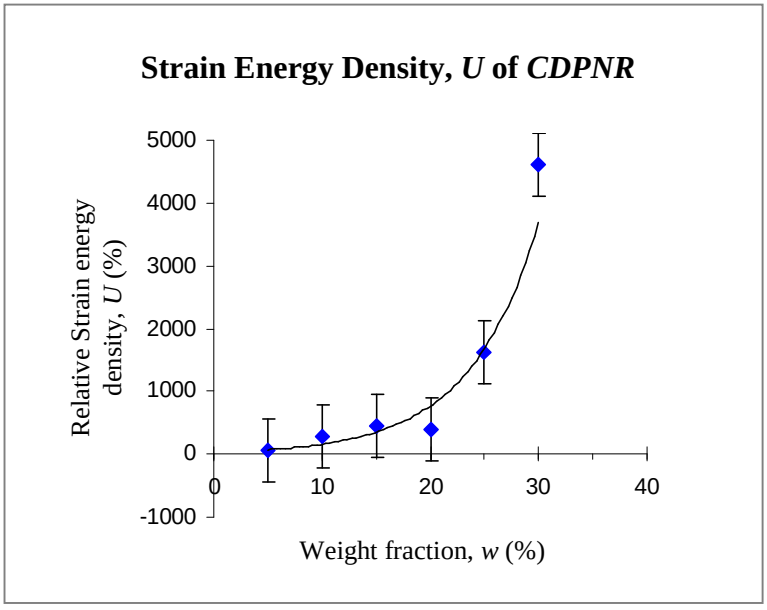

Figure 7.29: Relative strain energy density shows that improved interparticle bridging flocculated network structure in *CDPNR* increase toughness better than *CSMRL*.

Good stress distribution by the *flocculated network* in *CDPNR* is actually very important to avoid stress concentrators. The present of such concentrator can readily create weak points inside the composite system. On the other hand, close interactions with *OMON* silicates in *CENR-50* tend to create such weak points at phase boundaries. Physical crosslinkage with *OMON* silicate in addition can limit the spreading of applied forces. These effects therefore explain the weak toughness of *CENR-50*, despite its strong interfacial adhesions. Chemical crosslink in *interparticle bridging flocculated* network give better stress distribution. It was also functioning to slow down progressive failure in the *CDPNR* system. Such mechanisms by the *bridging flocculated* networks thus had changed *CDPNR* composite into a tougher material than its pristine polymer.

7.2.2.1.D. Composites OMON-Polyethylene, CPE

Mechanical study on *CPE* was carried out using samples with 1 %, 2 %, 3 %, 4 % and 5 % of *OMON* weight fractions. It was also including composite *PE* with 5 % of *Mon* content for comparison. Plots in Figure 7.30 show the stress-strain diagram of composites from the tensile test results in Table 7.6(a). They demonstrate the typical behavior of a composite with rigid filler inclusion [7.27 and 7.30]. Unlike the *natural rubber-OMON* composites, small fractions of *OMON* content were used in the *CPE* samples. In fact, it is a common practice to study the effect of small filler addition on composite properties. Particularly, composite with low molecular weight (MW) polymer matrix such as *PE*, where the high contain of rigid filler will easily lead polymeric composite to brittleness.

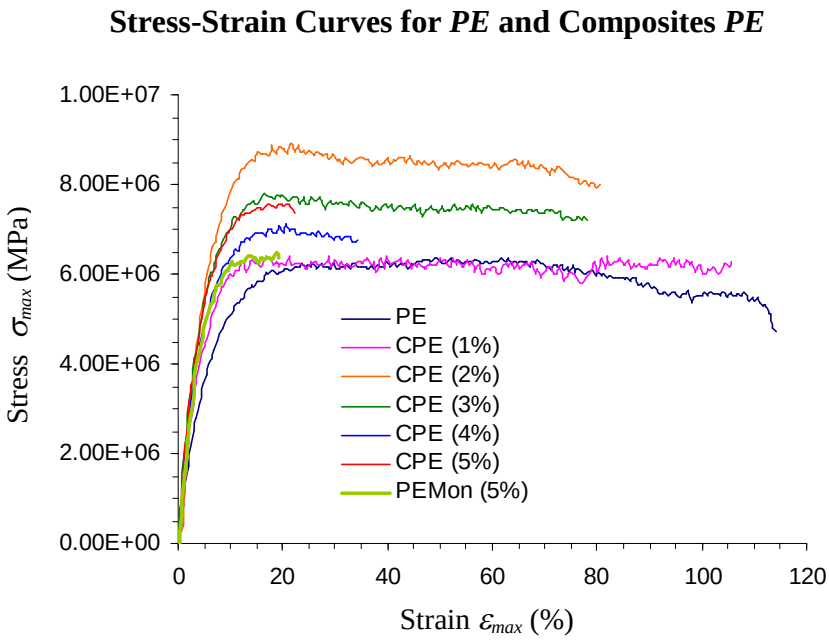

Figure 7.30: Stress-strain diagrams from tensile test on *PE* and composites *PE* with 1%, 2%, 3%, 4% and 5% of *OMON* content. *PEMon* (5%) represents composite with 5% of *Mon* for comparison.

PE is a non-polar polymer with very high hydrophobicity characteristic. For that reason, even the organophilic silicates such as *OMON* cannot be well dispersed inside the polymer. Therefore, it is hard to intercalate *PE* chains into *OMON* gallery especially via the method

Table 7.6(a)
Mechanical Properties of *PE* and Composite *PE*

Sample	PE	CPE(1%)	CPE(2%)	CPE(3%)	CPE4(%)	CPE(5%)	PEMon (5%)
Modulus, *Y* (MPa) (± 0.01)	179.94	187.95	190.04	197.99	205.07	210.44	180.55
PL Strength, PL_{st} (MPa) (± 0.01)	1.71	3.03	3.78	2.86	2.52	2.14	2.27
PL Strain, PL_{sn} (%) (± 0.01)	1.85	2.42	2.77	1.73	1.45	1.24	1.67
Tensile Strength, σ_{max} (MPa) (± 0.01)	6.63	6.86	9.09	8.30	7.83	8.13	6.82
Max elongation, ε_{max} (%) (± 0.01)	117.61	109.09	83.98	81.73	37.82	25.67	22.67
Strain energy density, *U* (MN/m^2) (± 0.01)	6.66	6.54	6.73	5.83	2.34	1.63	1.21

Table 7.6(a): Mechanical properties for *PE*, composite with *OMON*: *CPE* (1%), *CPE* (2%), *CPE* (3%), *CPE* (4%) and *CPE* (5%). It is including the composite with 5% of *Mon* inclusion *PEMon* (5%).

Table 7.6(b)
Relative Percentage for Mechanical Properties in *CPE* and *PEMon*

Sample	CPE(1%)	CPE(2%)	CPE(3%)	CPE4(%)	CPE(5%)	PEMon (5%)
Modulus, *Y* (%) (± 0.01)	4.45	5.62	10.03	13.97	16.95	0.34
PL Strength, PL_{st} (%) (± 0.01)	76.98	121.23	67.01	47.26	24.93	32.89
PL Strain, PL_{sn} (%) (± 0.01)	31.15	50.00	-6.56	-21.31	-32.79	-9.84
Tensile Strength, σ_{max} (%) (± 0.01)	3.53	37.11	25.29	18.10	22.63	2.87
Max elongation, ε_{max} (%) (± 0.01)	-7.24	-28.59	-30.51	-67.84	-78.18	-80.73
Strain energy density, *U* (%) (± 0.01)	-1.77	1.04	-12.40	-64.90	-75.51	-81.76

Table 7.6(b): Relative percentage for mechanical properties from composite *PE* with *OMON* (*CPE*) and *Mon* (*PEMon*) in comparison with their counterparts in case of *PE*.

of solution casting. In this work however, intercalation was detected on *CPE* (5%) with just about 5 % of *OMON* content. Mechanical analysis confirms the effect of *OMON* with a clear difference between the growth in elastic modulus, *Y* for *CPE* and *PE-Mon*. From Table 7.6(b), the modulus *Y* for *CPE* (5%) shows an increase about 16.95 % that is around 4885 % higher than the increase about 0.34 % in case of *PE-Mon* (5%).

The elasticity modulus *Y* for *CPE* in general rises linearly with the incorporation of *OMON* particles as shown in Figure 7.31(a). Again, penetration into *OMON* galleries by *PE* chains should have played significant role behind these observations. This is confirmed with the Halpin–Tsai estimation in Figure 7.31(b), which shows the growing effects of intercalation on the elasticity property. The remark actually is based on the fitted normalized modulus Y/Y_m for the *CPE* composites. It also proves the linear correlation between clay structure and modulus *Y*, as stated by the Halpin–Tsai theory for nanoclay composite with low filler content. This behavior is a result of intercalation process that gives wide contact surfaces for *polymer-OMON* interaction in the composite.

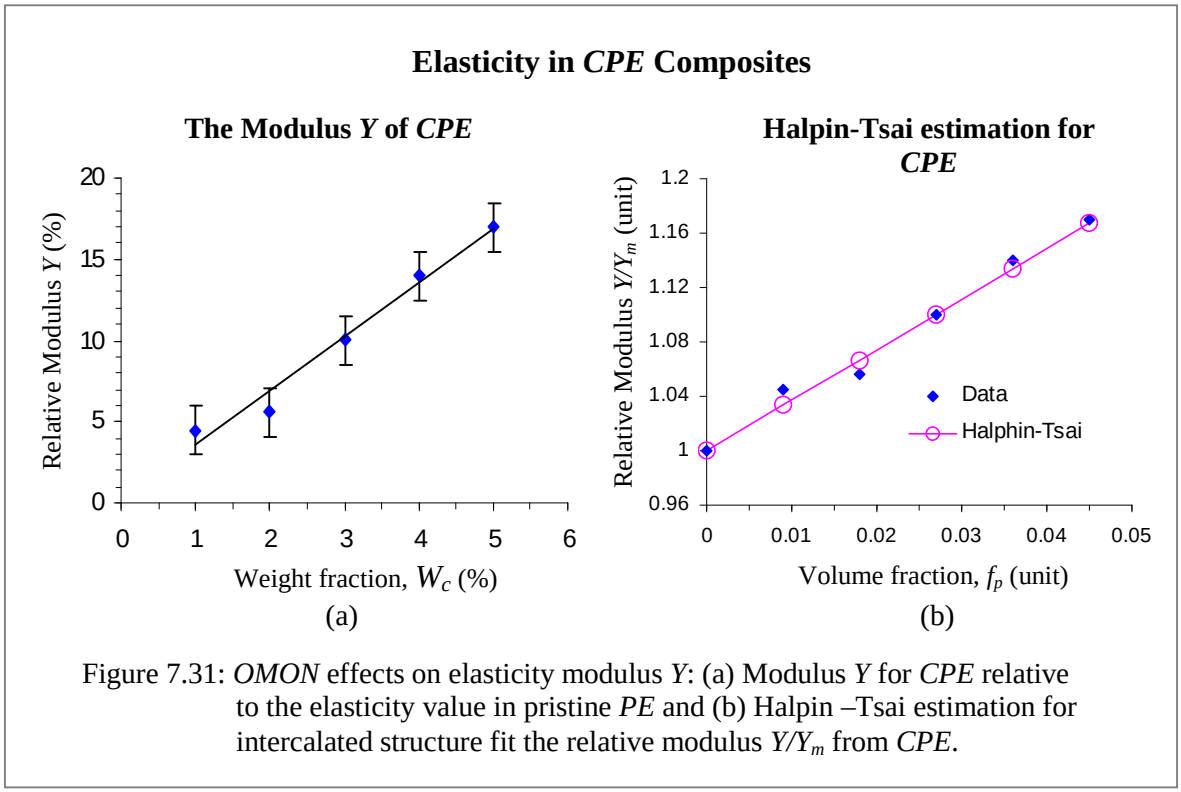

Figure 7.31: *OMON* effects on elasticity modulus *Y*: (a) Modulus *Y* for *CPE* relative to the elasticity value in pristine *PE* and (b) Halpin –Tsai estimation for intercalated structure fit the relative modulus Y/Y_m from *CPE*.

Besides the wide contact area, intercalation can also induce better matrix-filler interactions in *CPE*. Chains coiling between *PE* and *ODA* chains within *OMON* gallery for example produce physical linkage, which is important element for the composite reinforcement. The coiling mechanism itself is very useful in assisting van der Waals forces to bring *PE* chain closer toward *OMON* silicate surface. In that way, the non-polar matrix chains and filler particles were able to induce interfacial adhesion within the composite system. The binding forces at phase boundary in *CPE* had great potential to stimulate stacking layers structure on *OMON* units. During stress loading, such structure in response can generate mechanical frictions. This generated resistance force is also a part of the reinforcing mechanisms in the *CPE* composites.

Despite the improvement on modulus *Y*, structural effects from polymer intercalations can bring out different results on the linear elasticity behaviors. Table 7.6(b) reveals that *CPE* with *OMON* content up to 2 % of weight fraction had increment in both strength and strain at PL point. These growths on PL_{st} and PL_{sn} demonstrate that *OMON* was functioning as a *plasticizer* in *CPE* (1%) and *CPE* (2%). Even though intercalation in these composites was quite limited, but it did leave significant effect on the neighboring network of intercalated chains. Interruption caused by polymer intercalation on *PE* network reduced the interchain reaction and increased the matrix chains distances. Where, to some extent they will loosen the closed pack structure of *PE* chains. Chains uncoiling and lengthening therefore can be improved as shown by the growth of elastic strain PL_{sn} in both composites.

PE is a semi-crystalline polymer with both amorphous and also crystallite structures that can give weak points in its inner system. The loosened structure of *PE* in effect will lessen such weak points within *CPE*, which allowed better stress distribution and produced bigger reaction forces that improved the PL strength PL_{st}. However, *OMON* addition greater than 2 % in *CPE* had caused the reduction of PL_{st} and PL_{sn} (see Table 7.6(b)). This observation

suggests that further intercalation in the *CPE* composites gradually lessened the number of *PE* chain that can deform elastically. It thus distorted the stress distribution mechanism and the ability for chain extension in the non-polar polymer composites. These observe actually demonstrate the typical effect of matrix-rigid filler interactions.

The increase in Tensile strength, σ_{max} up to 2 % of *OMON* additions in Figure 7.32 adds more proof for the above discussed *plasticizer* effect. It tells that structural modification due to *OMON* intercalation effectively improved the stress distribution mechanism in *CPE*. However, the improvement is restricted within composite with more than 2 % of *OMON* content. In case of *CPE* (3%) and *CPE* (4%) in Table 7.6(b) for example, where distorted polymeric network is believed to cause the reductions on their Tensile strength σ_{max}. However, *CPE* (5%) shows an increase of about 23 % on the tensile strength. This finding can be related to the improved stacking order *N* of *OMON* structure inside the composite. Previously in Section 4.2.2.2.C, such structure with 6 successive layers of silicates was detected on *OMON* particles of the *CPE* (5%) composite. Mechanical frictions induced by the stacked structure in effect raised the amount of stress absorption through stress sharing at interphases. It thus contributes to the increased ultimate strength σ_{max} in the composite.

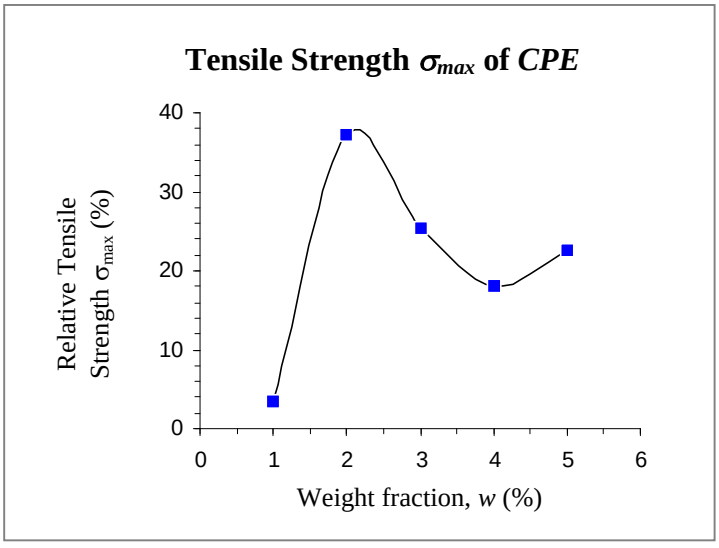

Figure 7.32: Relative tensile strength reveals structural effects caused by *OMON* Particles on the ultimate strength in *CPE*.

Despite the improvements on some mechanical properties, *OMON* distribution inside *CPE* basically had caused interruptions on its matrix network. Illustration in Figure 7.33 shows structural changes due to intercalation process and stacked layers structure. The disruptions can lead to distorted *PE* networks inside the *CPE* composites. The modifications as a result lessened the number of potential slippage that can take place among the *PE* chains. It was then reflected on the linear decrease of Maximum elongation $\varepsilon_{max,}$ as shown in Figure 7.34 for *CPE* composites.

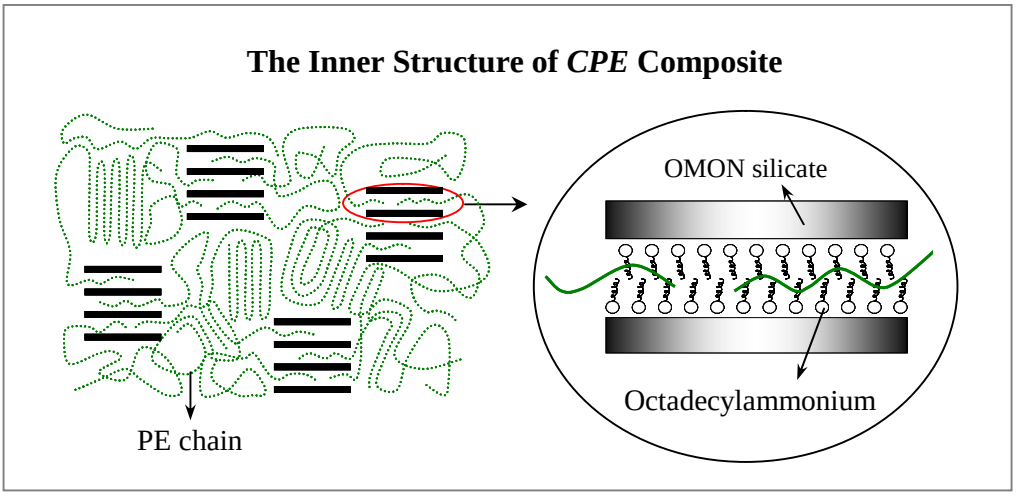

Figure 7.33: Intercalation of *PE* chains into *OMON* interlayer induce physical interaction with *OMON* particles that lead to structural changes on the *CPE* inner structure.

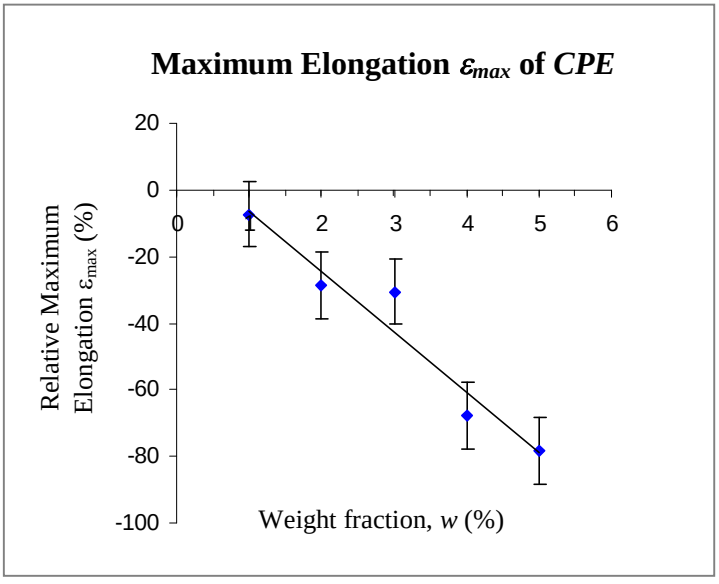

Figure 7.34: Relative maximum elongation shows a linear decrease as *OMON* content increase in *CPE* composites.

These drops on the elongation at break affected the ability of *CPE* to absorb energy during its deformations. Earlier discussion on the Tensile strength σ_{max}, *CPE* with *OMON* content from 1 % to 5 % in Table 7.6(b) demonstrate higher strength compare to that of pristine *PE*. These findings indicate the improved stress distribution mechanism in the composites. Even though the improvement could promote better energy absorption, but the reduction in ultimate elongation ε_{max} can reduce the strain energy *U*. This is shown in Figure 7.35 for *CPE*, which tells that the composite toughness is reducing with *OMON* addition.

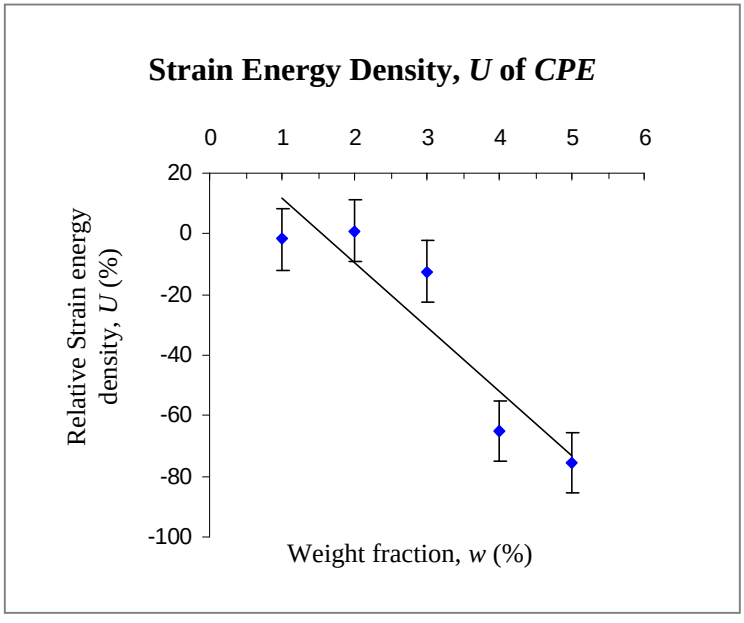

Figure 7.35: Relative strain energy density represents *CPE* toughness reduce as *OMON* weight fraction increase within the composites.

7.2.2.1.E Composites OMON-Plasticized Polyvinylchloride, CpPVC

In quest to understand the effect of *OMON* on polar polymer, plasticized *PVC* (*pPVC*) was used as the matrix component in *OMON* composite. The mechanical behaviors of *CpPVC* composite were then analyzed, based on the loading-extension curves in Figure 7.36. The graphs represent *CpPVC* specimens that contain about 1 %, 2 %, 3 %, 4 % and 5 % of *OMON* content. Along with these graphs, two other plots are added for comparisons. They are the *pPVC-Mon* (5%) plot for composite *pPVC* that is loaded with 5 % of *Mon* particles

and the plot of *CpPVC* (30%) which represent *pPVC* composite with high *OMON* content. Previously in Section 4.1.1.C, *pPVC* used in this work is supposed to have high content of plasticizer molecules, which had changed this polymer into an elastomeric material with good flexibility properties. The curve of *CpPVC* (30%) therefore is useful to study any mechanical effect on the elastomeric *pPVC* chains, which is caused by the big fraction of *OMON* constituent.

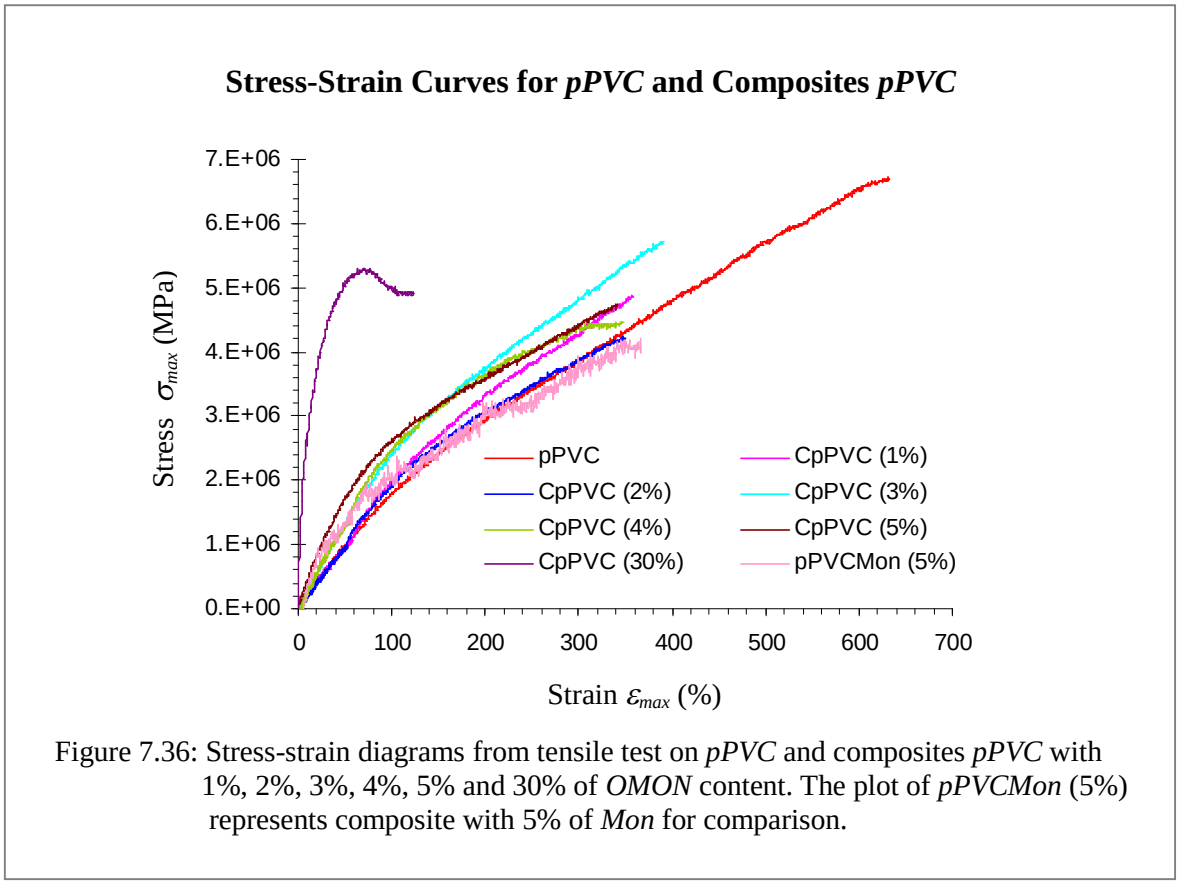

Figure 7.36: Stress-strain diagrams from tensile test on *pPVC* and composites *pPVC* with 1%, 2%, 3%, 4%, 5% and 30% of *OMON* content. The plot of *pPVCMon* (5%) represents composite with 5% of *Mon* for comparison.

Preliminary analyses on the *CpPVC* stress-strain curves show that in general they resemble similar curves for *CENR-50* and *CPE* composites. They are all demonstrating the typical behavior of reinforced polymeric composite, which had been subjected to external stresses. However, the developed trends for *CpPVC* mechanical properties are more or less the same with that of *CENR-50*. A plot for the elasticity modulus *Y* in Figure 7.37(a) gives a good example. This plot reveals an exponential growth of relative elastic modulus *Y* for *CpPVC*,

Table 7.7(a)
Mechanical Properties of *pPVC* and Composite *CpPVC*

Sample	pPVC	CpPVC (1%)	CpPVC (2%)	CpPVC (3%)	CpPVC (4%)	CpPVC (5%)	CpPVC (30%)	pPVCMon (5%)
Modulus, *Y* (MPa) (± 0.01)	2.10	2.23	2.31	3.28	3.51	4.87	50.80	4.84
PL Strength, *PLst* (MPa) (± 0.01)	0.85	1.06	0.91	1.01	0.72	0.73	1.29	0.29
PL Strain, PL_{sn} (%) (± 0.01)	41.78	57.25	47.17	35.19	23.68	16.40	2.00	9.27
Tensile Strength, σ_{max} (MPa) (± 0.01)	6.74	5.59	4.56	5.78	4.50	4.75	5.51	4.22
Max elongation, ε_{max} (%) (± 0.01)	635.78	452.14	417.42	394.28	365.56	345.25	127.00	369.87
Strain energy density, *U* (MN/m^2) (± 0.01)	24.81	15.07	12.00	13.69	11.35	10.80	5.78	9.76

Table 7.7(a): Mechanical properties for *PE*, composite with *OMON*: *CpPVC* (1%), *CpPVC* (2%), *CpPVC* (3%), *CpPVC* (4%), *CpPVC* (5%) and *CpPVC* (30%). It is including the composite with 5% of *Mon* inclusion, *pPVCMon* (5%).

Table 7.7(b)
Relative Percentage for Mechanical Properties in *CpPVC* and *pPVCMon*

Sample	CpPVC (1%)	CpPVC (2%)	CpPVC (3%)	CpPVC (4%)	CpPVC (5%)	CpPVC (30%)	pPVCMon (5%)
Modulus, *Y* (%) (± 0.01)	6.61	10.41	56.51	67.31	132.42	2323.39	131.07
PL Strength, PL_{st} (%) (± 0.01)	24.38	6.36	18.36	-16.14	-14.90	50.99	-66.07
PL Strain, PL_{sn} (%) (± 0.01)	37.02	12.90	-15.78	-43.33	-60.75	-95.21	-77.82
Tensile Strength, σ_{max} (%) (± 0.01)	-17.13	-32.38	-14.34	-33.27	-29.51	-18.27	-37.44
Max elongation, ε_{max} (%) (± 0.01)	-28.89	-34.34	-37.99	-42.50	-45.70	-80.02	-41.82
Strain energy density, *U* (%) (± 0.01)	-39.25	-51.65	-44.84	-54.27	-56.47	-76.71	-60.67

Table 7.7(b): Relative percentage for mechanical properties from composite *pPVC* with *OMON* (*CpPVC*) and *Mon* (*pPVCMon*) in comparison with the counterparts in case of pristine *pPVC*.

similar trend that characterize the elasticity of *CENR-50* in Figure 7.11(a). The growth in modulus *Y* for *CENR-50* (30%) was about 15420 %, which is significantly higher than the increase around 2323 % in case of *CpPVC* (30%) in Table 7.7(a). The big differences in these growths confirm the benefit of *OMON* exfoliation on the mechanical responses of *CENR-50* (30%). In general, the exponential trend of elasticity modulus *Y* demonstrates the remarkable effects of *OMON* as reinforcing agent on polar matrix chains.

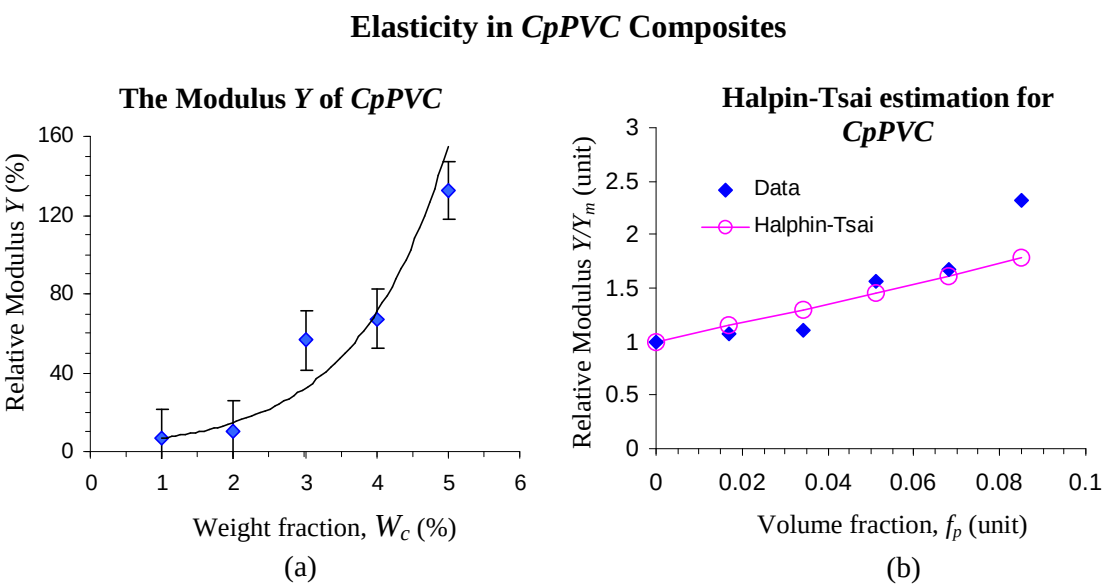

Figure 7.37: Low *OMON* content within *CpPVC* cause (a) the modulus *Y* increases exponentially, which indicate the outcomes from intercalation as shown by (b) Halpin-Tsai model.

From another perspective, it can also be considered as the benefit of using polar polymer as matrix elements in *polymer-OMON* composites. Actually, without organic modifier within *OMON* galleries, this smectite clay still can create physical linkage with the polar chains. Table 7.7(b) provides the evidence, where it shows an increase about 131 % on the elastic modulus *Y* for composite *pPVC-Mon* (5%). This value is close to the percentage increase around 132 % in case of *CpPVC* (5%) composite. The resemblance demonstrates by these two different composites indicates that similar reinforcing effect was generated by both

OMON and *Mon* particles. In that case, it draws attention to the physical reactions between the clays silicates and polar components in *pPVC* polymer.

Basically, silicate platelets in both *OMON* and *Mon* composites provide the potential sites for hydrogen bond formation. For example, hydroxyl groups on *Mon* structure can readily form hydrogen bonding with oxygen atom from *DOP*, the plasticizer molecules in *pPVC*. This secondary bonding in consequence can assist the non-bonded part of *pPVC* chains to verge upon silicate surfaces. In that way, it benefits the van der Waal forces to generate physical interactions that attach *pPVC* chains to the silicates. Therefore, both mechanisms contribute for the interfacial adhesions that operate at phase boundary. By this means, they could be the major contributors for mechanical reinforcements in both *OMON* and *Mon* composites.

The situation however is different when it involves composite with higher filler content. Table 7.7(b) reveals that 30 % of *OMON* incorporation gives about 2323 % increase on the elastic modulus *Y* of *CpPVC* (30%) sample. On the other hand, the same amount of *Mon* inclusion in *pPVC* had caused massive agglomerations on the clay particles. Apparently, two separate layers of *pPVC* polymer and *Mon* particles developed on the dried sample of *pPVC-Mon* (30%) composite. Great inhomogeneity demonstrated by this sample however eliminated it from tensile test in this work.

Different behaviors show by the composites enlightens the benefit of intercalated structure in *polymer-clay* composite. Penetration of *pPVC* chains into *OMON* interlayer increased its potential to be attached with more silicate surfaces. In fact, coiling process between *pPVC* and alkyl chains effectively had helped the matrix chains to approach the surfaces. More interactions by van der Waals forces thereby can be promoted within the *OMON* galleries. Similarly, hydrogen bonding was well induced where the hydroxyl group on *OMON* layers provided the potential sites for this linkage. The trapped *pPVC* chains inside such confine

space of *OMON* gallery also gave better chances for the chlorine atom on *PVC* backbone to interact with the existing exchangeable cations. The effects of chains intercalation thus had improved the physical interaction among polar matrix chains and *OMON* particles in *CpPVC* composites.

Particle dispersion within nanoclay composite in general depends on the ability of each component to interact at interfaces. Therefore, *OMON* particles are well dispersed within composite with good matrix-filler interactions. Wherein, particles agglomeration can be avoided especially in composite with high *OMON* content. However, it can also promote the formation of stacking layers structure as in case of *CPE*. In *CpPVC* (30%) for example, approximately 21 layers of silicate platelets were found stacking together in one unit of *OMON* particle. These stacked platelets as a response created frictions at interface during stress loading, which added more elements to the composite strengthening as demonstrated in Table 7.7(b). Sudden growth on the elastic modulus *Y* of *CpPVC* (5%), as well as in the PL strength PL_{st} for *CpPVC* (30%) support this believed.

More evidences in fact can be observed in Figure 7.37(b) for the plot of normalized elastic modulus Y/Y_m versus volume fraction f_p. This plot is consistent with the Halpin-Tsai model for *CpPVC* samples with low *OMON* content. By this means, it conform the importance of intercalation on elasticity modulus *Y* within the composites systems. Deviation from the estimated value however, occurs in the case of *CpPVC* (5 %) and *CpPVC* (30 %). It tells that *OMON* inclusion beyond the 0.07 volume fraction (about 4 % of weight fraction), produced additional reinforcing elements together with the intercalated structures. Notable improvements on the elastic modulus *Y* suggest that it was due to the improved stacking order *N* in these composites.

Plasticizing effect as previously detected in *CPE* composites also appear in case of *CpPVC* with small amount of *OMON* loading. Minimum dispersion of these tiny particles reduced

the structural resistance on matrix chains, which allowed them to deform elastically. It thus helps to improved the elasticity of *pPVC* chains and its composite. Table 7.7(b) shows the increase in PL strength, PL_{st} and PL strain, PL_{sn} for *CpPVC* (1%). On the other hand, these growths in general were decreasing as *OMON* content in the composites is increased. This is the disadvantage caused by the growing effect of binding forces at interfaces. In which, it reduced the great ability of *pPVC* chains for extension and stress dispersion.

Good matrix-filler interactions however allow stress transfer to operate at phase boundary, where the applied stress can be shared by both flexible matrix and rigid filler particles. In that way stress sharing in *CpPVC* (30%) for example, gave more strength to the composite. Likewise in *CpPVC* (5%), the small reduction on PL strength PL_{st} around 15 % compares to similar drop about 66 % in *pPVC-Mon* (5%) composite adds more evidence. Overall, the reductions on both strength and strain at PL points in *CpPVC* are much bigger than their counterparts in Table 7.6(b) for *CPE* composites. The observations highlight the effects of polar component that is good for strong interfacial adhesions within *CpPVC*. However, it caused chains interruption on matrix networks that contributed to the drops within elastic region. Strong adhesion at interfaces also increases the chances for stress concentration to take place in *CpPVC*. Stress sharing in that case turned out to be stress concentrator, which created weak points within the composites system. Such condition can lead to early failure that is believed responsible for the strength drops.

The great ability of matrix *pPVC* chains for extension in plastic region was distorted within *CpPVC* composites, despite their remarkable increases in modulus *Y*. Table 7.7(b) reveals the elastomeric feature of pristine *pPVC* chains, where its Maximum elongation ε_{max} gives about 636 %. On the other hand, the presence of *OMON* particles among *pPVC* chains had caused a significant drop in the ultimate elongation ε_{max} for *CpPVC*. Schematic diagram in Figure 7.38 illustrates the effect of *OMON* distributions on the composite inner structure.

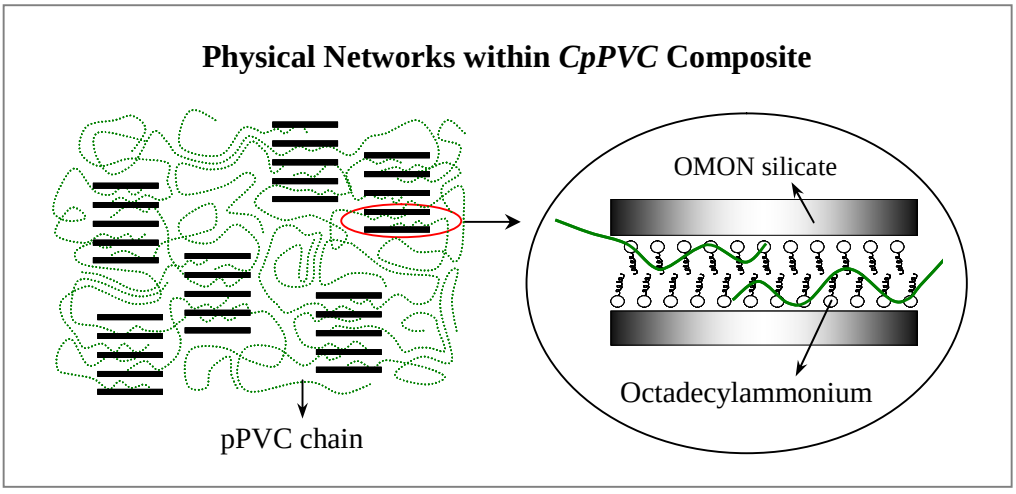

Figure 7.38: Physical interactions arise between polar *pPVC* chains and *OMON* silicates encourage intercalation processes. In which lead to structural changes on both *OMON* particles as well as the matrix chains.

Physical linkages with rigid fillers effectively can distort polymeric networks in flexible domain. It means that chain slippage between the adjacent matrix chains can be inhibited, especially with the increasing amount of *OMON* inclusion in the composites. Exponential decrease in Figure 7.39 demonstrates such effect on the relative Maximum elongation ε_{max}.

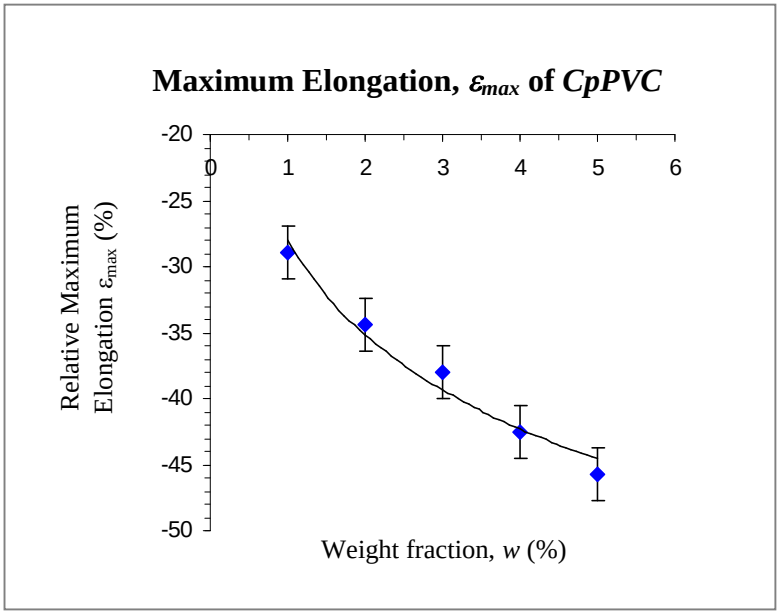

Figure 7.39: Intercalation in *CpPVC* with small fraction of *OMON* particles can cause the maximum elongation ε_{max} to reduce.

Another good example is given by the *CpPVC* (1%) in Table 7.7(b), which highlights the significant of polymeric networks on chain extension. Earlier on the *plasticizing effect*, this

composite was recognized to have strain increase within elastic region that gives the PL_{sn} about 37 %. However, the interrupted polymeric networks in this composite had restricted the chain slippage during plastic deformation, which had caused the drop of about 29 % on the Maximum elongation ε_{max} for *CpPVC* (1%).

Poor stress dispersion is another effect of the interrupted matrix networks within *CpPVC*. It manifested on the decrease in Tensile Strength σ_{max} as shown in Table 7.7(b). Relatively low reduction in the strength about 18 % for *CpPVC* (30%) however, indicates the effect of additional reinforcements inside this composite. Owing to its high *OMON* content thus, stress sharing and mechanical frictions produced by stacked layers structures are believed to cause the result. In spite of that, the tensile strengths of *CpPVC* in general give uncertain trend on their drops as shown in Figure 7.40. This behavior could be another effect from

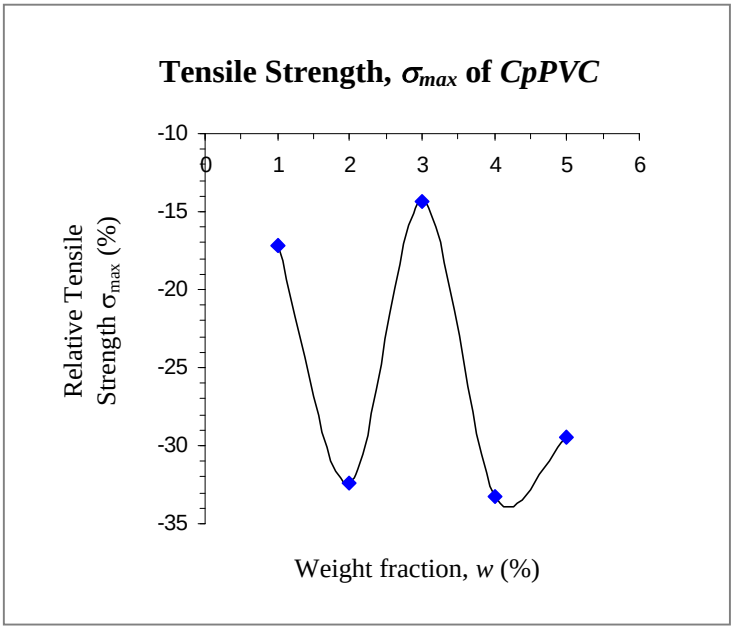

Figure 7.40: Structural modification induce by *OMON* particles cause the uncertainty in tensile strength behavior as *OMON* content increase in *CpPVC*.

good interaction between *OMON* platelets and elastomeric *pPVC* chains in the composites. Schematic representation in Figure 7.41 illustrates that some local physical network might arise as a result of extensive interaction by these chains. It links up several platelets from

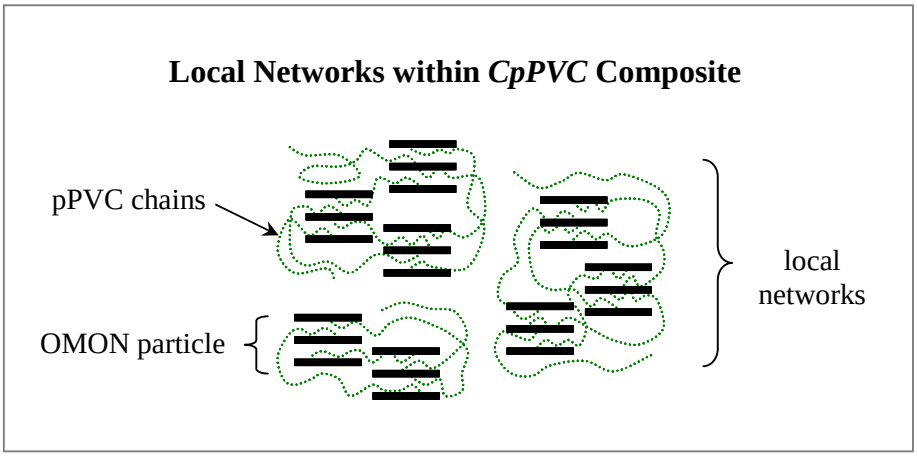

Figure 7.41: Small local networks that contribute for the uncertainty in tensile strength for *CpPVC* with relatively low *OMON* content.

neighboring particles into a small local physical network. Such networks within a distorted polymeric system will be useful to disperse applied stresses. Where, to certain extent it may reduce the drop in Tensile strength σ_{max} for *CpPVC*. The large number of *OMON* particles in *CpPVC* (30%) composite perhaps had induced this local network to expand, which then became more connected. In that way, it can facilitate the stress sharing that contributed for strength improvements in the composite.

The idea of local network inside *CpPVC* draws attention to its effect on mechanical failure. Poor dispersion of such networks within the tested area on a specimen can promote early break, which then influenced the Tensile strength σ_{max} in each composite. This remark may explain the uncertainty in Tensile strength σ_{max} of *CpPVC* composites, which practically had affected their toughness. Strain energy density *U* in Figure 7.42 however, shows that the decrease in Maximum elongation ε_{max} had more influence on the composite toughness. It tells that the reduced strain at break with the increased *OMON* content effectively limited the amount of energy absorbed in *CpPVC* composites.

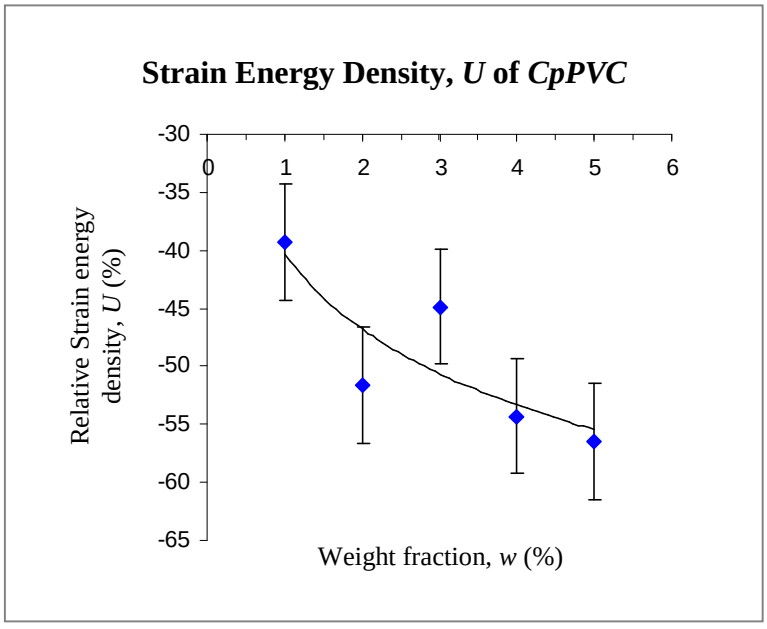

Figure 7.42: Relative strain energy density *U* shows that *CpPVC* toughness was more influenced with the drop in maximum elongation ε_{max} than it tensile strength σ_{max}.

The mechanical properties of *polymer-OMON* composites in general demonstrate notable changes. It proved that intercalation of polymeric chains into *OMON* interlayer manages to attach these elements from different origins into a renewed material. Reinforcing effects produced by *OMON* inclusion within the composites are reflected on the increments of elasticity modulus Young, *Y* and Tensile strength σ_{max}. While the disadvantage of this rigid filler can be seen in the drops of Maximum elongation, ε_{max} with *OMON* loading. There is an exception however in case of *CSMRL* and *CDPNR* composites, where the strain at break ε_{max} of these composites was remarkably increased with *OMON* content.

7.3 The Effects of *OMON* on Stress-strain Behaviors

Analyses on the tensile properties of *polymer-OMON* composites highlight the mechanical effects from matrix-filler interactions at phase boundaries. Basically, stress-strain diagrams for these composites are analogous to that of pristine polymers that made up their matrix domain. However, the presence of *OMON* distinguishes the stress-strain behavior from the reinforced polymers. This is attributable to structural modifications due to the rigid filler-flexible matrix interactions. In which, it effectively changed the initial behaviors of stress-strain diagram for the polymeric matrix. The modifications as a result had caused various mechanical effects in the composites. Significant role played by these effects can be seen in both elastic and plastic deformation behaviors.

7.3.1 Elastic Deformation

External forces experienced by *polymer-OMON* composites in response generated reaction forces. These forces can cause elastic deformations by stimulating temporary straightening and lengthening on the composite matrix chains. Structural changes within the composites could also involve the uncoiling of matrix main chains, a combination effect of elastic and plastic deformations. These processes subsequently affected the elasticity strain PL_{sn} and strength PL_{st} of the composites.

The variations in PL strength PL_{st} and PL strain PL_{sn} with *OMON* content as revealed in Figure 7.43 and 7.44 are useful to study elastic deformations. For instance, low inclusion of *OMON* in *CPE* (1%), *CPE* (2%), *CpPVC* (1%), *CSMRL* (5%) and *CDPNR* (5%) had increased both strength and strain at PL points. *OMON* particles in these cases should have acted as a *plasticizer*, where the intercalation at that stage was functioning to reduce the interchains reaction and raised their distances. In that way, it released any coiled chains which then promoted better chains extension compared to that of pristine polymers. More energy actually can be absorbed by these chains as stress distribution was improved. In

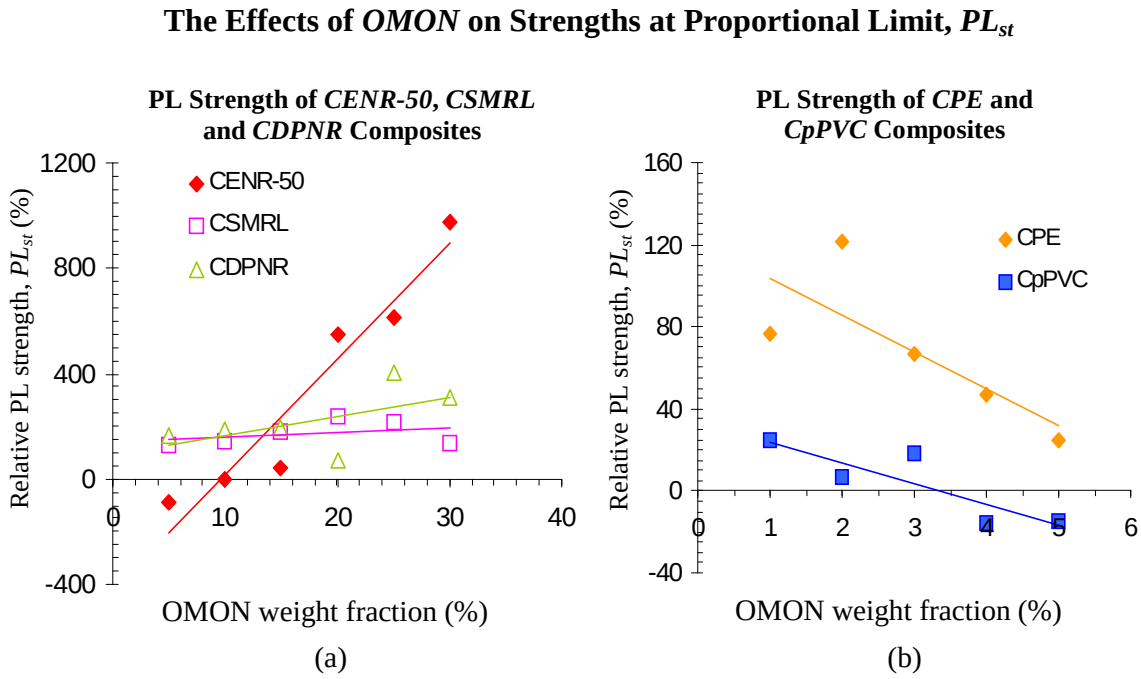

Figure 7.43: Elastic strength at Proprtional Limit, PL_{st} point for (a) *natural rubbers-OMON* composites and (b) *CPE* and *CpPVC*. The increase of *OMON* content generally raise the strength for *CENR-50*, *CSMRL* and *CDPNR*. While in case of *CPE* and *CpPVC* such increment leads to the reductions in PL_{st}.

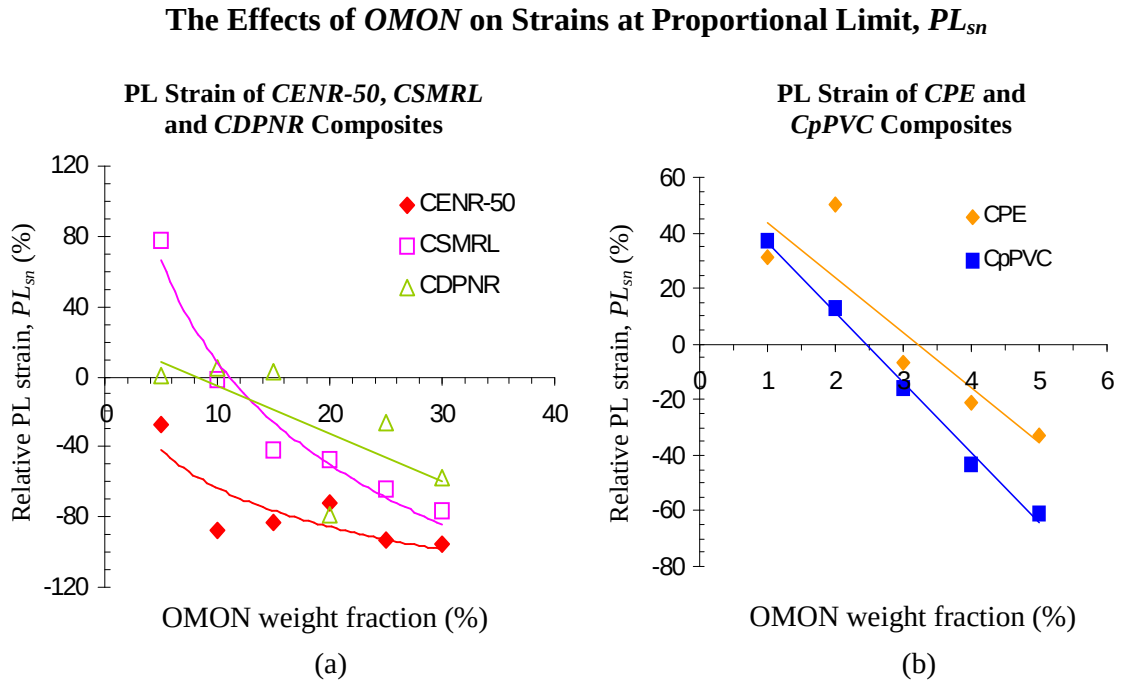

Figure 7.44: Elastic strains at proportional limit PL_{sn} for (a) *natural rubbers-OMON* composites and (b) *CPE* and *CpPVC* show that the inclusions of *OMON* particles reduce the elastic strain of matrix polymers in the composites.

contrast, PL_{st} together with PL_{sn} for *CENR-50* (5%) had a clear drop as shown in Figure 7.43(a) and 7.44(a) respectively. These are the effects of strong interfacial adhesion, which operated in the composite system. Besides the existing epoxide groups in *ENR-50* chains, the source for such binding forces could also come from chemical crosslinking within the composite. Moreover, hydrolyses on the epoxide groups produced hydroxyl molecules that can readily react with *OMON* silicate. In this case, *OMON* particle possibly had acted as a binder instead of *plasticizer* for the matrix chains. As a result, it connected a few adjacent particles into a small physical network. Good stress sharing by these scattered networks however turned it into stress concentrators. These weak points inside the *CENR-50* (5%) composite then led to the strain and strength drops in elastic region [7.31].

Similar observation can be seen in case of *CPE* and *CpPVC*, as *OMON* content increase in the composites. The reductions of elastic strength PL_{st} and strain PL_{sn} in Figure 7.43(b) and Figure 7.44(b) respectively demonstrate the effects of intercalations on matrix networks. Extensive penetration of *PE* and *pPVC* chains can reduce the generated reaction forces by the chains network, as well as its ability for extension. Schematic representations in Figure 7.45(a), (b), (c) and (d) for *CpPVC*, *CPE*, *CENR-50* and *CSMRL/CDPNR* in that order distinguish the effects of *OMON* intercalation by various type of polymers matrix. Despite the weak interaction in *CPE*, the strong interfacial adhesion of *CpPVC* was also incapable to generate good reaction force without effective network for stress dispersion mechanism. In case of *CpPVC* (30%) however, stress sharing and mechanical friction that were induced by stacked layers structures possibly had caused the increase in PL_{st}.

The benefit of material networks can be seen in Figure 7.43(a) in cases of *OMON-natural rubbers* composites. The growing number of *OMON* particles generally had increased the PL_{st} for *CSMRL*, *CDPNR* and *CENR-50*. Crosslink reactions that were assisted by amine molecules had induced chemical crosslink on adjacent polysioprene chains in these rubber

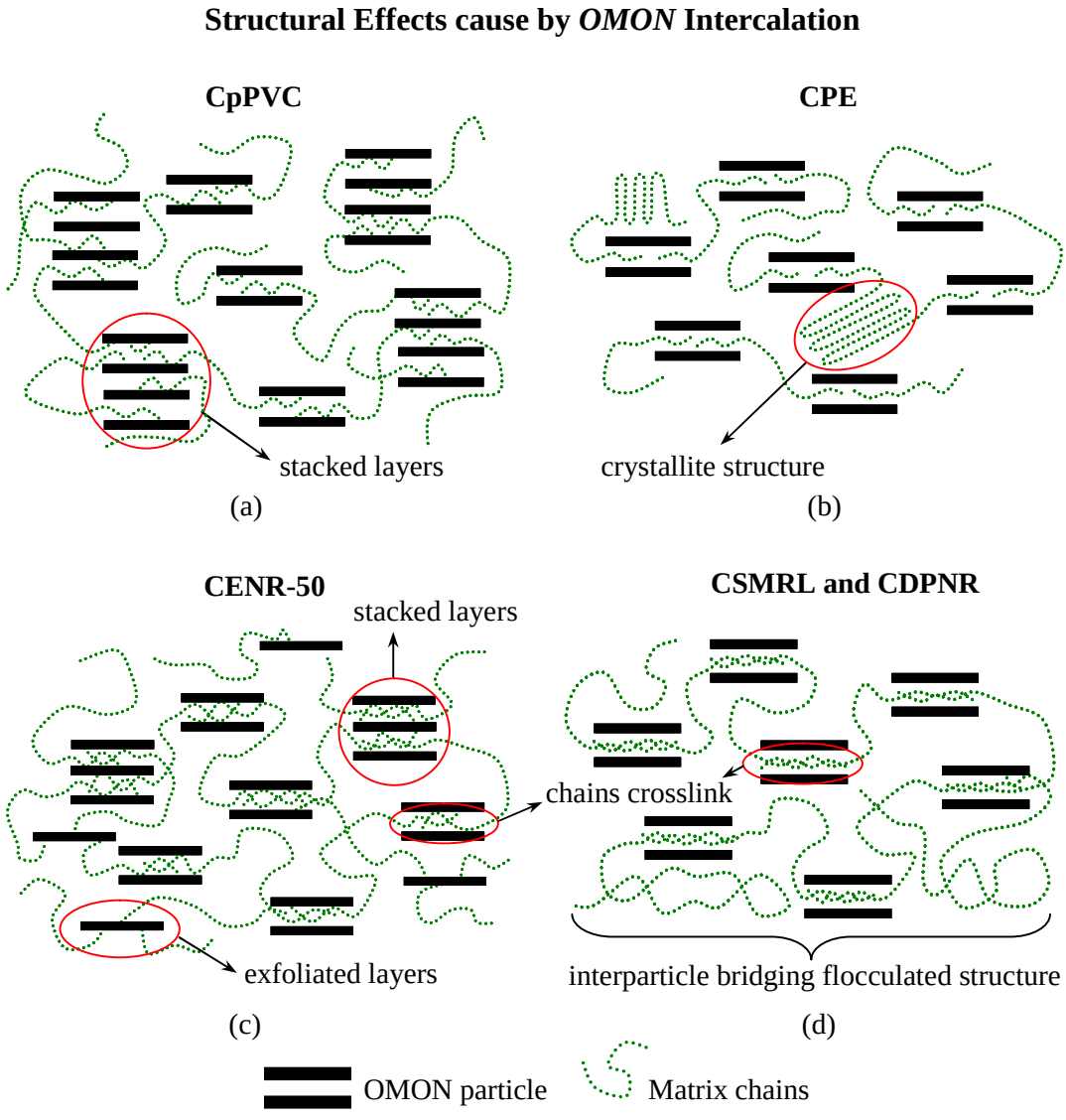

Figure 7.45: Schematic representations show structural effects produced from *OMON* intercalations in (a) *CpPVC*, (b) *CPE*, (c) *CENR-50* and (d) *CSMRL* and *CDPNR* composites.

composites. As a result, they linked up the matrix chains inside *OMON* gallery which then created chemical network. This network is illustrated in Figure 7.45(d) had a function to connect the elements within the *interparticle bridging flocculated* structure of *CSMRL* and *CDPNR* composites. In *CENR-50* however, the term chemical network is inappropriate to describe this composite system. This is due to the strong interfacial adhesions that bind together all its components into a big physical network. During elastic deformations, both

chemical and physical networks capable to absorb stresses, which then increased the elastic strengths PL_{st}. Physical network within *CENR-50* however had comparatively weak stress distribution mechanism compare to the chemical network. However, it gave an advantage for *CENR-50* with high *OMON* content. Physical network in *CENR-50* (30%) for example, promoted stress sharing to work at matrix-filler interphases particularly with the present of exfoliated *OMON* platelets. In that way, this network as shown in Figure 7.45(c) had cause remarkable increase in the elastic strength PL_{st}. The generated mechanical friction by some stacked layers structure in *CENR-50* should also contribute for the improvement. Besides the PL_{st} increase, the observed drops of PL strain PL_{sn} in Figure 7.44(a) adds more proves on the existence of physical networks. Matrix-silicates interactions that create the network in effect had made the uncoiling process of matrix chains more difficult. Therefore, chains straightening were greatly restrained in *CENR-50* composites, which subsequently led to the decrease in PL_{sn}.

The significant of stress-strain behaviors discussed above appears as they had affected the elasticity modulus *Y* and elastic toughness in each case of the *polymer-OMON* composites. It tells that the developed structures caused by matrix-filler interactions influenced the mechanical properties within the elastic region. Besides the initial structures of *OMON* and polymers matrix, their compositions also had great effect on the mechanical properties of *polymer-OMON* composites.

7.3.2 Plastic Deformation

Further increase of external forces on *polymer-OMON* composite subsequently will lead to plastic deformation. Additional load experienced by the straightened chains capable to stimulate slippage among adjacent chains in flexible domain. Therefore, strain increase in plastic region was then generated by this permanent deformation on the matrix structures.

In a composite system, stress distribution and stress sharing are equally important to give the Tensile strength, σ_{max}. However, their function on the Maximum elongation, ε_{max} works differently. Good stress distribution via chemical linkages can increase a composite strain before its break-off. On the contrary, stress sharing by physical linkages can create stress concentrator that leads to early failure and reduced the elongation at break ε_{max} [7.31 and 7.32].

Despite the plasticizing effect in elastic region, *OMON* intercalation basically had caused interruptions on the polymeric networks of matrix domain. This interrupted networks in consequence limited chains slippage, especially in composites with small *OMON* content. It was then reflected on the drops in Maximum elongation ε_{max} for *CPE* (1%) and *CpPVC* (1%) as shown in Figure 7.47(b). While the in case of *CENR-50* (5%), *CSMRL* (5%) and *CDPNR* (5%) in Figure 7.47(a), the increased ultimate strain ε_{max} indicates the presence of crosslinked chains from crosslink reaction in *OMON* galleries. Chemical networks in these composites increased their Tensile strength σ_{max} as shown in Figure 7.46(a), following the improved stress distribution mechanism. In fact, it could be the same reason behind the growth in Tensile strength σ_{max} of *CPE* (1%) and *CPE* (2%) in Figure 7.46(b). *Plasticizing* effects however, distinguished the origin for the improvements. This effect that was due to *OMON* intercalation facilitated matrix chains to uncoil easily, which then promoted better stress dispersion within the *CPE* composites.

Similar effect could have happened in *CpPVC* (1%) as well however, the drop in Tensile strength σ_{max} as shown in Figure 7.46(b) gives different picture. Good physical interactions in *CpPVC* encouraged the elastomeric *pPVC* chains to link up *OMON* particles into some small local networks. Schematic illustration for such network can be seen in Figure 7.41. Strong binding forces that operated at phase boundary gave this network great potential for

stress sharing. The scattered distribution however had changed these small networks into stress concentrators in the composite system. They created weak point, which then induced premature breaks and led to the decrease on the ultimate strength σ_{max}.

Furthermore, reduction in Tensile strength σ_{max} can be seen in Figure 7.46(b) for all cases of *CpPVC*. From the same figure, it shows that *OMON* addition in *CPE* composites overall had caused the σ_{max} to increase. These improvements on *PE* strength reveal the advantage of stress sharing in *CPE*. Physical linkage between *OMON* and the non-polar *PE* chains as shown in Figure 7.45(b) allowed stress transfer to work at their interphase [7.32]. It thus, explains the differences caused by the polarity of matrix chains on the composites strength. Distribution of small local network within the tested region on *CpPVC* sample has its own significance. A number of such networks inside the region for example put them into close interaction and induces more connections. In that way, it assisted better stress distribution that reduced the decrease in Tensile strength σ_{max}. This belief may describe the uncertainty shows by the σ_{max} of *CpPVC* composites in Figure 7.46(b).

More evidences on the significant of broad network for stress distribution mechanism is given by *CENR-50* composites. Crosslink reaction and good matrix-filler interaction in this composite effectively induced extensive physical bonding. These linkages as illustrated in Figure 7.45(c) capable to develop a wide *integrated network*. Stress concentration thereby should be lessened within the composite system. For that reason interfacial adhesion which promoted good stress sharing can assist better stress transport via the integrated physical network. As a result, the Tensile strength σ_{max} for *CENR-50* composites raise with *OMON* content as shown in Figure 7.46(a). This observation also demonstrates the growing effect of *OMON* addition on the physical network formation. In general, network that is capable to minimize stress loading at each point in its system can perform good stress distribution.

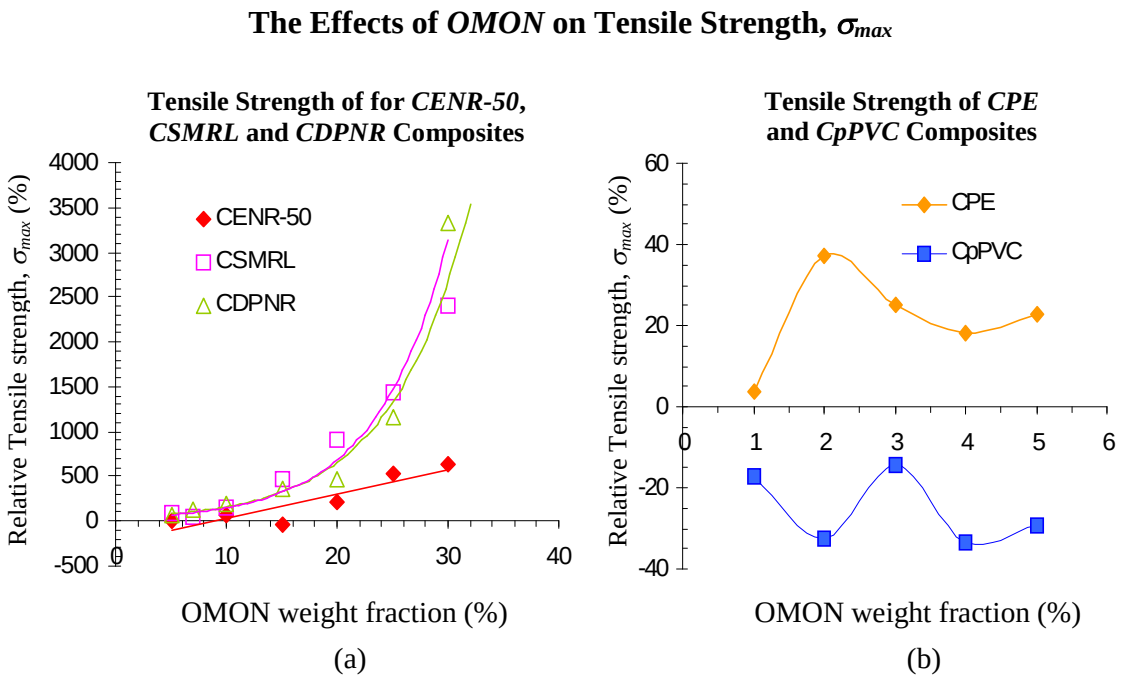

Figure 7.46: Tensile strength σ_{max} for (a) *natural rubbers-OMON* composites and (b) *CPE* and *CpPVC* composites. The growing numbers of *OMON* particles increase the tensile strength for *CENR-50*, *CSMRL* and *CDPNR*. While in *CPE* relatively small *OMON* content

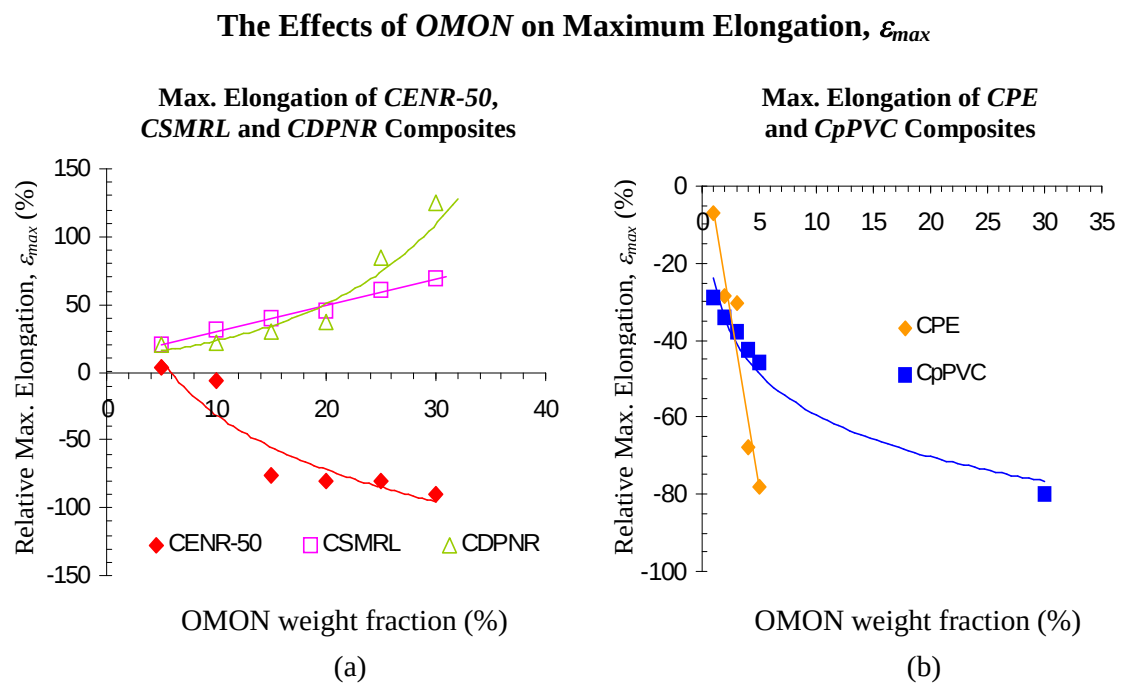

Figure 7.47: The effect of *bridging flocculated* structures differentiate the maximum elongation ε_{max} behaviors of natural rubbers composites in (a). The interrupted matrix network due to *OMON* inclusion in *CENR-50*, and also within *CPE* and *CpPVC* in (b) lead to strain reduction at the composites break-off point.

Mechanical studies in this work reveal that chemical linkages within *interparticle bridging flocculated* structures are more efficient than the physical bonding in *CENR-50* composite. Figure 7.45(d) gives the schematic illustrations for such flocculated structures within the *CSMRL* and *CDPNR* composites. Therefore, it explains the remarkable growths of Tensile strength σ_{max} as shown in Figure 7.46(a) for these composites.

Consistent trend is observed on the Maximum elongation, ε_{max} drops of *CpPVC* and *CPE* in Figure 7.47(b) with the increase of *OMON* content. This finding actually demonstrates the interrupted matrix network resulted from the intercalation process on *OMON* particles. Similar effect that had restrained chains slippage and thence reduced the strain at break ε_{max} of *CENR-50*. However, linear drops shows by the ultimate elongations ε_{max} in Figure 7.47(b) distinguish the fracture mechanism inside *CPE*. It indicates the presence of smooth fracture surface due to poor interfacial adhesions in the composite [7.33]. This condition had made the Maximum elongations ε_{max} of *CPE* drop more gradually than that of *CpPVC*, as well as the *CENR-50* in Figure 7.47(a). Where, a curve represents the ε_{max} drops in both cases of the polar composites. The curves demonstrate very dramatic decrease that can be stimulated by just a small amount of *OMON* loading. Rough fracture surface is supposed to cause these results, which can be generated by good interfacial adhesion that operates at interphases as shown in Figure 7.45(a) and 7.45(c) for *CpPVC* and *CENR-50* respectively. In such condition, the fracture path tends to go from one particle to another rather than giving a perfectly smooth fracture surface. These observations thus add more proof for the effect of chains polarity on *polymer-OMON* interactions.

On the other hand, the lack of polar component on matrix chains has its own benefit within *natural rubber-OMON* composites. Even tough it may reduce matrix-silicate interactions, but in that way it promoted extensive crosslink reaction on polyisoprene chains, which was assisted by amine cations. For example in case of *CSMRL* and *CDPNR*, where these chains

had better chances to simultaneously intercalate and crosslink inside several unit of *OMON* particles. As a result, a wide integrated network structure from this *interparticle bridging flocculation* process was created in the composites systems. During plastic deformations, slippage among the highly crosslinked chains were promoted in this chemical network as shown in Figure 7.45(d). The effect was manifested on the notable growths of Maximum elongation ε_{max} in Figure 7.47(a).

Various structures developed in *polymer-OMON* composites apparently had affected their Tensile strength σ_{max} and Maximum elongation ε_{max} in several different ways. Therefore, stress-strain behaviors within plastic region depend on the resultant structures, as *OMON* content increase in these composites. Most of the composite stress-strain outline typically falls within this region that represents plastic or permanent deformation. It thus, tells that structural modifications due to plastic deformations determined the composites toughness as a whole.

7.3.3 Discussion on The Structural Effects of *OMON*

It is understood thus far that *OMON* acts differently with various types of polymers, which depends on the polymer physical and chemical structures. In fact, *OMON* fraction within a composite also has great influence on the resultant structures. For that reason, the last two sections were dedicated to discuss possible structures and reactions that may influence the mechanical properties of *polymer-OMON* composites. Right through the discussions, three major influencing factors can be highlighted. They are the *interfacial adhesion*, *stacking order N* and *interparticle bridging flocculation*.

7.3.3.1 Interfacial Adhesion

In nanoclay composite, the term *interfacial adhesion* normally is connected to intercalation and exfoliation process. This is due to wide physical contacts they offer that provide good

grounds for *matrix-filler interaction*. Remarkable effect can be seen on the increment of elasticity modulus *Y* in *CENR-50* (30%) (*Y* = 15400 %) and *CpPVC* (30%) (*Y* = 2323 %). Notable growth in the modulus *Y* of *CENR-50* (30%) however, is inconsistent with the idea that weak entanglement dominates *ENR-50* chain interactions with alkyl tail inside *OMON* gallery. In fact, polar *pPVC* with higher dielectric constant, ε of about 6.5 [7.34] compares to 4.8 in case of *ENR-50* should promote better interactions with *OMON*. The remarkable growth in modulus *Y* is actually indicating the benefit of *OMON* exfoliation in *CENR-50* (30%). The exfoliated *OMON* silicates offered more contact area for extensive *matrix-filler interaction*, which then contributed to the increase.

Even though exfoliation is very often associated to good matrix-filler contact, but it does not always means a good *matrix-silicate interaction*. For example, exfoliated *CPVC* (5%) had an increment about 54 % on its elastic modulus *Y* [7.35]. This is much smaller than the increase about 132 % for the intercalated *CpPVC* (5%) in this work. It thus, highlights the importance of hydrogen bond formation between *OMON* and matrix chains. Such bonding could actually happen between the oxygen atom of plasticizer molecule *DOP* and hydroxyl groups on *OMON* silicates. This secondary bonding induced *matrix-silicate interaction* as illustrated in Figure 7.48. In that way, interfacial adhesion within *CpPVC* (5%) system was improved and contributed to the improvement. Hydrogen bonding is also another factor behind the remarkable growth of modulus *Y* in *CENR-50* composite. Since *ENR-50* chains contain both oxygen atom and hydroxyl groups, which stimulated more hydrogen bonding.

In this work, modifier tail is the alkyl chains from *ODA* cations within *OMON* interlayer. Significant role played by this element appears in case of exfoliated *PVA-Mon* against the intercalated *PVA-OMON* systems [7.27]. Where, the exfoliated composite had an increase of about 20 % on its modulus *Y* that is smaller than similar growth around 70 % by the intercalated composite. These results demonstrate that composite with both exfoliation and

hydroxyl groups do not always give a good *matrix-silicate interaction*. Alkyl tails in *PVA-OMON* was functioning to bring the matrix chains closer to silicate surfaces, which then promoted such interaction via hydrogen bonding and van der Waals forces. The generated interfacial adhesions at phase boundary therefore gave good reinforcing effects in this composite. In *PVA-Mon* system however, the interaction with *Mon* silicate was quite limited without the assistance of modifier chains.

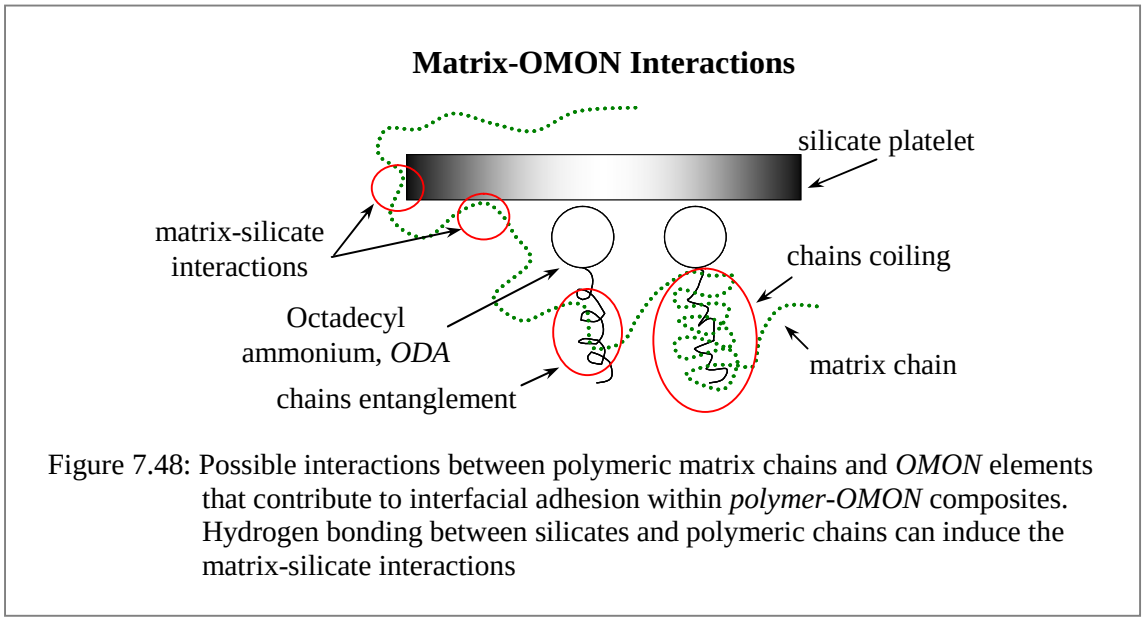

Figure 7.48: Possible interactions between polymeric matrix chains and *OMON* elements that contribute to interfacial adhesion within *polymer-OMON* composites. Hydrogen bonding between silicates and polymeric chains can induce the matrix-silicate interactions

Matrix-tail interaction actually give different effect depends on the matrix chains structure. Such as *chains entanglement* in Figure 7.48 that had helped bulky polyisoprene chains to encounter silicate surfaces within *natural rubbers-OMON* composites. In case of *CPE* and *CpPVC*, *chains coiling* were recognized to dominate their matrix chains interactions with the alkyl tails. The benefit of chains coiling can be seen in the increment of modulus *Y* for *CpPVC* (5%) about 132 %. This is relatively bigger than that of *CENR-50* (5%), which is around 32 %. It is to be noted that both composites had an intercalated system. In fact, it is also believed that *chains coiling* had helped the non-polar *PE* chains to intercalate into *OMON* galleries. Where, the generated reinforcement gave an increment about 16 % in the elasticity modulus *Y* of *CPE* (5%) composite.

Interfacial adhesion in *polymer-OMON* composite obviously is a result of various physical and chemical interactions. There is no simple explanation in fact to explain the mechanism involved in a composite system. However, it is understood that the ability of matrix chains to interact with both silicate surface and modifier tails is very important to generate the reinforcing effects in *polymer-OMON* composite.

7.3.3.2 Stacking Order, *N*

In the process of *OMON* intercalation, chains coiling can also improve the stacking order *N* that induced stacking layers structure as a result. Good matrix-filler interaction developed among the matrix chains and *OMON* helped to align the filler silicates into the stacked structure as illustrated in Figure 7.45(a) and 7.45(c). During stress loading, such structure generated mechanical frictions, which added more strengthening element in a composite. For example, *CPE* (5%) with six consecutive layers of *OMON* platelets shows the increase of modulus *Y* about 17 %. This increment is relatively higher compares to the 9 % increase in case of *CPE* that contains *OMON* particles with only three layers structures [7.36]. The generated frictions however may turn this stacked structure into stress concentrators, where they induced premature break that would lead a sample into premature failure. It thus, suggests additional reason behind the drop in Tensile strength σ_{max} for some *polymer-OMON* composite. Besides, the ability of matrix chains to slide on top one another can be affected by the stacked structure. This condition affects the extension of polymeric matrix chains in a composite. Such effect is reflected on the drops of Maximum elongation ε_{max} as observed in case of *CPE*, *CpPVC* and *CENR-50* samples.

Stacking layers basically is a result of matrix-filler interaction. Besides the van der Waals attraction forces, it should also be influenced by chain polarity especially with the presence of hydroxyl group. For example in the case of *CPLA* (5%), a Polylactide (*PLA*) composite with 5 % of *OMON* content. *PLA* is a polar polymer with both hydroxyl group and oxygen

atom on its backbones. These polar elements can promote hydrogen bond formation with *OMON* silicates. As a result, *CPLA* (5%) was able to stack about 7 to 17 layers of silicate platelets on *OMON* particles [7.37]. Polar *CpPVC* (30%) with 21 layers structure in this work adds more evidence on the benefit of polar matrix chains. In fact, the role of polar matrix chains is highlighted in case of *CENR-50* (30%). Where, around 5 layers of *OMON* silicate were stacked together even though chains entanglement dominated this composite system. The 6 layers structure in case of *CPE* (5%) composite that was assisted by chain coiling on the other hand, represent the disadvantage of non-polar chains for the stacking layers process.

Stacked layers structure in *polymer-OMON* composites is a unique structural effect due to the present of smectite *Mon* particles. This stacked structure is recognized to be influenced by both physical and chemical interactions among the composite components. Mechanical analyses reveal that the present of these stacking layers can be a sign of good matrix-filler interaction. However, the stress concentration it created has great potential to weaken some mechanical properties of these composites, such as the discussed Maximum elongation ε_{max} and Tensile strength σ_{max}.

7.3.3.3 Interparticle Bridging Flocculation

In composite study generally, it is rarely found that the raise of filler content is followed with the growth in Maximum elongation ε_{max}, elastic modulus Y and material toughness U. Some authors however reported a few cases on nanoclay composites with elastomer matrix [7.25, 7.38 and 7.39]. Unfortunately, it came without clear explanation regarding possible structural effects that can be related to such improvements. Throughout this work, stress-strain analyses demonstrate similar outcomes in *natural rubbers-OMON* composites except for *CENR-50*. Mechanical responses as shown by the *CSMRL* and *CDPNR* composites in fact point out the significant effects produced by the *interparticle bridging flocculation*

process. It is believed that the process responsible for the flocculated structures within the rubber composites.

Earlier in Section 7.2.2.1.B, crosslink reaction on the intercalated polyisoprene chains was recognized as the source for such flocculated structure as shown in Figure 7.45(d). By this means, chemical networks developed within this structure should have played significant role that improved some mechanical properties. Such as the growth in Tensile strength σ_{max} signifies the improvement on stress distribution mechanism, which is due to the chemical network. Extensive crosslinking in this network can make the process of chain uncoiling and straightening more difficult in elastic region. It thus, affected the composites elasticity as shown by the growths of modulus *Y* in Table 7.4(b) and 7.5(b). The improved elasticity actually means more strength was needed to induce just a small extension within the elastic region. From the tables, further applied of external forces however had caused the increase in Maximum elongation ε_{max} of *CSMRL* and *CDPNR* composite. Chains slippage normally takes place among the adjacent matrix chains as a response toward the applied forces. The crosslinked networks can promote this structural effect during plastic deformations. It thus, explains the great improvement in Maximum elongation ε_{max} of these composites.

The effect caused by *bridging flocculated structure* on the ε_{max} highlights the importance of amine assisted crosslink reaction in nanoclay composites. *CDPNR* (30%) for example, shows better improvement in the ultimate strain ε_{max} with 125.0 % increase compare to that of *CSMRL* (30%) with just about 69.8 %. This observes is consistent with the finding from FTIR spectroscopy in Section 4.3.2.4.A. It reveals that the crosslink reaction was more prominent in *CDPNR* if compare to the *CSMRL* composite. Possible explanation could be related to the presence of protein molecules in *CSMRL*. Polar elements from the molecules, such as ammonium ions and oxygen atoms have good potential to interact with *OMON* silicates. These interactions can bring the protein molecules, as well as the polyisoprene

chains within *SMRL* rubber into close contact with the silicates. The effect however had reduced the interchains reactions of the rubber matrix chains within *OMON* gallery. This condition could be the main reason behind the relatively less crosslink reaction in *CSMRL*. Such effect is more obvious in case of *CENR-50* composite, where polar matrix chains in this composite have great potential to form hydrogen bonds with *OMON* silicates. The lack of crosslink reaction in *CENR-50* significantly disadvantages the formation of interparticle flocculated structure. It thus, explains the observed drops in Maximum elongation ε_{max} as *OMON* content increases within the composite.

More prove actually demonstrated in the work of several authors on various modified clay composites, which can also be associated with the effect of crosslink reaction on the strain at break ε_{max}. Wang studies on *OMON* composite with epoxy elastomer [7.40] showed that *OMON* inclusion about 20 % of weight fraction had caused an increase around 45 % on the ε_{max}. It was possibly due to the chemical structure of epoxy elastomer, which is composed of epoxide groups as shown in Figure 7.49. Similarly as in case of *CENR-50*, these polar groups contributed to chains crosslinking via anti-oxidation reaction within *OMON* gallery. In fact, weak matrix-silicate interactions due to the presence of benzene rings promote this chemical process. For that reason, *interparticle bridging flocculation* structures could be dominating this composite system. In contrast to the *CENR-50* in this work, *OMON-epoxy* composite in that case showed the improved Maximum elongation ε_{max}.

Epoxy Resin

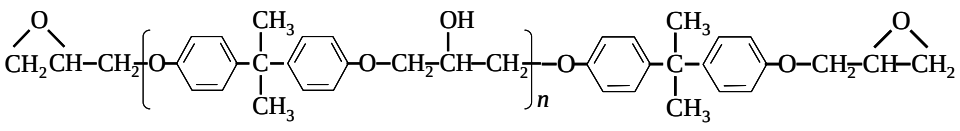

Figure 7.49: The chemical structure for poly(bisphenol A coepichlorohydrins), a type of epoxy resin [7.40].

The effect of chain crosslinking can also be connected with similar improvement in Mousa and Karger-Kocsis work on Styrene Butadiene Rubber *SBR* composite with *OMON* [7.41]. In this case however, double bonds on the *SBR* chains as illustrated in Figure 7.50 provided the potential sites for crosslink reaction. Perhaps, the lack of matrix-silicates interaction in the composite promoted the formation of interparticle bridging flocculated structure. This network structure within *SBR-OMON* composite therefore responsible for the increase in its Maximum elongation, ε_{max}.

Styrene Butadiene Rubber, *SBR*

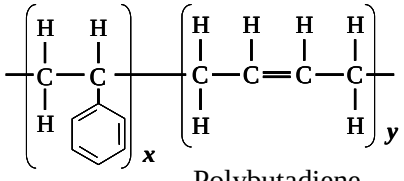

Polystyrene Polybutadiene

Figure 7.50: Chemical structure for Styrene-butadiene rubber, *SBR* [7.5].

The growth in ε_{max} with *OMON* loading is another aspect that suggests the involvement of crosslink reaction in structural modification. This behavior is established from series of *CDPNR* and *CSRML* tensile tests, using samples with *OMON* content up to 30 % of weight fraction. Results from Wang *et.al* works [7.42] on composite *OMON* with silicon rubber (*CSi*) give good comparison for the observations. Where, the growth in ultimate elongation ε_{max} was detected only for composites with less than 2 % of *OMON* loading. Illustration in Figure 7.51 for the chemical structure of silicon rubber might explain the results. It shows that no potential component in the structure that can participate either in anti-oxidation or crosslink reaction within *OMON* gallery. In that way, the flocculated network structure may not be developed within the *elastomer-OMON* composite system. The lack of such network structure therefore explains the drops in their Maximum elongation ε_{max}. On the

other hand, the growth in ε_{max} for *CSi* with small *OMON* content is most likely related to the *plasticizer* effect. This effect appeared as the structure of silicon matrix chains in *CSi* became loosen due to chains intercalation into *OMON* galleries. Hence, the unintercalated portions were allowed to straighten and slide on one another better than in pristine silicon rubber. This function of *OMON* as a plasticizer may explain the increase in strain at break, ε_{max} for the *CSi* composite with low *OMON* content.

Silicon Rubber

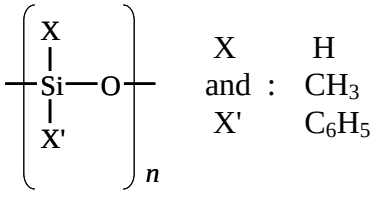

Figure 7.51: Chemical structure for silicon rubber where the X and X' could be hydrogen atoms or groups such as methyl (CH_3-) or phenyl (C_6H_5-) [7.5].

The idea of *interparticle bridging flocculation* thus far had helped to explain the growth in elongation at break ε_{max} with *OMON* loading. A big flocculated network in the *elastomer – OMON* composites is believed responsible for this unique structural effect. Further studies reveal the significance of crosslink reaction for the network creation. By this means, chain crosslinking on the elastomeric chains in *OMON* gallery has to be maximized in order to produce such mechanical behavior.

Stress-strain analysis on *polymer-OMON* composites overall reveals certain trends in both elastic and plastic regions. These trends demonstrate the importance of structural effects on composite deformations, in response towards external forces. Various structures created by a number of interactions between *OMON* and matrix chains contribute for these results. It thus highlights the significant of physical interaction such as chain entanglement and chain

coiling within *polymer-OMON* composite. This is including hydrogen bonding between the matrix chains and *OMON* silicates. Mechanical analyses also reveal the great contribution of chemical reaction on the composites structure. For example, anti-oxidation and crosslink reactions on matrix chains within *OMON* galleries.

7.4 Summary

- Preliminary analyses in mechanical studies were done on the stress-strain diagrams of pristine polymers. Section 7.1.1 highlights the potential elastic and plastic deformation in the polymers.
- Deformations in the polymers are reflected on their mechanical properties. Such as the elasticity modulus, *Y*, PL strength PL_{st}, PL strain PL_{sn}, Tensile strength σ_{max} and also the Maximum elongation ε_{max} that are tabulated in Table 7.1.
- Structural effects on the mechanical properties, such as stereoisomerism, crystallinity, chain crosslink and branching, and plasticizer molecule are discussed in Section 7.1.2. The effect of molecular weight (MW) is also highlighted in Section 7.1.3.
- Structural changes due to *OMON* existence in *polymer-OMON* composites had caused various mechanical reactions. Section 7.2.2 present the Halpin-Tsai equation that is a micromechanical model used to study the structural effect. This model is based on the concept of effective filler that describe the effects of *OMON* intercalation.
- Mechanical analyses on *CENR-50* composites in Section 7.2.3.A show the remarkable growths in modulus *Y* and Tensile strength σ_{max} as *OMON* content increases within the composites. The effect however, reduced their Maximum elongation ε_{max}.

- Physical network due to *matrix-silicate interaction* in *CENR-50* composite responsible for these results. *OMON* exfoliation in fact promoted better interactions that contribute to the great increase in modulus *Y*.

- The growth in modulus *Y* can also be seen in case of *CSMRL* and *CDPNR* composites that are discussed in Section 7.2.3.B and Section 7.2.3.C respectively. The normalized modulus *Y* manages to fit the Halpin-Tsai model up to 30 % of *OMON* inclusion in the natural rubber composites.

- Remarkable improvements in Maximum elongation ε_{max} highlight the importance of crosslink reaction within the composites. It created chemical network that generated *interparticle bridging flocculated* structure, which contribute to good stress distribution mechanism. The effects had increased the Tensile strength σ_{max} of *CSMRL*, as well as *CDPNR* composites.

- The interrupted matrix networks and stacked layer structures had caused the Tensile strength σ_{max} to reduce in case of *CPE* composites. Section 7.2.3.D reveals that these effects also affected the Maximum elongation ε_{max} of the composites. Matrix-silicate interactions however give the reinforcement effects in *CPE* composites, which had increased their modulus *Y*.

- Polar *pPVC* chains had induced good matrix-silicate interaction in *CpPVC* composites. It can be seen with the great increase of modulus *Y* in Section 7.2.3.E, which may also indicates the effect of stacked layer structure in the composites. Similarly as in *CPE*, this structure contributed to the drop in the Maximum elongation ε_{max} of *CpPVC*.

- The improved Maximum elongation ε_{max} observed in *polymer-OMON* composite with low *OMON* content suggests the plasticizer effect due to polymer intercalation. Section

7.3.1 and 7.3.2 discuss this effect that can reduce the interchain reactions among matrix chains. Chains extension thereby was promoted which then increased the ε_{max} and PL_{sn}.

- The importance of wide integrated networks for good stress distribution is highlighted in Section 7.3.2. It shows that physical and chemical networks within *natural rubber-OMON* composites distributed stress better than *CpPVC* and *CPE* system. The effects can be seen with the increases in Maximum elongation σ_{max} of the rubber composites.

- Mechanical analyses demonstrate the structural effects of *polymer-OMON* interactions on mechanical properties. Such as, *matrix-silicate interaction* that involves hydrogen bonding and van der Waals attraction force. Chains coiling and chains entanglement in matrix-alkyl chains interactions also contribute to structural effects.

- Section 7.3.3.A discuss the role of *interfacial adhesion* that had caused the growths in modulus *Y*. *Matrix-silicate* and *matrix-alkyl chains interactions* had great influence on this strength at interphases in the composites.

- The improved *stacking order, N* which is discussed in Section 7.3.3.B is another factor behind the improvement in modulus *Y*. However, it can also induce premature break that will reduce the Maximum elongation ε_{max}.

- *Interparticle bridging flocculation* in Section 7.3.3.C highlights the importance of anti-oxidation and crosslink reaction in *OMON* gallery. These amine assisted processes can crosslink the intercalated matrix chains, which then contributed to the improvements in Tensile strength σ_{max} and Maximum elongation ε_{max}.

References

7.1 J. R. Davis, "Tensile Testing", 2nd. Edition, *ASM International-The Material Information Society*, New York, (2004)

7.2 R. L. Timings, "Mechanical Engineer's Pocket Book", 3rd Edition, *Newnes- Elsevier*, Amsterdam, (2005)

7.3 A. Mubeen, "Experimental Strength of Materials", 3rd. Edition, *Khanna Publishers*, Delhi, (1997)

7.4 L. H. van Vlack, "Elements of Materials Science", 2nd. Edition, *Addison Wesley Publishing Company*, Massachusetts, (1959)

7.5 W. L. Smith, "Foundation of Materials Science and Engineering", 2nd. Edition, McGraw-Hill, New York, (1993)

7.6 M. F. Ashby and D. R. H. Jones – Translation: R. Othman, "Bahan Kejuruteraan", *Penerbit Uni. Sains Malaysia*, Pulau Pinang, (1996)

7.7 S. Fatahi, A. Ajji and P. G. Lafleur, "Correlation between different microstructural parameters and tensile modulus of various polyethylene blown films", *Poly. Eng. Sci.,* **V 47(9)**, (2007), pg. 1430 – 1440

7.8 R. K. Krishnaswamy, Q. Yang, L. Fernandez-Ballester and J. A. Kornfield, "Effect of the distribution of shortchain branches on crystallization kinetics and mechanical properties of high-density polyethylene", *Macromolecules,* **V 41**, (2008), pg. 1683 – 1704

7.9 S.L. Rosen, "Fundamental Principels of Polymeric Materials", 2nd. edt., *John Wiley & Sons*, New York,(1993)

7.10 D. Feldman, "Polymeric building materials", *Taylor & Francis*, New York, (1989)

7.11 F. E. Okieimen, T. O. Egbuchunam and D. Balkose, "The Effect of Bio-based Plasticizer on the Permanence and Water Vapour Transport Properties of PVC Plastigels", *Chem. Inds. & Chem. Eng.*, **V 14(1)**, (2008), pg. 11 – 15

7.12 R. Boughalmi, J. Jarray , F. Ben Cheikh Larbi , A. Dubault and J.L. Halary, "Molecular Analysis of the Mechanical Behavior of Plasticized Amorphous Polymers", *Oil & Gas Science and Technology – Rev. IFP*, **V 61(6)**, (2006), pg. 725 – 733

7.13 B.Y. Zhong, W.Z. Xue, H.Z. Ming and P.Z. Ren, "Effect of Physical Crosslinking on Properties of Plasticized High Molecular Weigh PVC", *J. Zhejiang Uni. Scie.*,**V 1(2)**, (2000), pg. 171-177

7.14 J. Black and G. Hastings, "Handbook of Biomaterial Properties**"**, *Chapman & Hall*, London New York, (1998) : http://www.matweb.com/

7.15 http://www.sdplastics.com/ polyeth.htlm

7.16 K. T. Cheng, A. R. Rais and K. B. Basir, "Deproteinised Natural Rubber", *Rubb. Res. Inst. Malaysia Bull No. 11*, The Rubber Research Institute of Malaysia, Kuala Lumpur, (1996)

7.17 Rubber Research Institute of Malaysia, "Epoxidised Natural Rubber", The Rubber Research Institute of Malaysia, Kuala Lumpur, (1984)

7.18 R. P. Sheldon, "Composite Polymeric Material", *Applied Science Publisher*, London and New York, (1982)

7.19 D. B. Miracle and S. L. Donaldson, "ASM Handbook: Composites", **V 21,** *ASM International Handbook Committee- ASM International*, US, (2001)

7.20 N. Sheng, M.C. Boyce, D. M. Parks, G. C. Rutledge, J. I. Abes and R. E. Cohen, "Multiscale micromechanical modeling of polymer/clay nanocomposites and the effective clay particle", *Polymer*, **V 45**, (2004), pg. 487 - 506

7.21 O. L. Manevitch and G. C. Rutledge, "Elastic properties of a single lamella of montmorillonite by molecular dynamics simulation", *J. Phy. Chem. B*, **V 108**, (2004), pg. 1428

7.22 C. J. Parez, V. A. Alvarez, I. Mondragon and A. Vazquez, "Mechanical properties of layered silicate/starch polycaprolatone blend nanaocomposites", *Poly. Int*., **V 56**, (2007), pg. 686 – 693

7.23 T. D. Fornes and D. R. Paul," Modeling properties of nylon 6/clay nanocomposites using composite theories", *Polymer*, **V 44**, (2003), pg. 4993 – 5013

7.24 Y. Dong, D. Bhattacharyya and P. J. Hunter," Experimental characterization and object-oriented finite element modeling of polypropylene / organoclay nanocomposites", *Comp. Sci. & Tech*., **V 68(14)** , (2008), pg 2864 – 2875

7.25 P. Li, L. Yin, G. Song, J. Sun, L. Wang and H. Wang, "High-perfomance EPDM/organoclay nanocomposites by melt extrusion", *App. Clay Sci*., **V 40**, (2008), pg. 38 - 44

7.26 Q. X. Jia, Y. P. Wu, Y. Q. Wang, M. Lu, J. Yang and L. Q. Zhang, "Organic Interfacial Tailoring of Styrene Butadiene Rubber-Clay Nanocomposites Prepared by Latex Compounding Method", *J. App. Poly. Sci*., **V 103**, (2007), pg. 1826 - 1833

7.27 J. H. Chang, T. G. Jang, K.J. Ihn, W. K. Lee and G. S. Sur, "Poly(vinyl alcohol) Nanocomposites with Different Clays: Pristine Clays and Organoclays", *J. App. Poly. Scie.,* **V 90**, (2003), pg. 3208 – 3214

7.28 A. Y. Rodriguez, P. A. Lloret, A. B. R. Navarro, J. D. M. Ramos and C. Cardell, "Thermo-XRD and differential scanning calorimetry to trace epitaxial crystallization in PA6/montmorillonite nanocomposites", *Mater. Lett*., **V 63**, (2009), pg.1159 – 1161

7.29 H. J. Bae, H. J. Park, S. I. Hong, Y. J. Byun, D. O. Darby, R. M. Kimmel and W. S. Whiteside, "Effect of clay content, homogenization RPM, pH and ultrasonification on mechanical and barrier properties of fish gelatin/montmorillonite nanocomposite films", LWT – *Food Sci. Technol.*, **V 42**, (2009), pg. 1179 – 1186

7.30 D. R. Paul and L.M. Robeson, "Polymer nanotechnology: Nanocomposites", *Polymer*, **V 49,** (2008), pg. 3187 – 3204

7.31 K. H. Wang, M. H. Choi, C. M. Koo, M. Xu, I. J. Chung, M. C. Jang, S. W. Choi and H. H. Song, "Morphology and Physical Properties of Polyethylene/Silicate Nanocomposite Prepared by Melt Intercalation", *J. Poly. Scie. B: Poly. Phys.,* **V 40**, (2002), pg. 1454 – 1463

7.32 M. M. Reddy, R. K. Gupta, S. N. Bhattacharya and R. Parthasarathy, "Structure-property relationship of melt intercalated maleated polyethylene nanocomposites", *Korea-Australia Rheo. J.,* **V 19(3)**, (2007), pg. 133 – 139

7.33 L. E. Nielsen and R.F. Landel, "Mechanical Properties of Polymers and Composites", 2nd Edition, *Marcel-Dekker*, New York, (1994)

7.34 P. J. Phillips, "Conduction Processes in Polymer" Electrical Properties of Solid Insulating Materials: *Molecular Structure and Electrical Behaviors* edited by R. Bartnikas and R. M. Eichhorn, Engineering Dielectrics **V IIA** - ASTM Special Technical Publication No. 783, Philadelphia, (1983)

7.35 F. Gong, M. Feng, C. Zhao, S. Zhang and M. Yang, "Particle configuration and mechanical properties of poly(vinylchloride)/montmorillonite nanocomposites via in situ suspension polymerization", *Poly. Test.,* **V 23**, (2004), pg. 847 – 853

7.36 C. Jo and H. E. Naguib, "Constitutive modeling of HDPE polymer/clay nanocomposite foams", *Polymer*, **V 48**, (2007), pg. 3349 – 3360

7.37 S. S. Ray and M. Okamoto, "Biodegradable Polylactide and Its Nanocomposites: Opening a New Dimension for Plastics and Composites", *Macromol. Rapid Commun.*, **V 24**, (2003), pg. 815 – 840

7.38 F. Avalos, J. C. Ortiz, R. Zitzumbo, M. A. L. Manchado, R. Verdejo and M. Arroyo, "Effect of montmorillonite intercalant structure on the cure parameters of natural rubber", *Euro. Poly. J*., **V 44**, (2008), pg. 3108 - 3115

7.39 G. Romario, F. Bignotti, S. Pandini and T. Ricco, "Mechanical reinforcement in natural rubber/organoclay nanocomposites", *Comp. Sci. Technol.*, (2009), in press

7.40 Z. Wang, J. Massam and T. J. Pinnavaia, "Epoxy-Clay Nanocomposites", Polymer-Clay Nanocomposites edited T. J. Pinnavaia and G. W. Beall, *Wiley*, Chichester and New York, (2000)

7.41 Karger-Kocsis and C. M. Wu, "Thermoset Rubber/Layered Silicate Nanocomposites: Status and Future Trends", *Poly. Eng. Sci.,* **V 44**, (2004), pg. 1083 – 1093

7.42 S. Wang, Q Li and Z Qi, "Studied on Silicon Rubber / Montmorillonite Hybrid Composites", *Eng Mater.,* (1998), pg. 87 – 93

Chapter 8

Conclusion and Future Work

Chapter 8: CONCLUSION AND FUTURE WORK

Section 8.1 reviews the aim and methodology of this research, which involve the approach taken to overcome several major obstacles in this work. It also highlights the contribution offered over the previous six chapters. Section 8.2 presents the conclusion of this research work, which underlines the thesis contributions to improve knowledge on *polymer-OMON* composites as well as experimental techniques. Finally, Section 8.3 considers future work possibilities.

8.1 Review of Reseach Objective

Earlier in Chapter 1, the main objective of this work was highlighted that is to characterize the thermo-electrical and mechanical properties of *polymer-OMON* composites. This work was done by means of *Thermally Stimulated Current* or *TSC* technique and *Tensile test* for thermo-electrical and mechanical studies, respectively. Chapter 2 briefly explains the basic principles behind these techniques and their theoretical backgrounds. However, there were a few obstacles arose in quest to fulfill the primary objective. Among the crucial problems faced are as follow,

a) The lack of knowledge on Montmorillonite (*Mon*) and *OMON* structures, as well as the mechanisms involve within the clay interlayer and also their interactions with the matrix chains of *polymer-OMON* composites

b) TSC is a sensitive measurement technique that must be carefully handled in order to generate reliable results. It was a big challenge to develop such system, as well as in the analysis of the TSC results.

c) Even though tensile test is a common mechanical study, it is very important to ensure proper methodology to bring out reliable results. It means that appropriate

experimental tools have to be prior designed and customized right to the type and dimensions of the studied samples.

Prior research therefore outlined three additional objectives for this project to overcome the major obstacles. They are

a) to improve the existing TSC set-up to develop a sensitive and reliable TSC system for thermo-electrical studies

b) to develop the right experimental method and apparatus for sample preparation and testing in tensile test for mechanical studies

c) to understand the characteristics and mechanisms involve in *Mon* and *OMON* clay, as well as their interactions with polymeric materials.

In order to accomplish these additional objectives, the research work was structured into three stages. They are known as *Methodology, Characterization* and *Thermo-electrical and Mechanical Studies*.

8.1.1 Methodology

In Chapter 3 of methodology, it was divided into two primary sections that comprised of *Sample Preparation* and *Instrumentation and Experimental Methods*. The modifications on *Mon* to produce *OMON* and the fabrication of *Mon* and *OMON* composites were explained in Section 3.1. The focus however was on the *Instrumentation and Experimental Method* to fulfill the outlined objectives.

8.1.1.1 TSC Measurement

Section 3.2.1.1 explains the instrumentations of TSC system, which were based on several fundamental principles in Section 2.1.1.1 and the experimental considerations outlined in Section 2.1.2. The *Thermally Stimulated Current, TSC* program that is a computer program

was developed to automated control this TSC system and for data acquisition. The system was calibrated with some known polymers, where the results confirmed the reliability of the developed TSC system.

8.1.1.2 Tensile Test

Section 3.2.2.1 describes the customized tools for sample preparation and sample holder in tensile test. The designs for these apparatus and the experimental consideration taken in tensile test were based on ASTM standards, as well as some basic principles summarized in Section 2.2.1.

The developed instrumentations and experimental methods in this work are able to carry out the TSC measurement and tensile test for thermo-electrical and mechanical studies in that order. Therefore, apart of the outlined objectives were achieved and these tools were ready to be used in the studies.

8.1.2 Characterization

Basic characterizations for *Mon*, *OMON* and their composites with polymers were done by means of Differential Scanning Calorimetry (*DSC*), X-ray Diffraction (*XRD*) and Fourier Transform Infrared (*FTIR*) spectroscopy.

8.1.2.1 Differential Scanning Calorimetry, DSC

Table 4.1 in Section 4.1.3 summarizes the observations on thermal features within the DSC thermograms of the studied materials. Analyses on DSC results suggested that *ODA* cation (*octadecylammonium*) was intercalated into *OMON* gallery. It also reveals the crystallinity of alkyl chains on these cations in most cases of *polymer-OMON* composites. The distorted endothermic peak within DSC thermogram of *CSMRL* and *CDPNR* composites indicate the interruptions on alkyl chains structures. Similarly, the lost of T_{m2} endothermic in case of *CpPVC* and *CPE* composites indicate the disruption of certain alkyl structure. DSC results

especially the temperature of thermal transition T_g and endothermic T_m are very useful for comparisons with the TSC results.

8.1.2.2 X-ray Diffraction, XRD

Section 4.2 discussed the XRD analyses carried out on *Mon, OMON* and their composites with polymers. Summarized analyses in Section 4.2.3 highlight important findings from the studies, such as the increased basal spacing d_{001} from 1.462 nm to 1.840 nm that proves the intercalation of *ODA* cations within *OMON* galleries. Table 4.3 shows that polar matrix chains promoted better intercalations, which had increased the basal spacing d_{001}. In case of *CENR-50*, it is believed that extensive increment in the interlayer height had caused the exfoliation of *OMON* silicate layer in the composite.

Further analyses in Section 4.2.2.2 revealed the effects of *bridging flocculation*, which described the interaction between silicate layers and polar matrix chains. *Ordering effect* that is also associated with matrix chains polarity explains the appearance of XRD peaks above the $2\theta = 6°$ in *Mon*. The importance of chain coiling in matrix-alkyl chains reactions was highlighted, where it was associated with the improved *stacked layer* (*N*) structure on *OMON* particles. Matrix chain polarity also contributes for such structure, as shown in case of *CpPVC* and *CENR-50* composites.

8.1.2.3 Fourier Transform Infra-red, FTIR

FTIR analyses carried out on pristine polymers, *OMON* and *polymer-OMON* composites were discussed in Section 4.3. For example, Table 4.6 shows the characteristic absorption bands of *SMRL, DPNR* and *ENR-50* natural rubbers, whereas the significant bands of *Mon, OMON* and *polymer-OMON* composites are listed in Table 4.7. Important findings from FTIR analyses were summarized in Section 4.3.3 with Table 4.8 lists all the related bands. FTIR characterizations on *polymer-OMON* composites catagorized various effects on these composites into four groups as follow.

i. ***Matrix-Alkyl Chains Interaction***

Analyses on several bands that are related to the methylene group (CH_2), methylene chains $(CH_2)_n$ and ammonium cation (NH_3^+) in Section 4.3.2 confirmed:

a) there exist the intercalation and interaction between matrix and alkyl chains

b) the chain coiling in matrix-alkyl chains interaction had distorted the structures of methylene groups as predicted in DSC analyses with the lost of T_{m2} endothermic

c) the interrupted alkyl structure as predicted in the DSC analyses for *CSMRL* and *CDPNR* composites. This effect was due to the interparticle bridging flocculation structure in the natural rubbers composites.

ii. ***Matrix chains-OMON Silicate Interaction***

Section 4.3.2.2 discussed some absorption bands that proved *OMON* silicate interactions with alkyl chains. These bands represent the vibration of (*Si-O-R*) and (*Si–H*) components. *OMON* exfoliation within *CENR-50* composite, as predicted by XRD analyses was proven with the appearance of ammonium cation ($–NH_3^+$) bands from amine salt.

iii. The Effects on OMON silicate – water removal

Extended hydrogen bonding between *OMON* silicate and water was reduced due to water removal as matrix chains inhabited the silicate surfaces. Section 4.3.2.3 explains the effects on the vibration bands of hydroxyl (*OH*) group from hydration in *OMON*. The effects can also be detected on some bands for alumina (*AlO*) and (*SiO*) from silicate groups.

iv. The Effects on Matrix chains

The trapped polyisoprene chains in *OMON* gallery had induced several chemical reactions in *natural rubber-OMON* composites. For example, *crosslink reaction* in Section 4.3.2.4.A that is believed facilitated by ammonium cation. This reaction promoted the formation of

interparticle bridging flocculation structure within *CSMRL* and *CDPNR* composites. *Anti-oxidation* reaction is also induced by these cations, which is discussed in Section 4.3.2.4.B. This reaction on oxygen related groups in the rubber matrix chains created hydroxyl group that contribute for good matrix-silicate reaction. In case of *CENR-50* composite, *hydrolysis* of the epoxide group on *ENR-50* chains generated more hydroxyl groups. It thus explained the strong matrix-silicate interaction as shown by the (*Si-O-R*) band in Section 4.3.2.2.

All through the analyses on DSC, XRD and FTIR results, the basic structures of *Mon* and *OMON* can be recognized. A lot of information gathered had helped to understand the clay minerals, especially the renewed *OMON* with organophilic property. Section 4.4 describes *OMON* structures within various types of polymers matrix. The characterizations therefore fulfilled one of the work objectives. The knowledge on *OMON* structures, as well as the mechanism involved in matrix-filler interaction is very useful for both thermo-electrical and mechanical studies.

8.1.3 Thermo-electrical and Mechanical Studies

Thermo-electrical and mechanical studies involve both measurements and data analyzing. The measurements were done using the developed TSC system and the customized tensile instrumentation as stated earlier in Section 8.1.1. Proper experimental procedures were also followed as suggested by the related ASTM standards. Two computer programs named as *TSC Analysis* and *Tensile Analysis* were developed for the purpose of data analyzing.

8.1.3.1 Thermally Stimulated Current, TSC Measurement

i. *TSC Thermogram*

TSC measurement create current-temperature plot or TSC thermogram, which is generated by the depolarization processes in an electret. Preliminary analyses on TSC thermograms for polymers, *Mon*, *ODA* (*octadecylamine*), *OMON* and *polymer-OMON* composites were

carried out in Chapter 5. The knowledge on glass transition temperature T_g and the melting temperature T_m had helped to recognize the α, β and ρ peaks of the polymers. Likewise, the α, ρ and ρ_1 peaks of *ODA* were identified where they can also be observed within *OMON* thermogram. Hence, these peaks must be related to the *ODA* cations inside *OMON* gallery. The α and ρ peaks of *OMON* appear in most cases of *polymer-OMON* composites, along with the TSC peaks from pristine polymers. The variations in maximum temperature T_{max} of these peaks prove various matrix-*OMON* interactions in the composites. The missing ρ_1 peak within the TSC plot for composites adds more evidence for such interactions.

ii. TSC Data Evaluation

Data evaluation is very important to bring out more information from TSC measurements. In this work, the effort was focused on activation energy E and pre-exponential factor τ_o that gives the characteristic time of the relaxation process. Peak decomposition carried out on various TSC peaks revealed that distributed relaxation processes involved behind the appearance of experimental peaks. In Section 6.1.2, analyses on the fitted energy E for decomposed α and ρ peaks confirmed that they are within the ranges for dipole and space charge relaxations, respectively. The analyses also reveal the presence of molecular-ion deep trap, as shown by a number of decomposed peaks with high energy E.

The origin of relaxation processes in electrets can be predicted with the knowledge on their characteristic relaxation time, τ_o. For example, a τ_o in the range of 10^{-18} to 10^{-25} s indicates the dipole-segmental relaxation, which is induced by local segmental motions on polymeric chains. Section 6.2.2 introduced the *N-fitting* method, a fitting technique that is capable to fit both experimental and numerical TSC data. From this fitting method, the characteristic relaxation time of *N-fitting* (τ_n) can also be calculated where it managed to demonstrate the occurrence of cooperative relaxation as highlighted in *William-Landel-Ferry* (*WLF*) theory.

Analyses on various TSC peaks of *OMON* and *polymer-OMON* composites also showed a range of dipole groups, dipole-segmental and space charge relaxations that contributed to depolarization processes. From this knowledge, different effects caused by *matrix-OMON* interaction within the composites can be investigated. For example, chain coiling and chain entanglement in matrix-alkyl chains reactions and the intermolecular reaction in crystalline structure that involved methylene groups. In Section 6.2.2.2.D, analyses on the τ_n from the experimental ρ peak of *pPVC* revealed the occurrence of segmental relaxation at the liquid-liquid transition temperature T_{ll}. The process of such thermal transition stimulated space charge release, as shown by the characteristic relaxation time τ_n of several decomposed ρ peaks. It thus, confirms the connection between space charge relaxation and the appearance of ρ peak within TSC thermogram.

8.1.3.2 Tensile Test

Tensile test basically is the measure of applied forces versus elongations on material. From the measurements, a stress-strain diagram can be plotted for data evaluations that reveals various mechanical properties. Such as the elastic modulus Young *Y*, Tensile strength α_{max} and Maximum elongation ε_{max}. Mechanical properties from pristine polymers in this work were used as references to study the effects of *OMON* inclusion within *polymer-OMON* composites. Structural modifications due to *matrix-OMON* interactions had caused various mechanical responses by the composites. Analyses on the generated mechanical properties revealed the importance role of *OMON* intercalation in polymer reinforcement. Halpin-Tsai equation in Section 7.2.3, which is a micromechanical model showed the effects caused by intercalated matrix chains on the normalized modulus *Y*. The intercalation and exfoliation of *OMON* particle offered remarkably wide contact area for polymer matrix to interact with *OMON* silicate, which then influence the mechanical property of a composite.

Matrix-silicate and matrix-alkyl chains interactions created various structural effects, which had improved some of the composites mechanical properties. For example, good interfacial adhesion promoted stress sharing at interphases that gave better modulus *Y* for *CENR-50* and *CpPVC* composites. The stacked layers structure on *OMON* particle in *CPE* composite also contributed to the increase in modulus *Y*. The stacked structure however, creates weak points that can induce early failure and contributes the drop in Maximum elongation ε_{max} of the composites. Significant increase of the ultimate strain ε_{max} in contrast can be seen in the case of *CSMRL* and *CDPNR* composites. Chemical network in these composites promoted chains slippage that was responsible for the improved strain at break. Such network that was discussed in Section 7.3.3.3 also contributed to the formation of interparticle bridging flocculated structure. This structure give good stress distribution mechanism in *CSMRL* and *CDPNR* composites that had caused the increase in Tensile strength σ_{max} and modulus *Y*.

The results and analyses of TSC measurements as well as tensile tests can be related to the findings from structural characterization in Chapter 4. Observations from the electrical and mechanical studies added more proofs that supported some suggestions in the preliminary work. In addition, they revealed a lot of information regarding the internal structure of *polymer-OMON* composites. From the studies, the importance of certain structural changes and their effects were also highlighted, such as interparticle bridging flocculated structures within *CSMRL* and *CDPNR* composites. Besides, they prove the reliability of methodology in Chapter 3, which is the major contributor in this work.

8.2 Conclusion

Physical and chemical reactions in matrix-filler interactions had caused various structural modifications in *polymer-OMON* composites. Physical reaction basically is associated with *matrix-silicate* reaction. However, *matrix-alkyl chains* reaction was also considered that involved chain coiling and chain entanglement in *OMON* gallery. **Basic characterization** on *Mon*, *ODA*, pristine polymers, *OMON* and *Polymer-OMON* composites reveals several valuable informations as follow:

- Comparisons on the DSC results of *ODA*, *OMON* and *OMON* composite show that the missing *ODA* endothermic (T_{m1} = 62.77 °C and T_{m2} = 89.53 °C) within *OMON* thermogram prove the intercalation of *ODA* cations.
- The increased basal spacing d_{001} of *OMON* from 1.840 nm to 3.86 nm proves the intercalation of polymers matrix chains within *OMON* gallery.
- The idea of bridging flocculation process explains the XRD peak of *Mon* composites, which appear above the d_{001} peak of *Mon* (2θ = 6.04 º).
- XRD peaks greater than the *Mon* d_{001} peak (2θ = 6.04 º) in case of *polar polymer-OMON* composites reveal the ordering effect due to *OMON* coherent structure.
- *Matrix-alkyl chain* coiling and matrix chain polarity improved the stacking order *N* of *OMON* particles. In case of *CpPVC*, the stacking order was increased from *N* about 4 layers to 21 layers of *OMON* silicates.
- *ODA* cations facilitated *crosslink reaction* on the polyisorene double bonds (*C=C*) of the intercalated natural rubber chains within *OMON* gallery.
- *ODA* cations induced *anti-oxidation reactions* on the oxygen related groups (*C-O-C*) from the intercalated polyisoprene chains within *OMON* gallery.

- Water molecules in *OMON* assisted *hydrolysis* process on epoxide groups (*C-O-C*) in *ENR-50* chains, which produced more hydroxyl groups (*OH*) that promoted *matrix-silicate* interaction within *CENR-50* composites.

The Effects of *OMON* modification in TSC and Tensile Studies

The mode of chain reaction in *matrix-alkyl chains* interactions can be recognized by means of *OMON* α peak within TSC plot, which is related to the methylene (CH_2) groups on alkyl chains. Several effects attributable to water removal from *OMON* confirm the inhabitation of matrix chains on *OMON* silicate surfaces. In fact, good *matrix-silicate* reaction by polar matrix chains improved the silicates arrangement on *OMON* structure. Hydrogen bonding and van der Waals forces had played significant role in this interaction, which produced the ordering effect in XRD spectroscopy. They can also promote extensive *matrix-alkyl chains* reaction. The effect was then reflected on the experimental *OMON* ρ peaks within the TSC plots for *CpPVC* and *CENR-50* composite. Where, their characteristic relaxation time, τ_n indicates the dipole-segmental relaxation by alkyl chains $(CH_2)_n$ on *octadecylamine* (*ODA*) cations within *OMON* gallery.

A number of chemical reactions were induced due to the trapped matrix chains with amine cations in such a confined space of *OMON* gallery. *Crosslink reaction* on the double bonds of natural rubbers chains promoted chains crosslinking inside *OMON* interlayer. Similarly, *anti-oxidation* reaction on oxygen related groups added more resources to the crosslinking process. In addition to the cations, chains entanglement in *matrix-alkyl chains* interactions promoted these chemical reactions. Where, the resultant crosslinked chains were important for the formation of interparticle bridging flocculated structure within *natural rubbers-OMON* composites. It resulted in the remarkable growths of Maximum elongation ε_{max} and Tensile strength σ_{max} of the composites. Several effects caused by the *hydrolysis* processes

of epoxide groups were also recognized in *OMON* composites with the epoxidised natural rubbers (*ENR-50*). Where, they had significantly improved *matrix-silicate* interaction that contributed to the significant growth in modulus *Y* of the rubber composite. *Matrix-alkyl chains* coiling that promoted stacking layer structure on *OMON* particles can also induce the increased modulus *Y*. This structure on the other hand stimulates premature failure that contributed to the drop in Maximum elongation ε_{max}.

Research Objective

The primary objectives to **thermo-electrically and mechanically study *polymer-OMON* composites** were succeeded by means of **TSC measurement** and **tensile test**, respectively. They can be concluded that:-

I. TSC study capable to demonstrate several effects from *matrix-OMON* reactions on the relaxation behaviors of *methylene groups* and *alkyl chains* within *OMON* gallery. From observation and analysis on the TSC result, it can also be suggested that:-

- The developed TSC technique is capable to reveal various relaxation effects within crystallite structure, as shown by the *OMON* thermogram with the appearance of α (28.03 °C), ρ (55.07 °C) and ρ_1 (75.66 °C) peaks
- The variation of T_{max} for *OMON* α and ρ peaks in TSC plots for *polymer-OMON* composites show that *OMON* act differently with various types of polymer matrix
- The lost *OMON* α peak at T_{max} = 34.87 °C within the TSC plot of *CPE* and *CpPVC* shows the effect of *matrix-alkyl* chains coiling on methylene groups (CH_2) mobility
- The ruined intermolecular reaction of methylene groups in the crystallite structure of alkyl chains $(CH_2)_n$ is responsible for the missing of *OMON* ρ_1 peak at T_{max} = 105.35 °C within the TSC plots of *polymer-OMON* composites

Data evaluation on the TSC result reveals that

- Decomposed TSC peaks with the activation energy *E* around 4 to 8 eV indicates the space charge released from molecular-ion deep traps
- *N-fitting* method that is a proposed fitting technique capable to fit both numerical and experimental data from the TSC peaks with data population, *P* around 76 % to 100 % for data deviation less than 5 % (< 5 %).
- The characteristic relaxation time or pre-exponential factor τ_n of *N-fitting* manage to confirm the cooperative relaxation of experimental α peak from polymers, where the τ_n is around 10^{+1} to10^{-4} s
- Analysis on various types of TSC peaks suggests that the characteristic relaxation time τ_n may indicate the dipole group (10^{-10} to 10^{-13} s), dipole-segmental (10^{-14} s to 10^{-17} s) and segmental (10^{-18} to 10^{-28} s) relaxations
- A number of decomposed peaks with high energy *E* (≥ 3eV) show characteristic time $\tau_n \leq 10^{-30}$ s, such low τ_n thus can be associated with space charge relaxations.
- *Matrix-alkyl* chains entanglement allows the cooperative relaxations by methylene groups. It is shown by the characteristic relaxation time τ_n of experimental *OMON* α peaks (10^{0} s to 10^{-2} s) in the TSC plot of *polymer-OMON* composites
- The characteristic relaxation time τ_n for the experimental *OMON* ρ peaks (10^{-16} s to 10^{-17} s) of *polymer-OMON* composites indicates the dipole-segmental relaxations due to extensive matrix-silicate interactions
- Decomposed *OMON* α and ρ peaks reveal partial dipole groups, dipole-segmental, segmental, space charge as well as the cooperative relaxations (10^{-5} to 10^{-9} s). They are representing the depolarizations at localized sites within *OMON* gallery.

II. Tensile study revealed various mechanical effects caused by different *matrix-OMON* reactions on the whole system of *polymer-OMON* composites. From observations and analysis on the stress-strain diagrams of polymers and their composites with *Mon* and *OMON*, it can be suggested that

- *Matrix-alkyl* chains and *matrix-silicate* interactions created structural effects, which influenced the mechanical properties of *polymer-OMON* composites. Among the prominent effects are the *interfacial adhesion*, *stacking layers* and *interparticle bridging flocculated* structure
- Wide integrated physical and chemical networks within *natural rubbers-OMON* composites give good stress distribution mechanism, which increased the Tensile strength σ_{max} (3332 %) and also modulus *Y*
- The effect of *OMON* intercalations on modulus *Y* was proven using the Halpin-Tsai fitting on data from *polymer-OMON* composites. In case of *CSMRL* and *CDPNR*, it was fitted up to 30 % of *OMON* inclusion
- Interfacial adhesion and physical network promoted stress sharing that contributed to significant growth in modulus *Y*. Particularly, in *CENR-50* (30%) composite with the exfoliated *OMON* platelets that give the increased *Y* about 15420 %
- Chemical networks within the interparticle bridging flocculated structure promoted chain slippage, which remarkably improved the Maximum elongation ε_{max} (125 %) with the increase of *OMON* content
- In non-network composite system such as *CpPVC*, the improvement in modulus *Y* (2323 %) is contributed by the interfacial adhesion and stacking layers structure (*N* ~21 layers in *CpPVC* (30%)) that facilitated the stress sharing at interphases

- Stacking layers in *polymer-OMON* composites created weak points that stimulated premature failure. It caused the drop about 80 % in the Maximum elongation ε_{max} of *CpPVC* (30%) compared to that of pristine *pPVC*.

8.3 Future Works

Based on the results and analyses from this research project, there are several potential directions that can be considered as future works. They are divided into four categories as follow:

A. Methodology

1) The developed TSC system can be improved with an integrated cooling system, such as a helium cryopump. In that way, the whole TSC system will be fully automated that can give better control on heating rate and temperature stabilization.

2) Electrode-sample interface in TSC system should be improved to avoid the formation of molecular-ion deep trap.

3) A proper sample cutter for tensile specimen should be designed to simplify the cutting process

B. Material

1) The intercalated polymeric chains into *OMON* interlayer normally will affect the air permeability of polymer. Therefore, the tortuosity of *polymer-OMON* composite is one more structural effect that should be investigated.

2) The addition of inorganic substance such as *OMON* into polymeric system can change the thermal behavior of a polymer. Therefore, the thermal stability of *polymer-OMON* composites should be investigated especially for application.

C. Thermo-electrical study

The proposed *N-fitting* method should be tested with various types of relaxation effects to see its reliability to differentiate relaxation behaviors in electrets

D. Mechanical study

1) Normally, the normalized modulus *Y* of nanoclay composite can fit Halpin-Tsai model just for a small filler addition (<10 %). Therefore, the ability of *CSMRL* and *CDPNR* composites system to fit the Halpin-Tsai equation up to 30 % of *OMON* content should be study in detail.

2) The idea of interparticle bridging flocculated structure influence mechanical properties should be tested with various combinations of matrix-silicate and matrix-alkyl chains systems.

All through the thermo-electrical and mechanical studies, a lot of information had been gathered that improved the knowledge on *OMON* and *polymer-OMON* composites. This research work also provided the opportunity to develop useful skills in instrumentation and experimental method. Physical set-up in the TSC system gives an advantage to diversify the studies on direct current DC (*I*), DC voltage (*V*), temperature (*T*) as well as the time (*t*) dependency of materials. Similarly as in case of TSC measurement, *Conductivity* that a computer program was developed to carry out the conductivity tests. This program can be used to perform the DC current *I* versus voltage *V* at temperature *T*, DC current *I* versus temperature *T* with voltage V and DC current *I* versus time *t* with voltage *V* at temperature *T*. The conductivity test of DC current *I* versus voltage *V* with variable temperature *T* and *OMON* content were done on *polymer-OMON* composites. The tests results however are not discussed in this thesis. Likewise, the generated results from thermo-mechanical study on these composites, where tensile tests were performed with variable temperature *T* will be discussed elsewhere.

This research work may not answer all the questions about nanoclay composites however, it adds a lot more information that can improve the understanding on these materials. From observations and analyses in this work, several directions were highlighted to further study this type of composite. The improved knowledge on structures and mechanisms involves in structural changes will be useful to expand the study on polymer nanocomposites, as well as their utility in various applications.

Appendix A

The Clay mineral Society

http://www.clays.org/SOURCE%20CLAYS/SCdata.html

SOURCE CLAY PHYSICAL/CHEMICAL DATA

Na-Montmorillonite (Wyoming) SWy-1(SWy-2)

ORIGIN:

Newcastle formation, (cretaceous)

County of Crook, State of Wyoming, USA

LOCATION:

NE 1/4 SE 1/4 Sec.18, T 57 N, R 65 W; 8, Topographic map: Seeley (15'), The upper 63 of recently stripped area was removed to expose clean,green upper Newcastle, Collected from which samples was taken, October 3,1972.

CHEMICAL COMPOSITION (%):

SiO2: 62.9, Al2O3: 19.6, TiO2: 0.090, Fe2O3:3.35, FeO: 0.32, MnO: 0.006, MgO: 3.05, CaO: 1.68, Na2O: 1.53, K2O: 0.53,F: 0.111, P2O5: 0.049, S: 0.05, Loss on heating: -550oC: 1.59; 550-1000oC:4.47, CO2: 1.33.

CATION EXCHANGE CAPACITY (CEC):

76.4 meq/100g, principal exchange cations Na and Ca.

SURFACE AREA:

N2 area: 31.82 +/- 0.22 m2/g

THERMAL ANALYSIS: DTA: endotherms at 185oC (shoulder at 235oC), desorptionof water: 755oC, dehydroxylation; shoulder at 810oC, exotherms at 980oC. TG: Loss in dehydroxylation range: 5.53% (theory: 5%).

INFRARED SPECTROSCOPY:

Typical spectrum for Wyoming bentonite with a moderateFe+3 content (band at 885 cm-1). Quartz is detectable (band at 780, 800,698, 400, and 373 cm-1), a trace of carbonate (band at 1425 cm-1).

STRUCTURE:

(Ca.12 Na.32 K.05)[Al3.01 Fe(III).41 Mn.01 Mg.54Ti.02][Si7.98 Al.02]O20(OH)4,Octahedral charge:-.53, Tetrahedral charge:-.02,Interlayer charge:-.55, Unbalanced charge:.05,

Appendix B

Lake Shore Model 330 Autotuning Temperature Controller Specifications

Lake Shore Model 330 Autotuning Temperature Controller User's Manual

Table 1-2. Model 330 Specifications

Thermometry:	
Number of Inputs:	Two
Sensor Types:	Model 330-1X – Silicon Diode
(Sensors Sold Separately)	Model 330-2X – Platinum RTD
	Model 330-3X – GaAlAs Diode
	Model 330-4X – Thermocouple
Accuracy:	Based on Model and Sensor Type (Refer to Table 1-1)
Update Rate:	Both Channels in 1 second
Precision Curve Storage:	Room for twenty 31-point Curves *
Standard Response Curves:	
DT-400 Series Silicon Diodes	Curve 10
DT-500 Series Silicon Diodes	DRC-D or DRC-E1 *(Obsolete)*
PT-100 Series Platinum RTDs	DIN 43760
Thermocouples	Ch-AuFe (0.07%), Ch-AuFe (0.03%), Type E (Chromel-Constantan), Type K (Chromel-Alumel), and Type T (Copper-Constantan)
SoftCal:	Entered in Voltage or Temperature *
Control:	
Control Type:	Digital, three term PID with Autotuning
Automatic Control Mode:	P, PI, or PID control, user selectable
Manual Control Mode:	Gain (Proportional) 1-999, Reset (Integral) 1-999 sec., and Rate (Derivative) 0 - 200% (0-500 sec.)
Control Stability:	To ±2.5 mK in a properly designed system for diode sensors (Refer to Table 1.1)
Setpoint Resolution:	0.01 K or °C below 200, least significant display digit in sensor units
Control Sensor Selection:	Front Panel
Ramp Rate:	0.1 to 99.9 K/min
Zones:	10 Zones with Setpoint, P, I, D, and Heater Range *
Heater Output Type:	Variable DC Current Source
Heater Setting Resolution:	15 bits
Max. Power To Heater:	50 Watts / 25 Watts (Field Configurable)
Heater Current by Range:	High (1 A), Medium (0.3 A), and Low (0.1 A)
Heater Output Compliance:	50 V (50 W) or 25 V (25 W)
Heater Load for Full Power:	50 Ω (50 W) or 25 Ω (25 W)
Minimum Heater Load:	35 Ω (50 W) or 10 Ω (25 W)
Heater Noise:	50 µV + 0.01% of output voltage (with Optional Model 3003 Heater Output Conditioner, heater noise is lowered by 20 dB)
Front Panel:	
Display:	Two, 4.5 digit LED
Display Units:	Temperature in K or °C. Sensor units in volts (330-1X & -3X), ohms (330-2X), or millivolts (330-4X)
Setpoint display:	Shared with control sensor
Heater output display:	20 digit LED bar graph, percent of full scale current for range
Annunciators:	Channel, units, heater range, interface mode
Temperature resolution:	0.01 below 200, 0.1 above
Sensor units resolution:	Refer to Table 1-1
Keypad:	Numeric plus special function
Computer Interfaces:	
IEEE-488 Capabilities:	Complies with IEEE-488.2 SH1,AH1,T5,L4,SR1,RL1,PP0,DC1, DT0,C0,E1
Serial Interface:	300 or 1200 baud, RJ-11 connector (RS-232C electrical standard)
General:	
Ambient Temperature Range:	20 to 30 °C (68 °F to 86 °F), or with reduced accuracy in range 15 °C to 35 °C (59 °F to 95 °F)
Power Requirements:	110, 120, 220, 240 VAC (+5%-10%), 50 or 60 Hz; 135 Watts
Size:	217 mm x 90 mm x 419 mm (8.5" x 3.5" x 16.5"), half-rack package
Weight:	5 kilograms (11 pounds)

* User-configurable with IEEE-488 or Serial Interface only.)

Lake Shore Cryotronics, "User's Manual Model 330 Autotuning Temperature Controller", *Lake Shore Cryotronics, Inc*., Westerville, Ohio, USA, (1994)

Appendix B

Lake Shore Model 330 Autotuning Temperature Controller Specifications

Electronic Information for Various Sensors and Temperature Ranges

Suffix	1	2	3	4 *
Sensor Type	Silicon Diode	100Ω Platinum RTD	GaAlAs Diode	Thermocouple
Sensor Temperature Coefficient	Negative	Positive	Negative	Positive
Sensor Units	Volts (V)	Ohms (Ω)	Volts (V)	Millivolts (mV)
Input Range	0–2.5 V	0–300 Ω	0–6 V	±15 mV
Sensor Excitation	10 µA ±0.1% constant current	1 mA ±0.01% constant current	10 µA ±0.1% constant current	N/A
The following specifications reflect operational characteristics with the specified Lake Shore Sensor.				
Example Lake Shore Sensor	DT-470-C0 with 1.4HS calibration	PT-103 with 1.4L calibration	TG-120P with 14J calibration	Ch-AuFe 0.07%
Sensor Temp. Range	1.4–475 K	30–800 K	1.4–325 K	1.4–325 K
Standard Sensor Curve	LSCI Curve 10	DIN 43760	Needs Calibration and 8001 Precision Option	NBS/NIST generated
Typical Sensor Sensitivity	–30 mV/K at 4.2 K –1.9 mV/K at 77 K –2.4 mV/K at 300 K –2.2 mV/K at 475 K	0.19 Ω /K at 30 K 0.42 Ω /K at 77 K 0.39 Ω /K at 300 K 0.33 Ω /K at 800 K	–180 mV/K at 4.2 K –1.25 mV/K at 77 K –2.75 mV/K at 300 K	16 µV/K at 4.2 K 20 µV/K at 300 K
Measurement Resolution:				
Sensor Units	0.04 mV	5 m Ω	0.09 mV	0.45 µV
Temperature Equivalence	1.3 mK at 4.2 K 21 mK at 77 K 16 mK at 300 K 18 mK at 475 K	26 mK at 30 K 12 mK at 77 K 13 mK at 300 K 15 mK at 800 K	0.5 mK at 4.2 K 72 mK at 77 K 32 mK at 300 K	30 mK at 4.2 K 22 mK at 300 K
Sensor Units Display Resolution	0.1 mV to 1 mV	0.01 Ω to 0.1 Ω	0.1 mV to 1 mV	1 µV
Measurement Accuracy	±125 µV ±0.015% RDG	±12 m Ω ±0.04% RDG	±200 µV ±0.035%	±1.5 µV + 0.1% RDG
Temperature Accuracy with Calibrated Sensor and 8001 Precision Option	±50 mK at 4.2 K ±120 mK at 77 K	±45 mK at 30K ±62 mK at 77K ±80 mK at 300 K ±75 mK at 475 K	±40 mK at 4.2 K ±350 mK at 77 K ±105 mK at 300K ±235 mK at 800K	±406 mK at 4.2K † ±110 mK at 300K ±150 mK at 300 K
Measurement Temperature Coefficient Sensor Units (%RDG/°C Ambient)	±0.002%	±0.004%	±0.006%	±0.01%
Control Stability:	±2.5 mK at 4.2 K ±25 mK at 77 K ±25 mK at 300 K	±15 mK at 30 K ±15 mK at 77 K ±15 mK at 300 K ±25 mK at 800 K	±5 mK at 4.2 K ±50 mK at 77 K ±50 mK at 300 K	±40 mK at 4.2 K ±40 mK at 300 K

* Thermocouple data is for uncompensated inputs.
† Sensor calibration and 8001 Precision Option are not available for thermocouples. The error listed is for the instrument only.

Lake Shore Cryotronics, "User's Manual Model 330 Autotuning Temperature Controller", *Lake Shore Cryotronics, Inc*., Westerville, Ohio, USA, (1994)

Appendix C

Keithley Electrometer / High Resistance meter Model 6517 Specifications

VOLTS

RANGE	5½-DIGIT RESOLUTION	ACCURACY (1 Year)[1] 18°–28°C ±(%rdg+counts)	TEMPERATURE COEFFICIENT 0°–18°C & 28°–50°C ±(%rdg+counts)/°C
2 V	10 µV	0.025 + 4	0.003 + 2
20 V	100 µV	0.025 + 3	0.002 + 1
200 V	1 mV	0.05 + 3	0.002 + 1

[1] When properly zeroed, 5½-digit, 1 PLC (power line cycle), median filter on, digital filter = 10 readings.

NMRR: 60dB on 2V, 20V, >55dB on 200V, at 50Hz or 60Hz ±0.1%.

CMRR: >120dB at DC, 50Hz or 60Hz.

INPUT IMPEDANCE: >200TΩ in parallel with 20pF, < 2pF guarded (10MΩ with zero check on).

SMALL SIGNAL BANDWIDTH AT PREAMP OUTPUT: Typically 100kHz (–3dB).

AMPS

RANGE	5½-DIGIT RESOLUTION	ACCURACY (1 Year)[1] 18°–28°C ±(%rdg+counts)	TEMPERATURE COEFFICIENT 0°–18°C & 28°–50°C ±(%rdg+counts)/°C
20 pA	100 aA[2]	1 + 30	0.1 + 5
200 pA	1 fA[2]	1 + 5	0.1 + 1
2 nA	10 fA	0.2 + 30	0.1 + 2
20 nA	100 fA	0.2 + 5	0.03 + 1
200 nA	1 pA	0.2 + 5	0.03 + 1
2 µA	10 pA	0.1 + 10	0.005 + 2
20 µA	100 pA	0.1 + 5	0.005 + 1
200 µA	1 nA	0.1 + 5	0.005 + 1
2 mA	10 nA	0.1 + 10	0.008 + 2
20 mA	100 nA	0.1 + 5	0.008 + 1

[1] When properly zeroed, 5½-digit, 1 PLC (power line cycle), median filter on, digital filter = 10 readings.

[2] aA =10–18A, fA=10–15A.

INPUT BIAS CURRENT: <3fA at T_{CAL}. Temperature coefficient = 0.5fA/°C.

INPUT BIAS CURRENT NOISE: <750aA p-p (capped input), 0.1Hz to 10Hz bandwidth, damping on. Digital filter = 40 readings.

INPUT VOLTAGE BURDEN at T_{CAL} ±1°C: <20µV on 20pA, 2nA, 20nA, 2µA, 20µA ranges. <100µV on 200pA, 200nA, 200µA ranges. <2mV on 2mA range. <4mV on 20mA range.

TEMPERATURE COEFFICIENT OF INPUT VOLTAGE BURDEN: <10µV/°C on pA, nA, µA ranges.

PREAMP SETTLING TIME (to 10% of final value): 2.5s typical on pA ranges, damping off, 4s typical on pA ranges damping on, 15ms on nA ranges, 2ms on µA and mA ranges.

NMRR: >95dB on pA, 60dB on nA, µA, and mA ranges at 50Hz or 60Hz ±0.1%.

COULOMBS

RANGE	5½-DIGIT RESOLUTION	ACCURACY (1 Year)[1,2] 18°–28°C ±(%rdg+counts)	TEMPERATURE COEFFICIENT 0°–18°C & 28°–50°C ±(%rdg+counts)/°C
2 nC	10 fC	0.4 + 5	0.04 + 3
20 nC	100 fC	0.4 + 5	0.04 + 1
200 nC	1 pC	0.4 + 5	0.04 + 1
2 µC	10 pC	0.4 + 5	0.04 + 1

[1] Specifications apply immediately after charge acquisition. Add

$$\left(4fA + \frac{|Q_{AV}|}{RC}\right) T_x$$

where T_x = period of time in seconds between the coulombs zero and measurement, Q_{AV} = average charge measured over T_x, and RC = 300,000 typical.

[2] When properly zeroed, 5½-digit, 1 PLC (power line cycle), median filter on, digital filter = 10 readings.

INPUT BIAS CURRENT: <4fA at T_{CAL}. Temperature coefficient = 0.5fA/°C.

OHMS (Normal Method)

RANGE	5½-DIGIT RESOLUTION	ACCURACY[1] (10–100% Range) 18°–28°C (1 Yr.) ±(% rdg+counts)	TEMPERATURE COEFFICIENT (10–100% Range) 0°–18°C & 28°–50°C ±(% rdg+counts)	AUTO V SOURCE	AMPS RANGE
2 MΩ	10 Ω	0.125+1	0.01 + 1	40 V	200 µA
20 MΩ	100 Ω	0.125+1	0.01 + 1	40 V	20 µA
200 MΩ	1 kΩ	0.15 + 1	0.015 + 1	40 V	2 µA
2 GΩ	10 kΩ	0.225+1	0.035 + 1	40 V	200 nA
20 GΩ	100 kΩ	0.225+1	0.035 + 1	40 V	20 nA
200 GΩ	1 MΩ	0.35 + 1	0.110 + 1	40 V	2 nA
2 TΩ	10 MΩ	0.35 + 1	0.110 + 1	400 V	2 nA
20 TΩ	100 MΩ	1.025+1	0.105 + 1	400 V	200 pA
200 TΩ	1 GΩ	1.15 + 1	0.125 + 1	400 V	20 pA

[1] Specifications are for auto V-source ohms, when properly zeroed, 5½-digit, 1 PLC, median filter on, digital filter = 10 readings. If user selectable voltage is required, use manual mode. Manual mode displays resistance (up to $10^{18}\Omega$) calculated from measured current. Accuracy is equal to accuracy of V-source plus accuracy of selected Amps range.

PREAMP SETTLING TIME: Add voltage source settling time to preamp settling time in Amps specification.

OHMS (Alternating Polarity Method)

The alternating polarity sequence compensates for the background (offset) currents of the material or device under test. Maximum tolerable offset up to full scale of the current range used.

Using Keithley 8002A or 8009 fixture

REPEATABILITY: $\Delta I_{BC} \times R / V_{ALT}$ + 0.1% (1σ) (instrument temperature constant ±1°C).

ACCURACY: $(V_{SRC}Err + I_{MAV}Err \times R)/V_{ALT}$

where: ΔI_{BC} is a measured, typical background current noise from the sample and fixture.

V_{ALT} is the alternating polarity voltage used.

$V_{SRC}Err$ is the accuracy (in volts) of the voltage source using V_{ALT} as the setting.

$I_{MAV}Err$ is the accuracy (in amps) of the ammeter using V_{ALT}/R as the rdg.

VOLTAGE SOURCE

RANGE	5½-DIGIT RESOLUTION	ACCURACY (1 Year) 18°–28°C ±(% setting + offset)	TEMPERATURE COEFFICIENT 0°–18°C & 28°–50°C ±(% setting+offset)/°C
100 V	5 mV	0.15 + 10 mV	0.005 + 1 mV
1000 V	50 mV	0.15 +100 mV	0.005 +10 mV

MAXIMUM OUTPUT CURRENT:
±10mA; active current limit at <11.5mA for 100V range.
±1mA; active current limit at <1.15mA for 1000V range.

SETTLING TIME: <8ms to rated accuracy for 100V range.
<50ms to rated accuracy for 1000V range.

NOISE: <150µV p-p from 0.1Hz to 10Hz for 100V range.
<1.5mV p-p from 0.1Hz to 10Hz for 1000V range.

Keithley Test Instrumentation Group, “Model 651 7 Electrometer User’s Manual”, *Keithley Instruments Inc.*, Cleveland, Ohio, U.S.A. (1995)

Appendix D

Keithley High Density Switch System Model 7001 Specifications

SYSTEM

CAPACITY: 2 plug-in cards per mainframe.

MEMORY: Battery backed-up storage for 100 switch patterns.

SWITCH SETTLING TIME: Automatically selected by the mainframe for each card. Additional time from 0 to 99999.999 seconds can be added in 1ms increments.

TRIGGER SOURCES:

External Trigger (TTL-compatible, programmable edge, 600ns minimum pulse, rear panel BNC).

IEEE-488 bus (GET, *TRG)

Trigger Link

Manual (front panel)

Internal Timer, programmable from 1ms to 99999.999 seconds in 1ms increments.

STATUS OUTPUT: Channel Ready (TTL-compatible signal, rear panel BNC). Low going pulse (10µs typical) issued after relay settling time. For two different switch cards, 7001 will be set to the slowest relay settling time.

SWITCHING SEQUENCE: Automatic break-before-make.

MAINFRAME DIGITAL I/O: 4 open-collector outputs (30V maximum pull up voltage, 100mA maximum sink current, 10Ω output impedance), 1 TTL compatible input, 1 common.

RELAY DRIVE: 700mA maximum for both card slots.

CARD SIZE: 32mm high × 114mm wide × 272mm long (1¼ in × 4½ in × 10¾ in).

CARD COMPATIBILITY: Fully compatible with all 7XXX cards.

THROUGHPUT

EXECUTION SPEED OF SCAN LIST[1]

	7011 Card	7015 Card
Individual channels:	130/second	500/second
Memory setups:	125/second	450/second

TRIGGER EXECUTION TIME (maximum time from activation of Trigger Source to start of switch open or close[2]**):**

SOURCE	LATENCY	JITTER
GET[3]	200 µs	<50 µs
*TRG[3]	5.0 ms	
Trigger Link	200 µs	<13 µs
External	200 µs	<13 µs

1 Rates include switch settling time of cards: 3ms for 7011 and 500µs for 7015 cards.

2 Excluding switch settling time.

3 Assuming no IEEE-488 commands are pending execution.

IEEE-488 COMMAND EXECUTION TIME

	EXECUTION TIME[1]	
COMMAND	DISPLAY OFF	DISPLAY ON
OPEN (@1!1)	7.5 ms	8.5 ms
CLOS (@1!1)	7.5 ms	8.5 ms
MEM:REC M1	5.0 ms	6.0 ms

1 Measured from the time at which the command terminator is taken from the bus to the time at which the relay begins to open or close.

ANALOG BACKPLANE

SIGNALS: Four 3-pole rows (Hi, Lo, Guard). These signals provide matrix and multiplexer expansion between cards within one mainframe.

MAXIMUM VOLTAGE: 250V DC, 250V RMS, 350V AC peak, signal path to signal path or signal path to chassis.

MAXIMUM CURRENT: 1A peak.

PATH ISOLATION:

$>10^{10}\Omega$, <50pF path to path (any Hi, Lo, Guard to another Hi, Lo, Guard).

$>10^{10}\Omega$, <50pF differential (Hi to Lo or Hi, Lo to Guard).

$>10^{9}\Omega$, <75pF path to chassis.

CHANNEL CROSSTALK: <–65dB @ 1MHz (50Ω load).

BANDWIDTH: <3dB loss at 100MHz (50Ω load).

IEEE-488 BUS IMPLEMENTATION

STANDARDS CONFORMANCE: Conforms to SCPI-1990, IEEE-488.2 and IEEE-488.1.

MULTILINE COMMANDS: DCL, LLO, SDC, GET, GTL, UNT, UNL, SPE, SPD.

UNILINE COMMANDS: IFC, REN, EOI, SRQ, ATN.

INTERFACE FUNCTIONS: SH1, AH1,T5, TE0, L4, LE0, SR1, RL1, PP0, DC1, DT1, C0, E1.

GENERAL

DISPLAY: Dual-line vacuum fluorescent.

1st line: 20-character alphanumeric.

2nd line: 32-character alphanumeric.

REAR PANEL CONNECTORS:

IEEE-488

8-pin micro DIN connector for digital I/O

8-pin micro DIN for Trigger Link

8-pin micro DIN for Trigger Link expansion

BNC for External Trigger

BNC for Channel Ready

POWER: 100V to 240V RMS , 50/60 Hz, 50VA maximum.

EMC: Complies with to European Union Directive 89/336/EEC, EN61326-1.

SAFETY: Conforms to European Union Directive 73/23/EEC, EN61010-1.

EMI/RFI: Meets VDE 0871B and FCC Class B.

ENVIRONMENT:

Operating: 0°–50°C, <80% relative humidity (0°–35°C).

Storage: –25° to +65°C.

DIMENSIONS, WEIGHT: 89mm high × 216mm wide × 375mm deep (3½ in × 8½ in × 14¾ in). Net weight 3.4kg (7½ lbs).

Specifications subject to change without notice.

Keithley Test Instrumentation Group, “Model 7001 Switch System Quick Reference Guide”, *Keithley Instruments Inc.*, Cleveland, Ohio, U.S.A. (1992)

Appendix E

Tensile Analysis Program

Front Panel

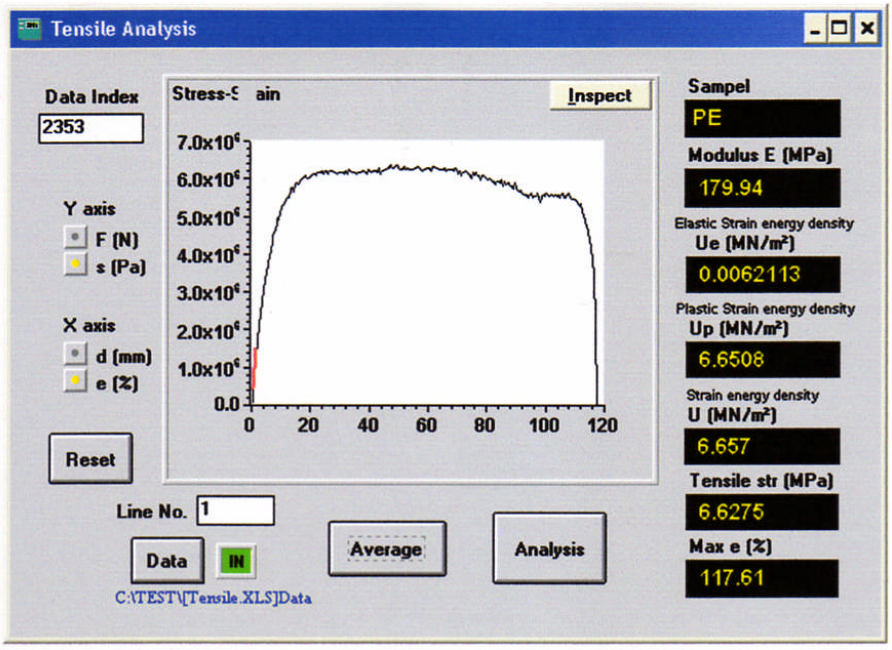

Analysis Panel

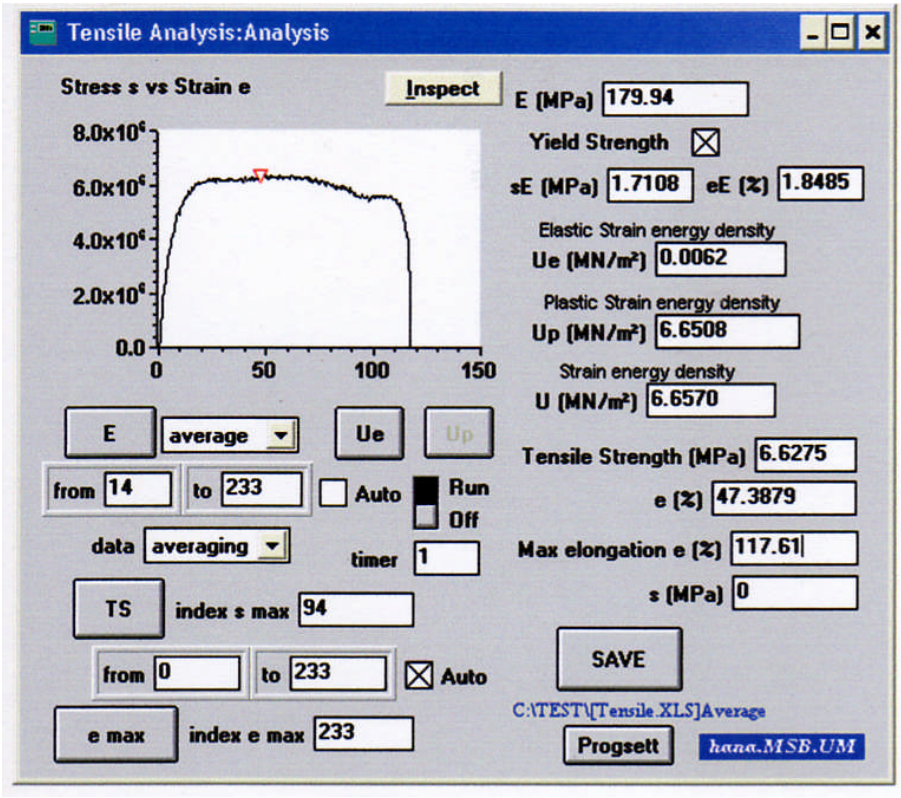

Tensile Analysis is a computer program that was developed for the purpose of data analyzing on tensile test data.

Appendix F

Kinetic Equations

The relation gives the thermoluminescence (TL) intensity for glow peaks of a first order-kinetic equation

$$I(T) = f_o n_o \exp\left(-\frac{E}{kT}\right)\exp\left[-\frac{f_o}{h}\int_{T_o}^{T}\exp\left(-\frac{E}{kT'}\right)dT'\right] \quad \ldots \text{(AF1)}$$

Where I = glow-peak intensity (current peak in TSC)

f_o = frequency factor (s^{-1})

n_o = the initial concentration of trapped carriers

k = Boltzman constant (eV K^{-1})

T = absolute temperature (K^{-1})

T_o = initial temperature (K)

h = heating rate (Ks^{-1})

For numerical calculation of the TL intensity (or TSC current) the integral part needs to be evaluated

$$F(T,E) = \int_{T_o}^{T}\exp\left(-\frac{E}{kT'}\right)dT' \quad \ldots \text{(AF2)}$$

According to Kitis [6.14], successive integrations by parts give

$$F(T,E) = T\exp\left(-\frac{E}{kT}\right)\sum_{n=1}^{\infty}\left(\frac{kT}{E}\right)^{n}(-1)^{n}\,n\,!.. \quad \ldots \text{(AF3)}$$

For limited number of terms (N), equation AF3 becomes

$$F(T,E) = T\exp\left(-\frac{E}{kT}\right)\left[\sum_{n=1}^{\infty}\left(\frac{kT}{E}\right)^{n}(-1)^{n}n! \;+\; \frac{1}{2}\left(\frac{kT}{E}\right)^{N+1}(-1)^{N}(N+1)!\right] \quad \ldots \text{(AF4)}$$

The second term is a correction factor and is taken into account because of the errors introduced from the limited number of terms. In most practical cases however, only the

first term of equation AF4 is taken into account. Where, in a second-order approximation it gives

$$F(T,E) = \frac{kT^2}{E}\exp\left(-\frac{E}{kT}\right)\left(1-\frac{2kT}{E}\right) \quad \ldots \text{(AF5)}$$

Using the approximation AF5 into equation AF1, it follows that

$$I(T) = f_o n_o \exp\left(-\frac{E}{kT}\right)\exp\left[-\frac{f_o kT^2}{hE}\times\exp\left(-\frac{E}{kT}\right)\left(1-\frac{2kT}{E}\right)\right] \quad \ldots \text{(AF6)}$$

By equating the derivative of equation AF1 to zero, the condition for maximum peak is found to be

$$\frac{hE}{kT_{\max}^2} = f_o \exp\left(-\frac{E}{kT_{\max}}\right) \quad \ldots \text{(AF7)}$$

or

$$f_o = \frac{hE}{kT_{\max}^2}\exp\left(\frac{E}{kT_{\max}}\right) \quad \ldots \text{(AF8)}$$

Substitution frequency factor f_o in equation AF6 with equation AF8 will give

$$I(T) = n_o \frac{hE}{kT_{\max}^2}\exp\left[\frac{E}{kT}\left(\frac{T-T_{\max}}{T_{\max}}\right)\right]\times\exp\left\{-\frac{T^2}{T_{\max}^2}\exp\left[\frac{E}{kT}\left(\frac{T-T_{\max}}{T_{\max}}\right)\right](1-\Delta)\right\} \quad \ldots \text{(AF9)}$$

where $\Delta = 2kT/E$

By inserting equation AF7 into equation AF6, TSC current I_m at the peak maximum is given by

$$I_{\max} = n_o \frac{hE}{kT_{\max}^2}\exp\left[-(1-\Delta_{\max})\right] \quad \ldots \text{(AF10)}$$

Where $\Delta_{\max} = 2kT_{\max}/E$. From equation AF10, it follows that

$$n_o \frac{hE}{kT_{\max}^2} = I_{\max}\exp(1-\Delta_{\max}) \quad \ldots \text{(AF11)}$$

By inserting equation AF11 into equation AF9, TSC current *I (T)* becomes

$$I(T) = I_{\max}\ \exp(1-\Delta_{\max})\exp\left\{\frac{E}{kT}\left(\frac{T-T_{\max}}{T_{\max}}\right)\times\exp\left\{-\frac{T^2}{T_{\max}^2}\exp\left[\frac{E}{kT}\left(\frac{T-T_{\max}}{T_{\max}}\right)\right]\right\}(1-\Delta)\right\}..$$

… (AF12)

Rearrangement of equation AF12 gives the final function for peak decomposition analysis

$$I(T) = I_{\max}\ \exp\left[1+\frac{E}{kT}\left(\frac{T-T_{\max}}{T_{\max}}\right)-\frac{T^2}{T_{\max}^2}\times\exp\left(\frac{E}{kT}\frac{T-T_{\max}}{T_{\max}}\right)(1-\Delta)-\Delta_{\max}\right] \quad \text{... (AF13)}$$

Appendix G

Conversion from clay weight fraction, W_c to particle volume fraction f_p

Clay content within composites typically is provided in weight fraction, W_c. Therefore, it is necessary to establish a quantitative connection between W_c and the volume fraction, f_p of "effective particle" t_{eff} which is a very important parameter in micromechanical model.

$$t_{eff} = (N-1)d_{001} + t_{sheet} \quad \text{... (AG1)}$$

where t_{eff} = effective thickness

N = number of platelets per stacked clay

d_{001} = basal spacing

t_{sheet} = silica sheet thickness

According to Sheng [7.17], volume fraction of silicate within the effective particle can be expressed as follow

$$\chi = \frac{V_{silicate}}{V_p} = \frac{Nt_{sheet}}{(N-1)d_{001} + t_{sheet}} \quad \text{... (AG2)}$$

where the number of silicate sheet per unit particle thickness

$$\chi_N = \frac{N}{t_{eff}} = \frac{N}{(N-1)d_{001} + t_{sheet}} \quad \text{... (AG3)}$$

The particle volume fraction f_p and particle weight fraction W_c are related according to

$$f_p = \frac{W_p/\rho_p}{W_p/\rho_p + (1-W_p)/\rho_m} \quad \text{... (AG4)}$$

where ρ_p and ρ_m are the mass densities of particles and matrix in composites.

In case of intercalated nanocomposites, W_c differs from typical particle weight fraction W_p. Since particles in such composites consists of both silicate sheets and interlayer galleries. The two quantities are relate through

$$\frac{W_p}{W_c} = \frac{\rho_p V_p}{\rho_{silicate} V_{silicate}} = \left(\frac{\rho_p}{\rho_{silicate}}\right) \Big/ \left(\frac{V_{silicate}}{V_p}\right)$$

$$= \frac{\rho_p}{\rho_{silicate}} \frac{1}{\chi} \equiv \alpha \qquad \text{... (AG5)}$$

Where $\rho_{silicate}$ is the mass density of silicate sheet and the ration W_p/W_c is defined as α. Taking $W_p = \alpha\, W_c$ into equation AG4, the volume fraction becomes

$$f_p = \frac{W_c \rho_p}{W_c/\rho_p + (1/\alpha - W_c)/\rho_m} \qquad \text{... (AG6)}$$

When Wc is small as it frequently found in case of nanocomposites, equation AG6 can be linearized as

$$f_p \approx \left(\frac{\alpha \rho_m}{\rho_p}\right) W_c = \left(\frac{\rho_m}{\rho_p} \bullet \frac{\rho_p}{\rho_{silicate}} \bullet \frac{1}{\chi}\right) W_c$$

$$= \left(\frac{\rho_m}{\rho_{silicate}} \bullet \frac{1}{\chi}\right) W_c \qquad \text{... (AG7)}$$

The density $\rho_{silicate}$ can be calculated from *Mon* lattice parameter given by Manevitch and Rutledge [7.18],

$$\rho_{silicate} = \rho_{lattice} = \frac{M_o}{A_o t_{sheet}} = \left(\frac{2.44}{t_{sheet}}\right) \text{ nm g/cm}^3 \qquad \text{... (AG8)}$$

where M_o = molecular weight = 720 g/mol

A_o = planar area = 0.49 nm^2

t_{sheet} = sheet thickness = 0.615 nm

If ρ_m = 1.0 g/cm^3 and taking equation AG8 into equation AG7, it will give the volume fraction

$$f_p = 0.41 t_{sheet} \frac{W_c}{\chi} = \left(\frac{0.41}{\chi_N} W_c\right) \text{nm}^{-1} \qquad \text{... (AG9)}$$